Segregation of late magmatic melt in mushes : experimental approach at high pressure

Monica Spagnoli

UNIVERSITÉ D'ORLÉANS

ÉCOLE DOCTORALE

ENERGIE, MATERIAUX, SCIENCES DE L'UNIVERS

Institut des Sciences de la Terre d'Orléans

THÈSE présentée par :

Monica SPAGNOLI

soutenue le : **15 octobre 2024**

pour obtenir le grade de : **Docteur de l'Université d'Orléans**

Discipline/ Spécialité : Sciences de l'Univers

Segregation of late magmatic melt in mushes: experimental approach at high pressure

THÈSE dirigée par :

M. Laurent ARBARET	Maître de conférence (HDR), Université d'Orléans

RAPPORTEURS :

M. Olivier BACHMANN	Professeur des universités, ETH Zürich
Mme Marian HOLNESS	Professeure des universités, University of Cambridge

---

JURY :

Mme Caroline MARTEL	Directrice de recherche, Université d'Orléans, Président du jury
M. Alain BURGISSER	Chargé de recherche, Université Savoie Mont Blanc
M. Luca CARICCHI	Professeur des universités, University of Geneva
M. Lyderic FRANCE	Maître de conférences, Université de Lorraine

Acknowledgements

Here I am at the end of this amazing journey. A PhD is not only a cultural enrichment, but a life experience that will stay with you forever. I have been lucky enough to work with and meet extremely knowledgeable people from all over the world. Each of them has given me so much, both academically and culturally.

I would like to thank my supervisor, Laurent Arbaret, for teaching me so much and for always being supportive.

I would also like to thank all the members of the jury, thanks to Olivier Bachmann and Marion Holness for revising my entire thesis, and thanks to Caroline Martel, Luca Caricchi, Alain Burgisser and Lyderic France for participating as members of the jury. Although we only spent a short time together, your opinions and advice were extremely helpful to me.

Thanks to the whole team that participated in my thesis. Thanks to the infinite patience of Remi Champallier for all the experiments we did together. Thanks to Jacques Precigout for all the EBSD analyses and to Aneta Slodczyk for the Raman analyzes and all her advice.

I have to thank all the researchers and staff at Isto who have always helped me. Thanks to Ida di Carlo and Patricia for all the analyses at the EPMA and the therapy sessions with Ida that we all enjoyed as students. Thanks to Giada Iacono-Marziano, Fabrice Gaillard, Juan Andújar and Bruno Scaillet for their support and help.

Thanks to my fellow travellers and colleagues, and future world-class researchers, Elena Nunez and Federica Faranda. I could not have imagined better friends by my side during these four years that have flown by thanks to you.

Thank you to all the other PhD students and postdocs who have been with me during these years. Thank you, Viktor, for being who you are, thank you, Carolina, it was short but intense, thank you Diletta, Alessandra, Hector, Khadija, Gina, Bence, Walid and all those I met, even if briefly. Each of you has left me something that I will always carry in my heart.

Thanks also to the people I met in Orléans and with whom we shared happy evenings.

Thanks to my family, my sister and my friends in Rome, who have always supported me from afar.

Last but not least, I would like to thank Claudio, my faithful life partner, who has always helped me and believed in me. Without you, I would not have been able to achieve this goal.

INDEX

Introduction

Volcanoes are geological structures found all over the world and by definition they are natural openings in the Earth's crust through which magma rises to the surface to forming lava, pyroclastic eruptions and gaseous emissions. Up to recent times, the magma was believed to reside only in magmatic chamber, but the scientific research has pushed its limits acquiring great geophysical and geochemical knowledge postulating new hypotheses for magma emplacement in the crust and mantle, where the magma is is found with a high crystal content. This physical state characterises the new concept of the magmatic body and defines it as a mush. A mush is described as a magmatic body dominated by crystals and containing a variable percentage of silicate fluid (Delph et al., 2017; Ward et al., 2014). The trans-crustal magmatic system (TCMS) model (Allan et al., 2013; Cashman et al., 2017; Holness, 2018) predicts the existence of a series of high-viscosity, interconnected mushes at different depths within the Earth's crust. Melt can be extracted from a mush to the surface through process of segregation, migration and extraction until it reaches the point of eruption. In both volcanic mush and magmatic chambers, a multitude of processes lead to a volcanic eruption. These include changes in temperature, pressure, mineralogical phases, and deformation processes. Recent studies have investigated the dynamics of magma ascent from a mush (Bachmann and Bergantz, 2004; Dufek and Bachmann, 2010; Jackson et al., 2018; Keller et al., 2013; Kohlstedt and Holtzman, 2009; Parmigiani et al., 2011; Phipps Morgan and Holtzman, 2005). However, experimental studies of the ascent of magmas undergoing deformation have not been able to fully clarify the mechanisms that dominate these processes. The study of deformation structures is essential for understanding the dynamics of magma transfer. Magma deformation can result in melt transfer through compaction or shear. Magma can move through porous flow, where the dominant parameter is porosity (Dufek and Bachmann, 2010), or through melt channel formation by shear localization (Katz et al., 2006). This type of deformation is a common occurrence in highly dynamic magmatic systems, such as those with high differential stress along the hanging walls of necks and dykes(Paterson et al., 1998; Smith, 1997), or within convective cells of magmatic chambers.

The objective of this thesis is to investigate the dynamics of melt migration subjected to shearing and to examine the deformation structures formed following deformation.

Torsion deformation experiments were conducted on synthetic samples with a haplotonalitic composition and a crystal content σ_s ranging from 0.52 to 0.95. Temperature and pressure conditions have been chosen to simulate the natural conditions of a magmatic mush (790°C - 810°C and 300 MPa). The strain rate $\dot{\gamma}$ ranged from $5.0*10^{-5}$ s^{-1} to $2.1*10^{-3}$ s^{-1}, which correspond to the deformation rates that commonly occur in volcanic environments (Chadwick Jr et al., 1988; Spera et al., 1988) while the finite strain γ ranged from 0.5 to 10. The crystal content from 0.52 to 0.95 was choosen because at these values the magmatic mush is formed by an interconnected network of crystals capable of spreading deformation occurs. The starting material is formed by only plagioclase crystals (excluding one experiment that shows quartz also) because their elongated shape makes them an ideal choice for studying the SPO (shape preferred orientation) and CPO (crystals preferred orientation).

Previous studies have experimentally investigated the structural and rheological relationships that occur when magmatic bodies are subjected to deformation (both shearing and compression) with crystal content between 0.1 and 0.5. However, experimental studies with high crystal content, starting from 0.5, are limited and do not provide clear insights into the dynamics of deformation, microstructure formation, and melt extraction phenomena. This study examines the deformational structures that appear at high crystal contents after torsion experiments, with the aspect ratio R of the crystals serving as a key value. The work of (Picard et al., 2011) demonstrates that synthetic mushes formed by plagioclases with an aspect ratio R = 4 subjected to shearing and with a crystal content between 0.40 and 0.58 show strong deformation structures, such as shear bands and crystal breakage, with no evidence of melt migration.

In this study, synthetic samples with plagioclases with an aspect ratio of R = 2 are subjected to torsion deformation. All synthetic samples were synthesized using an Internally Heated Pressure vessel. Deformation experiments were performed using a Paterson press. Subsequently, the samples were subjected to a series of analyses, including scanning electron microscopy (SEM) for 2D analysis, electron backscatter diffraction (EBSD) for 3D analysis, and electron microprobe analyzer (EPMA) for chemical compositions.

In parallel with the experimental study, an analytical study was conducted on natural samples to compare the results obtained during the experiments with the deformation structures found in the natural samples. Two series of samples were collected in the phonolitic volcanic province of Oriental Velay (French Massif Central) and they belong to a dike, Suc de Sara, and a neck, Petit Gerbier. The former represents a volcanic

structure that undergoes slow cooling, with deformation structures characteristic of an environment subject to rapid cooling. The second sample is subject to faster cooling, resulting in deformation structures that are slightly different.

The results obtained in this thesis permit a more precise definition of the concept and limits of a mush, the microstructural evolution of samples subjected to deformation, and finally, a more comprehensive understanding of the mechanisms that drive segregation, migration, and melt extraction in magmatic mushes.

State of the art

Résumé chapitre 1 - état de l'art

Ce chapitre d'introduction explique ce qu'est une mush volcanique. Sur le plan historique, il étudie l'évolution du concept de chambre magmatique et le passage de la chambre magmatique à la mush volcanique. Au cours des dernières décennies, le concept de mush volcanique s'est de plus en plus répandu. Des définitions de la mush ont été établies, avec des limites aux niveaux rhéologique, microstructural et environnemental. Le concept « Trans-Crustal Magmatic System » (TMC) a été établi, c'est-à-dire la zone dans laquelle le mush peut apparaître. À différentes profondeurs, le mush peut former un réseau interconnecté, où le liquide résiduel est capable de se déplacer et de s'élever. Le mush est un corps volcanique constitué en grande partie de cristaux, immergés dans une masse fondue généralement composée de silicates et de bulles. Pour que le liquide résiduel se déplace, certaines conditions de déformation, de teneur en cristaux, de température, de pression et de teneur en eau sont nécessaires. Toutes ces conditions forment ce que l'on appelle le " window of extraction ", c'est-à-dire toutes les conditions idéales qui rendent possible la mobilisation du liquide résiduel. Lorsque le mush est déformé, soit en compression, soit en torsion, le liquide résiduel à l'intérieur du mush peut ségréger, migrer et s'exsolver. L'objectif de cette thèse est d'étudier les processus de déformation en torsion qui génèrent le mouvement du liquide résiduel.

Au fil des années, différents mécanismes causant la ségrégation, la migration et l'exsolution de la matière fondue ont été proposés. Ces études sont principalement basées sur la modélisation numérique. Les travaux expérimentaux sur la mobilisation de la matière fondue dans le mush synthétique ont toujours porté sur des teneurs en cristaux inférieures à 60 %.

Dans cette thèse, des expériences de déformation par torsion ont été réalisées sur du mush synthétique avec des teneurs en cristaux comprises entre 0,52 et 0,95. Les objectifs sont d'étudier les microstructures formées dans les mushes soumise à la déformation, avec différentes vitesses de déformation et valeurs de déformation finie. Une première série d'expériences a été réalisée à faible teneur en cristaux et les résultats ont été comparés à ceux de travaux antérieurs (Picard et al., 2011). Il a été étudié comment la forme et le rapport d'aspect des minéraux affectent la propagation de la déformation et donc le développement des microstructures.

Une deuxième série d'expériences a été réalisée avec du mush hautement cristalline (0,73, 0,76 et 0,95). L'objectif est d'étudier la limite entre le mush et le système bloqué, c'est-à-dire à partir de quelle teneur en cristaux on passe d'un système qui peut être déformé à un système qui ne peut pas être déformé, car il est trop rigide.

I. State of the art

1. The birth of the mush idea

The concept of the magma chamber has evolved conceptually throughout history. In the 18th century, the scientific community attributed the origin of specific stratigraphic successions in mountain ranges to the phenomenon of 'Neptunism', named after the Roman god of the sea, as it represented a phenomenon related to water. Prof. Abraham Gottlob Werner (1749-1817) claimed that all rocks derived from crystallization from a primordial ocean. All the elements necessary for mineral crystallization were dissolved in water. Through cooling processes, the minerals could crystallize and deposit. Another concept introduced at the same time, but not accepted until years later, is the phenomenon of 'Plutonism' (from the Roman god of the underworld). James Hutton, a self-taught naturalist, claimed that rocks could form from magmatic intrusions and the slow cooling and crystallization of magma. Once the scientific community accepted the concept of Plutonism, another dilemma remained to be clarified: considering the Earth's

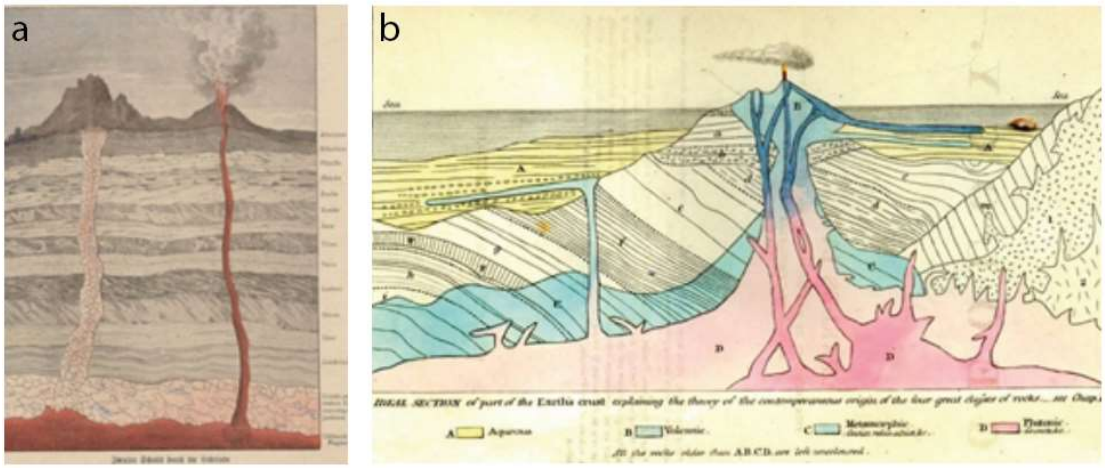

Figure I.1. a) An idealized section of earth´s crust, from Emile with "L´Ecorce terrestre" (1874), showing the stratigraphic order of the sediments deposited during various geological epochs. From https://blogs.scientificamerican.com/history-of-geology/granite-wars-episode-i-fire-water. b): Frontispiece of (Lyell, 1838). The ideal section of the Earth crust by Charles Lyell (1797-1875), Student of James Hutton, showing the -modern – concept of magma storage at depth, magma transfer and emplacement at the surface.

interior chemically homogenous (at the time it was imagined as a series of concentric shells), how could such mineralogically varying rocks can be formed?

Several hypotheses were formulated. The so-called granitisers thought that igneous rocks were formed by the fusion of pre-existing rocks (transformations by fluid). The group of so-called magmatists claimed that plutonic and granitic rocks resulted from the cooling of different melts. Norman Levi Bowen (1887-1956), after various petrological studies on the plagioclase-feldspar properties, published a famous petrological diagram, the phase diagram of plagioclase, showing how crystals form by cooling and how the chemism of the system can change during crystallization.

Once the concept of fractional crystallization was established, one question still remained to be answered: where did the huge amount of source magma come from? For more than a hundred years, the melt-dominated magma chamber has been regarded as the main volcanic supply mechanism (Cashman et al., 2017). All magmas are generated deep in the earth, and only a small percentage reaches the surface, thus causing volcanic eruptions. The magma, between its formation and the overflow to the surface, must transit and be stored inside the crust, or, more specifically, in the magma chambers.

Until the end of the twentieth century the most common conception was the magma chambers as large and homogeneous fused bodies, with a gaseous and crystalline component (fig. I.1a - b). However, in recent decades, the scientific consensus has shifted to a more complex picture: instead of mainly liquid, magmatic bodies are bound

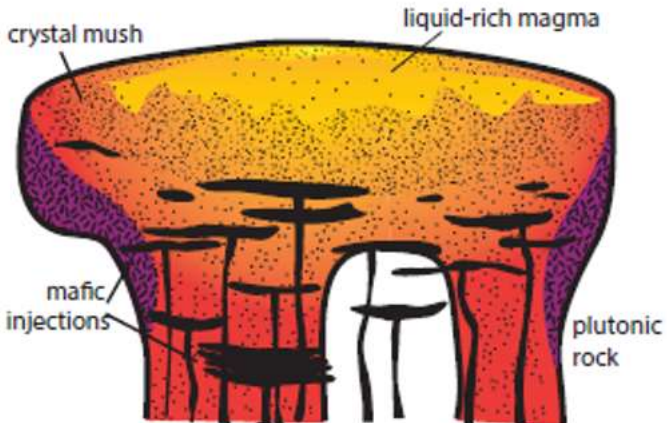

Figure I.2. Schematic diagram illustrating a crystal-mush dominated reservoir. Modified from Hildrethand Wilson (2007).

to bodies dominated by high crystalline mushes. These multiphase bodies can cover a large volume, up to 500,000 km^3 and they can come from the accumulation of crystals if the magma rises slow enough to crystallize them (Petford, 2003; Vigneresse et al., 1996). The mush is a partially molten system with temperatures at or above the solidus (Cashman et al., 2017), formed by a crystalline framework through which the melt is distributed (fig. I.2). Mushes are characterized as low-permeability, high-viscosity materials due to their high crystal fractions. The mush is called 'rigid' (Hildreth, 2004) if the crystals in a mush form an interconnected network. Conversely, if crystals are able to move and reorganize, the mush is called 'mobile' (Bachmann and Bergantz, 2008; Miller et al., 2014; Weinberg et al., 2021). Due to its high crystal content, its rheology is controlled by the deformation of the crystal framework. The mush is not erupted in its entirety, but the melt within it can be mobilized. A high crystalline content greatly increases the viscosity of the system (fig. I.3) and the strength of the crystal-melt aggregate (inset fig. I.3).

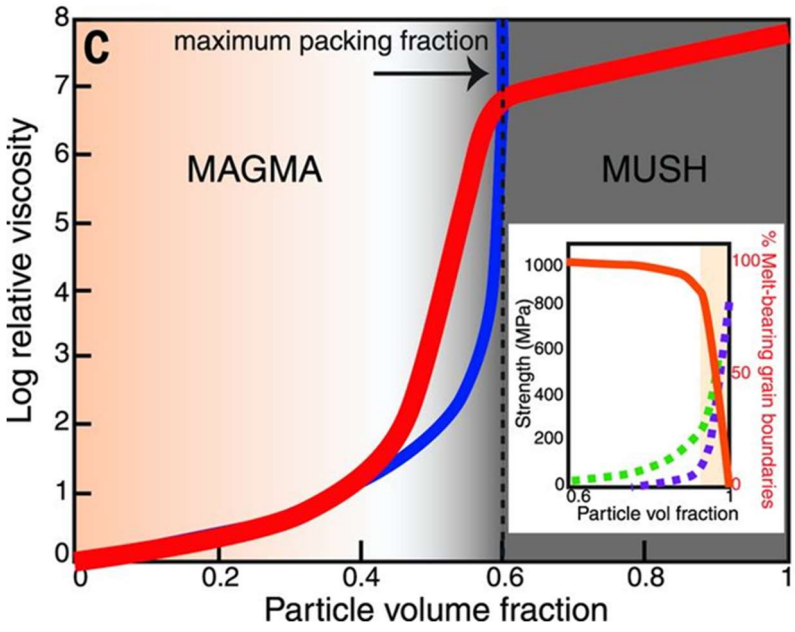

Figure I.3. Limit between magma and mush as function of particle volume fraction and viscosity. The inset shows the correlation between mush strengh and particle volume fraction (from Cashmann et al., 2017).

There have been several observations that have led to the replacement of the classic magma chamber model with the crystal mush model:

1) Seismic imaging frequently shows low percentage of melt in magma chambers (Lees, 2007; Huang et al., 2015; Kiser et al., 2016; Paulatto et al., 2022). Figure I.4 (Paulatto et al., 2022) shows the amount of melt found in 22 volcanoes, based on the depth of the seismic velocity anomaly and the volume anomaly. The results show a low percentage of melt storage (melt fraction between 0% and 20%).

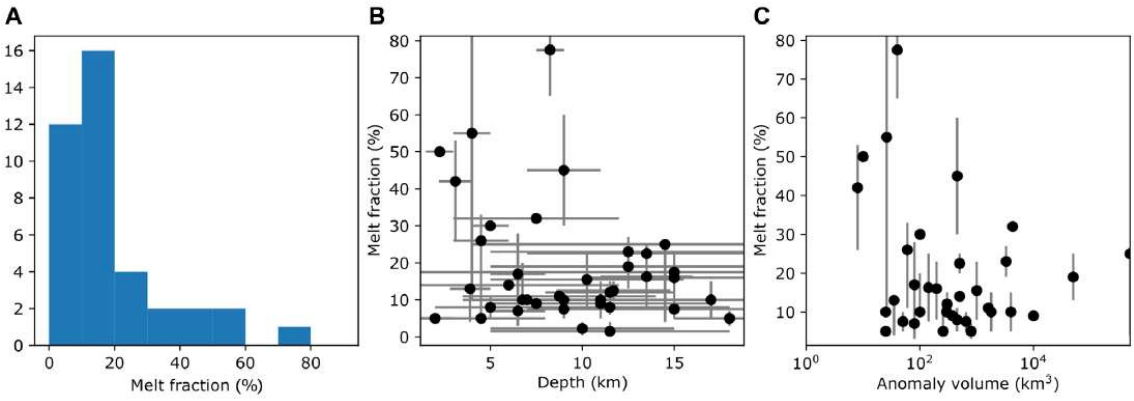

Figure I.4. a) Melt fraction histogram. b) Melt fraction vs low velocity anomaly. c) Melt fraction vs anomaly volume (Paulatto et al., 2022).

2) A considerable diversity in the ages and compositions of the crystals of volcanic rocks, which is inconsistent with the traditional mechanisms of cooling and crystallization (Reid and Rudnick, 2003; Schmitt, 2011)

3) Numerical models of magma injection recharging into a reservoir are in agreement with maintaining certain melt-dominated zones within a larger, partially molten region for long periods of time (Annen et al., 2015; Huber et al., 2012).

2. How does the melt move through mushes?

How the melt moves and rises is still deeply studied today, because it might lead to a better understanding how magmatic differentiation operates on the chemical evolution of the crust. Extensive knowledge has been acquired on the chemistry of magmatic bodies, but the rheology of their liquid and the domain controlled by the crystalline framework are still not thoroughly studied.

How the mushes can control the segregation and extraction of the melt? In this preliminary work, with an experimental approach, the effect of crystal fraction, size and aspect ratio on mush dynamics and its rheology with its related structures have been analysed. The hypothesis, according to the Trans-Crustal Magmatic System model TCMS (Cashman et al., 2017)(fig. I.5), is that volcanic mushes can be located at various depths in the crust, concentrated in pockets of mobile magma connected together by the warm and deep ductile crust to the more superficial open chambers. The rejuvenation and extraction of trapped melts from crystal-rich mushes are the fundamental processes of

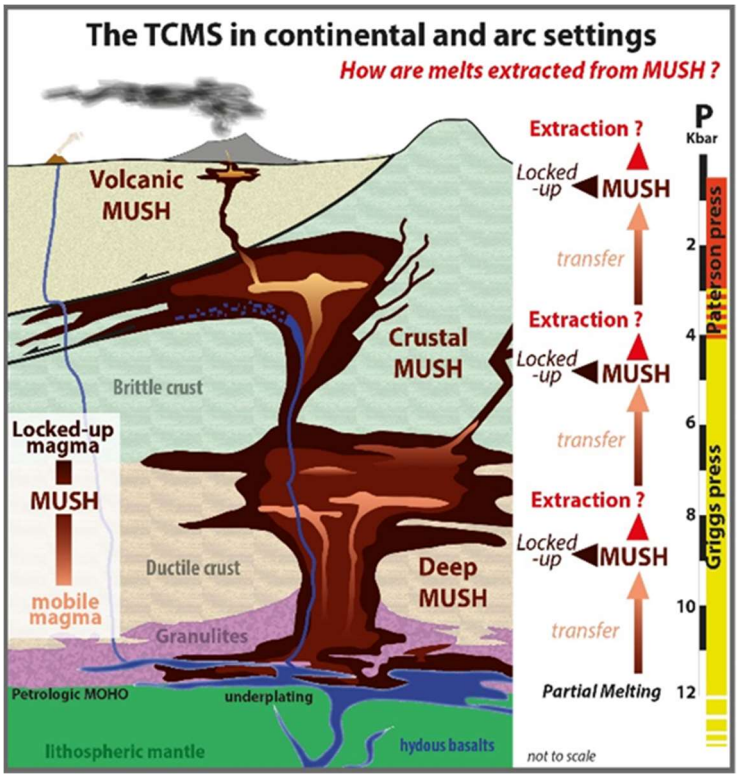

Figure I.5. Crustal scale: The Trans-Crustal Magmatic System (TCMS). Arbaret, unpublished.

differentiation. These processes need specific condition of crystals content, water content, temperature and pressure to be realized and they define the so-called window of extraction (Dufek and Bachmann, 2010; Burgisser and Bergantz, 2011). The window of extraction is highlighted in the red circled area of the mush (fig. I.6), where the rheological conditions allow the extraction of magma from the latter. The numerical values that can delimit the extraction window to a specific interval of crystalline content are not well identified yet, and it will be the purpose of this work to find out if there is migration of melt even for greater crystalline contents than those stated by previous works.

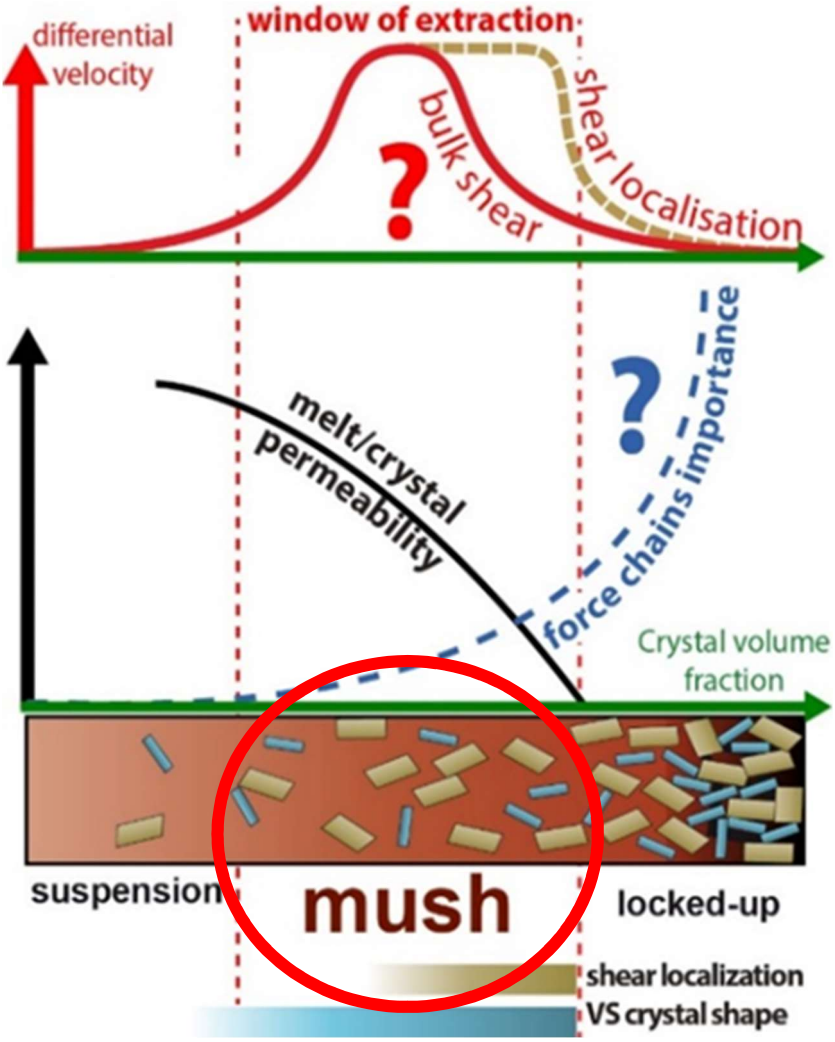

Figure I.6. Crystal scale: the window of extraction (Arbaret, Unpublished).

The aim of this work is also to determine the crystal content at which there is a transition from a mush system to a locked-up system (a system that cannot be deformed due to the very high crystal content). From previous works, different mush/locked-up system

limits were assumed. At extremely high crystal contents (approximately ϕ_s: 0.8), a critical threshold has been defined as the rheological critical melt percentage, RCMP (Arzi, 1978). Other experimental studies (Lejeune and Richet, 1995; Van Der Molen and Paterson, 1979) define this transition at crystal contents between 0.4 and 0.9. In the work of (Vigneresse et al., 1996), a limit called Particle Locking Threshold (PLT) was defined, which should occur for crystal contents between 0.0 and 0.9. Another threshold was defined by (Rosenberg and Handy, 2005). They collected a number of existing experimental data on partial melting and defined a threshold called the Melting Connectivity Transition (MTC), which appears at crystal contents above 0.93. Compared to the RCMP, the MTC is characterized by a higher viscosity and can be formed by a breakdown of the interconnectivity of the liquid without a change in the solid structure. This is a parameter still not well defined, as through experimental studies it can vary between 0.4 and 0.9, depending on the shape, size, viscosity, SPO of the solid fraction (Dingwell et al., 1993; Saar et al., 2001).

The mechanisms by which melt migration occurs are not well understood. However, melt mobilization mechanisms can be classified into 3 different types. The first is melt segregation, where residual melt from a sample is concentrated in specific areas, forming enriched and depleted regions in the melt on length scales longer than the grain size (Kohlstedt and Holtzman, 2009). The second is melt migration, where melt moves over a pressure gradient on length scales longer than the grain size but shorter than the compaction length (Kohlstedt and Holtzman, 2009). The third is melt extraction, which includes all processes that can segregate and migrate melt, leading to the emplacement of magmas.

Although the precise mechanisms of melt mobilisation are not fully understood, it is clear that many factors influence magma mobilisation. These factors can include pore-pressure lubrication, buoyancy, contact friction interaction and hydrodynamic. Besides the buoyancy effect, the other factors depend on intrinsic properties, such as the roughness and viscosity of the melt, and the shape of the crystal (Saar et al., 2001), rate of deformation and imposed stress.

From the work of (Kohlstedt and Holtzman, 2009), it is clear that one of the main driving force for melt movement could be buoyancy (due to density differences between the melt and the rock, fig. I.7a-b) or shear (due to the pressure gradient created by shear deformation, fig. I.7c-d). From other works, the mechanisms that have been hypothesized and studied are reactive porous flow (Aharonov et al., 1995; Jackson et al.,

2018), porous flow (Scott and Stevenson, 1986) porosity waves (Scott and Stevenson, 1984), the development of melt-rich transport channels, dykes or shear bands (Keller et al., 2013; Kohlstedt and Holtzman, 2009), diapiric melt enhancement or floating magmas (Seropian et al., 2018) or melt segregation processes (Bachmann and Bergantz, 2004; McKenzie, 1984).

It is the latter process that is the focus of this work. Melt segregation is defined as the formation of melt-rich or melt-poor regions due to a pressure gradient at the largest grain size.

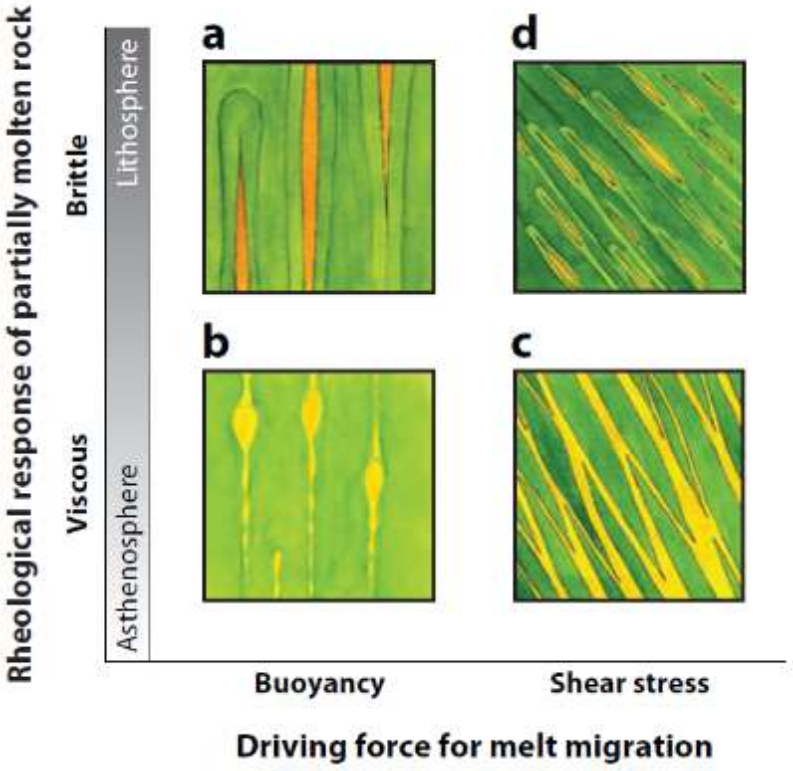

Figure I.7. Mechanisms of melt migration in the asthenosphere and lithosphere. a) brittle regime and dominated by buoyancy, there is tensile dike propagation. b) viscous regime and dominated by buoyancy, there is porous flow. c) viscous regime, stress driven melt segregation. d) brittle regime dominated by shear crack propagation (from Kohlstedt et al., 2009).

3. Melt segregation models

Some models of melt mobilization in a mush from previous works are shown in this section. Each study describes a different element as a key parameter for melt migration (crystal content, permeability, strain rate, etc.). This further emphasizes that the processes of melt mobilization are extremely complex and require further study from both a geochemical and geophysical perspective.

Starting with low crystalline content (<45%) magma suspensions, a magma mobilization model was developed by (Bachmann and Bergantz, 2004). The mobilization of a rhyolitic fluid from a volcanic mush is possible if the crystalline content reaches 45%. As shown in figure I.8, a magmatic suspension with crystal content <45% exhibits convective movements, which allow the movement of the crystals. At values of ± 45-50%, the system changes from liquid to solid, convection ends and crystal frameworks are formed. The melt extraction begins through compaction, micro-settling and hindered settling processes.

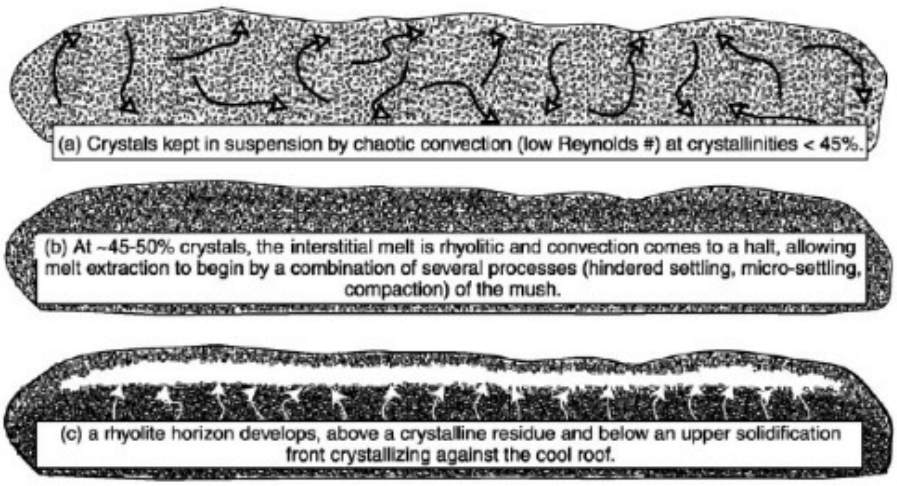

Figure I.8. Schematic illustration of the melt expulsion model for the generation of crystal-poor rhyolites (Bachmann and Bergantz, 2004).

In a context of higher crystalline content (50-60%), density contrast can be another key factor in the mobilization of a volcanic mush. (Burgisser and Bergantz, 2011) hypothesize a two-stage mobilization model (fig. I.9). The first phase involves a decrease in the crystallinity of a magma through heating. This generates an underlying mobile layer, and when this becomes sufficiently buoyant, it penetrates the overlying magma, which is

highly viscous, generating a mechanism of mixing and homogenization. If the process in strong enough, the decompression could generate the moving magma necessary for an eruption.

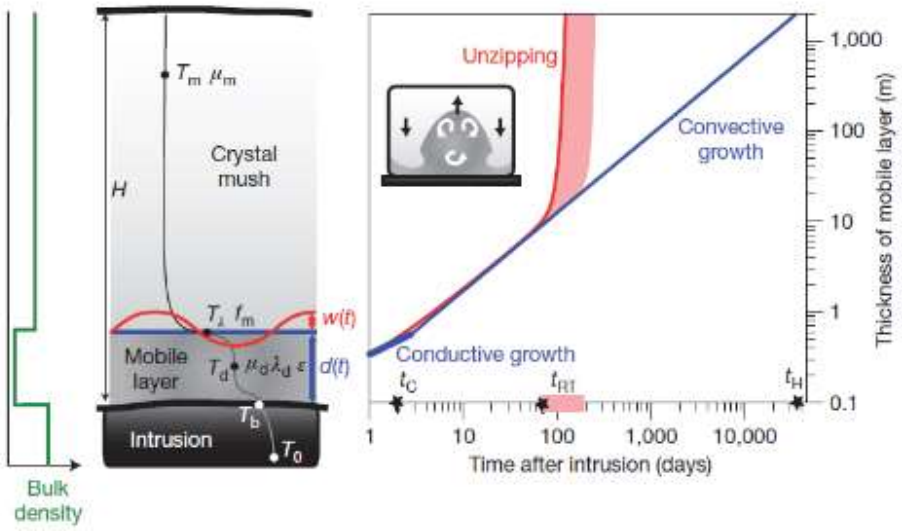

Figure I.9. Schematic of a stagnant mid-crustal reservoir being reheated from below by an intrusion. d: layer thickness, w: interface instability amplitude, w+d: unstable front. The horizontal axis indicates the time at which the layer starts convecting tc. (from Burgisser and Bergantz, 2011).

By strain localization it is possible to have melt channel formation (Katz et al., 2006). These melt channels can be preferential channels for melt migration and extraction. By modelling laboratory experiments (Cooper, 1990; Spiegelman, 2003), (Katz et al., 2006) explain the formation of localized shear bands, emerged at 15°-25° to the plane of shear. In a viscous and porous material, after a simple shear deformation experiment, the melt flows and converges in the area with low pressure, creating melt bands at about 20° to the direction of maximum shear (fig. I. 10).

According to the work of (Dufek and Bachmann, 2010; Parmigiani et al., 2011) the right permeability value allows the melt transfer by porous flow. As illustrated in figure I.11, at low crystal content the crystals are immersed in the melt, they move following the magmatic flow lines. Some of them are deposited, separated from the melt going to the base of the flow (detrainment thickness). The convection currents are generated by variation in density, due to cooling and consequent crystallization. When a slight

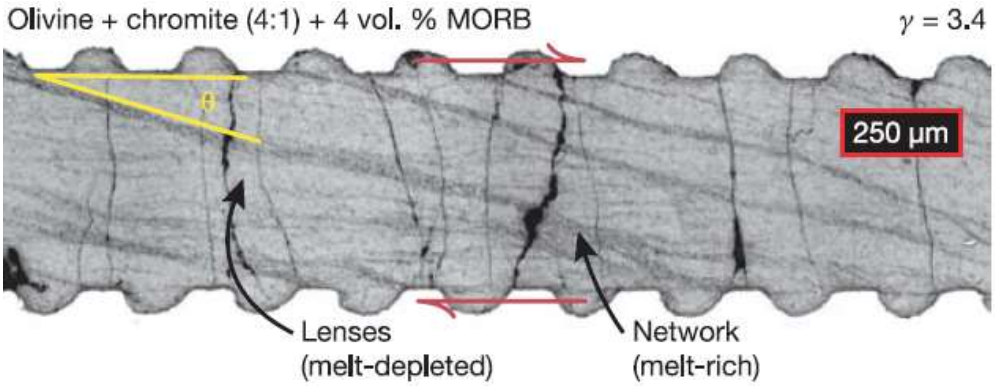

Figure I.10. Cross section of a simple shear experiment on a partially molten aggregated. The melt-rich bands are the dark gray region, and sub-vertical black features are decompression cracks (from Katz et al.,2006)

interconnected crystalline network begins to form, and therefore the crystals approach lock-up, the melt could be separated, through hindered settling and compaction phenomena. By increasing the crystalline content, the mush has a very low permeability, which prevents crystal-melt separation. The total volume of melt that will be extracted depends on thermal parameters such as the latent heat of crystallization and the geothermal gradient. With crystallinity higher than 70%, the low permeability prevents the separation of the melt, and the crystal-liquid separation occurs mainly by low melt fraction compaction (McKenzie, 1985; Bachmann and Bergantz, 2004). Therefore, the best range to favor the separation of the melt from the crystals is between 0.5 and 0.7. This specific extraction window interval makes melt extraction in a cooling magma chamber is more likely to be accepted for the following reasons: 1) decrease in thermal gradients between chamber wall 2) absence of convection inside the chamber leads to a greater segregation of the melt, 3) buffering by latent heat of crystallization.

The partial melting mechanism of the pre-existing crust leads to a compositional gap if there is a critical amount of non-modal melt. At low crystallinity, convection currents are formed due to the density variations induced by cooling and crystallization. The crystals remain in suspension, following the flow lines of the high crystalline fluid (Thompson, 1972; Brophy, 1991; Burgisser et al., 2005).

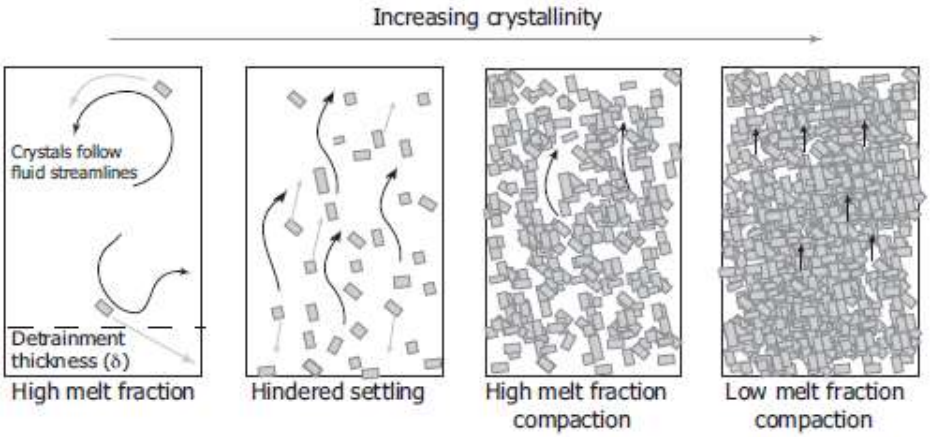

Figure I.11. Conceptual model of crystal-melt dynamics at range of melt fractions. From Dufek et al., 2010.

4. Rheological behaviour of magmatic suspensions

Depending on the crystalline content, magma has a different behavior. Considering the shear stress (σ) and the strain rate (ἐ), figure I.12 shows the rheological behaviors chart

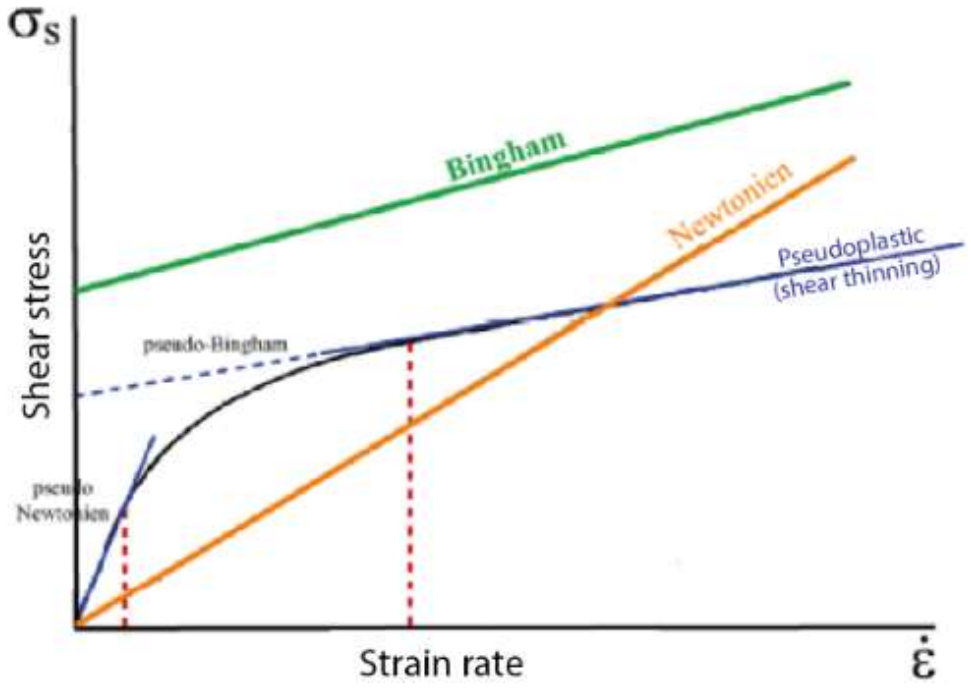

Figure I.12. Rheological behaviors defined for magmatic suspensions (modified after Fernandez and Gasquet, 1994).

that could be used as comparison of magmas behaviors (Fernandez et al., 1983). At a low σ value, the behavior is Newtonian, and can be simulated through the Einstein-Roscoe equation. By increasing the crystalline percentage, the behavior becomes non-Newtonian (Arbaret et al., 2007; Bagdassarov and Pinkerton, 2004; Fernandez et al., 1983; Lejeune and Richet, 1995; Saar et al., 2001), shifting to a Binghamian or pseudoplastic behavior, the latter divided into shear thinning and shear thickening, depending on the rheology of the magma. When the crystalline content reaches ± 30%, a stress threshold appears and the flow has a shear thinning behavior, due to the crystalline structure that must be destructured to allow the detachment (fig. I.13).

As shown in figure I.6, depending on the crystal content, the volcanic body can be defined as a suspension, mush or locked-up system. The limits of these ranges have not yet been exactly defined. The mechanical notion of a 'locked system' is not a univocal definition, limited to a particular fraction of crystalline content. The work of (Bergantz et al., 2017) shows a number of elements that can make a system deformable, even at high crystalline content. In addition, they analyze magmatic mechanisms and processes that can 'deform' a mush prior to eruption or mixing. However, theoretical boundaries can be established by observing the rheological and microstructural behaviour of each volcanic body considered. Based on numerical modelling, studies of natural samples and experimental studies, five domains can be defined.
At crystalline contents below 20% ($\phi_s < 0.20$), the crystals are not in contact with each other and the volcanic body can be defined as a suspension. It behaves like a Newtonian fluid, it has a constant viscosity and its behavior can be modeled by the Einstein-Roscoe

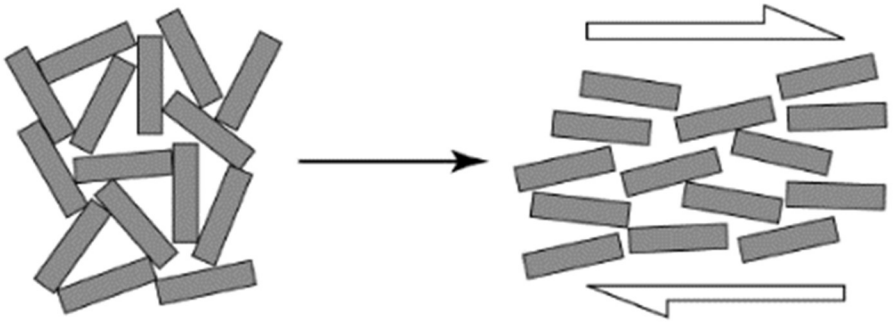

Figure I.13. Destructuring of the crystalline framework allowing the flow (Picard, 2009).

equation (Ishibashi and Sato, 2007; Roscoe, 1952). As crystallization continues, the crystalline content increases, and the suspension shifts from Newtonian to non-Newtonian behavior, creating a crystalline framework that can transmit deviatory stress (Petford, 2003).

There are several structures that are typical of low crystalline environments that can give an indication of the nature of the deformation. The few crystals present could begin to have a preferential orientation in the direction of deformation, schlieren and compositional layering (fig. I.14a), pillar structures and enclaves could form.

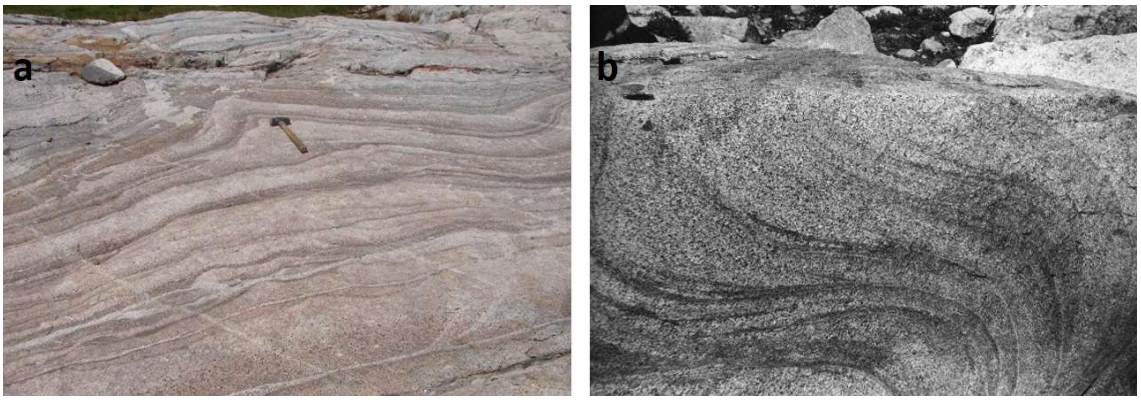

Figure I.14. a) Schlieren structure with low crystal content. b) Schlieren structure with high crystal content.

From https://earth.usc.edu/research/tuolumne/schlieren/schlierenlayers.htm

At higher crystal content ($0.20 < \phi_s < 0.40$), there is a Bingamian behavior, which reflects the same behavior as the Newtonian fluids but only after exceeding a critical stress value, the so-called RPT (Rigid Percolation Threshold) defined by (Vigneresse et al., 1996). Interconnectivity is generated between crystals with a crystalline structure capable of transmitting stresses (Petford, 2003) and with an increase in viscosity. Therefore, there is a shear thinning behavior. This is also the area where penetrative-type crystal fabric develops by rotation of crystals (Ildefonse et al., 1992; Arbaret et al., 1996; Vigneresse et al., 1996). This domain would correspond to the PLT (Particle Locking Threshold) defined by (Vigneresse et al., 1996). This crystal range produces more intense deformation structures with deformation of enclaves, complex schlieren formations (fig. I.14b) and orientation of the crystals in the direction of the deformation. When the crystal content is high enough to create interactions between the different crystals, the suspension becomes 'dense' (Petford, 2009). To achieve this condition, the

distance between the granules (h) is equal to or less than the particle size (d, fig. I.15). The melt streamlines, which in a low crystallinity body are straight and follow the direction of deformation, follow a more tortuous path in a high crystallinity body and increase in viscosity until they reach the maximum packing fraction. In these magmas there is an increase in viscosity as the number of particles increases and the streamlines become more tortuous.

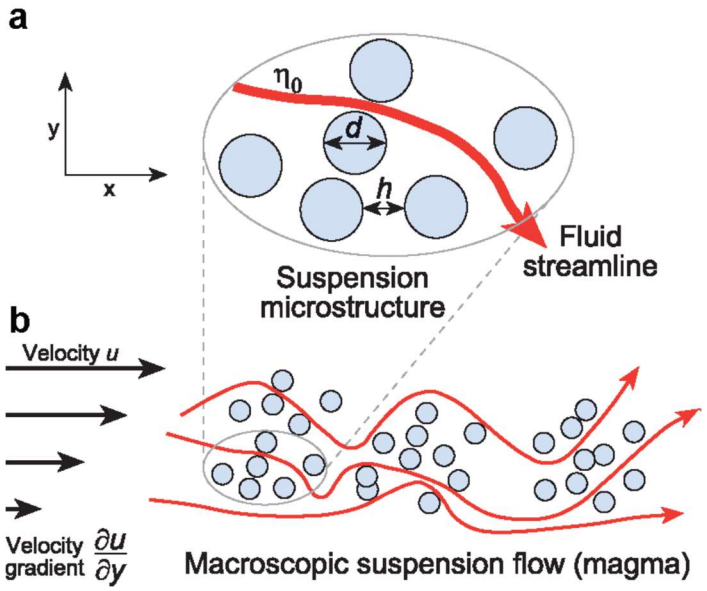

Figure I.15. Magma undergoing shear deformation. a) The particles forming the magma have a diameter d and a spacing h. The particles are immersed in a magmatic fluid of viscosity μ_0 which follows a streamline. b) The particles move by interacting with each other, the viscosity of the body increases and the streamlines follow a tortuous direction. From Petford, 2009.

At crystal content $0.40 < \phi_s < 0.52$, the behavior is still shear thinning with the development of penetrative fabric and shear bands (Picard et al., 2011). Suspension viscosity is further increased, favouring brittle deformation process. As the crystal content increases, the behaviour of the suspension can be shear thickening type. The shear thickening can be related to the phenomenon of dilatancy. The particles that form the suspension reorganise during shearing, increasing the pore space and volume of the sample (fig. I.16).

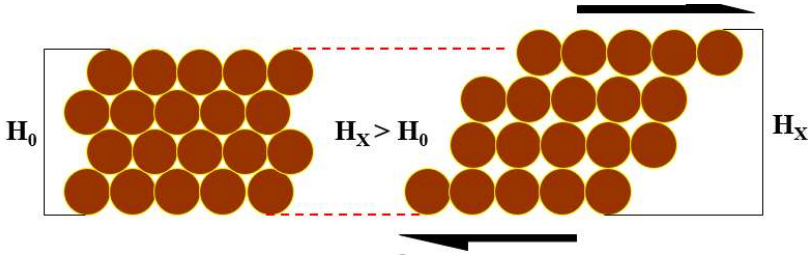

Figure I.16. Graphical representation of the dilatancy phenomenon. The sample, initially unformed, undergoes shearing. This leads to a different arrangement of the particles, with an increase in the final height (H_x) compared to the initial height (H_0).

For $0.52 < \phi_s < 0.58$, the shear thinning and shear thickening behaviors are even more marked. Due to the high crystal content and high viscosity of the suspension, deformation is concentrated in certain areas of the sample, resulting in the formation of diffuse shear bands (Picard et al., 2011). The deformation processes can be so intense that a large part of the suspension forms cataclasite in particular with increasing strain rate (Forien et al., 2011). The crystals generally show a bimodal preferred shape orientation in the foliation and shear directions. The most common deformation structures are S/C/C' geometries (fig. I.17a) and shear bands (fig. I.17b).

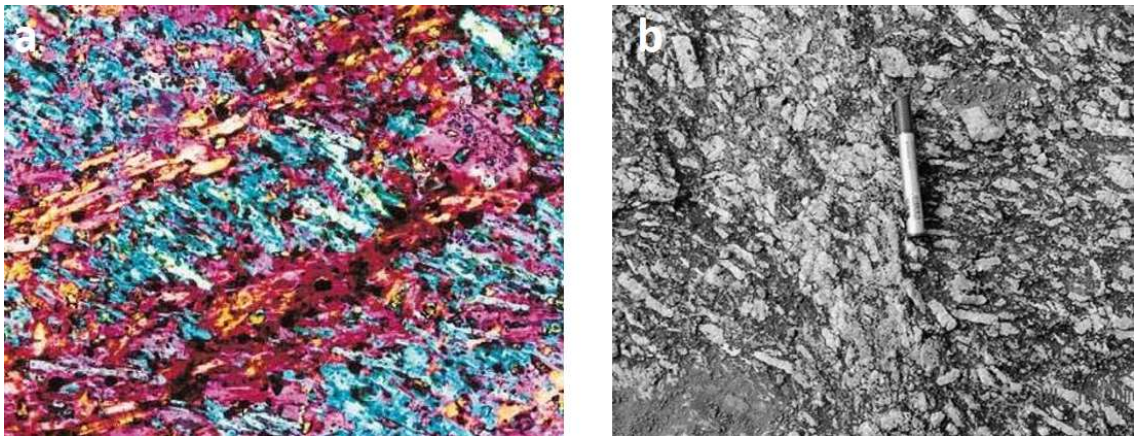

Figure I.17. a) Trachytic texture with S/C' geometry. From Smith, 1996. b) Shear band, from Sen K, 2006.

For $\phi_s > 0.58$, viscosity increases slightly and the behavior is shear thickening. The sample is very resistant to deformation. The crystalline structure is a rigid localization of forces, resulting in brittle deformation and fracture. Distributed tension gashes can be form (Arbaret et al., 2007; Bouchez et al., 1992), which can be intersected by shear

bands. If the deformation is particularly intense and localized, cataclasite can cover a large part of the sample.

For crystal contents above 0.30, deformation structures can be related to either brittle deformation (Riedel system, fig. I.18a, common for crystal contents above 50%) or ductile deformation (S/C/C' system, fig. I.18b, (Bauer et al., 2000), common for crystal contents above 40%).

The Riedel cataclastic system develops in a simple shear environment and is formed by a network of conjugated and unconjugated shear bands. In high crystal content natural samples subjected to shear, the Y, R_1 and P bands are easy to find. The high angle bands (R_2 and X) are less stable and can appear, rotate and disappear.

In the ductile S/C/C' system, the formation of the S and C structures can occur simultaneously to ensure a constant volume, while the C' bands generally form when there is very strong strain and the sample volume is changed.

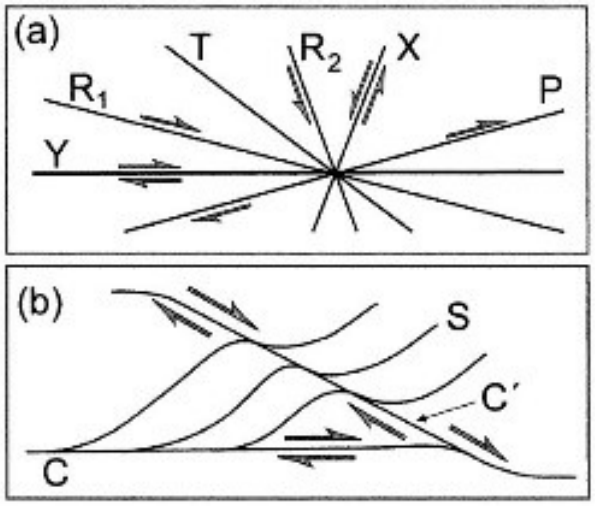

Figure I.18. Deformation structures formed in a simple shear environment. a) Riedel's (1929) cataclasitic system. b) S/C/C' ductile system (Bouchez et al., 1992).

Figure I.19 shows a summary diagram of all the structures analysed in this section, with increasing viscosity and crystal content.

At low crystal content, there is Newtonian behaviour and the viscosity remains constant. At contents of around 0.40 the suspension is solid. The viscosity increases rapidly, there is Binghamian behaviour and shear softening. As the crystallinity increases, shear thickening occurs.

At crystal contents above 0.60 the suspension is granular. Viscosity increases more slowly, deformation is brittle or the system can be blocked.

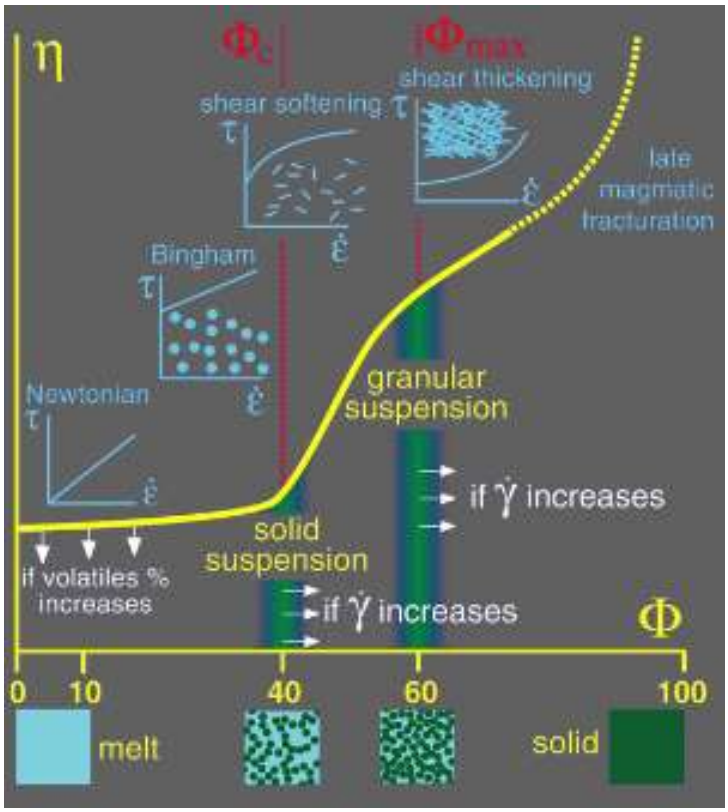

Figure I.19. General model of magma rheology. At low crystal contents, the suspension has Newtonian behaviour and moves by fluctuation and convection. At crystal contents between 40% and 60% a solid suspension forms, with shear softening behaviour if deformation is applied. At crystal contents of around 60%, the suspension is granular and the behaviour is shear thickening. At crystall contents above 70%, deformation results in the formation of late magmatic fracturation. (Arbaret 2021, unpublished).

5. Influence of bubbles on melt migration

At low crystal contents, useful indicators of deformation directions can be bubbles. Although is not the main purpose of this work, bubbles can be considered as deformable objects, hence strain markers in volcanic melts (Arbaret et al., 2007). In samples without crystals, the bubbles behave as "passive markers", actively deforming without undergoing the viscosity contrast between them and the melt. The finite strain ellipse theory (Ramsay, 1967) is used to calculate the relationships between the orientation of the bubbles α, R and the finite shear strain γ. The relationship between the applied finite strain and the orientation of the theoretical long axis follows the equation below (March, 1932):

$$\alpha = \frac{1}{2}\arctan\frac{2}{\gamma}$$

At crystal contents greater than 0.16, the bubbles no longer have a passive behavior as an ideally deformable marker, but they have a different orientation. This expresses a change in the flow of the liquid enveloping solid particles, documented by simple shear experiments (Ildefonse et al., 1992).

Bubbles in a silicate liquid display a double behavior: they can decrease the viscosity of a rhyolitic liquid (Bagdassarov and Dingwell, 1992) or they can increase it, depending on the crystal content (Stein et al., 1992). The limit between one behavior and the other is given by the capillary number Ca, which represents the ratio between the shear stress that tends to deform the bubble and the tension surface which instead resists deformation (Manga et al., 1998). The bubbles remain spherical and resist the flow if Ca is less than 0.5, slightly increasing their viscosity (fig. I.20). The bubbles line up with the flow for Ca values greater than 0.5, lowering the viscosity. Another parameter that

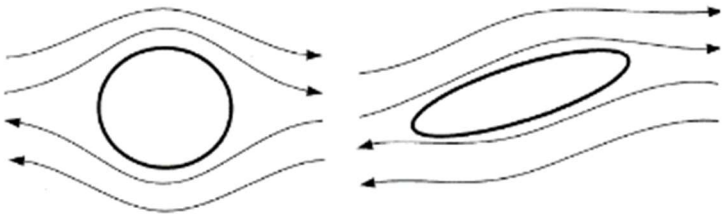

Figure I.20. Illustration of bubble shape and flow lines for low Ca (left) and high Ca (right). Deformed bubbles are less resistant to deformation (Manga et al., 1998).

influences the effect of the bubbles is their total quantity. For bubble fractions up to 32% by volume, the viscosity of the silicate liquid is not affected by the bubble phase (Lejeune et al., 1999), while for higher percentages, the viscosity decreases (fig. I.21).

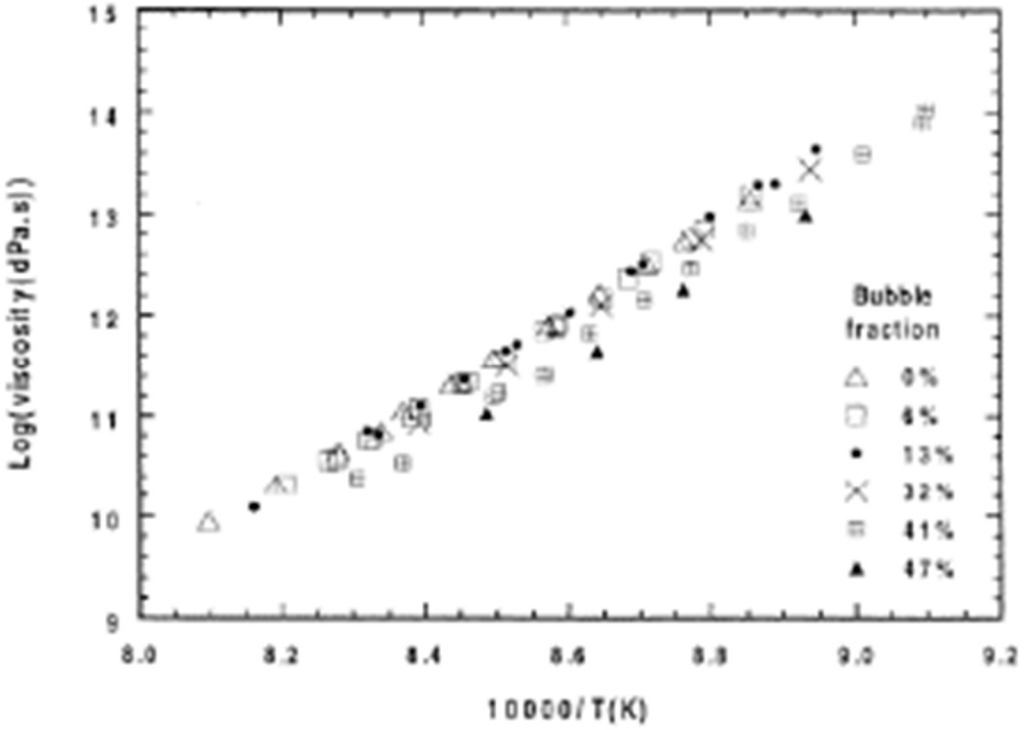

Figure I.21. Viscosity log as a function of temperature and the bubble fraction. Up to 32% of bubbles the viscosity of the silicate liquid is not affected by the bubble phase (Lejeune et al., 1999).

It has been noticed (Bagdassarov and Dingwell, 1992) that the stronger influence on the viscosity is given by the effect o the crystallization, which can increase the viscosity by a factor of 6, while the influence of the bubbles reduces the viscosity by a factor of 1.4.

Bubbles can be key elements in magma mobilization, especially in siliceous and viscous magmas. During the ascent of a water-saturated magma, there is exsolution of the magmatic volatiles with subsequent expansion and coalescence of bubbles (Gonnermann and Manga, 2007). Degassing processes take place through the permeable deformation of networks of bubbles. Outgassing is favored by the formation of shear localization, which focuses the escape routes of the gas (Okuma 2009, 2013). According to the model of (Crozier et al., 2022) magma ascent takes account for gas

escape through permeable bubble networks, magmatic fractures, and wall rock (fig. I.22). In order to have the degassing, magmatic fractures are necessary which they require the shear localization.

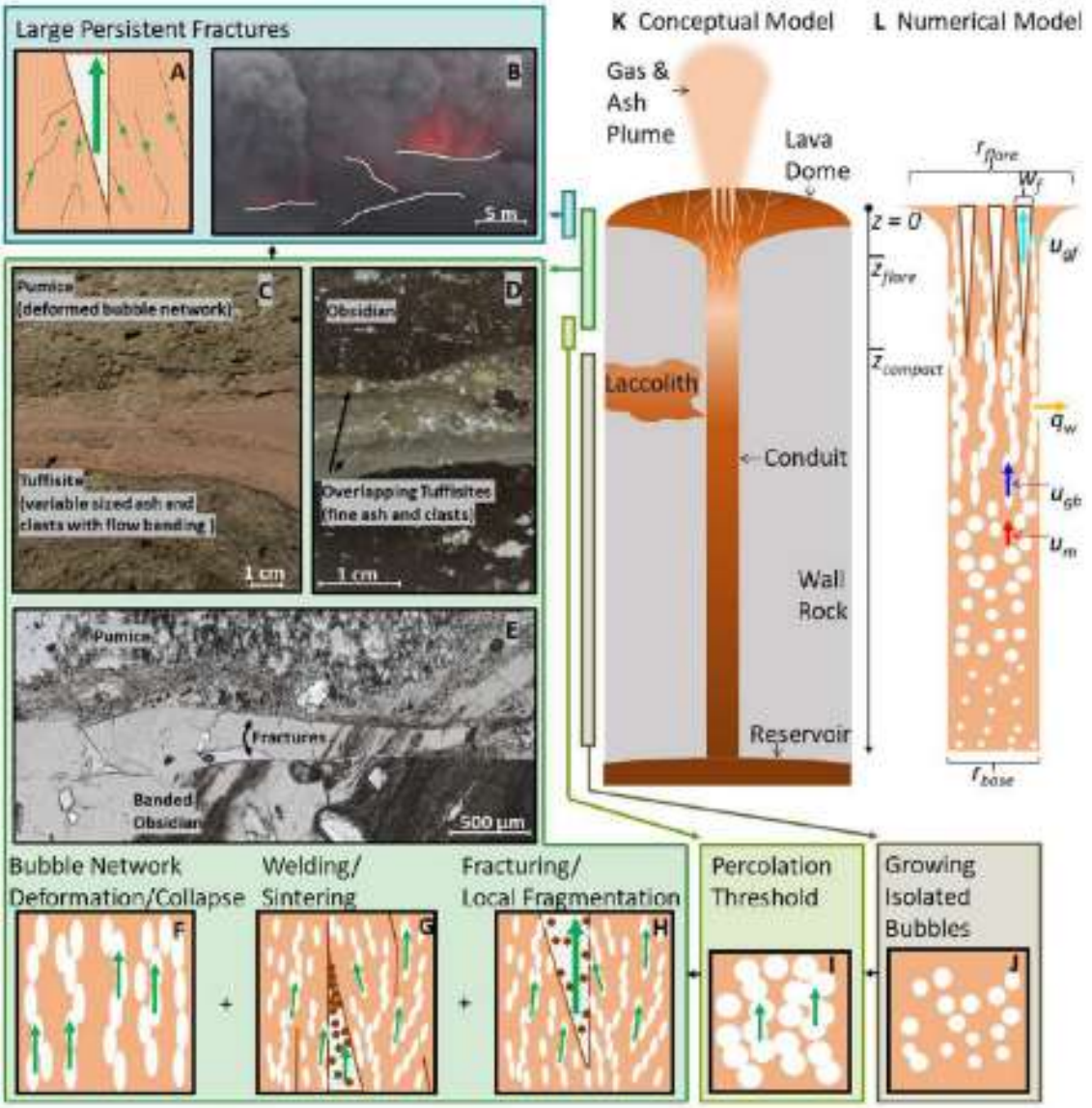

Figure I.22. Conceptual model of volcano eruption from Crozier et al., 2022.

6. Force chains

Mushes are a multiphase systems made of a connected network of crystals located in a silicate melt reservoir (Bergantz et al., 2017), so their dynamics are controlled by crystal interactions and fluid interactions. Through these contacts stress can be propagated, creating an inhomogeneous distribution of force contacts and producing the so-called force chains (fig. I.23). Whenever there are mechanisms of shear thickening and jamming in crystal-rich suspension, they play a decisive role in the formation of shear zone and localization of forces (Tordesillas, 2007).

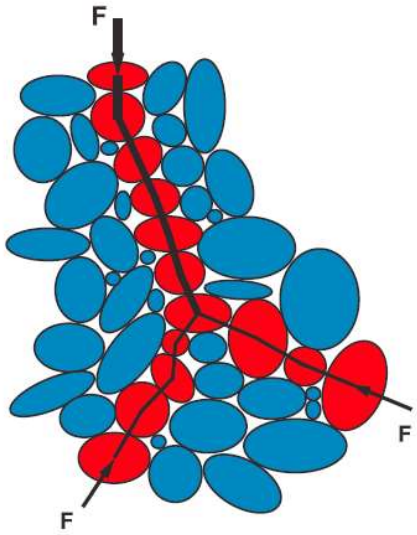

Figure I.23. Schematic representation of force chain propagation. In a granular system subjected to deformation, the red particles represent the branching region of the force chain (from Bergantz et al., 2017)

The first observations regarding the inhomogeneous transmission of stresses were made through photoelastic experiments (fig. I.24, from http://www.lmgc.univ-montp2.fr/perso/franck-radjai/research/stress-transmission/), with birefringent particles. The photoelastic image shows filaments of bright grains subject to high loads against a background of dark areas formed by less loaded grains. The first measurement of the force chains was made using carbon paper to record the normal forces propagated at the boundaries of the particles.

There is no definition of a force chain, but it can be described as a set of particles (at least three, up to an unlimited number) in contact with each other that carry and

propagate a force greater than the mean force (Cates et al., 1998; Muthuswamy and Tordesillas, 2006; Peters et al., 2005; Wambaugh, 2010).

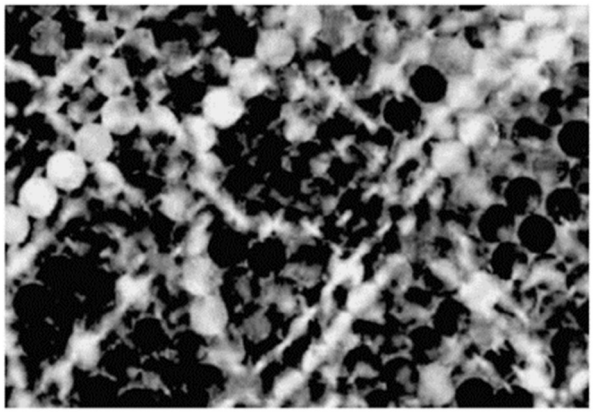

Figure I.24. Stress chains in a photoelastic image of a packing of beads, from http://www.lmgc.univ-montp2.fr/perso/franck-radjai/research/stress-transmission/.

Force chain propagation can occur in branching patterns, forming arcs and transmitting force on a macro scale (Bergantz et al., 2017). Therefore, the distribution of forces in these suspensions is bimodal (Majmudar and Behringer, 2005; Radjai et al., 1998). The bimodality of the force chain is given by the formation of two distinct classes of force: a stronger one that moves in a direction parallel to the load, and a weaker one that propagates isotropically and slightly perpendicular to the load, behaving as if it were a 'pressure' (Bergantz et al., 2017). An example of the bimodality of force chains and their direction of propagation is illustrated in figure I.25 (Bergantz et al., 2017), which shows a discrete element simulation (DEM) of a basaltic intruding into a basaltic mush. Normal forces that are greater than the average force are coloured red, normal forces that are lower than the average force are coloured blue. As the fluid intrusion enters the system, a system of forces develops with a branching pattern, where the mean forces are distributed almost linearly over many particles.

The force chains have different intensities and propagations depending on several factors. Starting from the shape, with elongated particle the force distributions become wider as the length increases (Azéma et al., 2011).

Furthermore, when considering a polydisperse system, shear forces are mainly captured by the longer and larger particles. This means that larger particle sizes correspond to larger force chains and smaller particle sizes do not strongly influence the direction of force propagation.

In addition to crystal shape, a parameter that strongly influences the propagation of the force chain is the mobility of the system.

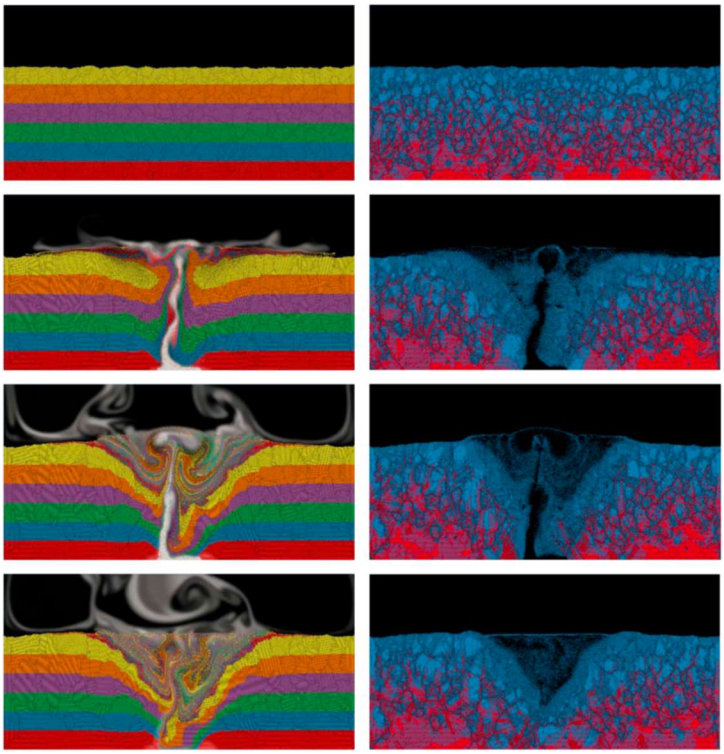

Figure I.25. Simulation of discrete elements for an intrusion into a mush. There are four time phases. On the left is the fluidization and crystal mixing process, on the right the force propagation (Bergantz et al., 2017).

This parameter is closely related to crystal shape, as the larger the aspect ratio of the particles in contact, the lower the mobility of the system. There are other factors that influence the mobility of the system such as the crystal content, viscosity and permeability of the suspension. As a result, the suspension does not behave elastically, as there is a reorganisation of the suspension when deformation is applied (Ness et al., 2017). The number of contacts between the crystals is not kept constant and consequently the force chains are not stable over time. A plastic state called 'fragility' is created (Bergantz et al., 2017). In this state, there is an initial phase of rapid micro-fragile deformation associated with contact failure. The second phase involves a macro-fragile structural response where there is local reconfiguration (Cates et al., 1998; Ness et al., 2017; Ness and Sun, 2016). Thus, the strength of the system changes over time, as do its force chains, particularly when particles are free to rotate and translate. Force chains

migrate, abandoning previous force chains and forming new ones. This creates what is known as "force chain instability" (Cundall and Strack, 1983; Guo, 2012; Tordesillas, 2007; Tordesillas et al., 2014, 2009). These instabilities generate and underlie the localization of deformation and shear bands (Tordesillas, 2007). For this reason, large part of this thesis focuses on the study of force chains.

It has been observed (Radjai et al., 1998) that a packaging of granular materials subjected to shear develops a network of anisotropic contacts. Despite the mobility of the particles and their disorder, the packing of particles shows a finite shear strength. This is due to the formation of new contacts along the main major axis of the strain rate tensor, while some of them are lost if perpendicular to the tensor. Thus, two distinct classes of forces are formed, involving strong force chains and weak force chains (fig. I. 26).

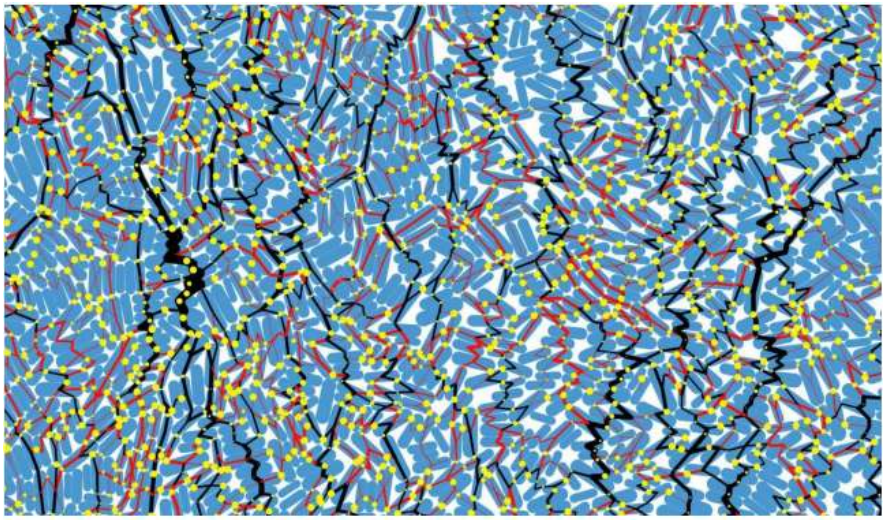

Figure I.26. A snapshot of the force-bearing particle. The strong forces are in black, the weak forces are in red (Azema et al., 2011).

After exceeding a certain limit threshold, the weak force network shift from a passive stabilizing agent in comparison to strong force chains to a transmitting active force.

In case of disk packing, the contacts in the weak network are perpendicular to the contacts in the strong forces. In case of packing in elongated particles, both strong and weak networks are oriented parallel to the stronger force chains. In this situation, the average normal force in the weak network has a maximum value in the contacts

perpendicular to the strong network. This means that the weak forces change their behavior depending on the shape of the particles. In case of circular particles, many weak side contacts support the strong force chains. With elongated particles, the strong force chains are supported laterally by fewer contacts but with high weak forces (Azéma et al., 2011).

The shape that best represents plagioclase crystals, which are the minerals used for the deformation experiments used in this thesis, is the RCR (fig. I.27). It is a rounded-cap-rectangle, modeled as the juxtaposition of two semi-discs with a rectangle (Azema and Radjaï, 2012).

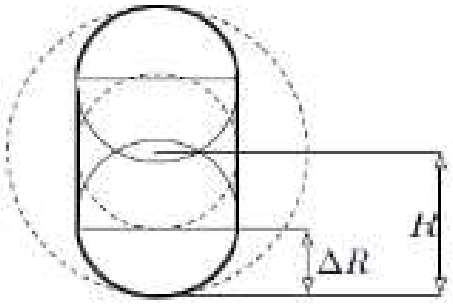

Figure I.27. Shape of a Rounded-Cap-Rectangle (RCR)

Contacts between RCR particles can be classified into three categories (Azema and Radjaï, 2012) namely cap-to-cap (C-C), cap-to-side (C-S) and side-to-side (S-S) (fig. I.28). A study conducted by Azéma and Radjaï (2012), analyses the contact forces in terms of branch vectors that unite the centers of the particles that shows how the side-side

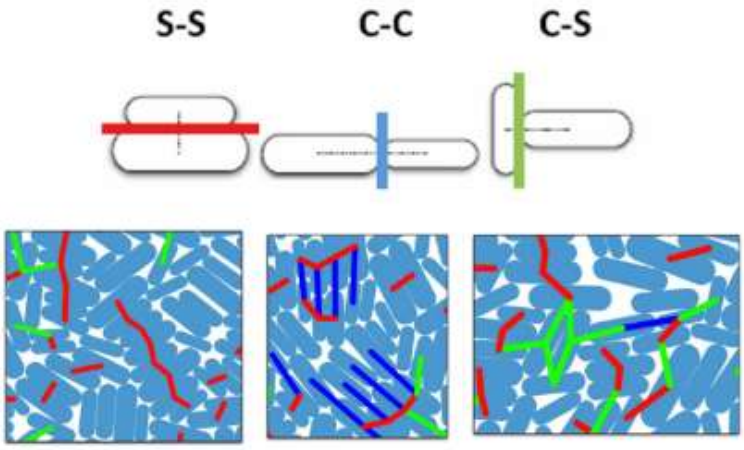

Figure I.28. a) Principal contact modes: side-side (S-S), cap-cap (C-C), cap-side (C-S). b) Direction of force contacts. Modified from Azema and Radjaï, 2012.

contacts, oriented orthogonally to the major principal stress direction, capturing the strongest force chains. The largest and most intense force chains are therefore found where there is a majority of side-to-side contact.

A quantification of force propagation in particles of granular systems is shown in figure 29. The branch vector is defined as a line connecting the centre of the particles. For spherical particles, the branch vector is equal to the sum of the radii of the circumferences. For non-spherical particles, the branch vector has different values that change as the particles translate and rotate (Bergantz et al., 2017).

How is stress transmitted between particles? There is a statistical approach (Azema and Radjaï, 2012) through branch vectors (defined as the vector that connects the center of the particles, to describe the fabric anisotropy (fig. I.29), and contact force orientations. The formula for calculating the stress tensor is:

$$\sigma = \frac{1}{v}\sum_{c\in v} f_\alpha^c l_\beta^c$$

Where σ is the stress tensor, V is the volume of the sample, l^c are the branch vectors and f^c are the contact force vectors (force vector that is formed in contact between two granules) at contact c.

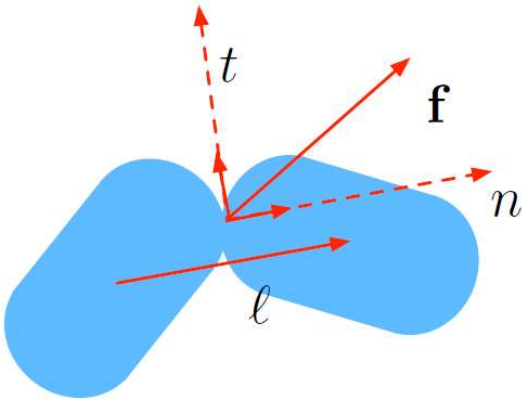

Figure I.29. Branch vector; f: force vector; n,t: local contact frame. From Azema and Radjaï, 2012.

In this thesis, the force chains were studied from a quantitative and statistical point of view. After the deformation experiments, the samples were photographed by SEM and the types of contacts formed between the plagioclases were studied. Although the

samples show good correlations to the information provided by the bibliography above, the studies performed still remain preliminary. Force chains play a very important role in the propagation of deformation and the formation of shear bands, so further numerical modelling and experimental studies are needed to better understand this phenomenon.

7. Comparison with previous experimental works

The first experimental studies on the rheology of magmatic suspensions were done on almost isometric particles, such as quartz (Caricchi et al., 2007), corundum (Champallier et al., 2008), alumina grains (Arbaret et al., 2007), or natural suspensions (Caricchi et al., 2008; Cordonnier et al., 2009). In recent years, due to developments in this area of research and technological advances, it has been possible to expand the field of study not only to circular particles, but also to more complex shapes, through numerical modeling.

High pressure and high temperature deformation experiments on magmatic suspensions consisting of anisometric plagioclase particles were carried out by (Picard et al., 2011). In his experiments, it is noted how the crystal content and the aspect ratio of the crystals strongly influence the rheology of the volcanic mush. Viscosity increases by about five orders of magnitude compared to samples made of isometric quartz particles. The samples considered have a crystal content of 0.38 and 0.52. The first was subjected to compression deformation experiments, while the second was subjected to torsion deformation experiments, both using a Paterson apparatus (fig. I.30). The parameters of the experiments were a confinement pressure of 300 MPa, temperatures of 900°C and 800°C for ϕ_s = 0.38 and 0.52 respectively and strain rates ranging from 1 x 10^{-5} s^{-1} to 1 x 10^{-3} s^{-1}. Analyzing the post deformation samples, they have a non-Newtonian, shear-thinning rheological behavior, as observed also for anisometric and near isometric particles (Caricchi et al., 2008, 2007; Champallier et al., 2008; Cordonnier et al., 2009; Lavallée et al., 2007). His experiments are comparable to natural systems: alignments and tilting of feldspar crystals in igneous rocks (Vernon, 2018) were found in samples with low crystalline content (ϕ_s <0.4) where the rotation and translation of the

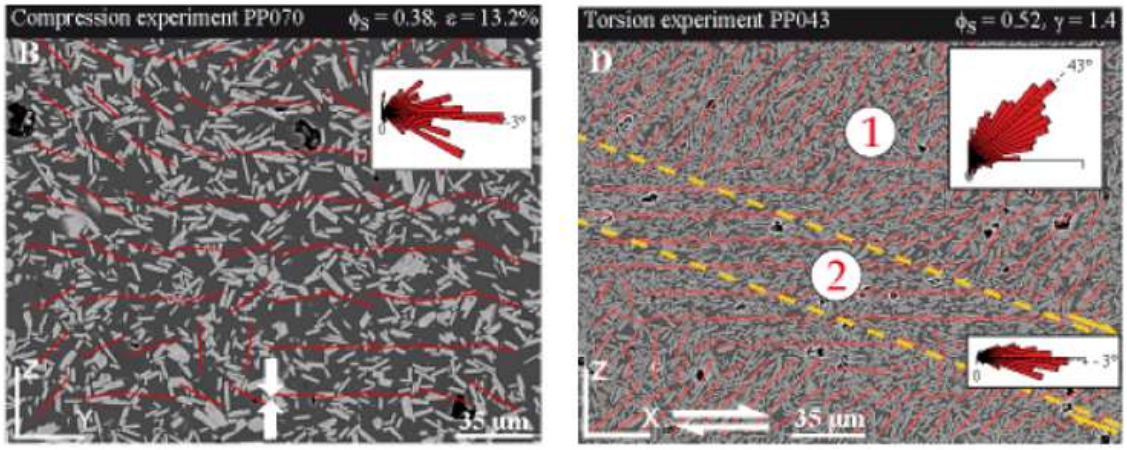

Figure I.30. SEM images of deformed sample with Paterson apparatus. Left: sample with ϕ_s = 0.38 (PP070). Right: sample with ϕ_s = 0.52 (PP043). In the upper and lower insets are shown the rose diagrams of the local plagioclase fabric in the penetrative zone (zone 1) and in the shear zone. Silicic glass is in dark grey, plagioclase in light grey and gas bubble in black. The red lines are the long axes of the local crystal fabric. The type of deformation is indicated by white arrows (Picard et al., 2011).

crystals generates a pervasive fabric (Fernandez et al., 1983). Thus by increasing the strain, there is a stabilization of stress, as also occurs in Picard's experiments, and this fabric can represent cinematic indicators of an early magmatic flow (Philpotts and Asher, 1994). Reaching crystalline contents of 0.5, structures called "trachyte weaving" (Smith, 2002) are formed, where strain partitioning and the development of two fabrics take place (Vigneresse and Tikoff, 1999). This has been seen in lavas rich in feldspar and have similarly oriented structures to S/C and can give information on shear directions (Nicolas, 1992). These textural domains can be found on the walls of the conduit and on the bases and flanks of trachytic lava domes (Zavada et al., 2009). By increasing the crystal content, the viscosity also increases by at least five orders of magnitude, due to the formation of background masses filled with microliths (up to 50% by volume) of plagioclase (Burgisser et al., 2010). This could strongly influence the occurrence of an explosive eruption of gas-bearing magmas: the reduction in the ascent rate of the magma flow could cause the formation of a magma plug and an over pressurization of the underlying magma. The conclusion is that by increasing the crystalline fraction, the system pass from a nearly steady-state flow to a strain weakening behavior, due to the transition from pervasive to fabric to strain-partitioning fabric.

For higher crystalline contents, deformation experiments at high pressures and deformations were performed by (Arbaret et al., 2007). His results show how rheological evolution of magma flow can be during ascent and location, although deformation rate, magma composition and temperature could be different. The analyzed samples consisted of alumina grains, with a crystalline content between 0 and 76%. The conditions of the torsion experiments are pressure of 300 MPa, temperatures between 475°C and 1000°C and shear strain rate between 2×10^{-5} and 2×10^{-3} s^{-1}.

For crystalline fractions between 0.0 and 0.16, there is a Newtonian behavior, with a viscosity of 10.3 Pa.s. By increasing the crystalline content, between 0.16 and 0.54, the viscosity increases by an order of magnitude and the crystals are oriented almost parallel to the shear direction, undergoing a rotation (fig. I.31). Between 0.54 and 0.65, viscosity increases by 1.5 orders of magnitude, and 2 domains of alternating orientations appear. At 0.65 and temperature below 550°C, tensile and intergranular fractures appear, with an extensional fabric almost parallel to the shortening direction. At crystalline fractions $\phi_s \geq 0.54$, the deformation is more and more heterogeneous, shear bands and S/C structures are formed. Due to the high crystalline content, the granules in contact with each other are not able to accommodate local stress through rotation and tilting, but develop intergranular fractures. If the fracturing process is strong, cataclastic behavior

occurs. The deformation process ends when crystal contents equal to 0.76 are reached, where no deformation structures develop.

Magmas located in depth have deformation rates around 10^{-10} s^{-1} (Petford, 2003) while

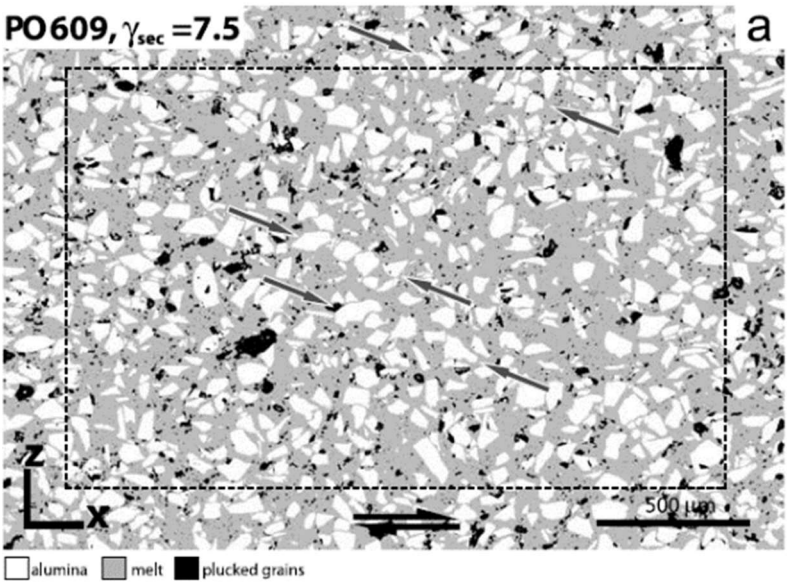

Figure I.31. False grey-level image of [XZ] of PO609 with crystal content of 0.34. Dark grey arrows point out the orientation of 20° (Arbaret et al., 2007).

those reached in Arbaret's experiments represent volcanic dike or sill placed at low depths, or silicic magmas erupted on the surface to form domes and lava flows from 10^{-3} to 10^{-7} s^{-1} . In this environment, the generation of ductile to brittle shear faults on the surface of near-solid spines and along sidewalls of magma conduits can be more easily generated due to the development of localization microstructures, such as intergranular fracturing and melt-filled shear bands.

Further deformation experiments were carried out by (Caricchi et al., 2007). The high temperature and pressure conditions are 500-900°C and 250 MPa respectively, crystal content between 0.5 and 0.8 and different strain rates. The conditions analysed are comparable to those that can be found in volcanic conduits. By studying results and numerical modeling that simulate the ascent of the magma, it is shown how the strain rate modifies the behavior inside the volcanic conduit.

For crystal contents between 0.1 and 0.6 (fig. I.32a), considering a silicate melt suspension, the formation of microstructures occurs with the transition from Newtonian to shear thinning behavior, increasing the strain rate. The application of high strain rates

or high stress causes particles aggregation, which align following the flow direction (Lyon et al., 2001).

For high crystalline contents (fig. I.32b), the dynamics are different because the particles are in contact with each other. It is possible to have a flow only when there are expansion phenomena, which allows the particles to move.

Experiments at high pressures and temperatures in partially molten rocks have been carried out in the past to study melt migration processes. Stacked discs of haplotonalitic glass and natural basalt were deformed in torsion by (Laumonier, 2013; Laumonier et al., 2015). The crystalline fraction of the basalt changed with temperature. At lower temperatures, there was no interaction between the haplotonalitic melt and the basalt, as the basalt had a high crystalline fraction and behaved as a rigid mush. At higher temperatures, the basaltic mush broke.

Another work is by (Pistone et al., 2013, 2012). They deformed haplogranitic mush with bubbles in torsion. Rich bands of molten material formed in some mush samples due to the accommodation of heterogeneous deformation during deformation.

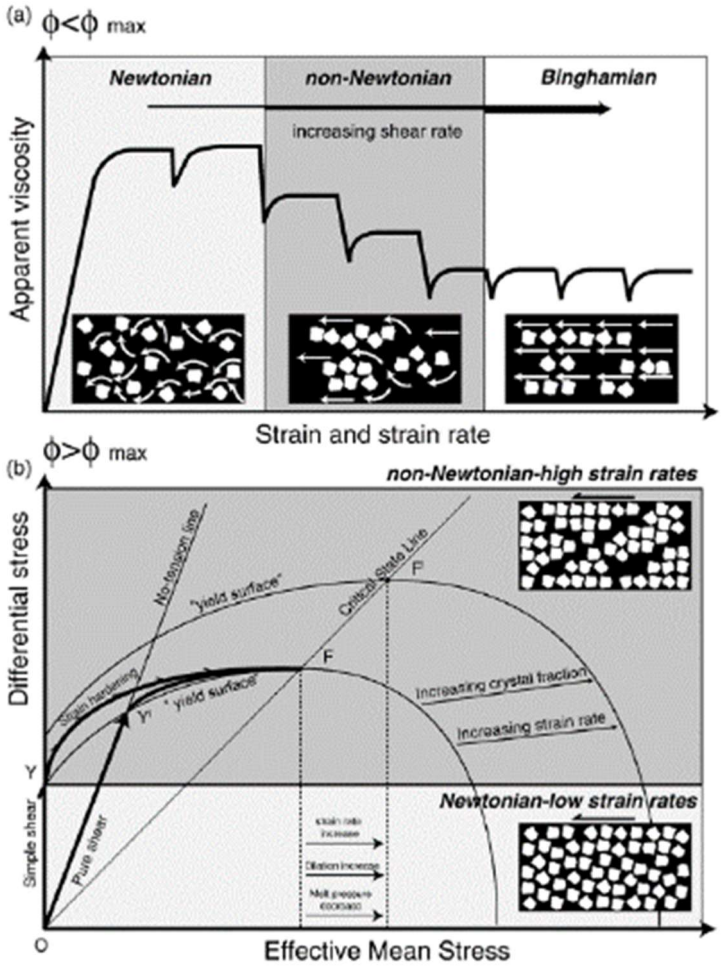

Figure I.32. Diagram shows the relationships between microstructures and rheological behavior of the experiments. a) Apparent viscosity plotted against strain. In the lower part of the diagram are shown the microstructures generated during the experiments that are responsible for the observed rheological transitions. At low strain rates, there is Newtonian behavior and viscosity does not vary. By increasing the strain rate, the system shifts from a non-Newtonian behavior to a Binghamian behavior. b) Diagram illustrating the relationship between differential stress and effective mean stress, considering the samples subjected to a deformation experiment in torsion and one in compression. The paths OY and OYI represent the loading trajectories for torsion and compression experiments, respectively. When the lines meet the yield surface, irreversible deformation begins. The dilation, following the deformation, decreases the melt pressure driving the loading path toward the critical state line. In F, the flow of the material continues at constant differential stress and constant effective mean stress. The amount of dilation is directly proportional to strain rate and inversely proportional to the melt pressure. The increase of dilation with strain rate promotes the localization (Caricchi et al.,2007).

8. Crystal morphology

The interconnected network of crystals found in mushes gives rise to characteristic rheological and microstructural features. In particular, the results of this work show that the aspect ratio R of the particles is very important for the propagation of deformation in the suspension and thus for the formation of localized deformation structures. Plagioclase crystals are the starting material for deformation experiments. Experiments have been carried out on both high aspect ratio (R = 2) and low aspect ratio (R = 4) plagioclase crystals. For this reason, a section is dedicated to the shape of the crystals and how it can influence the behaviour of a mush.

Jeffery's model (1922) is one of the first works that describes the rotation of particles inside a viscous suspension subjected to a homogeneous shear stress, considering the long axis a and the short axis b. The particles rotate continuously following an orbit whose period depends on the aspect ratio R when this is greater than 1. When the value is equal to 1, there is a continuous rotation at a constant speed equal to half the speed of deformation. Analogous deformation experiments with symmetries higher than monocline confirm this rotation model (Willis, 1977; Arbaret et al., 2001), therefore it can be used to simulate the behavior of solid particles during a simple shear deformation.

(Graham et al., 2023) investigate how crystal shape can affect the behaviour of volatiles and outgassing processes in crystal-rich magmas. They carry out decompression experiments at high pressure and high temperature. The starting materials are rhyolitic glasses with corundum crystals (aspect ratio R = 1.8 ± 0.6) and wollastonite crystals (aspect ratio R = 10 ± 5.5). These crystals are added to the starting material in different percentages in order to study the influence of the aspect ratio R on the outgassing processes (fig. I.33). The results show how the crystals with a high aspect ratio R (wollastonite) favour the permeability at a critical melt porosity ϕ_c-melt at vesicle values to lower values compared to experiments performed without crystals, such as the experiments of (deGraffenried et al., 2019; Lindoo et al., 2016). The high crystal content and the high aspect ratio R of the crystals favour the formation of random loose packing (RLP), where the crystals move and touch each other. The bubbles have less melt and less space to form, causing the bubbles to coalesce and connect. Therefore, permeability is reached faster when there are crystals with a high aspect ratio R.

In addition, a high aspect ratio R corresponds to greater bubble connection and coalescence. With a high aspect ratio, the size of the bubbles is smaller than those formed with low aspect ratio crystals.

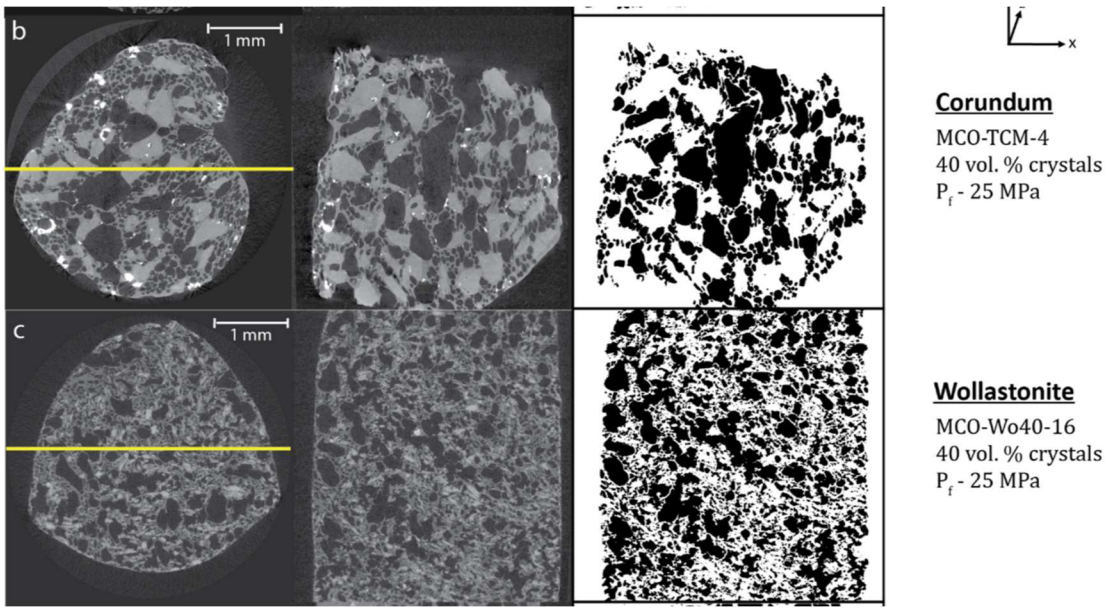

Figure I.33. Slices from decompression experiments. The images are X-ray computed tomography (XCT) images. At the top, experiment carried out on crystals with a low aspect ratio R (corundum). At the bottom, experiments carried out on crystals with a high aspect ratio (wollastonite). The bubbles are black. From Graham et al., 2023.

(Hoyos et al., 2022) performed compaction experiments with particles of different geometries and aspect ratios R (1:1, 2:1 and 4:1). They investigated how the aspect ratio R can influence melt extraction processes by analysing repacking mechanisms following pore space reduction. They measured the resistance to deformation over the time of each experiment with different aspect ratios R. The results of the experiments are shown in figure I.34. The behaviour of spherical particles, 2:1 particles and 4:1 particles has been plotted. As the load increased, the spherical particles show a regular behaviour with an increase in displacement. The 2:1 particles show one drop at load values around 20. The 4:1 particles show two drops, stronger than the 2:1 particles. The regularity of the curve without drops (spherical particles) is due to the movement of the particles, which rotate and translate. A low aspect ratio R of the particles makes their motion continuous without the formation of strong force chains. Curves with drops (2:1, 4:1)

reflect a more rigid structure, with particles that can move less due to their shape and the formation of strong force chains. If the deformation is too great, the force chains break and the drop is formed. In conclusion there are two mechanisms that can cause melt extraction. The first is widespread frictional dissipation between adjacent particles. This leads to continuous deformation and melt extraction. The second is associated with the development of force chains that produce localised and instantaneous deformation. Depending on the shape and aspect ratio R of the particles, one deformation mechanism will predominate over the other. The largest deformations were found for samples with a higher aspect ratio R.

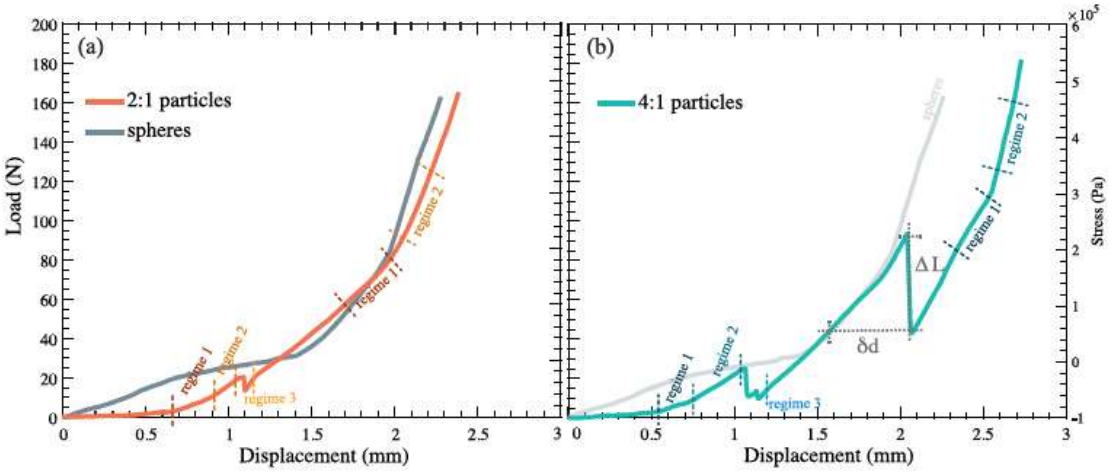

Figure I.34. Load vs. displacement graphs. Each curve represents a sample with a different R aspect ratio (grey 1:1, red 2:1, blue 4:1). From (Hoyos et al., 2022).

In (Amirrahmat et al., 2019), the aspect ratio R of the particles is studied in relation to the number of average contacts (ANC) in the suspension. They analysed the kinematic behaviour of particles in granular samples under triaxial deformation using 3D analysis and discrete element DEM studies. The applied deformation induced the formation of shear micro-bands (MSBs), which vary as a function of the parameters density, confining pressure, particle aspect ratio R and number of contacts. The results show that the greater the number of contacts, the greater the deformation of the sample. Samples with a higher aspect ratio R show a greater variation in ACN value and therefore a greater number of contacts with deformation. Thus, a higher aspect ratio R produces more deformation in the sample, as expressed by the formation of micro-shear bands.

9. Mush classification

Many factors can change the mush characteristics and this makes their classification very difficult. Considering the factors analyzed in this work (crystal content, crystal morphology and strain rate), a classification has been established (fig. I.35). Based on the crystal content, a magmatic body is divided into solid suspension (crystals are not in contact, the body has viscous behaviour), loose mush (crystals are in contact, there is propagation of deformation with foliation and C' shear bands formation), locked-up mush (crystals are in contact, there is strong localized deformation with shear band and crystal breakage due to the high crystal content) and solid-like system (the crystal content is extremely high, the melt is unable to move and the magmatic body can only be deformed by fracturing). Depending on crystal morphology and deformation rates, these boundaries could shift to higher or lower crystal contents. It will be the task of this thesis to investigate these boundaries.

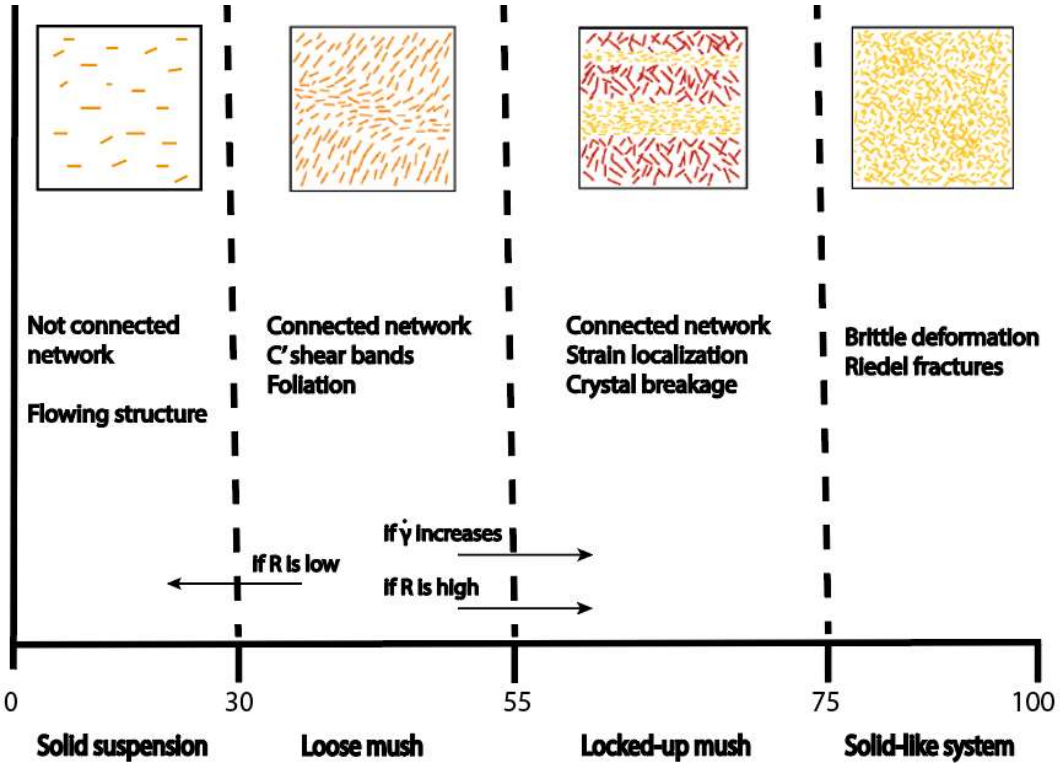

Figure I.35. Mush classification depending on crystal content.

Experimental method and analytic techniques

Résumé Chapitre II - Méthode expérimentale et techniques d'analyse

Dans cette thèse de doctorat expérimentale, les matériaux de départ synthétisés l'ont été avec une composition aplotonique, la teneur en cristaux variant entre 0,58 et 0,95. Les poudres de verre préalablement synthétisées ($HAn_{20}Q_{15}$ et $HAn_{50}Q_{15}$, (Laumonier, 2013)) ont été placées dans des capsules d'or. De l'eau à 3 wt% a ensuite été ajoutée. Les capsules ont été soudées et placées dans un four à 100°C pendant une journée pour vérifier l'étanchéité. Ensuite, les capsules ont été placées dans un IHPV à des températures de 790°C à 810°C et à une pression de 300 MPa. La durée de l'expérience était variable, allant de 7 à 21 jours. Après les expériences de synthèse, les échantillons ont été retirés de la capsule en or, coupés, limés et préparés pour les expériences de déformation. Les expériences de déformation réalisées dans cette thèse sont des expériences de torsion, effectuées avec la presse Paterson. Les échantillons ont été déformés dans différentes conditions de déformation (déformation finie et vitesse de déformation). Les conditions de déformation, de pression et de température choisies reproduisent un environnement volcanique naturel. Les expériences de déformation ont duré de 20 minutes à 24 heures. À la fin de l'expérience, l'échantillon a été retiré de l'autoclave et photographié pour les reconstructions panoramiques. L'échantillon a ensuite été coupé, limé et analysé en 2D, 3D et chimiquement. Les analyses des images 2D ont été réalisées au MEB (microscope électronique à balayage). Des photographies de tous les échantillons ont été prises à différents grossissements et les microstructures ont été observées. Les analyses en 3D ont été effectuées à l'EBSD (Electron Backscatter Diffraction), où des cartes d'orientation des minéraux ont été réalisées. Les analyses chimiques ont été effectuées à l'EPMA (microanalyse par sonde électronique). L'analyse des images a été réalisée à l'aide d'Adobe Illustrator, l'analyse statistique de l'orientation préférentielle de la forme des cristaux (SPO) à l'aide de SPO2003 et d'Intercept, et les résultats ont été représentés graphiquement à l'aide du logiciel Grapher. Les analyses sur l'orientation préférentielle des cristaux (CPO) ont été effectuées à l'aide des logiciels AZtecCrystal et Matlab. Les données ont été traitées numériquement à l'aide du logiciel Excel.

II. Experimental method and analytic techniques

1. Internally heated pressure vessel (IHPV)

The internally heated pressure vessels (Gros bleu, Gros vert, Alambic; ISTO) have been used to synthesized all the starting materials for the deformation experiments. They consist to a high pressure chamber, compressed with argon. The maximum temperature is 1400°C and it is checked costantly by the double type K thermocouples (5 cm spacing between the two reading points, type K is Nickel / Chromium - Nickel / Aluminum) made up of two nested cylinders (fig. II. 1a). The high pressure chamber is made of two nested cylinders and between these two there is a water cooling circuit (fig. II.1b).

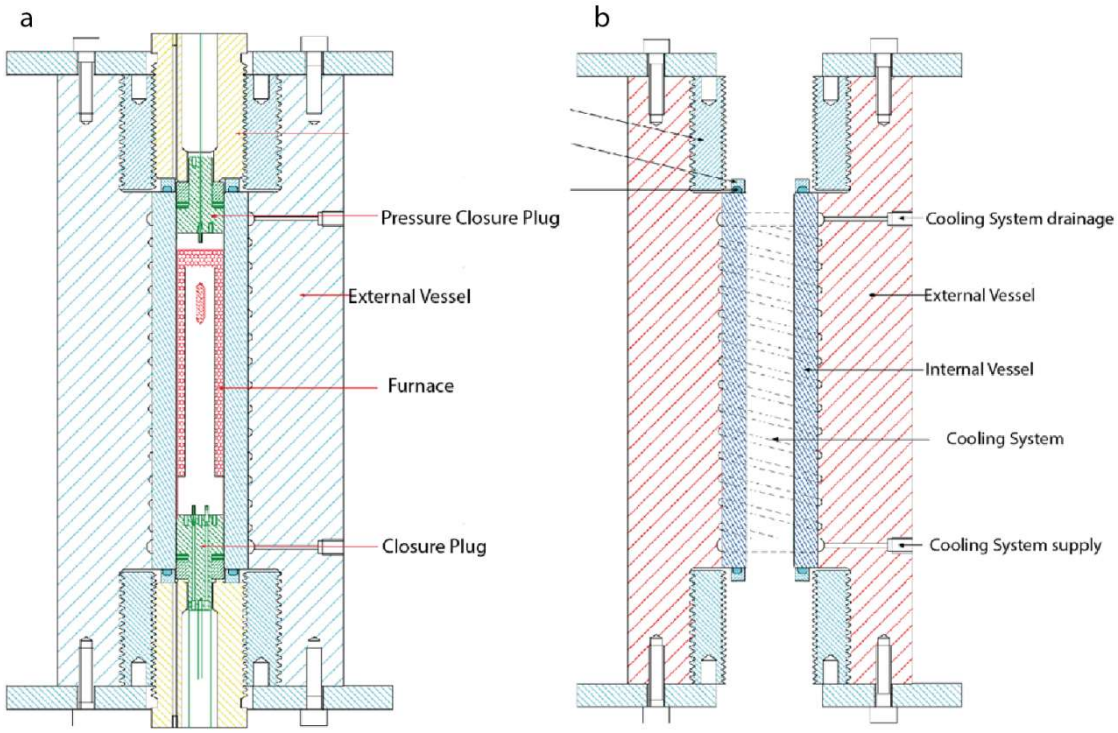

Figure II.1. Internally heated pressure vessel. a) In blue, the high pressure enclosure, in red: the oven, in green: the obturators, in yellow: the plugs. b) Longitudinal section. In red: the external cylinder, in blue: the internal cylinder, in black: the cooling circuit (after Champallier, 2005).

The Kanthal resistance is located inside the autoclave. To ensure the sealing of the experiments, the autoclave is closed by two obturator, while to ensure the flow of the gas, there is another pressure shutter on the back of the autoclave. The obturators located at the front allows passage of the furnace power, the thermocouples and the rapid quench system. They are surrounded by wool silica that, being a thermal insulator, can reduce convection and focus on the working area of the oven, the hot spot.

The hot spot represents an isothermal area (approximately + 1 ° C) located between the two reading points in which the capsules containing the samples are placed (fig. II.2).

The temperature is gradually increased, causing the thermal expansion of the argon. In this way it is possible to reach the desired pressure (200 MPa). Once the synthesization is over, the furnace power is turned off and an isobaric quenching, keeping the pressure constant to avoid the nucleation of bubbles, is performed. The cooling rate is 100°C/minute circa, which is a value fit for the oven. It has not been possible to perform a rapid quench, because the size of the capsules were too big (Roux and Lefèvre, 1992; DiCarlo et al., 2006). Furthermore the cinetic of microlite cristallisation from an haplotonalitic melt is low enough to avoid any significant cristalisation during the cooling stage. Finally, when the temperature is around 100°C (much below the glass transition temperature), the autoclave is decompressed and the sample is removed.

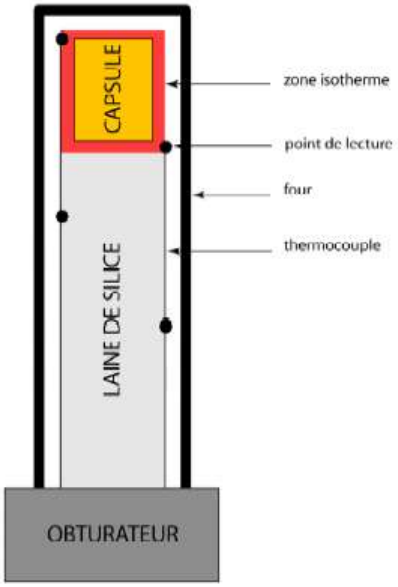

Figure II.2. Schematic layout of the thermocouples and the capsule in relation to the isothermal zone of the oven.

2. Pressure and temperature procedures in synthesis experiments

The first step is to reach a pressure of 50 MPa. To obtain this pressure, the system is pressurised by injecting argon, or another inert gas, through an air pump. Once the pressure of 50 MPa is reached, the argon injection is stopped. Higher pressure values are achieved through the action of one or two hydraulic multipliers, depending on the pressure required. In this work the final pressure for the experiments is 300 MPa. To reach this pressure, the system is pressurised up to 200 MPa, then the temperature is raised manually, which allows 300 MPa to be reached by thermal expansion of the argon. A regulator in the control panel of the autoclave is able to stabilise the temperature plateau. The controller can be used to programme decreasing temperature ramps for synthesis experiments. Once the experiment is finished, the temperature is lowered at a constant pressure (isobaric quenching, fig. II.3). The temperature is lowered at a rate of approximately 80-100°C/min in order to preserve dissolved volatiles and reduce the nucleation of a gas phase (Champellier, 2005). Non-equilibrium crystalline fractions, or quenching phases, may appear before the glass transition temperature (Tg). However, the cooling rate is enough to prevent quenching phases from crystallising (Champellier, 2005). Finally, a temperature slightly below the glass transition temperature is reached and maintained for six hours (fig. II.3). This process prevents fracturing of the experimental sample, as it promotes 'relaxation' of the silicate glass and it decreases the surface tension.

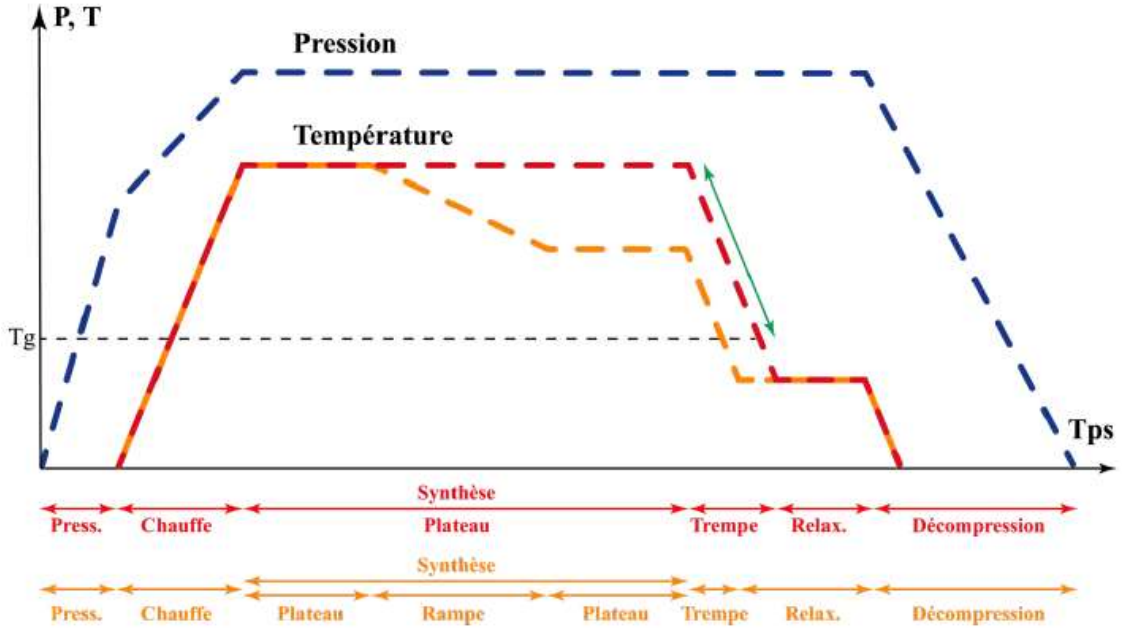

Figure II.3. Pressure and temperature paths in synthesis experiments (modified from Laumonier, 2013). The orange line represents the dynamic condition of the experiment with a progressive drop in temperature at constant pressure. If the experiment is conducted in a constant state, pressure is represented by the blue line and temperature by the red line. Tg = glass transition. Press = first pressure phase. Relax = period in which the glass is 'relaxed', after passing the glass transition phase. glass transition.

3. Paterson press

The Paterson press (fig.II.4) is a gas-powered, internally heated autoclave designed for the study of rock deformation at high pressure (P<7 kbar) and high temperature (T<1400°C).

The sample is deformed by an engine located outside the autoclave at atmospheric pressure. Through the "internal load cell" it is possible to precisely measure the deformation and the stress applied to the sample subjected to pressure, expressed in axial force (N) and / or moment (N.m) applied to the sample.

The components and parts of the Paterson press are shown in figure II.5. The resistance is made of molybdenum. Under the furnace there is the internal measuring cell, while the external measuring cell is located under the autoclave, the latter allows to measure the force applied by the motor and the deformation of the sample.

The action of the motor located under the autoclave allows the coaxial deformation, which is transmitted through a piston and through the internal cell. Using a system of dynamic joints, the piston passes through the obturators.

Figure II.4. Paterson press pictures. Left: front press, right: back press.

In the case of torsional deformation, the motor is located above the autoclave. The angular displacement of the sample is measured by a rotary displacement converter. The torsion module initiates the action of a gear that allows a rotational movement of the upper half column. The lower half-column, on the other hand, does not rotate, so the sample must accommodate by deformation the angular displacement between the upper half-column and the lower half-column. As with the coaxial deformation, the transmission of the deformation occurs through the pressure shutter and the dynamic sealing system. The joints are equal to the difference between the forces measured by the two cells, internal and external.

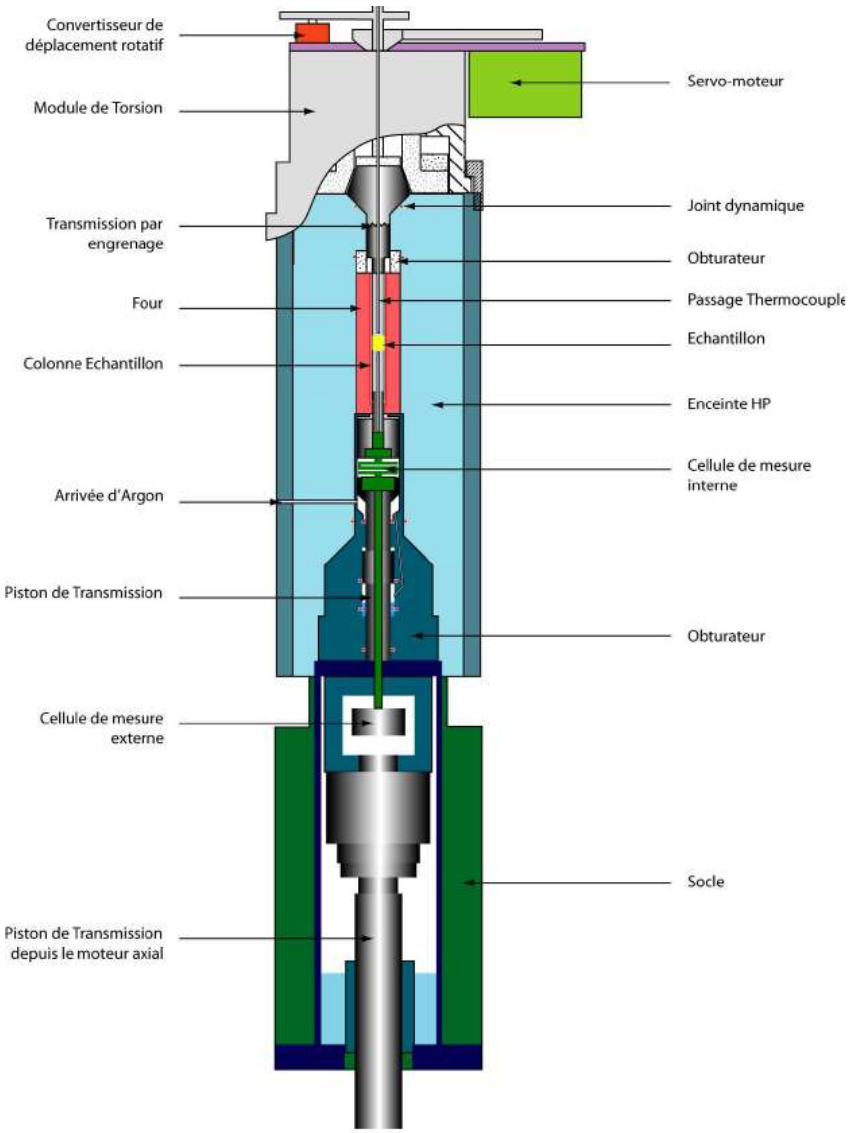

Figure II.5. Paterson press with torsion module (Champallier, 2005).

The sample column is a set of pistons covered with a "jaquette" which allows to transmit the stress to the sample (fig. II.6). The sample is located in the center, and is bordered both above and below by two 3 mm alumina discs (spacer), two alumina pistons and two zirconia pistons (PSZ). The surfaces of the discs must be perfectly flat, parallel to each other and perpendicular to the axis of the jacket in order to ensure a perfect tranfer of the stress to the sample without any slip between the solid cylinders (see example below). A hole in their center lets the thermocouples get throught them, so the temperature can be read throughout the experiment. Everything is inserted inside a copper or iron jacket which has the task of keeping the structure in position. The choice of jacket depends on the temperatures reached during the deformation experiments. At low temperatures, copper jackets are used (melting point at 1084°C, at 1 atm). Copper is an element that tends not to react with silicate melts, so chemical exchanges between jacket and sample during the experiment are prevented. At high temperatures, iron jackets are used, as the melting point of iron is 1535°C at 1 atm, despite iron being a very reactive element with silicate melts. The jacket is about 25 cm long, 15 mm diameter, 0.2 mm thick. Steel pistons are positioned externally in order to increase the seal of the column and to let not the argon escape. A drive piston is placed at the top of the column in order to link the deformation motor and a steel piston is placed at the bottom of the column to link the measurement cell.

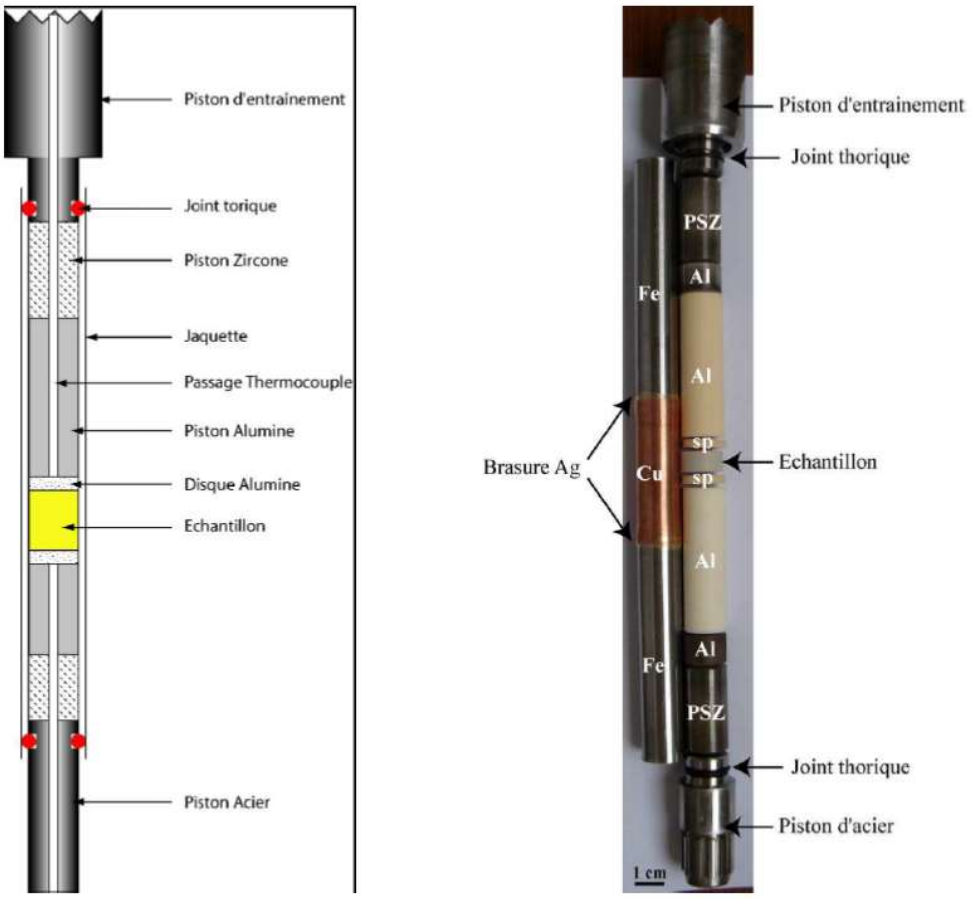

Figure II.6. Sample column illustrations. (a) Section of the sample column. (b) Photograph of aCu jacket and sample column assembly (Champallier, 2005).

The temperature is read using a type K thermocouple which passes through the sample column to come into contact with the top spacer and therefore very close to the sample.

During the deformation experiments, the sample could be blocked and be subjected to flattening (coaxial experiments) or the top part of the column could be mobile (the bottom is fixed) creating a torsional deformation in the sample. Some problem could arise if the resistance of the sample is similar to the resistence of the alumina, because a contact between the alumina components could happen, generating a deformation and leading to non-deformation of the sample (fig. II.7).

For torsion experiments, there is no theoretical limit to the maximum displacement, and the resolution of the displacement reading is 0.001 radians. The internal cell can detect

a moment between 1 and 1000 N.m, with a resolution of 0.1 N.m. The practical deformation rate can be between 10^{-3} to 10^{-7} s^{-1}.

Figure II. 7. Slip at the interface between the alumina disc and the sample (modified after (Arbaret et al., 2007).

4. Mathematical constrain in torsion

The following mathematical relations are used for data analysis and they were developed by Paterson and Olgaard (2000). The samples used in the experiments are cylinders with diameter d, length l and radius R. The sample has 3 characteristic planes: [xy] corresponding to the shear plane; [yz], plane perpendicular to the shear plane and centered and [xz], tangential plane perpendicular to the shear plane (fig. II.8).

The value r is the distance between a point located on one of the faces of the cylinder and the center of this face.

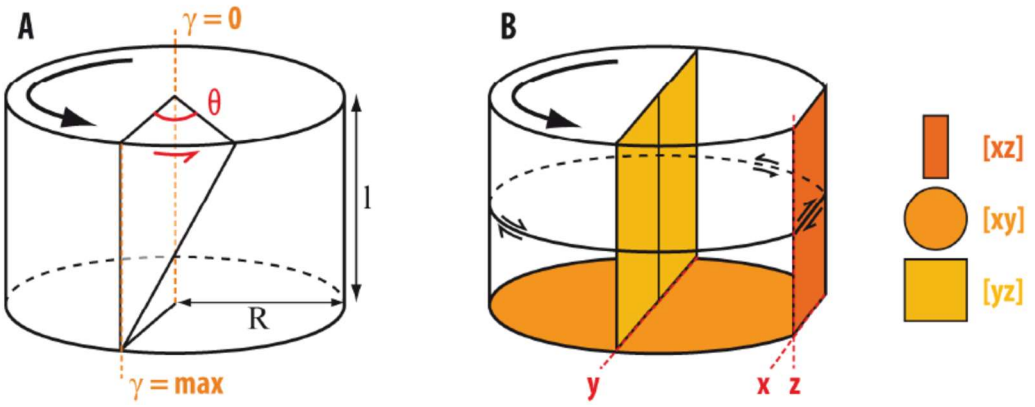

Figure II.8. Geometry of a cylindrical sample for the mathematical relations of a deformation in the Paterson press. A) annotations for torsion, B) observed sections (Laumonier, 2013).

During an experiment, the angular rate of deformation θ is set by the operator. The internal measuring cell measures the applied moment. The maximum strain rate γ is calculated with the equation:

$$\gamma = \frac{R\,\theta}{l}$$

The angular velocity applied to the sample is calculated by deriving the angular displacement with respect to time:

$$\dot{\gamma} = \frac{R\,\dot{\theta}}{l}$$

The deformation rate and deformation speed are not constant during the torsion experiments, the deformation is greater going distant from the center of the sample. If the deformation is considered homogeneous over the whole sample, the deformation increases linearly between the center and the periphery of the sample and it is possible to replace R with r in the equations above.

5. Sample preparation for deformation

For the deformation experiments, about 13 grams of starting material plus 3wt% of water demineralized was placed inside gold capsules (fig. II.9) of 3.5 cm long, 22 mm in diameter and 250 µm thick, then closed and welded with a gold hat.

The first step is welding the base of the capsule, introducing water, and then adding well pressed glass powder in order to avoid empty spaces. The capsule is weighed at each step to ensure that the right percentages of water have been introduced. To verify correct welding three steps are carried out: the first is to insert the capsule in boiling oil at temperature of 200°C. If the capsule is not well sealed, bubbles can be observed. The second step is to put the capsule in an oven at a temperature of 120°C for a day. This allows to check the integrity and also to homogenize the water in the sample. The last step is to insert the sample into the autoclave at pressure of 500 bar. If after this the capsule is still intact, it will most likely withstand the temperature and pressure conditions of the planned experiments. The sample is now ready to be experimented on.

Figure II. 9. Sample preparation. Left: gold capsule after synthesis. Centre: sample taken from the gold capsule. Right: sample drilled and cut into a 15 mm diameter cylinder.

The last welded part of the capsule is to be placed always in the upper isothermal zone of the vessel. Consequently, the lower part is the one welded first, where water has been deposited and placed in the lower and isothermal zone of the furnace. The dynamics of crystallization of plagioclases during the experiment is very slow, and during the cooling process there is no nucleation of any plagioclase crystals. SEM analyzes are performed on the upper, lower and central part of the sample to ensure its homogeneity. The deformation rate and deformation speed are not constant during the torsion experiments, the deformation is greater going distant from the center of the sample. If the deformation is considered homogeneous over the whole sample, the deformation increases linearly between the center and the periphery of the sample and it is possible to replace R with r in the equations above.

6. Scanning electron microscope (SEM)

The samples chosen for analysis were cut along a plane parallel to the mineral lineation and orthogonal to the foliation, corresponding to the [x;z] structural plane, where x represents the mineral lineation and z is the normal to the foliation plane.

All the samples, both experimental and natural, are observed through the use of a scanning electron microscope (SEM, model JEOL JSM-6400, ISTO). The analysis can be carried out with two different imaging modes:

- Secondary electron emission (SEI imaging) - the morphology of the sample is observed, and the contrasts depend on the reliefs of the samples.

- Emission of backscattered electrons (BSE imaging) - the contrasts are given by the average atomic numbers of the phases and an image of the chemical composition is obtained.

In this work is paramount to obtain images with high resolution, in order to recognize the different textures formed during the experiments. For this reason, the SEM analysis were performed using BSE imaging, to obtain the morphology of the smallest plagioclase crystals and to be able to process them with software's such as Adobe Illustrator, Gimp, SPO2003 and Intercept2003.

7. Electron micro probe analyzer (EPMA)

Electron microprobe analysis is a non-destructive analysis to determine the chemical composition of a phase. The instrument used in this study, located at ISTO, is a Cameca SX50 (Merlin Compact ZEISS) equipped with 5 spectrometers. The sample to be analyzed is bombarded by an electron beam. The analyzed crystals or glasses will react by emitting radiation whose angle is characteristic for each element. The detectors, positioned at different inclinations, will record some elements in the form of intensity of radiation. These radiation intensities are then compared with calibrated intensities on samples of known chemical composition. In this study four elements (Na, Al, Si, and Ca) were analyzed, since the phases analyzed are experimental plagioclases and glasses. For plagioclases analysis, the instrument was set with the following parameters: acceleration voltage of 15 kV, working distance of 10 mm, with focused incident electrons beam (for glass analysis, the beam is defocalized 6 x 6 μm).

8. Measurements of crystallographic orientations by EBSD

Electron backscatter diffraction (EBSD), also known as backscatter Kikuchi diffraction (BKD), is a diffraction technique that precisely measures the orientation of a crystal lattice for any crystallized material. As coupled to a scanning electron microscope (SEM), the EBSD camera is able to image a phosphor screen that captures the diffracted electrons and gives rise to a diffraction pattern of the crystal lattice (fig. II.10). The resulting electron backscatter diffraction pattern (EBSP) is composed of Kikuchi bands that cross each other and correspond to lattice planes with their respective miller indices (hkl). The relationship between the diffraction pattern and crystal lattice is given by the Bragg's law: $2d_{hkl}.\sin\theta = n.\lambda$, where d_{hkl} is the distance between given lattice planes, as defined by their miller indices (hkl), θ is the Bragg angle, n is an integer and λ, the electrons wavelength.

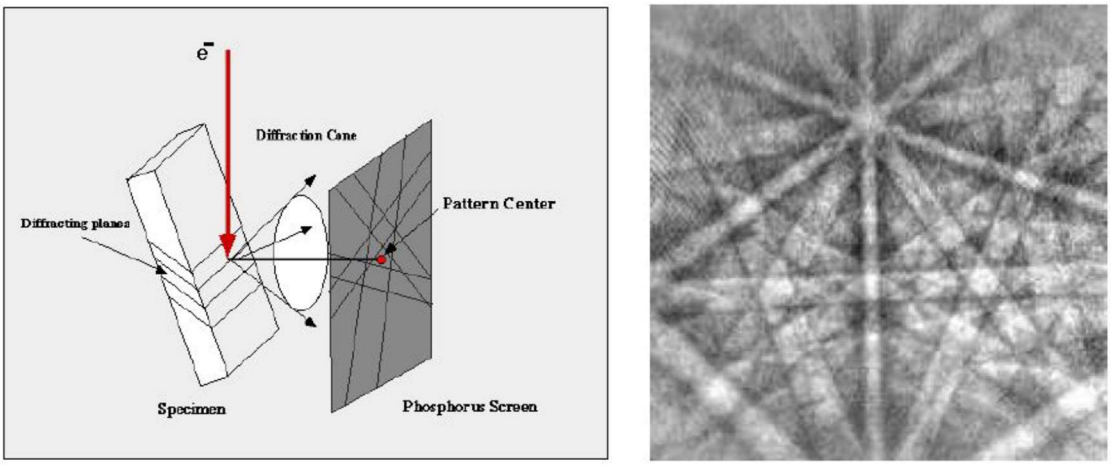

Figure II.10. Left: Schematic representation of the principle of EBSD. Right: Example of a diffraction pattern with Kikuchi bands.

Once the diffraction pattern is captured, the Kikuchi bands are automatically detected using the Hough's transform method, and then compared to a database using distances and angles between reticular planes, grouping them by triplet or quadruplet. In the Oxford system (here using the Aztec 6.0 software), a solution of crystal orientation (within the list of crystal phases provided before analysis) is then proposed or not, depending on different parameters (Mean Average deviation (MAD), number of quadruplets, etc.) that define the quality of indexation (fig. II.11). For instance, no solution is given for a MAD higher than 1.4° and a solution is commonly considered as a good one for a MAD lower than 1. For most cases, data are acquired within a defined area and using a given step size on multiple rows, producing an EBSD map.

After acquisition, the EBSD map is cleaned by removing wild spikes (isolated non-indexed pixels) and removing zero solutions, particularly along grain boundaries. The sample map is finally "reconstructed" by defining grain boundaries and intragranular boundaries as a function of misorientation angles between indexed EBSD pixels. The misorientation angle is defined as the minimum rotation angle (and related rotation axis) required for two patterns to superpose each other. While a value of 10° has been applied for grain boundaries, it has been used angles between 2° and 10° to define intragranular boundaries. Grains with less than 10 pixels are also not considered as grain and removed from the map. EBSD data are finally exploited using the MTEX toolbox for Matlab (version 5.10), giving access to multiple plots that characterize the crystallographic information of our sample, including map representations (intragranular misorientations, grain orientation spread, kernel average

misorientations, etc.) and grain-related features (lattice preferred orientation, grain size, aspect ratio, etc.) collected into pole figures, inverse pole figures and/or graphs.

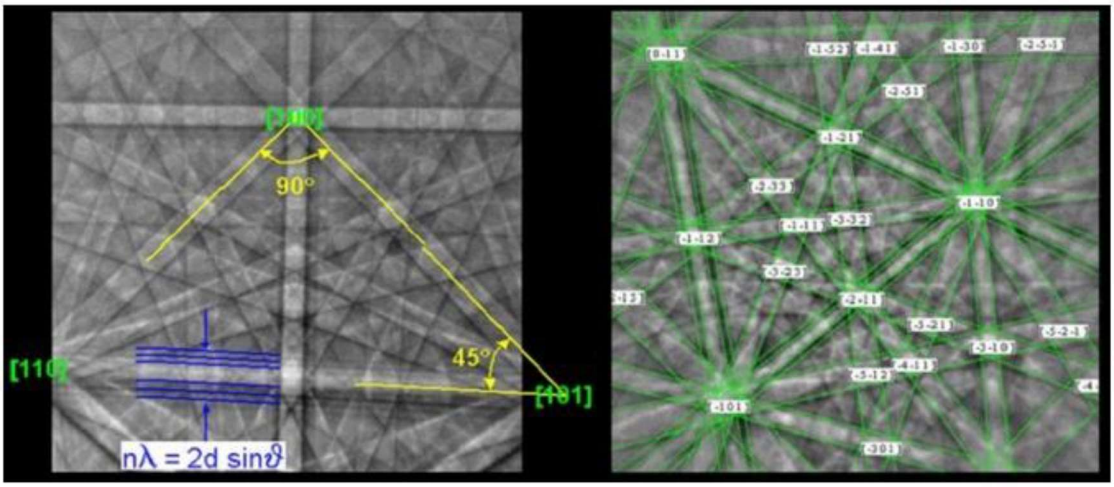

Figure II.11. Left: Example of band detection with angular calculation between Kikuchi bands. Right: Example of indexed diffraction pattern where miller indices are superposed on Kikuchi bands. In this case, the solution is characterized by a MAD far lower than 1. From www.ebsd.info/

9. SPO2003 and Intercept2003 image software

The SEM acquired images of the samples are analyzed through SPO2003, a free software developed by P. Launeau, University of Nantes, France. The moments of inertia method (Launeau, 2004) is used to detect the plagioclase crystals and to obtain parameters of their long axis a, short axis b, the aspect ratio R and their orientation (fig. II.12).

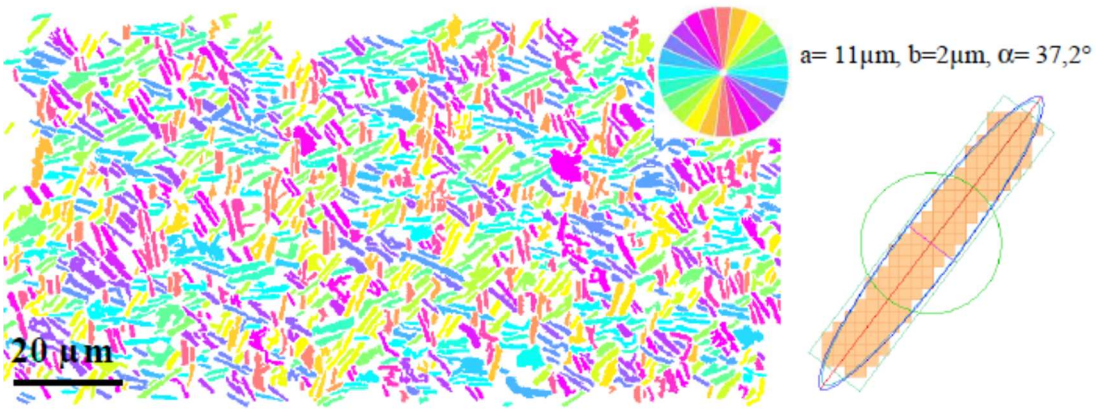

Figure II.12. Left: plagioclase SEM picture composed of plagioclases isolated by hand with Illustrator and colored using SPO2003. The different colors represent different orientations of the crystals. Right: the long axis a, short axis b and orientation angle α values with respect to the vertical of a plagioclase crystal (Picard, 2009).

In case the crystalline content is too high and there is the formation of a connected network of crystals, it will not be possible to measure the preferential orientation of the shape of each particle with the SPO software. In this case it is possible to calculate the shape fabric of the whole population of particles by using the intercept method (Intercetp2003 software from P. Launeau). This APP virtually divides the image into a specific number of sections, defined by the user, which can vary from 1 to 900 (30 x 30) and each one covers the neighboring section by 50% in X and Y, allowing to measure the orientation of local forms (fig. II.13). Graphically, the intercept method is based on a grid with a defined inclination and formed by lines j parallel to each other. The software counts the number of inputs and outputs for each line, and the intercept will be equal to the number of changes in value, calculated for all directions and lines. After completing this operation, a map is obtained that has detected all the contours of the crystals.

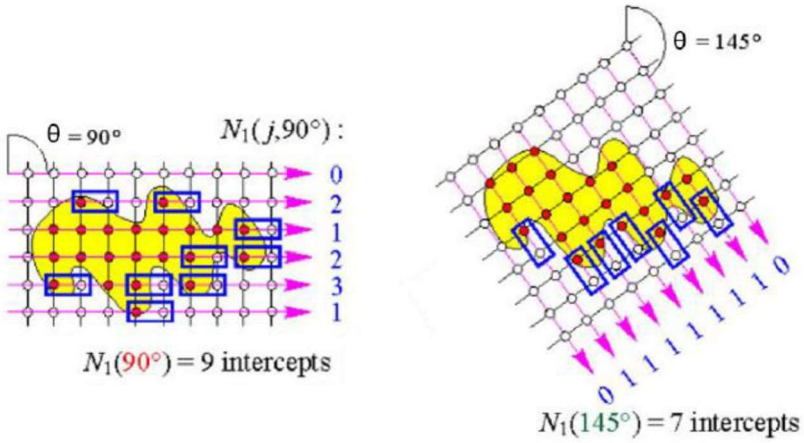

Figure II.13. Illustration of the intercept method (Launeau and Robin, 1996), with an angle grid α = 90° and α = 145°. The white circles represent the analysis points outside the object and the red circles the analysis points inside the object. The number of intercepts for each angular step is equal to the number of times the cursor leaves the object multiplied by the number of lines.

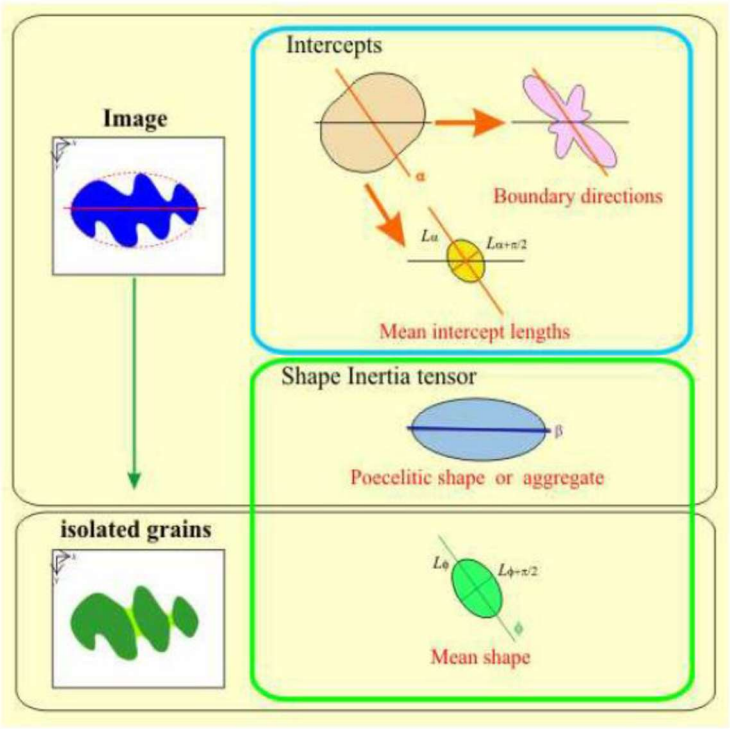

Figure II.14. On the top: Intercept method for an aggregate. On the bottom: Moment of inertia method for a crystal (Launeau, 2004)

For each section analyzed, there will be an ellipse of the mean orientations of the fabric, defined by its long axis a, its short axis b, its eccentricity r (also called aspect ratio r = a / b) and the direction of its long axis a (fig. I.14). An average tensor ellipse of the shape fabric defined by a mean tensor eccentricity R, its long axis a, its short axis b and the direction of its long axis a is then computed.

In figure II.15 the local ellipses is highlighted in green, the long axes in orange and the short axes in blue. For the average values, the colors are dark green, red and dark purple respectively.

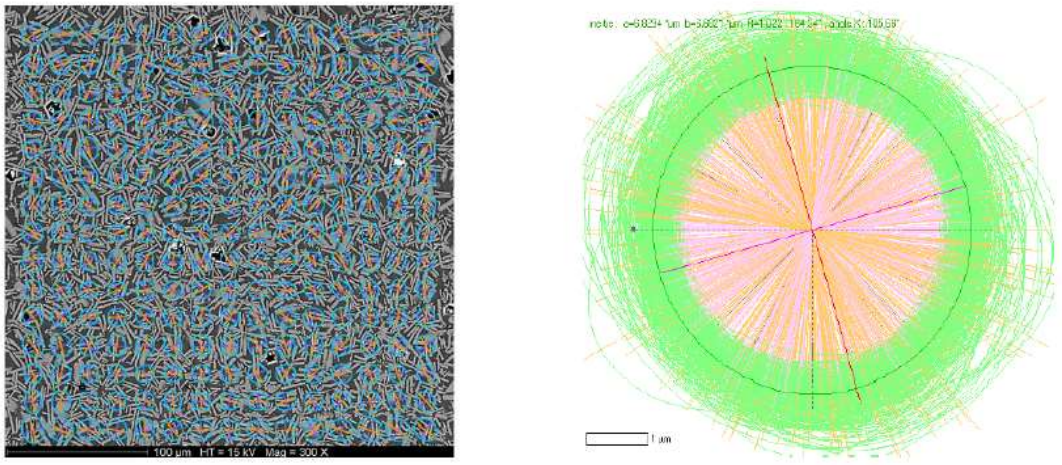

Figure II.15. Left: Local tensor ellipses obtained using Intercept2003 software. The sem picture is composed of plagioclase crystals, divided into 15 x 15 sections. The long axis is in orange, the short axis in purple and the ellipse in blue. Right: Representation of all calculated tensor ellipses. The long axes are orange, the short axes in purple and the tensor ellipses in green. The mean tensor ellipse is in dark green, the long axis in red and the conrto axis in dark purple. At the top of the imagine there are the values of its eccentricity R, its long axis a, its short axis b and its direction of orientation with respect to the vertical.

In this work, the orientation of the starting materials is calculated with respect to the X axis, while for the deformed samples the calculation direction is perpendicular to the shear direction (fig. II.16.)

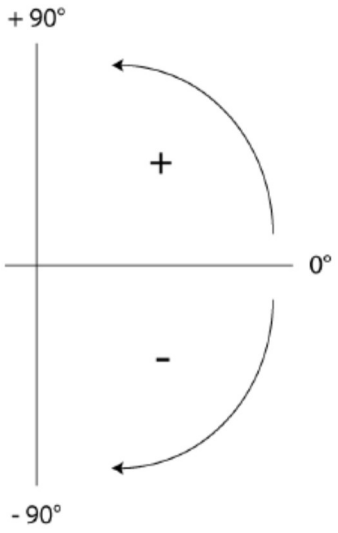

Figure II.16. Orientation directions used in this study, between -90 ° and + 90 °. 0 ° is parallel to the shear direction.

10. Contacts and clusters

After obtaining SEM images of the deformed samples, the proportions and contact relationships between the plagioclase crystals were studied. The contacts between the plagioclases were visualised and drawn by hand using Illustrator software. Type and orientation of contacts between plagioclase crystals were classified and studied following the definition of (Azema and Radjaï, 2012): S-S, side-side, long axis in contact; C-C, cap-cap, short axis in contact; S-C, side-cap, long axis and short axis in contact (fig. II.17)

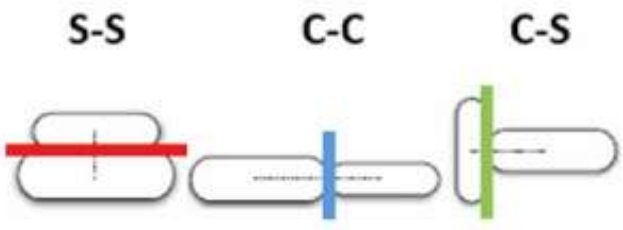

Figure II.17. Principal contact modes: side-side (s-s), cap-cap (c-c), cap-side (c-s). Modified from (Azema and Radjaï, 2012).

Once the contact measurements were complete, the clusters were examined. Clusters are defined as a series of particles in contact with each other, formed by a minimum of 3 particles and with no maximum number (fig. II.18). The contacts considered for the formation of clusters are the S-S and the C-C. For each deformed sample, the orientations of the clusters and the orientations of the contacts of the clusters were studied. The method used is the same as for the study of the contacts: from the SEM images, the clusters and the orientations of the clusters' contacts are drawn by hand using Adobe Illustrator. The data obtained are then plotted using Grapher software.

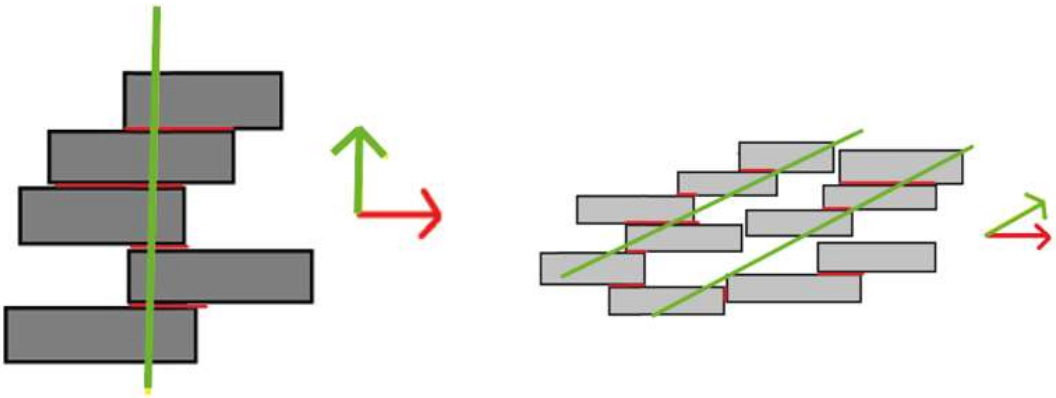

Figure II.18. Plots of different cluster arrangements. Green line: orientation of the cluster, red line: orientation of the contacts in the cluster.

Starting materials

Résumé Chapitre III - Matériaux de départ

Dans cette thèse, plusieurs tests de matériaux de départ ont été effectués avant de choisir le matériau synthétique utilisé pour les expériences de déformation. L'objectif était de trouver un matériau synthétique capable de reproduire une mush volcanique, avec une teneur en cristaux comprise entre 0.50 et 0.90 et composée principalement de plagioclase. Ces minéraux ont une forme allongée, il est donc facile d'étudier leur SPO et CPO. Dans un premier temps, une modélisation a été réalisée à l'aide du logiciel Melts. Différentes compositions chimiques ont été étudiées dans différentes conditions de température, de pression et de teneur en eau. Considérant les résultats obtenus avec le logiciel Melts et des expériences de synthèse réalisées dans des travaux antérieurs avec des compositions chimiques similaires (Laumonier, 2013; Picard, 2009), des expériences de "synthèse test" ont été réalisées. Des matériaux synthétiques ont été placés dans de capsules d'or. Plusieurs expériences de synthèse ont été réalisées à l'aide IHPV, en suivant les conditions de température, de pression et de teneur en eau obtenues avec Melts. Les matériaux de départ pour les tests étaient $HAn_{20}Q_{15}$ (un mélange de compositions d'anorthite et de quartz), $HAn_{50}Q_{15}$ (un mélange de compositions d'anorthite et de quartz), HGN + cristaux de plagioclase (une composition haplogranitique mélangée à des cristaux de plagioclase de la dimension micrométrique. Les teneurs en eau étaient comprises entre 2.0 et 6.0 wt%. Les pressions ont toujours été maintenues constantes à 300 MPa. Les températures ont toujours été maintenues très proches de la température du solidus (730°C- 810°C), car c'est dans cette range de température que se produit la plus grande partie de la nucléation des cristaux. La durée de l'expérience et les rampes de température étaient très variables. Il a été constaté qu'une teneur en eau plus élevée diminuait les processus de nucléation des cristaux, mais qu'une faible teneur en eau favorisait la nucléation du quartz. Une teneur en eau de 3 wt% en poids a donc été choisie. Les températures finales utilisées pour les expériences de synthèse et de déformation étaient comprises entre 790°C et 810°C, avec des durées d'expérience comprises entre 7 et 21 jours et la présence de rampes de température pour quelques expériences seulement. Cela a permis d'obtenir une teneur en cristaux comprise entre 0.58 et 0.95. Le matériau de départ final utilisé pour toutes les expériences était $HAn_{50}Q_{15}$, qui a formé des synthétiques riches en plagioclase avec un rapport d'aspect R = 2.

III. Starting materials

1. Determination of the starting composition

The aim of this work is to study the microstructural and rheological behavior of magmatic suspensions that have different crystalline contents subjected to torsion deformation experiments. Crystals of homogeneous size and shape, anisotropic, immersed in a silicate liquid are the best starting materials. All these criteria can be achieved with plagioclase crystals, and given their strong anisotropy, it is easy to study their shape preferred orientation (mineral fabrics) and their breakage.

All synthesis experiments were performed using an Internally Heated Pressure Vessel (IHPV). The experiments are divided into "test series" and "series".

The "test series" are synthesis experiments performed with small gold capsules (15 mm high, 2.5 mm wide and 400 µm thick). The small capsule size allows more capsules to be placed in the IHPV during the same experiment. In this way it is possible to study the behaviour of samples with different compositions and different water contents.

The "series" are the synthesis experiments carried out with large gold capsules (35 mm high, 22 mm wide and 250 µm thick). The composition, water content and temperature of the experiment are chosen according to the best results of the "test series". For each synthesis experiment, only one capsule is placed in the IHPV. The best starting material for synthesis experiments turned out to be haplonalite. This starting material is consisted by 4 elements: SiO_2, Al_2O_3, Na_2O and CaO, making the crystallization of ferrous and mangnesiferous phases easily prevented. A haplotonalitic composition (HTN) was synthesized during (Champallier, 2005) showing plagioclase and quartz samples under magmatic conditions of 300 MPa and temperatures of 775°C. In order to lower the quartz content, the HTN composition was mixed with a 20% (An_{20}) and with 50% (An_{50}) of anorthite composition by Picard's thesis (fig. III.1a-b. For further details, see Picard's thesis, 2009). The two final mixtures are called $HAn_{20}Q_{15}$ and $HAn_{50}Q_{15}$. Their chemical compositions are shown in table III.1. These samples are the material used for the deformation experiments on the Paterson press.

All the synthesis experiments are shown in table III.2. As shown in table III.2, different compositions are used for the test syntheses in series 5 (pieces of material already synthesised in series 3, which were re-synthesised in the IHPV to test whether the crystal content could be increased) and series 6 (haplogranitic plagioclase crystals mixed with powder of $HAn_{50}Q_{15}$ composition). Both series failed. Series 5 maintained the crystal content of plagioclase, but also nucleated quartz. Series 6 showed strong dissolution phenomena of plagioclases due to non-equilibrium chemical compositions.

The syntheses performed with the chosen starting materials ($HAn_{20}Q_{15}$ and $HAn_{50}Q_{15}$) were carried out with different water percentage and temperatures in order to vary the crystalline content. For both compositions, undercooling during the synthesis experiments reduced the final crystal content of the samples. This is probably due to the unstable temperature condition caused by the undercooling. The continuous and gradual change in temperature does not create a state of equilibrium and therefore the crystals nucleate less and more slowly.

An important difference created by the two different compositions of the starting material is the morphology of the crystals. The two different compositions lead to the nucleation of plagioclases with different aspect ratio R. The $HAn_{20}Q_{15}$ starting material nucleates plagioclase crystals with a high aspect ratio (R ~ 4). The starting material $HAn_{50}Q_{15}$ nucleated plagioclase with a lower aspect ratio (R ~ 2). This difference is extremely important as it generates different microstructural behaviors of the samples when subjected to deformation.

a

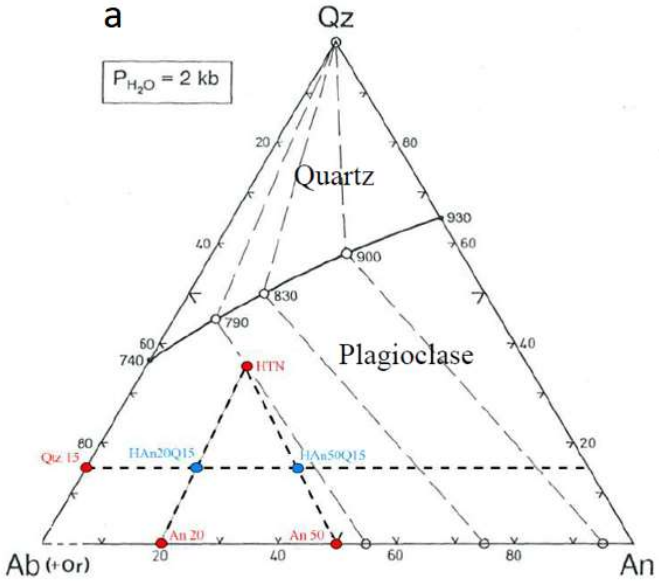

b

	$HAn_{20}Q_{15}$	$HAn_{50}Q_{15}$
Qtz	15	15
Ab	68	50
An	17	35

Figure III.1. a) Compositions of the mixtures reported in a Qz-Ab-An ternary diagram. The cotectic curve (in black) and the compositions of the coexisting phases are indicated for PH_2O = 2kbar ((Johannes, W. and Holtz, F., 1996)). The starting compositions are represented by a red circle and the mixtures obtained from these compositions by blue circles (from Picard's thesis, 2009). b) Nominative composition of the two starting materials ($HAn_{20}Q_{15}$ and $HAn_{50}Q_{15}$). Qtz = quartz, Ab = albite, An = anorthite (from Picard's thesis, 2009).

a	Starting glass ($HAn_{20}Q_{15}$) n = 46
Na_2O	7.88 (± 0.15)
SiO_2	69.34 (± 0.26)
Al_2O_3	19.35 (± 0.26)
CaO	3.43 (± 0.10)
Total	100

b	Starting glass ($HAn_{50}Q_{15}$) n = 20
Na_2O	5.93 (± 0.13)
SiO_2	63.89 (± 0.32)
Al_2O_3	22.83 (± 0.20)
CaO	7.35 (± 0.05)
Total	100

Table III.1. Chemical analysis of the two starting glasses. The analyses have been performed using an electron microprobe with a defocused beam of 20 x 20 µm. a) Starting glass $HAn_{20}Q_{15}$. b) Starting glass $HAn_{50}Q_{15}$.

Sample	Composition	Aspect ratio R	Capsule size (h x w x d)	H_2O (wt%)	P (MPa)	T (°C)	Synthesis time	Crystals fraction
Series 1.								
#6	HTN + $An_{20}Q_{15}$	4	35 mm x 22 mm x 250 µm	3.0	300	800	7 days	0.58
#7	HTN + $An_{20}Q_{15}$	4	35 mm x 22 mm x 250 µm	3.0	300	1000 - 800	1 h 1000 - ramp for 2 days - 5 days 800	0.52
Test series 2.								
$HAn_{50}Q_{15}$ 1a	HTN + $An_{50}Q_{15}$	2	15 mm x 2 mm x 250 µm	2.0	330	1000 - 825	1 day 1000 - ramp for 9 days - 4 days 825	n.d. (low crystal fraction)
$HAn_{50}Q_{15}$ 2a	HTN + $An_{50}Q_{15}$	2	15 mm x 2 mm x 250 µm	2.5	330	1000 - 825	1 day 1000 - ramp for 9 days - 4 days 825	n.d. (low crystal fraction)
$HAn_{50}Q_{15}$ 3a	HTN + $An_{50}Q_{15}$	2	15 mm x 2 mm x 250 µm	3.0	330	1000 - 825	1 day 1000 - ramp for 9 days - 4 days 825	n.d. (low crystal fraction)
$HAn_{50}Q_{15}$ 4a	HTN + $An_{50}Q_{15}$	2	15 mm x 2 mm x 250 µm	3.5	330	1000 - 825	1 day 1000 - ramp for 9 days - 4 days 825	n.d. (low crystal fraction)
$HAn_{50}Q_{15}$ 1b	HTN + $An_{50}Q_{15}$	2	15 mm x 2 mm x 250 µm	2.0	300	1000 - 825	4 days 1000 - ramp for 11 days - 1 day 825	n.d. (low crystal fraction)
$HAn_{50}Q_{15}$ 2b	HTN + $An_{50}Q_{15}$	2	15 mm x 2 mm x 250 µm	2.5	300	1000 - 825	4 days 1000 - ramp for 11 days - 1 day 825	n.d. (low crystal fraction)
$HAn_{50}Q_{15}$ 3b	HTN + $An_{50}Q_{15}$	2	15 mm x 2 mm x 250 µm	3.0	300	1000 - 825	4 days 1000 - ramp for 11 days - 1 day 825	n.d. (low crystal fraction)
$HAn_{50}Q_{15}$ 4b	HTN + $An_{50}Q_{15}$	2	15 mm x 2 mm x 250 µm	3.5	300	1000 - 825	4 days 1000 - ramp for 11 days - 1 day 825	n.d. (low crystal fraction)
$HAn_{50}Q_{15}$ 5b	HTN + $An_{50}Q_{15}$	2	15 mm x 2 mm x 250 µm	4.0	300	1000 - 825	4 days 1000 - ramp for 11 days - 1 day 825	n.d. (low crystal fraction)
$HAn_{50}Q_{15}$ 6b	HTN + $An_{50}Q_{15}$	2	15 mm x 2 mm x 250 µm	5.0	300	1000 - 825	4 days 1000 - ramp for 11 days - 1 day 825	n.d. (low crystal fraction)
$HAn_{50}Q_{15}$ 7b	HTN + $An_{50}Q_{15}$	2	15 mm x 2 mm x 250 µm	6.0	300	1000 - 825	4 days 1000 - ramp for 11 days - 1 day 825	n.d. (low crystal fraction)
Series 3.								
HTN4	HTN + $An_{50}Q_{15}$	2	35 mm x 20 mm x 250 µm	3.0	300	1000 - 800	5 h 1000 - ramp for 2 days - 5 days 800	0.58
HTN8	HTN + $An_{50}Q_{15}$	2	35 mm x 20 mm x 250 µm	3.0	300	1000 - 800	5 h 1000 - ramp for 2 days - 5 days 800	0.58
HTN9	HTN + $An_{50}Q_{15}$	2	35 mm x 20 mm x 250 µm	3.0	300	1000 - 800	5 h 1000 - ramp for 2 days - 5 days 800	0.59

Table III.2. Synthesis conditions and characteristics of the different starting materials.

Sample	Composition	Aspect ratio R	Capsule size (h x w x d)	H_2O (wt%)	P (MPa)	T (°C)	Synthesis time	Crystals fraction
Test series 4.								
$HAn_{50}Q_{15}$ 1c	HTN + $An_{50}Q_{15}$	2	15 mm x 2 mm x 250 µm	2.5	300	730	7days	n.d. (almost fully crystallized)
$HAn_{50}Q_{15}$ 2c	HTN + $An_{50}Q_{15}$	2	15 mm x 2 mm x 250 µm	3.0	300	730	7 days	n.d. (almost fully crystallized)
$HAn_{50}Q_{15}$ 3c	HTN + $An_{50}Q_{15}$	2	15 mm x 2 mm x 250 µm	2.5	300	760	7days	n.d. (low crystal fraction)
$HAn_{50}Q_{15}$ 4c	HTN + $An_{50}Q_{15}$	2	15 mm x 2 mm x 250 µm	3.0	300	760	7 days	n.d. (low crystal fraction)
$HAn_{50}Q_{15}$ 5c	HTN + $An_{50}Q_{15}$	2	15 mm x 2 mm x 250 µm	2.5	300	790	7days	n.d. (good crystal fraction)
$HAn_{50}Q_{15}$ 6c	HTN + $An_{50}Q_{15}$	2	15 mm x 2 mm x 250 µm	3.0	300	790	7 days	n.d. (good crystal fraction)
$HAn_{50}Q_{15}$ 7c	HTN + $An_{50}Q_{15}$	2	15 mm x 2 mm x 250 µm	3.5	300	790	7days	n.d. (good crystal fraction)
$HAn_{50}Q_{15}$ 8c	HTN + $An_{50}Q_{15}$	2	15 mm x 2 mm x 250 µm	4.0	300	790	7 days	n.d. (good crystal fraction)
Test series 5.								
HTN9 tris	HTN9	2	15 mm x 2 mm x 250 µm	3.0	300	730	7 days	-
HTN9 bis	HTN9	2	15 mm x 2 mm x 250 µm	3.0	300	760	7 days	-
Test series 6.								
1 mix	PG crystals (50-90 µm) + HTN + $An_{50}Q$	2	15 mm x 2 mm x 250 µm	2.5	300	730	7 days	-
2 mix	PG crystals (50-90 µm) + HTN + $An_{50}Q$	2	15 mm x 2 mm x 250 µm	3.0	300	730	7 days	-
3 mix	IPG crystals (50-90 µm) + HTN +$An_{50}Q$	2	15 mm x 2 mm x 250 µm	2.5	300	760	7 days	-
4 mix	PG crystals (50-90 µm) + HTN + $An_{50}Q$	2	15 mm x 2 mm x 250 µm	3.0	300	760	7 days	-
Series 7.								
HTN11	HTN + $An_{50}Q_{15}$	2	35 mm x 20 mm x 250 µm	3.0	300	810	7 days	0.73
HTN13	HTN + $An_{50}Q_{15}$	2	35 mm x 20 mm x 250 µm	3.0	300	810	7 days	0.76
HTN14	HTN + $An_{50}Q_{15}$	2	35 mm x 20 mm x 250 µm	3.0	300	810	7 days	0.76
HTN12	HTN + $An_{50}Q_{15}$	2	35 mm x 20 mm x 250 µm	3.0	300	790	7 days	0.95
HTN15	HTN + $An_{20}Q_{15}$	4	35 mm x 20 mm x 250 µm	3.0	300	810	7 days	-

Table III.2. Synthesis conditions and characteristics of the different starting materials.

1.2 Series 1.

These samples were synthesized by Picard during his PhD (2009). The starting materials have a haplotonalitic composition ($HAn_{20}Q_{15}$), with content water of 3 wt%. The aim was to create a mineralogically homogenous sample, with as few bubbles as possible and well-developed plagioclase phenocrysts. The samples considered for this work were synthesized in a HIPV, with pressure of 300 MPa and different temperatures. The temperature of the first sample (#6) was 800°C, maintained for 7 days. The temperature of the second sample (#7) was initially 1000°C for 1 hour, then an undercooling process was implemented to bring the temperature from 1000°C to 800°C. Finally, the sample remained at 800°C for 7 days. The undercooling was done because, according to work by (Lofgren, 1974), this process affects the shape and size of the crystals. In Picard's samples, undercooling only caused a difference in crystal content, resulting in a delay in crystal nucleation. Sample #7 (with undercooling) has a crystal content ϕ_s of 0.52 (fig. III.2) and sample #6 (no undercooling) has a crystalline content ϕ_s of 0.58 (fig. III.3).

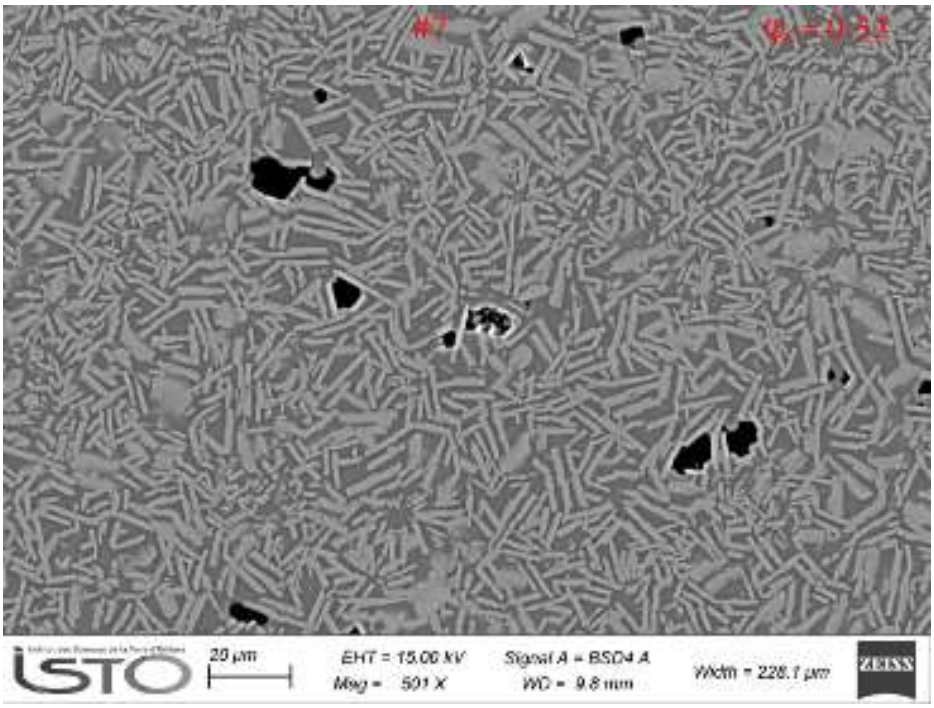

Figure III.2. SEM picture of #7 sample. Black: bubbles, light grey: plagioclase crystals, dark gray: glass.

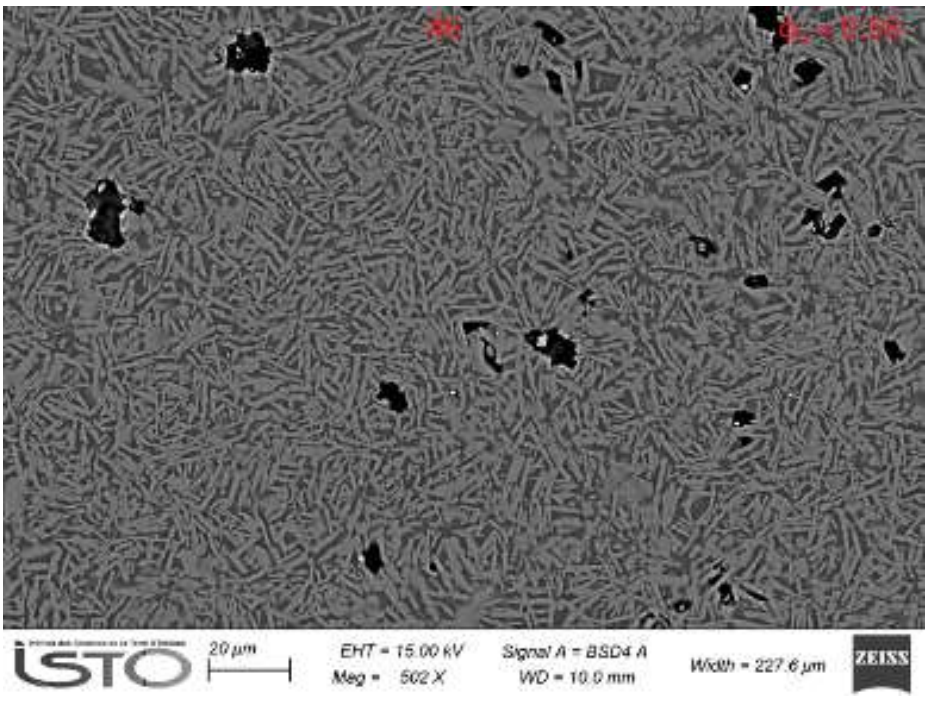

Figure III.3. SEM picture of #6 sample. Black: bubbles, light grey: plagioclase crystals, dark gray: glass.

1.3. Test series 2.

The starting material of this test series is with $HAn_{50}Q_{15}$ composition. The experiment was performed with a pressure of 300 MPa, varying the water content and undercooling rates. The aim was to find the best conditions for producing a starting material with a crystal content ϕ_s around 0.60. The first experiment was carried out at constant pressure (330 MPa), with content water ranging from 2.0 to 3.5 wt% and temperature subjected to undercooling. The starting temperature was 1000°C and then it was gradually reduced over 9 days to 825°C (19.5°C per day). The temperature remained stable for a further 4 days. All the samples show less crystallinity than expected (fig. III.4a), with higher crystallinity at lower water contents. Furthermore, the crystals have a low aspect ratio (R = 2), whereas the initial aim of the work was to produce a high crystal content starting material formed by crystals with a high aspect ratio (R = 4).

To increase the crystallinity and the aspect ratio R, another experiment was carried out with the same starting material. The pressure was 300 MPa, the water content varied between 2.0 and 6.0 wt% and the temperature was subjected to a slower undercooling. The temperature was reduced from 1000°C to 825°C in 11 days, with a cooling rate of 15.9°C per day. Temperature stayed at 825°C for a day. The samples show a lower crystalline content than the first experiment, showing that a slower cooling rate did not increase crystals nucleation (fig. III.5a). Furthermore, the shape of the crystals remained unchanged, with an aspect ratio of R = 2.

The more important factor may be the temperature kept stable at 825°C. In this equilibrium condition, the first experiment nucleated more crystals because the temperature of 825°C was maintained for 4 days, whereas in the second experiment the temperature was stable at 825°C for only 1 day.

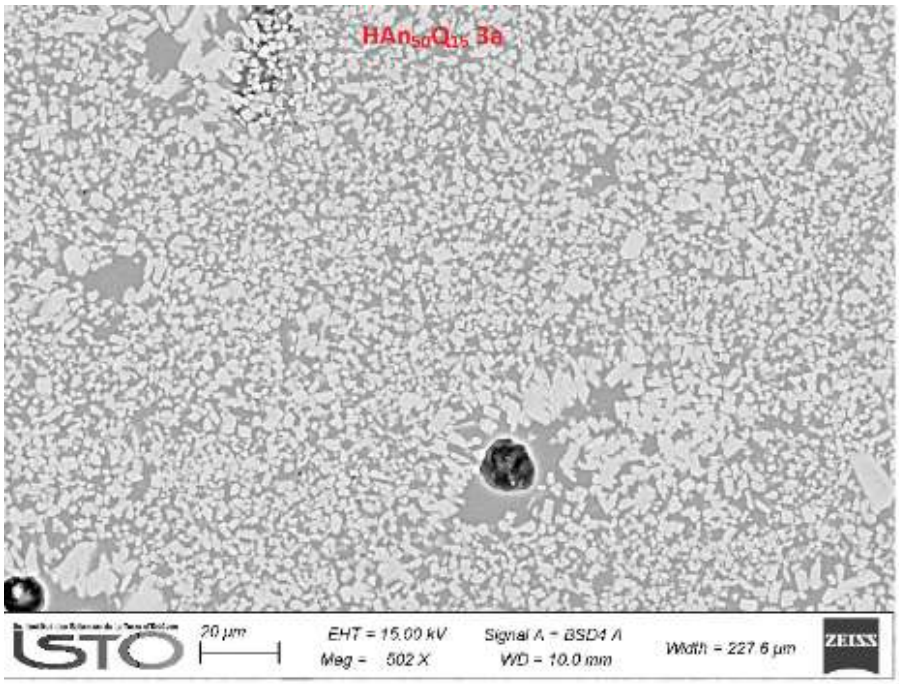

Figure III.4. SEM picture of $HAn_{50}Q_{15}$ 3a sample. Black: bubbles, light grey: plagioclase crystals, dark gray: glass.

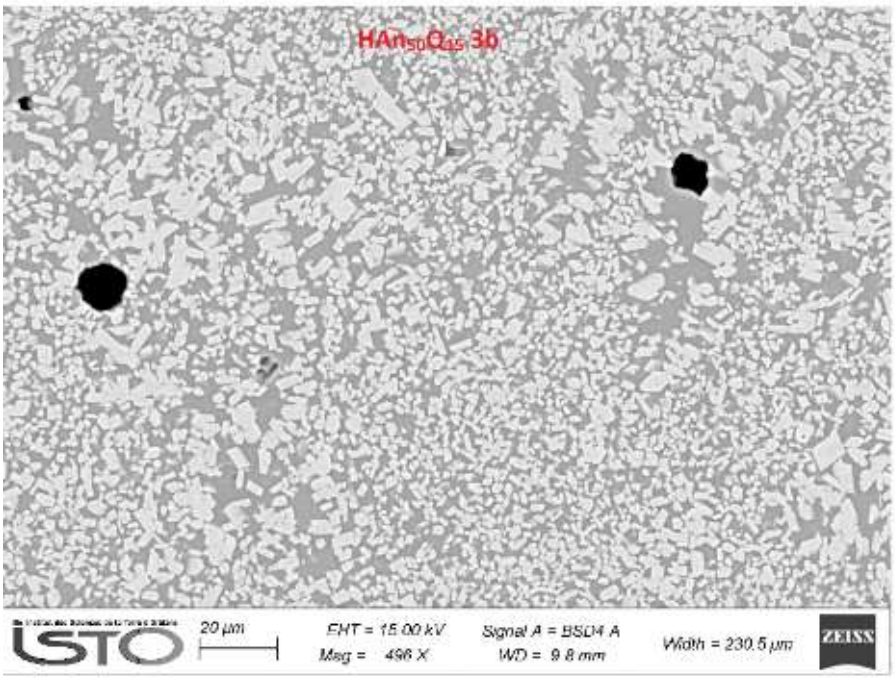

Figure III.5. SEM picture of $HAn_{50}Q_{15}$ 3b sample. Black: bubbles, light grey: plagioclase crystals, dark gray: glass.

1.4 Series 3.

Gold capsules were filled with haplotonalitic glass powder ($Han_{50}Q_{15}$), with water content of 3 wt%. The aim was to synthesize samples with only plagioclase crystals and a crystal content around 0.60. This crystal content was chosen for different reason: it represents the content required to have the physical conditions of a solid mush and it is good for strain experiments with the Paterson press, in order to investigate strain localization, sample rheology and possible melt migration. The pressure and temperature conditions were chosen on the basis of (Picard, 2009) experiments, as he synthesized samples with a crystalline content of 0.58. In addition, previous test synthesis (see test series 2) shows a low crystal content at temperatures of 825°C. Therefore, it was decided to set the temperature at 800°C in order to increase crystals nucleation.

The samples were placed in an IHPV for 7 days, with a pressure of 300 MPa and temperatures ranging between 1000°C and 800°C. The samples were at 1000°C for 5 days, then the temperature was reduced from 1000°C to 800°C in 2 days (100°C per day). The temperature remained stable at 800°C for 5 days. The materials obtained were prepared and analyzed with SEM (fig. III.6a-b).

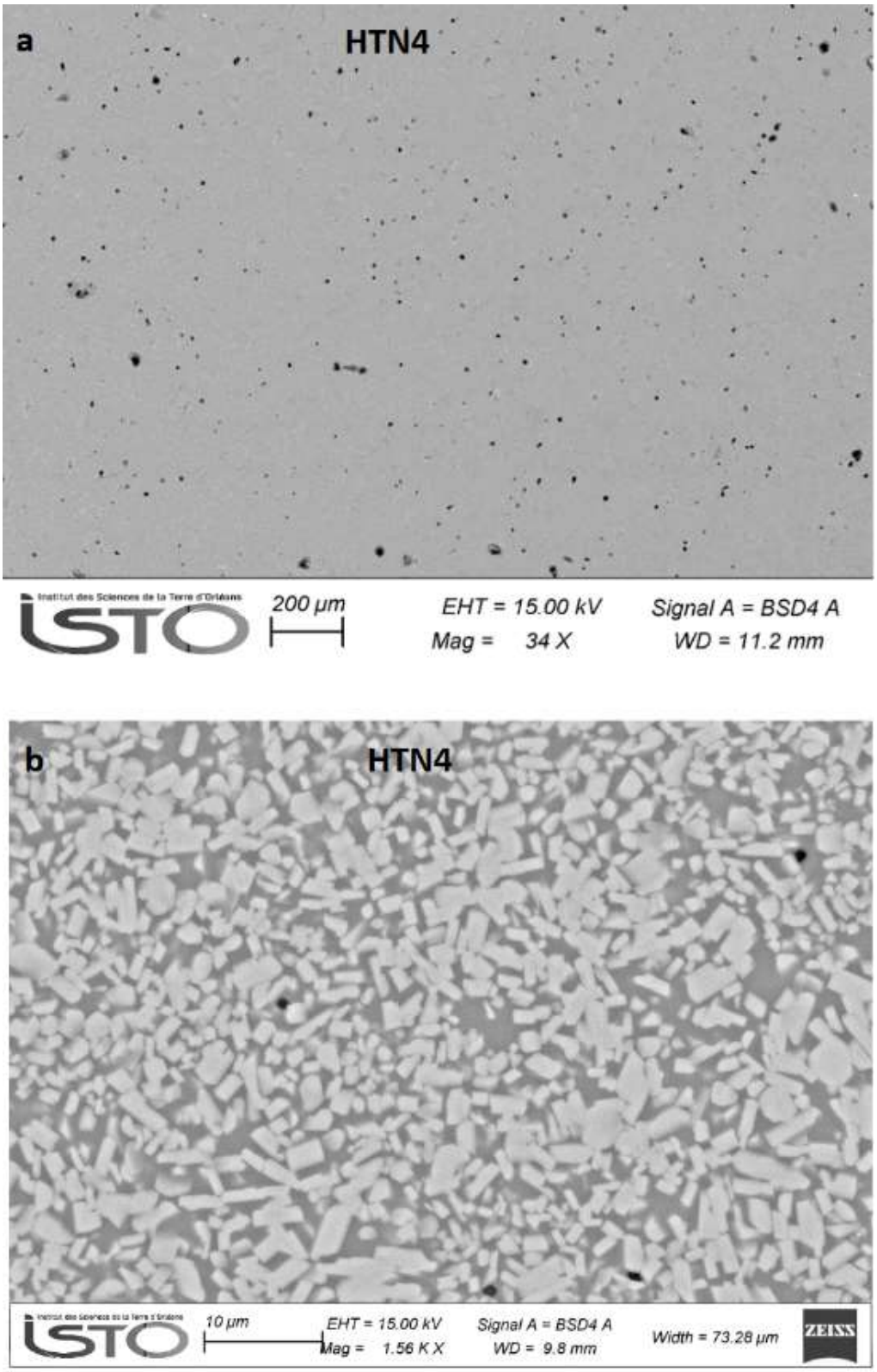

Figure III.6. SEM picture of HTN4 sample. a) Magnification: 34 X. b) Magnification: 1.56 X. Black: bubbles, light grey: plagioclase crystals, dark gray: glass.

1.5. Test series 4.

As in test series 2, the synthesis experiments were carried out with small gold capsules (15 mm high, 2.5 mm wide and 400 µm thick). The composition used for this set of experiments is $HAn_{50}Q_{15.}$ The aim was to synthesize several capsules in the same experiment and to investigate the best conditions of temperature and water content to produce a starting material with a crystal content higher than 0.70. Through crystallization modeling with MELTS software, it has been seen how compositions reach the solidus temperature at about 760°C. In order to increase the crystalline content as much as possible, the experiments were carried out with low temperatures. The samples were placed in an IHPV, at pressures of 300 MPa, temperatures between 790°C and 730°C, for 7 days. As the temperature decreases, the crystalline content increases. As the water content increases, the crystalline content decreases. The samples are shown in the fig. III.7.

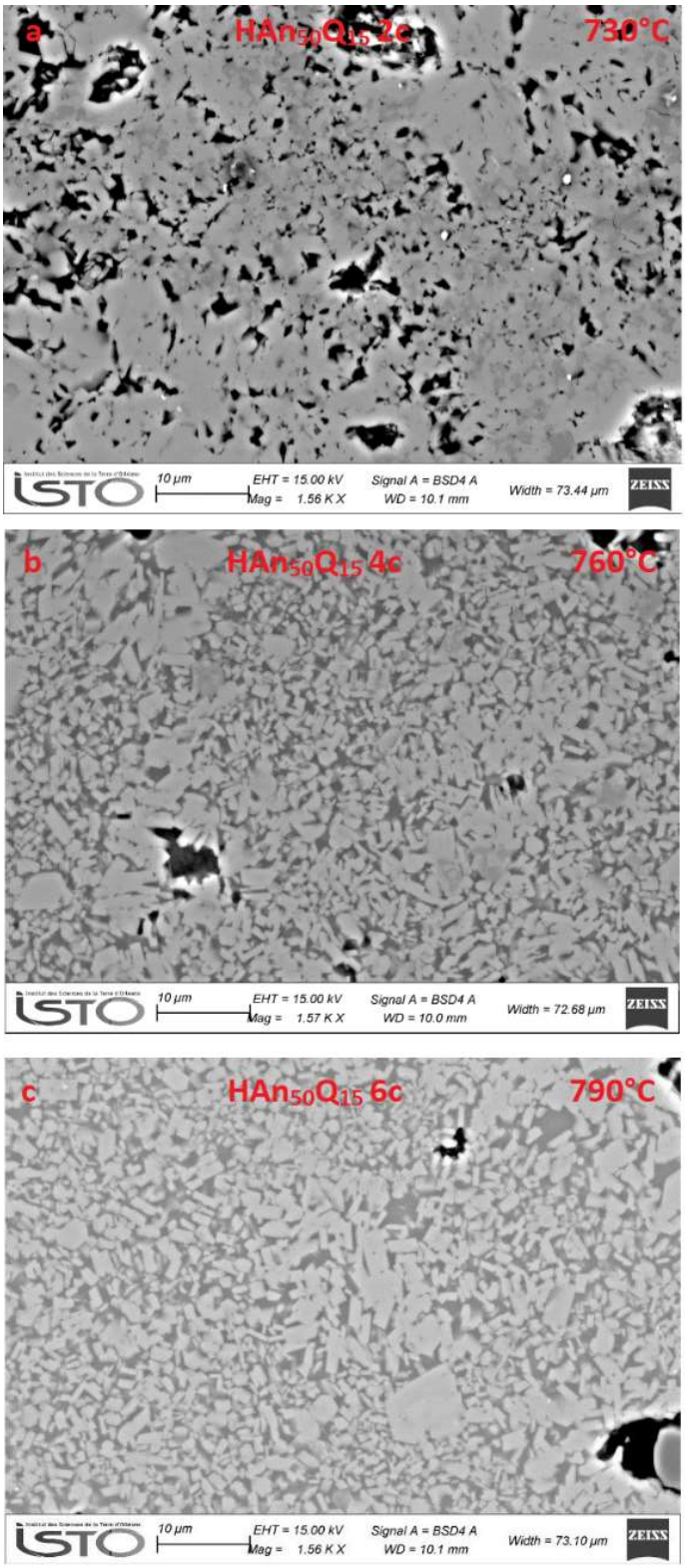

Figure III:7. SEM pictures of samples from test series 4. a) Sample synthetized at 730°C ($HAn_{50}Q_{15}$ 2c). b) Sample synthetized at 760°C ($HAn_{50}Q_{15}$ 4c). c) Sample synthetized at 790°C ($HAn_{50}Q_{15}$ 6c). Black: bubbles, light grey: plagioclase crystals, dark gray: glass.

1.6. Test series 5.

Series number 5 was carried out with parts of the already synthesized HTN9 sample to see if further days of synthesis could change the crystallinity of the already highly crystallized sample. The experiments were carried out at temperatures of 730°C and 760°C. The HTN9bis and HTN9tris samples showed no difference in crystal content compared to the HTN9 sample, but they did nucleate quartz (fig. III.8).

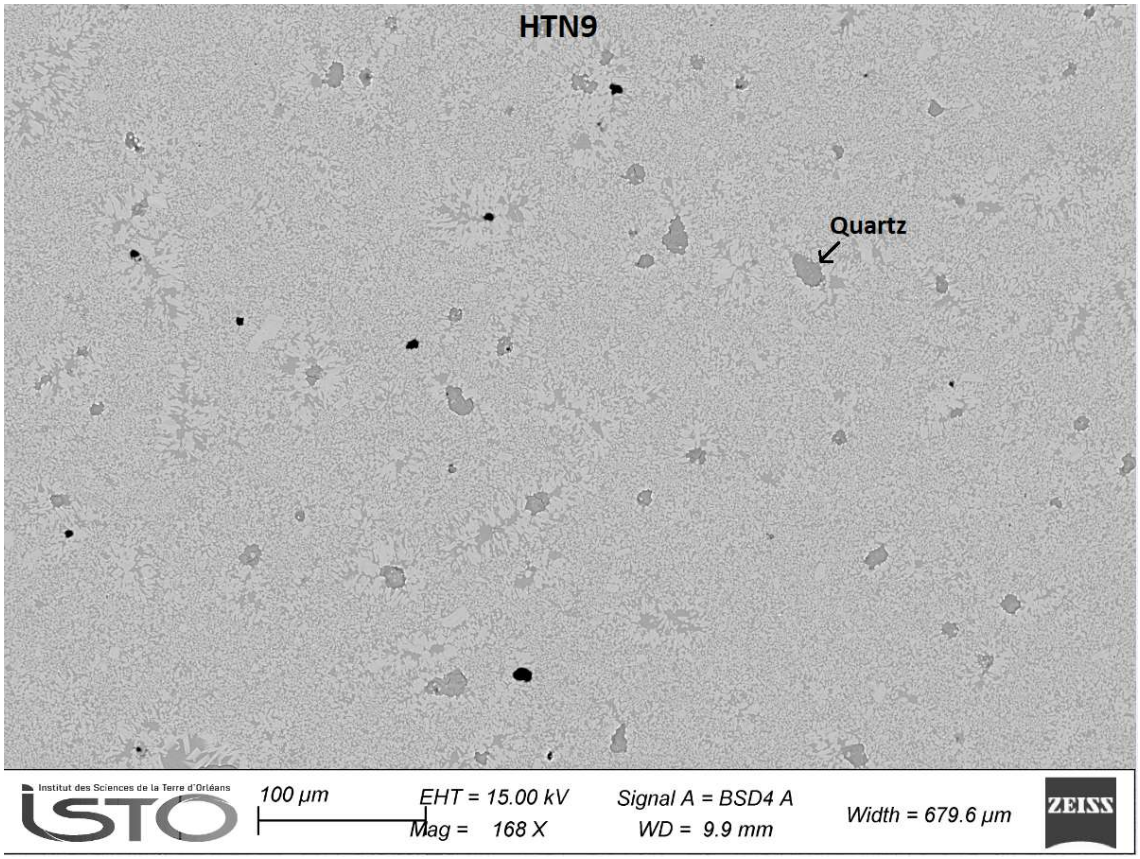

Figure III.8. SEM picture of HTN9bis sample. Black: bubbles, light grey: plagioclase crystals, gray: glass, dark grey: quartz.

1.7. Test series 6.

Natural idiomorphic plagioclase crystals with haplogranitic composition (HPG8), 20 µm in length in average (crystals from Puy de Dome, (Miallier D. et al., Submitted), fig. III.9a and b), were mixed with haplotonalitic powder ($HAn_{20}Q_{15}$) in order to create a concentrated suspension with a specific crystalline percentage. The starting material was placed in an IHPV for 7 days, at temperatures of 730°C and 760°C. The different composition between the plagioclase crystals and the glass has produced strong dissolution phenomena in the crystals, thus making impossible their use (fig. III.9).

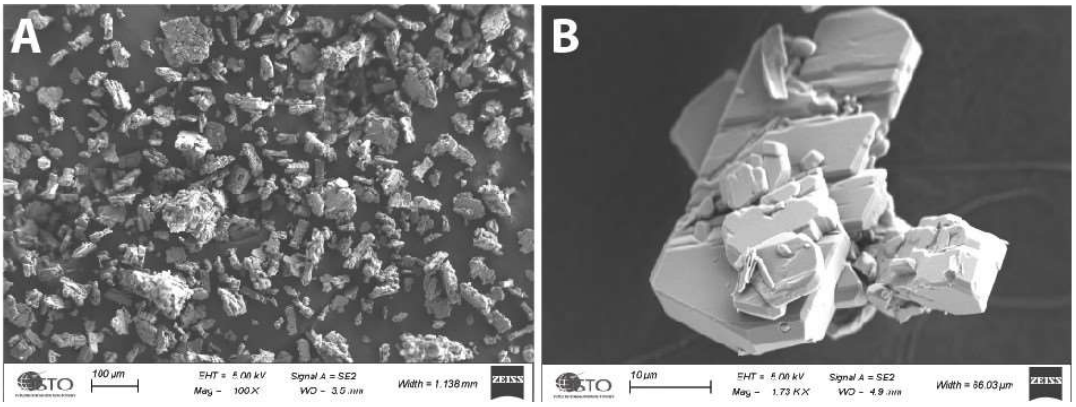

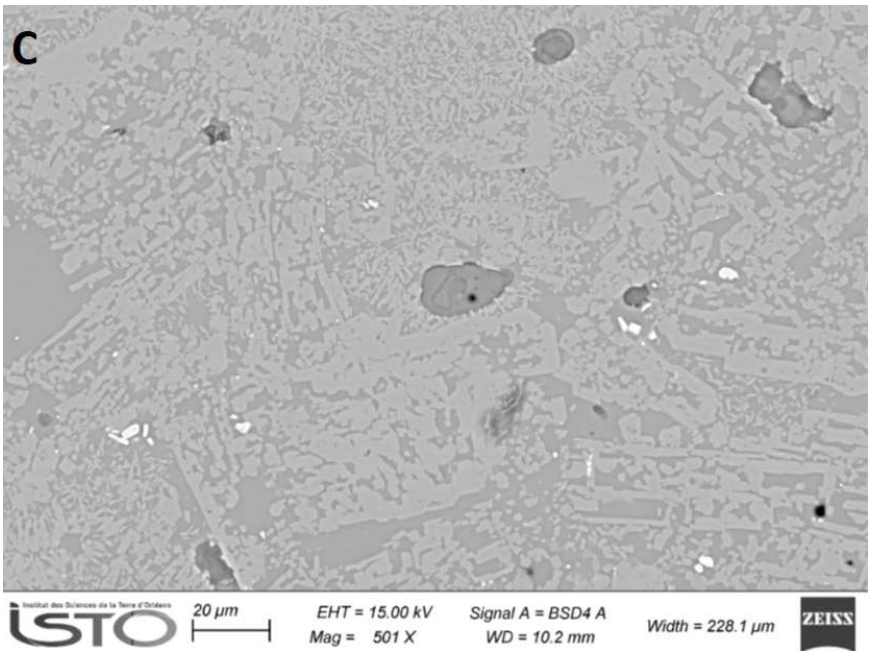

Figure III.9. a and b) idiomorphic K-feldspar microlites from Puy de Dôme ash deposit. Modified from Miallier et al. (Submitted). c) Sem picture of mix sample, with dissolution phenomena.

1.8. Series 7.

These starting materials were synthesized in large gold capsules (35 mm high, 22 mm wide and 250 µm thick). These are the highly crystalline synthetic samples used for the deformation experiments in the Paterson press. Pressure and water content were kept constant for all experiments (300 MPa and 3 wt% respectively), while the temperature has been varied in a range between 790°C and 810°C to obtain different crystal contents. Two different compositions were used, $HAn_{50}Q_{15}$ and $HAn_{20}Q_{15}$. The former is the composition used in most of the previous experiments. The second is the composition used in Picard's thesis (2009) and it generates the sample HTN15. This HTN15 synthesis was carried out in order to perform high crystallinity deformation experiments on plagioclase crystals with an aspect ratio R of 4. Unfortunately, the deformation experiment with the Paterson press could not be carried out due to lack of time. However, the synthesis shows how a small variation in composition changes the morphology of the crystals (figure III.10).

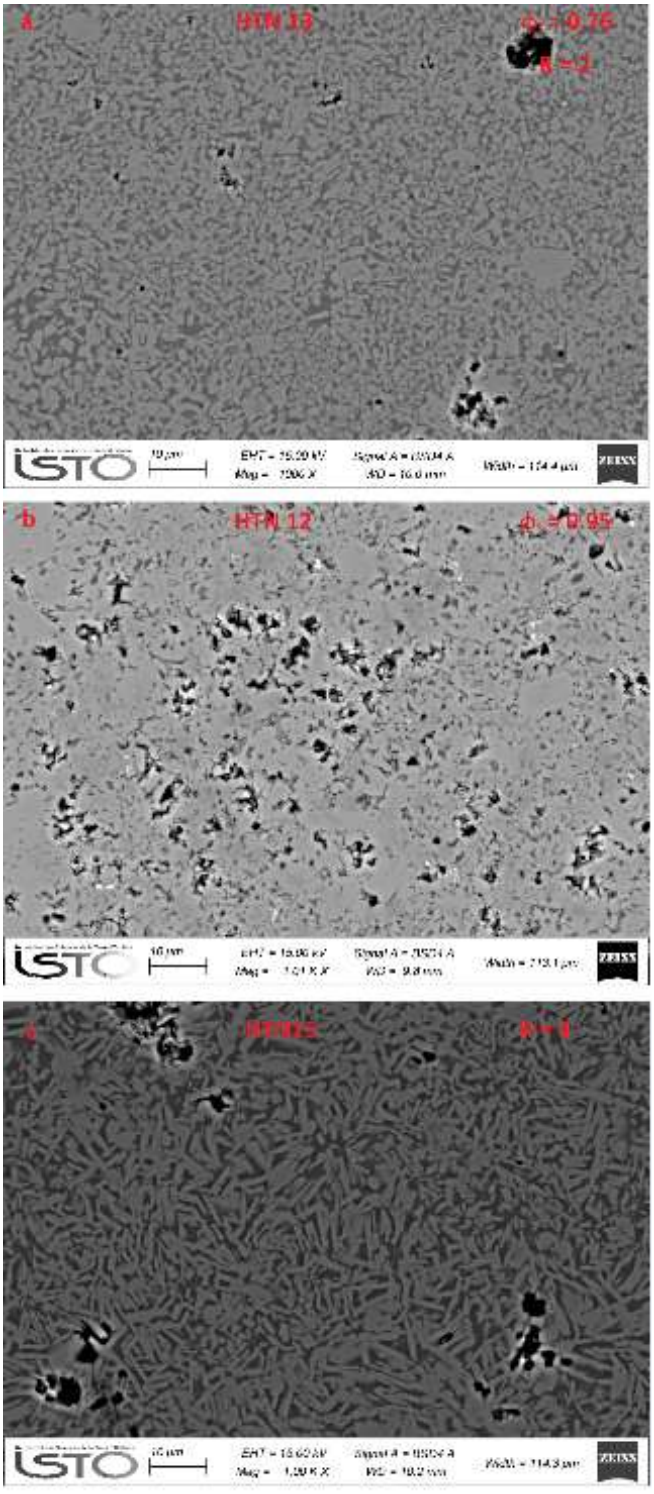

Figure III.10. SEM pictures of samples from series 7. a) Sample synthetized at 810°C with $HAn_{50}Q_{15}$ composition (HTN13). b) Sample synthetized at 790°C with $HAn_{50}Q_{15}$ composition (HTN12). c) Sample synthetized at 810°C with $Han_{20}Q_{15}$ composition (HTN15). Black: bubbles, light grey: plagioclase crystals, dark gray: glass.

Although the samples have a non-uniform crystal size, the elongated shape can be seen in the SEM images in figure III.11.

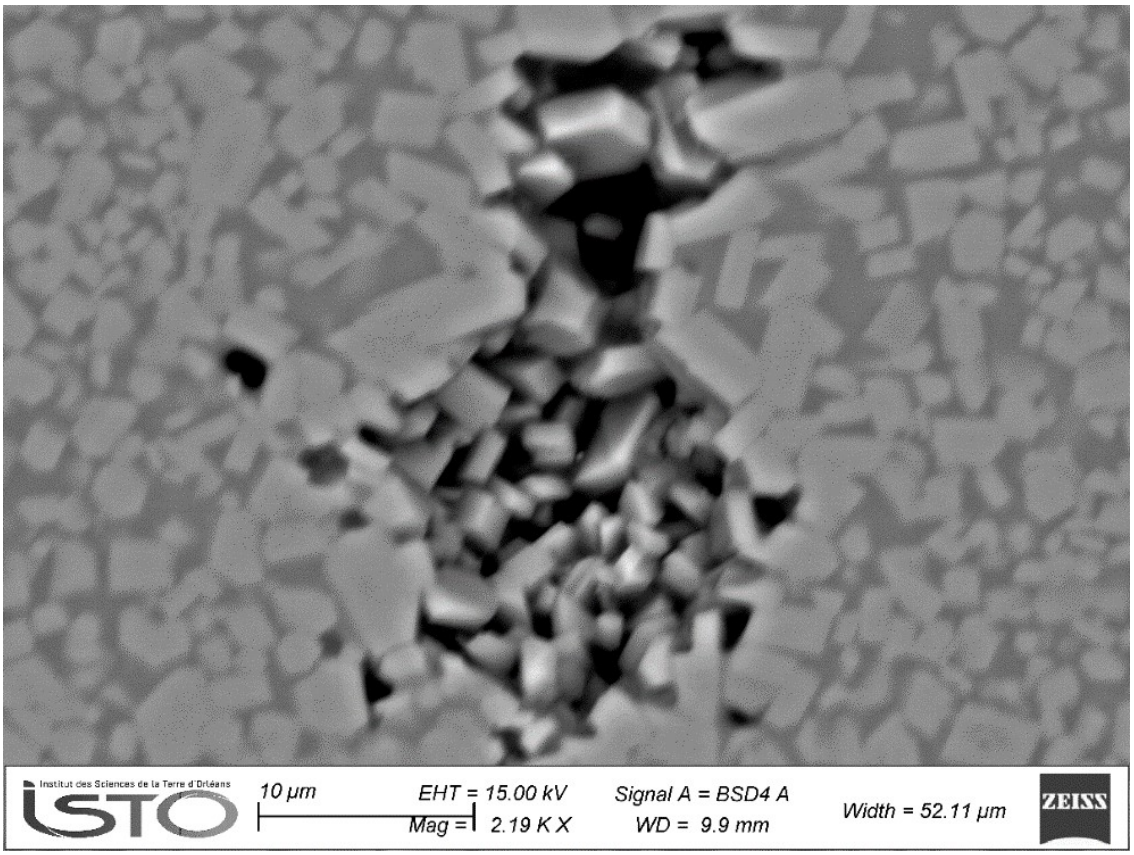

Figure III.11. SEM picture of plagioclase crystals.

2. Crystal morphology

The plagioclase crystals of all the starting materials were studied for their morphological characteristics of equivalent diameter ϕ and aspect ratio R. Analyses were carried out by SEM analysis with a size of approximately 75µm x 85µm. This allowed the analysis of a minimum crystal number of 270 and a maximum number of 976. This different number depends on the crystal size: samples with aspect ratio R = 4 (#7 and #6) have a larger equivalent diameter than samples with aspect ratio R = 2 (HTN4, HTN8, HTN9, HTN11, HTN13, HTN14).

2.1. Equivalent diameter ϕ

The figure III.11 represents the histograms of the equivalent diameters Φ of all the starting materials.

Sample #7 (fig. III.11a) has an arithmetic mean equivalent diameter of 3.00±1.52 µm and a harmonic mean of 2.00 µm. The mode has a value of 2.18 µm.

Sample #6 (fig. III.11b) shows an arithmetic mean of equivalent diameter equal to 2.29±1.09. Its harmonic mean is 1.78 µm and its mode is 1.82 µm.

The HTN4 sample (fig. III.11c) has an equivalent diameter of 1.52±0.69 µm with a harmonic mean of 1.23 µm and with a mode of 1.1 µm.

The HTN8 sample (fig. III.11d) shows an equivalent diameter of 2.04±0.83 µm and a harmonic mean of 1.59 µm. Its mode is equal to 1.48 µm.

The HTN9 sample (fig. III.11e) shows an equivalent diameter of 1.99±0.93 µm, a harmonic mean of 1.48 µm and a mode of 1.2 µm.

The HTN11 sample (fig. III.11f) has a mean equivalent diameter value of 1.14±0.48 µm, a harmonic mean value of 0.97 µm and a mode of 0.95 µm.

The HTN13 sample (fig. III.11g) has an equivalent diameter of 1.67±0.69 µm, with a harmonic mean of 1.31 µm and a mode of 1.35 µm and 1.90 µm.

The HTN14 sample (fig. III.11h) shows an equivalent diameter of 1.40±0.62 µm. Its harmonic mean value is equal to 1.15 µm and its mode is equal to 1.08 µm.

By comparing the arithmetic mean, harmonic mean and mode and analyzing their deviation, it is possible to check the symmetry of the size distributions. For all

histograms, the mean and mode do not coincide, indicating a log-normal population and therefore a non-symmetric distribution.

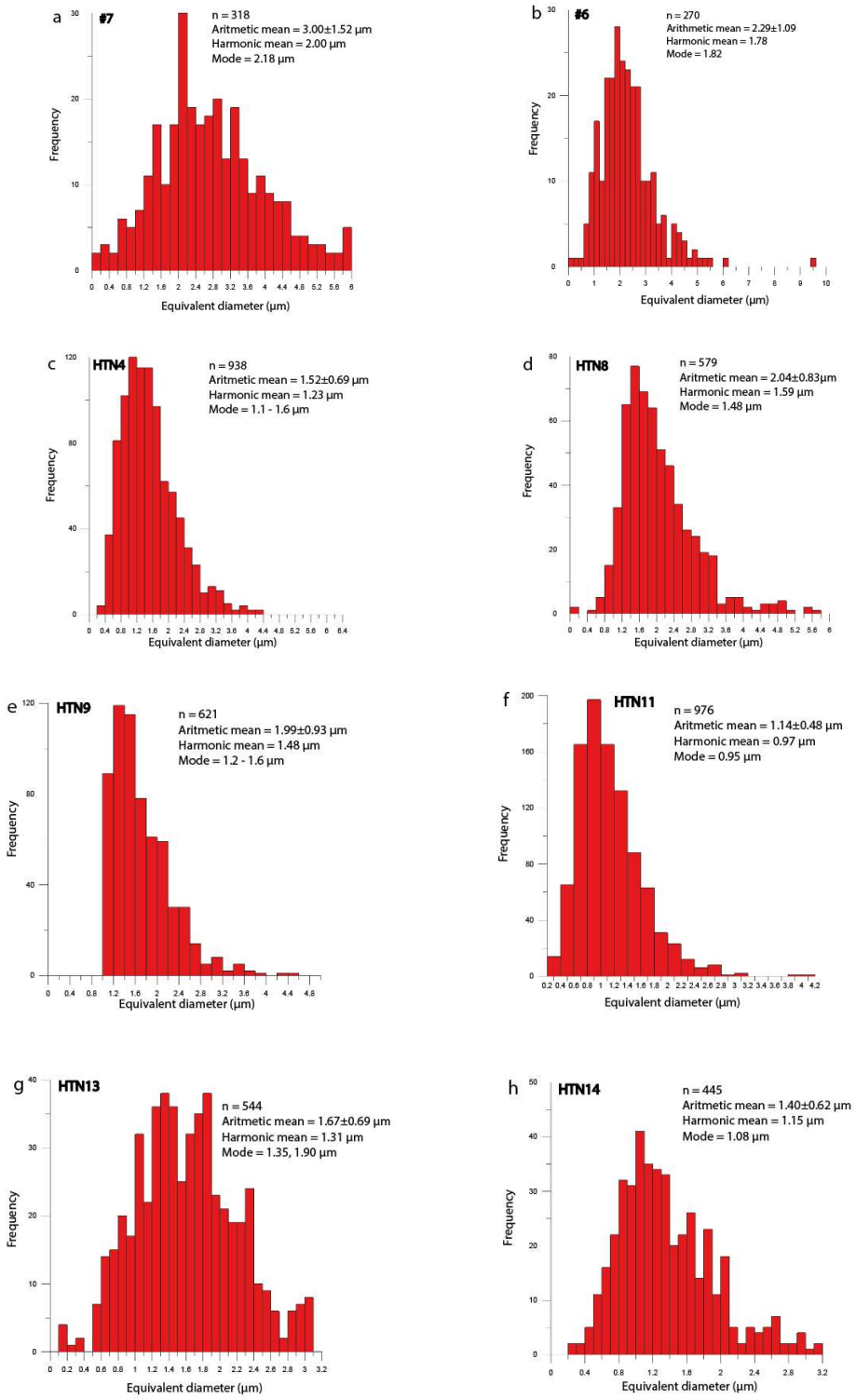

Figure III.11. Histograms of equivalent diameters of all the starting materials. a) #7. b) #6. c) HTN4. d) HTN8. e) HTN9. f) HTN11. g) HTN13. h) HTN14.

2.2. Aspect ratio R

The histograms in figure III.12 show the aspect ratio R for all the starting materials. The values of aspect ratio R are calculated for the arithmetic mean, harmonic mean and mode.

Sample #7 (fig. III.12a) has an arithmetic mean R of 4.03±2.22, a harmonic mean of 3.15 and a mode of 2.21.

Sample #6 (fig. III.12b) shows an arithmetic mean R of 3.65±2.23. The harmonic mean is 2.79 and the mode is 2.20.

Sample HTN4 (fig. III.12c) has an arithmetic mean R of 1.99±0.82 and a harmonic mean of 1.76. The mode of 1.55.

The HTN8 sample (fig. III.12d) shows an arithmetic mean R of 1.86±0.63. The harmonic mean is 1.69 and the mode is 1.2.

The HTN9 sample (fig. III.12e) has an arithmetic mean R of 1.72±0.57 and a harmonic mean of 1.58. Its mode of 1.56.

The HTN11 sample (fig. III.12f) has an arithmetic mean R of 1.89±0.87 with a harmonic mean of 1.71 and a mode of 1.45.

Sample HTN13 (fig. III.12g) shows an arithmetic mean R of 2.02±0.99 and a harmonic mean of 1.77. Its mode is 1.58.

Sample HTN14 (fig. III.12h) has an arithmetic mean of 1.87±0.76, a harmonic mean of 1.67 and a mode of 1.54.

As with the equivalent diameters, the samples have different arithmetic means, harmonics and modes. This indicates a log-normal trend and non-symmetric populations.

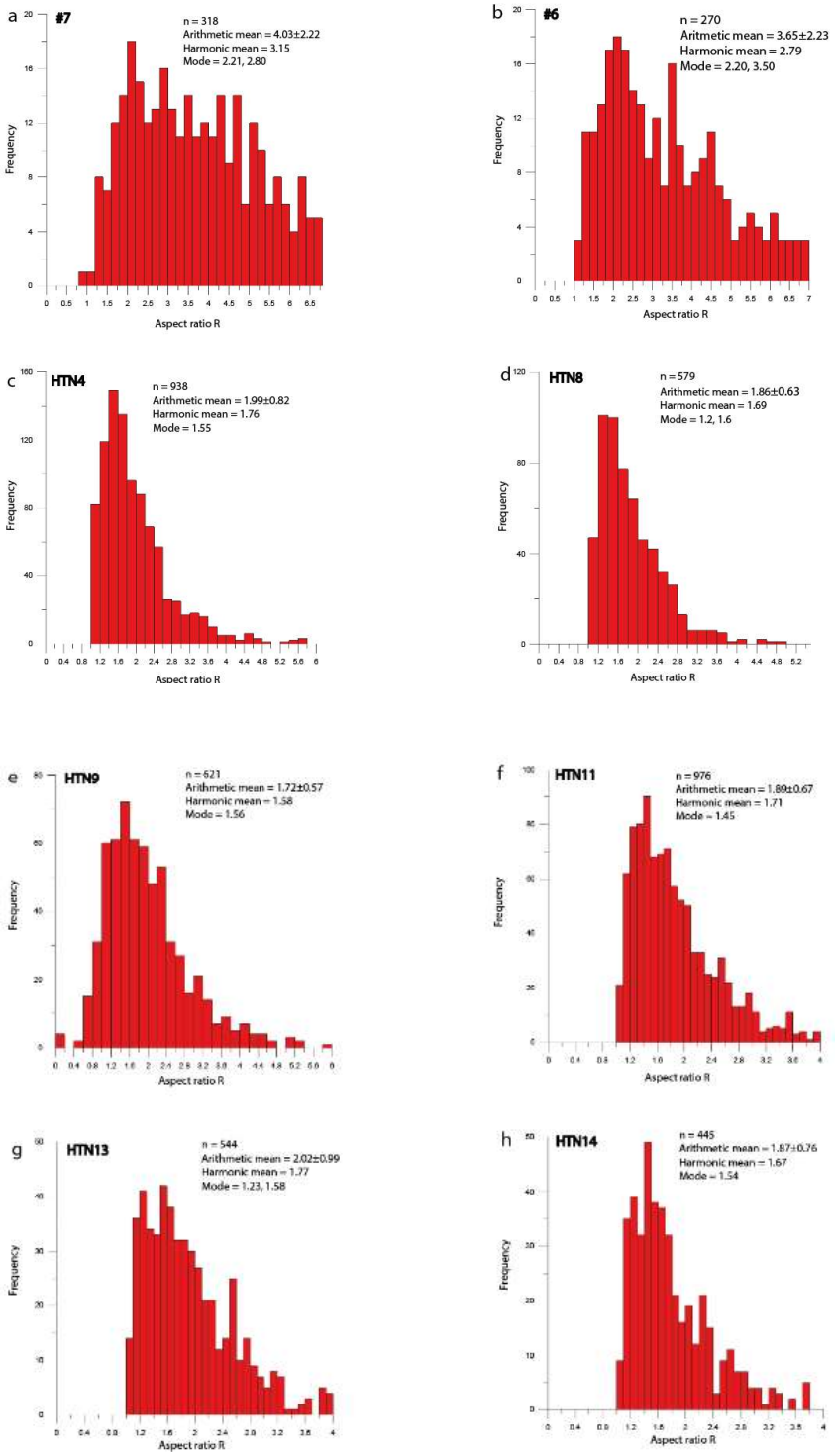

Figure III.12. Histograms of aspect ratio R of all the starting materials. a) #7. b) #6. c) HTN4. d) HTN8. e) HTN9. f) HTN11. g) HTN13. h) HTN14.

3. Chemical composition of the crystals

This paragraph shows the chemical analyses carried out on all the starting materials, in their plagioclases crystals. Due to the high crystalline content, the residual melt areas appear extremely small. Chemical analyses performed in these areas show a high error and are unreliable, therefore they are not shown. Table III.3a shows the chemical analyses of the plagioclases of samples #7 and #6, while table III.3b shows the chemical analyses of the plagioclases of samples HTN4, HTN8, HTN9, HTN11, HTN12, HTN13 and HTN14.

a

Mineral	Plagioclase		Plagioclase	
Sample	#7		#6	
n	12		12	
		±		±
Na_2O	7.33	0.37	7.84	0.39
SiO_2	64.70	2.32	64.61	1.34
Al_2O_3	22.05	1.61	22.42	0.85
CaO	5.02	1.01	4.72	0.48
Total	99.10		99.59	

b

Mineral	Plagioclase		Plagioclase		Plagioclase		Plagioclase		Plagioclase		Plagioclase		Plagioclase	
Sample	HTN4		HTN8		HTN9		HTN11		HTN12		HTN13		HTN14	
n	20		17		10		63		16		24		12	
		±		±		±		±		±		±		±
Na_2O	5.57	0.68	5.53	0.59	5.50	0.35	5.78	0.40	6.09	0.75	6.17	0.50	5.90	0.31
SiO_2	57.34	2.40	58.29	2.77	59.35	2.61	59.76	1.84	60.96	5.29	60.03	2.28	25.08	2.03
Al_2O_3	26.78	1.46	25.83	1.59	25.81	1.84	25.37	1.24	24.02	3.09	24.56	1.42	59.63	3.29
CaO	9.55	1.04	9.13	1.25	8.98	1.24	8.64	0.68	8.03	1.22	8.26	0.57	8.47	0.99
Total	99.24		98.78		99.64		99.55		99.10		99.02		99.08	

Table III.3. Chemical composition of all the starting materials analyzed by electron microprobe. a) Samples #7 and #6. b) Samples HTN4, HTN 8, HTN9, HTN11, HTN12, HTN13, HTN14. n = number of analyses.

4. Control of crystal size and morphology of #6 and #7 samples

The samples appear homogeneous with an average crystal lenth of 10 μm in average. Both samples have the same chemical composition and water content. The aspect ratio R of plagioclase crystals is close to 4.

The samples containing ϕ_s = 0.52 (from #7, fig. III.13a) and ϕ_s = 0.58 (from #6, fig. III.14a) show a main tensor ellipse with an eccentricity R of 1.034 (fig. III.13b) and of 1.008 (fig. III.14b) respectively, calculated by the analysis of the preferential shape orientation. The samples show a slight preferential orientation of the long axis of the crystals in the rose diagrams at -88° (fig. III.13c) and -88° (fig. III.14c). This is probably due to the internal pressure of the autoclave and the shape of the capsules which favour a weak vertical orientation as already noticed by Picard (2009) in its syntheses. This trend should not be considered binding for the deformation experiments, since the vertical orientation is weak and the deformation experiments have a shear direction parallel to the x-axis. The long axis of the plagioclases crystals of samples #6 and #7, analyzed by the inertia tensor method (fig. III.15a and III.16a, each color represents a different direction of the crystal, fig. III.15b and III.16b), do not show any preferential orientation (figures III.15c and III.16c).

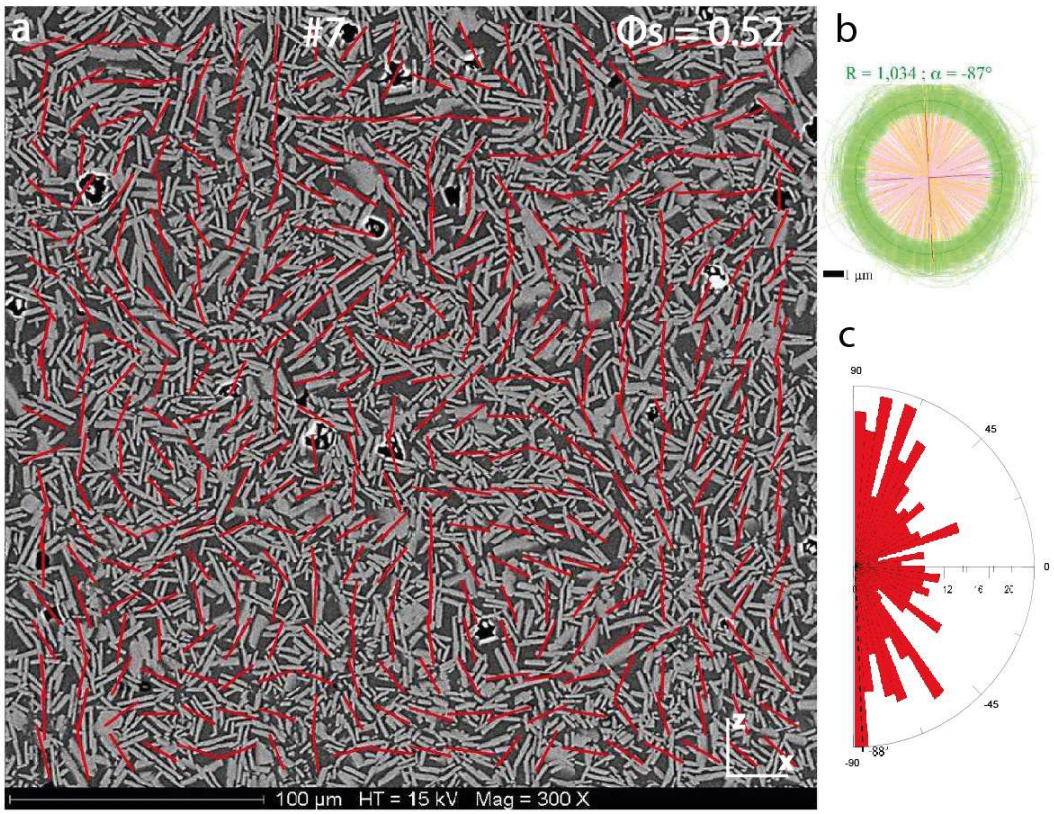

Figure III.13. Determination of textures for undeformed starting material containing ϕs = 0.52 (sample #7). SEM image in backscattered electrons. The red lines represent the long axes of the local ellipses of form fabric. (b) Local tensor ellipses of shape fabric. The values of eccentricities of the mean ellipses (R) as well as their directions of orientation (α) are indicated above the ellipse. (c) Rose of the directions of the long axes of local shape fabric ellipses. The maximum orientation direction is shown in black (modified from Picard's thesis, 2009).

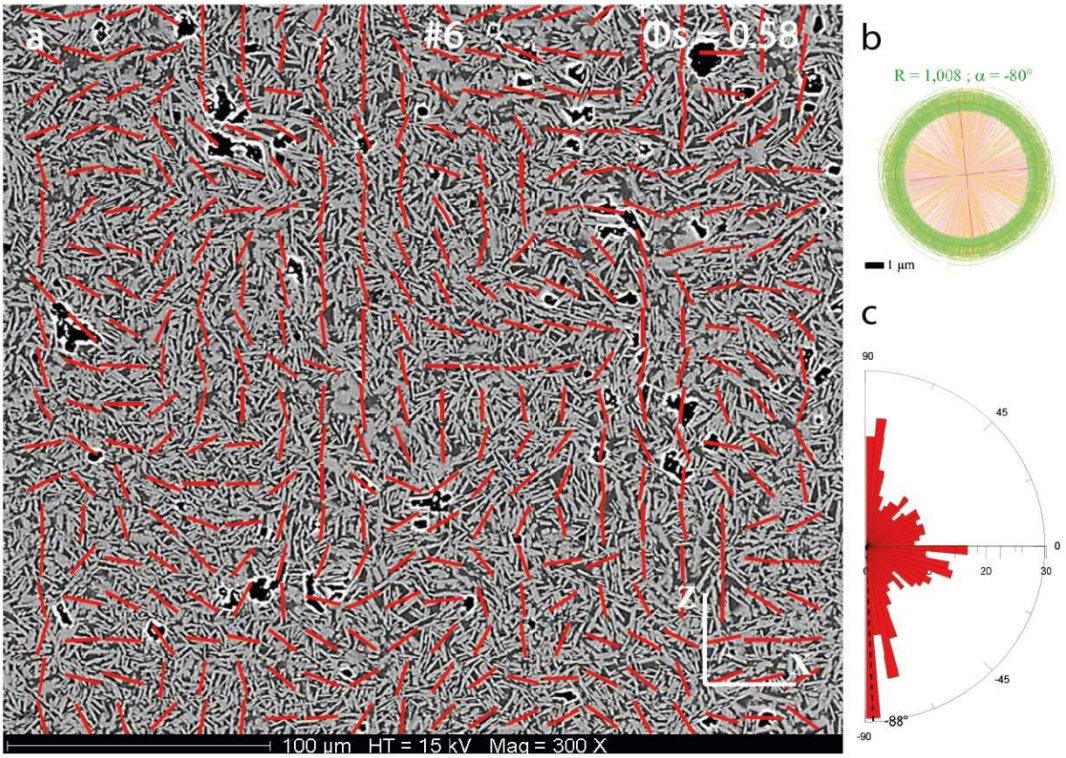

Figure III.14. Determination of textures for undeformed starting material containing ϕs = 0.58 (sample #6). SEM image in backscattered electrons. The red lines represent the long axes of the local ellipses of form fabric. (b) Local tensor ellipses of shape fabric. The values of eccentricities of the mean ellipses (R) as well as their directions of orientation (α) are indicated above the ellipse. (c) Rose of the directions of the long axes of local shape fabric ellipses. The maximum orientation direction is shown in black (modified from Picard's thesis, 2009).

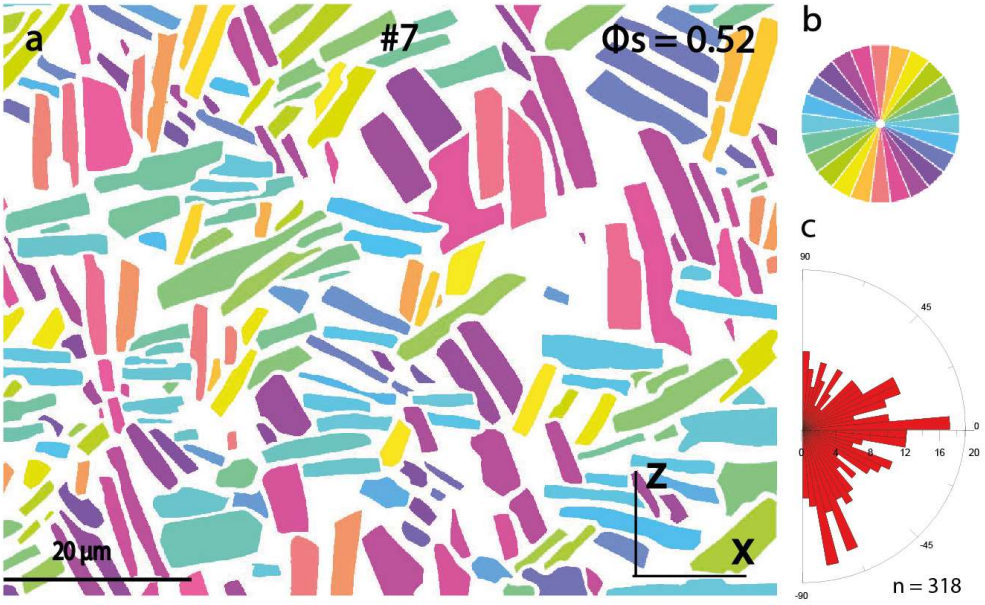

Figure III.15. Crystals orientation of undeformed sample containing $\phi_s = 0.52$ (a) Crystals are colored according to their orientations. (b) Rose of orientation colors. (c) Rose of directions of individual crystal orientation. n = number of measures.

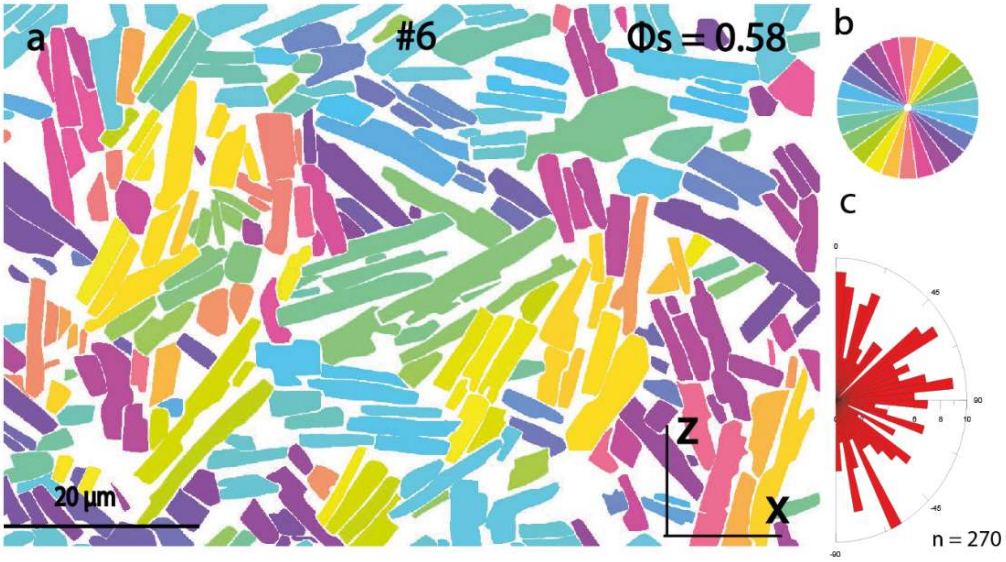

Figure III.16. Crystals orientation of undeformed sample containing $\phi_s = 0.58$. (a) Crystals are colored according to their orientations. (b) Rose of orientation colors (c) Rose of directions of individual crystal orientation. n = number of measures.

5. Control of crystal size and morphology of HTN4, HTN8 and HTN9 samples

The samples HTN4, HTN8 and HTN9 are homogeneous and the average size of the crystals is between 2 and 10 µm. Unlike the previous samples, these starting materials have an aspect ratio of R = 2 and they were studied in a different paragraph.

Sample HTN4

Sample HTN4 (fig. III.17a) shows an eccentricity value R = 1.009 and the direction of orientation of the main tensor ellipse is α = 20.07° (fig. III.17b). The orientations of the long axes of the local tensor is without any preferential direction, as it is shown in the rose diagram (fig. III.17c). The rose of the directions of the long axes of plagioclases calculated on each crystal by using the inertia method (fig. III.18a) does not show any preferential direction (fig. III.18c).

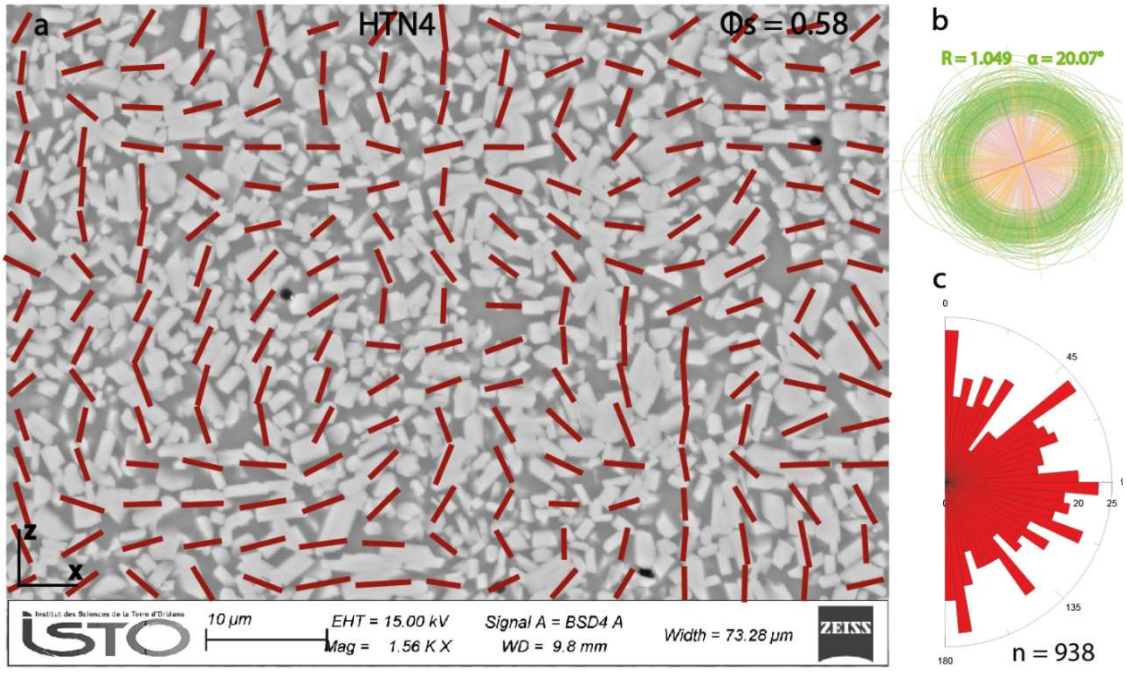

Figure III.17. Determination of textures for HTN4 sample. SEM image in backscattered electrons. (b) Local tensor ellipses of shape fabric. c) Rose of the directions of the long axes of local shape fabric ellipses. n = number of measures.

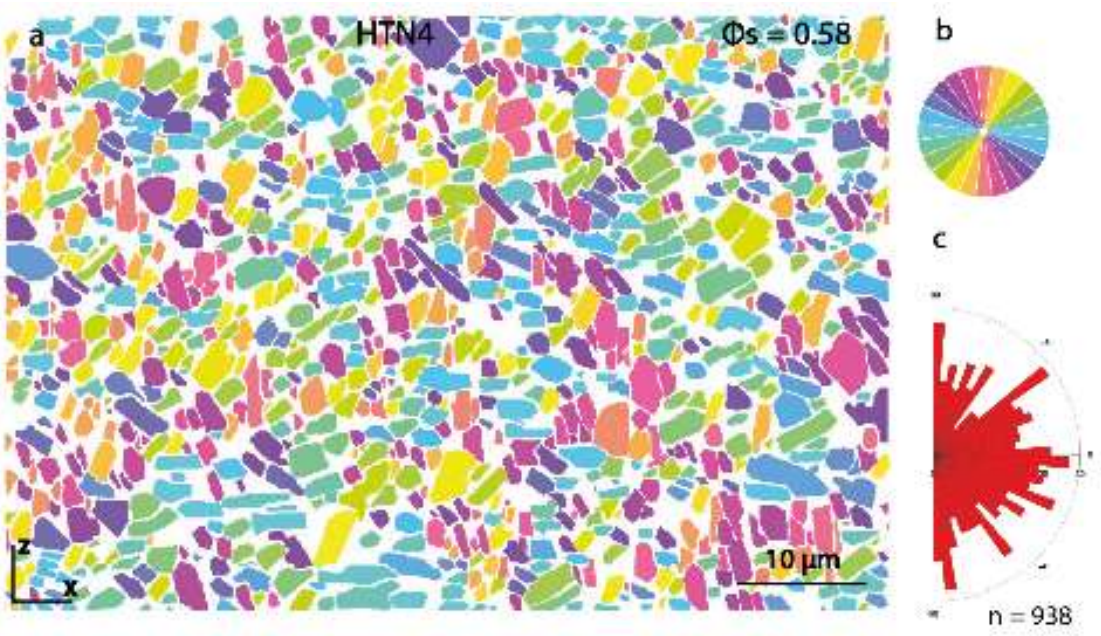

Figure III.18. Crystals orientation of undeformed sample HTN4. (a) Crystals colored according to their orientations. (b) Rose of orientation colors (c) Rose of directions of individual crystal orientation. n = number of measures.

Sample HTN8

The samples HTN8 (fig. III.19a) show a main tensor ellipse with an orientation of α = 19.43° and an eccentricity R = 1.031, calculated by the analysis of the preferential shape orientation. The long axis plagioclases orientation (fig. III.19c) show an orientation at -45° with respect to the X axis, as it is shown in the rose diagram . The crystals were drawn by hand (fig. III.20a, ellipse of direction fig. III.20b). The rose of the directions of the long axes of plagioclase crystals obtained by the inertia method has no preferential orientation (fig. III.20c).

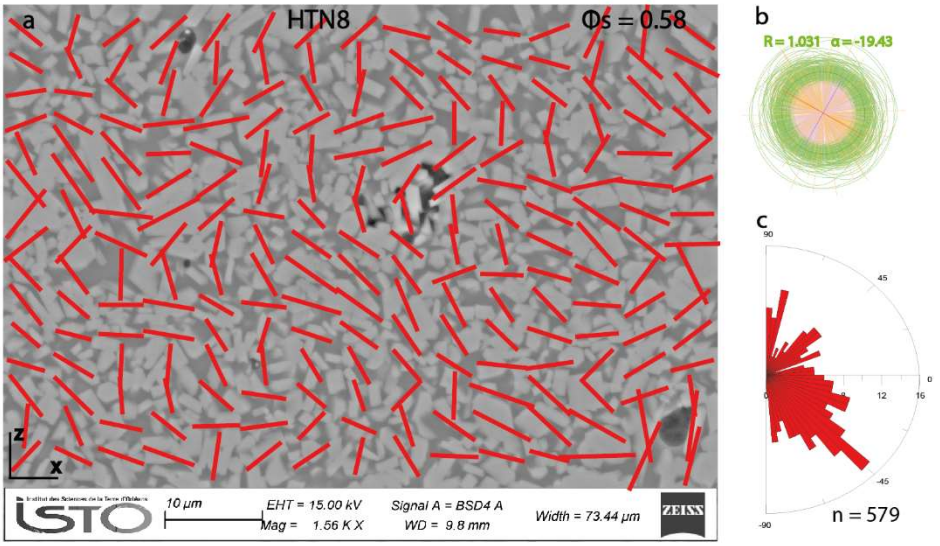

Figure III.19. Determination of textures for HTN8 sample. SEM image in backscattered electrons. (b) Local tensor ellipses of shape fabric. (c) Rose of the directions of the long axes of local shape fabric ellipses. n = number of measures.

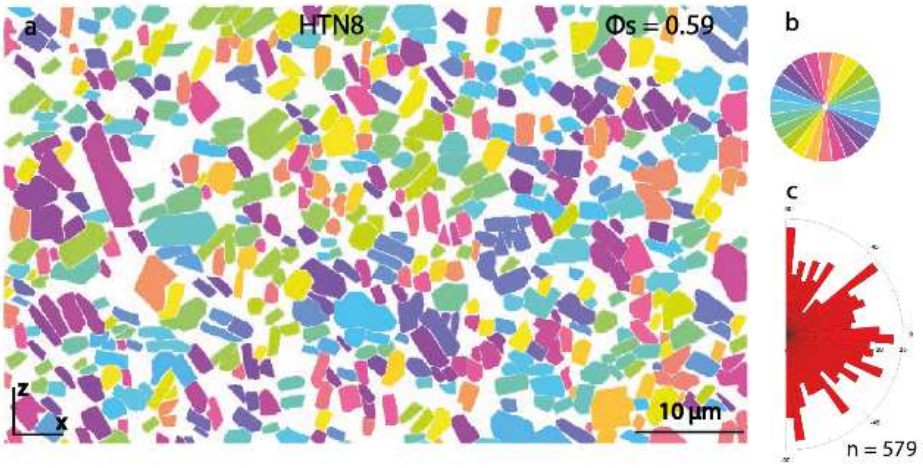

Figure III.20. Crystals orientation of undeformed sample HTN8. (a) Crystals colored according to their orientations. (b) Rose of orientation colors (c) Rose of directions of individual crystal orientation.

Sample HTN9

The samples HTN9 (fig. III.21a) has the main tensor ellipse with R = 1.050, calculated by the analysis of the preferential shape orientation. The long axis orientation of the main tensor ellipse has values of -33° (fig. III.21b). The rose of the directions of the long axes

of plagioclase crystals does not show any preferential direction (fig. III.21c). The hand-drawn crystals of sample HTN9 (fig. III.22a) studied by the inertia method show a light orientation of the crystals between 0° and -45° (fig. III.22c).

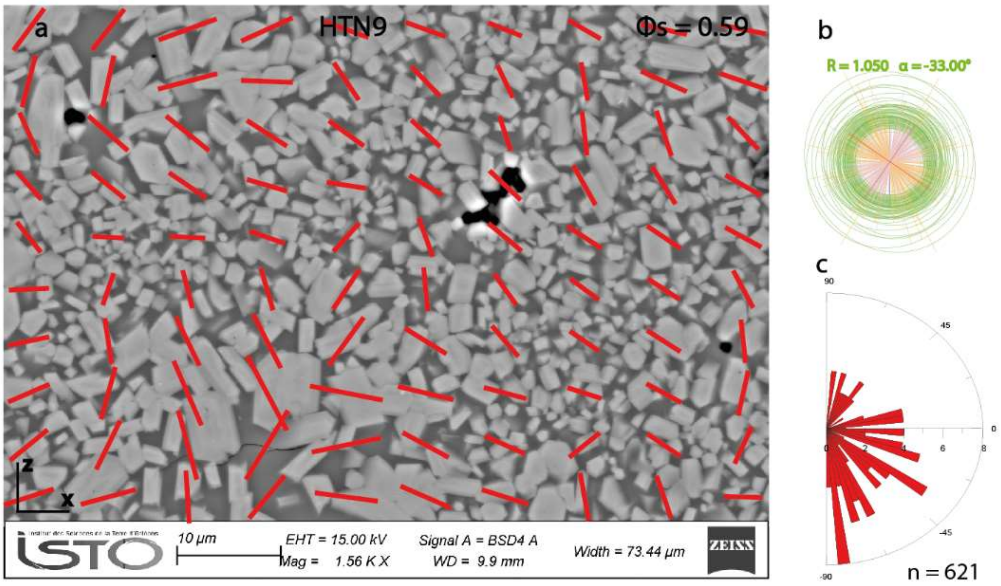

Figure III.21. Determination of textures for HTN9 sample. SEM image in backscattered electrons. (b) Local tensor ellipses of shape fabric. (c) Rose of the directions of the long axes of local shape fabric ellipses. n = number of measures.

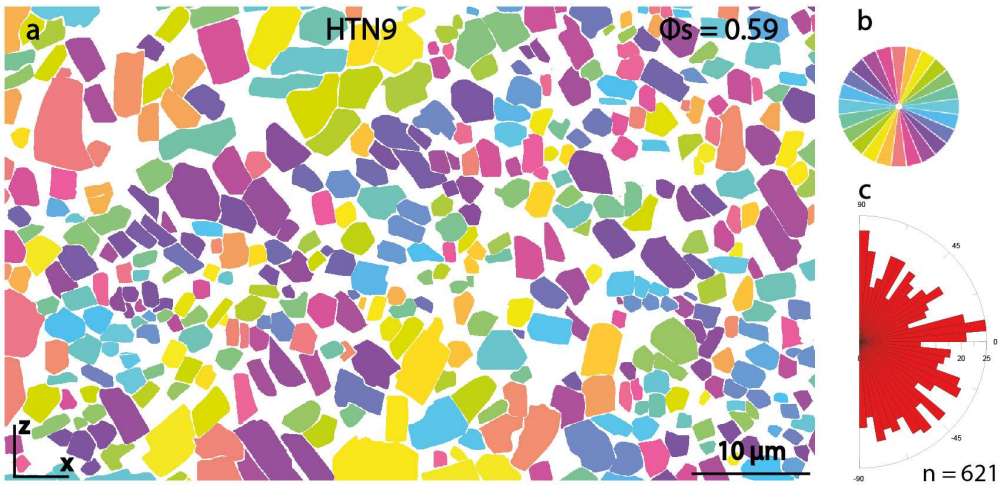

Figure III.22. Crystals orientation of undeformed sample HTN9. (a) Crystals colored according to their orientations. (b) Rose of orientation colors (c) Rose of directions of individual crystal orientation. n = number of measures.

6. Control of crystal size and morphology of HTN11, HTN13 and HTN14 samples

Samples HTN11, HTN13 and HTN14 show an aspect ratio R = 2 and a high crystal content compared to the previously analyzed samples. For this reason, these starting materials were analyzed in a separate paragraph. Due to the very high crystal content (ϕ_s = 0.73 - 0.76) the crystals often overlap. This overlap makes 2D analysis of the samples difficult as the edges of the plagioclases are not clearly visible. Morphological and preferential orientation analyses of samples HTN11, HTN13 and HTN14 may be more subject to error than samples with lower crystal content. Sample HTN12, which has a crystalline content ϕ_s of 0.95, was not analysed in 2D because the amount of crystals is so high that the plagioclase boundaries cannot be discerned.

Sample HTN11 (fig. III.23a) has an eccentricity of the main tensor ellipse R = 1.034 and an orientation direction α of 25.33° (fig. III.23b). The orientations of the long axes of the local ellipses show no specific orientation (fig. III.23c).

In the HTN13 sample (fig. III.24a) the eccentricity of the ellipse of the mean tensor of the shape fabric has a value of R = 1.109, associated with a main orientation direction α of 29.51° (fig. III.24b). The orientations of the long axes of the local ellipses show an orientation between 10° and 70° (fig. III.24c).

The sample HTN14 (fig. III.25a) shows an eccentricity of the main ellipse R of 1.012 with a mean orientation direction of the tensor ellipse α of 61.15° (fig. III.25b) with respect to the shear direction. The orientations of the long axes of the local ellipses do not show any orientation (fig. III.25c).

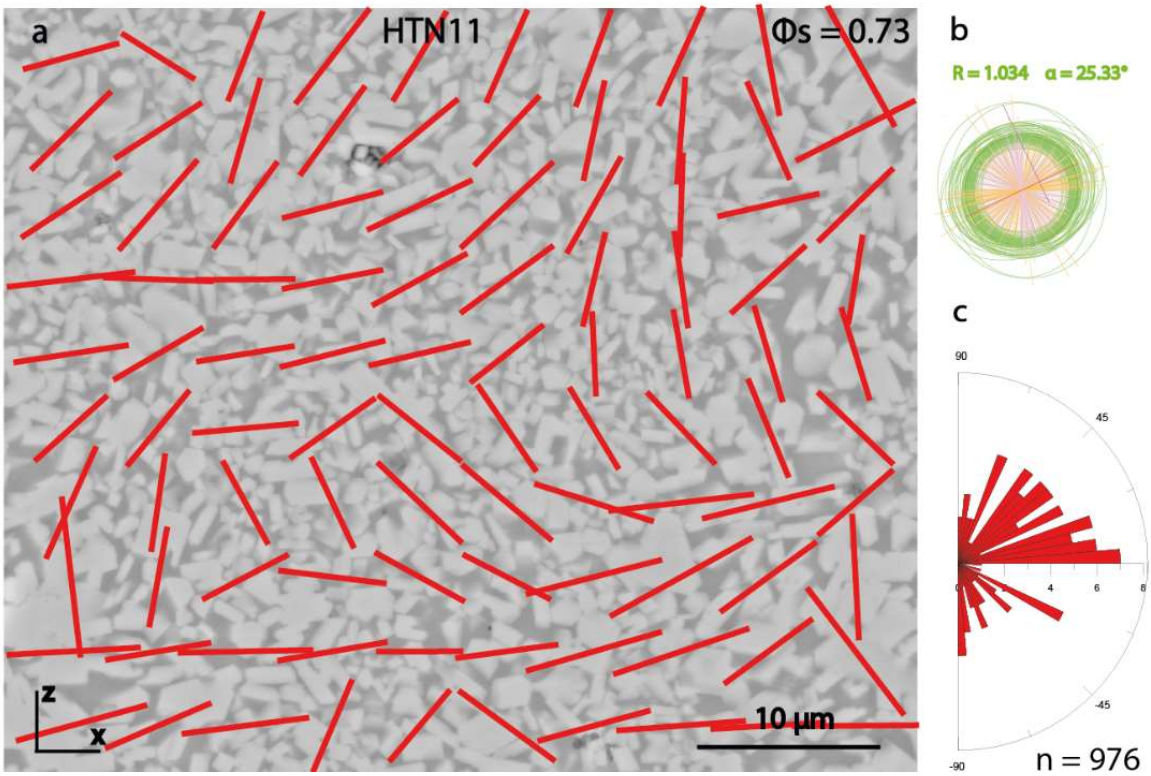

Figure III.23. Determination of textures for HTN11 sample. SEM image in backscattered electrons. (b) Local tensor ellipses of shape fabric. (c) Rose of the directions of the long axes of local shape fabric ellipses. n = number of measures.

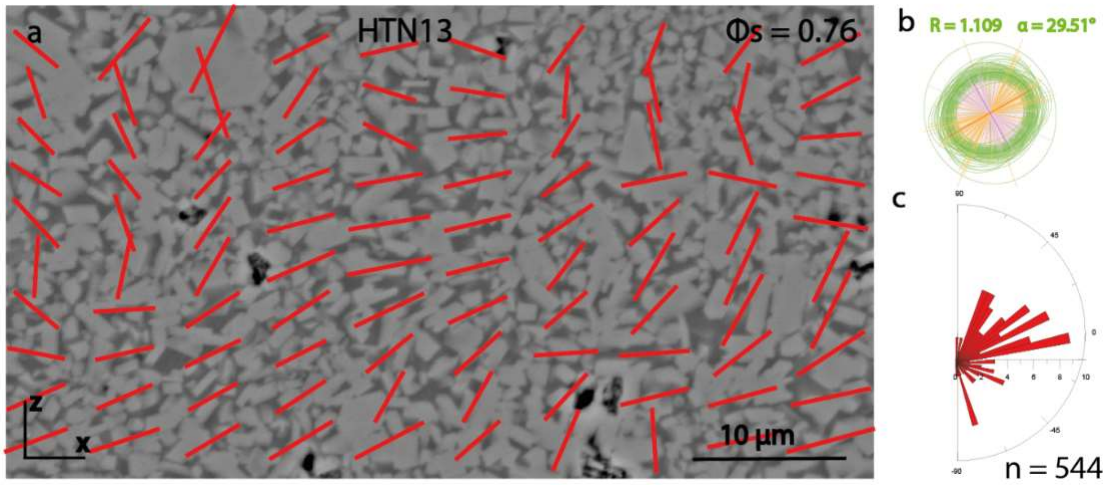

Figure III.24. Determination of textures for HTN13 sample. SEM image in backscattered electrons. (b) Local tensor ellipses of shape fabric. (c) Rose of the directions of the long axes of local shape fabric ellipses. n = number of measures.

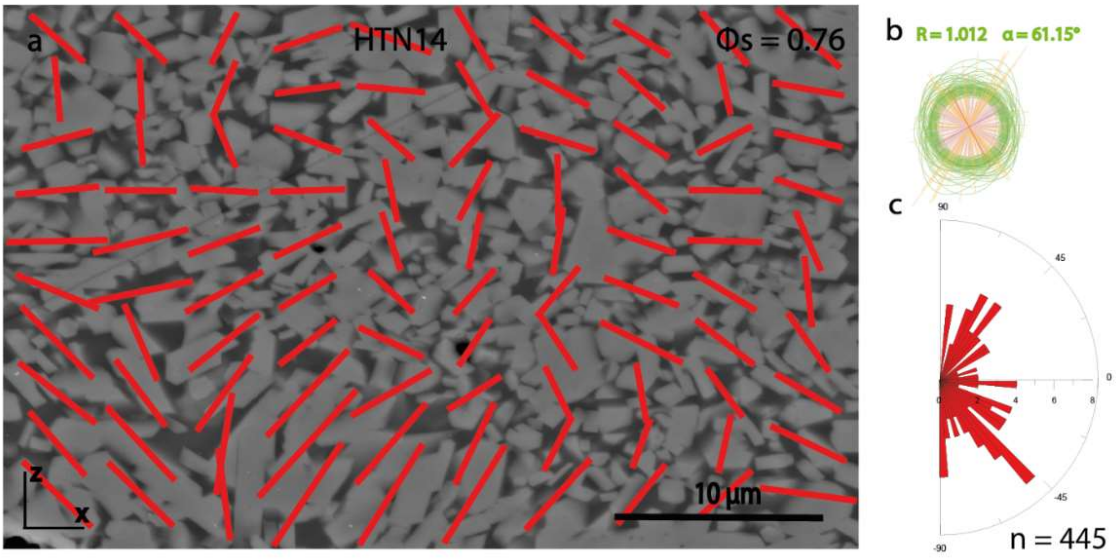

Figure III.25. Determination of textures for HTN14 sample. SEM image in backscattered electrons. (b) Local tensor ellipses of shape fabric. (c) Rose of the directions of the long axes of local shape fabric ellipses. n = number of measures

The hand-drawn crystals of samples HTN11 (fig. III.26a) and HTN14 (fig. III.28a) studied by the inertia method do not show any preferential orientation of the crystals (fig. III.26c and 28c). The sample HTN13 (fig. III.27a) show a preferential direction at 0° and 48° (fig. III. 27c).

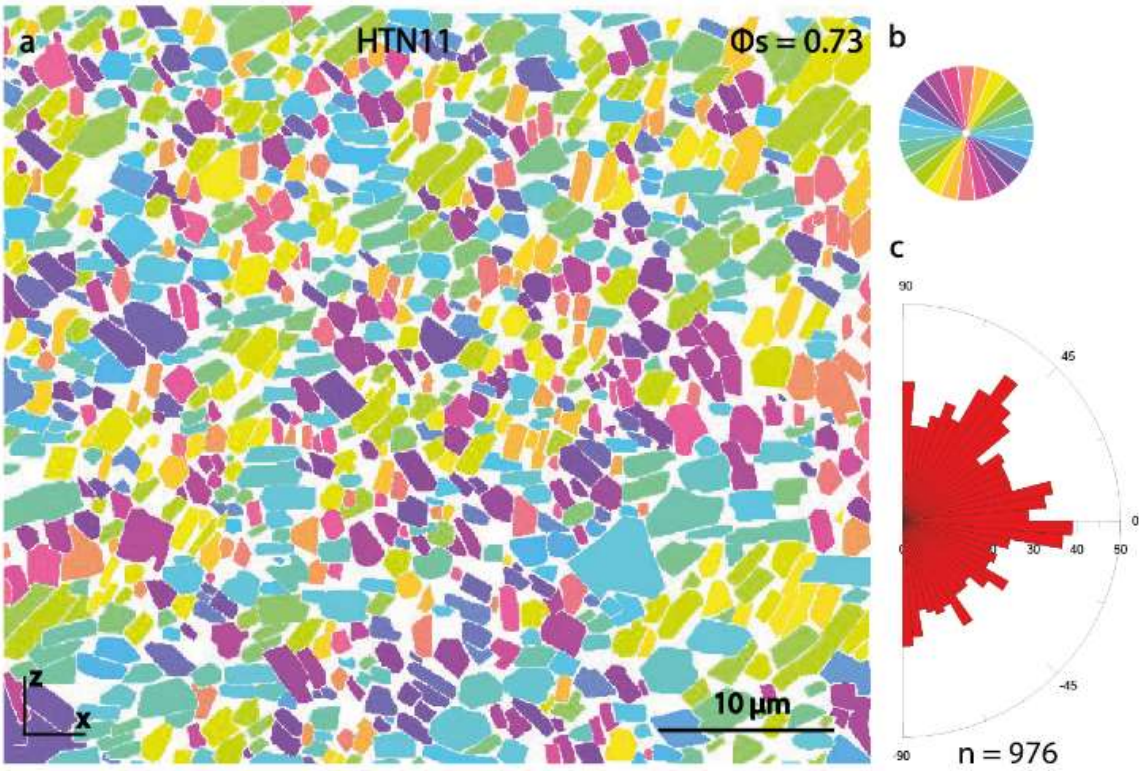

Figure III.26. Crystals orientation of undeformed sample HTN11. (a) Crystals colored according to their orientations. (b) Rose of orientation colors (c) Rose of directions of individual crystal orientation. n = number of measures.

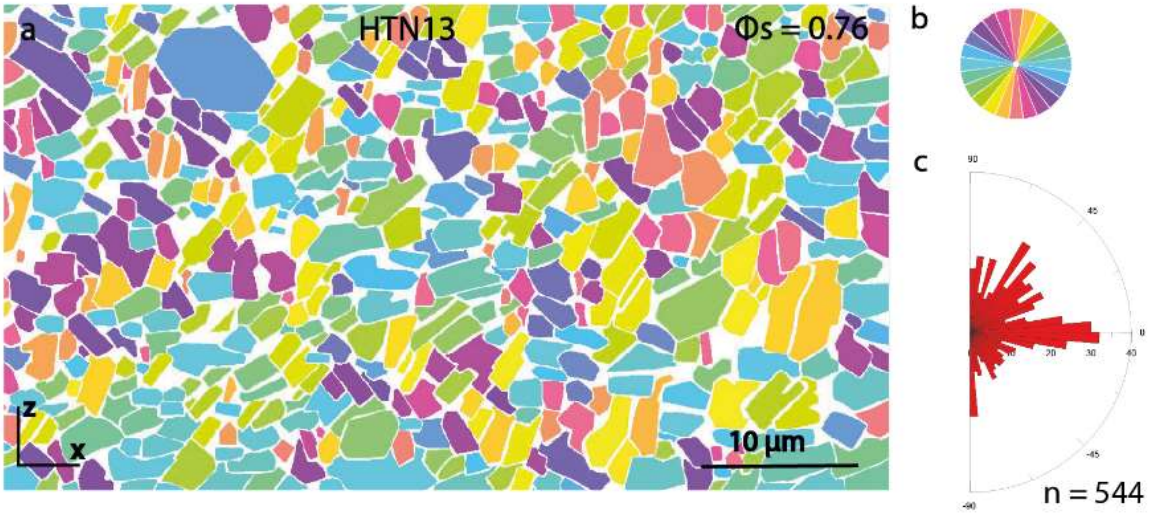

Figure III.27. Crystals orientation of undeformed sample HTN13. (a) Crystals colored according to their orientations. (b) Rose of orientation colors (c) Rose of directions of individual crystal orientation. n = number of measures.

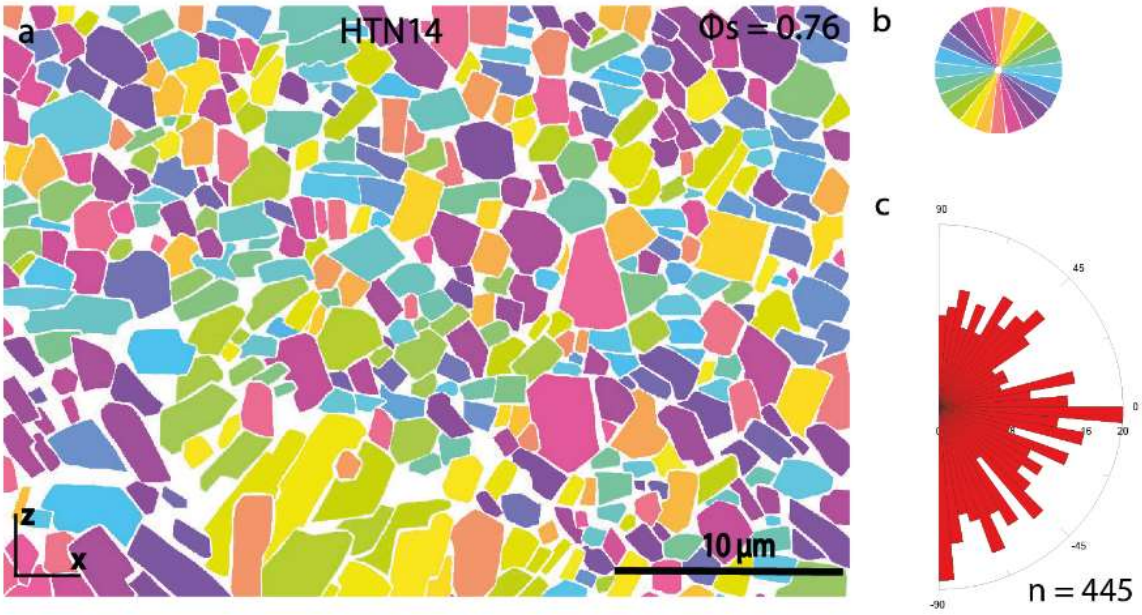

Figure III.28. Crystals orientation of undeformed sample HTN14. (a) Crystals colored according to their orientations. (b) Rose of orientation colors (c) Rose of directions of individual crystal orientation. n = number of measures.

7. Shape fabric of bubbles

Figure III.29 shows the bubbles from samples #7 (fig. III.29a) and #6 (fig. III.29d). The bubbles show no preferred direction (#7 fig. III.29b, #6 fig. III.29e).
The aspect ratio R for sample #7 (fig. III. 29c) has an arithmetic mean of 1.45±0.34 and a harmonic mean of 1.51. The total bubble content of sample #7 is 1.2%.
The aspect ratio R of sample #6 (fig. III.29f) has an arithmetic mean of 1.60±0.44 and a harmonic mean of 1.51. Its total bubble content is 1.2%.

Figure 30 shows the bubbles of samples HTN 4 (fig. III.30a), HTN 8 (fig. III.30d) and HTN 9 (fig. III.30g). None of the samples shows a preferred bubble direction (HTN4 fig. III.30b, HTN8 fig. 30e and HTN9 fig. III.30h).
The aspect ratio R of sample HTN4 (fig. III.30c) has an arithmetic mean of 1.50±0.36 and a harmonic mean of 1.43. Its total bubble content is 3.5%.
Sample HTN8 has an arithmetic mean aspect ratio R (fig. III.30f) of 1.52±0.38 and a harmonic mean of 1.62. Its total bubble content is 2%.

The aspect ratio R of sample HTN9 (fig. III.30i) has an arithmetic mean of 1.45±0.33 and a harmonic mean of 1.40. Its total bubble content is 3.6%.

Figure 31 shows the bubbles of samples HTN 11 (fig. III.31a), HTN 13 (fig. III.31d) and HTN 14 (fig. III.31g). As with the previous samples, these starting materials do not show any preferential bubble direction (HTN11 fig. 31b, HTN13 fig. III.31e and HTN14 fig. III.31h).

The aspect ratio R for sample HTN11 (fig. III.30c) has an arithmetic mean of 1.41±0.25 and a harmonic mean of 1.37. The total bubble content of sample HTN11 is 4.5%.

The aspect ratio R of sample HTN13 (fig. III.30f) has an arithmetic mean of 1.53±0.47 and a harmonic mean of 1.44. Its total bubble content is 3.3%.

The aspect ratio R of sample HTN14 (fig. III.30i) shows an arithmetic mean of 1.47±0.34. The harmonic mean is 1.41 and the total bubble content is 5.1%.

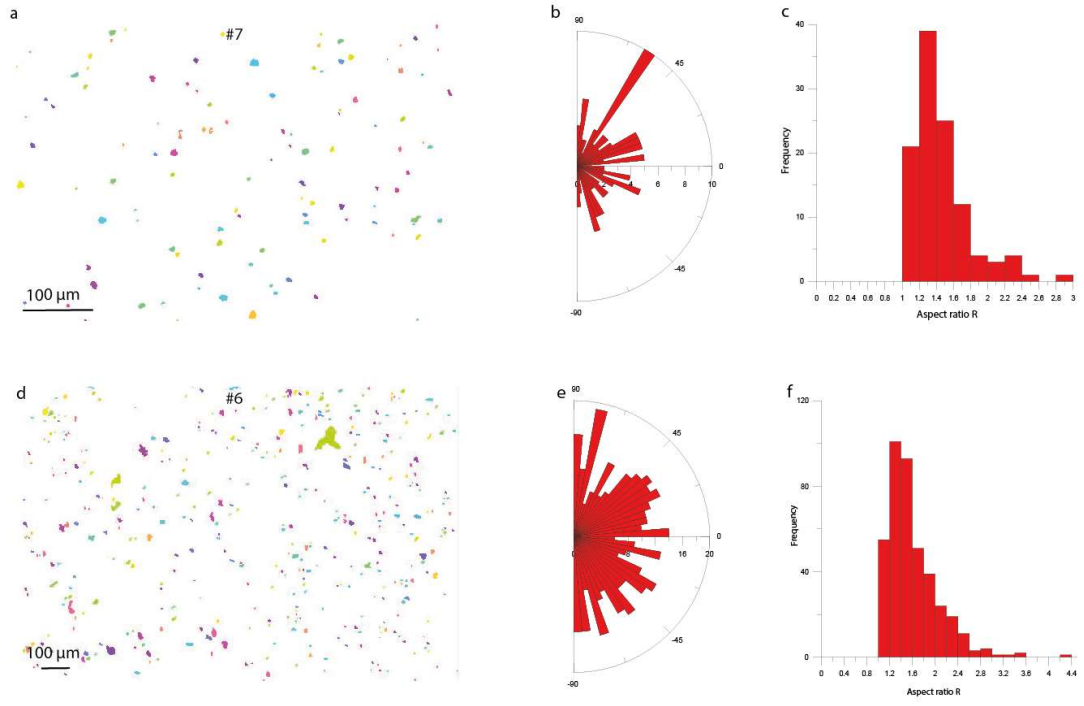

Figure III.29. Bubbles orientation of the sample #7 (top) and #6 (bottom) a) Crystals colored according to their orientations for sample #7. b) Rose of directions of individual bubbles orientation for sample #7. c) Aspect ratio R histogram of bubbles from sample #7. d) Crystals colored according to their orientations for sample #6. e) Rose of directions of individual bubbles orientation for sample #6. f) Aspect ratio R histogram of bubbles from sample #6.

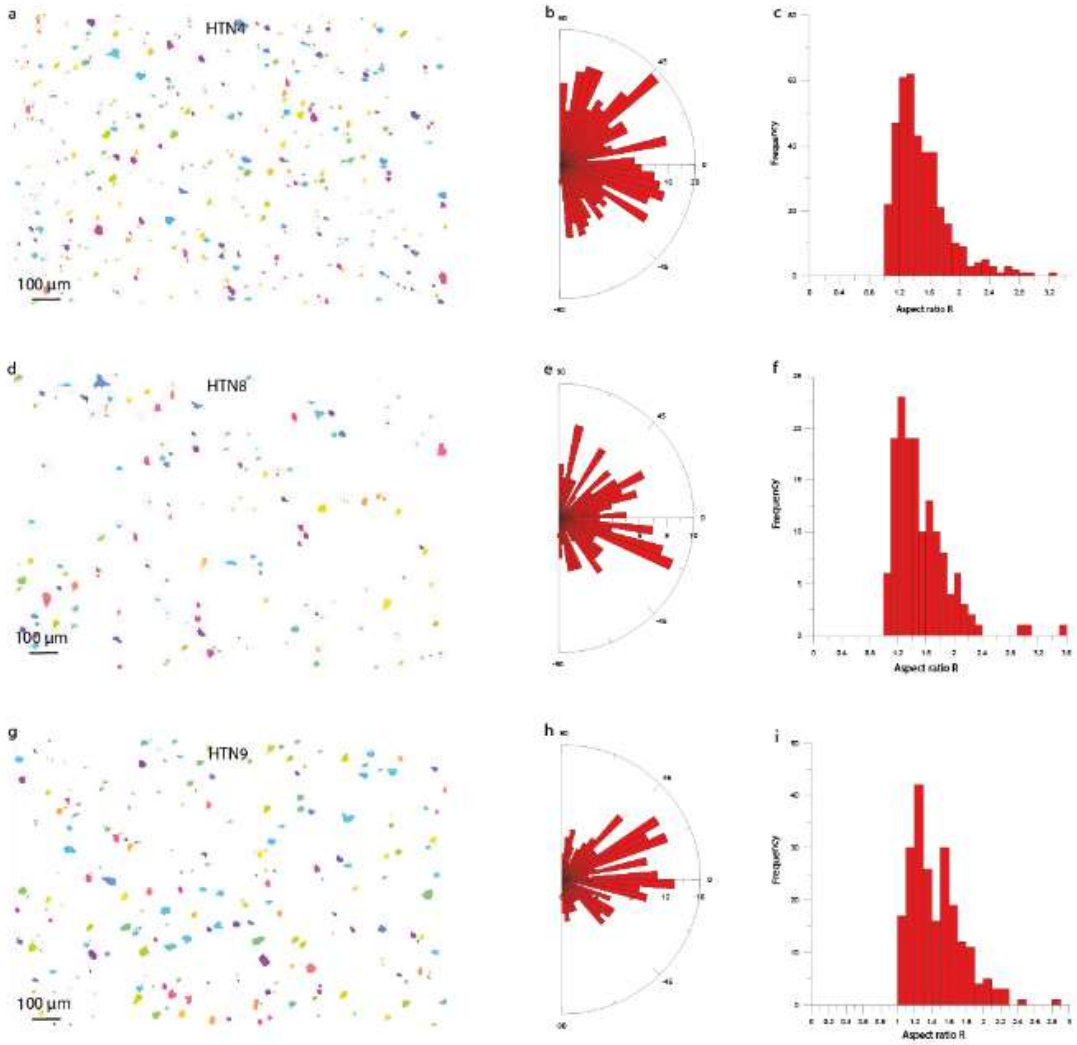

Figure III.30. Bubbles orientation of the sample HTN4 (top), HTN8 (center) and HTN9 (bottom) a) Crystals colored according to their orientations for sample HTN4. b) Rose of directions of individual bubbles orientation for sample HTN4. c) Aspect ratio R histogram of bubbles from sample HTN4. d) Crystals colored according to their orientations for sample HTN8. e) Rose of directions of individual bubbles orientation for sample HTN8. f) Aspect ratio R histogram of bubbles from sample HTN8. g) Crystals colored according to their orientations for sample HTN9. h) Rose of directions of individual bubbles orientation for sample HTN9. i) Aspect ratio R histogram of bubbles from sample HTN9.

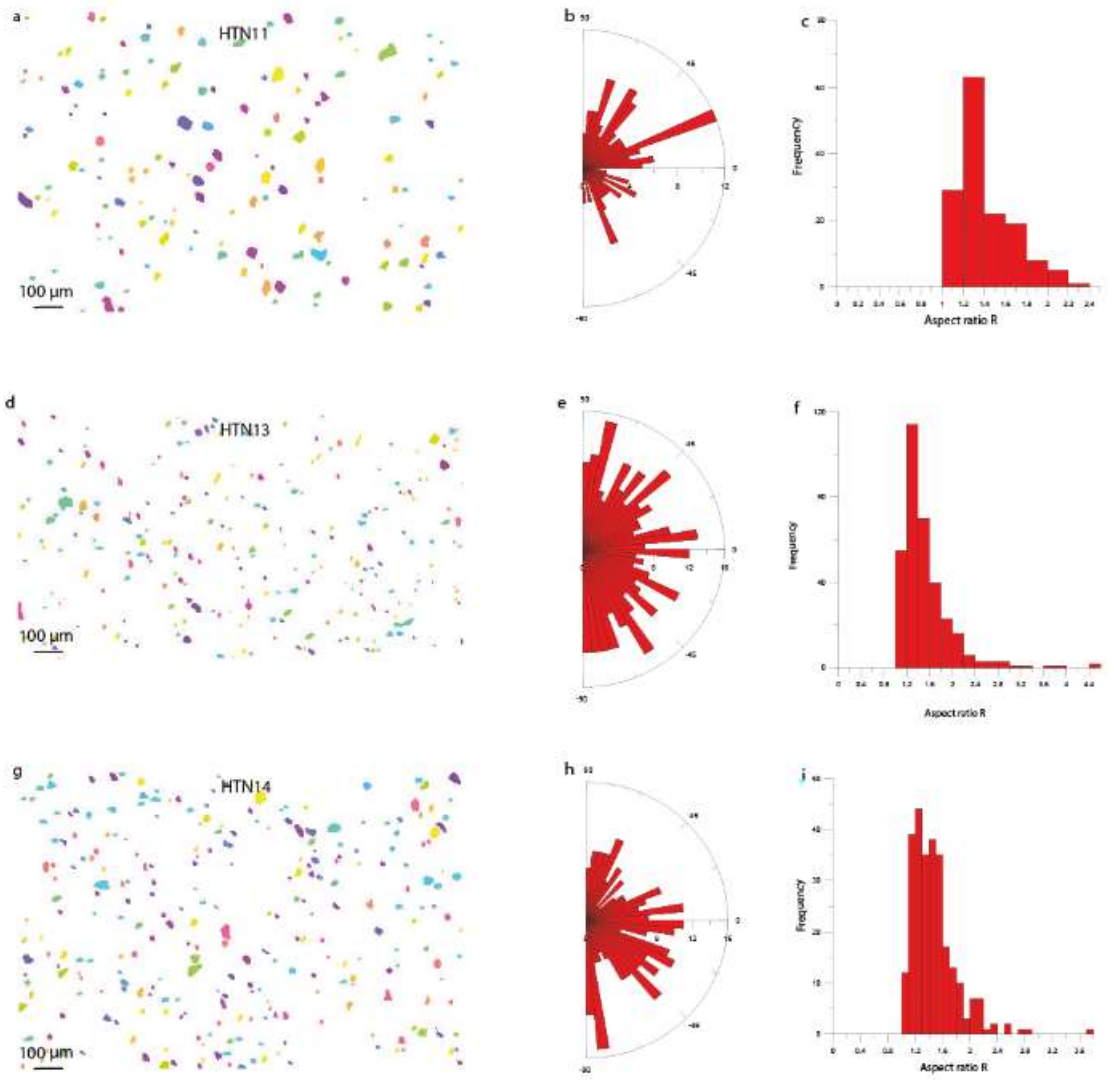

Figure III.31. Bubbles orientation of the sample HTN11 (top), HTN13 (center) and HTN14 (bottom) a) Crystals colored according to their orientations for sample HTN11. b) Rose of directions of individual bubbles orientation for sample HTN11. c) Aspect ratio R histogram of bubbles from sample HTN11. d) Crystals colored according to their orientations for sample HTN13. e) Rose of directions of individual bubbles orientation for sample HTN13. f) Aspect ratio R histogram of bubbles from sample HTN13. g) Crystals colored according to their orientations for sample HTN14. h) Rose of directions of individual bubbles orientation for sample HTN14. i) Aspect ratio R histogram of bubbles from sample HT14.

Results locked-up mush - R = 4

Résumé du chapitre IV - Résultats - Locked-up mush - R = 4

Dans ce chapitre, tous les résultats sont rapportés pour des échantillons synthétiques de composition haplotonalitic formés à partir de plagioclase avec un rapport d'aspect R = 4 et une teneur en cristaux = 0,52 et 0,58. Les échantillons ont été synthétisés à l'aide d'un IHPV et déformés par torsion à l'aide d'une presse Paterson pendant la thèse de doctorat de Picard.
Les valeurs de déformation finie sont comprises entre 0.5 et 10, tandis que les valeurs de vitesse de déformation sont comprises entre $5.0*10^{-5}$ s^{-1} et $2.1*10^{-3}$ s^{-1}.
Les échantillons ont été photographiés pour réaliser des reconstructions panoramiques. Ils ont été étudiés du point de vue de leurs caractéristiques morphologiques (rapport d'aspect R et diamètre équivalent), de leurs microstructures et de l'orientation préférentielle de leur forme, ainsi que de leur chimisme. Enfin, les types de contacts et d'e clusters développés ont été étudiés.

Tous les échantillons avec un rapport d'aspect R = 4 sont caractérisés par la localization des forces et la formation de bandes de cisaillement.
Lorsque les échantillons avec ϕ_s = 0,52 sont déformés, les cristaux se translatent et tournent pour former une foliation. La déformation est répartie sur l'ensemble de l'échantillon et des chaînes de force et les clusters se forment dans toute la zone déformée. L'étape finale est la formation de bandes de cisaillement C' par dilatation.

L'échantillon avec ϕ_s = 0,58 et un taux de déformation $\dot{\gamma}$ = 8,9*10-4 s-1 présente un comportement différent. En raison de la teneur élevée en cristaux, les cristaux ne peuvent pas tourner ni se déplacer. Cela conduit à une accumulation de déformation dans certaines zones de l'échantillon avec la formation de chaînes et d'amas de force importants. Au stade final, des bandes de cisaillement C sont formées en raison de la forte accumulation de déformation.

L'échantillon avec ϕ_s = 0,58 et un taux de déformation $\dot{\gamma}$ = 2,1*10-3 s-1 présente le même comportement que l'échantillon précédent. En raison de la vitesse de déformation rapide, une seule région centrale déformée est formée par des bandes de cisaillement C, C' et des thrust shear bandes.

Les bulles ont conservé les mêmes propriétés que le matériau de départ et n'ont donc pas été déformées. Elles ne présentent une orientation que pour l'échantillon PP249.

IV. Results - Locked-up mush - R = 4

This section reports the results of the deformation experiments for the samples with an aspect ratio R ≃ 4. The samples have a variable crystal content ϕ_s between 0.52 and 0.59 and were subjected to different strain rate $\dot{\gamma}$ and finite strain γ (for more details on synthesis and deformation experiments on samples with R = 4, see the work of Picard (PhD thesis), 2009, and the work of Laumonier, 2013). Each sample is studied individually, analyzing the SPO and CPO of the different sample areas. The following sections show the first results on the contacts and clusters formed in the samples. The table IV.1 below shows the experiments performed at Paterson press. The values of aspect ratio R and equivalent diameter Φ correspond to the harmonic mean values, so they are lower than the arithmetic mean values, but are more representative. As can be seen from the figure IV.2 and figure IV.3, the histograms have a log-normal trend, with the highest values on the x-axis being unrepresentative due to their small number. In order to minimize these values, the harmonic mean is considered to be the most representative and it was decided to show the harmonic mean values in table IV.1.

A summary table with all deformation experiments performed for both samples with aspect ratio R = 4 and aspect ratio R = 2 is shown in Appendix A.

Starting material	Aspect ratio R	Equivalent diameter Φ (μμ)	H_2O content (wt.%)	P (MPa)	T (°C)	Finite strain γ	Strain rate $\dot{\gamma}$ (s^{-1})
#7	2.73 ± 1.51	2.37 ± 1.23	3	300	800	1.4	$1.1*10^{-4}$
#6	2.74 ± 1.53	2.85 ± 1.45	3	300	800	1.4	$8.9*10^{-4}$
#6	2.13 ± 1.29	1.84 ± 1.53	3	300	700	2.0	$2.1*10^{-3}$

Table IV.1. Deformation experiments for the samples with R ≃ 4 and ϕ_s = 0.52 – 0.59. The values for aspect ratio R and equivalent diameter Φ are the harmonic mean values, which are more representative of the samples.

1. Panoramic reconstruction

Figure IV.1 shows the panoramic reconstructions of the samples after the deformation experiments. All the samples were subjected to rightward torsion. Sample PP043 (fig. IV.1a) shows a homogenous deformation with a break in the copper cover. This is probably due to a localization of the deformation at the end of the experiment. Sample PP029 (fig. IV.1b) shows inhomogeneous deformation, with more intensely deformed areas (dashed red lines). Sample PP249 (fig. IV.1c) shows very inhomogeneous deformation with localization of the deformation.

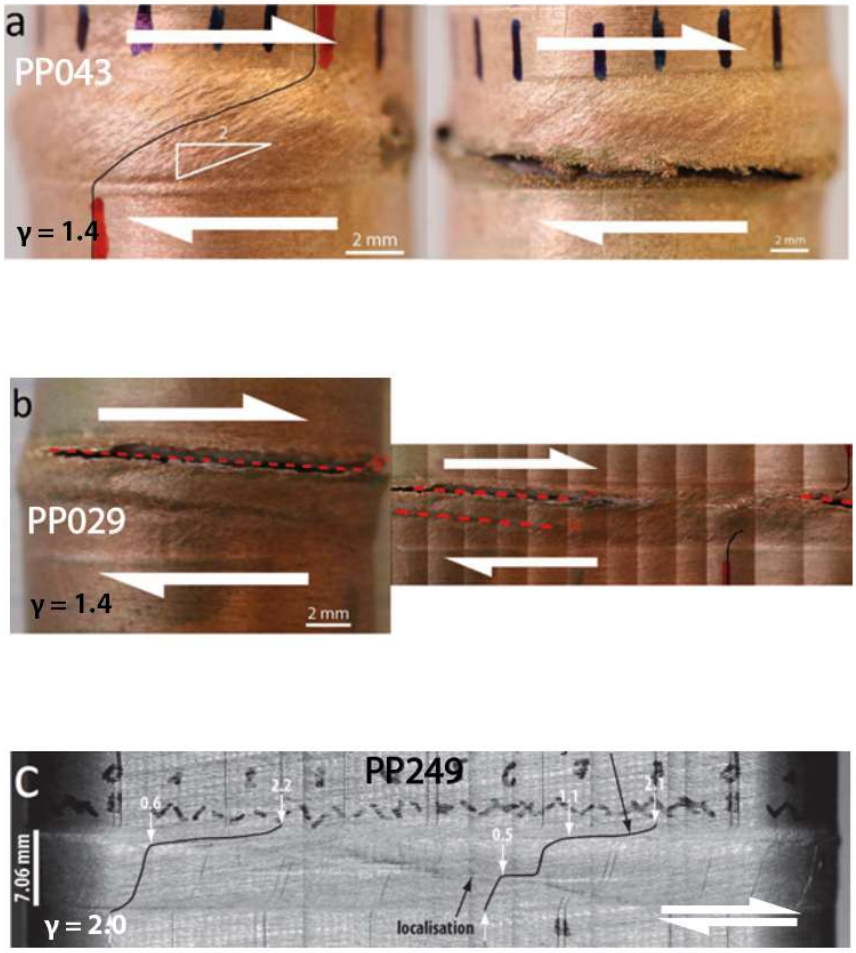

Figure IV.1. Panoramic reconstruction of the samples still embebbed in their copper jacket subject to torsion deformation. a) PP043, b) PP029, c) PP249. Deformation rates (black line) are indicated on each image. Modified from (Laumonier, 2013; Picard et al., 2011).

2. Crystal morphology

For all the experiments, the aspect ratio R and equivalent diameter Φ were calculated, considering the mode, the arithmetic and the harmonic mean.

2.1 Equivalent diameter Φ

Figure IV.2 shows the distribution of the equivalent diameter values for the experiments PP043, PP029 and PP249. Groups of crystals were analyzed in the penetrative fabric and in the shear bands.

Sample PP043 in its penetrative fabric (fig. IV.2a) has an average equivalent diameter of 2.87±1.23 µm, with a harmonic mean of 2.37 µm. The mode is 2.5 µm. The shear bands area (fig. IV.2b) shows a slightly smaller equivalent diameter, with an arithmetic mean of 2.45±1.0 µm and harmonic mean of 2.03 µm. The mode is 2.0 µm.

The crystals of the penetrative fabric of sample PP029 (fig. IV.2c) have a mean equivalent diameter values of 3.44±1.45 µm and a harmonic mean of 2.85 µm. The mode is 2.5. The shear bands of sample PP029 (fig IV.2d) have an equivalent diameter of 2.43±1.02 µm, with a harmonic mean of 2.01 µm. The mode is 1.6 µm.

Sample PP249 has an equivalent diameter value in its penetrative fabric of 2.58±1.53 µm (fig. IV.2e), with a harmonic mean of 1.84. The mode is 1.4. In the shear bands, the equivalent diameter is 1.95±0.84 µm with a harmonic mean of 2.11 µm. The mode is 2.2 µm (fig. IV.2f).

All samples show larger equivalent diameters in the penetrative fabrics than in the shear bands. The mode and harmonic mean values are similar for all samples, except for the shear band of sample PP249. The arithmetic mean, however, is different and always significantly higher. This indicates a log-normal population with not too much inhomogeneity in the equivalent granule diameters. The most representative value is the harmonic mean. The numerical data can be found in Appendix B.

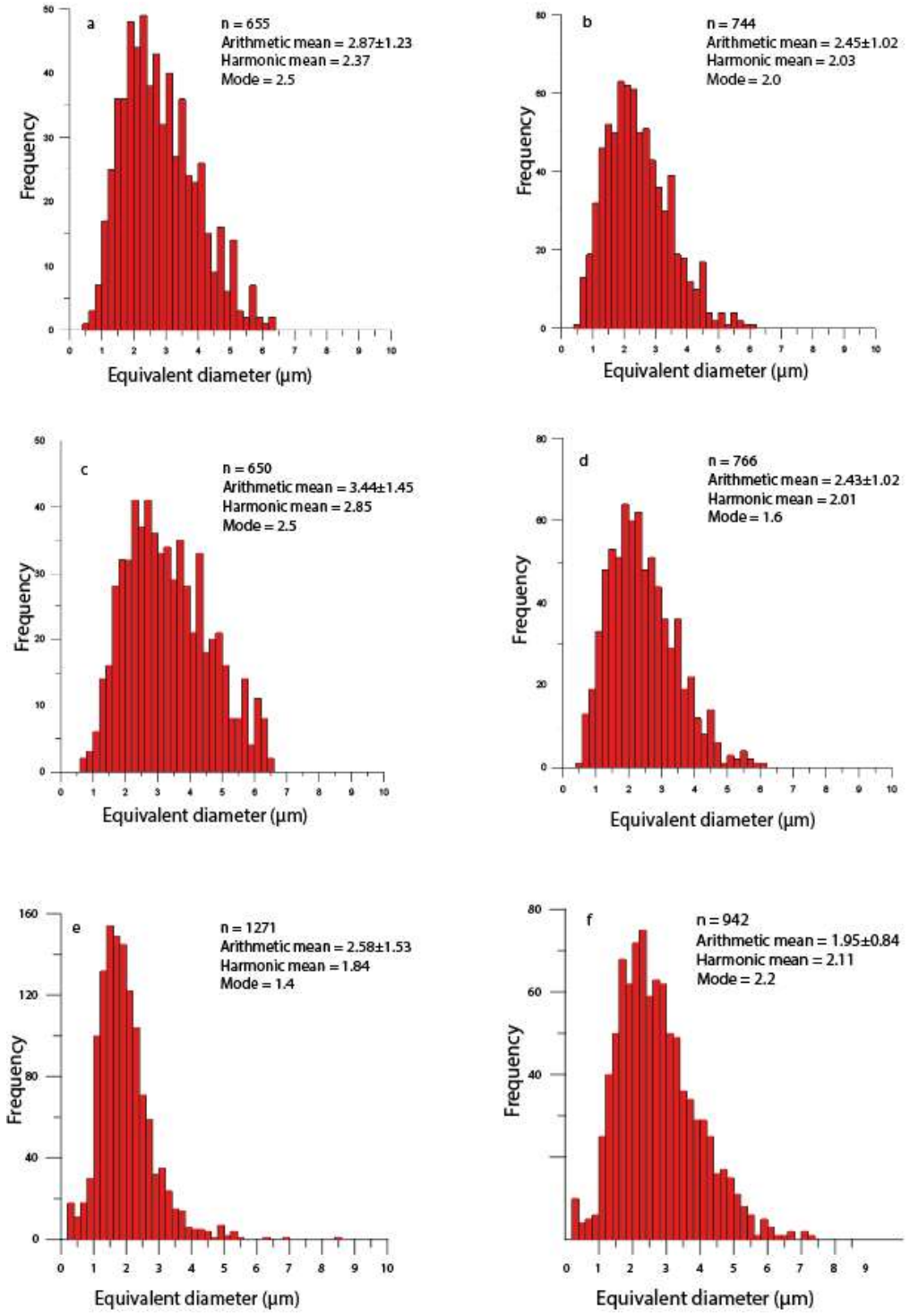

Figure IV.2. Histograms of equivalent diameters calculated in groups of crystals in deformation experiments. a) PP043 penetrative fabric, b) PP043 shear band, c) PP029 penetrative fabric, d) PP029 shear band, e) PP249 penetrative fabric, f) PP249 shear band.

2.2 Aspect ratio R

Figure IV.3 represents the aspect ratio R in arithmetic mean, in harmonic mean and in mode for each population of crystals divided into main/penetrative fabric - shear bands.

Sample PP043 in the penetrative fabric (fig. IV.3a) shows a maximum R value of 7, a minimum value of 1, an arithmetic mean of 3.29±1.51 and a harmonic mean of 2.73. The mode is 2.3. In the shear bands (fig. IV.3b), the maximum and minimum R value is the same of the penetrative fabric, with a maximum of 7 and a minimum of 1. The arithmetic mean is 3.33±1.48 and the harmonic mean is 2.77. The mode is 2.2. There are no significant numerical variations between the penetrative fabric and the shear bands.
The penetrative fabric of PP029 sample (fig. IV.3c) shows a maximum R value of 7 and a minimum value of 1. The arithmetic mean is 3.31±1.53, the harmonic mean is 2.74 and the mode is 2.5. Again, the shear bands of sample PP029 have a maximum R value of 7 and a minimum of 1, with an arithmetic mean of 3.26±1.46 and a harmonic mean of 2.70. The mode is 2.2 (fig. IV.3d). As in the previous sample, the R values in the penetrative fabric and shear bands are similar.
Sample PP249 has a maximum R value of 7 and a minimum of 1 in its penetrative fabric (fig. IV.3e), with an arithmetic mean of 2.54±1.29, a harmonic mean of 2.13 and a mode of 1.4. The values in the shear bands (fig. IV.3f) are lower, with the maximum R equal to 4.2, minimum R equal to 1, an arithmetic mean of 2.46±0.90 and a harmonic mean of 2.21. The mode is 1.8.
The aspect ratio R values are similar for samples PP043 and PP029, while sample PP249 shows lower values. The arithmetic mean and harmonic mean never coincide, while the mode values are similar to the harmonic mean. This makes the harmonic mean the most reliable value, showing log-normal populations.

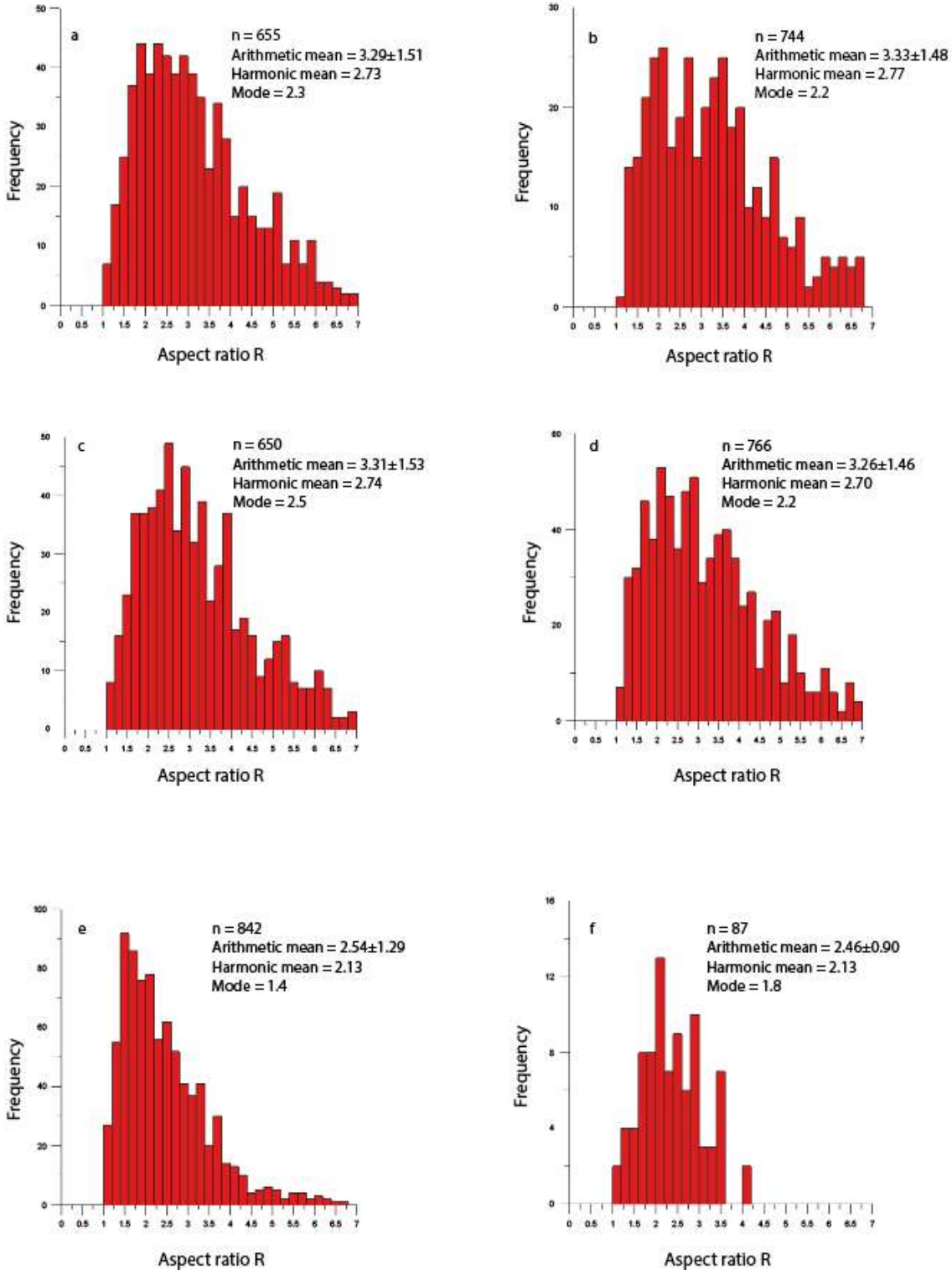

Figure IV.3. Histograms of aspect ratio calculated in groups of crystals in deformation experiments. a) PP043 penetrative fabric, b) PP043 shear band, c) PP029 penetrative fabric, d) PP029 shear band, e) PP249 penetrative fabric, f) PP249 shear band.

3. Chemical composition of plagioclases and residual glass

The chemical compositions of the crystals and glass of experiments PP043, PP029 and PP249 are shown in the table IV.2a and IV.2b. The analyses were carried out in the penetrative fabric and in the shear bands, on the crystals and on the glass. The results show homogeneous compositions, similar to those of the starting materials. This proves that there was no dissolution or crystallization processes during the deformation experiments. The plagioclase crystals of samples PP043 and PP249 show similar chemical analyses and the results are comparable. Sample PP029 has a high Na_2O content. This may be due to the formation of two generations of plagioclase during synthesis. The first generation nucleated during the initial phase and has a sodium content of about 7. The second generation shows an enrichment of sodium with values of about 10. Further chemical analyses can be found in Appendix D.

a

Mineral	**Plagioclase**		**Plagioclase**		**Plagioclase**	
Sample	**PP043**		**PP029**		**PP249**	
n	**12**		**15**		**11**	
		±		±		±
Na_2O	7.68	0.15	10.60	1.53	7.19	0.48
SiO_2	61.86	1.79	67.79	1.01	62.40	2.54
Al_2O_3	24.22	1.12	20.26	0.85	23.69	1.53
CaO	6.15	0.75	4.46	0.09	6.64	1.43
Total	99.90		103.11		99.91	

b

Glass	**PP043**		**PP029**		**PP249**	
Sample	**10**		**15**		**10**	
n						
		±		±		±
Na_2O	6.62	0.69	5.09	1.26	6.00	1.00
SiO_2	67.6	1.57	70.84	3.81	69.72	1.86
Al_2O_3	17.39	2.63	14.01	2.69	15.93	2.03
CaO	2.82	0.85	1.77	0.60	2.04	1.02
Total	94.43		91.71		93.69	

Table IV.2. a) Plagioclase chemical composition from deformed samples. b) Residual glass chemical composition from deformed samples.

4. Study of the microstructures

This section shows the results of 2D analysis of samples with aspect ratio R = 4. Samples are classified according to their crystal content ϕ_s, finite strain γ and strain rate $\dot{\gamma}$.

ϕ_s = 0.52, γ = 1.4 and $\dot{\gamma}$ = 1.1*10^{-4} s^{-1} (PP043)

Sample PP043 (fig. IV.4a) shows a pervasive fabric crossed by shear bands oriented at -20° / -25° to the shear direction. The shear bands have a thickness of 40 µm. The pervasive fabric shows an orientation of the long axes of the crystals at 45° and 70° (fig. IV.4c) and the mean value of the eccentricity of the mean tensor ellipse of the shape fabric is 1.27 (fig. IV.4b), with an average inclination α of 52.39°.
In the shear band, the average eccentricity of the mean tensor ellipse of the shape fabric is 1.60 and α is 3.01° (fig. IV.4d). The orientation of the crystals is between +10° and -10°, aligned close to the bulk shear direction (fig. IV.4e).
A part of the sample was analyzed with the SPO software in order to better characterize the crystal orientations. The plagioclase crystals were individually hand-drawn using Illustrator software. The figures IV.5a and IV.5d show the analysis of the individual crystals in the penetrative fabric and shear bands. In the penetrative fabric there is unimodal distribution of the crystals with a mean tensor ellipse of 1.31 (fig. IV.5b) and a preferential orientation between 30° and 75° (fig. IV.5c) to the shear direction. In the shear bands, the mean tensor ellipse R_x of 2.09, an inclination α of 53.67° (fig. IV.5e). The orientation of the crystals is well defined and it is between -10° and 15° (fig. IV.5f) with respect to the shear direction. These results are very similar to those obtained with the intercept method.

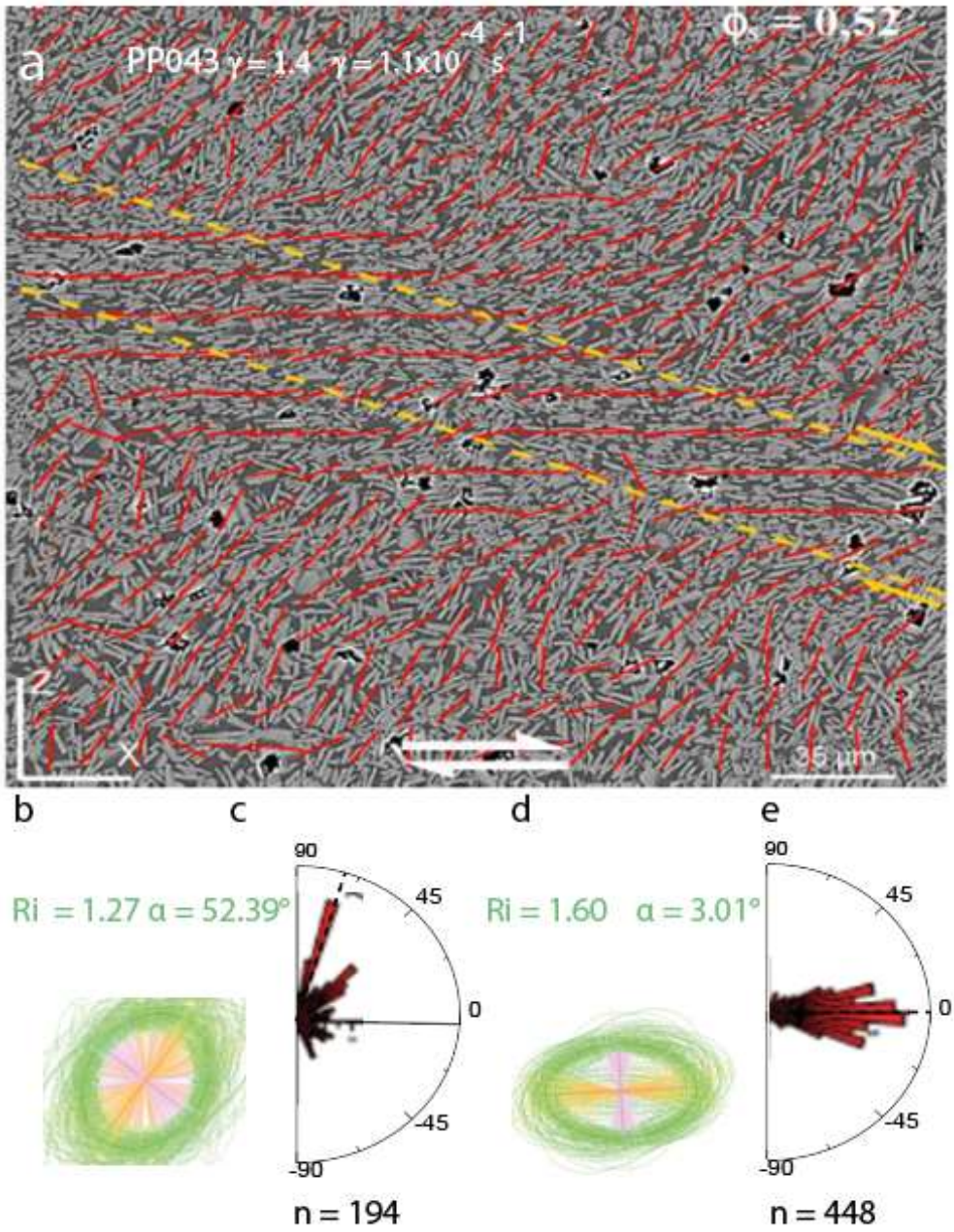

Figure IV.4. Preferential orientation of sample PP043 a) [XZ] section SEM image of the sample PP043. Dashed yellow lines delimit the shear band. The red lines represent the long axes of the local tensor ellipses of the shape fabrics. b) Mean tensor ellipse of the shape penetrative fabric. R_i = eccentricity of the mean ellipse, α = orientation of the long axis of the ellipse. c) Rose diagram of long axes of local tensor ellipses of penetrative fabric. d) Mean tensor ellipse of the shape fabric in the shear band. e) Rose diagram of long axes of local tensor ellipses of shear band. Modified from Picard et al., 2011.

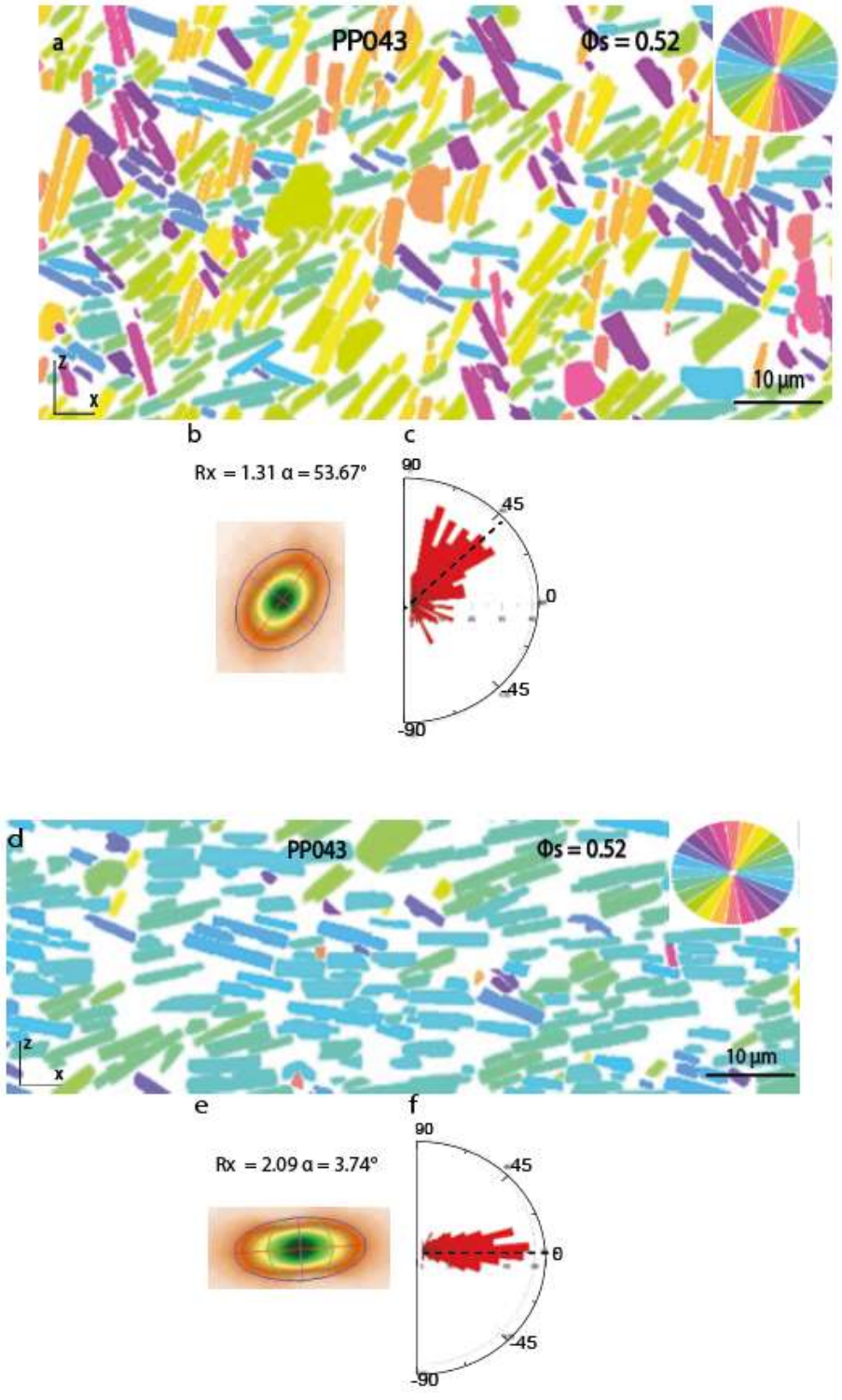

Figure IV.5. Orientation of the long axes of the plagioclases of sample PP043 in the penetrative fabric (a) and in the shear band (d). b) Mean tensor ellipse for the penetrative fabric. c) Rose diagram of individual crystal orientation for the penetrative

fabric. e) Mean tensor ellipse for the shear band. f) Rose diagram of individual crystal orientation for the shear band.

ϕ_s = 0.58, $\dot{\gamma}$ = 1.4 and $\mathring{\dot{\gamma}}$ = 8.9*10^{-4} s^{-1} (PP029)

The sample PP029 (fig. IV.6a) shows no pervasive structure or crystals orientation in the penetrative fabric (fig. IV.6c). In the penetrative fabric, the eccentricity of the mean tensor ellipse of the shape fabric has a value of R_i = 1.07 and an inclination α of 28.93° (fig IV.6d).

The shear bands crossing the sample have an inclination of -10° and a thickness between 40 μm and 50 μm (fig. IV.6a). The orientations of the long axes of the local ellipses in the shear bands show an orientation between 20° and -15° (fig. IV.6b). The values of eccentricity R_i and inclination α of the mean tensor ellipse are 1.61 and 3.01°, respectively (fig. IV.6e).

By analyzing the individual crystals, shown in fig. IV.7a for the non-penetrative area and in fig. IV.7d for the shear band, it can be observed that the penetrative fabric there is a slight orientation between 10° and 75°, (fig. IV.7c) while the shear bands have a preferential orientation between +10° and -10° (fig. IV.7f). The mean tensor ellipse for the penetrative fabric is 1.10 with α = 15.74° (fig. IV.7b) and for the shear band is 2.04 with α = 3.20° (fig. IV.7e).

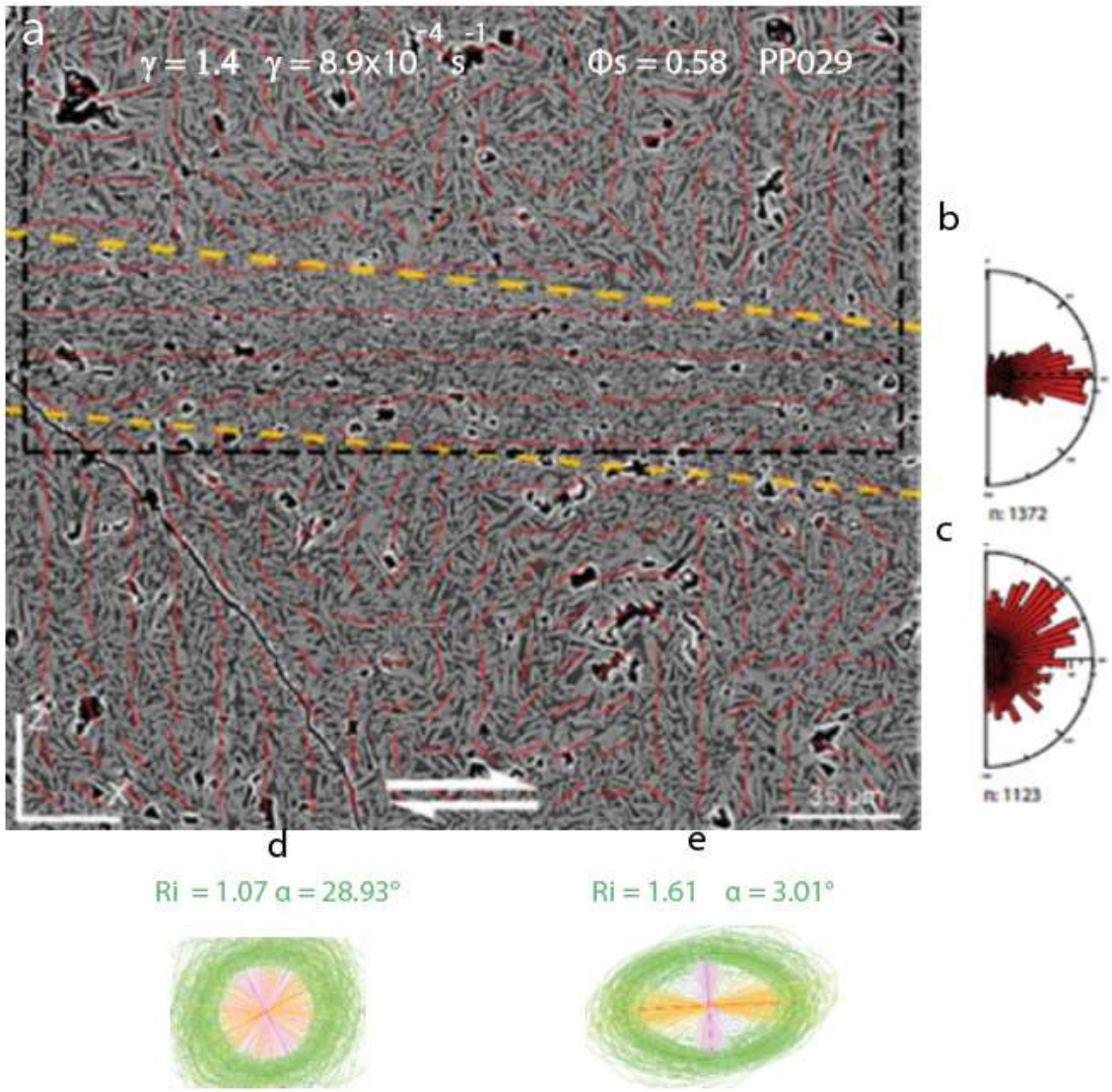

Figure IV.6. Preferential orientation of sample PP029 ϕs = 0.52 a) [XZ] section SEM image of the sample. The shear bands are delimited by dashed yellow lines. The red lines represent the long axes of the local tensor ellipses of the shape fabrics. b) Rose diagram of long axes of local tensor ellipses for the shear band. c) Rose diagram of long axes of local tensor ellipses for the penetrative fabric. d) Mean tensor ellipse of the shape fabric for the shear band. e) Mean tensor ellipse of the shape fabric for the penetrative fabric. R_i = eccentricity of the mean ellipse, α = orientation of the long axis of the ellipse. Modified from Picard et al., 2011.

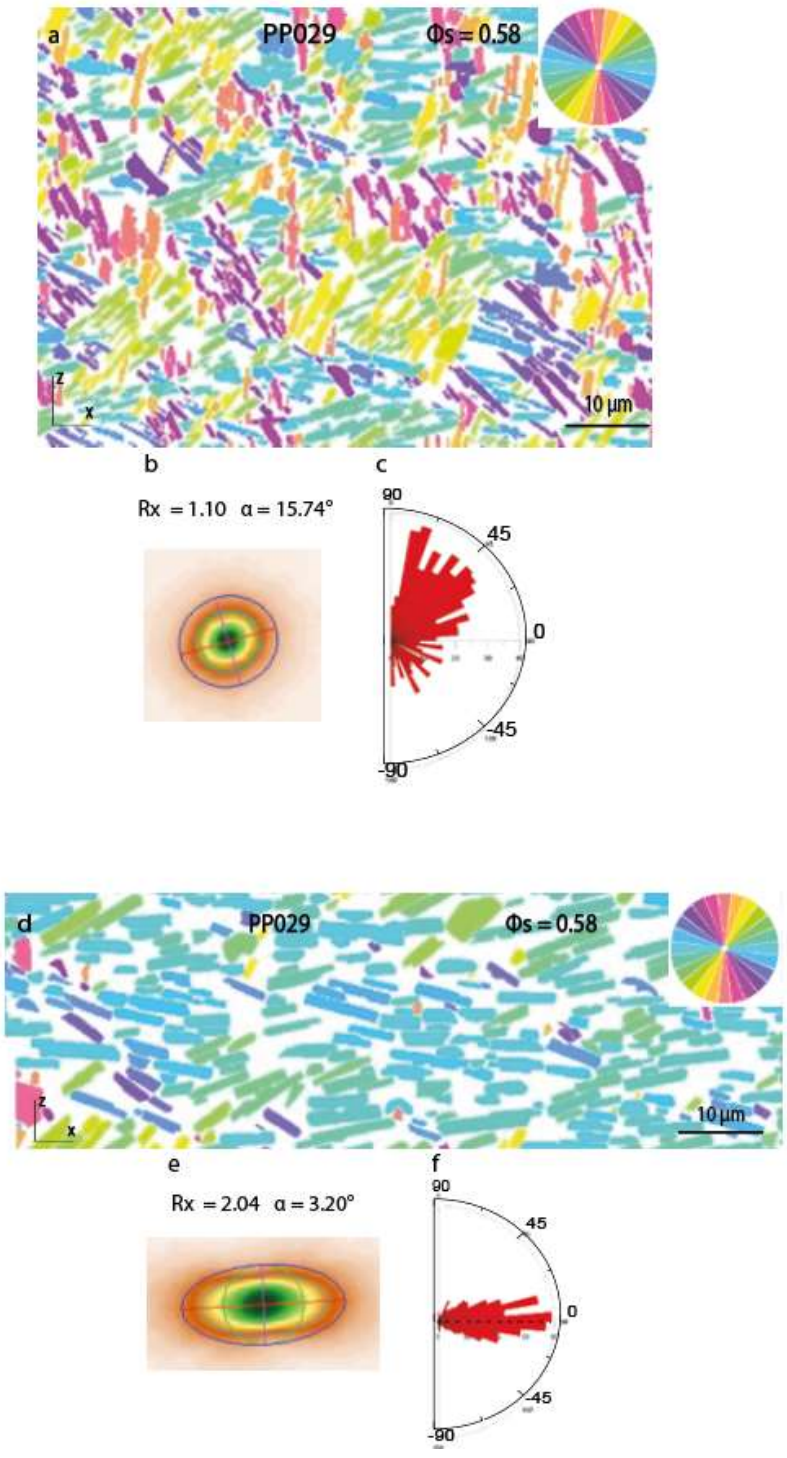

Figure IV.7. Orientation of the long axes of the plagioclases of sample PP029 in the penetrative fabric (a) and in the shear band (d). b) Mean tensor ellipse for the penetrative fabric. c) Rose diagram of individual crystal orientation for the penetrative fabric. e) Mean tensor ellipse for the shear band. f) Rose diagram of individual crystal orientation for the shear band.

ϕ_s = 0.58, γ= 2.0 and $\dot{\gamma}$ = 2.1*10^{-3} s^{-1} (PP249)

The sample PP249 (fig. IV.8a) has a penetrative fabric with no specific crystals orientation, as shown by the rose diagram of the long axes of the local tensor (fig. IV.8c). The eccentricity of the mean tensor ellipse of the penetrative fabric is 1.02 and the inclination of the tensor ellipse α is 40.66° (fig IV.8d).

For the shear bands, the rose diagram of the long axis shows a strong orientation between 15° and -18° (fig. IV.8b), the eccentricity of the mean ellipse R is 1.41, and the direction of orientation of the mean tensor ellipse α is 3.40° (fig. IV.8e).

Using the inertia method, and considering the plagioclase crystals one by one (fig. IV.9a - d), the mean tensor ellipse is 1.07 with α = 32.98° for the penetrative fabric (fig. IV.9b). There is no crystal orientation (fig IV.9c). For shear bands, the mean tensor ellipse R_x is 1.88 with α = 2.35° (fig. IV.9e) and the rose of the direction of plagioclases shows an orientation of 5° (fig. IV.9f).

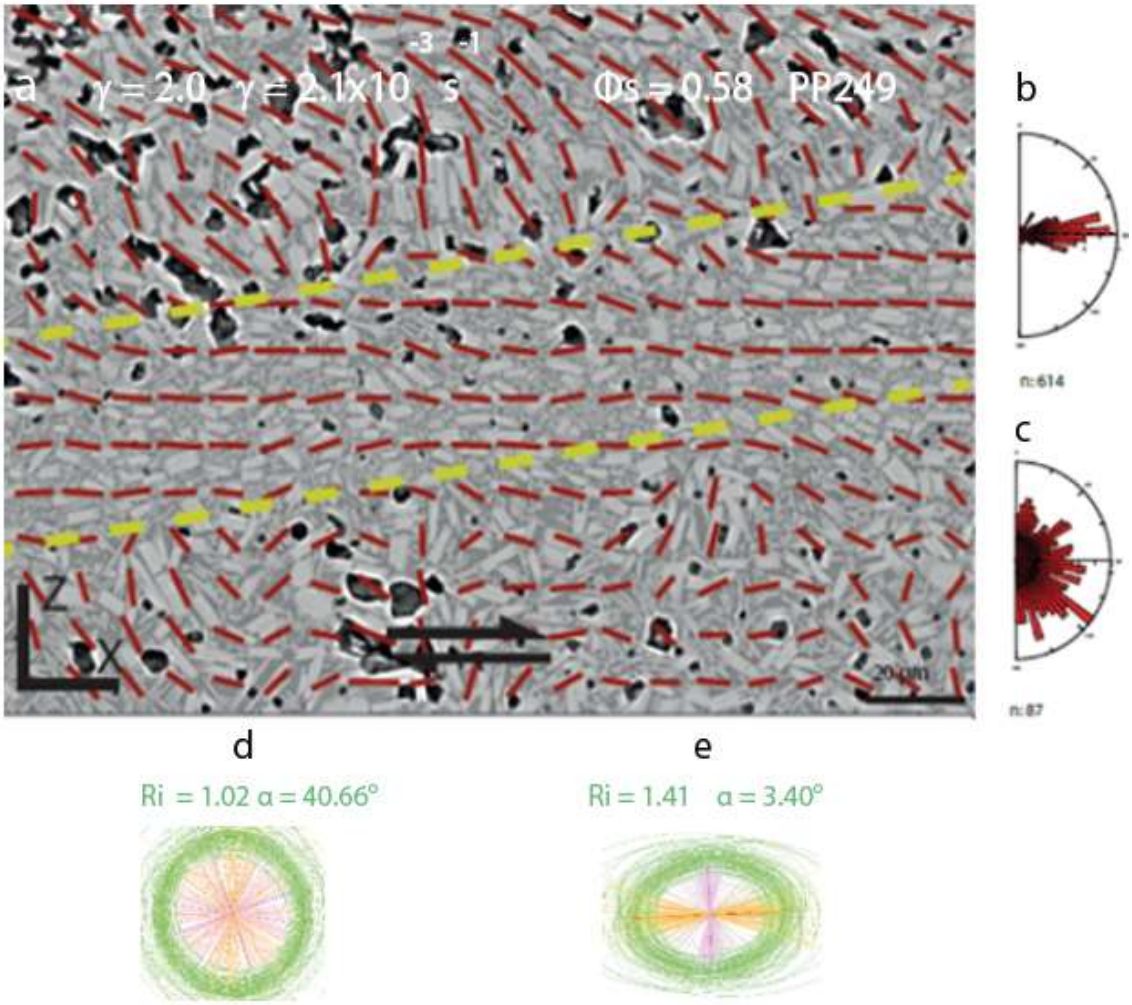

Figure IV.8. Preferential orientation of sample PP249 (ϕ_s = 0.58). The red lines represent the long axes of the local tensor ellipses of the shape fabrics. The shear band is delimited by dashed yellow lines. a) [XZ] section SEM image of the sample. b) Rose diagram of long axes of local tensor ellipses of the penetrative fabric. c) Rose diagram of long axes of local tensor ellipses of the shear band. d) Mean tensor ellipse of the shape fabric in the penetrative fabric. e) Mean tensor ellipse of the shape fabric in the shear band. R_i = eccentricity of the mean ellipse of the penetrative fabric, α = orientation of the long axis of the ellipse.

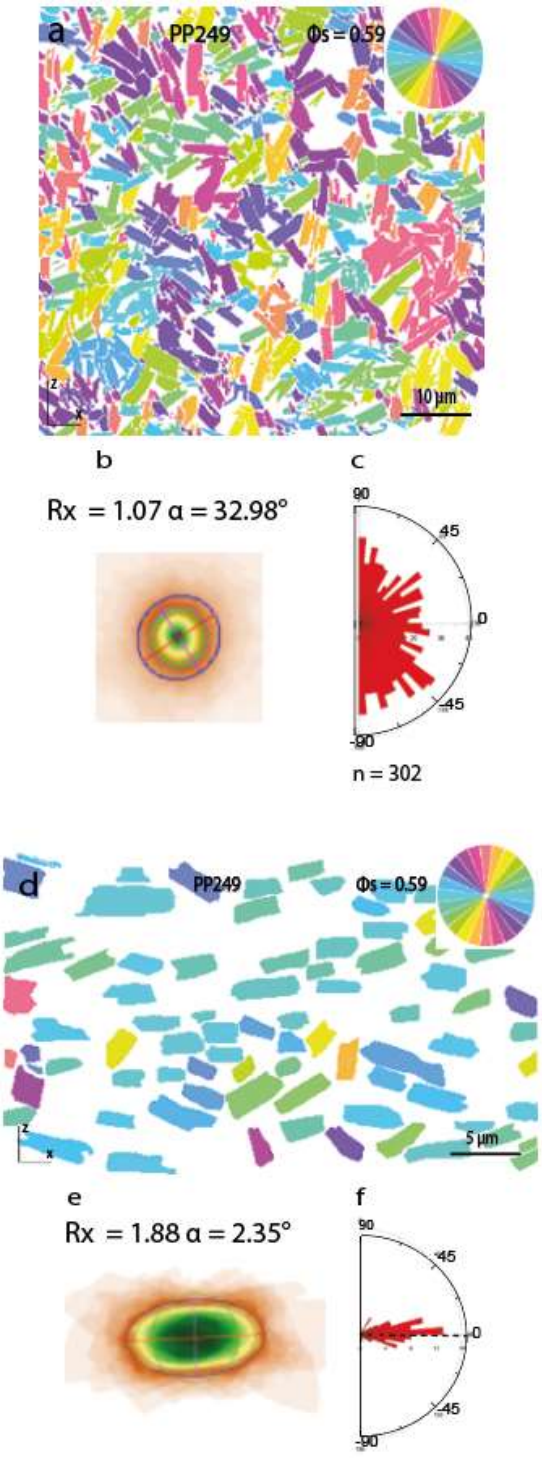

Figure IV.9. Orientation of the long axes of the plagioclases of sample PP249 in the penetrative fabric (a) and in the shear band (d). b) Mean tensor ellipse for the penetrative fabric. c) Rose diagram of individual crystal orientation for the penetrative fabric. e) Mean tensor ellipse for the shear band. f) Rose diagram of individual crystal orientation for the shear band.

The original preserved fabric is crossed by an anastomosing network of shear bands between 30 and 50 µm thick (fig. IV.10a). Within these shear bands, the plagioclase crystals show two different crystal generations. The first has a grain size between 1 and 10 µm, the second has a grain size of less than 1 µm and represent broken crystals (fig. IV.10b).

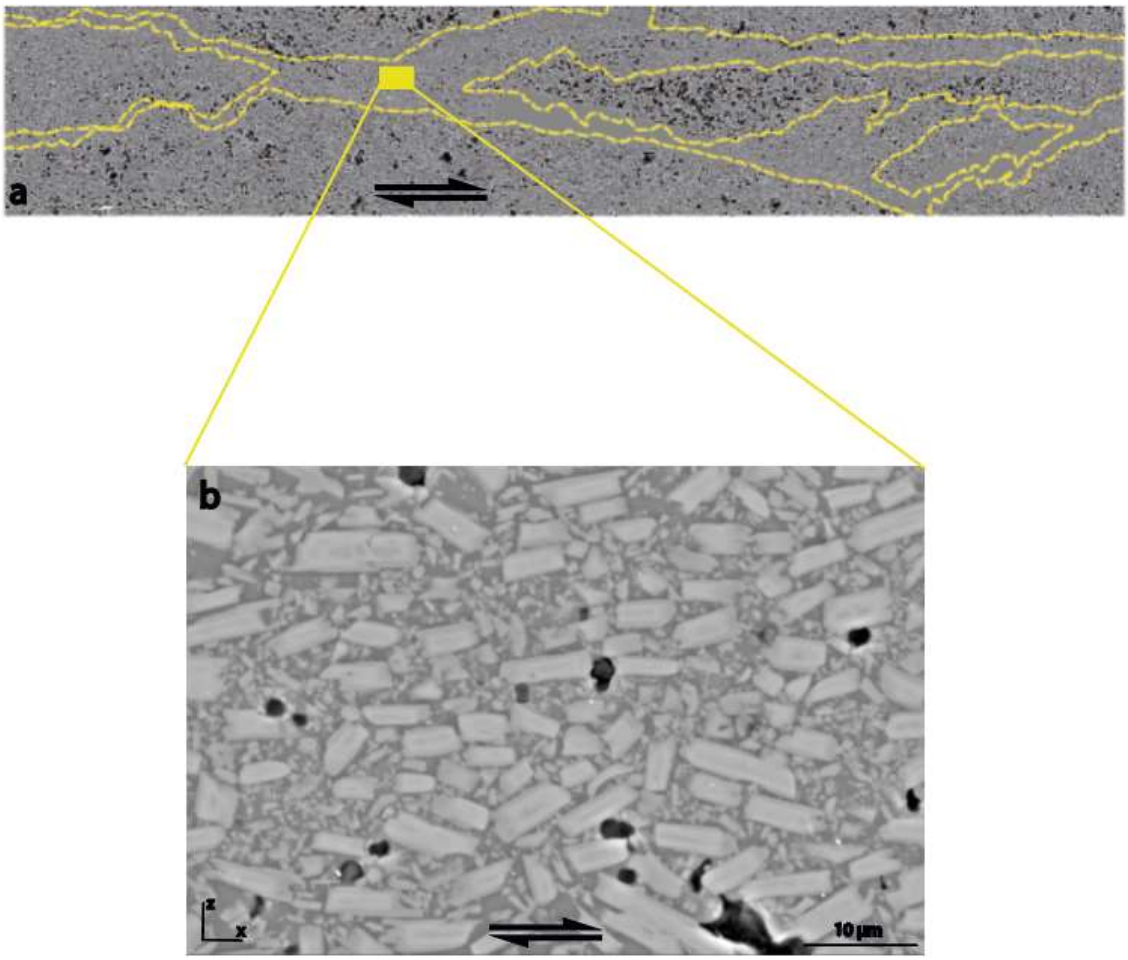

Figure IV.10. a) SEM pictures of sample PP249 with anastomosing network of shear bands. b) [XZ] section SEM image of the sample PP249 in a shear band, with broken crystals.

5. Contacts

The contacts between the plagioclase crystals have been classified following the definition of (Azema and Radjaï, 2012): S-S, side-side, long axis in contact; C-C, cap-cap, short axis in contact; S-C, side-cap, long axis and short axis in contact (fig. IV.11).
The proportions of each type of contact for each sample are shown in table IV.3. The contacts were considered in the penetrative fabric and in the shear bands.

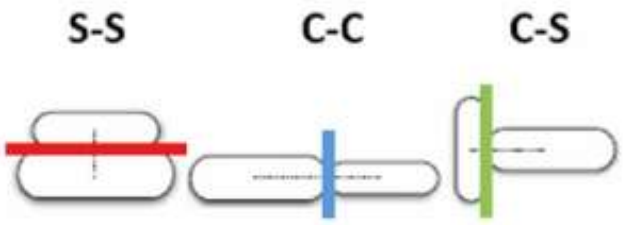

Figure IV.1. Principal contact modes: side-side (s-s), cap-cap (c-c), cap-side (c-s). Modified from (Azema and Radjaï, 2012).

Samples PP043 and PP029 show similar proportions of contacts in the main and penetrative fabric. The lower crystal content of sample PP043 could have caused greater crystals movement, facilitating the formation of S-C contacts. Sample PP249 shows a higher proportion of S-C contacts. This is probably due to the higher strain rate, which causes intense and inhomogeneous deformation of the sample.
In the shear bands, all samples show a higher proportion of S-S contacts. This is due to the localization of the deformation, which oriented the crystals in the direction of the deformation, increasing the S-S contacts.

Sample	$\dot{\gamma} = 1.4, \mathring{\gamma} = 1.1*10^{-4}$	$\dot{\gamma} = 1.4, \mathring{\gamma} = 8.9*10^{-4}$	$\dot{\gamma} = 2.1, \mathring{\gamma} = 1.0*10^{-3}$
	PP043 penetrative fabri	**PP029 main fabric**	**PP249 main fabric**
S-S proportion	0.44	0.44	0.20
C-C proportion	0.18	0.29	0.10
S-C proportion	0.37	0.26	0.70

Sample	$\dot{\gamma} = 1.4, \mathring{\gamma} = 1.1*10^{-4}$	$\dot{\gamma} = 1.4, \mathring{\gamma} = 8.9*10^{-4}$	$\dot{\gamma} = 2.1, \mathring{\gamma} = 1.0*10^{-3}$
	PP043 shear bands	**PP029 shear bands**	**PP249 shear bands**
S-S proportion	0.60	0.50	0.43
C-C proportion	0.21	0.17	0.28
S-C proportion	0.19	0.33	0.29

Table IV.3. Contacts proportion for each type of contact and for each sample. Top: penetrative fabric area. Bottom: shear bands area.

ϕ_s = 0.52, $\dot{\gamma}$ = 1.4 and $\mathring{\gamma}$ = 1.1*10^{-4} s^{-1} (PP043)

Sample PP043 in the penetrative fabric (fig. IV.12a) has a percentage of S-S contacts of 44%, C-C contacts of 18% and S-C contacts of 37%. The S-S contacts have an orientation of 45° and 75° (fig. IV.12b) C-C contacts show a slight orientation at -70° (fig. IV.12c) and S-C contants a slight orietnation at 22° (fig. IV.12d).

The shear band of sample PP043 (fig. IV.12e) has a percentage of S-S contacts increasing to 60%, while S-C contacts decrease to 19%. The proportion of C-C contacts remains similar, at 21%. The S-S and C-C contacts are strongly oriented, with a direction between 15° and -5° and 80° -65° respectively (fig. IV.12f-g). The S-C contacts show a preferred orientation at -15° (fig. IV.12h)

In both the penetrative fabric and the shear bands, the contacts are representative of the deformation experienced.

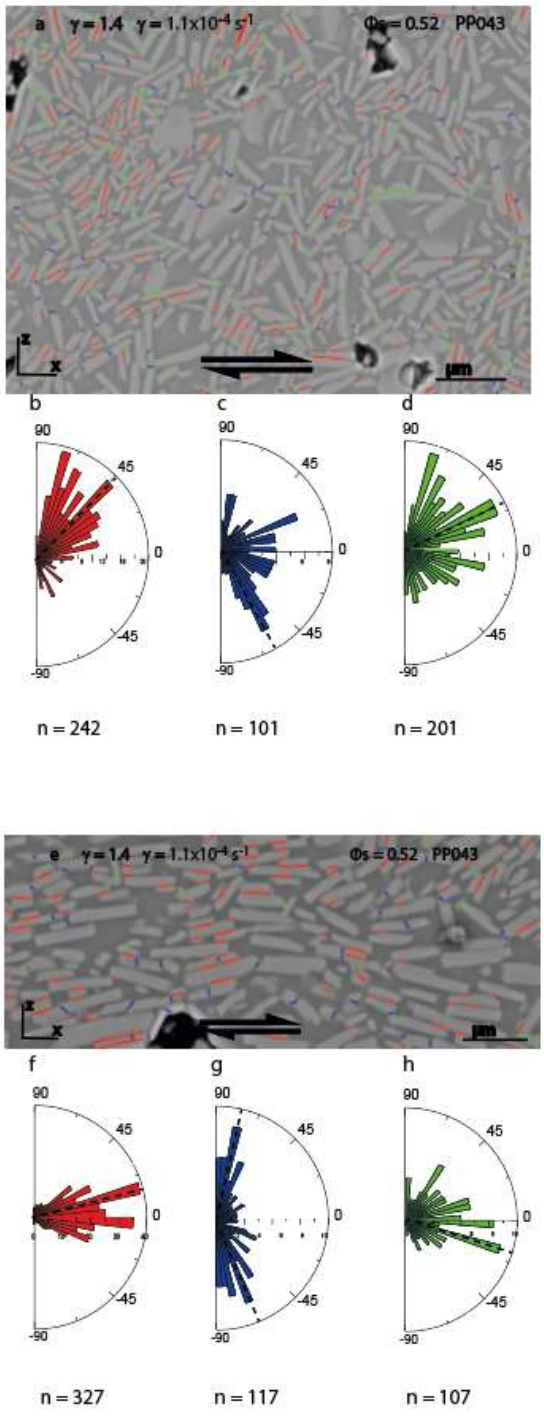

Figure IV.12. Penetrative fabric (a) and shear band (e) of PP043 sample. a) SEM picture of the penetrative fabric with hand drawn the contacts (red: S-S, blue: C-C, green: S-C). Below: Rose diagram for the orientation of the contacts S-S (b), C-C (c) and S-C (d) of the penetrative fabric. e) SEM picture of the shear band with hand drawn the contacts (red: S-S, blue: C-C, green: S-C). Below: Rose diagram for the orientation of the contacts S-S (f), C-C (g) and S-C (h) of the penetrative fabric. n = number of measurements.

ϕ_s = 0.58, γ = 1.4 and $\dot{\gamma}$ = 8.9*10^{-4} s^{-1} (PP029)

The penetrative fabric of the sample PP029 (fig. IV.13a) has no specific contact orientation (fig. IV.13b-c-d), with an S-S contact percentage of 44%, C-C of 20% and S-C of 26%.

The shear band (fig. IV.13e) shows an increase in contacts, with S-S contacts oriented between 28° and -20° (fig. IV.13f), C-C contacts at 85° and between -45° -85° (fig. IV.13g), S-C contacts without orientation (fig. IV.13h). The percentage of S-S contacts is 50%, C-C is 17% and S-C is 33%.

Again the orientation of the contacts is representative of the deformation. In the penetrative fabric there is no preferred direction of contacts, whereas in the shear band the S-S contacts follow the direction of deformation and the C-C contacts are perpendicular to S-S contacts.

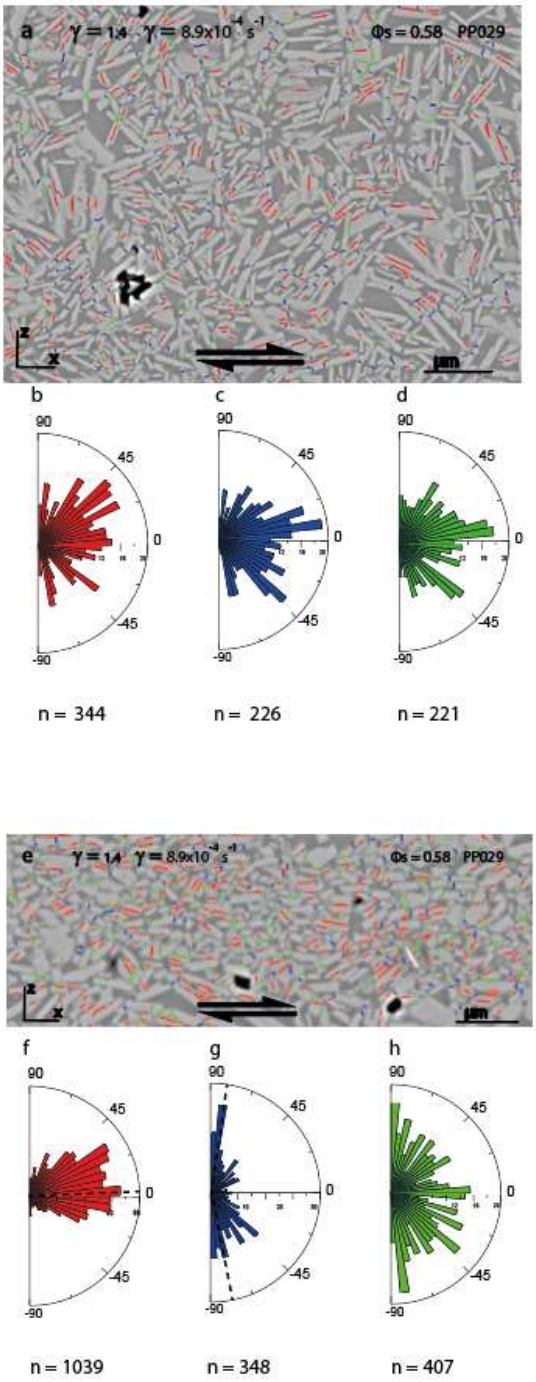

Figure IV.13. Penetrative fabric (a) and shear band (e) of PP029 sample. a) SEM picture of the penetrative fabric with hand drawn the contacts (red: S-S, blue: C-C, green: S-C). Below: Rose diagram for the orientation of the contacts S-S (b), C-C (c) and S-C (d) of the penetrative fabric. e) SEM picture of the shear band with hand drawn the contacts (red: S-S, blue: C-C, green: S-C). Below: Rose diagram for the orientation of the contacts S-S (f), C-C (g) and S-C (h) of the penetrative fabric. n = number of measurements.

ϕ_s = 0.58, γ= 2.0 and $\dot{\gamma}$ = 2.1*10^{-3} s^{-1} (PP249)

The penetrative fabric of sample PP249 (fig. IV.14a) has contacts with no preferred orientation (fig. IV.14 b-c-d). The percentage of S-S contacts is 20%, C-C is 10% and S-C is 70%.

The shear band (fig. IV.14e) shows that the S-S contacts are oriented at 0° and 23° (fig. IV.14f), the C-C contacts at +80° and -80° (fig. IV.14g) and the S-C contacts at 0° and -25° (fig. IV.14h). S-S contacts have a higher percentage, 43%, C-C has 28% and S-C has 29%. For this sample it is difficult to interpret the contacts, in the shear band the broken crystals are in large quantities and do not allow contact interpretation.

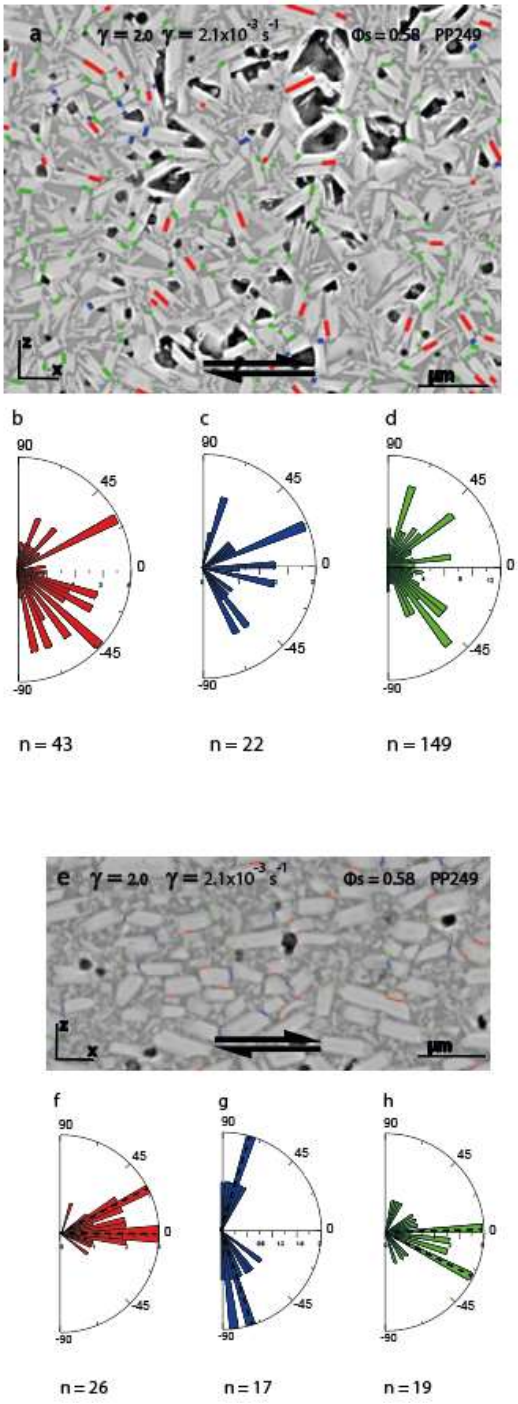

Figure IV.14. Penetrative fabric (a) and shear band (e) of PP249 sample. a) SEM picture of the penetrative fabric with hand drawn the contacts (red: S-S, blue: C-C, green: S-C). Below: Rose diagram for the orientation of the contacts S-S (b), C-C (c) and S-C (d) of the penetrative fabric. e) SEM picture of the shear band with hand drawn the contacts (red: S-S, blue: C-C, green: S-C). Below: Rose diagram for the orientation of the contacts S-S (f), C-C (g) and S-C (h) of the penetrative fabric. n = number of measurements.

6. Clusters

In this paragraph, clusters formed by more than 3 contacts S-S or C-C have been considered. The analysis were performed on both the penetrative fabric and the shear area for the samples with localized deformation.

ϕ_s = 0.52, $\dot{\gamma}$ = 1.4 and $\dot{\gamma}$ = 1.1*10^{-4} s^{-1} (PP043)

The clusters studied in the penetrative fabric of sample PP043 (fig. IV.15a) show a 45° clusters orientation (fig. IV.15b) and a preferred orientation of the contacts in the clusters of -43° (fig. IV.15c). In the penetrative fabric, foliation favours the formation of clusters. However, in numerical terms they are not very numerous and they are more concentrated in the areas with the highest crystal content. All the samples show crystal contents that can vary depending on the area analyzed, with a variation that is generally around 2-3%. It is also noticeable that clusters form more easily where the crystal size is larger. This is probably due to the greater amount of force accumulated along the larger surface area of the crystal. Clusters are formed from a minimum of 3 to a maximum of 13 crystals.

The clusters in the shear area of sample PP043 (fig. IV.15d) are oriented between-5° and 20°, with a mean value ad 5° (fig. IV.15e). The preferred orientations of the contacts in the clusters are at 90° and -55° (fig. IV.15f). In the shear bands the clusters are evenly distributed over the surface and are more numerous than in the penetrative fabric of the sample. Numerically they are formed from a minimum of 3 to a maximum of 16 crystals.

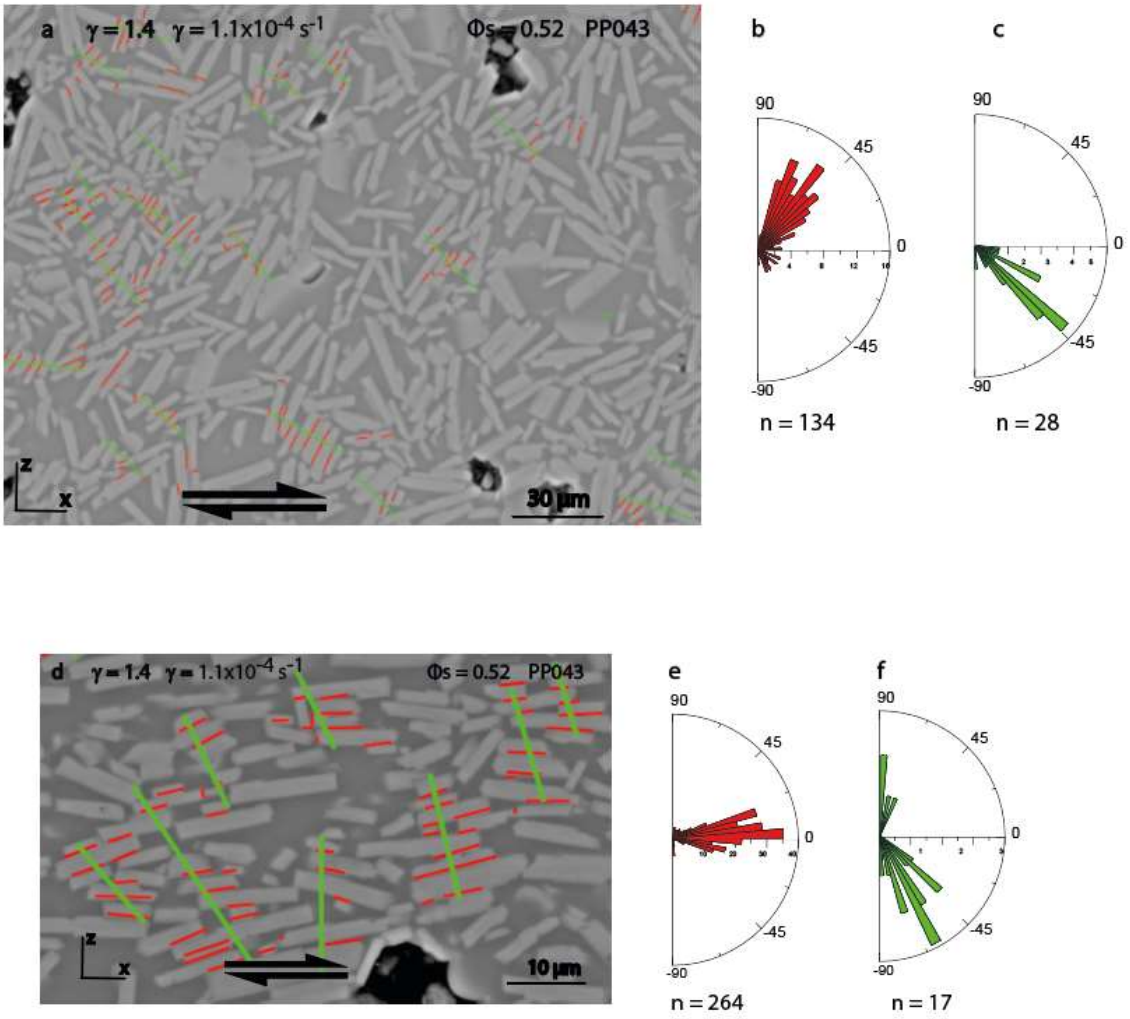

Figure IV.15. SEM image of sample PP043 in the penetrative fabric (a) and shear band (d) with hand-drawn orientation of the clusters. b) Rose diagram of the preferred orientations of the clusters in the penetrative fabric. c) Rose diagram of orientation of the contacts in the clusters in the penetrative fabric. e) Rose diagram of the preferred orientations of the clusters in the shear band. f) Rose diagram of orientation of the contacts in the clusters in the shear band.

ϕ_s = 0.58, $\dot{\gamma}$ = 1.4 and $\mathring{\dot{\gamma}}$ = 8.9*10^{-4} s^{-1} (PP029)

The sample shows sporadic clusters in the penetrative fabric (fig.16a), with no preferential orientation (fig. IV.16b). The orientation of the clusters does not show a preferred direction (fig. IV.16c). The penetrative fabric of the sample numerous clusters with a weak preferential orientation. The clusters consist of a minimum of 3 to a maximum of 8 crystals and are concentrated where the crystal grain size is largest.

Unlike sample PP043, the deformed area of sample PP029 (fig. IV.16d) shows sets of clusters separated by nonoriented particles, usually of smaller particle size. The clusters are oriented with a preferred orientation between 25° and - 15° (fig. IV.16e) and the orientations of the contacts of the clusters are at 90°, -60° and -82° (fig. IV.16f). As in with the shear band of the sample PP043, the clusters are more numerous, more oriented and formed by a greater number of crystals, with a minimum of 3 and a maximum of 20. The distribution of the clusters is homogeneous over the entire surface. However, due to the broken crystals, distribution of the clusters in the shear bands is less homogeneous and less numerous compared to the sample with crystal content of 0.52.

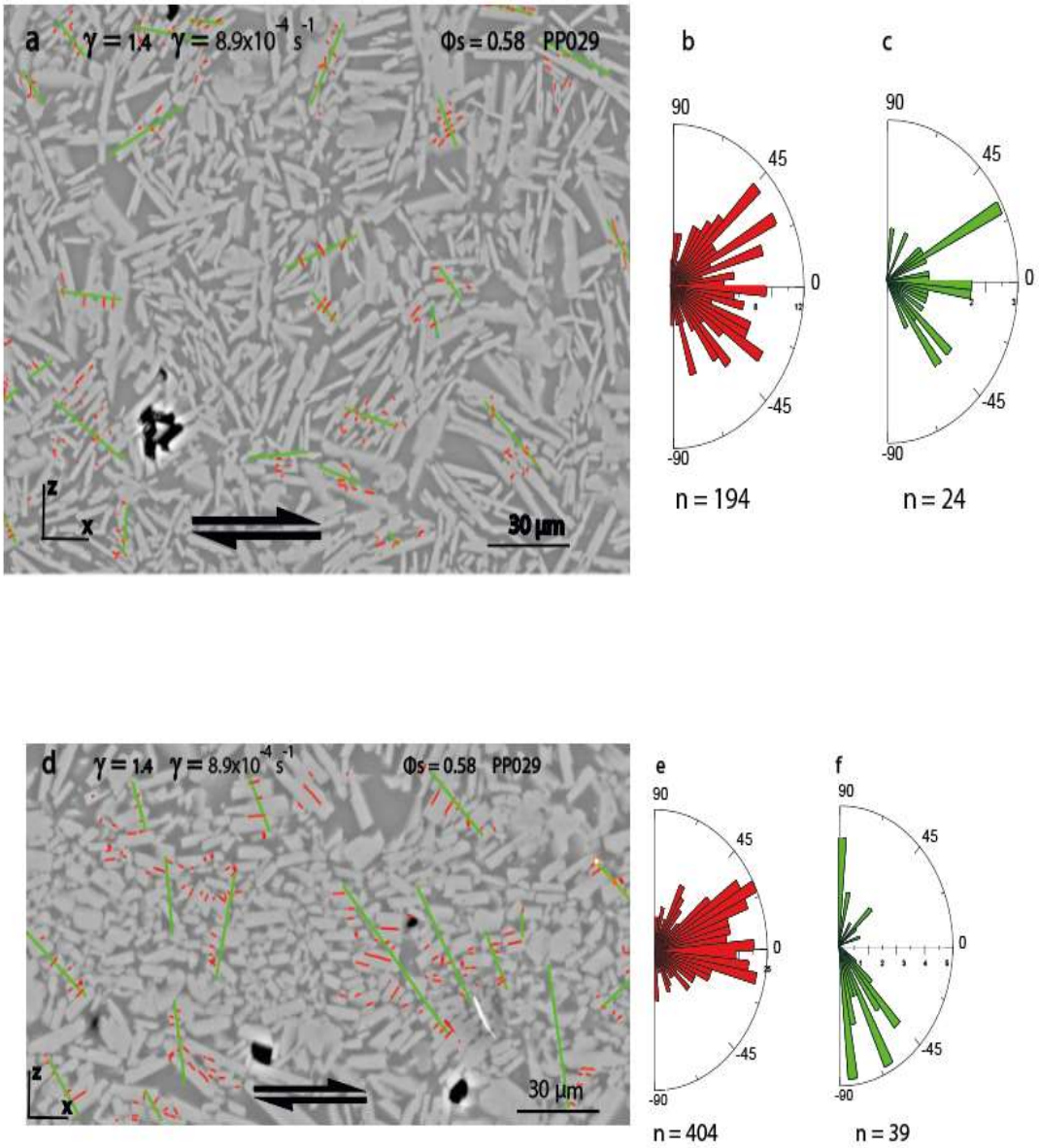

Figure IV.16. SEM image of sample PP029 in the penetrative fabric (a) and shear band (d) with hand-drawn orientation of the clusters. b) Rose diagram of the preferred orientations of the clusters in the penetrative fabric. c) Rose diagram of orientation of the contacts in the clusters in the penetrative fabric. e) Rose diagram of the preferred orientations of the clusters in the shear band. f) Rose diagram of orientation of the contacts in the clusters in the shear band.

ϕ_s = 0.58, γ= 2.0 and $\dot{\gamma}$ = 2.1*10^{-3} s^{-1} (PP249)

For this sample, there is no formation of clusters, noth for the penetrative fabric and for the shear bands. In the penetrative fabric there is a strong majority of S-C contacts, so there are no clusters.
The shear bands are strongly cataclased. Each crystal is surrounded by crystals of lower granulometry with absence of clusters connection.

7. Shape fabric of bubbles

Bubbles from all samples were analyzed using SPO software, studying their preferential direction, content, and aspect ratio. Samples PP043 and PP029 were analyzed without distinction of mean fabric and shear bands, as the bubbles content is homogeneous throughout the surface of the samples. Sample PP249 shows a variation in bubble content between mean fabric and shear bands, therefore the two areas were analyzed separately.
The bubble content of sample PP043 (fig. IV.17a) is 1.5%. The mean tensor ellipse R_x is 1.10 with an orientation α of 45. 03° (fig IV.17b). The bubbles have no preferential direction (fig. IV.17c). The arithmetic mean of their aspect ratio is 1.80±0.61, and the harmonic is 1.65 (fig. IV.17d).
Sample PP029 (fig. IV.17e) shows a slightly higher crystalline content of 1.7%. The mean tensor ellipse R_x is 1.10 with an orientation α of 41.43° (fig IV.17f). The rose of directions shows no preferential orientation (fig. IV.17g). The R values are similar to the previous sample, with the arithmetic mean of 1.87±0.72 and the harmonic mean of 1.67 (fig. IV.17h). Sample PP249 has a different bubble content, both in the penetrative fabric (fig. IV.18a), with a content of 4.7%, and in the shear band (fig. IV.18e), with a content of 0.9%. The mean tensor ellipse in the penetrative fabric is R_x = 1.03 with α = 81.60° (fig. IV.18b). The bubbles follow no particular direction (fig. IV.18c), while in the shear bands they are weakly oriented in the direction of deformation, between 45° and -45° (fig. IV.18g).
The aspect ratio is held constant, with an arithmetic mean of 1.61±0.46 in the penetrative fabric and 1.60±0.44 in the shear band, and a harmonic mean of 1.51 and 1.50, respectively (fig. IV.18d and fig. IV.18h).

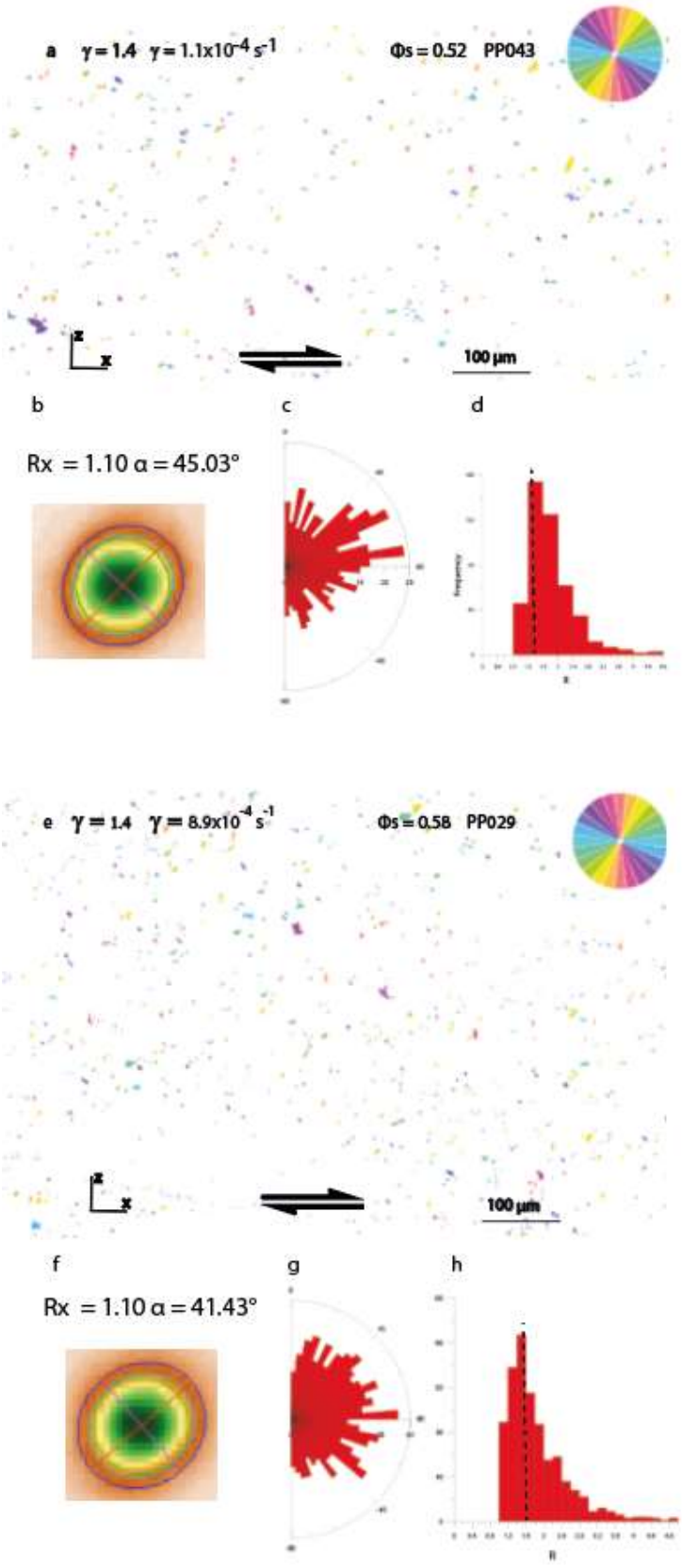
a γ = 1.4 γ = 1.1x10-4 s-1
Φs = 0.52 PP043
100 µm
b
c
d
Rx = 1.10 α = 45.03°
e γ = 1.4 γ = 8.9x10-4 s-1
Φs = 0.58 PP029
100 µm
f
g
h
Rx = 1.10 α = 41.43°

Figure IV.17.

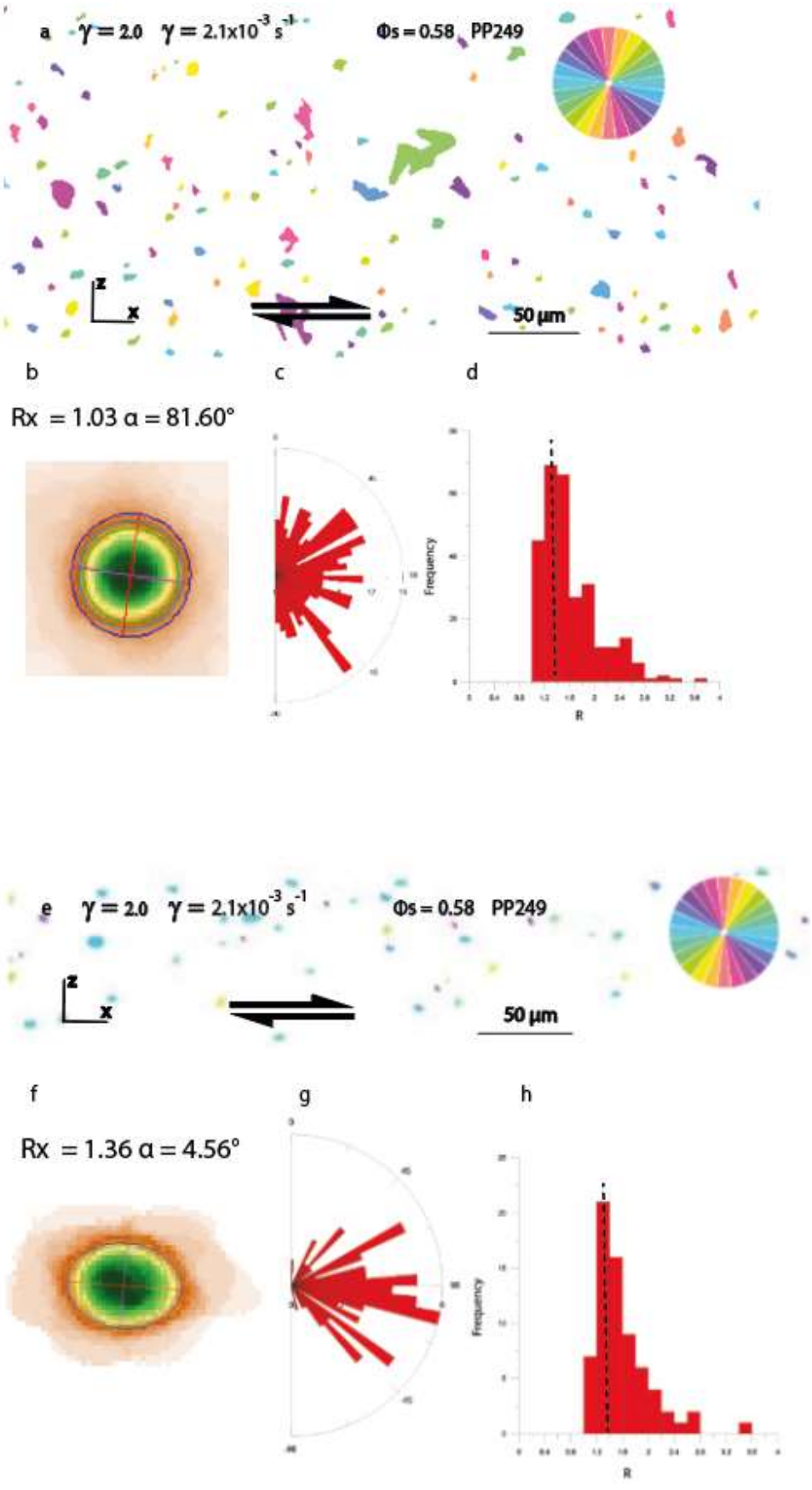
a
γ = 2.0 γ = 2.1x10-3 s-1
Φs = 0.58 PP249
z
x
50 µm
b
c
d
Rx = 1.03 α = 81.60°
Frequency
R
e
γ = 2.0 γ = 2.1x10-3 s-1
Φs = 0.58 PP249
z
x
50 µm
f
g
h
Rx = 1.36 α = 4.56°
Frequency
R

Figure IV.18.

Figure IV.17. Bubbles shape fabric of sample PP043 (a) and PP029 (e). b) Mean tensor ellipse of sample PP043 c) Rose of directions of individual bubbles orientation for sample PP043. d) Aspect ratio histogram for groups of bubbles for sample PP043. f) Mean tensor ellipse of sample PP029 g) Rose of directions of individual bubbles orientation for sample PP029. h) Aspect ratio histogram for groups of bubbles for sample PP029.

Figure IV.18. Bubbles shape fabric of sample PP249 in the penetrative fabric (a) and in the shear band (e). b) Mean tensor ellipse of the penetrative fabric c) Rose of directions of individual bubbles orientation for the penetrative fabric. d) Aspect ratio histogram for groups of bubbles for the penetrative fabric. f) Mean tensor ellipse of the shear band. g) Rose of directions of individual bubbles orientation for the shear band. h) Aspect ratio histogram for groups of bubbles for the shear band.

8. Summary

All samples with aspect ratio R = 4 are characterized by localization of forces and formation of shear bands.

The deformation process of the sample with $\phi_s = 0.52$ is schematized in fig. IV.19a. When the sample is subjected to deformation, the crystals translate and rotate to form a foliation. The deformation is distributed throughout the sample and medium force chains and clusters are formed throughout the deformed area. The final stage is the formation of C' shear bands by dilatancy.

The sample with $\phi_s = 0.58$ and strain rate $\dot{\gamma} = 8.9*10^{-4}\ s^{-1}$ shows a different behaviour (fig. IV.19b). Due to the high crystal content, the crystals cannot rotate and translate. This leads to an accumulation of strain in certain areas of the sample with the formation of strong force chains and clusters. In the final stage, C shear bands are formed due to the strong strain accumulation.

The sample with $\phi_s = 0.58$ and strain rate $\dot{\gamma} = 2.1*10^{-3}\ s^{-1}$ shows the same behaviour as the previous sample. Due to the fast strain rate, a single central deformed region is formed by C, C' shear bands and thrust bands.

The bubbles retained the same properties as the starting material, so they were not deformed. They show orientation only for the sample PP249.

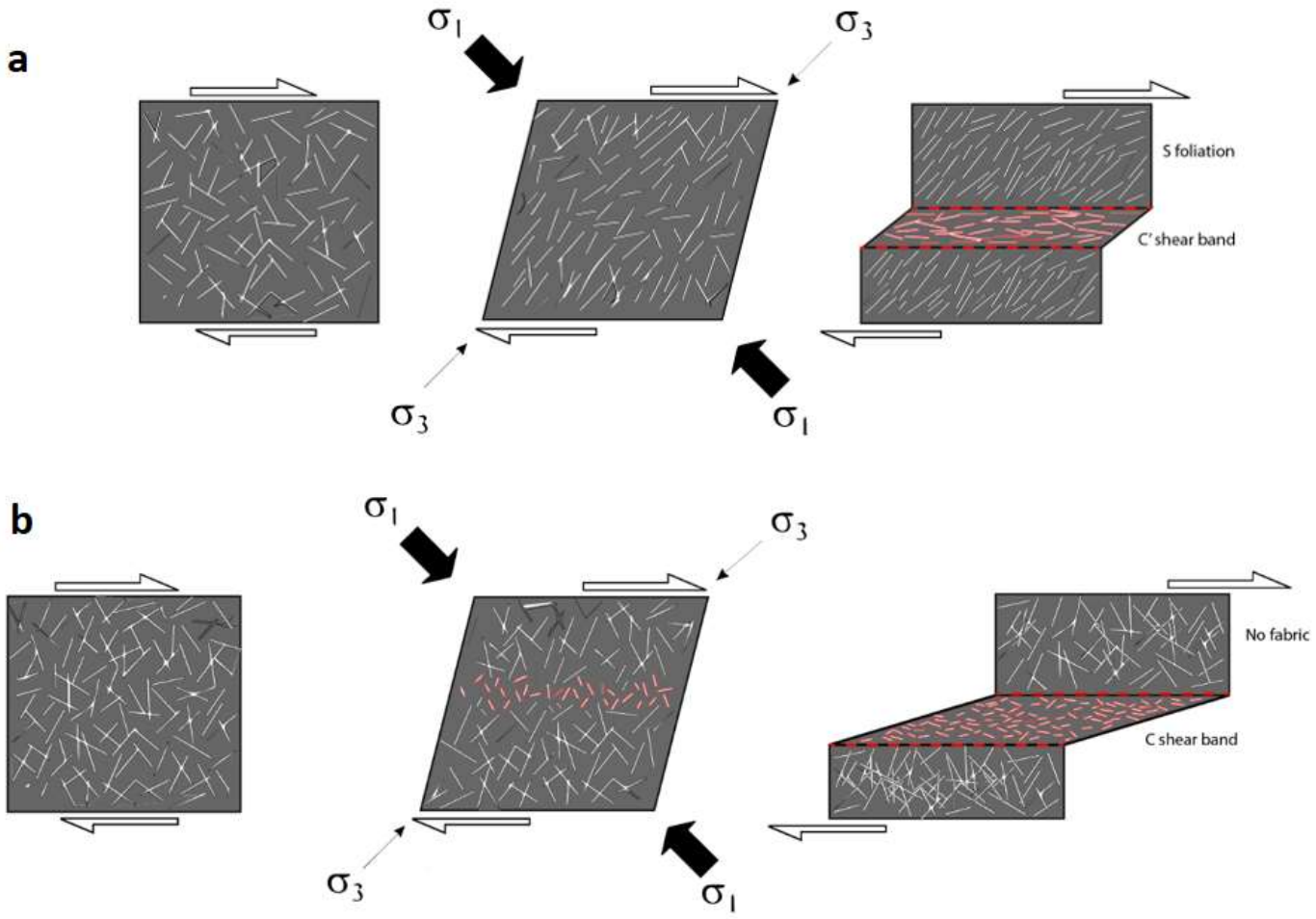

Figure IV.19. a) Deformation stages for sample with ϕs = 0.52. b) Deformation stages for sample with ϕs = 0.58.

Results loose mush - R = 2, ϕ_s = 0.58, 0.59

Résumé du chapitre V - Résultats - R = 2, ϕ_s = 0,58 - 0,59

Dans ce chapitre, les résultats sont décrits pour les échantillons synthétiques avec un rapport d'aspect R = 2 et une teneur en cristaux = 0,58 et 0,59.

Les échantillons ont été déformés avec une déformation finie de 0,5 à 2,0 et une vitesse de déformation de $1.0*10^{-4}$ s^{-1} a $2.1*10^{-3}$ s^{-1}.

La figure 1 montre les reconstructions panoramiques des échantillons après les expériences. La déformation est uniformément répartie sur toute la surface de l'échantillon. Ceci est mis en évidence par les rainures sur le cuivre droit. L'échantillon PP6985 s'est cassé lors de la phase finale de l'expérience de déformation. Les structures de déformation ayant été préservées, cet échantillon a également été analysé et étudié. Les caractéristiques morphologiques du plagioclase sont rapportées, et le rapport d'aspect R et le diamètre équivalent ont été étudiés. Les analyses chimiques EPMA effectuées sur les cristaux de plagioclase sont présentées.

Les microstructures des échantillons sont rapportées et étudiées, avec l'analyse SPO. Les types de contact développés dans ces échantillons sont également illustrés, en subdivisant les contacts en types S-S, C-C et S-C (d'après la définition d'Azema et al., 2011).

Les échantillons avec un rapport d'aspect R = 2 et une teneur en cristaux ϕ_s = 0,58 et 0,59 ne présentent pas de structure due à la localization du cisaillement et il existe des tissus de forme homogène pour les plagioclases et les bulles. Lorsque la déformation est appliquée, on observe l'apparition d'un domaine d'orientation dû au tiling des particules. Les cristaux suivent la direction de la déformation et sont orientés à ±45° et ±0°.

La forme légèrement allongée des cristaux leur permet de se déplacer. Contrairement aux plagioclases dont le rapport d'aspect R = 4, les cristaux peuvent se déplacer et se translater, formant un réseau homogène de contacts sur toute la surface de l'échantillon, mais avec peu clusters. Cela pourrait être l'une des raisons de l'absence de localization des déformations : il n'y a pas d'accumulation de force puisque la position des cristaux change constamment.

La mobilité des cristaux est confirmée par l'absence de cataclastite, qui est très abondante dans les échantillons avec R = 4 à un taux de déformation élevé.

V. Results loose mush - R = 2, ϕ_s = 0.58, 0.59

This chapter illustrates the results of samples with R = 2 with a crystal content between 0.58 and 0.59. The temperature and pressure remained the same during all the experiments (800°C, 300 MPa), while the values of finite strain and strain rate were changed (table V.1). The samples were studied in their morphology, chemical compositions, microstructures, contacts and clusters.

A summary table with all deformation experiments performed for both samples with aspect ratio R = 4 and aspect ratio R = 2 is shown in Appendix A.

Sample	Crystal content	Starting material	Aspect ratio R	Equivalent diameter Φ (μμ)	H_2O content (wt.%)	P (MPa)	T (°C)	Finite strain γ	Strain rate $\dot{\gamma}$ (s^{-1})
PP669	0.58	HTN4	1.81 ± 1.15	1.47 ± 1.17	3	300	800	0.5	$1.0*10^{-4}$
PP676	0.58	HTN8	1.72 ± 0.62	1.62 ± 0.79	3	300	800	1	$1.0*10^{-4}$
PP684	0.59	HTN9	1.62 ± 0.69	1.26 ± 0.77	3	300	800	2	$2.1*10^{-3}$
PP685	0.59	HTN9	1.66 ± 0.76	1.50 ± 0.75	3	300	800	2.3	$1.0*10^{-4}$

Table V.1. Paterson press experiments for the sample with R = 2 and ϕ_s = 0.58 0.59. The values for aspect ratio R and equivalent diameter are the harmonic mean values, which are more representative of the samples.

1. Panoramic reconstructions

Figure V.1 represents a panoramic reconstruction of all samples with aspect ratio R = 2 and crystal content ϕ_s = 0.58 - 0.59 after torsion deformation. In contrast to the samples with aspect ratio R = 4 and the same crystal content (fig. IV.1, ch. results R = 4), the samples show a homogenous distribution of deformation along the entire outer surface. The grooves appear well aligned and straight. Their inclination increases with increasing strain rate. This deformation homogeneity is not typical for samples with such a high crystal content, which is why it is important to investigate the factors that can lead to this kind of behaviour. Sample PP685 (ϕ_s = 0.59, γ = 2.3, $\dot{\gamma}$ = 1.0*10^{-4}) broke, fortunately in the final stage of the experiment, so the material was preserved and ready for analysis.

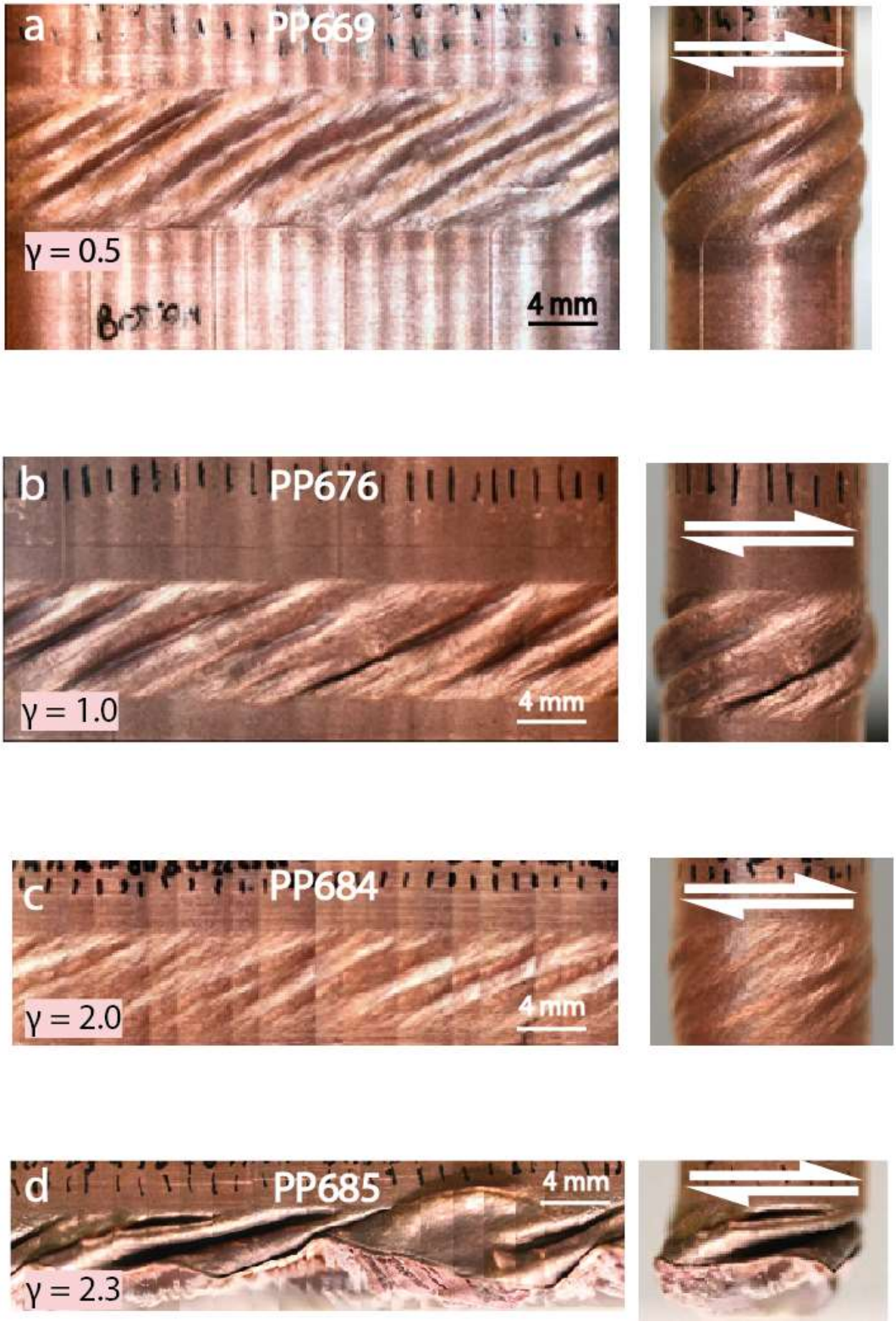

Figure V.1. Panoramic reconstruction of the samples still embebbed in their copper jacket subject to torsion deformation. a) PP669 (ϕ_s = 0.58, γ = 0.5, $\dot{\gamma}$ = 1.0*10^{-4}), b) PP676 (ϕ_s = 0.58, γ = 1.0, $\dot{\gamma}$ = 1.0*10^{-4}), c) PP684 (ϕ_s = 0.59, γ = 2.0, $\dot{\gamma}$ = 2.1*10^{-3}), d) PP685 (ϕ_s = 0.59, γ = 2.3, $\dot{\gamma}$ = 1.0*10^{-4}).

2. Crystal morphology

For each deformed sample the aspect ratio R and equivalent diameter Φ of the crystals were analyzed on SEM images with a picture size ~ 60 µm x 90 µm. This ensured to analyze a representative population of at least 650 crystals.

2.1. Equivalent diameter Φ

Figure V.2 represents the histograms of equivalent diameters Φ for samples PP669, PP676, PP684 and PP685.

Sample PP669 (fig. V.2a) shows a mean equivalent diameter of 1.81±1.17 µm and an arithmetic mean of 1.47 µm. The mode is 1.3.
Sample PP676 (fig. V.2b) displays an equivalent diameter of 1.93±0.79 µm with a harmonic mean of 1.62 µm and a mode of 1.9.
Sample PP684 (fig. V.2c) has an equivalent diameter of 1.58 ± 0.77 µm, a harmonic mean of 1.26 µm and a mode of 1.2.
Sample PP685 (fig. V.2d) shows an equivalent diameter of 1.79 ± 0.75 and a harmonic mean of 1.50 µm. The mode is 1.7.

The values of the arithmetic mean, harmonic mean and mode do not match, although the values of the harmonic mean and mode are quite similar. This indicates a non-symmetry of the crystal populations, which have a log-normal trend, so the most representative value is the harmonic mean.

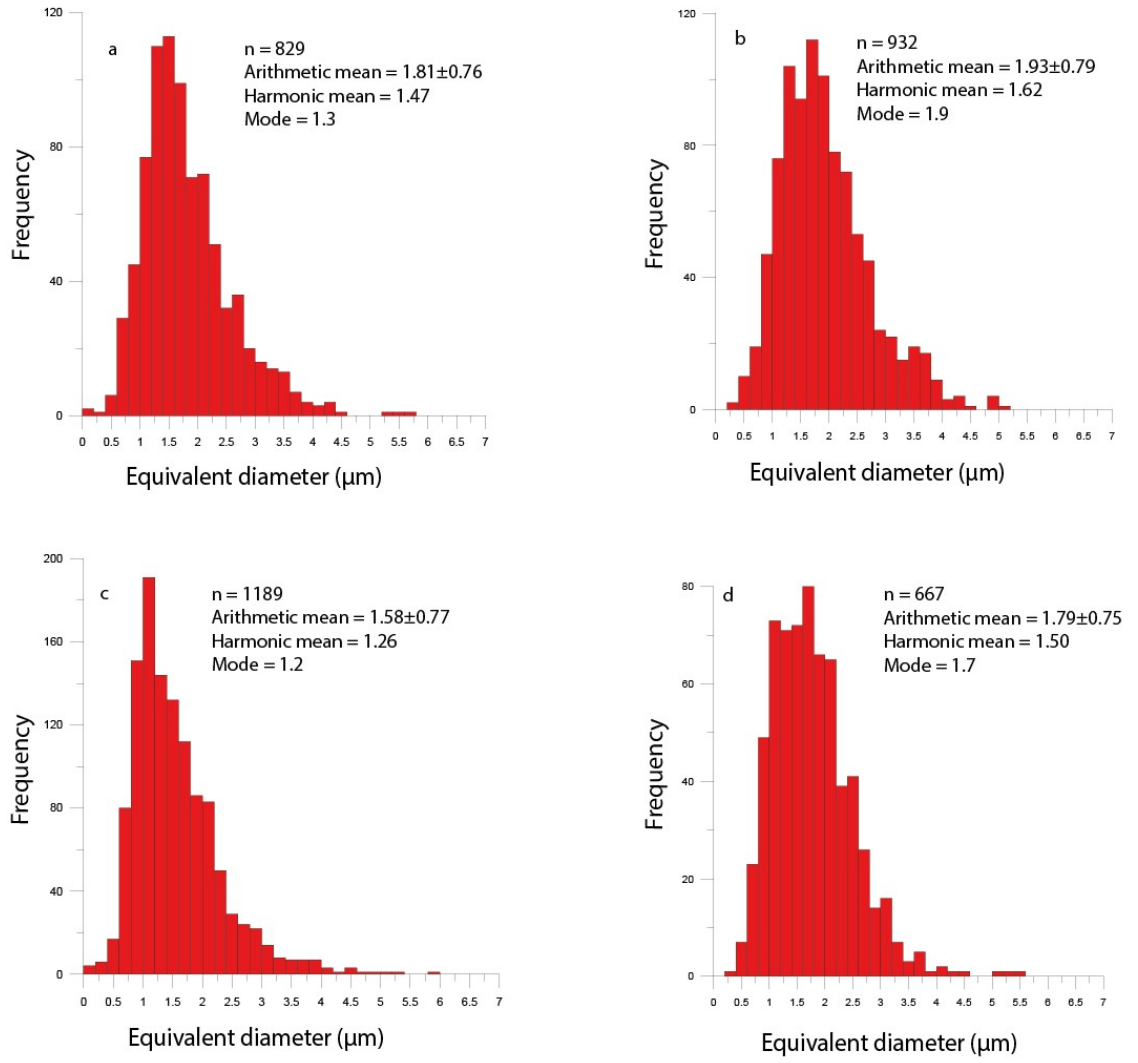

Figure V.2. Histograms of equivalent diameters calculated in groups of crystals in deformation experiments. a) PP669 (ϕ_s = 0.58, $\dot{\gamma}$ = 0.5, $\dot{\gamma}$ = 1.0*10^{-4}), b) PP676 (ϕ_s = 0.58, $\dot{\gamma}$ = 1.0, $\dot{\gamma}$ = 1.0*10^{-4}), c) PP684 (ϕ_s = 0.59, $\dot{\gamma}$ = 2.0, $\dot{\gamma}$ = 2.1*10^{-3}), d) PP685 (ϕ_s = 0.59, $\dot{\gamma}$ = 2.3, $\dot{\gamma}$ = 1.0*10^{-4}).

2.2. Aspect ratio R

The histograms in figure 3 represent the aspect ratio R for samples PP669, PP676, PP684 and PP685. The values of R are calculated for the arithmetic mean, the harmonic mean and the mode.

Sample PP669 (fig. V.3a) has R values ranging from 1 to 5.6, with an arithmetic mean of 2.05±1.15 and a harmonic mean of 1.81. The mode is at 1.5.
Sample PP676 (fig. V.3b) shows an arithmetic mean of R of 1.88±0.62, a harmonic mean of 1.72 and a maximum and minimum value of 6 and 1 respectively. The mode is at 1.2.
Sample PP684 (fig. V.3c) has an aspect ratio ranging from 1 to 5.7, with an arithmetic mean of 1.79±0.69 and a harmonic mean of 1.62. The mode is at 1.4.
Sample PP685 (fig. V.3d) shows a minimum R value of 1 and a maximum value of 4.4. The arithmetic mean is 1.83±0.76 and the harmonic mean is 1.66. The mode is at 1.5.

As with the equivalent diameters, the arithmetic mean, the harmonic mean and the mode do not coincide. The arithmetic mean is always the largest, while the harmonic mean and mode are only slightly different. The most realistic values to consider for aspect ratio R are those of the harmonic mean. Crystalline populations have a log-normal trend. The aspect ratio R values range in similar proportions for all samples, with the exception of sample PP669, which has slightly higher values.

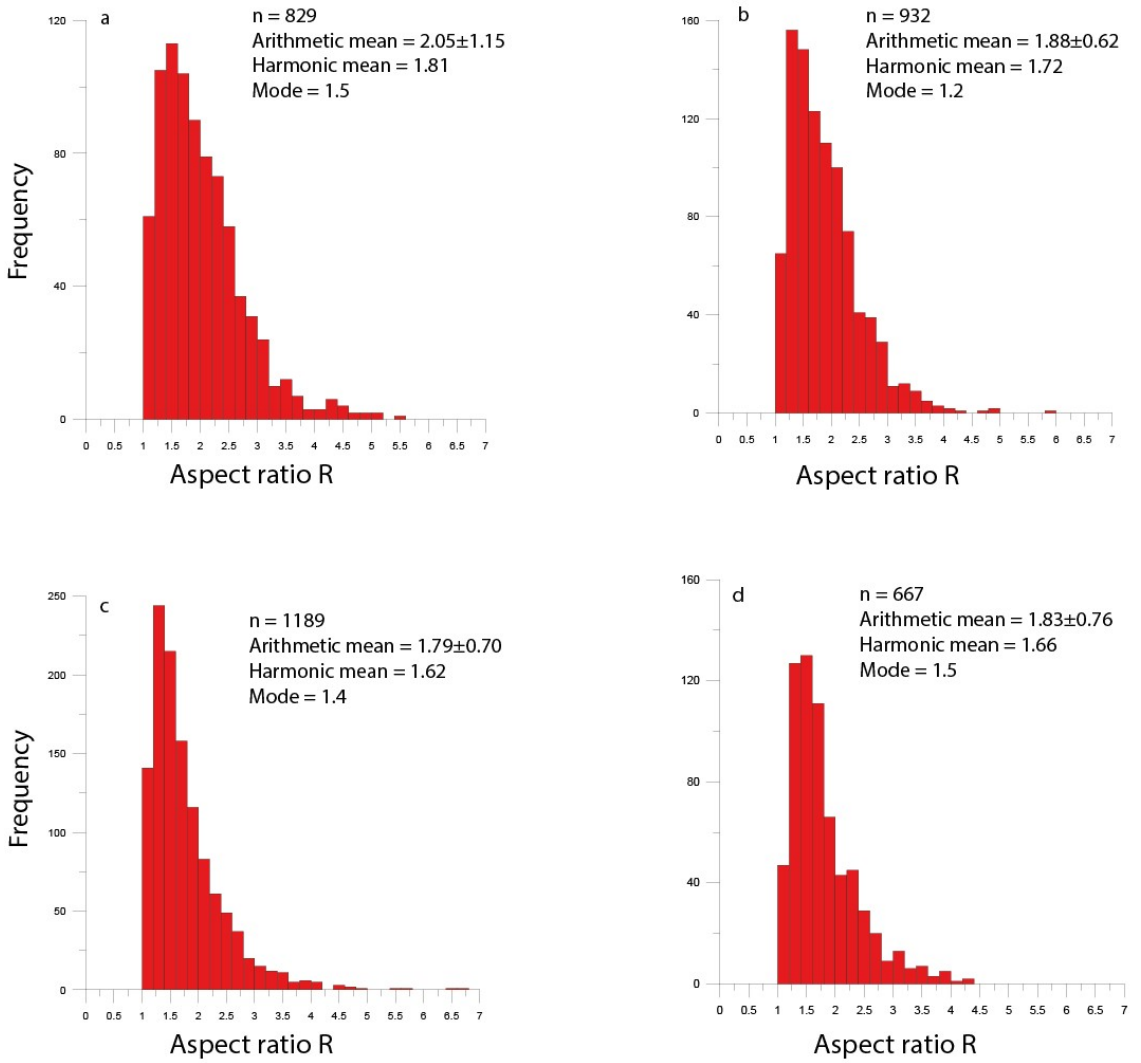

Figure V.3. Histograms of aspect ratio calculated in groups of crystals in deformation experiments. a) PP669 (ϕ_s = 0.58, $\dot{\gamma}$ = 0.5, $\mathring{\gamma}$ = 1.0*10^{-4}), b) PP676 (ϕ_s = 0.58, $\dot{\gamma}$ = 1.0, $\mathring{\gamma}$ = 1.0*10^{-4}), c) PP684 (ϕ_s = 0.59, $\dot{\gamma}$ = 2.0, $\mathring{\gamma}$ = 2.1*10^{-3}), d) PP685 (ϕ_s = 0.59, $\dot{\gamma}$ = 2.3, $\mathring{\gamma}$ = 1.0*10^{-4}).

3. Chemical composition of plagioclases and residual glass

Table V.2 shows the chemical analysis of plagioclase crystals in deformed samples obtained with EMPA analysis. Since no shear bands are visible in the deformed samples PP669, PP676, PP684 and PP685, the measurements were done randomly over the whole studied sections. Due to the large quantity of crystals, the glass areas of samples PP676 and PP684 could not be analyzed, as the glass analyses were mixed with the plagioclase analyses. Further chemical analyses can be found in Appendix D.

a

Mineral	Plagioclase		Plagioclase		Plagioclase		Plagioclase	
Sample	PP669		PP676		PP684		PP685	
n	32		10		13		23	
		±		±		±		±
Na_2O	5.29	0.53	5.28	0.21	5.32	0.28	5.07	0.23
SiO_2	57.84	2.71	57.79	2.91	57.18	2.98	55.99	2.56
Al_2O_3	26.87	1.67	26.79	1.81	27.26	1.76	28.01	1.49
CaO	9.87	1.28	9.95	1.26	10.06	1.15	10.78	1.12
Total	99.87		99.82		99.82		99.85	

b

Mineral	Glass		Glass		Glass		Glass	
Sample	PP669		PP676		PP684		PP685	
n	17		12		12		17	
		±		±		±		±
Na_2O	2.54	0.66	n.d	-	n.d	-	3.12	0.39
SiO_2	78.67	2.93	n.d.	-	n.d.	-	78.95	1.24
Al_2O_3	15.63	1.70	n.d.	-	n.d.	-	14.94	0.56
CaO	2.64	0.95	n.d.	-	n.d.	-	2.36	0.38
Total	99.48						99.38	

Table V.2. EPMA analysis for sample with R = 2 and ϕ_s = 0.58 – 0.59. a) Plagioclases chemical composition. b) Residual glass chemical composition.

The plagioclases of the deformed samples have a chemical composition very similar to that of the starting materials. Therefore, no nucleation and alteration processes took place during the deformation experiments.

4. Microstructural analysis

Unlike the R = 4 samples, the R = 2 samples do not show shear bands, but they have crystals orientation along the entire surface of the samples. For this reason, several randomly area were chosen over the XZ section with an average size between 30 µm x 70 µm and 70 µm x 90 µm.

ϕ_s = 0.58, $\dot{\gamma}$ = 0.5, $\mathring{\dot{\gamma}}$ = 1.0*10^{-4} (PP669)

In the sample PP669 (fig. V.4a) the eccentricity of the ellipse of the mean tensor ellipse shows a low value of R = 1.12, associated with a mean orientation direction α of 20.16° (fig. V.4b). The orientations of the long axes of the local ellipses show an orientation between 30° and -5° (fig. V.4c).

Although the sample appears homogeneous in the area analyzed by the intercept method, the analysis of the individual crystals by the inertia method shows a slightly different situation (fig. V.5a). The inertia tensor ellipse has R_x = 1.11 and α = 13.83° (fig. V.5b). The crystals are oriented in three main directions. The first, the most intense, which corresponds to the preferred direction found with Intercept, is oriented between -5° and 20°. The second, slightly less intense, is oriented close to 45°. The third, the least intense, shows a population at -45° (fig. V.5c).

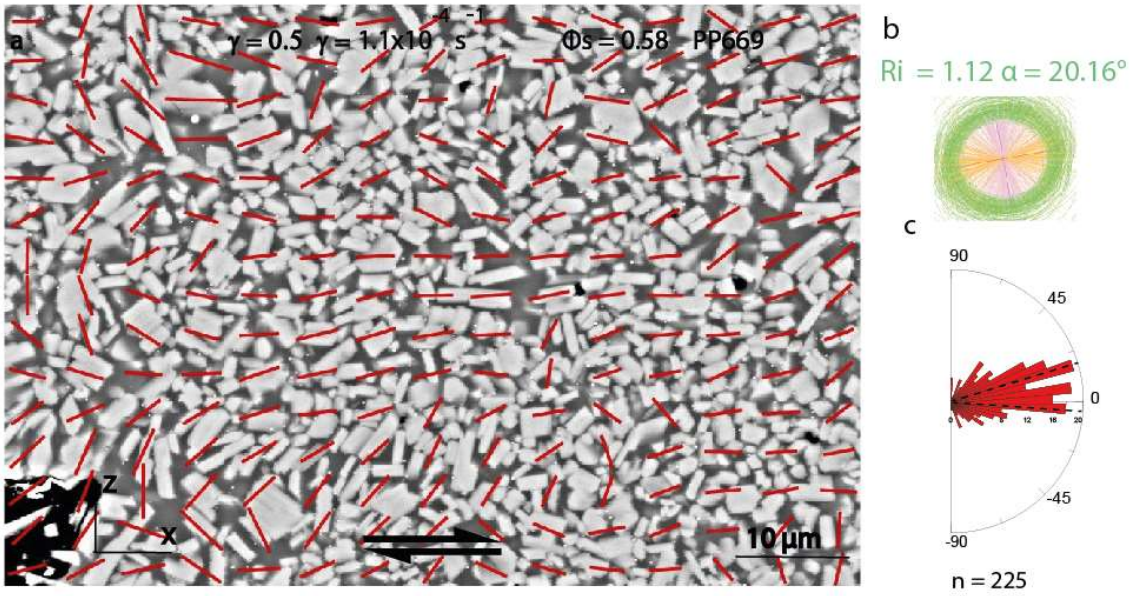

Figure V.4. Preferential orientation of sample PP669. a) [XZ] section SEM image of the sample. b) Mean tensor ellipse of the shape fabric. R_i = eccentricity of the mean ellipse, α = orientation of the long axis of the ellipse. c) Rose diagram of long axes of local tensor ellipses. n = number of measures.

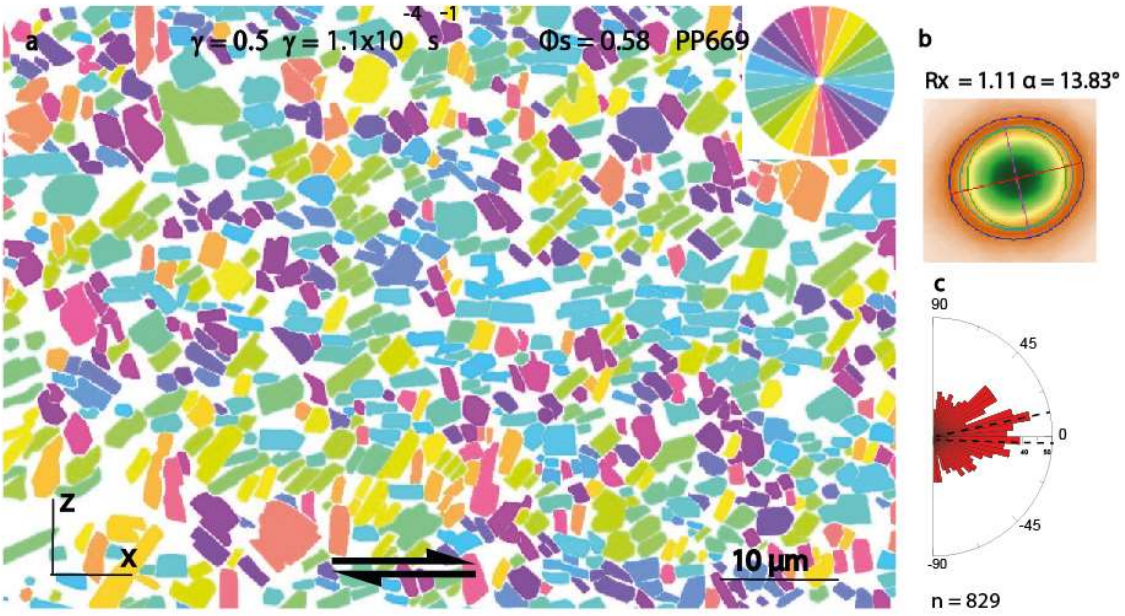

Figure V.5. a) Individual crystal orientations of sample PP699. Crystals are colored according to their orientations. b) Intertia tensor ellipse R_x. c) Roses diagram of individual crystals orientations. n = number of measures.

ϕ_s = 0.58, $\dot{\gamma}$ = 1.0, $\mathring{\dot{\gamma}}$ = 1.0*10^{-4} (PP676)

The sample PP676 (fig. V.6a) shows an eccentricity of the mean tensor ellipse R_i of 1.07 with a direction of orientation of the mean tensor ellipse α of 16.36° (fig. V.6b) with respect to the shear direction. The orientations of the long axes of the local ellipses show an orientation at 30° (Fig. V.6c). The crystals orientation, calculated using the inertia method (fig. V.7a), show a intertia tensor ellipse with R_x = 1.14 and α = 16.83° (fig. V.7b). The preferential directions of the crystals have 2 trends: the first at -5° and the second at 40° (fig. V.7c).

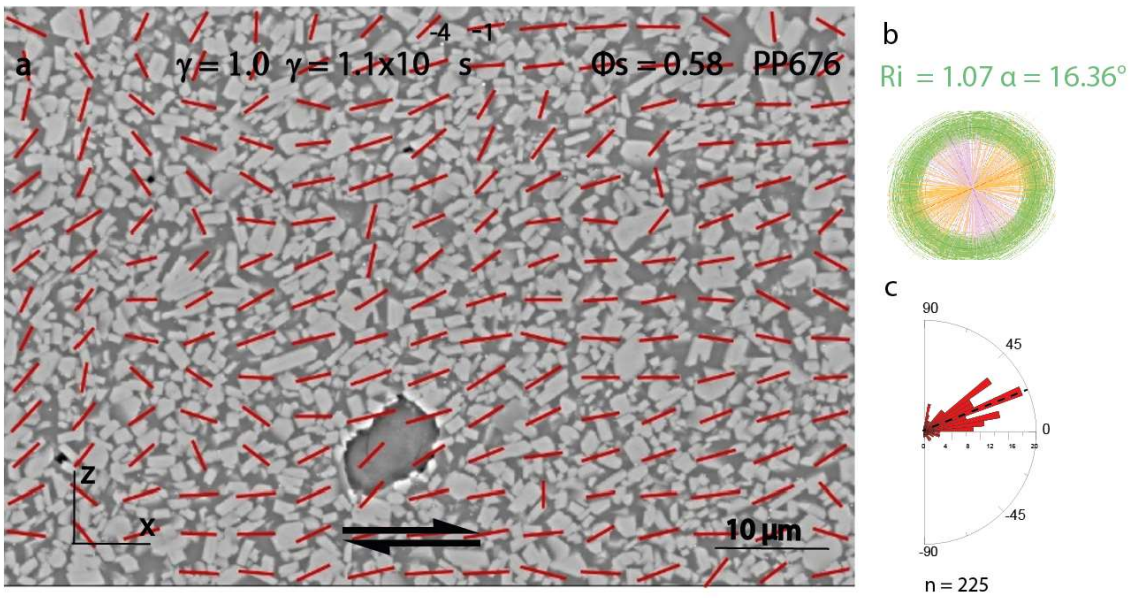

Figure V.6. Preferential orientation of sample PP676. a) [XZ] section SEM image of the sample. The red lines represent the long axes of the local tensor ellipses of the shape fabrics. b) Mean tensor ellipse of the shape fabrics. R_i = eccentricity of the mean ellipse, α = orientation of the long axis of the ellipse. c) Rose diagram of long axes of local tensor ellipses. n = number of measures.

.

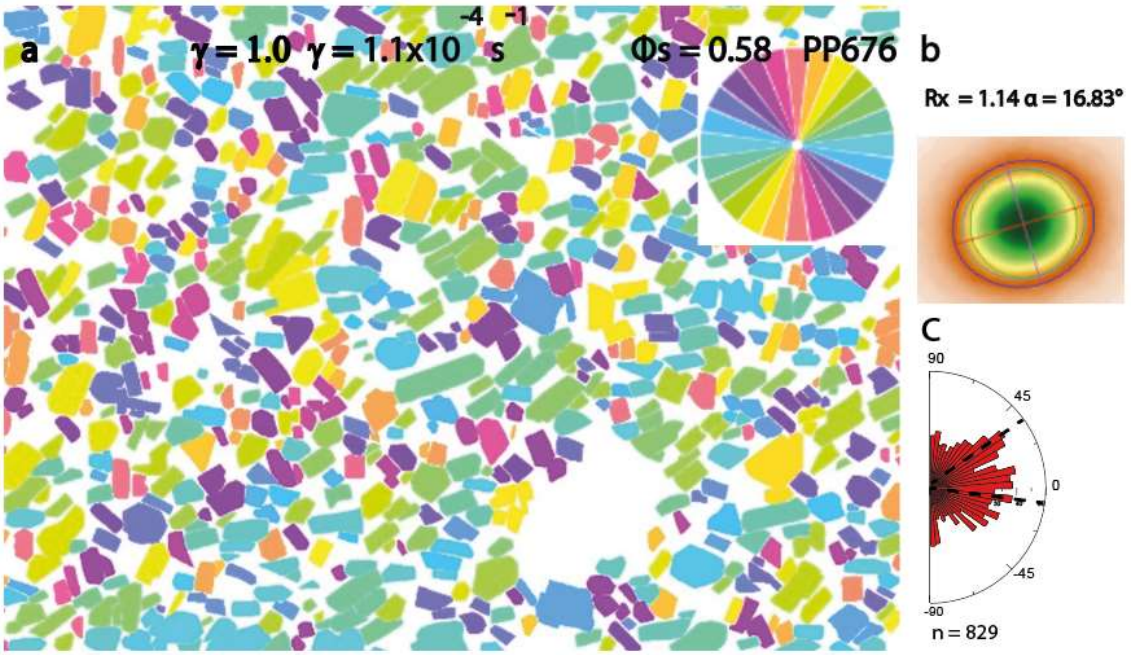

Figure V.7. Individual crystal orientations of the sample PP676. a) [XZ] section SEM image. The crystals of plagioclases were separated manually. b) Intertia tensor ellipse Rx. c) Roses diagram of individual crystals orientations. n = number of measures.

ϕ_s = 0.59, $\dot{\gamma}$ = 2.0, $\mathring{\dot{\gamma}}$ = 2.1*10^{-3} (PP684)

In the sample PP684 (fig. V.8a) the eccentricity of the mean tensor ellipse has a value R_i = 1.06 and an orientation α of 42.17° (fig. V.8b). The rose diagram of the long axes of the ellipse shows two preferential directions: 20° and 65° (fig. V.8c). The orientations of the plagioclase crystals analyzed with the inertia method (fig. V.9a) show an eccentricity of the intertia ellipse R_x = 1.17 and an orientation α = 44.05° (fig. V.9b). The rose of orientation shows light preferred range of orientation of the crystals between -15° and 45° (fig. V. 9c).

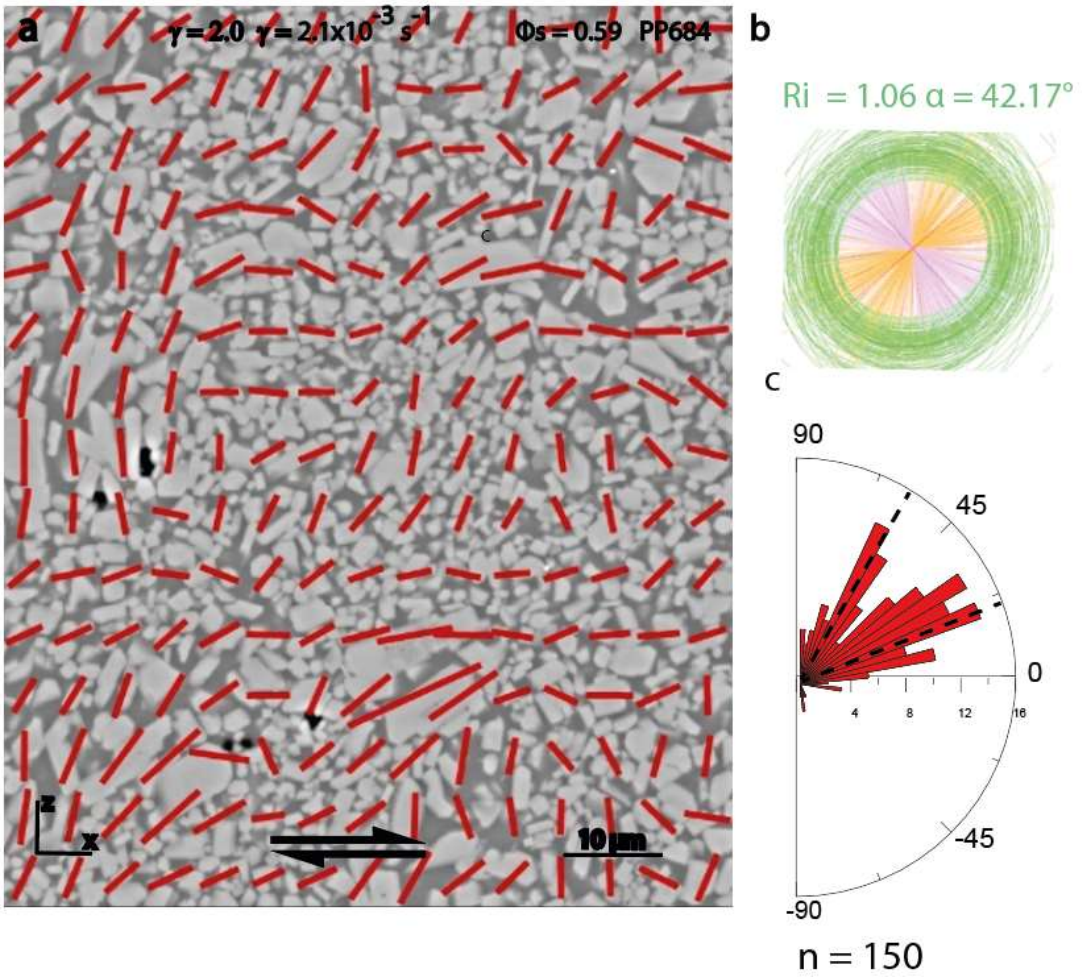

Figure V.8. Preferential orientation of sample PP684. a) [XZ] section SEM image of the sample. The red lines represent the long axes of the local tensor ellipses of the shape fabrics. b) Mean tensor ellipse of the shape fabric. R_i = eccentricity of the mean ellipse, α = orientation of the long axis of the ellipse. c) Rose diagram of long axes of local tensor ellipses. n = number of measures.

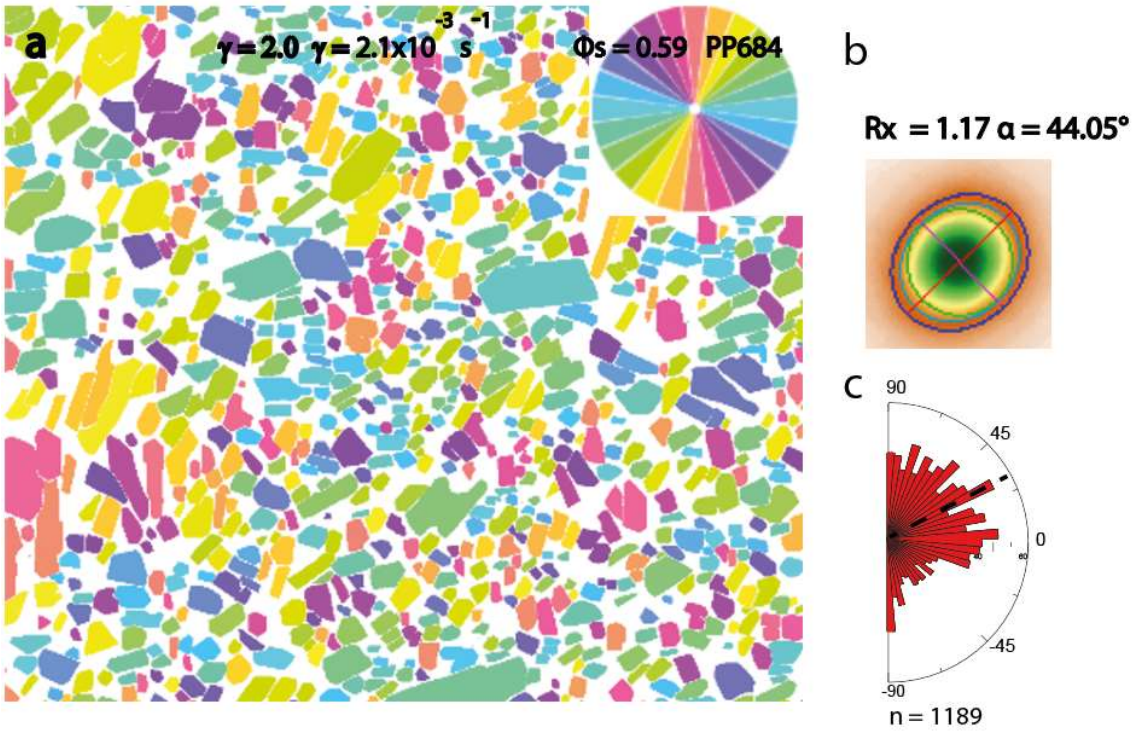

Figure V.9. Individual crystal orientations of PP684 sample. a) [XZ] section SEM image. The crystals of plagioclases were separated manually. b) Intertia tensor ellipse R_x. c) Roses diagram of individual crystals orientations.

ϕ_s = 0.59, γ = 2.3, $\dot{\gamma}$ = 1.0*10^{-4} (PP685)

In the sample PP685 (fig. V.10a) the eccentricity of the ellipse of the mean tensor shows a value of R_i = 1.50 associated with an orientation α of 21.70° (fig. V.10b). The rose diagram of the long axes of the ellipse shows a preferred orientation at 25° (fig. V.10c). Analysis of the preferential orientation of the crystals with the inertia method (fig. V.11a) show the eccentricity of the inertia tensor is R_i = 1.22 and the orientation α = 29.10° (fig. V.11b). The orientations of the crystals are at 40° - 45° and close to 10° (fig. V.11c).

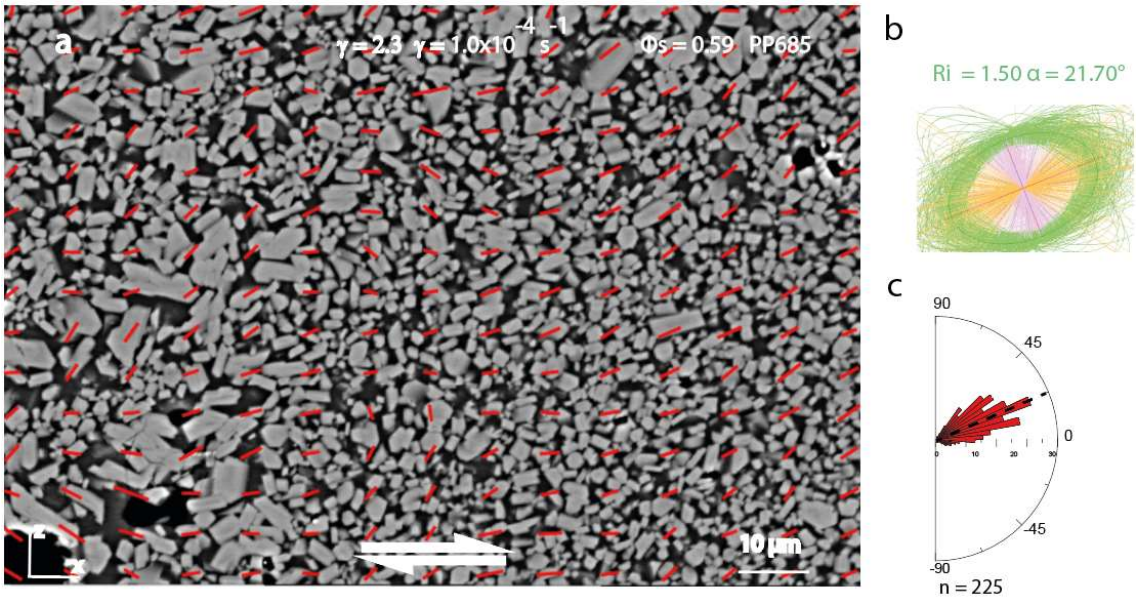

Figure V.10. Preferential orientation of sample PP685. a) [XZ] section SEM image of the sample. The red lines represent the long axes of the local tensor ellipses of the shape fabrics. b) Mean tensor ellipse of the shape fabric. R_i = eccentricity of the mean ellipse, α = orientation of the long axis of the ellipse. c) Rose diagram of long axes of local tensor ellipses. n = number of measures.

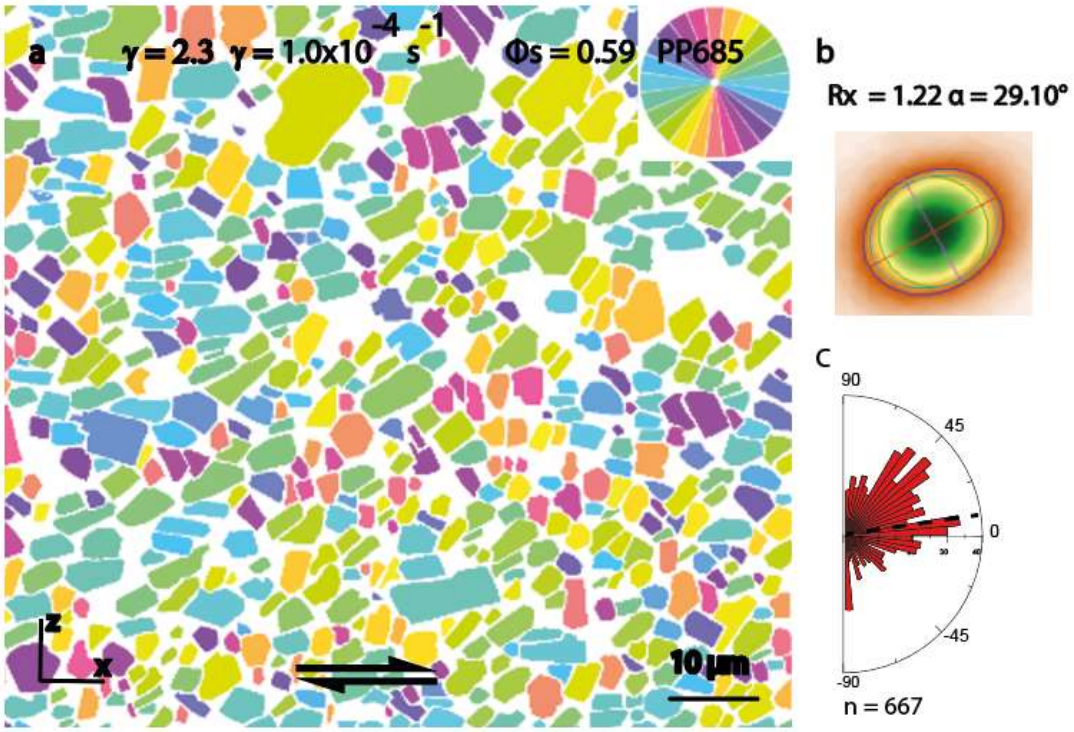

Figure V.11. Individual crystal orientations of PP685 sample. a) [XZ] section SEM image. The crystals of plagioclases were separated manually. b) Intertia tensor ellipse R_x. c) Roses diagram of individual crystals orientations. n = number of measures.

5. Aspect ratio R versus orientation α

The aspect ratio R and orientation α of each crystal of all the experiments were diagrammed in figure V.12 to investigate any correlation between these two parameters.

Sample PP669 (fig. V.12a) shows no correlation between aspect ratio and crystal orientation.
Samples PP676 (fig. V.12b), PP684 (fig. V.12c) and PP685 (fig. V.12d) have very similar results. Crystals with an aspect ratio R greater than 4 have a weak preferred orientation. Higher aspect ratio values show orientation values closer to 0°.

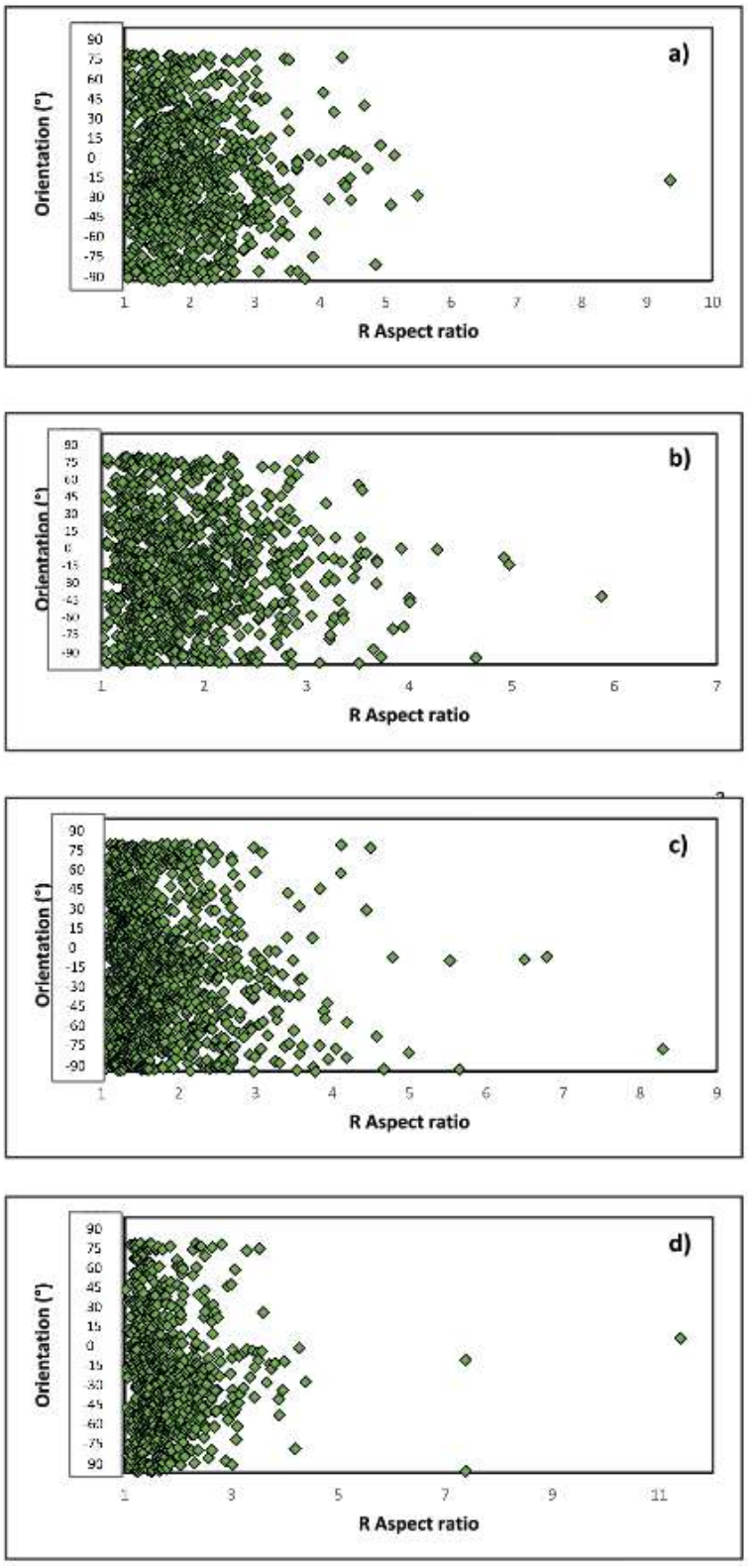

Figure V.12. Diagrams of all samples showing the aspect ratio vs orientation of the crystals. a) PP669 (ϕ_s = 0.58, $\dot{\gamma}$ = 0.5, $\dot{\gamma}$ = 1.0*10^{-4}), b) PP676 (ϕ_s = 0.58, $\dot{\gamma}$ = 1.0, $\dot{\gamma}$ = 1.0*10^{-4}), c) PP684 (ϕ_s = 0.59, $\dot{\gamma}$ = 2.0, $\dot{\gamma}$ = 2.1*10^{-3}), d) PP685 (ϕ_s = 0.59, $\dot{\gamma}$ = 2.3, $\dot{\gamma}$ = 1.0*10^{-4}).

6. Contacts

Type and orientation of contacts between plagioclase crystals were classified and studied following the definition of (Azema and Radjaï, 2012): S-S, side-side, long axis in contact; C-C, cap-cap, short axis in contact; S-C, side-cap, long axis and short axis in contact (fig. V.13).

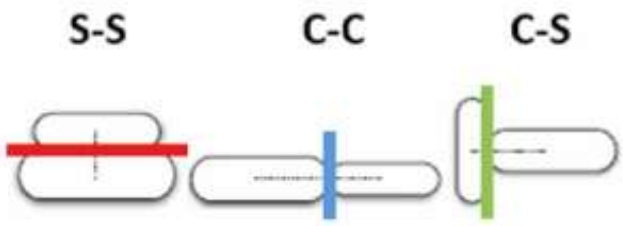

Figure V.13. Principal contact modes: side-side (s-s), cap-cap (c-c), cap-side (c-s). Modified from (Azema and Radjaï, 2012).

Samples PP669, PP676, PP684 and PP685 do not show shear bands, so the contacts were studied along the entire surface of the samples, without any distinction of area. Table V.3 shows the proportion of each contact for all the samples.

Sample	$\gamma = 0.5, \dot{\gamma} = 1.0*10^{-4}$	$\gamma = 1.0, \dot{\gamma} = 1.0*10^{-4}$	$\gamma = 2.0, \dot{\gamma} = 2.1*10^{-3}$	$\gamma = 2.3, \dot{\gamma} = 1.0*10^{-4}$
	PP669	PP676	PP684	PP685
S-S proportion	0.52	0.53	0.54	0.43
C-C proportion	0.04	0.08	0.06	0.21
S-C proportion	0.44	0.39	0.40	0.36

Table V.3. Contacts proportion for each type of contact and for each sample.

Despite the progressive increase in finite strain, the samples show very similar contact proportions, particularly for S-S contacts. Sample PP685 shows a lower proportion of S-S contacts and an increase in C-C and S-C contacts. This indicates a lower symmetry of the sample, which could be caused by sample breakage in the final part of the experiment.

ϕ_s = 0.58, γ = 0.5, $\dot{\gamma}$ = 1.0*10^{-4} (PP669)

Sample PP699 (fig. V.14a) shows no strong preferential contact directions. The S-S contacts have an orientation at 75°, weak orientation between 0° and 45° and a very weak orientation at -80° (fig. V.14b). The S-C contacts show a weak orientation between 0° and 45°, with a maximum at 5° (fig. V.14d), while the C-C contacts have no preferential orientation (fig. V.14c). S-S contacts account for 52% of the total contacts, C-C contacts for 4% and S-C contacts for 44%. Due to the small number and non-orientation of C-C contacts, these cannot be representative of the sample statistics.

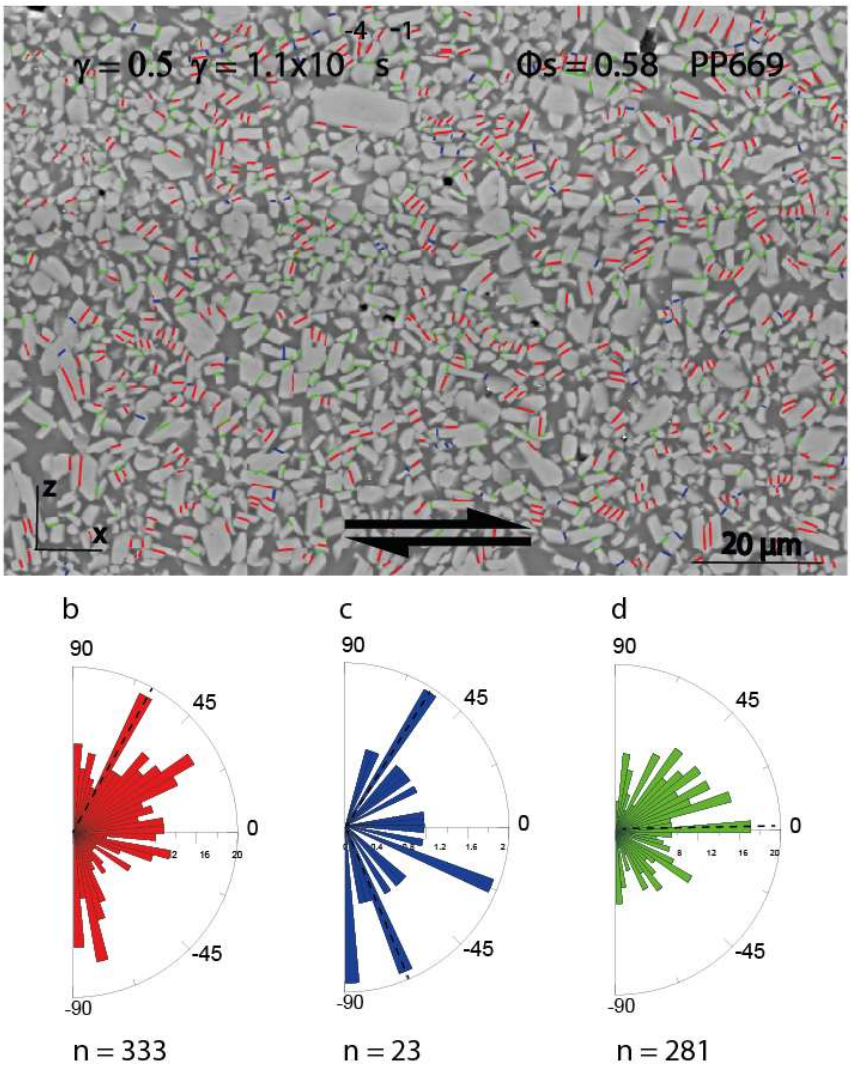

Figure V.14. a) SEM picture of the sample PP669 with hand drawn the contacts (red: S-S, blue: C-C, green: S-C). b) Rose diagram for the orientation of the contacts S-S (b), C-C (c) and S-C (d). n: number of measurements.

ϕ_s = 0.58, γ = 1.0, $\dot{\gamma}$ = 1.0*10^{-4} (PP676)

Sample PP676 (fig. V.15a) shows a stronger preferential orientation of the contacts than the previous sample. S-S contacts are oriented 35°-45° (fig. V.15b) and they represent 53% of the total contacts. C-C contacts show a less defined direction, around -80° (fig. V.15c) and they represent a small proportion of the contacts, 8%. S-C contacts have a preferential direction between 0° and 45° (fig. V.15d), with the strongest at 20°. Their proportion is 39%. Although the C-C contacts have a stronger orientation than the previous sample, they are not representative of the sample statistics as they are too few in number.

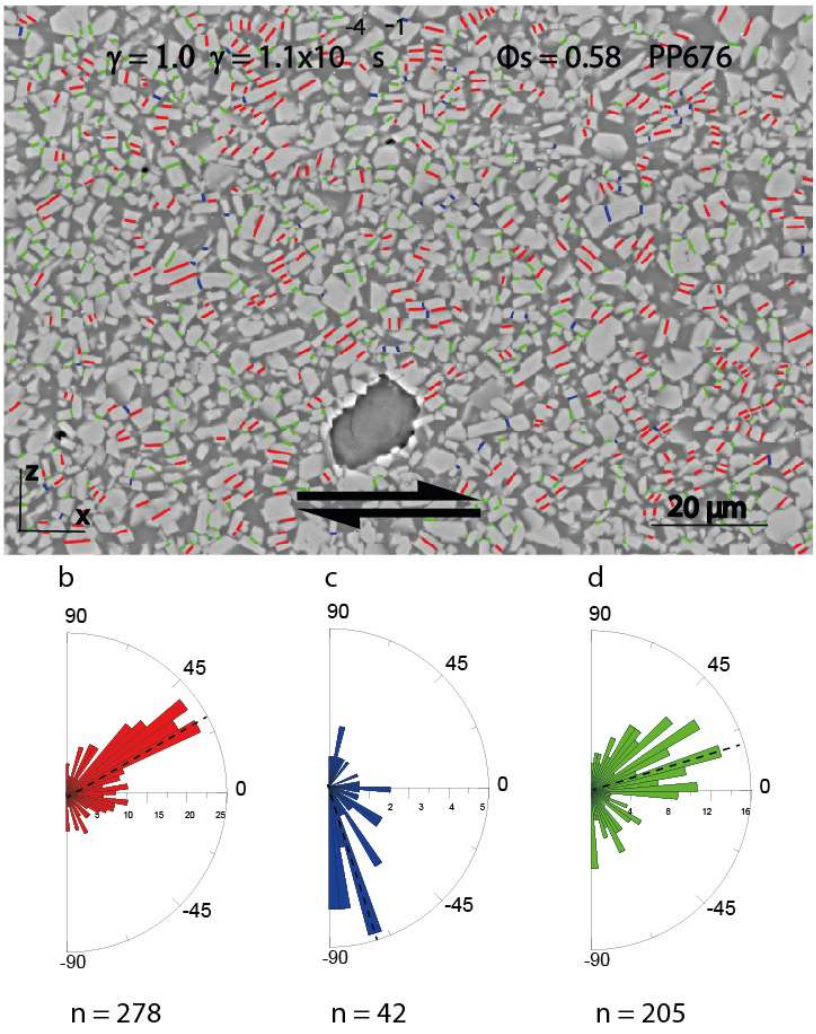

Figure V.15. a) SEM picture of the sample PP676 with hand drawn the contacts (red: S-S, blue: C-C, green: S-C). c) Rose diagram for the orientation of the contacts S-S (b), C-C (c) and S-C (d). n: number of measurements.

ϕ_s = 0.59, γ = 2.0, $\dot{\gamma}$ = 2.1*10^{-3} (PP684)

The S-S contacts of sample PP684 (fig. V.16a) have a preferred orientation between 0° and 75° (fig. V.16b), with a stronger concentration at 40° and their percentage is 54%. The C-C contacts, representing 6% of the total contacts, are oriented at 80°, 45°, -40° and -80° (fig. V.16c). The percentage of S-C contacts is 40% and they are oriented at 24° and slightly at -80° (fig. V.16d). As in the previous sample, the C-C contacts show a preferred orientation, but are not representative of the C-C contact population as they are too few in number to produce realistic statistics.

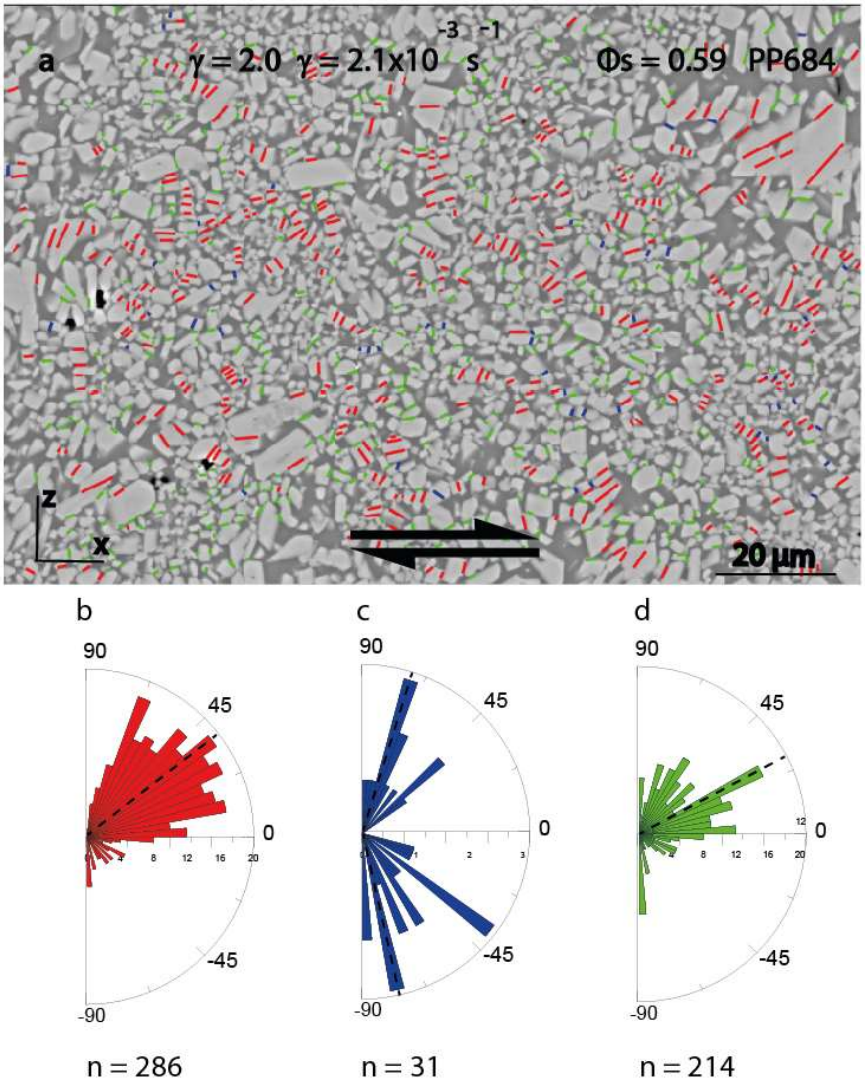

Figure V.16. a) SEM picture of the sample PP684 with hand drawn the contacts (red: S-S, blue: C-C, green: S-C). b) Rose diagram for the orientation of the contacts S-S (b), C-C (c) and S-C (d). n: number of measurements.

ϕ_s = 0.59, γ = 2.3, $\dot{\gamma}$ = 1.0*10^{-4} (PP685)

Sample PP685 (fig. V.17a) shows a slightly different percentage of contacts than the other samples: 43% for S-S contacts, 21% for C-C contacts and 36% for S-C contacts. The direction of the S-S contacts is between 20° and 45° (fig. V.17b), with a maximum at 30°, the C-C contacts are oriented between -40° and -70° (fig. V.17c), while the S-C contacts have no preferred orientation (fig. V.17d). Interesting information can be deduced from the orientation of the S-S and C-C contacts. In this sample, the number of C-C contacts is unusually high, so it can represent a population statistic of the contact C-C.

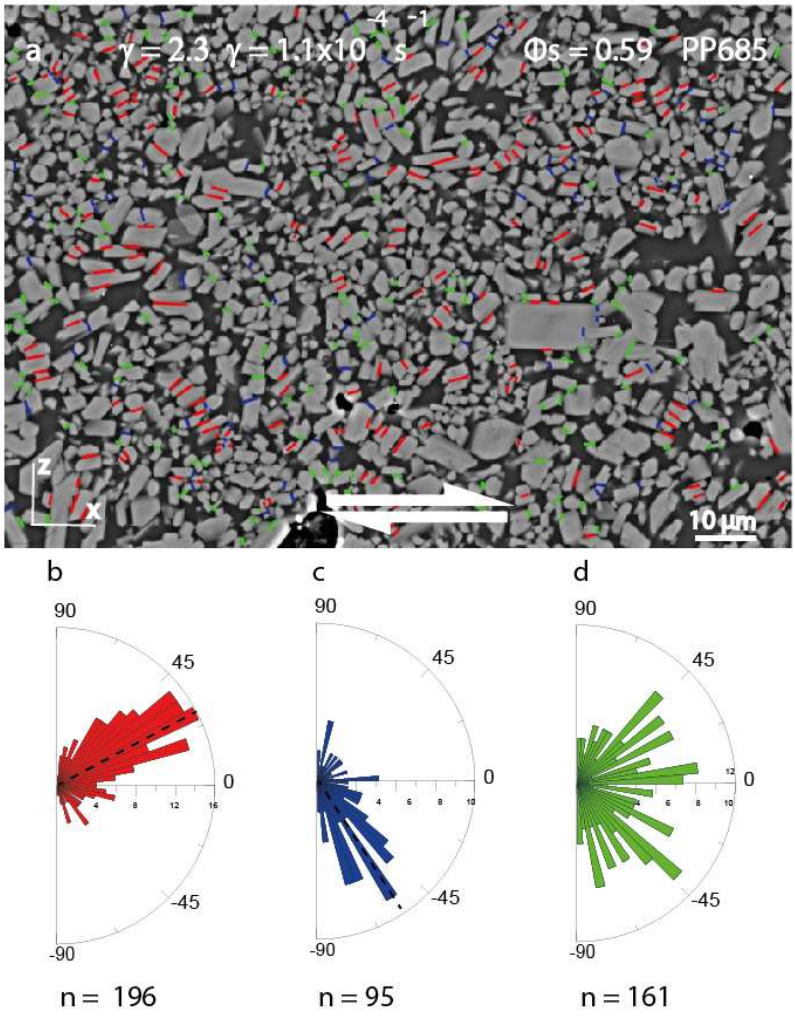

Figure V.17. SEM picture of the sample PP685 with hand drawn the contacts (red: S-S, blue: C-C, green: S-C). Below: Rose diagram for the orientation of the contacts S-S (b), C-C (c) and S-C (d). n: number of measurements.

Figure V.18 shows zoomed images of the contacts in each sample to examine their differences. For samples PP669, PP676 and PP684 the contacts are evenly distributed over the entire surface of the samples.

Sample PP669 (fig. V.18a) shows the S-S contacts oriented at a lower inclination than samples PP676 and PP684, which maintain the same inclination (fig. V.18b-c). In addition, sample PP669 shows more sporadic concentrations of S-S contacts than samples PP676 and PP684, which instead show larger amounts of adjacent S-S contacts. Sample PP685 (fig. V.18d) is not included in these statistics because its breakage at the end of the experiment probably altered the geometry of the contacts.

Thus, higher finite strain correspond to greater inclination of the S-S contacts and greater density of the contacts.

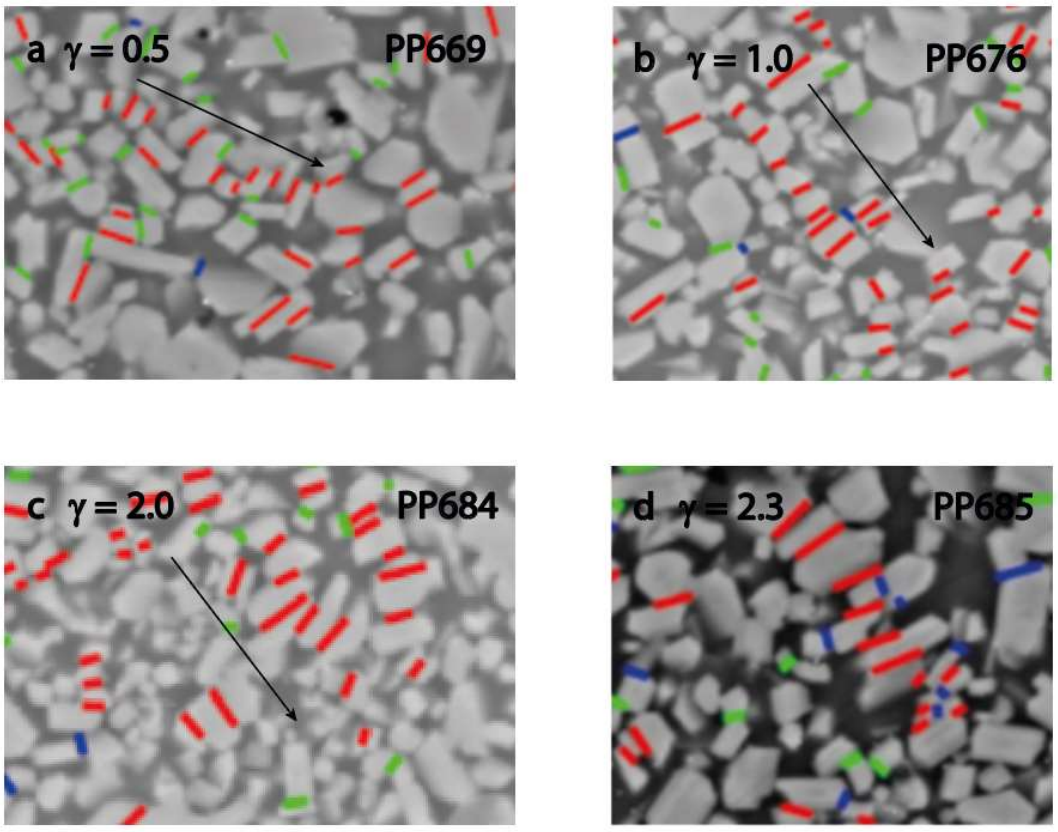

Figure V.18. Zoom on the contacts of samples a) PP669 (ϕ_s = 0.58, γ = 0.5, $\dot{\gamma}$ = 1.0*10^{-4}), b) PP676 (ϕ_s = 0.58, γ = 1.0, $\dot{\gamma}$ = 1.0*10^{-4}), c) PP684 (ϕ_s = 0.59, γ = 2.0, $\dot{\gamma}$ = 2.1*10^{-3}), d) PP685 (ϕ_s = 0.59, γ = 2.3, $\dot{\gamma}$ = 1.0*10^{-4}). The arrows indicate the different inclinations of the contacts directions.

7. Clusters

In this section, all clusters formed by a minimum of 3 adjacent S-S and C-C contacts were considered (as defined in chapter methods). Both clusters orientation (green line, fig. V.19) and orientation of the contacts in the clusters (red line, fig. 19) are indicated. Depending on the arrangement of the crystals, there can be different orientations of the clusters, which can lead to different force localization structures. Therefore, it is necessary to study all the relationships between crystals, contacts and clusters.

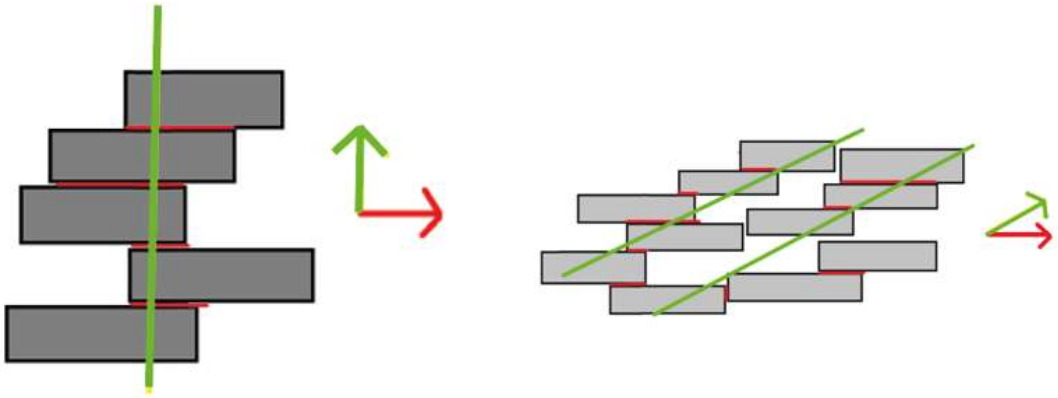

Figure V.19. Plots of different cluster arrangements. Green line: orientation of the cluster, red line: orientation of the contacts in the cluster.

ϕ_s = 0.58, $\dot{\gamma}$ = 0.5, $\mathring{\gamma}$ = 1.0*10^{-4} (PP669)

The sample PP669 (fig. V.20a) has the orientation of the contacts in the clusters with preferential orientations at 45° (fig. V.20b). The orientations of the clusters are -40° and 0° (fig. V.20c).

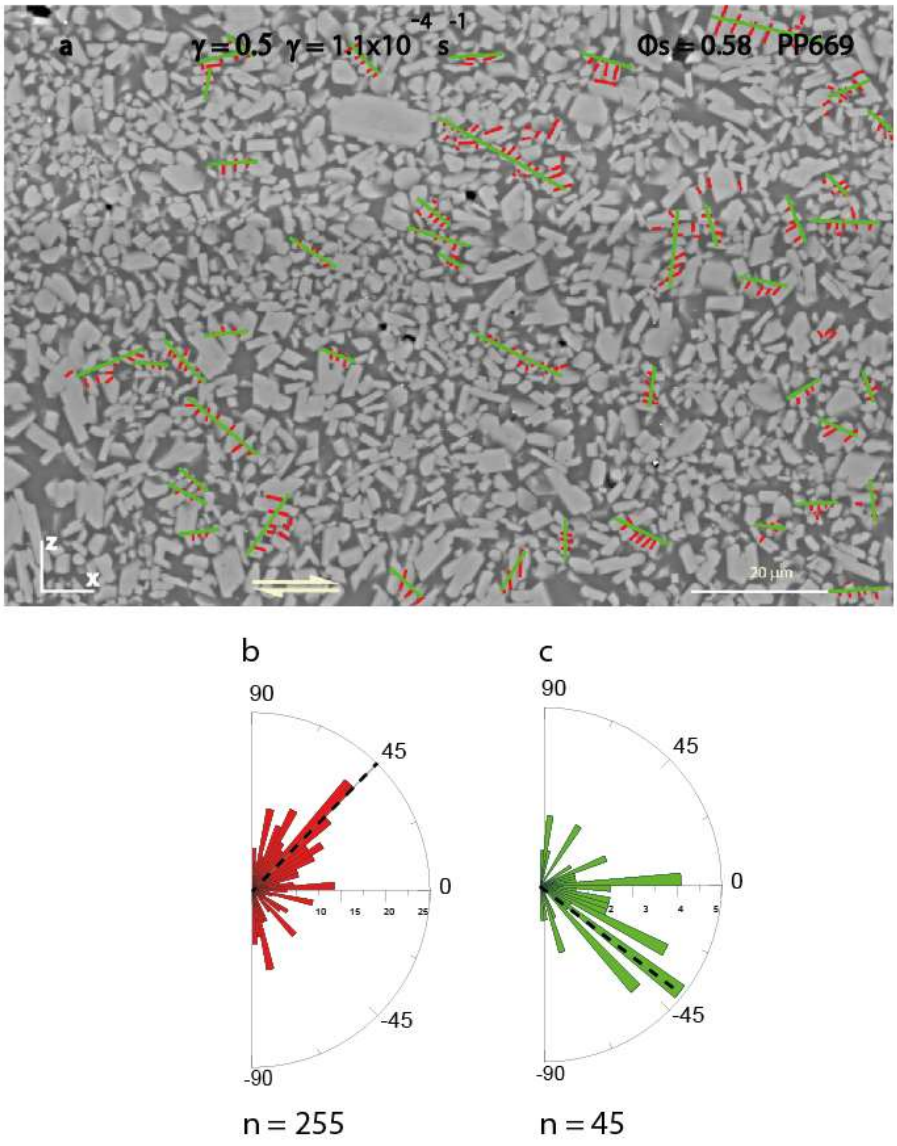

Figure V.20. a) SEM image of sample PP669 with hand-drawn orientation of the clusters. b) Rose diagram of orientation of the contacts in the clusters, c) rose diagram of the preferred orientations of the clusters. n = number of measures.

ϕ_s = 0.58, γ = 1.0, $\dot{\gamma}$ = 1.0*10^{-4} (PP676)

The sample PP676 (fig. V.21a) shows a strong orientation of the contacts in the clusters with preferred orientation at 30° (fig. 21b). The orientation of the clusters is at -45° (fig. V.21c).

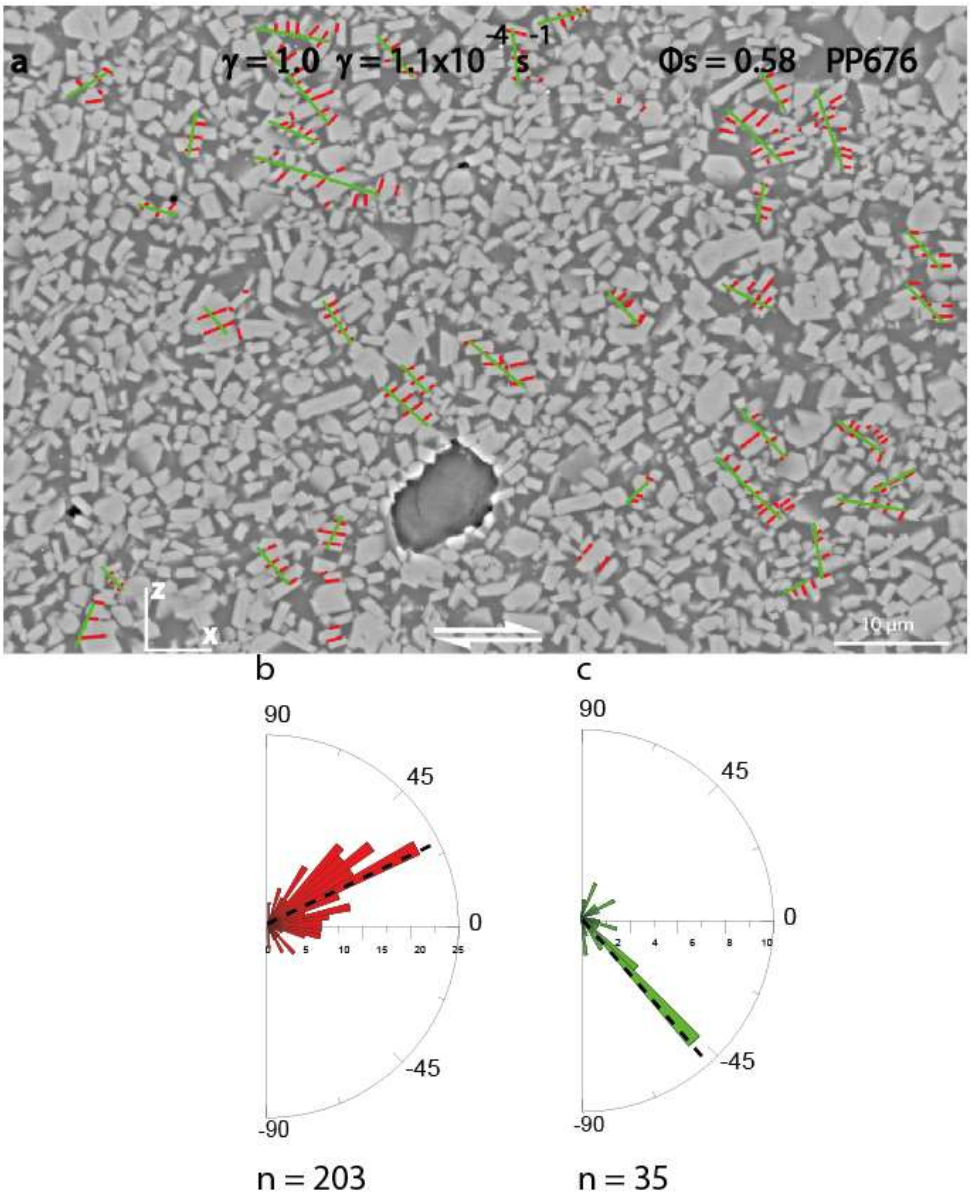

Figure 2 V.1. a) SEM image of sample PP676 with hand-drawn orientation of the clusters. b) Rose diagram of orientation of the contacts in the clusters, c) rose diagram of the preferred orientations of the clusters. n = number of measures.

ϕ_s = 0.59, $\dot{\gamma}$ = 2.0, $\dot{\gamma}$ = 2.1*10^{-3} (PP684)

The PP684 sample (fig. V.22a) has a very similar behavior to the PP676 sample, with an orientation of the contacts in the clusters at 30° and 50° (fig. V.22b). The orientations of the clusters are -45° and 35° (fig. V.22c).

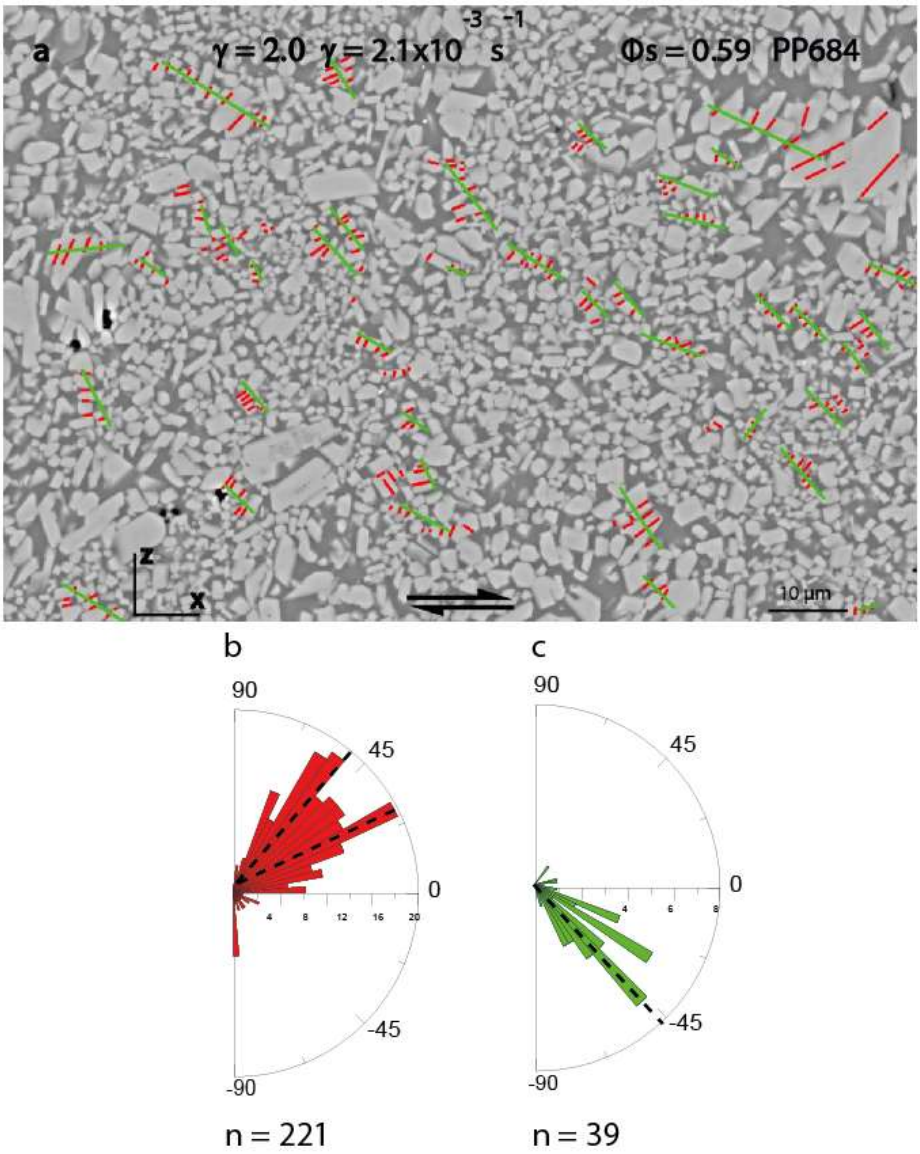

Figure V.22. a) SEM image of sample PP684 with hand-drawn orientation of the clusters. b) Rose diagram of orientation of the contacts in the clusters, c) rose diagram of the preferred orientations of the clusters. n = number of measures.

ϕ_s = 0.59, $\dot{\gamma}$ = 2.3, $\mathring{\dot{\gamma}}$ = 1.0*10^{-4} (PP685)

Sample PP685 (fig. V.23a) has a preferential orientation of the contacts in the clusters at 35° (fig. V.23b) and the orientation of the clusters shows a preferential direction at 55° (fig. V.23c).

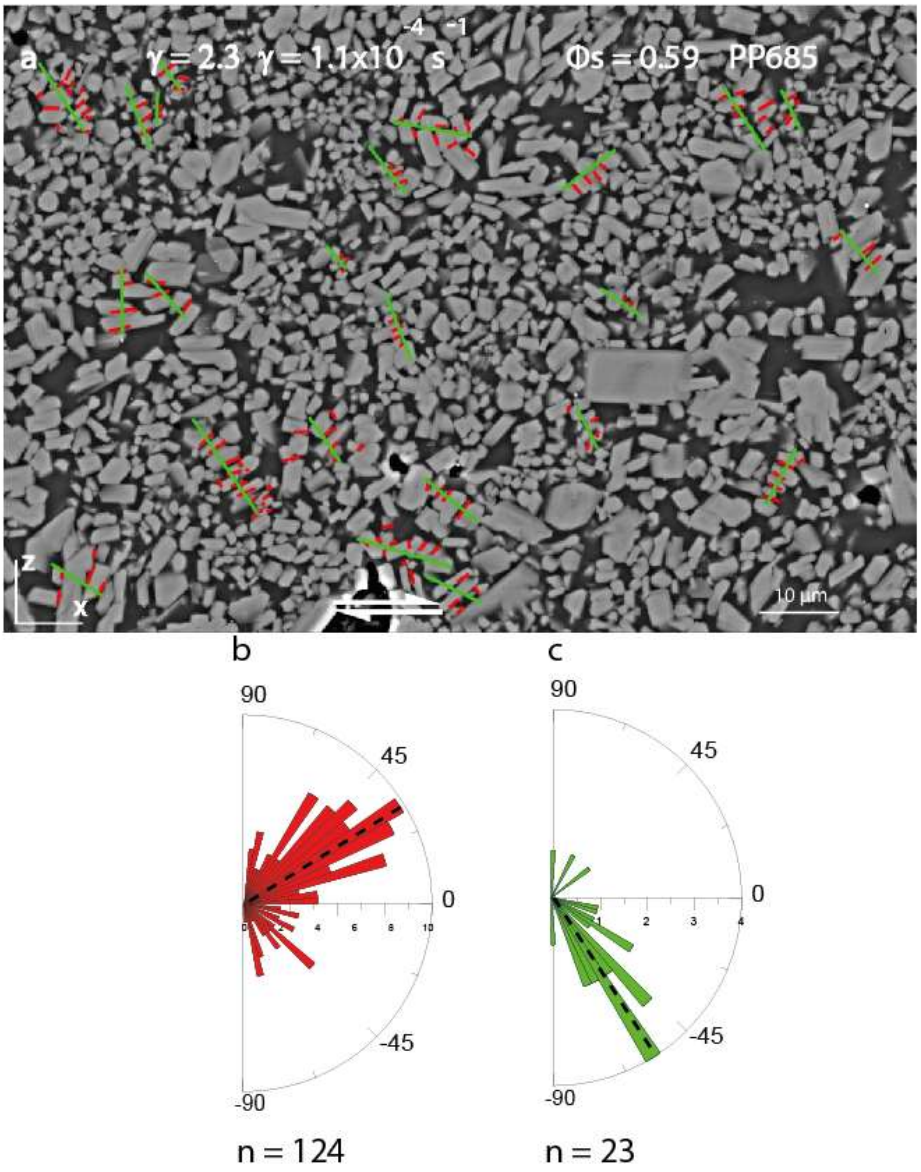

Figure V.23. a) SEM image of sample PP685 with hand-drawn orientation of the clusters. b) Rose diagram of orientation of the contacts in the clusters, c) rose diagram of the preferred orientations of the clusters. n = number of measures.

8. Shape fabrics of bubbles

Sample PP669 (fig. V.24a) has a bubble content of 1.8%. The inertia tensor ellipse shows an eccentricity R_x = 1.55 and an inclination α = 37.64° (fig. V.24b) The bubbles show a preferential orientation between 68° and 40° (fig. V.24c). The arithmetic mean aspect ratio of the bubbles is 1.55±0.32, with a harmonic mean of 1.52 (fig. V.24d).
The bubble content for sample PP676 (fig. V.24e) covers the 1.4% of the total area, with an eccentricity R_x of the inertia tensor ellipse of 1.31 and with α = 31.55° (fig. V.24f). The preferred orientation of the crystals is between 15° and 45° (fig. V.24g), with a maximum at 20°. The aspect ratio is very similar to the previous sample, with an arithmetic mean of 1.56±0.41 and a harmonic mean of 1.51 (fig. V.24h).
Sample PP684 (fig. V.25a) shows a bubble content of 1.2%. The inertia tensor ellipse shows an eccentricity R_x = 1.51 and an inclination α = 27.78° (fig. V.25b). The preferred direction of the bubbles is between 0° and 45° (fig. V.25c), the arithmetic mean value of the aspect ratio is 1.94±0.63 and the arithmetic mean is 1.78 (fig. V.25d).
Sample PP685 (fig. V.25e) has a bubble content of 1.4%, with an eccentricity R_x of the inertia tensor ellipse of 1.53 and with α = 10.55° (fig. V.25f). The preferred orientation of the bubbles is between 0° and 20° (fig. V.25g). The aspect ratio has an arithmetic mean value of 1.72±0.36 and a harmonic mean value of 1.66 (fig. V.25h). The numerical data can be found in Appendix C.

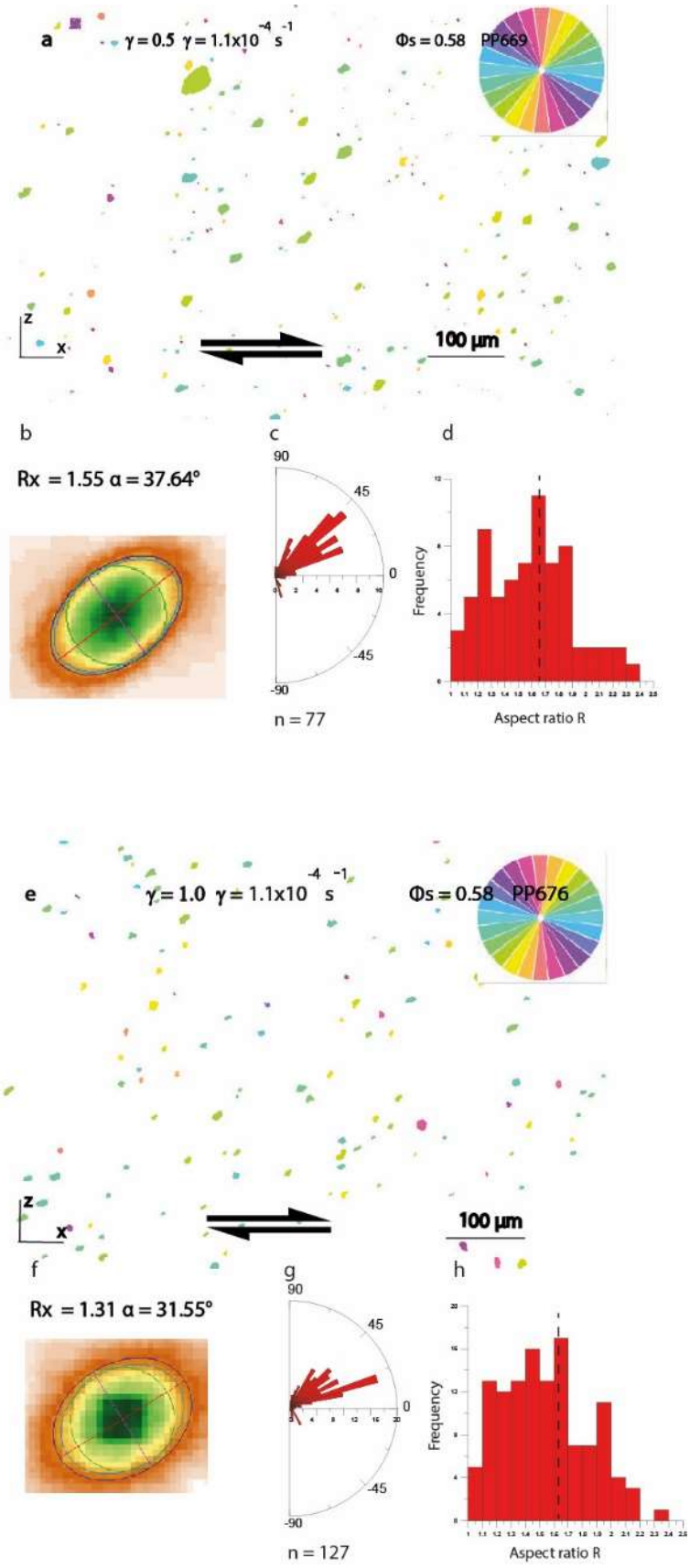
a
γ = 0.5 γ = 1.1x10 -4 -1 s
Φs = 0.58 PP669
z
x
100 µm
b
c
d
Rx = 1.55 α = 37.64°
90
45
0
-45
-90
n = 77
Frequency
Aspect ratio R
e
γ = 1.0 γ = 1.1x10 -4 -1 s
Φs = 0.58 PP676
z
x
100 µm
f
g
h
Rx = 1.31 α = 31.55°
90
45
0
-45
-90
n = 127
Frequency
Aspect ratio R

Figure V.24.

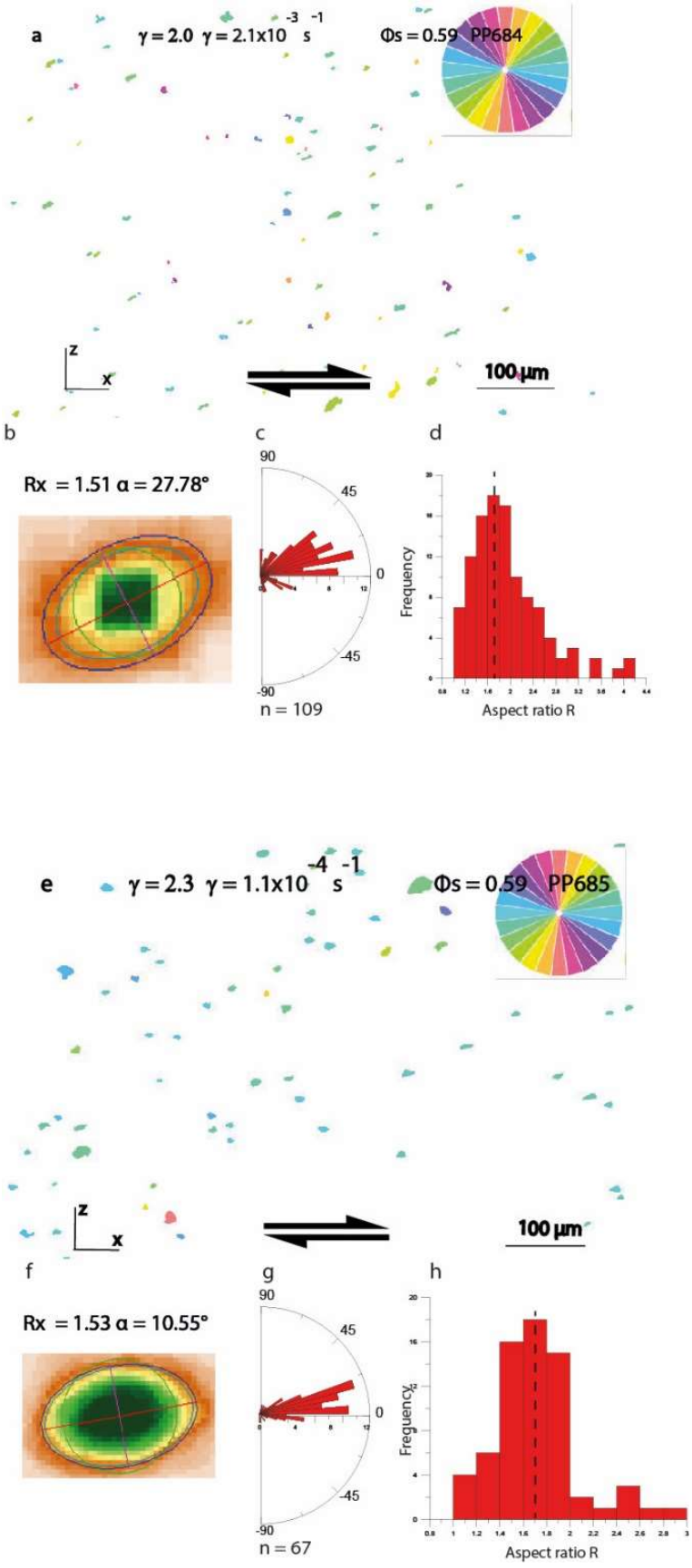
a
γ = 2.0 γ = 2.1x10 -3 -1 s
Φs = 0.59 PP684
z
x
100 µm
b
c
d
Rx = 1.51 α = 27.78°
90
45
0
-45
-90
n = 109
Frequency
Aspect ratio R
e
γ = 2.3 γ = 1.1x10 -4 -1 s
Φs = 0.59 PP685
z
x
100 µm
f
g
h
Rx = 1.53 α = 10.55°
90
45
0
-45
-90
n = 67
Frequency
Aspect ratio R

Figure V.25.

Figure V.24. Bubbles orientation of sample PP669 (a) and PP676 (e). a) Bubbles colored according to their orientations for sample PP669. b) Inertia tensor ellipse of PP669 sample. c) Rose of directions of individual bubbles orientation of PP669 sample d) Aspect ratio histogram for groups of bubbles of PP669 sample. e) Bubbles colored according to their orientations for sample PP676. f) Inertia tensor ellipse of PP676 sample g) Rose of directions of individual bubbles orientation of PP676 sample. h) Aspect ratio histogram for groups of bubbles of PP676 sample.

Figure V.25. Bubbles orientation of sample PP684 (a) and PP685 (e). a) Bubbles colored according to their orientations for sample PP684. b) Inertia tensor ellipse of PP684 sample. c) Rose of directions of individual bubbles orientation of PP684 sample d) Aspect ratio histogram for groups of bubbles of PP684 sample. e) Bubbles colored according to their orientations for sample PP685. f) Inertia tensor ellipse of PP685 sample g) Rose of directions of individual bubbles orientation of PP685 sample. h) Aspect ratio histogram for groups of bubbles of PP685 sample.

9. Summary

Samples with aspect ratio R = 2 and crystal content ϕ_S = 0.58 and 0.59 show no structure from shear localization and there are homogeneous shape fabrics for both plagioclases and bubbles. As can be seen in figure V.26, when deformation is applied there is the onset of an orientation domain due to particles tiling. The crystals follow the direction of the deformation and they are oriented at ±45° and ±0°.

The slightly elongated shape of the crystals allows them to move. Unlike plagioclases with aspect ratio R = 4, the crystals can move and translate, forming a homogeneous network of contacts over the entire surface of the sample, but with few clusters. This could be one of the reasons for the lack of strain localization: there is no accumulation of force as the position of the crystals is constantly changing.

The mobility of the crystals is confirmed by the absence of cataclastite, which is very abundant in samples with R = 4 at high strain rate.

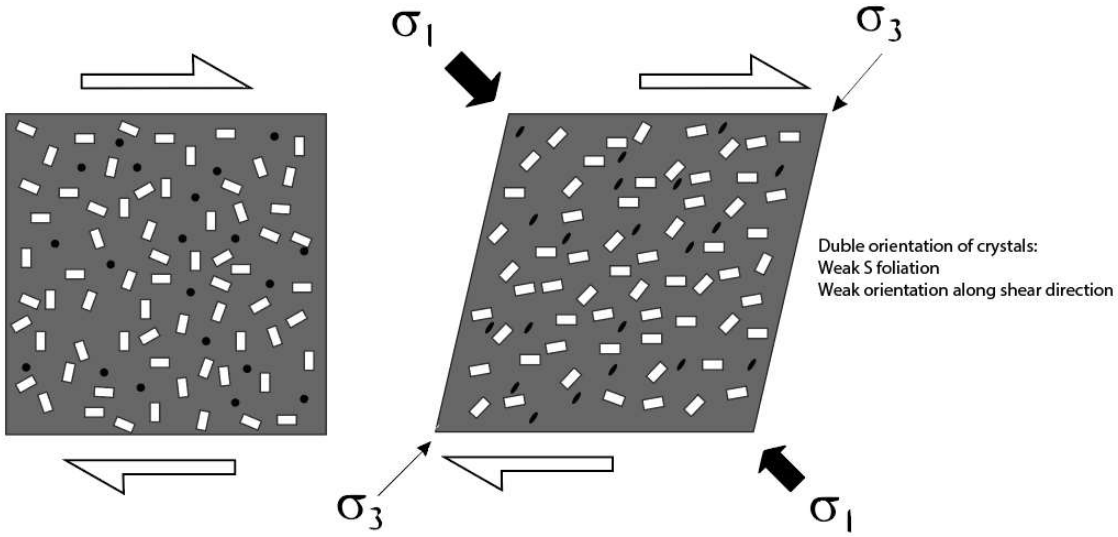

Figure V.26. Deformation stages for samples with R = 2 and ϕ_s = 0.58 – 0.59.

Results loose mush - R = 2, ϕ_s = 0.73 - 0.76 - 0.95

Résumé du chapitre VI - Résultats R = 2, ϕ_s = 0,73, 0,76 et 0,95

Les échantillons étudiés dans ce chapitre ont un rapport d'aspect R = 2 et une teneur en cristaux ϕ_s = 0,73, 0,76 et 0,95.

Les valeurs de déformation finie sont comprises entre 2,0 et 10, tandis que les valeurs de vitesse de déformation sont comprises entre $1*10^{-3}$ s^{-1} et $5*10^{-5}$ s^{-1}.

Comme pour les échantillons synthétiques précédents, tous les échantillons ont été photographiés après les expériences de déformation. Des reconstructions panoramiques ont été réalisées, où une déformation homogène est observée pour l'échantillon avec une déformation finie γ = 2, tandis qu'une tendance ondulatoire est observée pour les échantillons avec une déformation finie γ = 5. L'échantillon PP699 s'est cassé à la fin de l'expérience. Cependant, l'échantillon a conservé toutes ses caractéristiques intactes et a donc été analysé et étudié.

Les échantillons sont étudiés du point de vue de leur morphologie (rapport d'aspect R et diamètre équivalent), de leurs caractéristiques microstructurelles et de leur chimisme. Enfin, les types de contacts et de clusters qui se développent dans chaque expérience sont étudiés.

Les échantillons avec des teneurs en cristaux ϕ_s = 0,73 - 0,76 ne présentent pas de localization de la déformation. Après les expériences de déformation, les échantillons développent un motif ondulé composé de cristaux avec une orientation moyenne entre 0° et 45°. Les bulles sont orientées dans la direction du cisaillement et présentent des phénomènes de coalescence. A partir d'une déformation finie ɣ = 5, les échantillons développent un banding, qui est formé par des bandes interconnectées enrichies en liquide résiduel et formant un réseau anastomosé. Les contacts sont répartis sur toute la surface des échantillons. En raison de la mobilité des cristaux, le nombre de clusters est toujours faible.

L'échantillon avec ϕ_s = 0,95 a un comportement granulaire. Lorsqu'il est soumis à une déformation, il développe une orientation des plagioclases entre 0° et 45° et une série de bandes interconnectées avec un motif anastomosé. Ces bandes sont enrichies en liquide résiduel et en bulles. Elles ont une taille de grain cristallin inférieure à celle du tissu principal. Ceci démontre la localization de la déformation dans ces bandes.

VI. Results loose mush - R = 2, ϕ_s = 0.73 - 0.76 - 0.95

This chapter ilustrates the results for the samples PP693, PP695, PP698, PP699, PP701. The conditions of all deformation experiments are shown in table VI.1. The samples were studied in their morphological characteristics (equivalent diameter Φ and aspect ratio R), chemical composition, microstructures, contacts and clusters. Sample PP701 was only analysed in terms of microstructures and chemical composition, as its morphology and its very high crystal content did not consent morphological and contact analysis. As with the samples studied in chapters IV and V, the morphological characteristics are analysed using both the arithmetic mean and the harmonic mean. The values of aspect ratio R and equivalent diameter in the harmonic mean are given in table VI.1. The use of the harmonic mean was chosen because it is more representative of the samples, although the values of aspect ratio R and equivalent diameter Φ are lower than those obtained with the arithmetic mean.

A summary table with all deformation experiments performed for both samples with aspect ratio R = 4 and aspect ratio R = 2 is shown in Appendix A.

Sample	Crystal content	Starting material	Aspect ratio R	Equivalent diameter Φ (μμ)	H_2O content (wt.%)	P (MPa)	T (°C)	Finite strain γ	Strain rate $\dot{\gamma}$ (s^{-1})
PP693	0.73	HTN11	1.95 ± 0.96	1.54 ± 0.74	3	300	810	2	$2.5*10^{-4}$
PP695	0.76	HTN13	1.87 ± 0.92	1.24 ± 0.62	3	300	810	5	$2.5*10^{-4}$
PP698	0.76	HTN14	1.85 ± 1.18	1.20 ± 0.71	3	300	810	5	$1.0*10^{-3}$
PP699	0.76	HTN14	1.84 ± 0.80	1.43 ± 0.75	3	300	810	10	$2.5*10^{-4}$
PP701	0.95	HTN12	n.d.	n.d.	3	300	790	1.8	$5.0*10^{-5}$

Table VI.1. Paterson press experiments for the sample with R = 2 and ϕ_s = 0.73 - 0.76 – 0.95. The values for aspect ratio R and equivalent diameter Φ are the harmonic mean values, which are more representative of the samples.

1. Panoramic reconstructions

Figure VI.1 shows the panoramic reconstructions of all samples with aspect ratio R = 2 and crystal contents ϕ_s = 0.73, 0.76 and 0.95 after the torsion experiments. The directions of deformation are indicated by the black lines.

Sample PP693 (fig. VI.1a) was deformed with a finite strain ɣ = 2.0 and shows a homogeneous deformation distributed over the whole sample with straight grooves.
Sample PP695 (fig. VI.1b), deformed at a finite strain ɣ of 5, shows a curvilinear pattern with the maximum deformation in the central area.
Sample PP698 (fig. VI.1c) was deformed with a finite strain ɣ = 5.0 and shows a homogeneous deformation with grooves slightly wavy.
Sample PP699 (fig. VI.1d) was subjected to a finite strain ɣ of 10 and broke at the end of the experiment. Observations from the outer copper show how the deformation propagates in a wavy pattern.
Sample PP701 (fig. VI.1e) was subjected to a finite strain ɣ of 1.8 as the high crystal content made this sample particularly stiff and it was not possible to achieve higher finite strain without breaking the sample. The strain is evenly distributed on the surface and there is an onset of sample breakage.

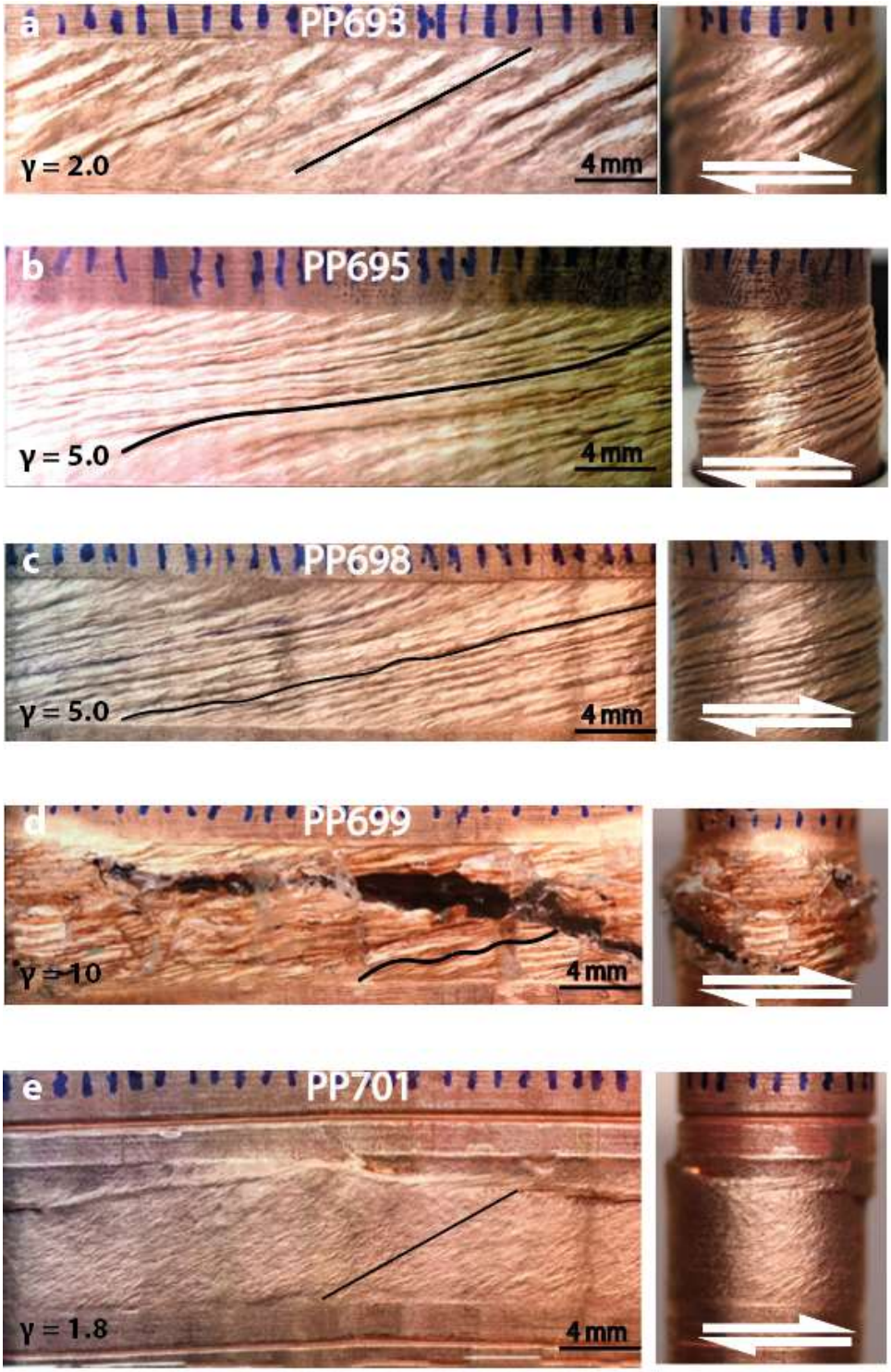

Figure VI.1. Panoramic reconstruction of the samples still embebbed in their copper jacket subject to torsion deformation. a) PP693 (ϕ_s = 0.73 γ = 2.0, $\dot{\gamma}$ = 2.5*10^{-4}) b) PP695(ϕ_s = 0.76, γ = 5.0, $\dot{\gamma}$ = 2.5*10^{-4}), c) PP698(ϕ_s = 0.76, γ = 5.0, $\dot{\gamma}$ = 1.0*10^{-3}), d) PP699 (ϕ_s = 0.76 γ = 10.0, $\dot{\gamma}$ = 2.5*10^{-4}), e) PP701 ($\phi_s \simeq$ 0.95, γ = 1.8, $\dot{\gamma}$ = 5.0*10^{-5}). The deformation is highlighted but the black line.

2. Crystal morphology

Histograms of the distribution of equivalent diameters Φ and aspect ratio R were made. It has been considered the mode, the arithmetic and the harmonic mean.

2.1. Equivalent diameter Φ

Sample PP693 has a arithmetic mean of 1.60±0.74 µm, with a harmonic mean of 1.25 µm and a mode of 1.1 µm (fig. VI.2a). All values sway in a range of 0.4 µm to 6.4 µm.
Sample PP695 shows values slightly lower than the previous sample. The equivalent diameter ranges from 0.2 µm to 4.5 µm with an arithmetic mean of 1.49±0.62 µm and a harmonic mean of 1.24 µm The mode is at 1.3 µm (fig. VI.2b).
Sample PP698 has very similar values to sample PP695. The arithmetic mean of the equivalent diameter is 1.49±0.68, the harmonic mean is 1.23 µm with values ranging from 0.2 µm to 4.6 µm and the mode at 1.2 µm (fig. VI.2c).
Sample PP699 shows an arithmetic mean equivalent diameter of 1.70±0.75 µm, a harmonic mean of 1.43 µm with values ranging from 0.2 µm to 4.2 µm (fig. VI.2d). The mode is at 1.1 µm.

The equivalent diameter values are similar in all the experiments. However, the arithmetic mean, harmonic mean and mode values do not coincide, indicating that the crystal populations are log-normal and that the harmonic mean is the best parameter to consider for averaging.

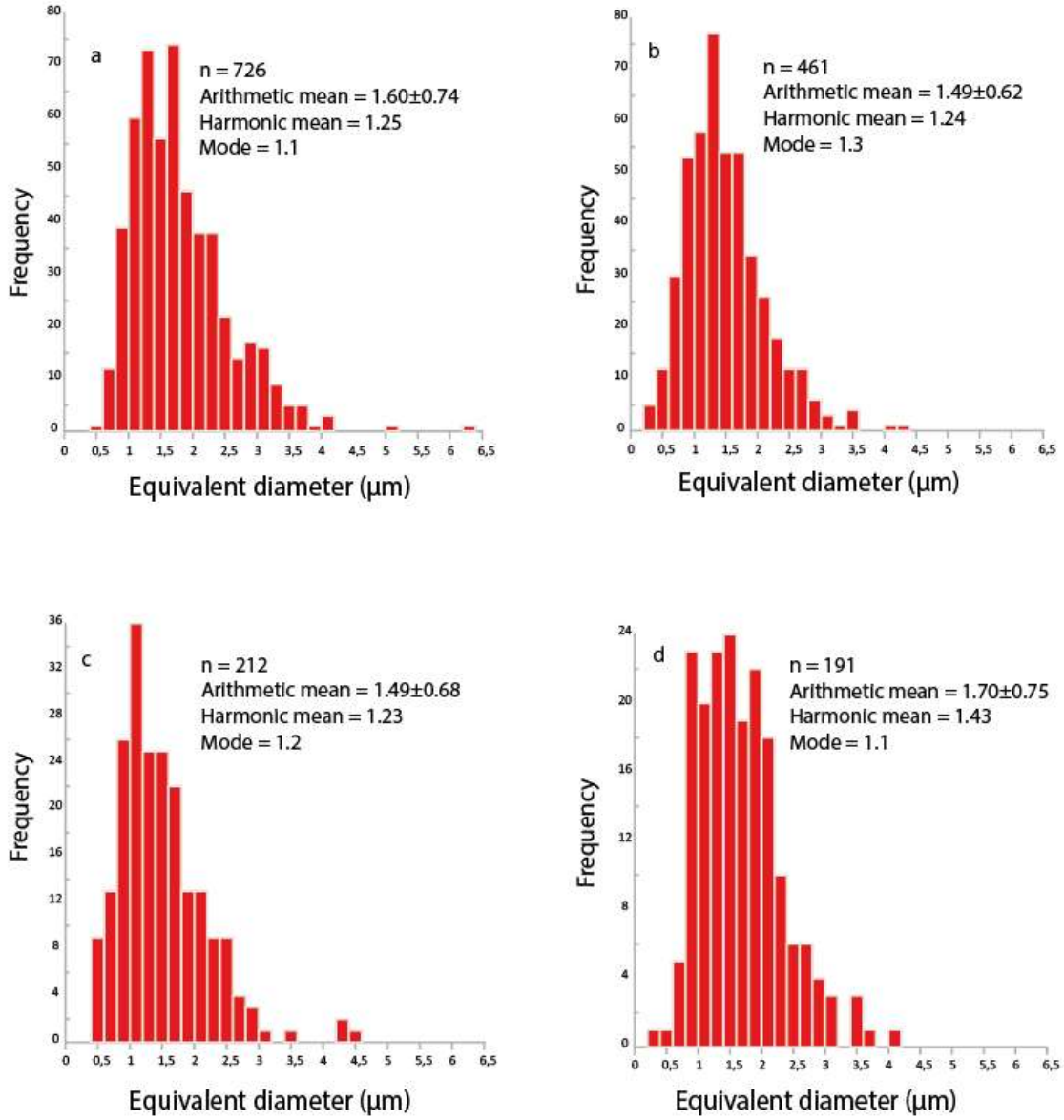

Figure VI.2. Histograms of equivalent diameters calculated in groups of crystals in deformation experiments. a) PP693 (ϕ_s = 0.73 $\dot{\gamma}$ = 2.0, $\dot{\gamma}$ = 2.5*10^{-4}) b) PP695(ϕ_s = 0.76, $\dot{\gamma}$ = 5.0, $\dot{\gamma}$ = 2.5*10^{-4}), c) PP698(ϕ_s = 0.76, $\dot{\gamma}$ = 5.0, $\dot{\gamma}$ = 1.0*10^{-3}), d) PP699 (ϕ_s = 0.76 $\dot{\gamma}$ = 10.0, $\dot{\gamma}$ = 2.5*10^{-4}).

2.2. Aspect ratio R

Sample PP693 has an arithmetic mean of 2.22±0.96 and a harmonic mean of 1.95. The mode is at 1.5. The minimum value is 1 and the maximum value is 6.8 (fig. VI.3a).
Sample PP695 has aspect ratio values ranging from 1 to 5.6, with an arithmetic mean of 2.15±0.92 and a harmonic mean of 1.87 (fig. VI.3b). The mode is at 1.3.
The R values for sample PP698 range from 1 to 5.5, with an arithmetic mean of 2.03±0.82, a harmonic mean of 1.77 and a mode at 1.4 (fig. VI.3c).
Sample PP699 has a maximum R value of 4.6 and a minimum value of 1. The arithmetic mean is 2.08±0.80 and the harmonic mean is 1.84 (fig. VI.3d). The mode is at 1.7.

All samples show similar aspect ratio values, so the samples are homogeneous. As for the equivalent diameter, the arithmetic mean, harmonic and mode values do not coincide. The geometry of the system is log-normal and the best interpretation is with the harmonic mean.

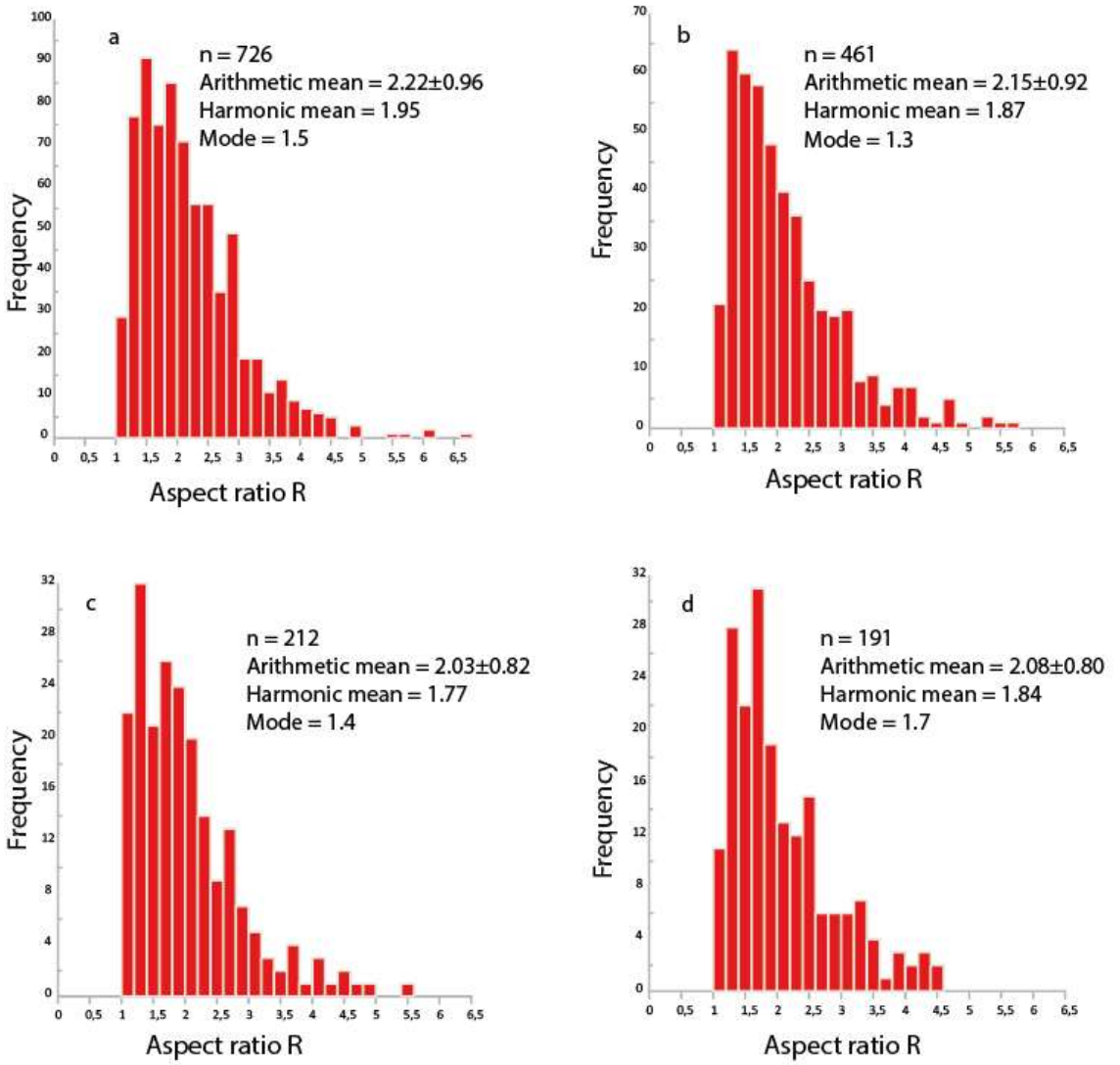

Figure VI.3. Histograms of aspect ratio calculated in groups of crystals in deformation experiments. a) PP693 (ϕ_s = 0.73 $\dot{\gamma}$ = 2.0, $\dot{\gamma}$ = 2.5*10^{-4}) b) PP695(ϕ_s = 0.76, $\dot{\gamma}$ = 5.0, $\dot{\gamma}$ = 2.5*10^{-4}), c) PP698(ϕ_s = 0.76, $\dot{\gamma}$ = 5.0, $\dot{\gamma}$ = 1.0*10^{-3}), d) PP699 (ϕ_s = 0.76 $\dot{\gamma}$ = 10.0, $\dot{\gamma}$ = 2.5*10^{-4}).

3. Chemical composition of the crystals

The chemical analyses of plagioclase crystals obtained with EPMA are shown in the table VI.2. Analyses were carried out at the top, middle and bottom of the samples. It was not possible to analyse the residual glass, as the high crystal content did not allow the formation of sufficiently large melt areas.

All the chemical analyses show similar values from one sample to another, making the analyses comparable. However, there is a large error in the SiO_2 content due to the high crystal content and small crystals size. It is possible that analyses carried out on individual crystals include some glass. For the same reason no analysis was performed on the glass as the residual melt areas are extremely small.

Mineral	**Plagioclase**		**Plagioclase**		**Plagioclase**		**Plagioclase**		**Plagioclase**	
Sample	**PP693**		**PP695**		**PP698**		**PP699**		**PP701**	
n	**25**		**10**		**18**		**22**		**20**	
		±		±		±		±		±
Na_2O	5.63	0.31	5.70	0.26	6.02	0.56	5.48	0.43	5.77	0.62
SiO_2	59.63	1.57	57.76	1.50	58.58	1.77	60.14	1.79	62.72	3.88
Al_2O_3	24.99	1.32	25.36	0.94	25.74	1.15	24.66	1.11	22.45	2.34
CaO	8.49	0.64	8.59	0.59	8.59	0.86	8.06	0.68	7.15	0.83
Total	98.74		97.40		98.93		98.33		98.10	

Table VI.2. Plagioclase chemical composition from deformed samples.

4. Study of the microstructures

Φ_s = 0.73 $\dot{\gamma}$ = 2.0, $\dot{\gamma}$ = 2.5*10^{-4} (PP693)

Figure VI.4a shows the structures produced by the sample PP693. The sample shows a penetrative fabric distribuited along the entire surface of the sample.
The direction of orientation of the mean tensor ellipse is 29.95° with respect to the shear direction, associated with an eccentricity of 1.46 (fig. VI.4b). The orientation of the long axes of the local tensor ellipses is at 40° with respect to the shear direction (fig VI.4c).
The crystals were hand drawn and analyzed using the SPO software, in order to characterize the orientations of each single crystal (fig. VI.5a). The inertia tensor ellipse has an eccentricity R_x = 1.36 and an inclination α = 26.36 (fig. VI.5b). The orientation of the crystals is in a range between -5° and 45° with respect to the shear direction (fig. VI.5c).

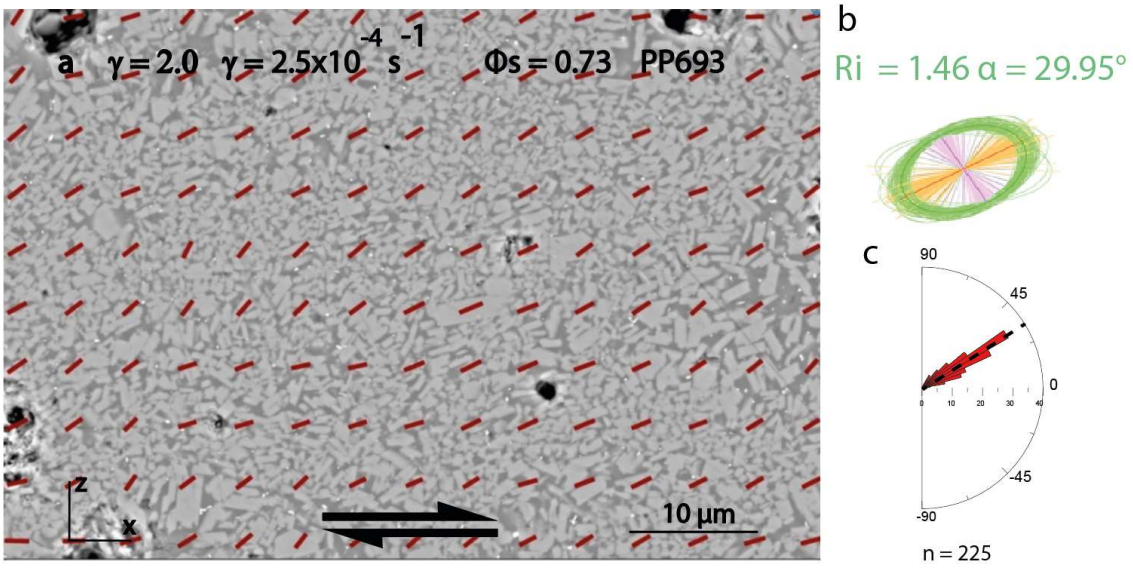

Figure VI.4. Preferential orientation of sample PP693 a) [XZ] SEM image of the sample. The red lines represent the long axes of the local tensor ellipses of the shape fabrics. b) Mean tensor ellipse of the shape fabric. R_i = eccentricity of the mean ellipse, α = orientation of the long axis of the ellipse. c) Rose diagram of long axes of local tensor ellipses.

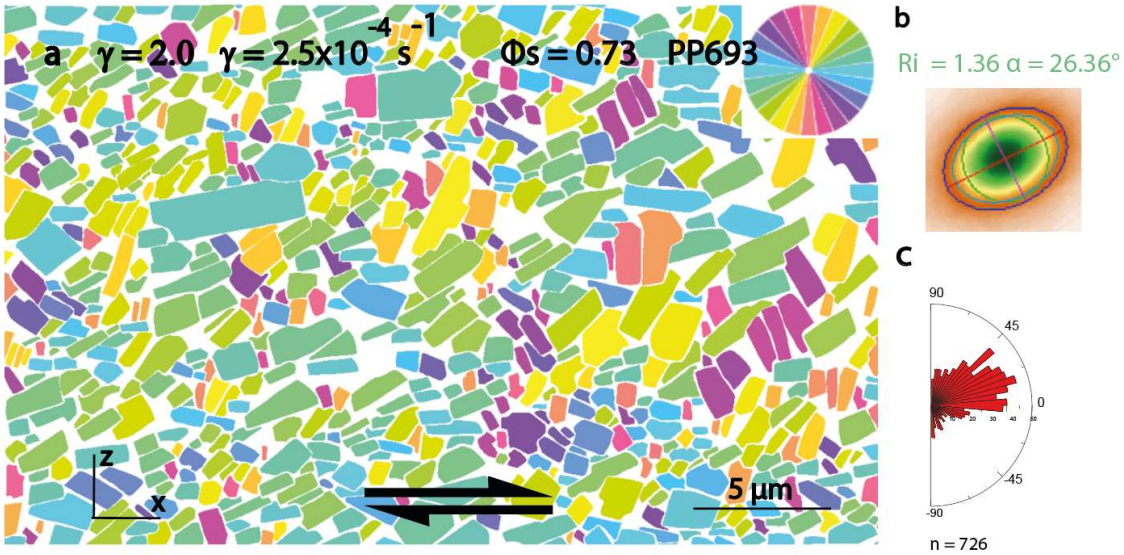

Figure VI.5. a) Orientation of the long axes of the plagioclases of sample PP693. b) Inertia ellipse tensor. R_x = eccentricity of the mean ellipse, α = orientation of the long axis of the ellipse. c) Roses diagram of individual crystal orientations.

4.2 Samples with $\phi_s = 0.76$

Samples with ϕ_s = 0.76 were grouped in a single paragraph divided into two sub-paragraphs: banding and penetrative fabric.

All the samples develop banding, which is a deformed structure formed by interconnected bands with an anastomosing pattern. These bands are rich melt area compared to the surrounding areas of the sample. Figure VI.6 shows comparison between two samples, the first without banding (a) and the second with banding (b), the last being subjected to higher strain.

The second sub-section analyses the deformation structures, as previously done for the other samples, using the inertia and intercept method.

Sample PP699 broke in the last part of the experiment and was studied by considering the top and broken area separately from the central area.

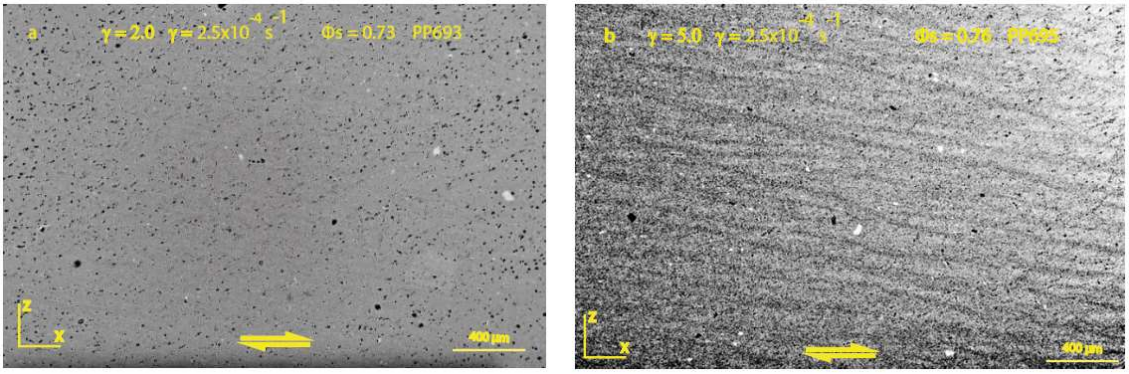

Figure VI.6. SEM images of a sample without banding (a) and with banding (b). The ligh grey are the crystals rich area, the dark gray are the bands and the black are the bubbes.

4.3 Banding

Figure VI.7 shows all the samples with a crystal content between 0.73 and 0.76 that developed banding. In figures VI.7a, VI.7c and VI.7e the bands are underlined in red.
All samples show bands with widths between 20 µm and 50 µm. The distances between the bands are very variable as they form an interconnected network. The distances range from few microns to 200 µm.
All samples are flanked by the rose of band directions. The double orientation of the roses (figures VI.7b, VI.7d, VI.7f) is due to the connecting lines between the bands. All the bands have an inclination between -5° and -20°, while the connecting lines are shorter bands with an inclination between 0° and 45°. The bands are enriched in residual melt by an average of between 7 and 10%.

In order to better characterise the bands in the sample, EDS mappings were carried out on random areas of a sample with banding (fig. VI.8, PP695 sample). The maps show a lineation corresponding to enrichment or depletion of a specific element (Ca, Na, Al and Si).

The next sub-paragraph analyses the penetrative fabric of each sample, highlighting the differences between the bands and the surrounding crystal-rich areas.

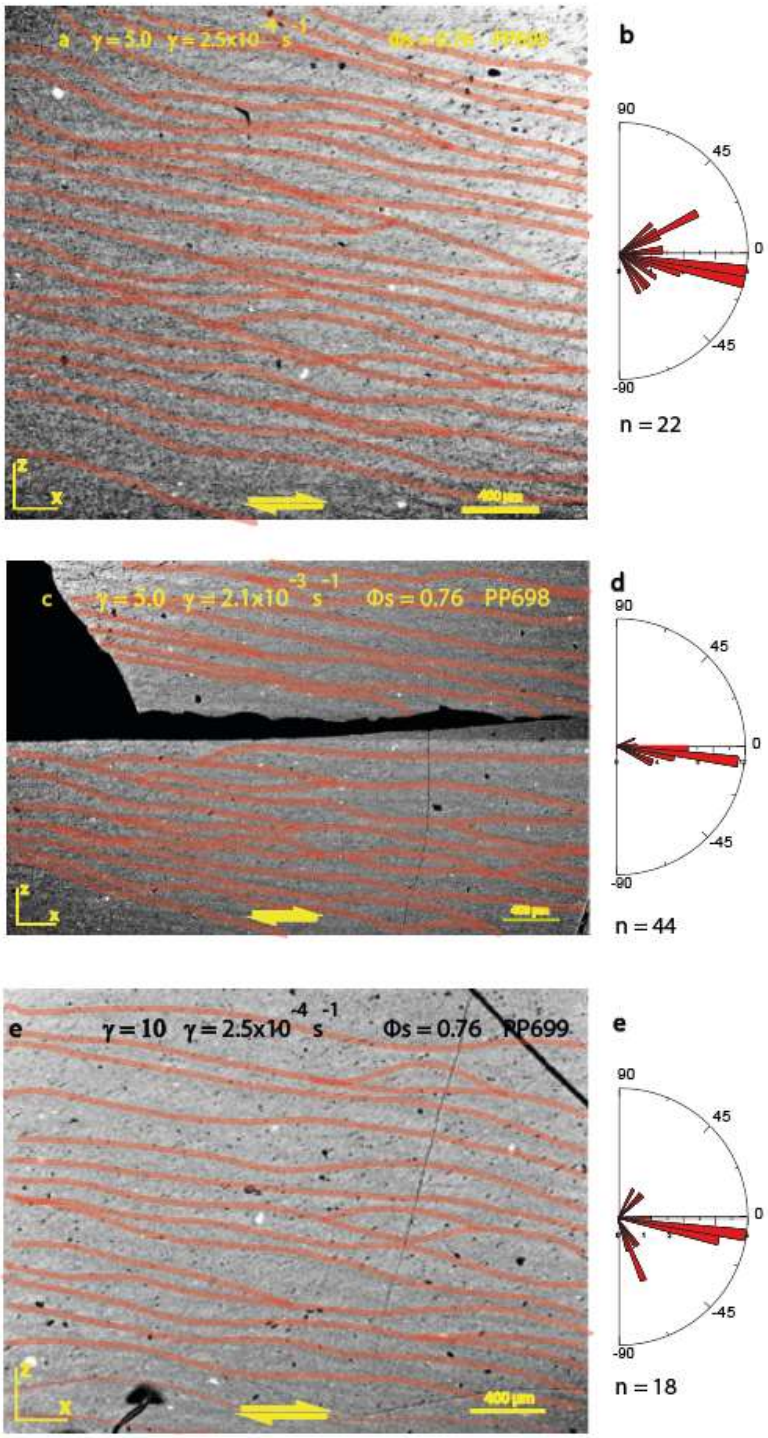

Figure VI.7. SEM images of all samples showing banding. The development of banding is highlighted by the red lines. a) SEM image of sample PP695, b) rose diagram of long axes of local tensor ellipses of sample PP695, c) SEM image of sample PP698, d) rose diagram of long axes of local tensor ellipses of sample PP698, e) SEM image of sample PP699, f) rose diagram of long axes of local tensor ellipses of sample PP699. n = numbr of measures.

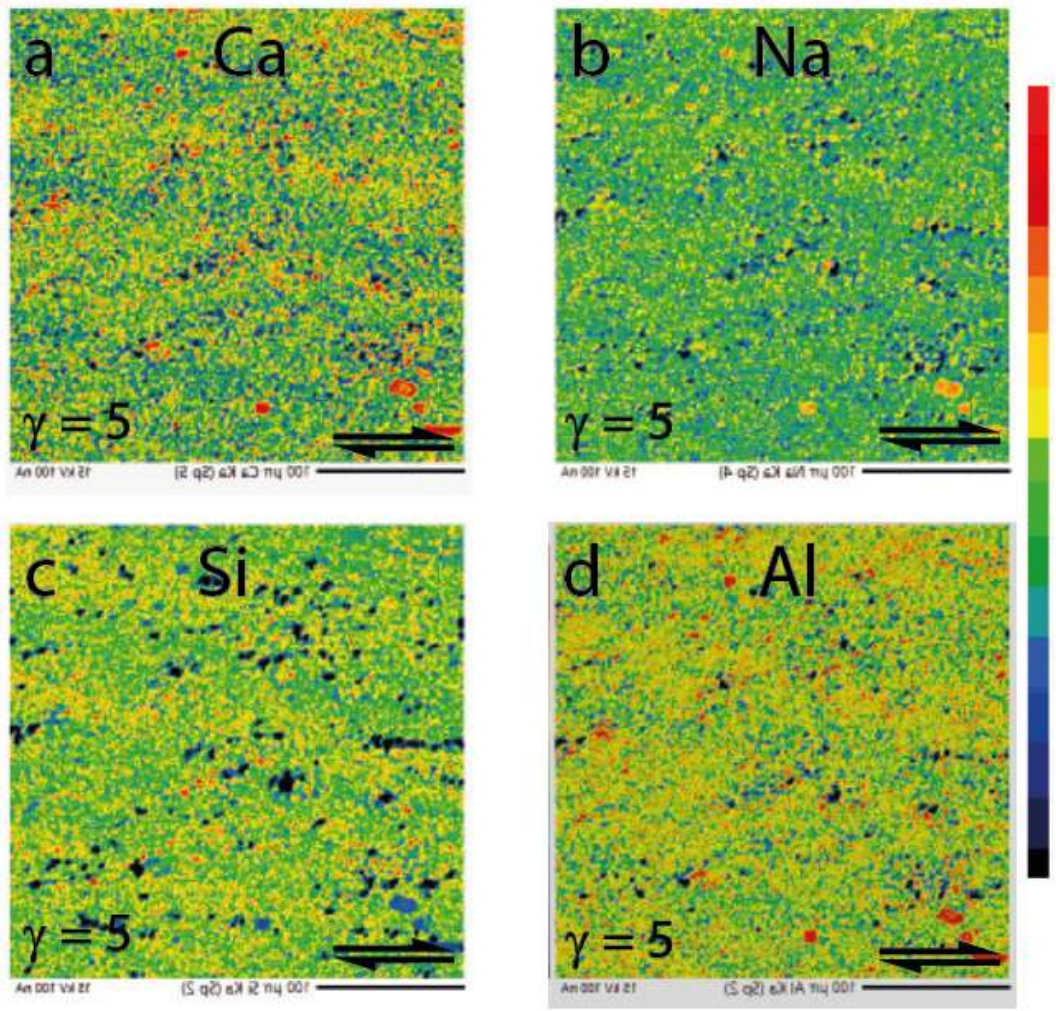

Figure VI.8. EDS mapping of a) Ca, b) Na, c) Al, d) Si on a selected area of PP695 sample.

Main shape fabrics

ϕ_s = 0.76, γ = 5.0, $\dot{\gamma}$ = 2.5*10^{-4} (PP695)

The analysis of the sample PP695 using the Incercept software (fig. VI.9a) shows that the mean tensor ellipse has an eccentricity of 1.87 with α = 18.45° (fig. VI.9b). The orientations of the long axes of the local ellipses shown by the rose diagram indicate a preferred orientation between 2° and 25° (fig. VI.9c)

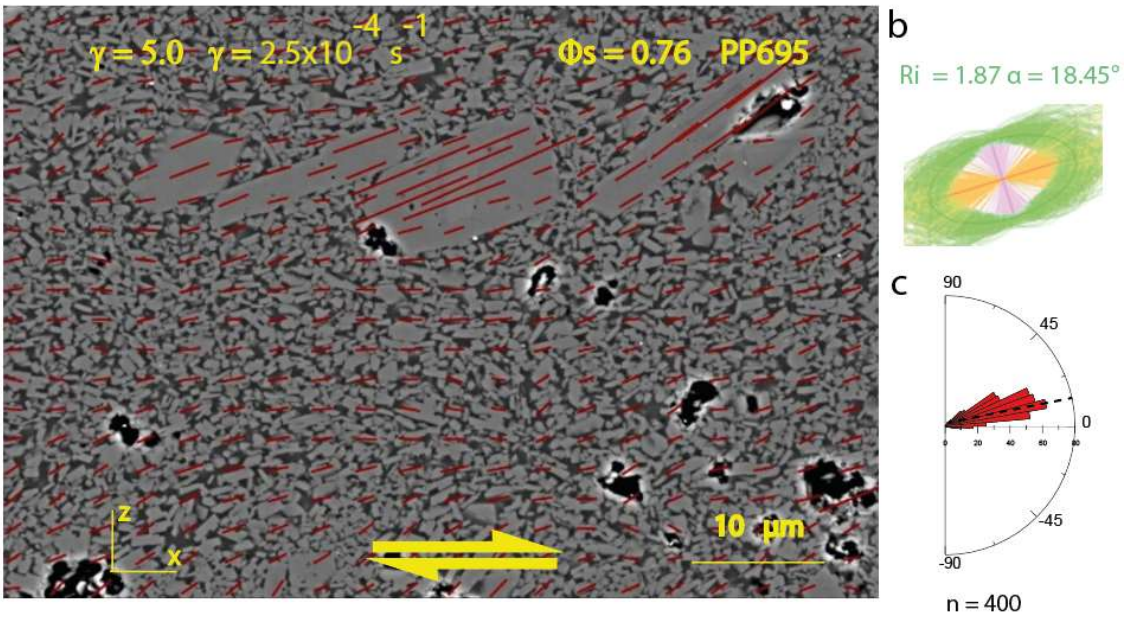

Figure VI.9. Preferential orientation of sample PP695 a) [XZ] SEM image of the sample. The red lines represent the long axes of the local tensor ellipses of the shape fabrics. b) Mean tensor ellipse of the shape fabric. R_i = eccentricity of the mean ellipse, α = orientation of the long axis of the ellipse. c) Rose diagram of long axes of local tensor ellipses. n = numbr of measures.

Crystals were hand-drawn in both banding and crystal-rich areas to compare their characteristics. The banding area is outlined by the dotted red line.

The rose diagrams of the high-crystalline areas (fig. VI.10 b – d) have the intertia tesors with R_x = 1.74, α = 28.97° and with R_x = 1.34, α = 26.23° (fig. VI.10b_2 – d_2). The rose of the preferred orientations shows a concentration between 0° and 45°. The areas with low crystal content (the band) show more defined preferential direction in a single range, with orientations ranging from 10° to -5° (fig. VI.10c_3). The eccentricity R_x of the

inertia tensor is 1.53 and the α is 1.34° (fig. VI.10c_2). The crystal content ϕ_s of the crystal rich areas varies from 0.66 to 0.77, while in the bands (low crystal content area) varies from 0.59 to 0.66.

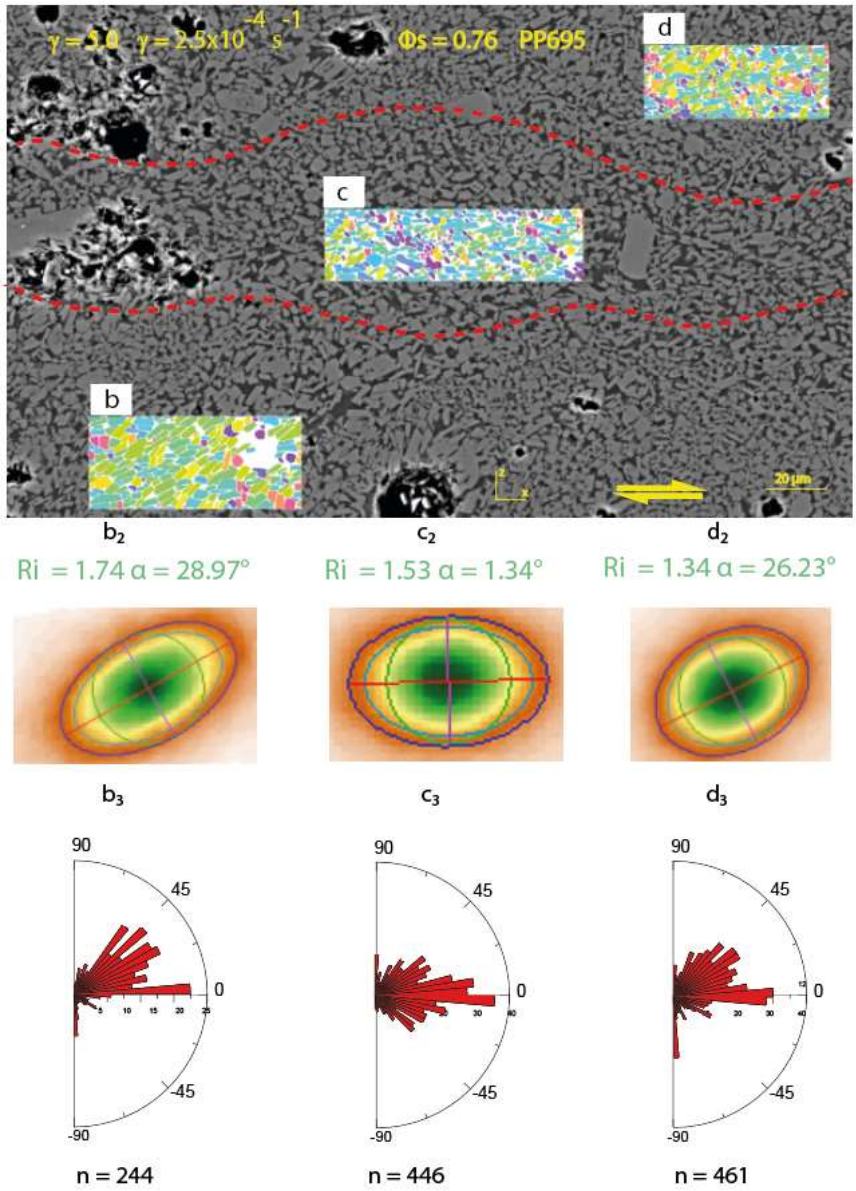

Figure VI.10. Preferential crystal orientation of sample PP695. Crystals were hand-drawn in the high crystal content and low crystal content areas. b - d) High crystal content areas (ϕ_s = 0.66 – 0.77), c) low crystal content area (ϕs = 0.59 – 0.66), b_2 – d_2) Inertia tensor for the high crystal content areas, c_2) Intertia tensor for the low crystal content area, b_3 – d_3) rose diagram of the preferential direction of the crystals in the high crystal content area, c_3) rose diagram of the preferential direction of the crystals in the low crystal content area. n = numbr of measures.

ϕ_s = 0.76, γ = 5.0, $\dot{\gamma}$ = 1.0*10^{-3} (PP698)

Analysing the sample with the intercept method, it shows a wavy pattern (fig. VI.11a), with the eccentricity of the local tensor ellipse R of 1.80 and α of 16.95° (fig. VI.11b). The rose diagram shows a preferred orientation between 20° and 40° (fig. VI.11c).

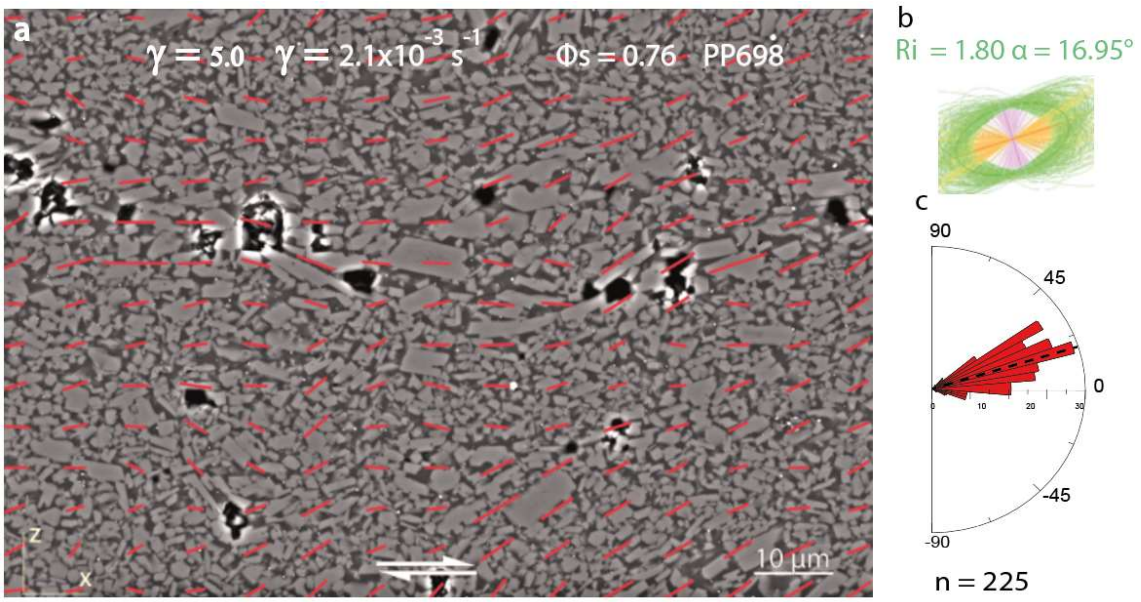

Figure VI.11. a) SEM image of sample PP698. The red lines represent the long axes of the local tensor ellipses of the shape fabrics. b) Mean tensor ellipse of the shape fabric. α = orientation of the long axis of the ellipse, R_i = eccentricity of the mean ellipse. c) Rose diagram of long axes of local tensor ellipses. n = numbr of measures.

Figure VI.12 shows 2 analysed areas of the same sample. The areas correspond to those enriched in crystals (penetrative fabric, outside of the bands). From the images analysed by the intercept method (fig. VI.12), the wavy orientation of the crystals is clear, so 2 different areas of the same sample were analysed by the inertia method to check whether the orientation is homogeneous or follows a wavy pattern. The first area analysed (fig. VI.12a) shows a long axis orientation rose with preferred orientation between 15° and -20° (fig. VI.12b), while the intertia tensor ellipse has R_x = 1.36 α= -7.30° (fig. VI.12c). The second analysed area (fig. VI.12d) shows a long axis orientation rose with preferential orientation between 5° and 35° (fig VI.12e), while the intertia tensor ellipse has R_x = 1.52 and α = -25.57° (fig. VI.12.f). These area show a crystal content between ϕ_s 0.66 and 0.77.

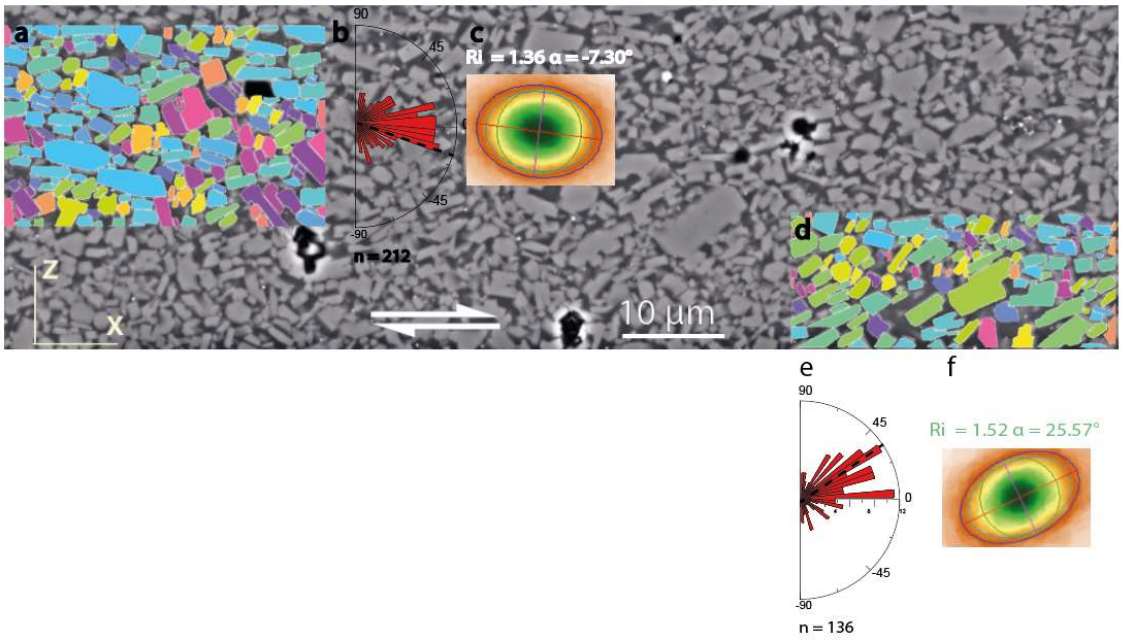

Figure VI.12. Preferential crystal orientation of sample PP698. Crystals were hand-drawn in the high crystal content areas. b - c) high crystal content areas (ϕ = 0.66 – 0.77), d) low crystal content area (ϕ = 0.58 – 0.65), b_2 - c_2) rose diagram of the preferential direction of the crystals in the high crystal content area, d_2) rose diagram of the preferential direction of the crystals in the low crystal content area. n = number of measures

In figure VI.13 an area of low crystal content (a band) of sample PP698 (fig. VI.13a) has been examined by drawing the crystals by hand (fig. VI.13b). The boundaries of the band are indicated by the dashed red line. The inertia tensor ellipse shows R_x = 1.53 and α = 17.16° (fig. VI.13c). The crystals within the bands have a preferential direction between 5° and 10° (fig. VI.13d). The crystal content ϕ_s of this area is ± 0.60.

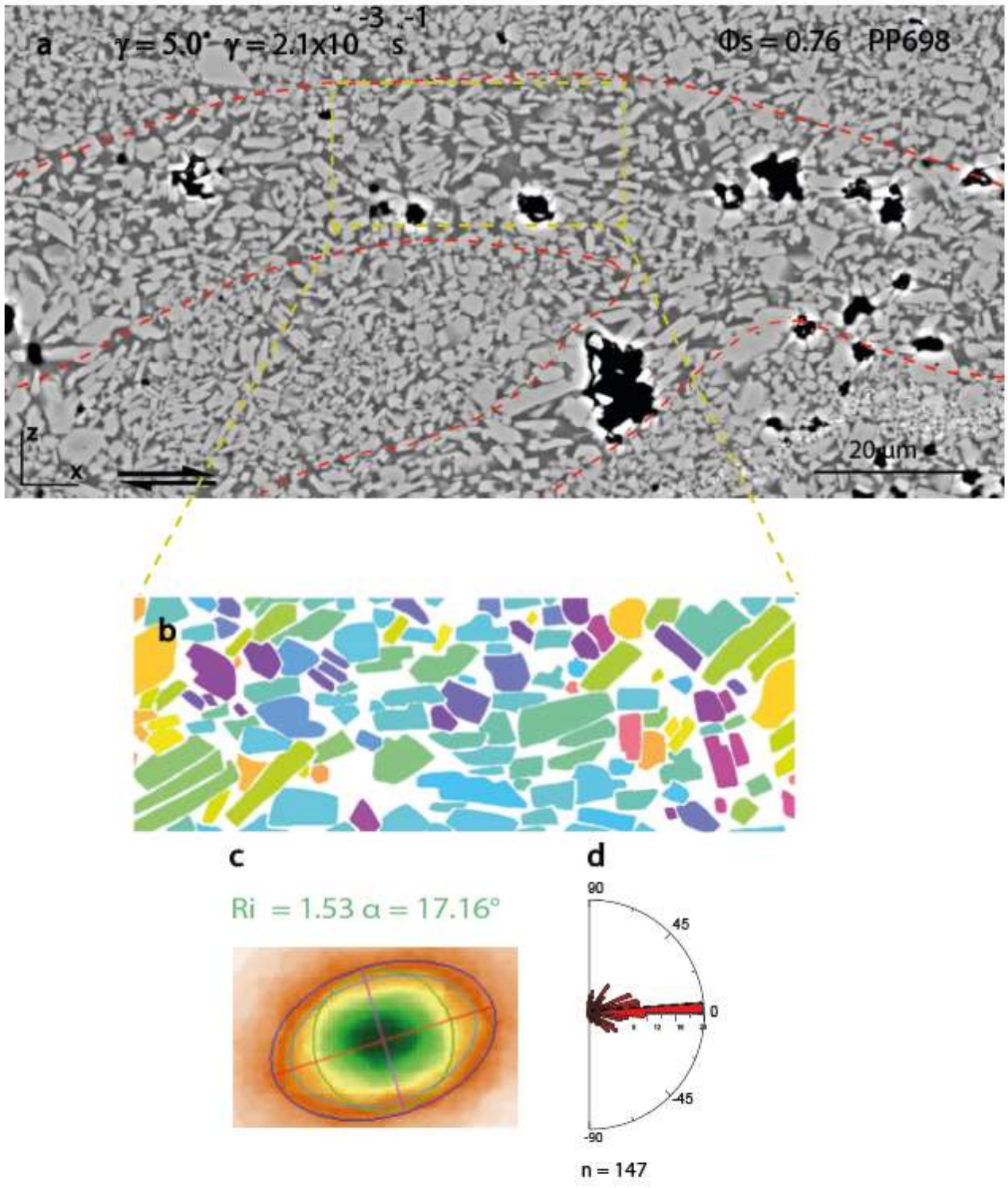

Figure VI.13. a) SEM picture of sample PP698. b) Crystals are hand-drawn in the low crystal content area (band), c) Intertia tensor ellipse of the low crystal content area, d) rose diagram of the preferential direction of the low crystal content area. The area of low crystal content is outlined by the dashed red line. The area of hand drawn crystals is outlined by the dashed yellow line. n = number of measures.

ϕ_s = 0.76 γ = 10.0, $\dot{\gamma}$ = 2.5*10^{-4} (PP699)

The sample broke at the end of the deformation experiment, but the microstructures and crystals remained well preserved. Given the different characteristics of the sample depending on the area analysed, the sample was studied and the results were reported considering the top part (fractured area) and the central part (unfractured area) separately (fig. VI.14). These 2 areas have been described in two different sub-sections.

In the top part (fractured area, fig. VI.14a), there is strain localization and the sample has developed a complex fracture system with different orientation.
In the central part (unfractured area, fig. VI.14b), the sample shows weak banding phenomena and crystals orientation.

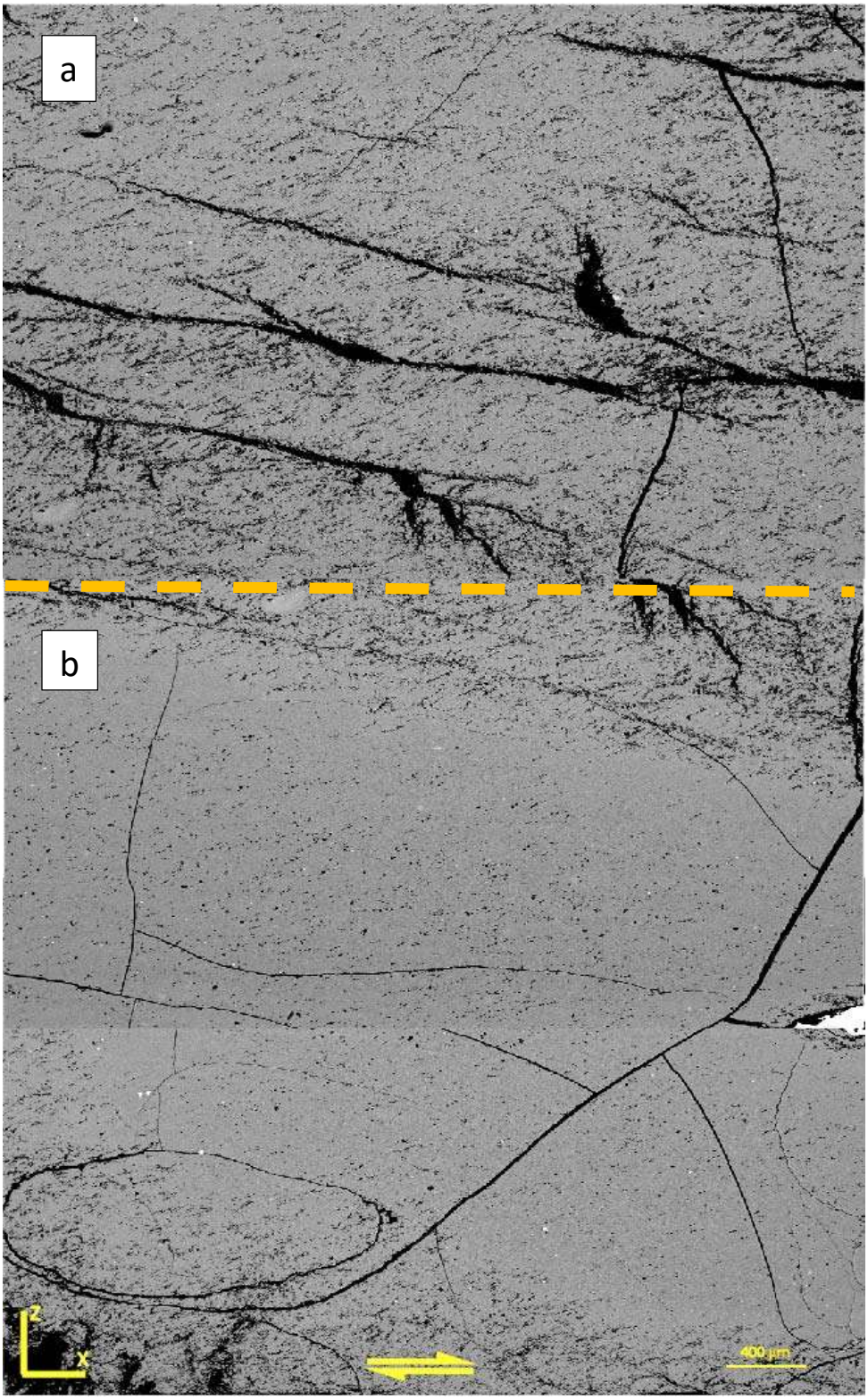

Figure VI.14. Panoramic photo of sample PP669. The sample was studied by dividing the top part (fractured area, a) and the central part (unfractured area, b).

Central part

As with the previous samples, sample PP699 shows bands enriched in residual melt (areas of low crystal content).

In the central part, several areas were hand-drawn and analysed using the inertia method (fig. VI.15a) to check the crystals orientation and crystal content. In the area b) of figure VI.15, the crystals have a crystal content ϕ_s of 0.73 and a preferred orientation between 5° and -5° (fig. VI.15b_2) In the area c, the crystal content ϕ_s decreases (0.65) and the preferred directions are at 5° and -32° (fig. VI.15c_2). In the area d, the crystal content ϕ_s is 0.77 and the crystal orientation is at 45° (fig. VI.15d_2).

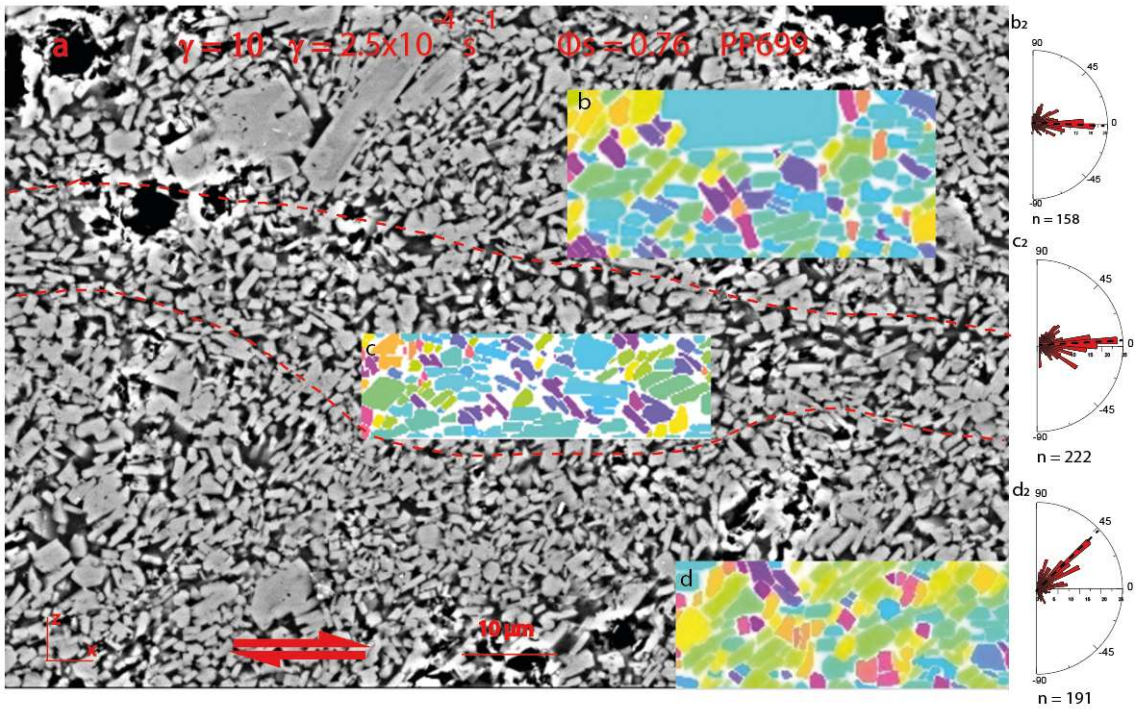

Figure VI.15. Preferential crystal orientation of sample PP699. Crystals were hand-drawn in the high crystal content and low crystal content areas. b - d) high crystal content areas (ϕ_s = 0.73 – 0.77), c) low crystal content area (ϕ_s = 0.65), b_2 - d_2) rose diagram of the preferential direction of the crystals in the high crystal content area, c_2) rose diagram of the preferential direction of the crystals in the low crystal content area. n = number of measures.

The same area was also analysed using the intercept method (fig. VI.16a). As in the previous samples, there is a wavy regime. The local tensor ellipse of the shape fabric has an eccentricity R_i of 1.78 (fig. VI.16b) and the long axis directions are oriented between 18° and 40° (fig. VI.16c).

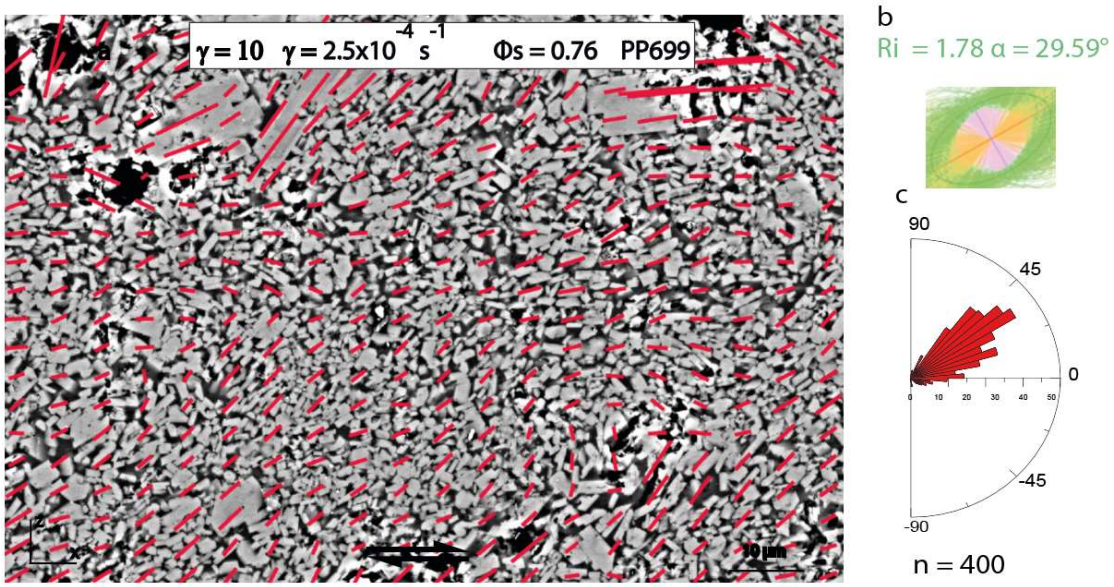

Figure VI.16. a) SEM image of sample PP699. The red lines represent the long axes of the local tensor ellipses of the shape fabrics. b) Mean tensor ellipse of the shape fabric. α = orientation of the long axis of the ellipse, R_i = eccentricity of the mean ellipse. c) Rose diagram of long axes of local tensor ellipses. n = number of measures.

Top part

Figure VI.17a shows an overview of the fractured area of the sample. There are two sets of fractures, the first generation formed, with a preferential direction at 30° (fig. VI.17b – green) and the other, the second generation formed, with a preferential direction at -15° (fig. VI.17b – red).

Preferential orientations of the plagioclase crystals were studied using the inertia method and the intercept method. A section between two sets of fractures was chosen. The area considered is highlighted in the yellow rectangle in fig. VI.18.

Figure VI.19a shows the section of hand-drawn crystals within two fractures. The crystals, analyzed with the inertia method, display a preferred orientation at 30° (fig. VI.19b).

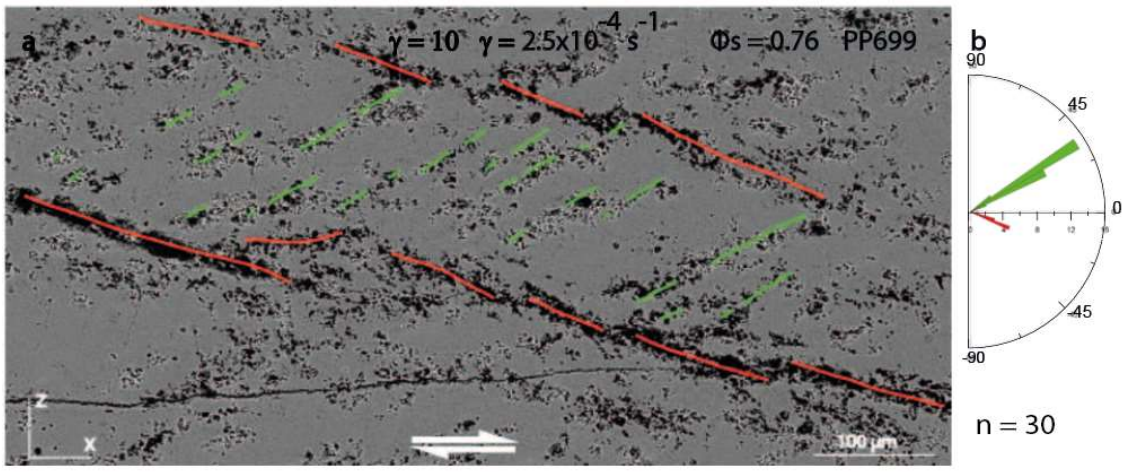

Figure VI.17. a) SEM picture of PP699 sample in the fractured area. b) Roses diagram of the preferential direction of the fractures. Green: first generation fractures, red: second generation fractures. n = number of measures.

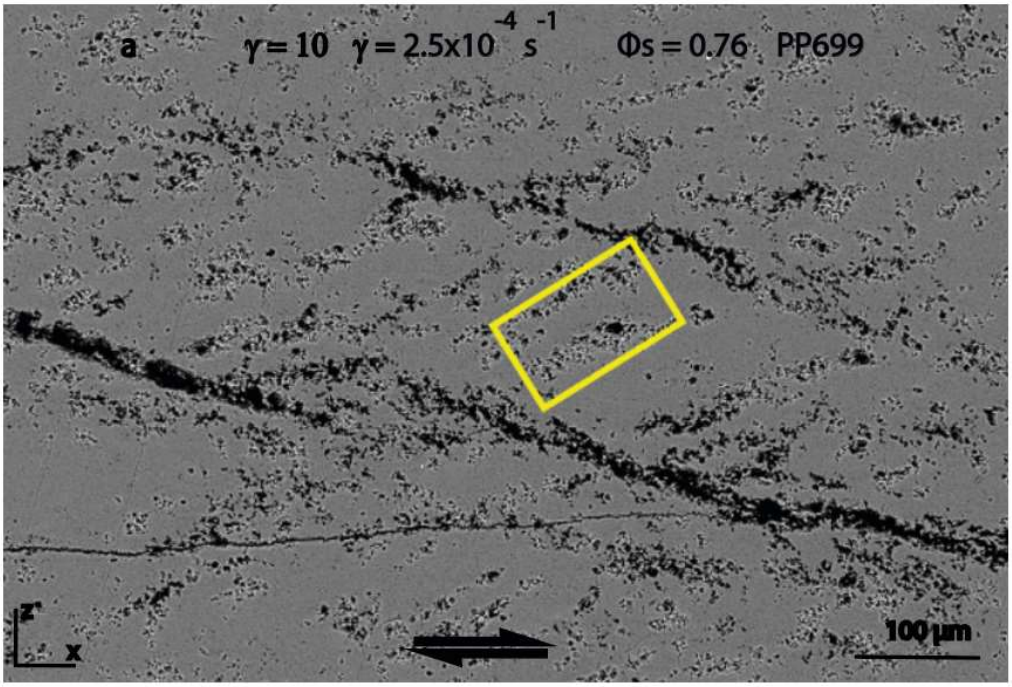

Figure VI.18. SEM picture of sample PP699. The crystal area studied is highlighted by the yellow rectangle.

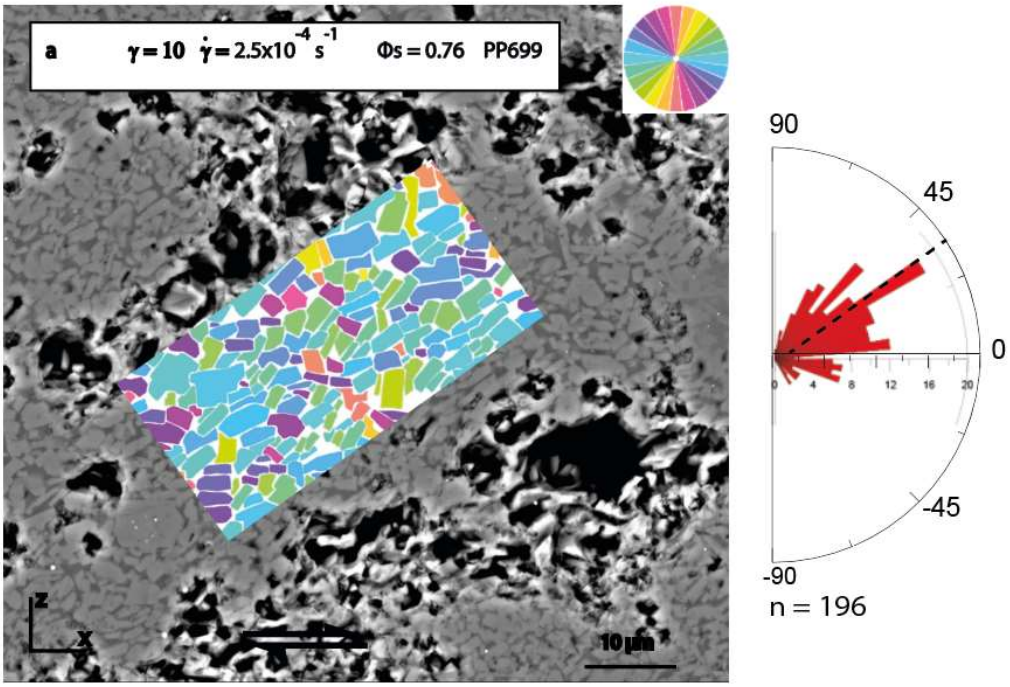

Figure VI.19. a) Preferential crystal orientation of sample PP699 in fractured area. Crystals were hand-drawn in the high crystal content and low crystal content areas. b) Rose diagram of the preferential direction of the crystals. n = number of measures.

Analysis of the sample using the intercept method (fig. VI.20a) shows an eccentricity value R_i of 1.67 (fig. VI.20b) and α = 38.15°. The orientation of the long axes of the local ellipse is more constrained in a defined range, between 30° and 45° (fig. VI. 20c).

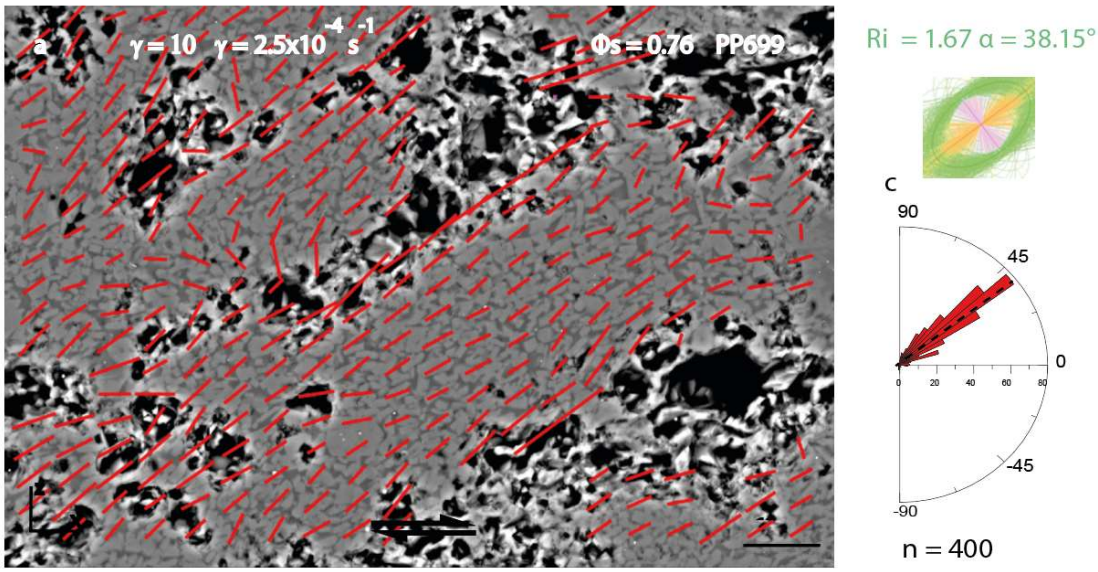

Figure VI.20. Preferential orientation of sample PP699 in fractured area a) [XZ] SEM image of the sample. The red lines represent the long axes of the local tensor ellipses of the shape fabrics. b) Mean tensor ellipse of the shape fabric. R_i = eccentricity of the mean ellipse, α = orientation of the long axis of the ellipse. c) Rose diagram of long axes of local tensor ellipses. n = number of measures.

$\phi_s \simeq 0.95$, $\gamma = 1.8$, $\dot{\gamma} = 5.0*10^{-5}$ (PP701)

Sample PP701 (ϕ_s = 0.95) shows a stronger banding phenomena than samples with ϕ_s = 0.76 (fig. VI.21a). As shown in the rose diagram (fig. VI.21b) the bands have a -5° orientation, and are connected to each other through a series of smaller bands oriented at 25° -30°, forming an anastomosing network. Their thickness ranges from 5 µm to 20 µm and the spacing ranges from a few microns to 300 µm.

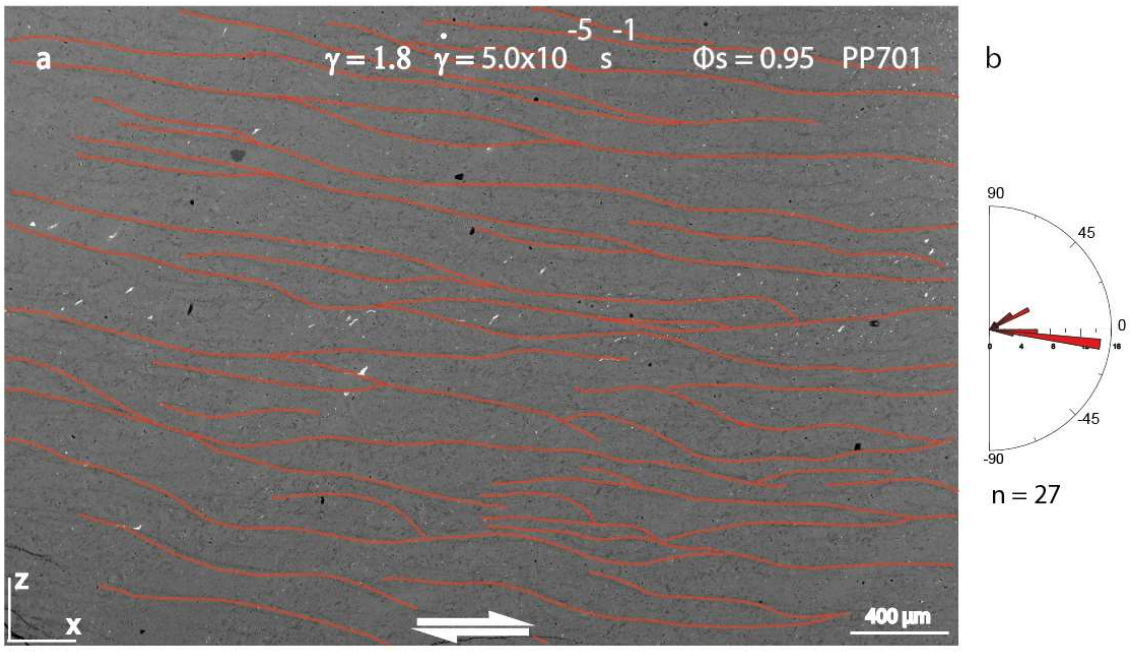

Figure VI.21. SEM image of sample PP701. The red lines follow the direction of the bands. b) Rose diagram for bands directions. n = number of measures.

Unlike all the other samples, PP701 shows a new mineralogical phase, quartz (fig. VI.22), which appears both in the penetrative fabric and in the bands. The sample consists of plagioclase, quartz, melt and bubbles, at different proportions in the penetrative fabric and bands.

The penetrative fabric is composed of plagioclase, elongated quartz, a small amount of melt and bubbles (fig. VI.22).

The bands are composed of the same constituents, but they are enriched in bubbles and melt, and show a smaller grain size of plagioclases than the penetrative fabric (fig VI.23).

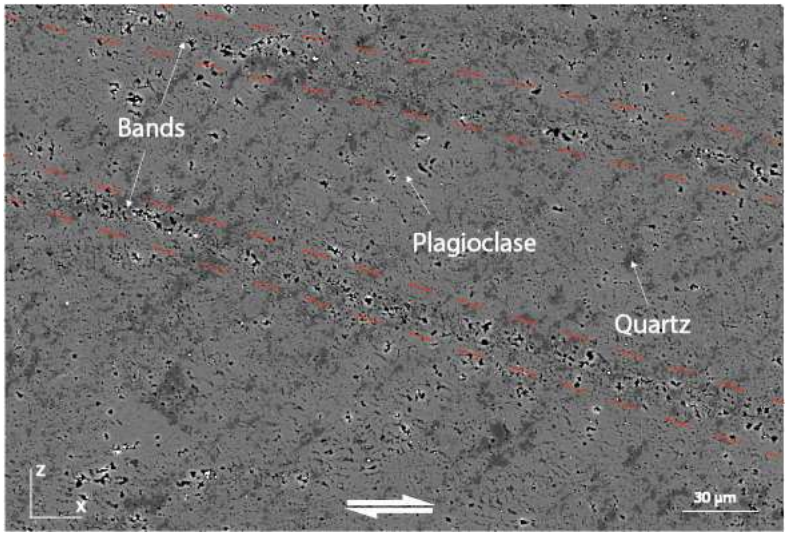

Figures VI.22. SEM image of sample PP701. Bands are highlighted by dotted red lines.

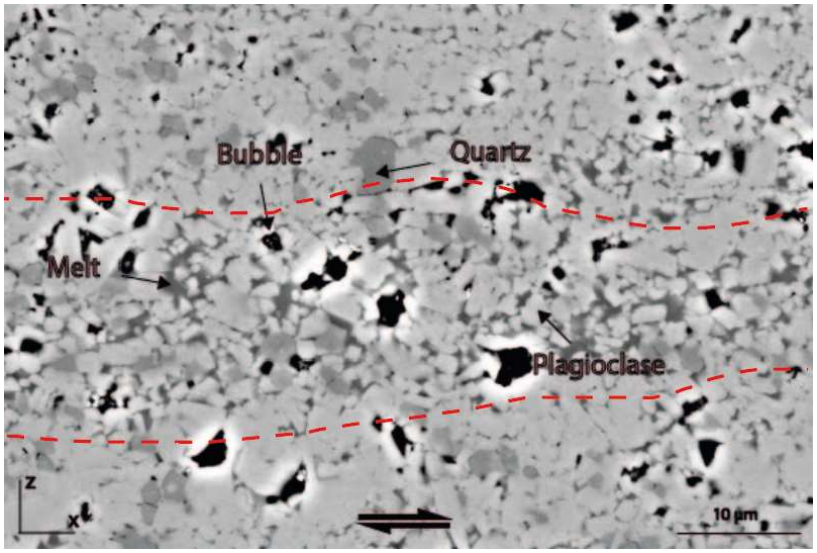

Figure VI.23. SEM image of sample PP701. Zoom on a band. The band is highlighted by dotted red lines.

Figure VI.24 shows SEM/EDS analyses of two areas of the sample: the melt-rich band (fig. VII.24a) and the melt-poor area (fig. VII.24b, melt-poor matrix, corresponding to the penetrative fabric). EDS analysis of the melt rich area (fig. VII.24a) shows areas of silica richness corresponding to quartz compositions (red areas), areas of Na and Si depletion corresponding to plagioclase crystals (light blue areas), areas of slight Na and Si

enrichment corresponding to the melt rich band (dark blue areas), and black areas corresponding to bubbles or voids.

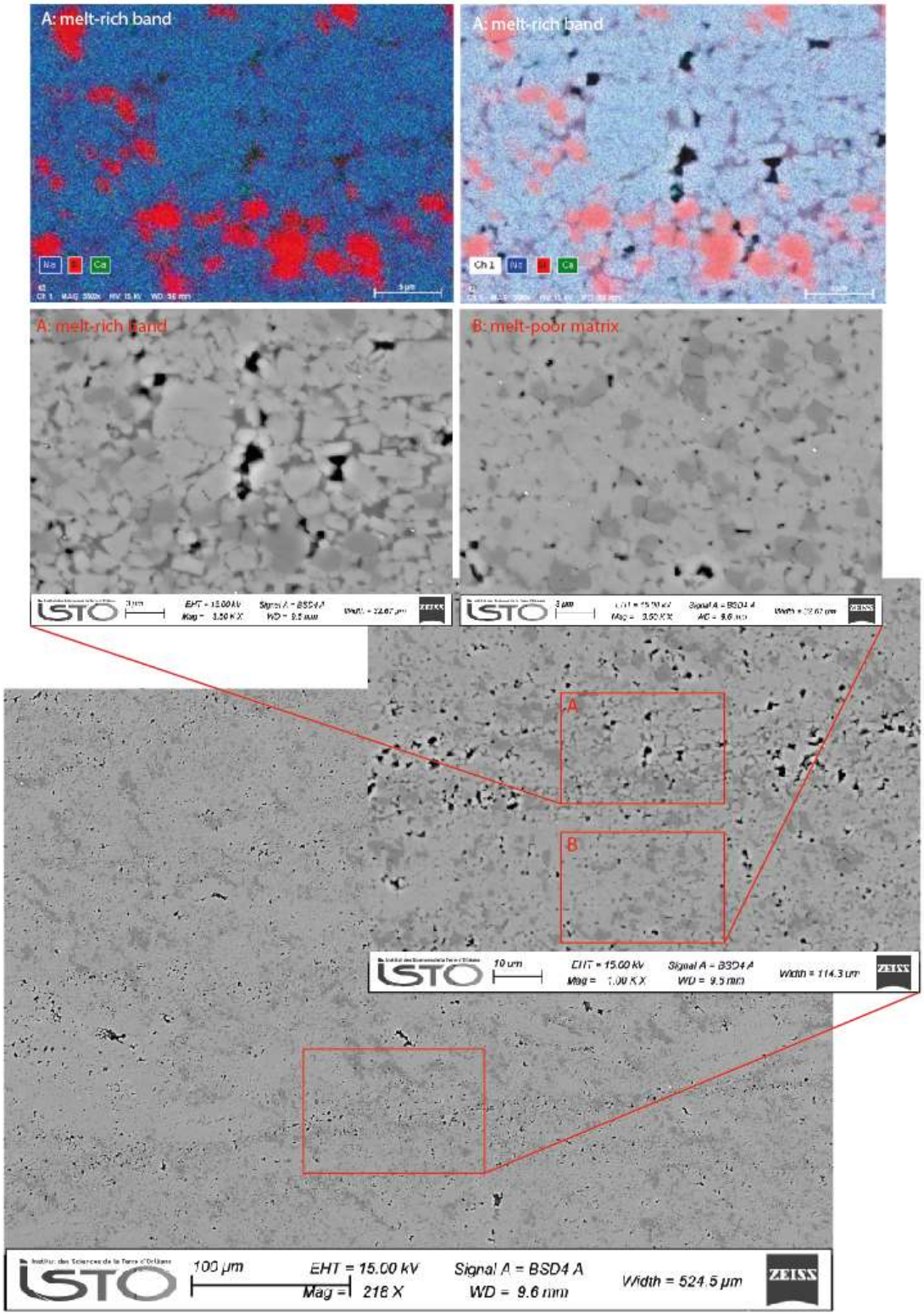

Figure VII.24. SEM and EDS images of sample PP701. a) melt-rich band, b) melt-poor penetrative fabric.

The bands were studied by EDS analysis in order to better understand the composition (tab. VI.3). The elements analysed are sodium, calcium, aluminium and silica.

	Melt	Plagioclase	Quartz
Na_2O	4.25	5.93	-
SiO_2	73.17	61.53	100
Al_2O_3	16.75	23.27	-
CaO	4.85		-

Table VI.3. EDS analysis on PP701 band.

Main shape fabric

For the crystals orientation analysis, the sample was studied by the inertia method in both the bands and adjacent area, the penetrative fabric (fig. VI.25a).
Figure VI.25b shows the preferential plagioclases directions in the penetrative fabric at 50° and 10°, with a rose diagram with a preferential plagioclases direction that ranges from 0° to 50° (fig. VI.25c).
In the band (the area highlighted by the red dottered lines) the intertia mean tensor has R_x = 1.29 and α = -7.91° (fig. VI.25d). The rose diagram shows a preferential direction between 5° and -35° (fig. VI.25e).
The quartz (fig. VI.26a) has an eccentricity of the intertia mean tensor at 1.14 and α = 48.99° (fig. VI.26b). The rose diagramshows a preferential direction at 90°, 45° and 20° (fig. VI. 26c).

Histograms of the equivalent diameters Φ of plagioclases in the penetrative fabric (fig. VI.27a) and in the bands (fig. VI.27b) show the difference in their grain size. The crystals in the penetrative fabric are larger, thus subject to less deformation.

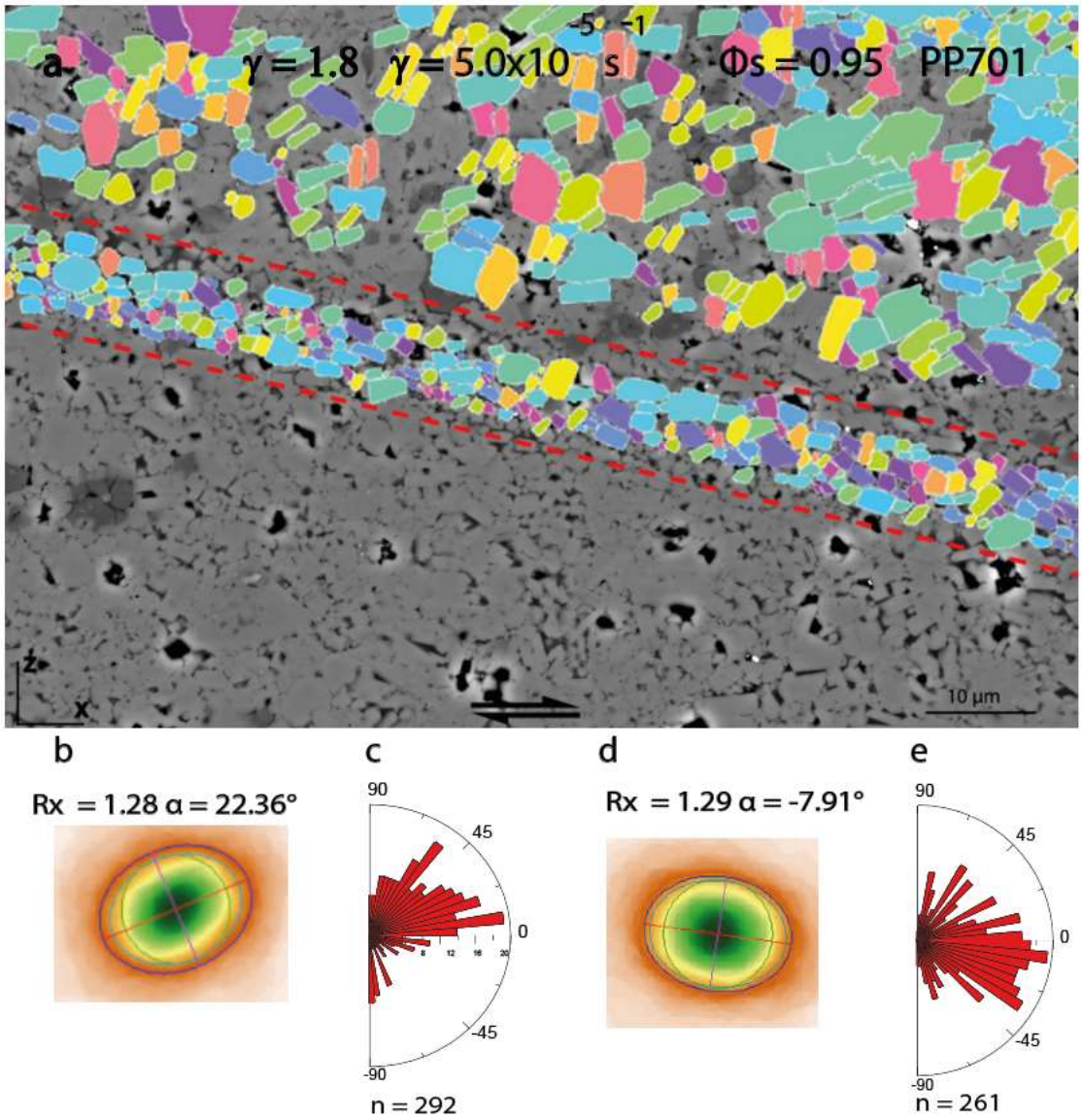

Figure VI.25. a) Preferential plagioclase orientation of sample PP701. Crystals were hand-drawn in the high crystal content and low crystal content areas. The band is bordered by the dashed red line. b) Inertia tensor ellipse of the penetrative fabric. c) Rose diagram of the preferential direction of the plagioclase in the penetrative fabric. d) Inertia tensor ellipse of the band. e) Rose diagram of the preferential direction of the plagioclase in the band. n = number of measures.

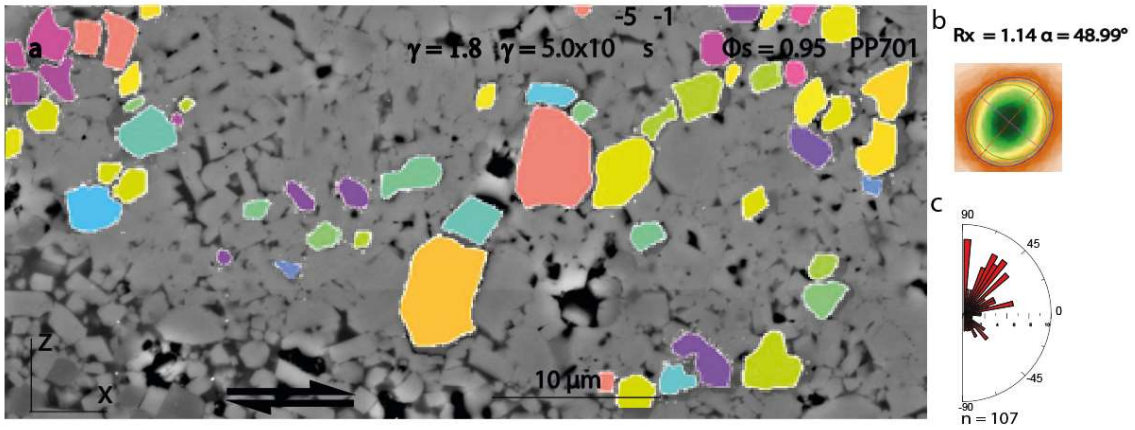

Figure VI.26. a) Preferential quartz orientation of sample PP701. Crystals were hand-drawn in the high crystal content and low crystal content areas. b) Inertia tensor ellipse of quartz. c) Rose diagram of the preferential direction of the quartz. n = number of measures.

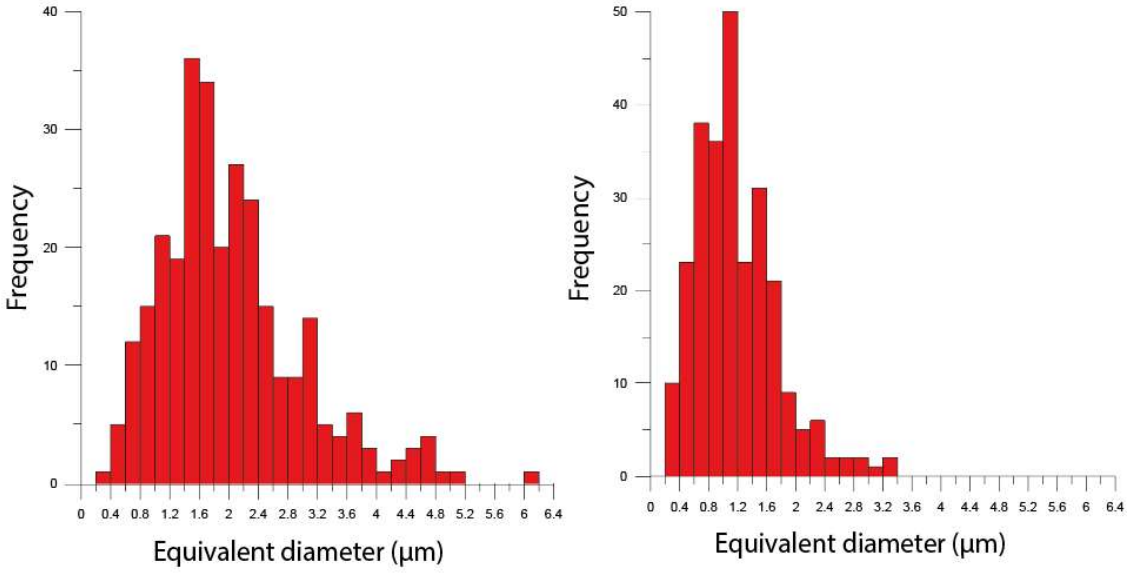

Figure VI.27. Histograms of equivalent diameters Φ of plagioclases in the penetrative fabric (a) and bands (b).

EDS maps were made on random areas of the sample in order to highlight the banding phenomenon (fig. VI.28).

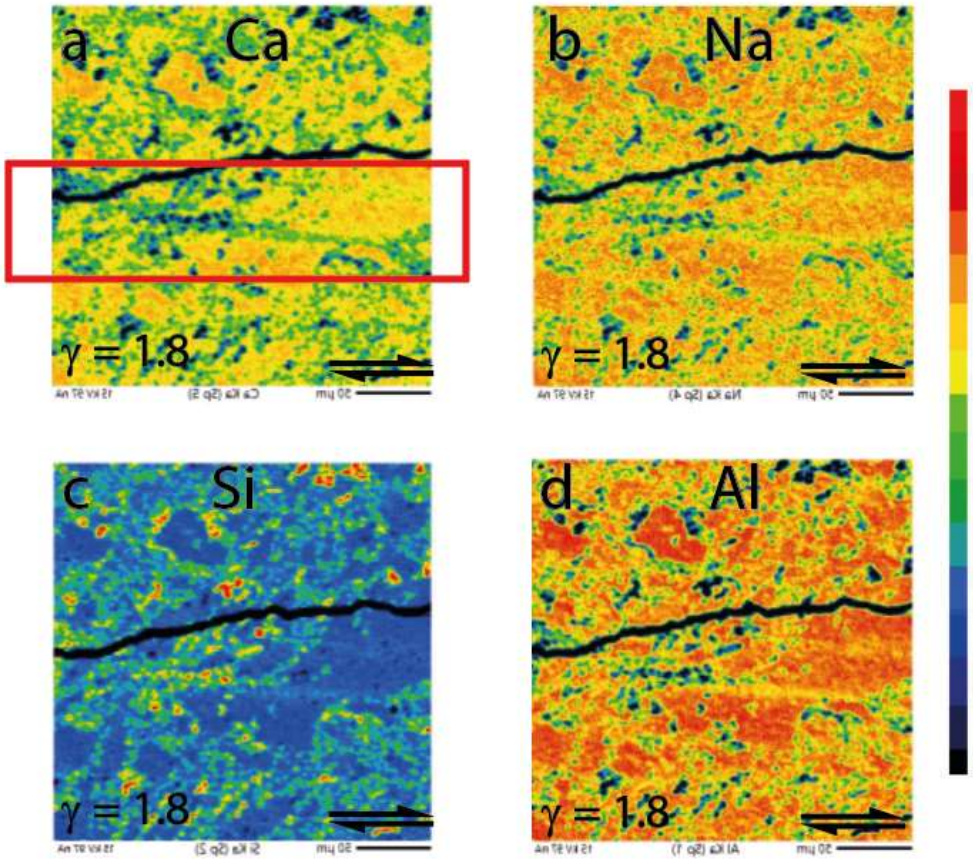

Figure VI.28. EDS mapping on PP701 sample of Na, Ca, Al and Si elements. The band is located inside the red triangle.

5. Main shape of bubbes

The bubbles of sample PP701 (fig VI.29a) were studied in two different areas: the penetrative fabric and the bands. In both areas, the bubbles show a similar light preferential direction, between -10° and -75° for the penetrative fabric (fig. VI.29b) and between -15° and -80° for the band (fig. VI.29c).

The bubble content changes considerably, with 4.2% in the penetrative fabric and 16.2% in the bands. The shape of the bubbles is highly irregular and affected by crystal morphology, so the aspect ratio has not been calculated.

The equivalent diameter Φ of the bubbles in the penetrative fabric has a arithmetic mean of 0.73±0.39 µm, with a harmonic mean of 0.60 µm and a mode of 0.5 µm (fig. VI.30a). In the band, the arithmetic mean is 1.16±0.89 µm, the harmonic mean is 0.64 µm and the mode is 0.7 µm (fig. VI.30b).

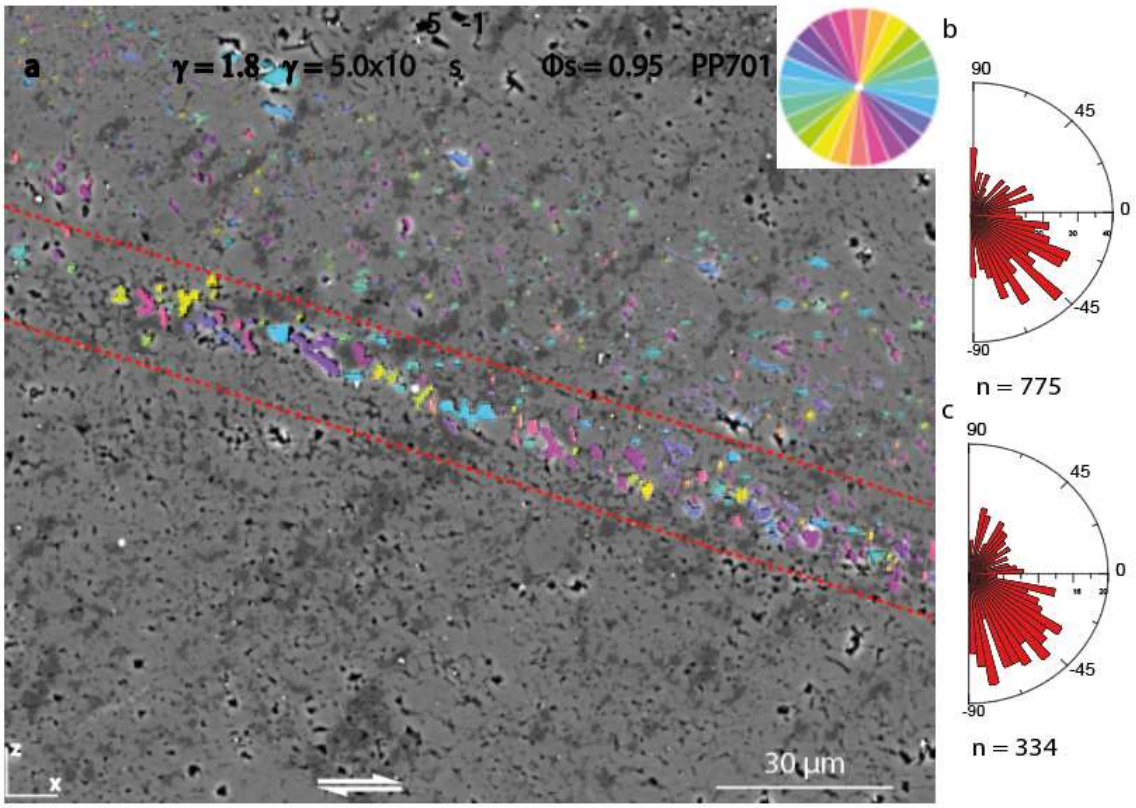

Figure VI.29. a) SEM picture of sample PP701. The band is delimited by the dotted red lines. Bubbles are colored according to their orientations. b) Rose of directions of individual bubbles orientation for the penetrative fabric c) Rose of directions of individual bubbles orientation for a band. n = number of measures.

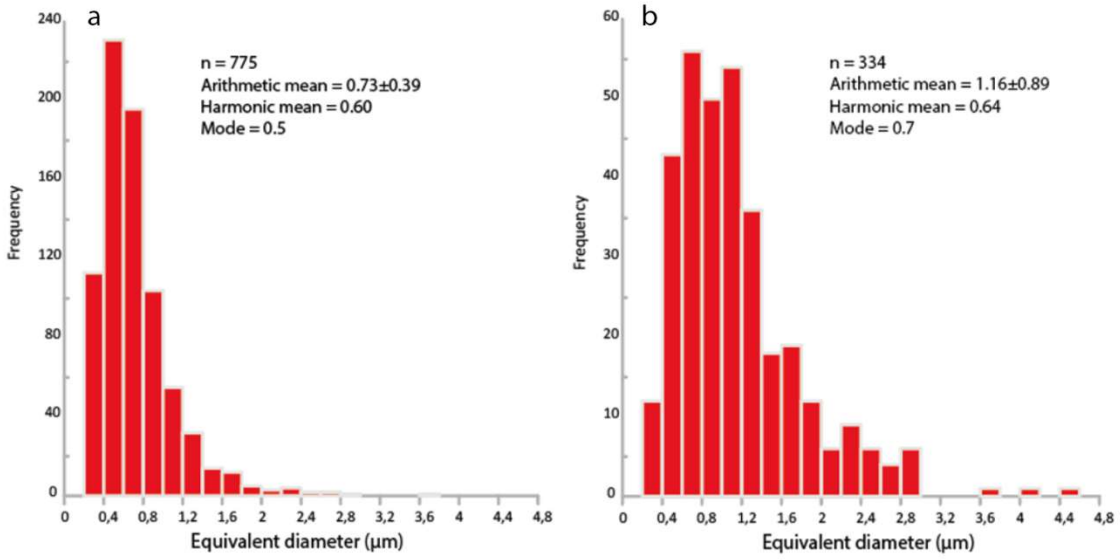

Figure VI.30. Histograms of equivalent diameters Φ for the penetrative fabric (a) and the band (b).

6. Aspect ratio R vs orientation of the crystals α

In order to study the correlations between aspect ratio R and crystal orientation α, these parameters were diagrammed for each sample (PP693 fig. VI.31a, PP695 fig. VI.31b, PP698 fig. VI.31c, PP699 fig. VI.31d).

At 1<R<2, the orientation of the crystals does not follow any preferred direction.
At 2<R<5, increasing the aspect ratio also changes the orientation of the crystals, moving its values closer to zero.
At R >5, all crystals have a preferential direction at 0°.

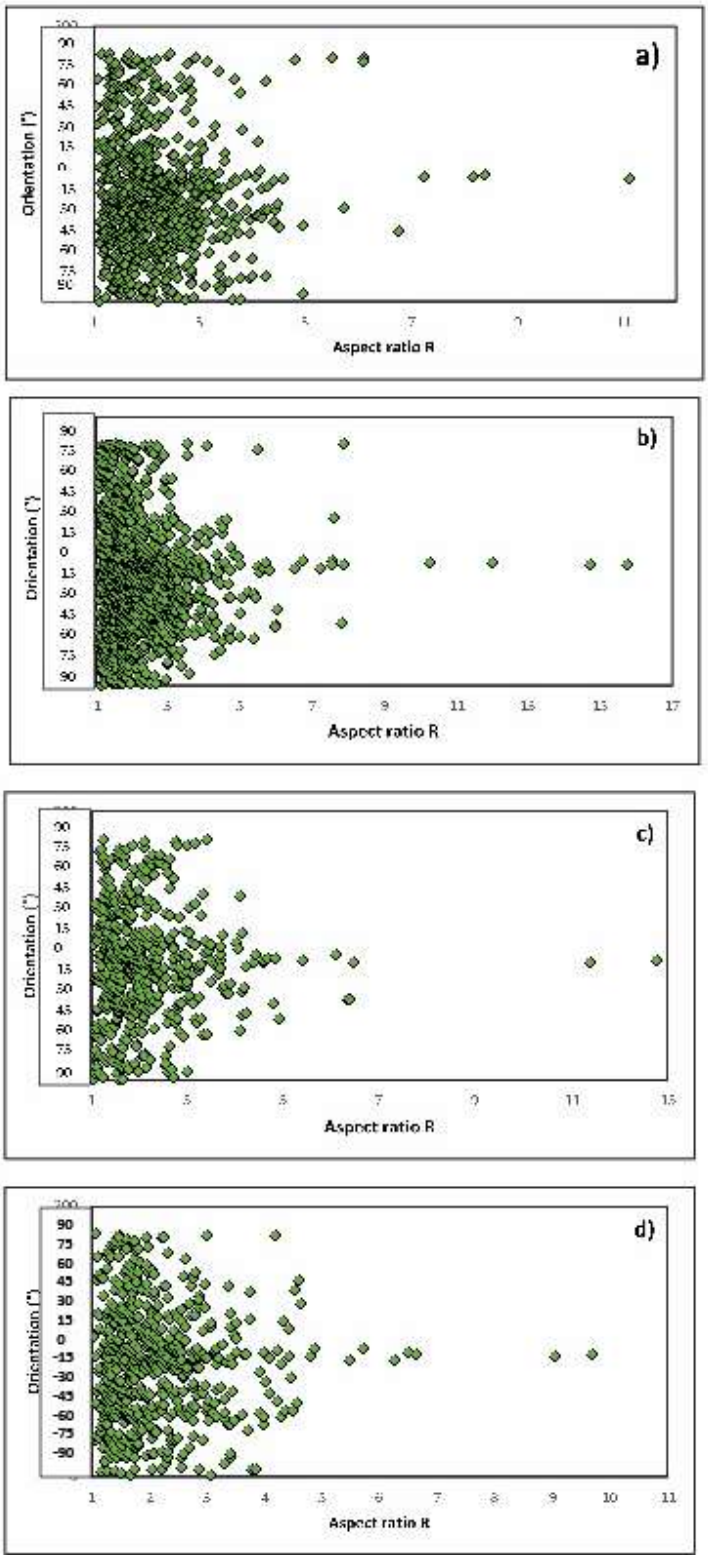

Figure VI.31. Diagrams of all samples showing the aspect ratio vs orientation of the crystals. a) PP693 ($\dot{\gamma}$ = 2.0, $\mathring{\gamma}$ = 2.5*10^{-4}), b) PP695 ($\dot{\gamma}$ = 5.0, $\mathring{\gamma}$ = 2.5*10^{-4}), c) PP698 ($\dot{\gamma}$ = 5.0, $\mathring{\gamma}$ = 1.0*10^{-3}), d) PP699 ($\dot{\gamma}$ = 10.0, $\mathring{\gamma}$ = 2.5*10^{-4}).

7. Contacts

The contacts between plagioclase crystals in all samples were studied, classifying them according to the types of sides in contact and following the definition of (Azema and Radjaï, 2012): S-S, side-side, long axis in contact; C-C, cap-cap, short axis in contact; S-C, side-cap, long axis and short axis in contact (fig. VI.32).
Table VI.4 show the proportion of each contact for all the samples.

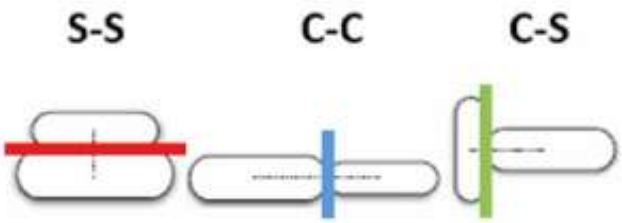

Figure VI.32. Principal contact modes: side-side (s-s), cap-cap (c-c), cap-side (c-s). Modified from (Azema and Radjaï, 2012).

Sample	$\gamma = 2.0, \dot{\gamma} = 2.5*10^{-4}$	$\gamma = 5.0, \dot{\gamma} = 2.5*10^{-4}$	$\gamma = 5.0, \dot{\gamma} = 1.0*10^{-3}$	$\gamma = 10, \dot{\gamma} = 2.5*10^{-4}$
	PP693	PP695	PP698	PP699
S-S proportion	0.69	0.67	0.65	0.59
C-C proportion	0.08	0.11	0.10	0.15
S-C proportion	0.23	0.22	0.25	0.26

Table VI.4. Contacts proportion for each type of contact and for each sample.

The proportions of S-S, C-C and S-C contacts are similar for the samples with crystal content ϕ_s of 0.73-0.76 and finite strain γ of 2 - 5. Surprisingly, the highest values of S-S are found in the sample with the lowest finite strain (PP693, $\gamma = 2$), but given the small difference with the other samples (S-S difference ± 0.2- 0.4), this is probably just a random occurrence. In contrast, sample PP699 ($\gamma = 10$) shows a lower proportion of S-S contacts and a higher proportion of C-C and S-C contacts. This is probably due to the breakage of the sample in the final part of the experiment.

ϕ_s = 0.73 γ = 2.0, $\dot{\gamma}$ = 2.5*10^{-4} (PP693)

The PP693 sample (fig. VI.33a) shows oriented contacts, with a majority of S-S contacts (69%), a minimal amount of C-C contacts (8%) and an intermediate amount of S-C contacts (23%). S-S contacts have a preferred direction between 22° and 50° (fig. VI.33b), C-C contacts at -90° (fig. VI.33c) and S-C contacts at -90° (fig. VI.33d). Due to the small number of C-C contacts, they are not statistically meaningful.

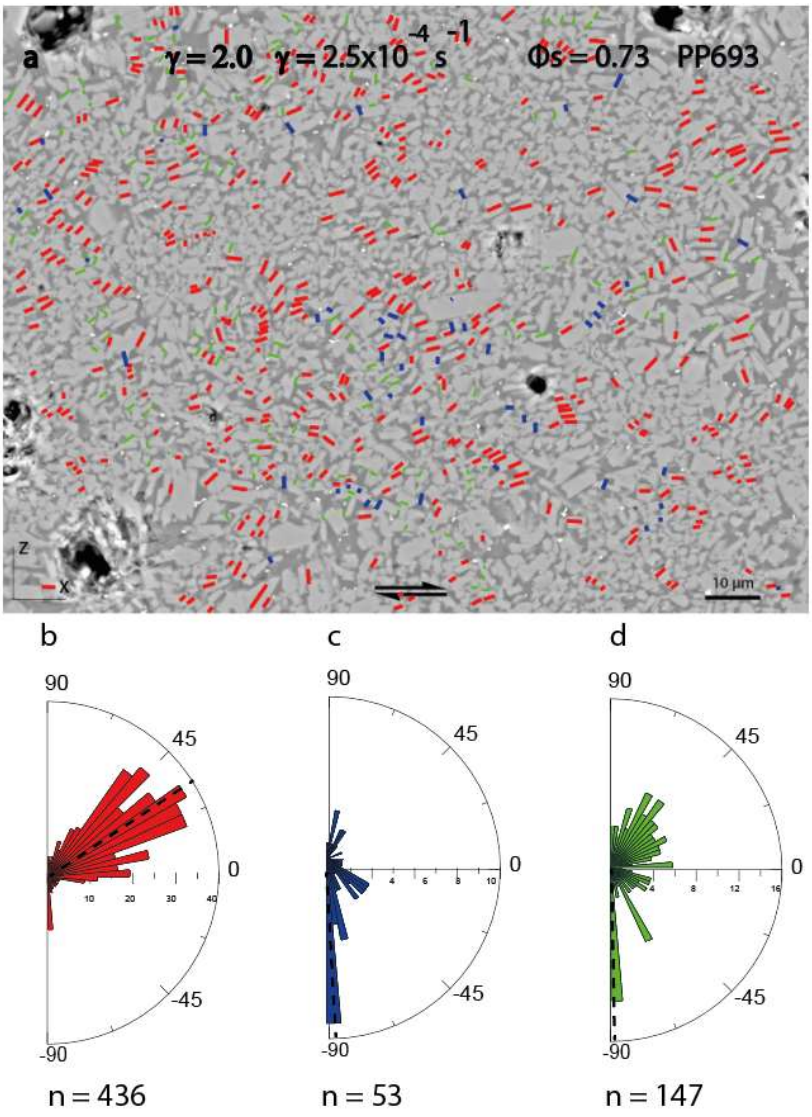

Figure VI.33. a) SEM picture of the sample PP693 with hand drawn the contacts (red: S-S, blue: C-C, green: S-C,). Rose diagram for the orientation of the contacts b) S-S, c) C-C, d) S-C. n = number of measuraments.

ϕ_s = 0.76, $\dot{\gamma}$ = 5.0, $\dot{\gamma}$ = 2.5*10^{-4} (PP695)

Sample PP695 (fig. VI.34a) shows very similar contact proportions to sample PP693, with S-S at 67%, C-C at 11% and S-C at 22%. The S-S contacts have preferred orientation at 0° and between 20° and 35° (fig VI.34b). The C-C contacts show a preferential orientation at -90° (fig. VI.34c), and S-C contacts are lightly oriented at 0° (fig. VI.34d).

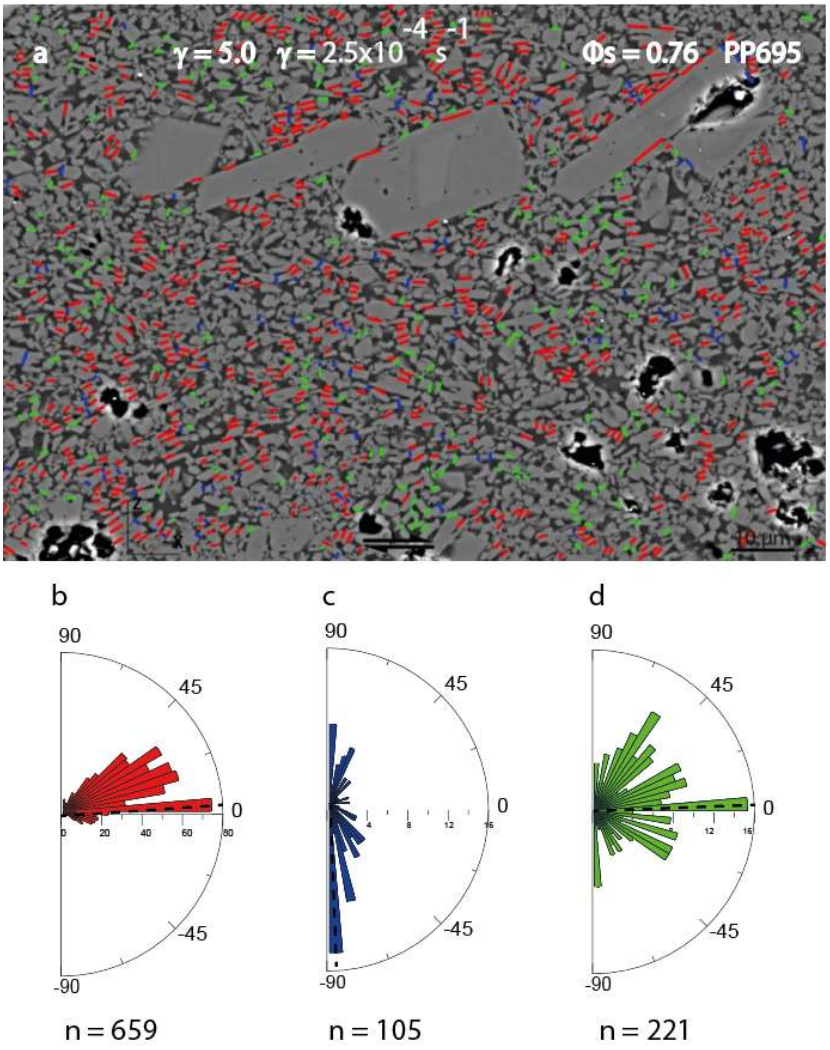

Figure VI.34. a) SEM picture of the sample PP695 with hand drawn the contacts (red: S-S, blue: C-C, green: S-C). Rose diagram for the orientation of the contacts b) S-S, c) C-C, d) S-C. n = number of measuraments.

ϕ_s = 0.76, γ = 5.0, $\dot{\gamma}$ = 1.0*10^{-3} (PP698)

In the sample PP698 (fig. VI.35a) the proportion of S-S contacts sample is 65%, of C-C contacts 10% and of S-C contacts 25%. The preferred directions of the S-S are 2, at 0° and between 20° and 30° (fig. VI.35b), the orientations of the C-C are at -90° and between -60° and -70° (fig. VI.35c) and the orientations of the S-C are at 35°, 0° and -90° (fig. VI.35d). Again, the C-C contacts are few in number. However, their orientations are constant in all experiments, so they can be partially taken into account.

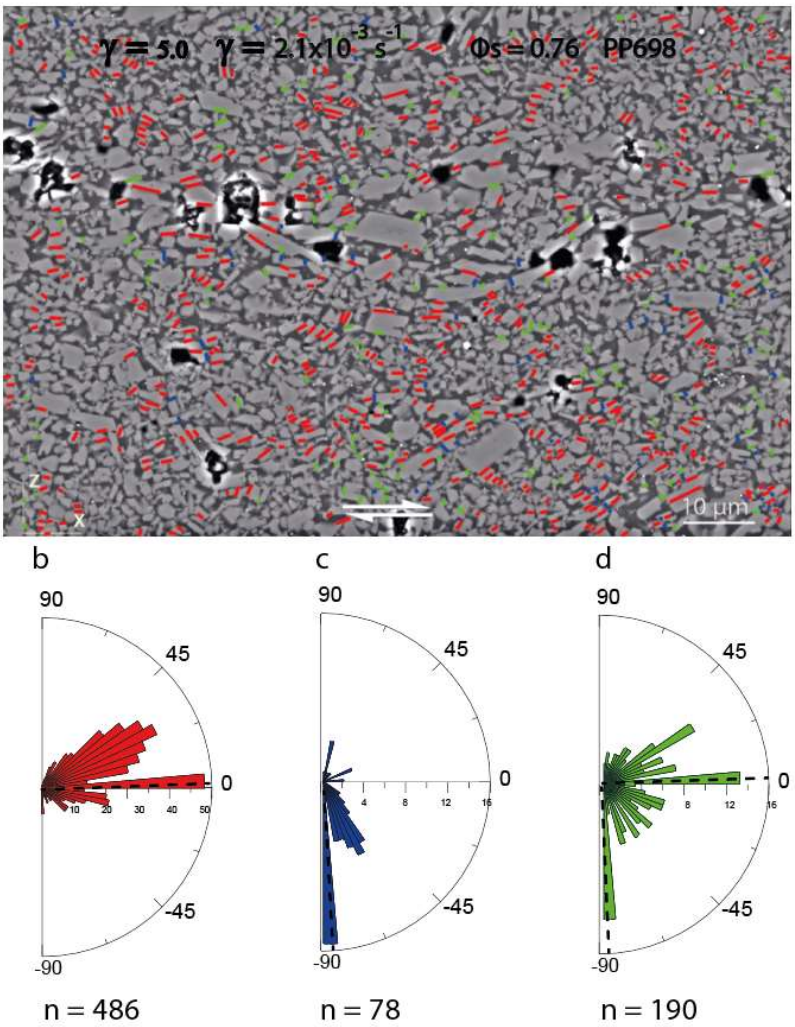

Figure VI.35. a) SEM picture of the sample PP698 with hand drawn the contacts (red: S-S, blue: C-C, green: S-C,). Rose diagram for the orientation of the contacts b) S-S, c) C-C, d) S-C. n = number of measuraments.

ϕ_s = 0.76 γ = 10.0, $\dot{\gamma}$ = 2.5*10^{-4} (PP699)

Sample PP699 (fig. VI.36a) have a proportion of S-S contacts of 59%, C-C contacts of 15% and S-C contacts of 26%. The preferential orientation of S-S contacts is between 40° and 60° (fig. VI.36b), of C-C contacts is at 90° and -90°, (fig. VI.36c), while S-C contacts have no preferential orientation (fig. VI. 36d).

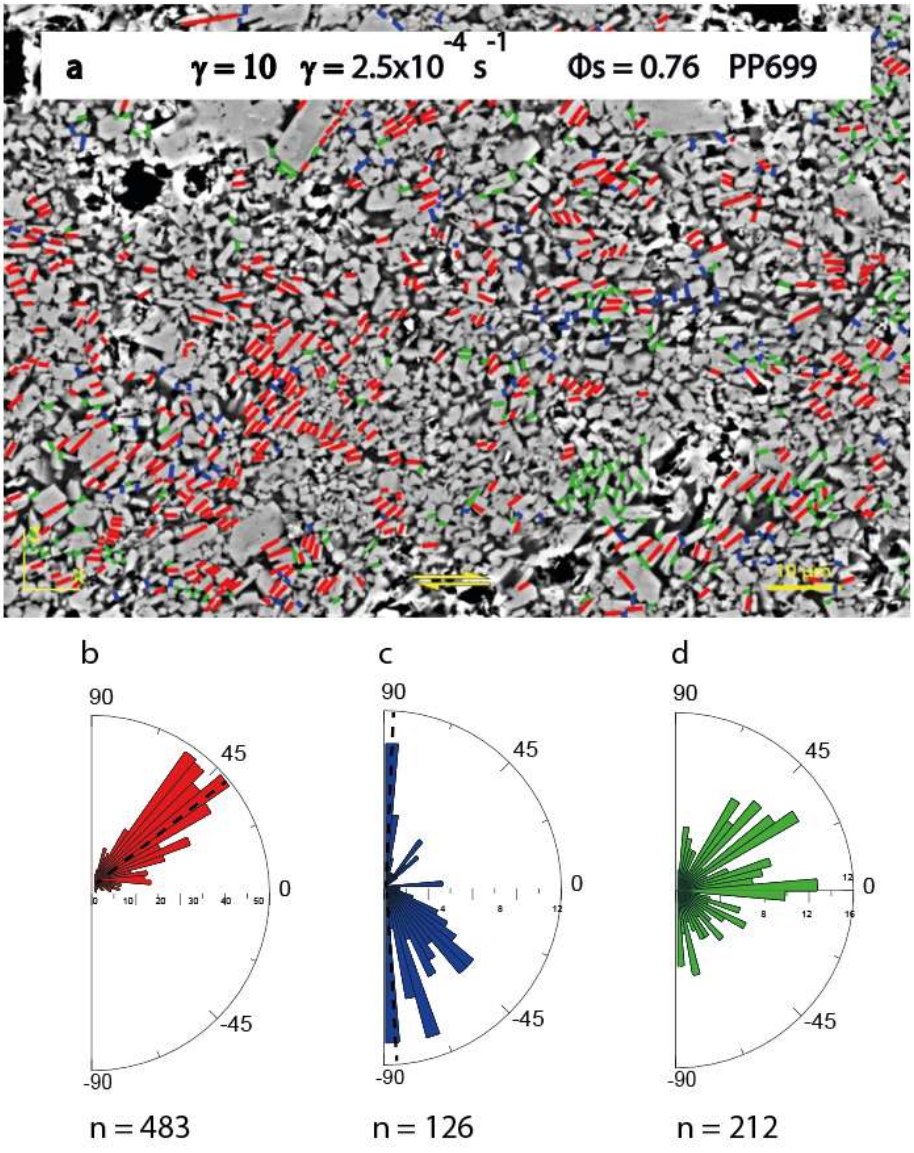

Figure VI.36. a) SEM picture of the sample PP699 with hand drawn the contacts (red: S-S, blue: C-C, green: S-C,). Rose diagram for the orientation of the contacts b) S-S, c) C-C, d) S-C. n = number of measuraments.

Figure VI.37 shows zooms on the contacts of all samples at 0.73 and 0.76 crystal content. Figure VI.37a is the sample at ϕ_s = 0.73 and ɣ = 2.0. Contacts are few and concentrated in certain areas of the sample. This is probably due to the low finite strain ɣ, that does not give contacts time to spread.

Increasing the finite strain (ɣ = 5, fig. VI.37b-c) increases the number of contacts. The difference between sample PP695 (fig. VI.37b) and PP698 (fig. VI.37c) lies in the strain rate $\dot{\gamma}$. The high strain rate does not allow the contacts to be evenly distributed, creating areas where there are more contacts and areas where there are fewer contacts. This is the case of sample PP698, deformed with $\dot{\gamma} = 2.1 \times 10^{-3}\ s^{-1}$.

Figure VI.37d shows the sample subjected to finite strain ɣ = 10. There are many contacts but they are localised in specific areas. The location of the contacts also differs by contact type: there are areas rich in S-S contacts, areas rich in C-C and S-C contacts. The mechanism that led to this subdivision is unclear, but it is likely to be related to the breaking of the sample in the final phase of the experiment.

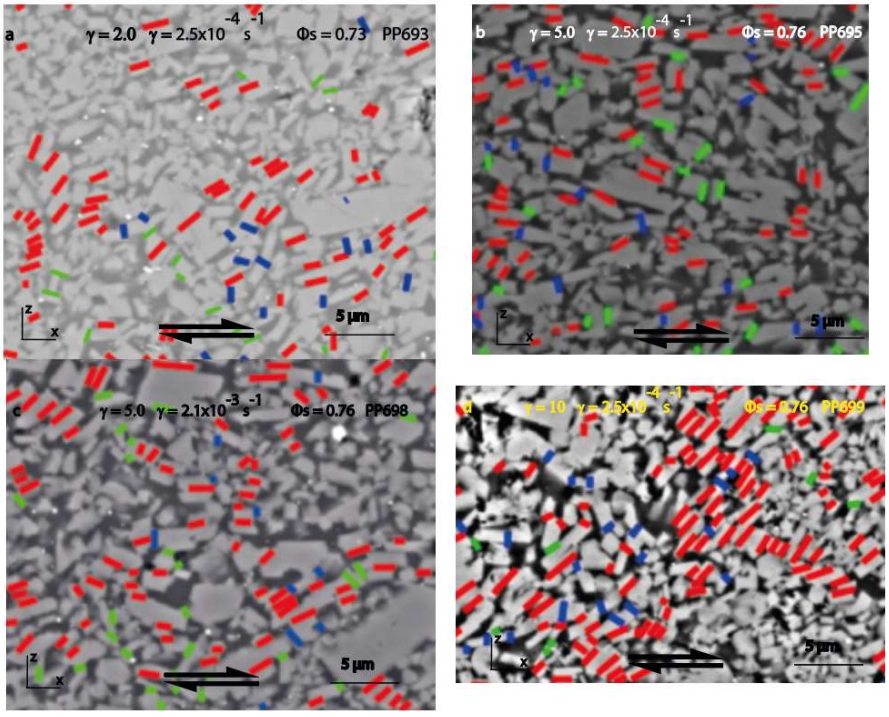

Figure VI.37. Zoom on the contacts of samples a) PP693 (ɣ = 2.0, $\dot{\gamma} = 2.5*10^{-4}$), b) PP695 (ɣ = 5.0, $\dot{\gamma} = 2.5*10^{-4}$), c) PP698 (ɣ = 5.0, $\dot{\gamma} = 1.0*10^{-3}$), d) PP699 (ɣ = 10.0, $\dot{\gamma} = 2.5*10^{-4}$).

8. Clusters

In this paragraph the orientation of the clusters and the orientation of the contacts forming the clusters are considered (fig. VI.38). By definition, clusters are formed by a minimum of 3 contacts of type S-S or C-C, with unlimited maximum value. The greater the number of elements forming a cluster, the greater the deformation that can be propagated.

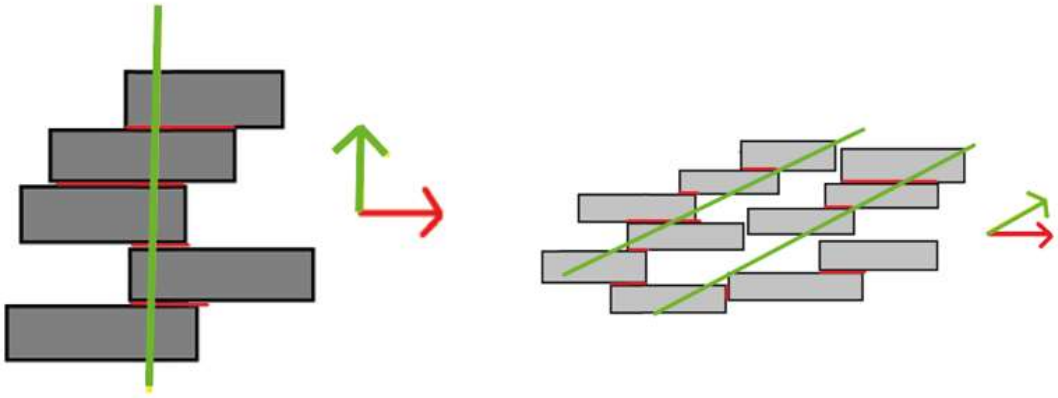

Figure VI.38. Plots of different cluster arrangements. Green line: orientation of the cluster, red line: orientation of the contacts in the cluster.

ϕ_s = 0.73 γ = 2.0, $\dot{\gamma}$ = 2.5*10^{-4} (PP693)

Sample PP693 (fig. VI.39a) shows an orientation of the contacts in the clusters at 25° and 50° (fig. VI.39b), and the orientation of the clusters at -35° (fig. VI.39c).

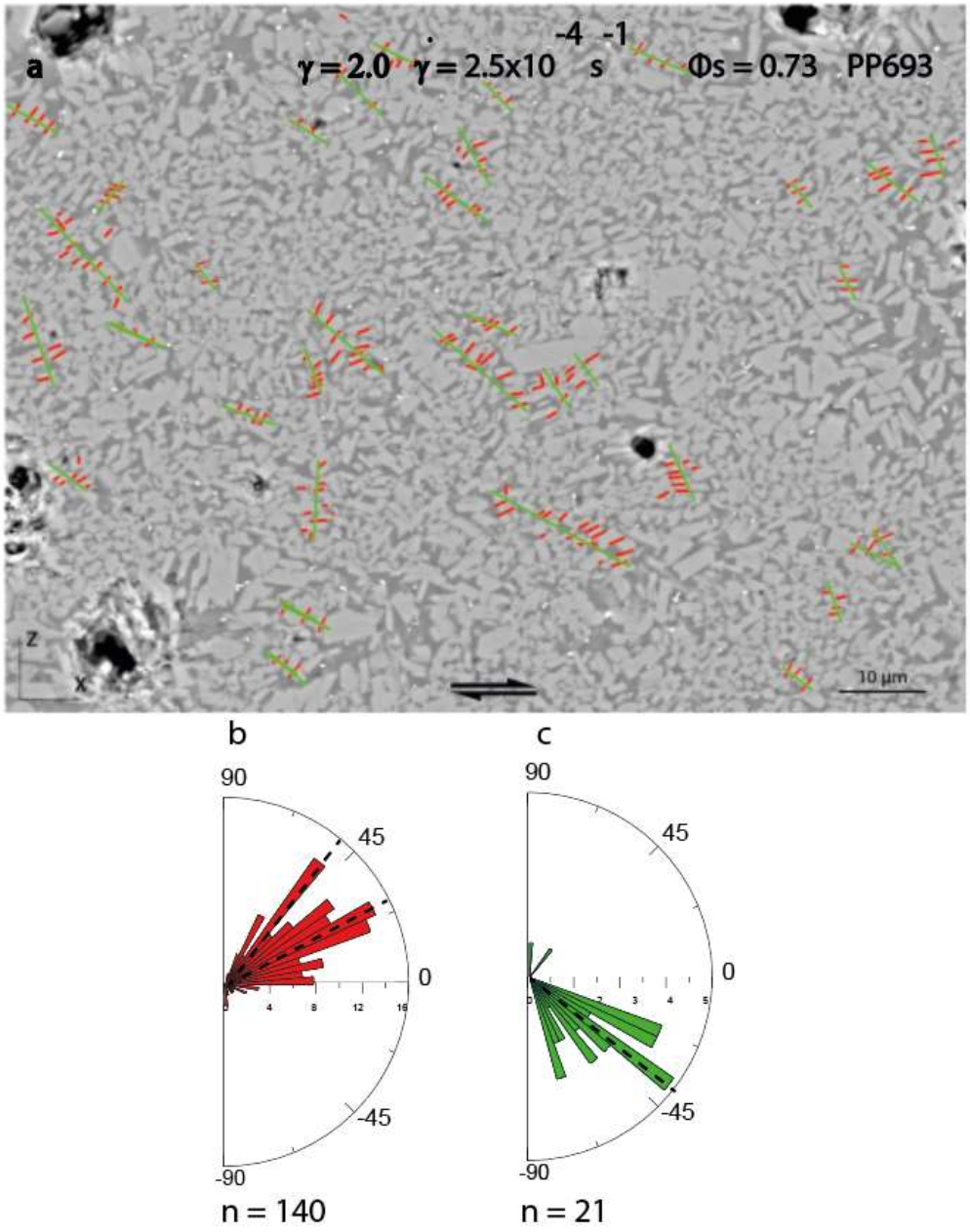

Figure VI.39. a) SEM image of sample PP693 with hand-drawn orientation of the clusters. b) Rose diagram of orientation of the contacts in the clusters**,** c) rose diagram of the preferred orientations of the clusters. n = number of mesures.

ϕ_s = 0.76, $\dot{\gamma}$ = 5.0, $\dot{\gamma}$ = 2.5*10^{-4} (PP695)

Sample PP695 (fig. VI.40a) has an orientation of the contacts in the clusters at 0° and 25° (fig. VI.40b) and orientation of the clusters at 80° and -45° (fig. VI.40c).

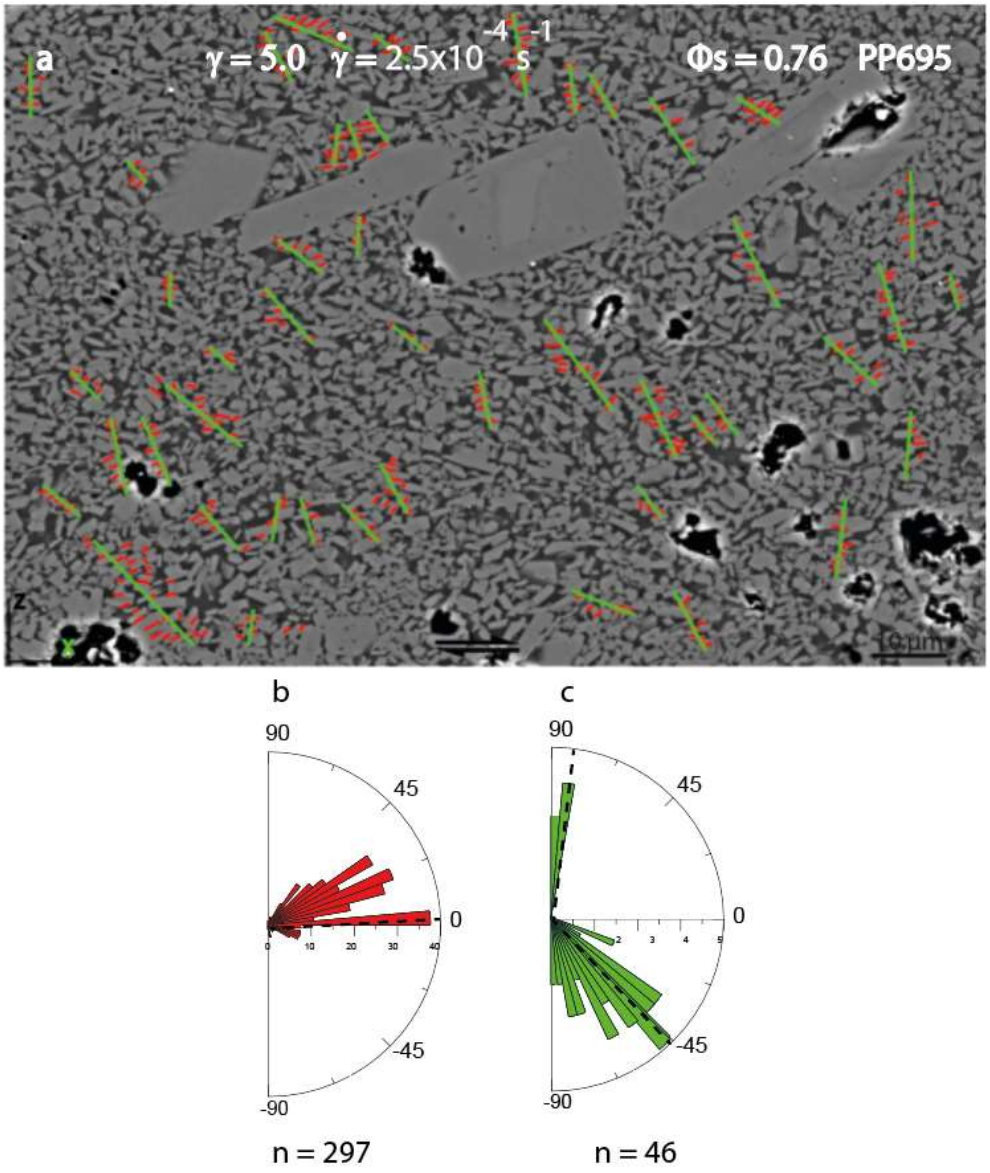

Figure VI.40. a) SEM image of sample PP695 with hand-drawn orientation of the clusters. b) Rose diagram of orientation of the contacts in the clusters, c) rose diagram of the preferred orientations of the clusters.

ϕ_s = 0.76, $\dot{\gamma}$ = 5.0, $\dot{\gamma}$ = 1.0*10^{-3} (PP698)

Sample PP698 shows very similar values to the sample PP695, with an orientation of the contacts of the clusters at 0° and 25° (fig. VI.41a) and an orientation of the clusters at -45° (fig. VI.41c).

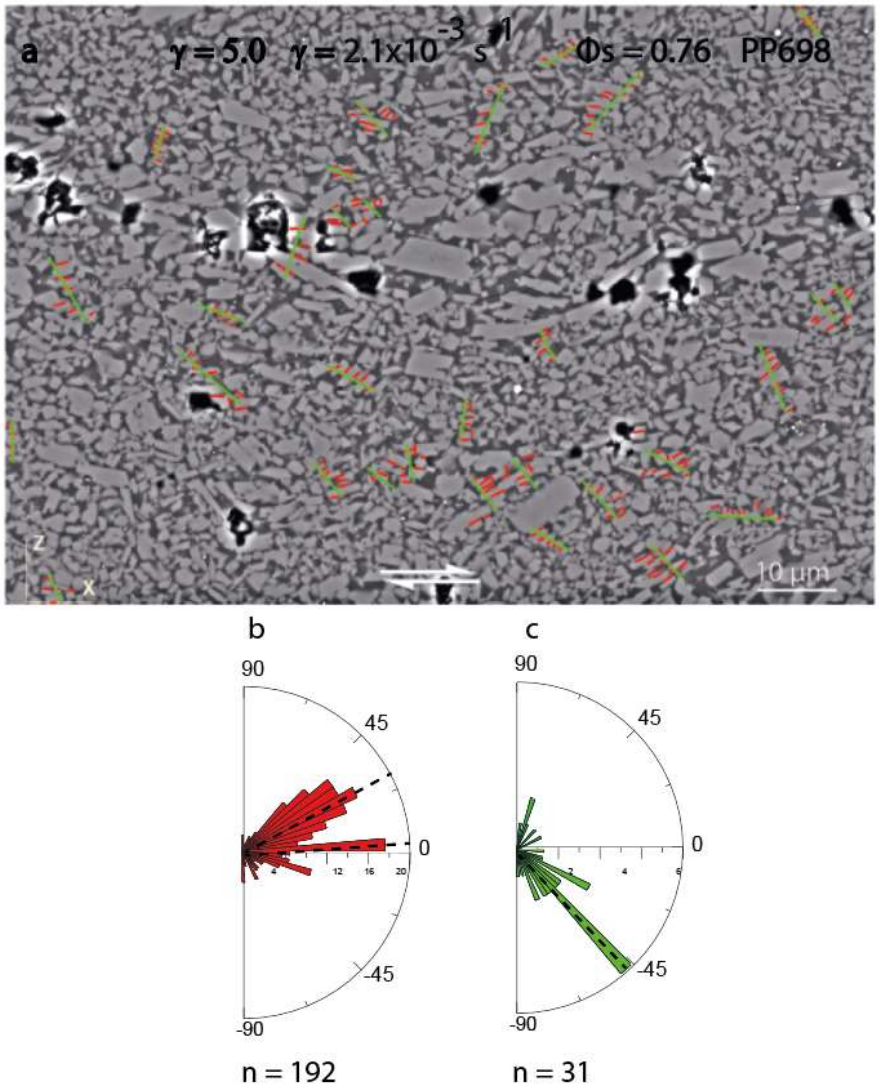

Figure VI.41. a) SEM image of sample PP698 with hand-drawn orientation of the clusters. b) b) Rose diagram of orientation of the contacts in the clusters**,** c) rose diagram of the preferred orientations of the clusters.

ϕ_s = 0.76 γ = 10.0, $\dot{\gamma}$ = 2.5*10^{-4} (PP699)

Sample PP699 (fig. VI.42a) has the most directional contacts, with an orientation of the contacts of the clusters between 50° and 35° (fig. VI.42b) and an orientation of the clusters at -45° (fig. VI.42c).

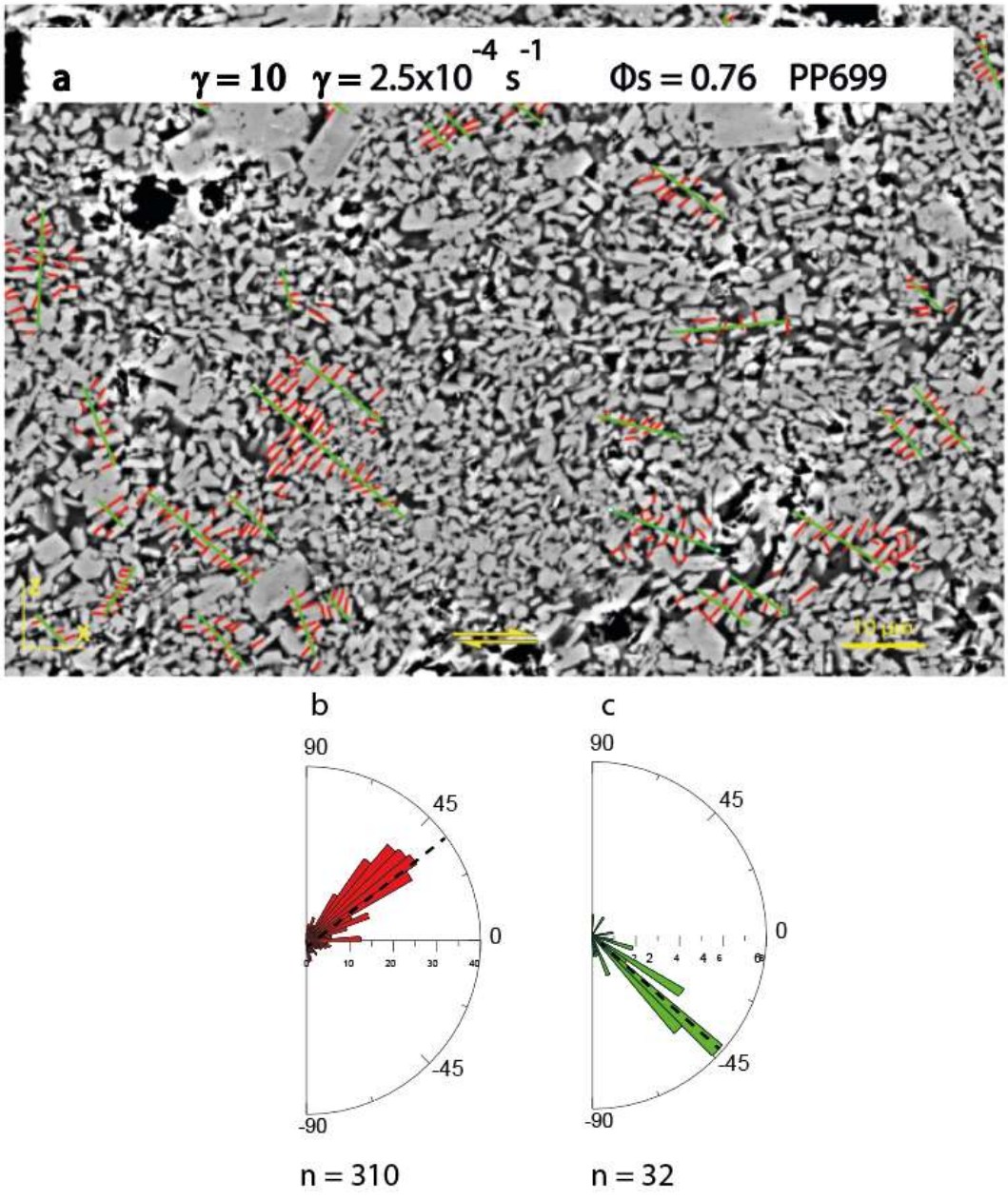

Figure VI.42. a) SEM image of sample PP699 with hand-drawn orientation of the clusters. b) b) Rose diagram of orientation of the contacts in the clusters, c) rose diagram of the preferred orientations of the clusters.

Higher values of finite strain ɣ correspond to more defined angular ranges of the clusters. Longer strains give the clusters a stronger orientation.

The number of contacts forming the clusters remains very similar in the experiments up to strain rate ɣ = 5, with clusters formed by 3 to 15 elements. In the deformed experiment at finite strain ɣ = 10, the clusters are formed by a larger number of elements, up to 27.

9. Shape fabric of bubbles

ϕ_s = 0.73 ɣ = 2.0, $\dot{\gamma}$ = 2.5*10^{-4} (PP693)

Sample PP693 (fig. VI.43a) shows a bubbles content of 2.4%. Their mean aspect ratio R is 1.67±0.52 (fig. VI.43b). The bubbles were drawn by hand (fig. VI.42c). They show a inertia tensor ellipse with R_x = 1.54 and α = 26.33° (fig. VI.43d). The rose diagram shows light preferential direction between 0° and 50° (fig. VI.43e), with no coalescence phenomena.

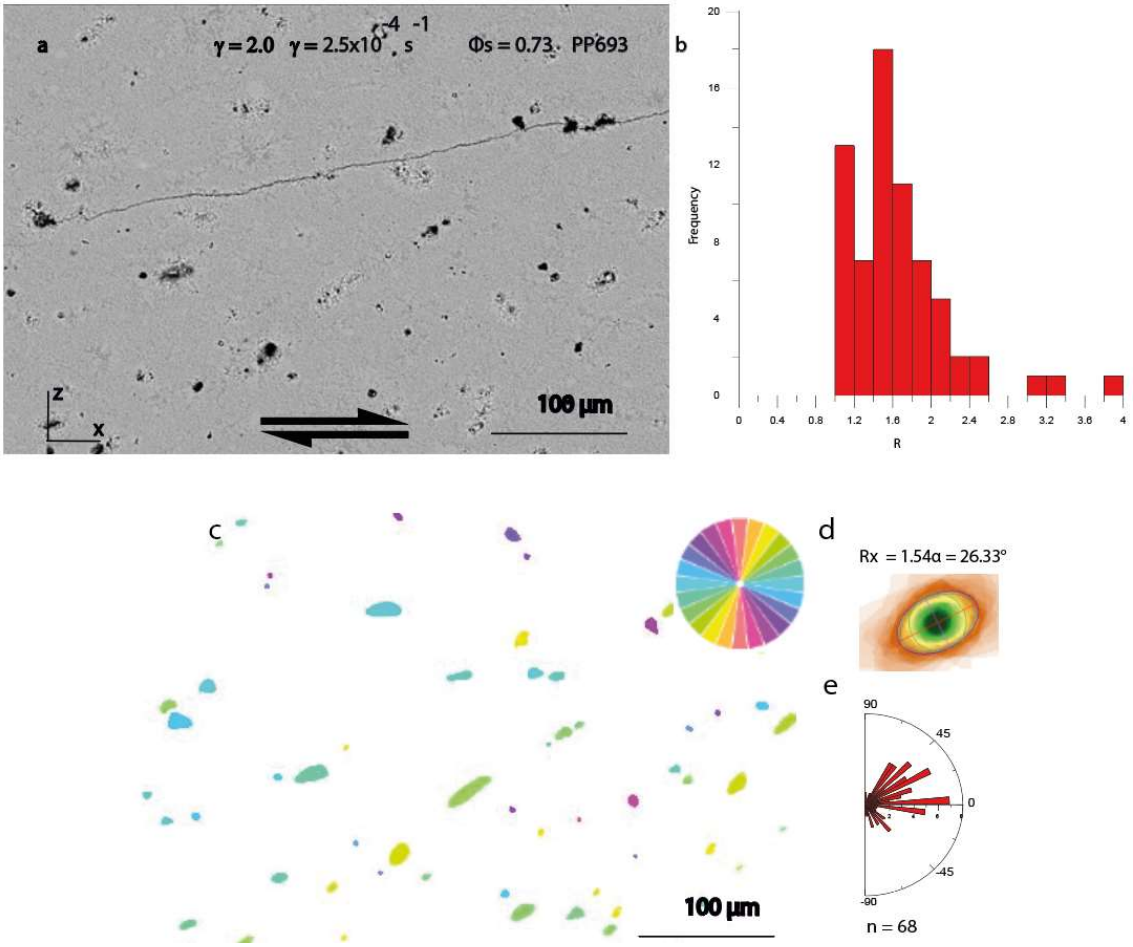

Figure VI.43. a) SEM picture of sample PP693. b) Aspect ratio R histogram of the bubbles. c) Bubbles colored according to their orientations. d) Inertia mean tesnor of the bubbles. e) Rose of directions of individual bubbles orientation. n = number of measures.

ϕ_s = 0.76, $\dot{\gamma}$ = 5.0, $\dot{\gamma}$ = 2.5*10^{-4} (PP695)

Sample PP695 shows a higher bubbles content than the previous sample with a higher orientation and coalescence phenomena in different direction (fig. VI.44a and VI.44b). Coalescent bubbles are found scattered along the entire surface of the sample, without any correlation with the bands.

Bubbles (fig. VI.45a) cover 7% of the total area, with an eccentricity of the inertia tensor ellipse R_x = 1.42 (fig. VI.45b) and with an orientation ranging between 45° and -10° (fig. VI.45c), creating an wavy pattern. The mean aspect ratio R is 1.83±0.71 (fig. VI.45d).

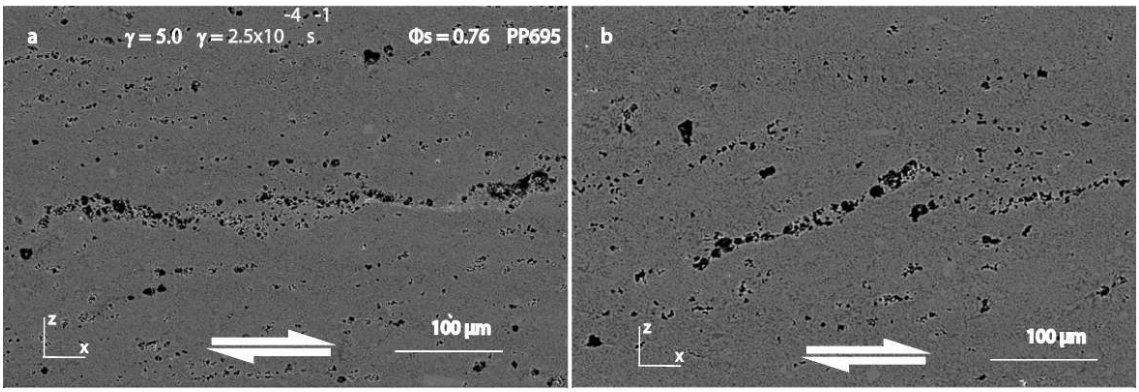

Figure VI.44. SEM pictures of sample PP695. a - b) Focus on bubbles cohalescence with different orientation.

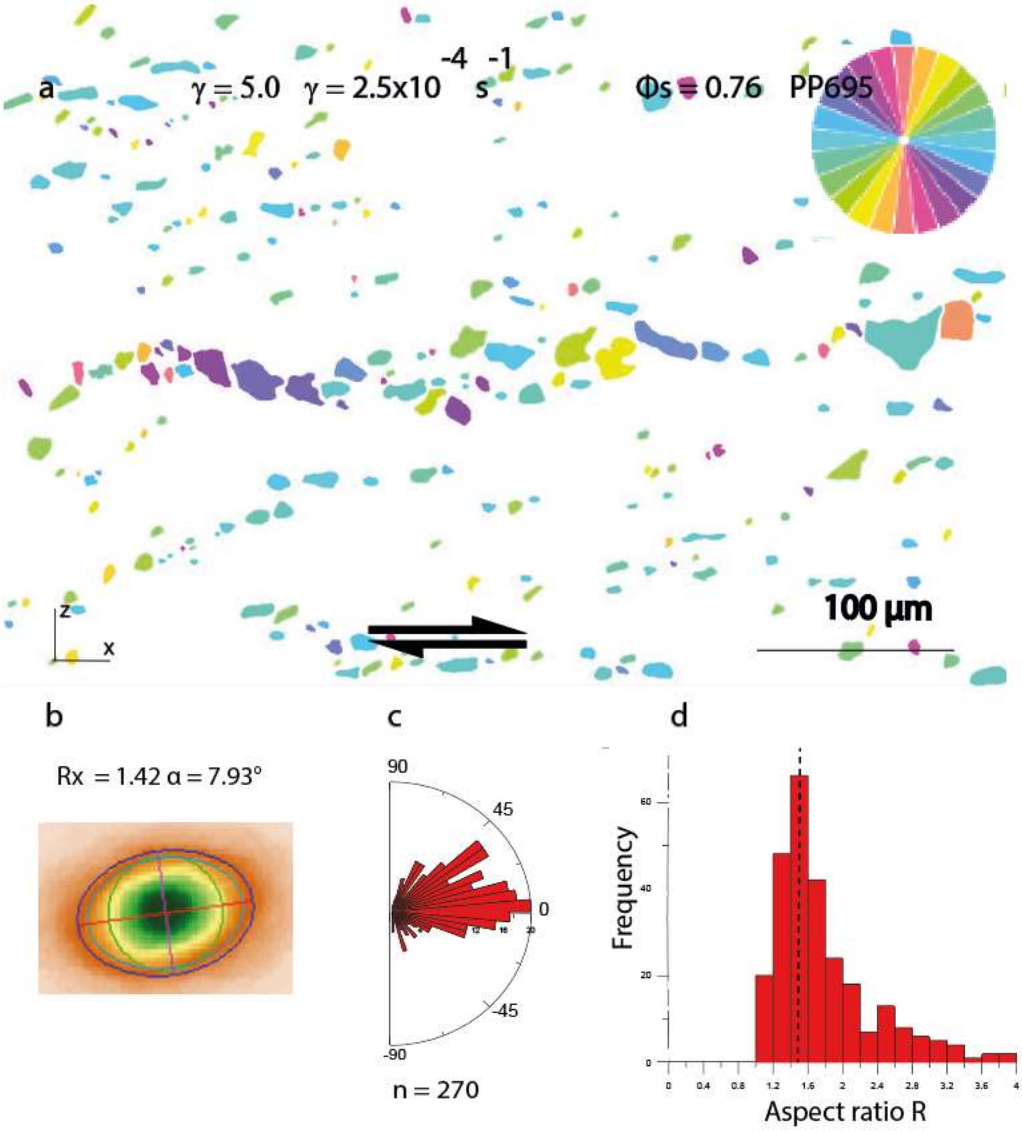

Figure VI.45. Bubbles orientation of the sample PP695. a) Bubbles colored according to their orientations. b) Inertia tensor ellipse of the bubbles. c) Rose of directions of individual bubbles orientation. d) Aspect ratio histogram of the bubbles. n = number of measures.

ϕs = 0.76, ɣ = 5.0, $\dot{\gamma}$ = 1.0*10^{-3} (PP698)

In sample PP698 (fig. VI.46a) there are slight coalescence phenomena between bubbles, which are strongly oriented. There is a weaker coalescence phenomena compared with sample PP695. The area occupied by the bubbles is 9.9%.

The bubbles were hand-drawn (fig. VI.47a) and the show a inertia tensor ellipse with R_x = 1.50 and α = 28.52° (fig. VI.47b). From the rose diagram, the preferred orientations of the bubbles are at 45° and 25° (fig. VI.47c). The aspect ratio R is 1.83±0.83 (fig. VI.47d).

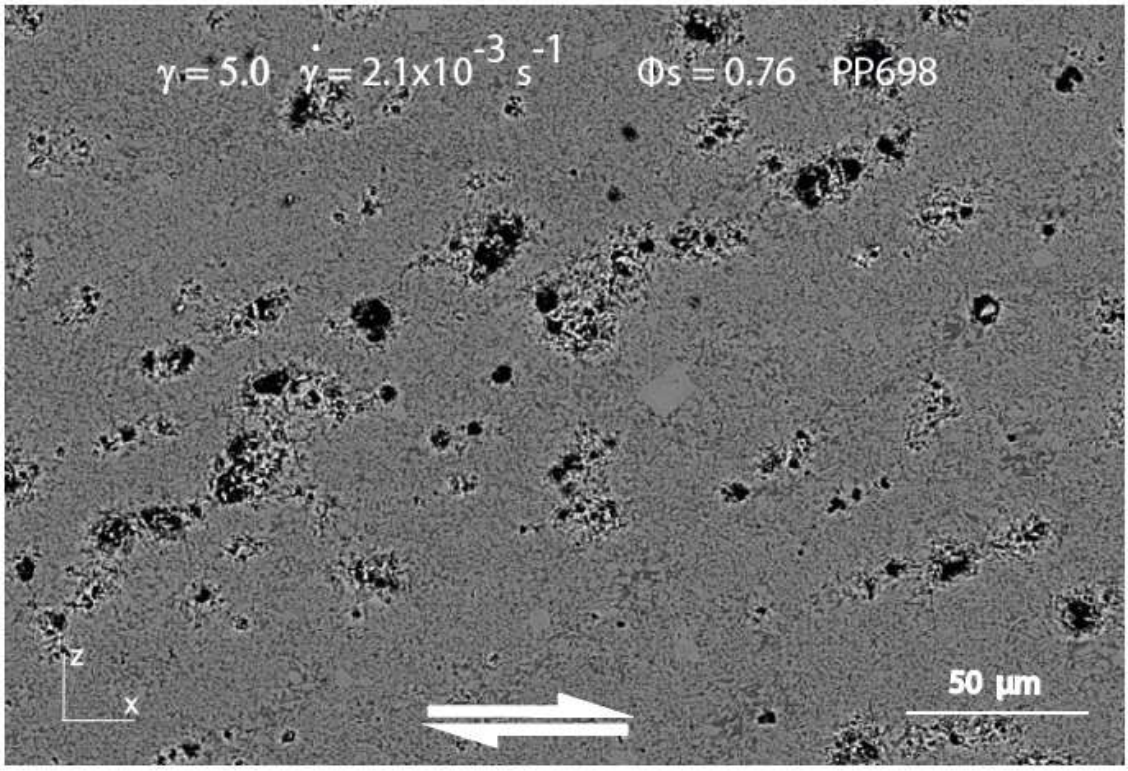

Figure VI.46. a - b) SEM pictures of sample PP698.

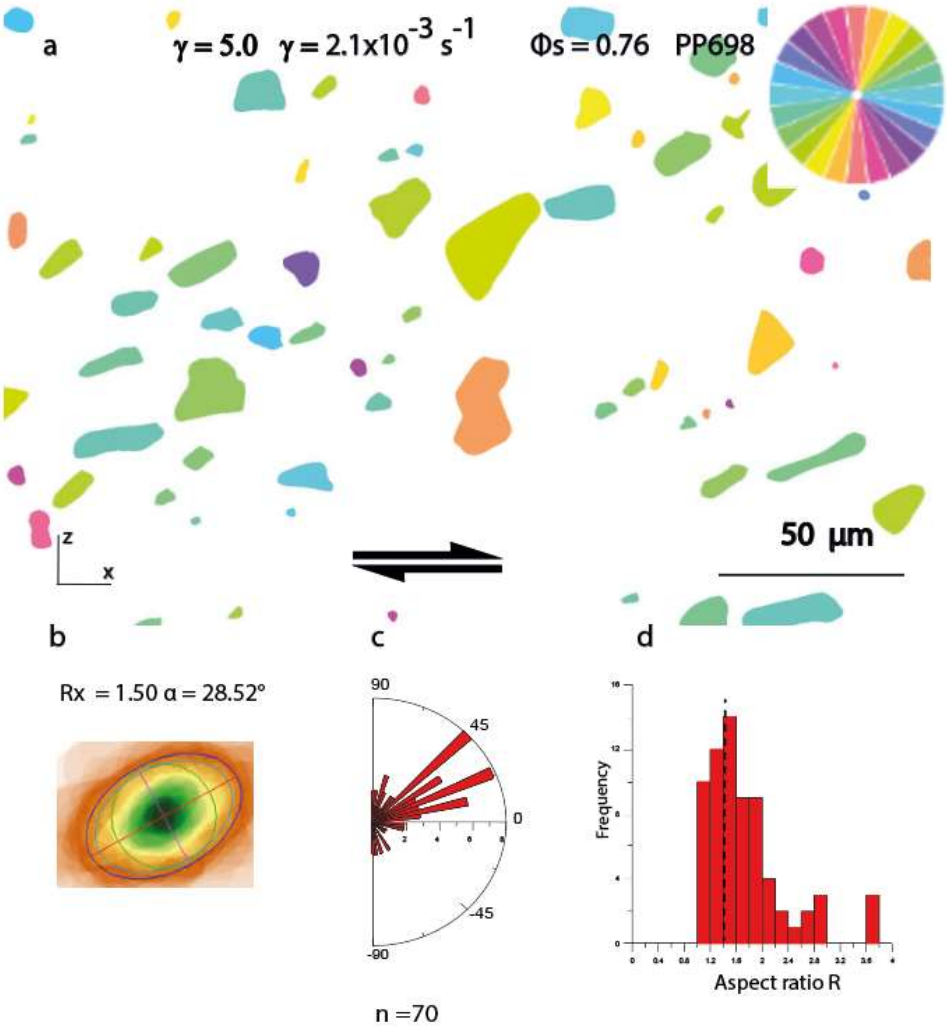

Figure VI.47. Bubbles orientation of the sample PP698. a) Bubbles colored according to their orientations. b) Inertia tensor ellipse of the bubbles. c) Rose of directions of individual bubbles orientation. d) Aspect ratio histogram of the bubbles. n = number of measures.

ϕs = 0.76, ɣ = 10.0, $\dot{\gamma}$ = 2.5*10^{-4} (PP699)

Sample PP699 (fig. VI.48) shows different bubble behaviour depending on the area taken into consideration. For this reason, the sample was analysed in 4 different areas, representative of all bubble behaviours.

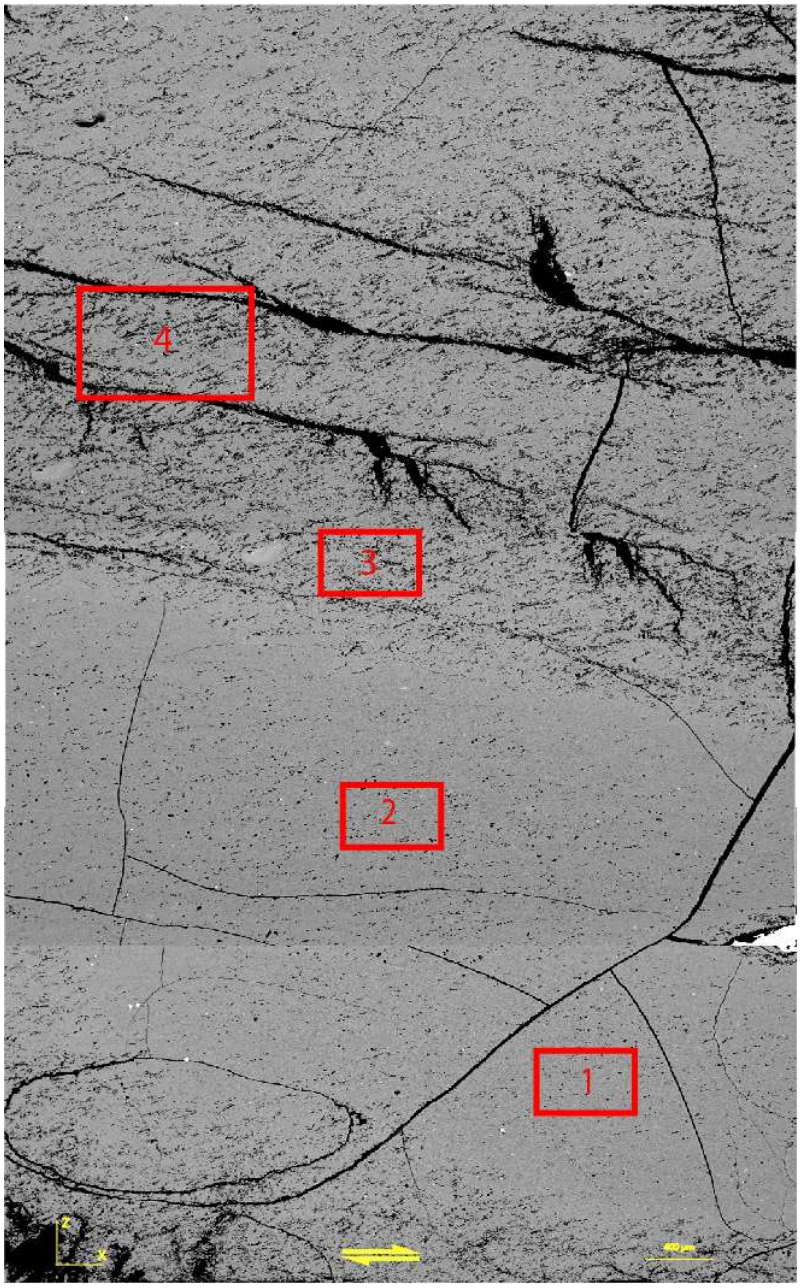

Figure VI.48. Panoramic image of sample PP699. The areas analysed are enclosed in red rectangles.

Centre - Area n.1

Area no. 1 of sample PP699 (fig. VI.49) is part of the unfractured area and it has a bubble content of 3.4%.The bubbles were drawn by hand (fig. VI.50a) and they show an ecentriity of the intertia tensor ellipse R_x = 1.36 and α = 19.08° (fig. VI.50b). The preferential orientation of the bubbles is at 35° (rose diagram, fig. VI.50c). The mean aspec ratio R is 1.49±0.35 (fig. VI.50d).

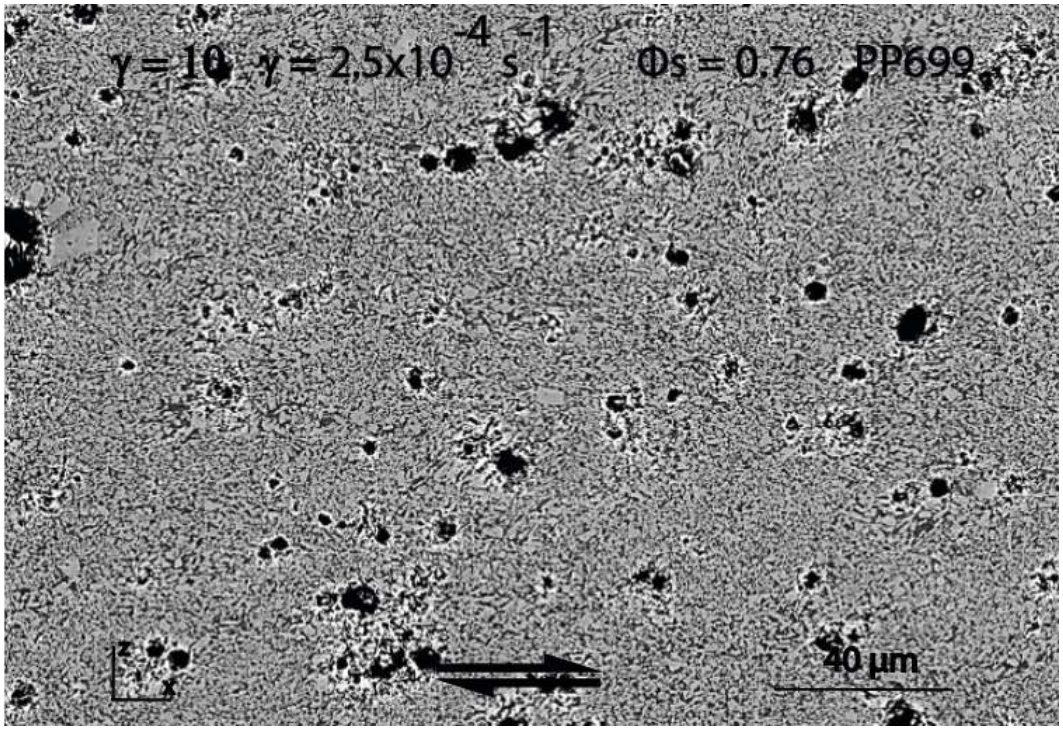

Figure VI.49. a) SEM picture of bubbles in the area n.1. b) Aspect ratio histogram for groups of bubbles.

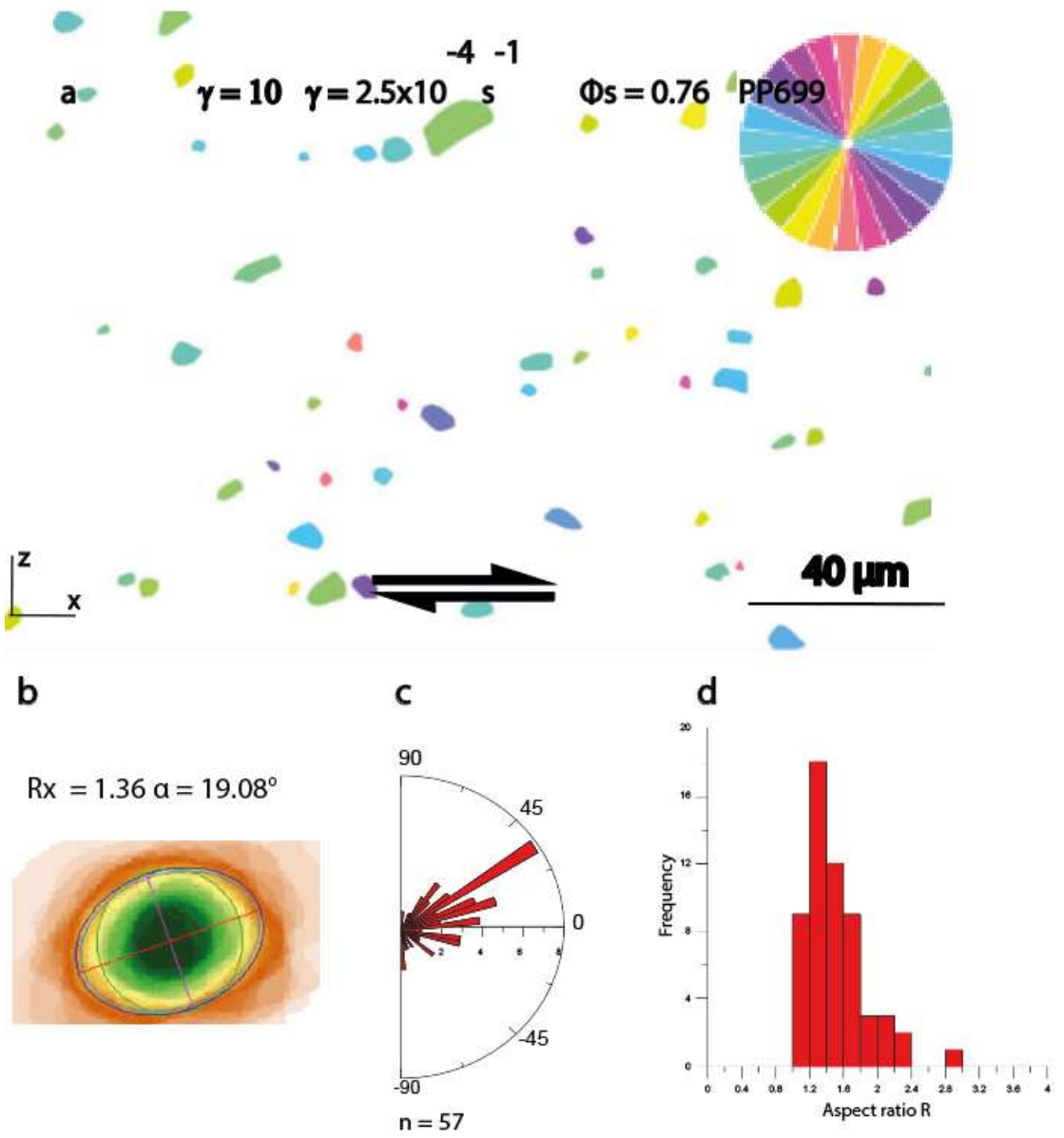

Figure VI.50. Bubbles orientation of the area n.1 (PP699) a) Bubbles colored according to their orientations. b) Inertia tensor ellipse of the bubbles. c) Rose of directions of individual bubbles orientation. d) Aspect ratio histogram of the bubbles. n = number of measures.

Centre - Area n.2

The analysed area is part of the unfractured area of the sample and it shows how the bubbles begin to coalesce (fig. VI.51a). The total area covered by the bubbles is 12.7%. The bubbles were hand-drawn (fig. VI.52a) and the show a inertia tensor ellipse with R_x = 1.76 and α = 1.88° (fig. VI.52b). From the rose diagram, there is no preferred orientation of the bubbles (fig. VI.52c). The mean aspect ratio R is 2.15±0.84 (fig. VI.52d).

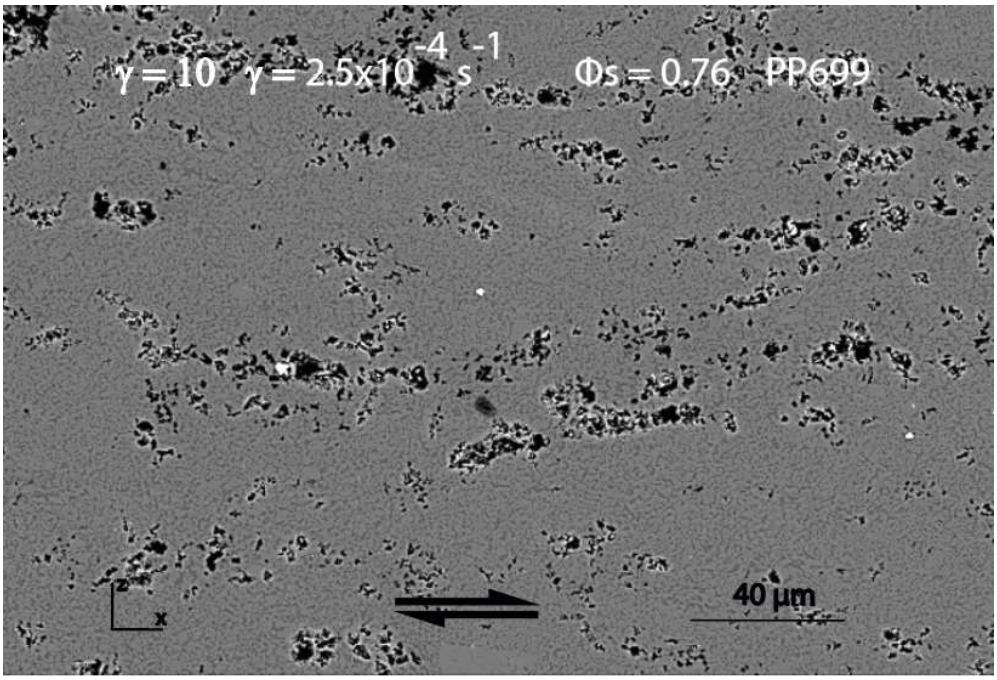

Figure VI.51. a) SEM picture of bubbles in the area n. 2

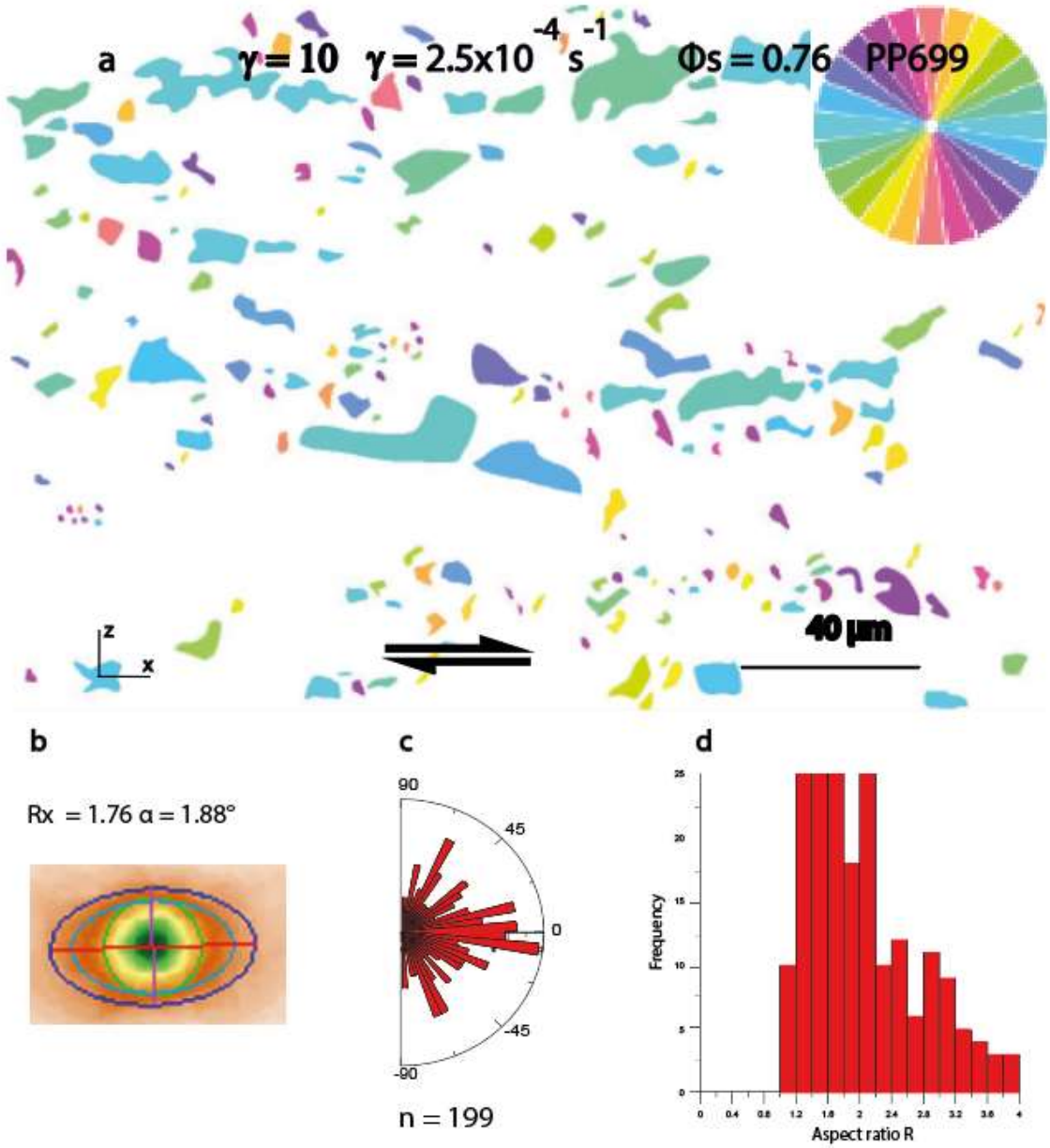

Figure VI.52. Bubbles orientation of the area n.2 (PP699) a) Bubbles colored according to their orientations. b) Inertia tensor ellipse of the bubbles. c) Rose of directions of individual bubbles orientation. d) Aspect ratio histogram of the bubbles. n = number of measures.

Top – Area n.3

This area is part of the fractured area. The bubbles occupy 19% of the total area (fig VI.53). The bubbles were hand-drawn (fig. VI. 54a) and the show a inertia tensor ellipse with R_x = 1.18 and α = 14.36° (fig. VI.54b). From the rose diagram, there is no preferred orientation of the bubbles (fig. VI.54c). The mean aspect ratio R is 2.00±0.74 (fig. VI.54d).

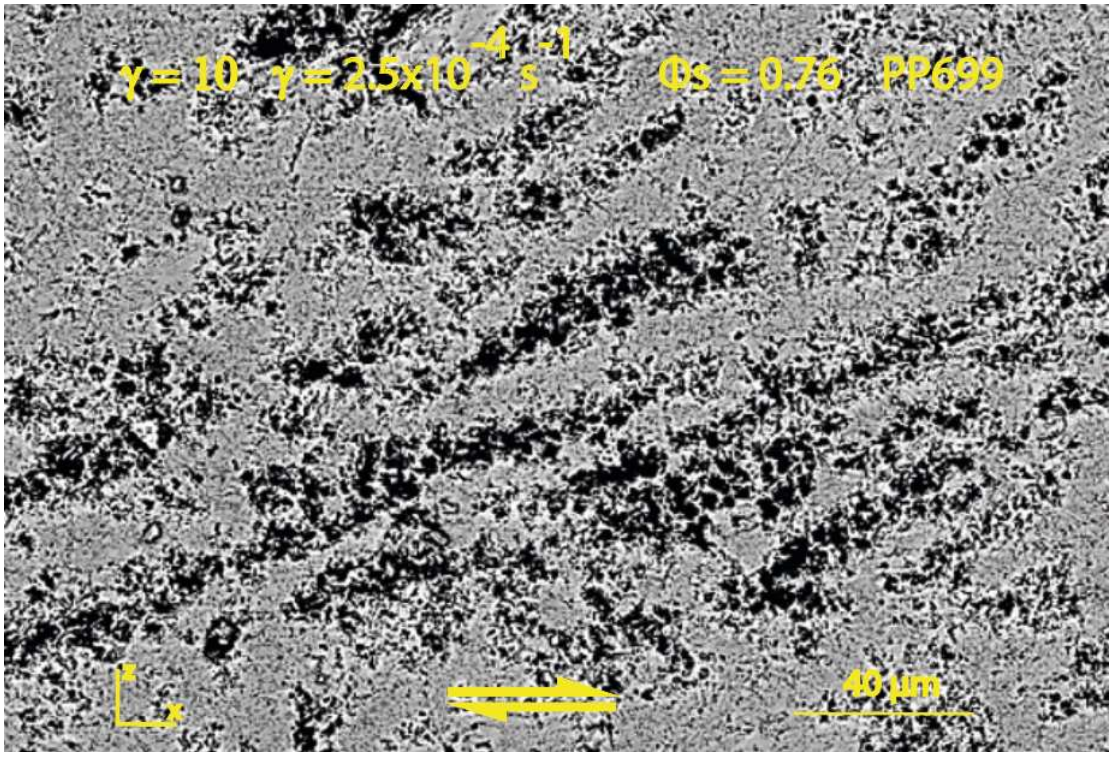

Figure VI.53. a) SEM picture of bubbles in the area n. 3 (fractured area).

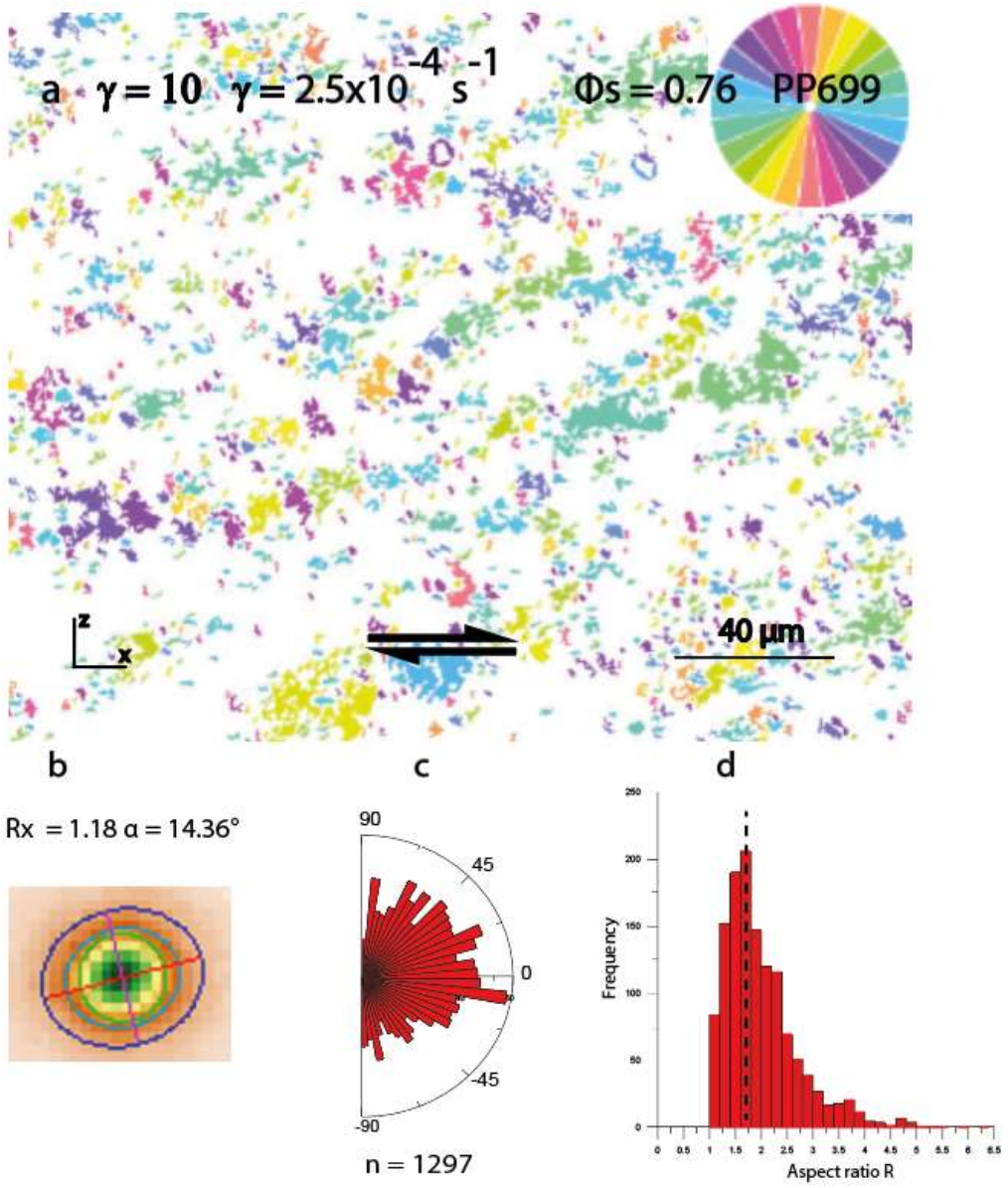

Figure VI.54. Bubbles orientation of the area n.3 (PP699) a) Bubbles colored according to their orientations. b) Inertia tensor ellipse of the bubbles. c) Rose of directions of individual bubbles orientation. d) Aspect ratio histogram of the bubbles. n = number of measures.

Top – Area n.4

Area no. 4 of sample PP699 (fig. VI.55) shows a crystalline content of 12%.

The bubbles were studied using the inertia method (fig. VI.56a) and show an eccentricity of the inertia tensor ellipse R_x = 2.50 and α = 14.92° (fig. VI.56b). No preferential orientation was found in the bubble direction (fig. VI. 56c). The bubbles have mean R value of R 1.99±0.79 (fig. VI.56d).

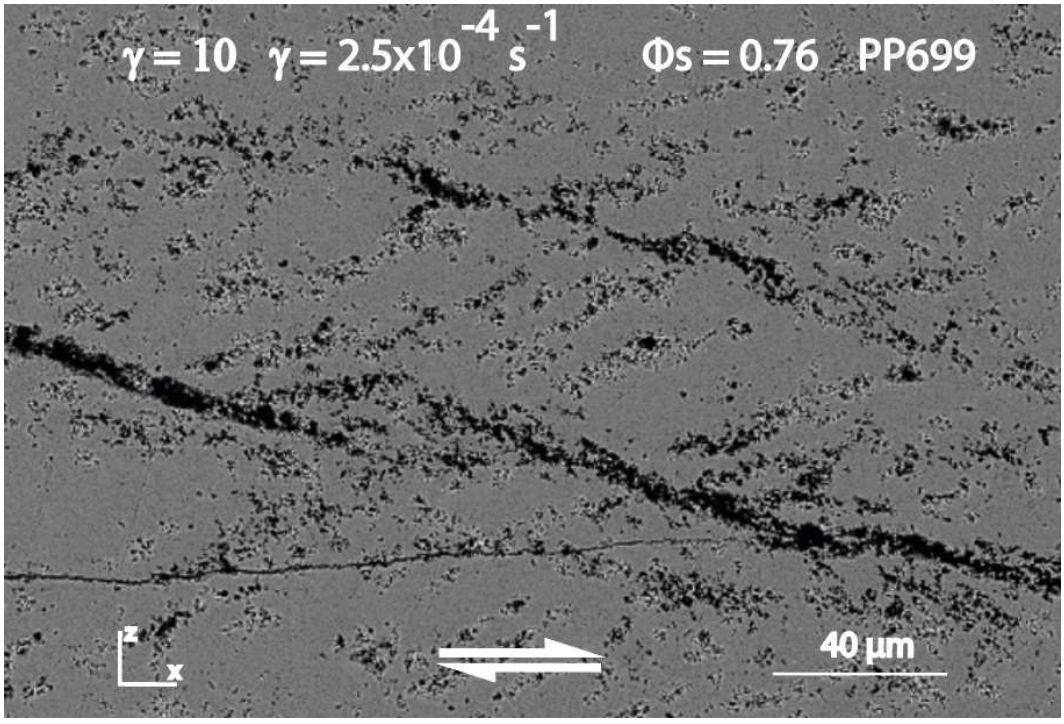

Figure VI.55. a) SEM picture of bubbles in the area n. 4.

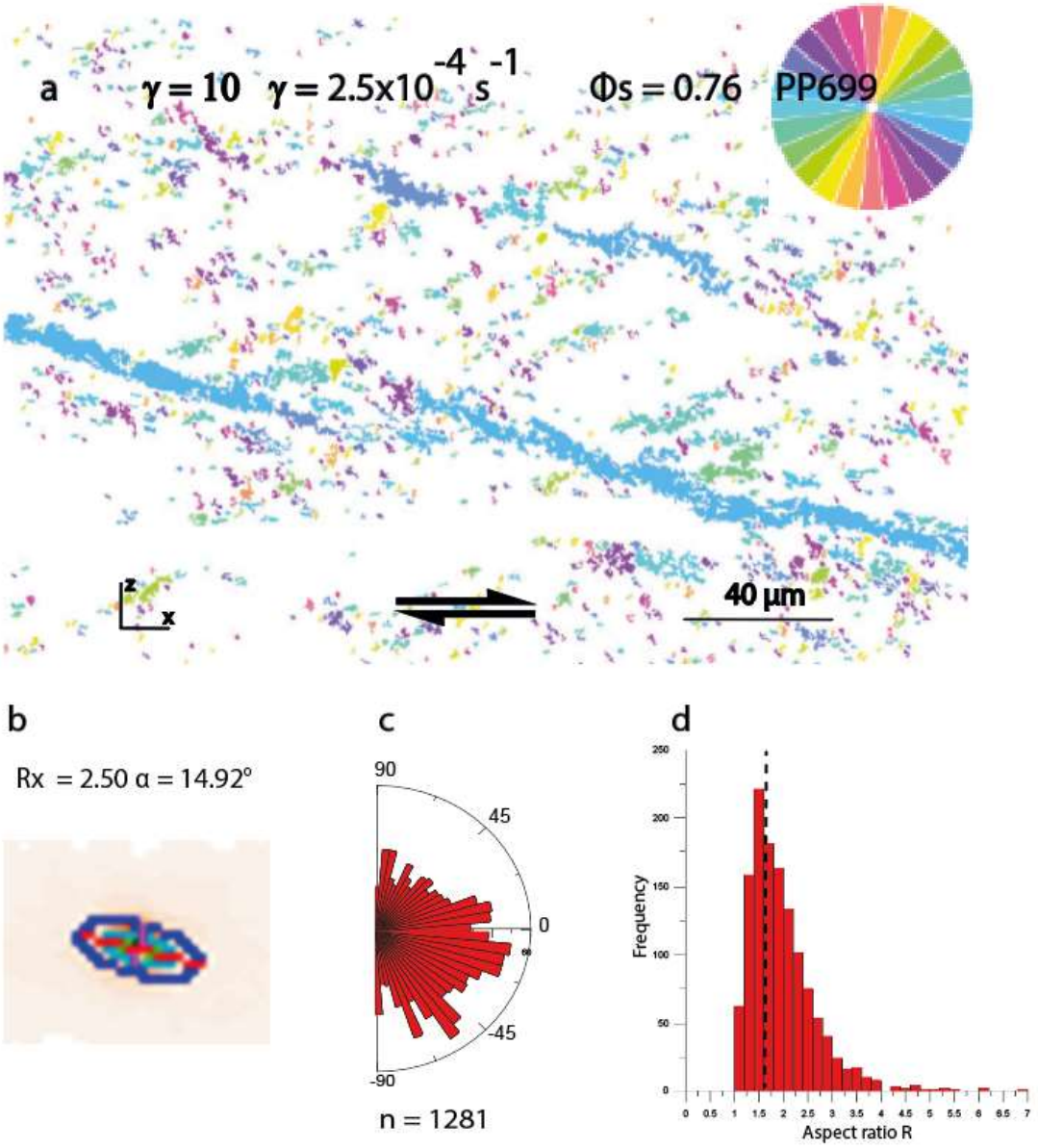

Figure VI.56. Bubbles orientation of the area n.4 (PP699) a) Bubbles colored according to their orientations. b) Inertia tensor ellipse of the bubbles. c) Rose of directions of individual bubbles orientation. d) Aspect ratio histogram of the bubbles. n = number of measures.

10. Summary

Samples with crystal contents ϕ_s = 0.73 - 0.76 show no strain localization. After the deformation experiments, the samples develop a wavy pattern consisting of crystals with an average orientation between 0° and 45°. The bubbles are oriented in the direction of shear and show coalescence phenomena. Starting from finite strain γ = 5, the samples develop banding, which is formed by interconnected bands enriched in residual melt and forming an anastomosing network (fig. VI.56a). The contacts are distributed over the entire surface of the samples. Due to the mobility of the crystals, the number of clusters is always small.

The sample with ϕ_s = 0.95 has granular behaviour. When subjected to deformation, it develops plagioclases orientation between 0° and 45° and a series of interconnected bands with an anastomosing pattern. These bands are enriched in melt and bubbles. They have a smaller crystal grain size than the penetrative fabric. This demonstrates the localization of deformation in these bands (fig. VI.57b).

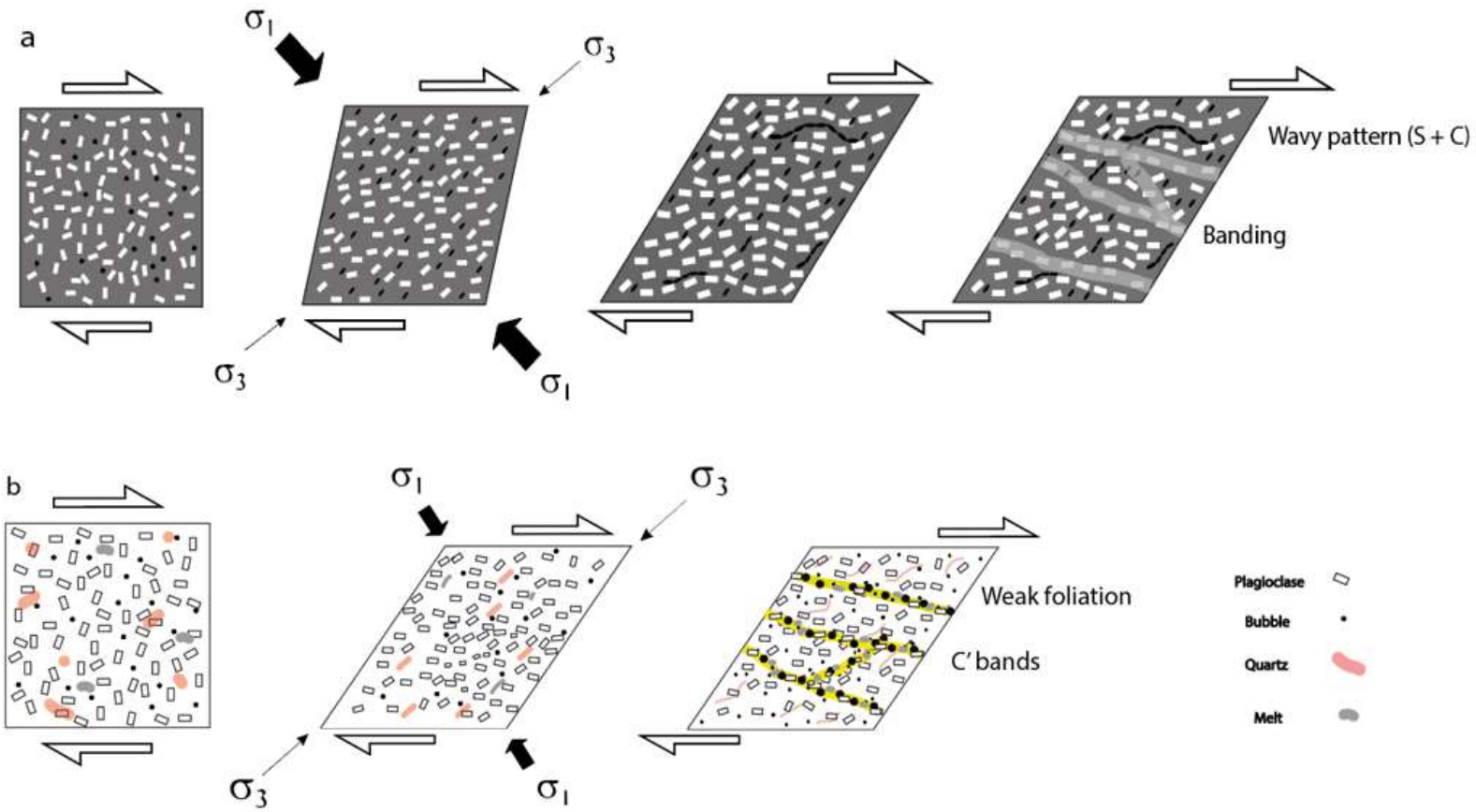

Figure VI.57. a) Deformation stages for samples with R = 2 and ϕ_s = 0.73 – 0.76. b) Deformation stages for samples with R = 2 and ϕ_s = 0.95.

11. Synthesis of all the experimental results

Figure VI.58 shows a summary diagram of all the deformation structures formed in the deformed samples with aspect ratio R = 2 and R = 4 at different crystal contents.

The samples with aspect ratio R = 2 at crystal contents of 0.58, 0.59 and 0.73 show a pervasive fabric with more pronounced wave-like trends with increasing crystal content and finite strain values. At crystal contents greater than 0.73, finite strain values between 5 and 10 form interconnected melt-enriched bands relative to the surrounding areas, producing melt segregation phenomena. This phenomenon has been observed in experiments up to crystal contents of 0.95.

Samples with aspect ratio R = 4 show strain localization expressed by the formation of shear bands at crystal contents between 0.52 and 0.59. No experiments were carried out at high crystal contents (greater than 0.70), but it is hypothesised that a sample with aspect ratio R = 4 may exhibit melt migration when deformed to high values of finite strain.

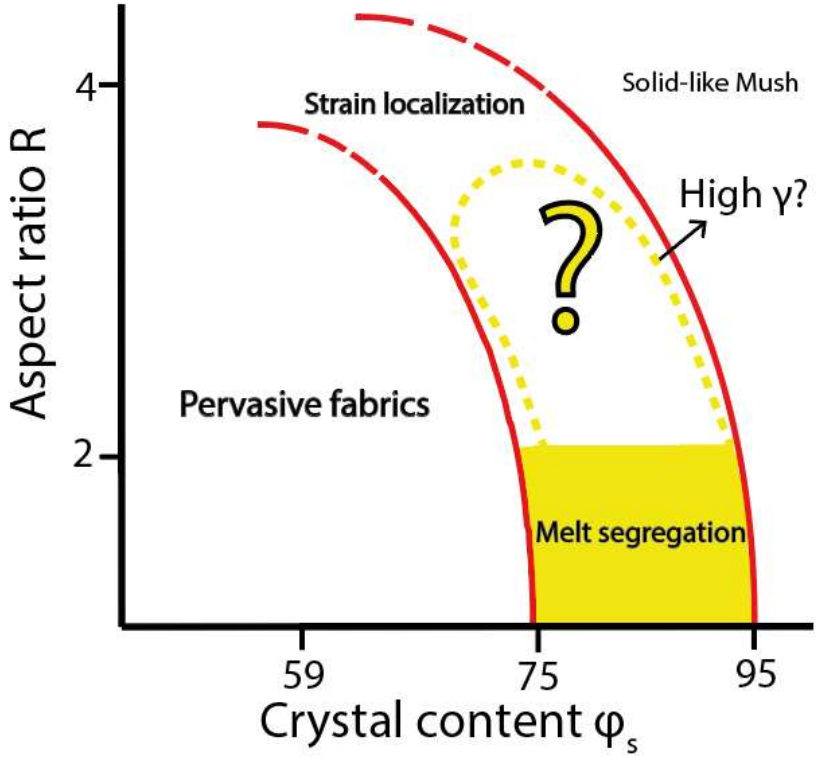

Figure VI.58. Crystal content ϕ_s vs aspect ratio R diagram showing all deformation structures formed in samples with aspect ratio R = 4 and aspect ratio R = 2.

Results natural samples
Study cases: phonolitic intrusions

Résumé du chapitre VII - Résultats des échantillons naturels

Les échantillons naturels présentés dans ce chapitre sont des corps volcaniques du Massif Central français. Les échantillons ont une composition phonolitique et proviennent de deux corps géologiques différents : le Petit Gerbier (ou Gouleou, un neck volcanique) et le Suc de Sara, un dyke volcanique. L'objectif de ces travaux est d'étudier comment le liquide résiduel se déplace à partir du corps volcanique et quels types de microstructures sont formés pendant les événements de déformation.

Les zones sélectionnées pour l'échantillonnage sont représentatives des différentes intensités de déformation : des échantillons ont été prélevés le long des marges et le long des zones centrales des corps volcaniques. Cela permet d'étudier les structures de déformation résultant d'une forte déformation (zones le long des marges) et d'une faible déformation (zones intérieures).

Le Petit Gerbier et le Suc de Sara sont des structures volcaniques tardives qui ont subi des déformations au cours de la dernière phase de cristallisation et qui présentent une teneur élevée en cristaux. Ces zones présentent une foliation, des alignements de cristaux et des bandes de cisaillement. Ce sont des indicateurs importants du comportement rhéologique non linéaire du magma. Il est primordial d'étudier la géométrie de ces structures car elle pourrait fournir des renseignements sur le type de déformation et des informations sur la paléocontrainte qui a initié la déformation.

Le chapitre commence par une introduction expliquant les principales caractéristiques des corps volcaniques étudiés et l'endroit où ils se trouvent. Dans le paragraphe suivant, l'histoire volcanique de la province magmatique est décrite, en particulier l'histoire géologique du Suc de Sara et du Petit Gerbier.

La section des résultats étudie les échantillons naturels dans leurs caractéristiques morphologiques (rapport d'aspect R et diamètre équivalent). Les analyses chimiques effectuées sur les minéraux et le verre résiduel des échantillons sont ensuite présentées. Un paragraphe présente les analyses Raman effectuées sur les fuseaux résiduels des échantillons. Les analyses microstructurales étudient l'orientation des cristallins, en particulier sur les cristaux de feldspath, car ils sont les plus abondants et ont une forme allongée. Enfin, les types de contacts (S-S, C-C, S-C) présents dans le tissu pénétrant de l'échantillon du Petit Gerbier et les orientations des bulles sont étudiés.

Les valeurs du rapport d'aspect R et du diamètre équivalent ϕ de l'échantillon PG1 indiquent un refroidissement lent et une déformation moins sévère, avec des cristaux peu allongés et beaucoup plus grands que ceux de l'échantillon PG3.

Les cristaux présentent une orientation préférentielle de la forme en fonction de la direction de la déformation. Dans le tissu pénétrant, les cristaux présentent un motif ondulé. Les échantillons les plus déformés présentent des bandes de cisaillement, les échantillons modérément déformés présentent des bandes et les échantillons les plus internes présentent une foliation.

Les contacts entre les cristaux sont bien orientés mais peu nombreux en raison des différentes phases minéralogiques présentes dans le tissu de pénétration de l'échantillon PG.

Les forces peuvent être localisées de deux manières : en augmentant la concentration des chaînes de force stables ou en formant des zones de faiblesse avant le début de la déformation. L'échantillon PG1, qui représente la phase initiale de la déformation, présente des zones de fusion concentrée disséminées dans l'échantillon. Il est probable que ces zones représentent des faiblesses où la déformation se localise, comme les bandes de cisaillement présentes dans l'échantillon PG1.

Le pourcentage de bulles dans le Petit Gerbier est si faible que les résultats de leur analyse peuvent être négligeables.

VII. Melt and fluid segregation in phonolitic systems: the studied cases of Petit Gerbier neck and Suc de Sara dyke (Velay Volcanic Province, France)

1. Introduction

In addition to the experimental approach, the link between shear deformation and seggregation of late magmatic melts and fluids was explored in representative, effusive and shallow emplaced, volcanic bodies. The chosen examples comprise two volcanic phonolitic bodies emplaced in the Velay volcanic province located Souteast of the French Massif Central: the Petit Gerbier neck (named also Gouleiou, DMS latitude 44° 53' 40.8336'' N, DMS longitude 4° 13' 17.8068'' fig. VII.1a (Arbaret et al., 1993)) and the Suc de Sara dike (DMS latitude 44° 52' 26.706'' N, DMS longitude 4° 13' 17.544'' E, fig. VII.1b; (Pereira et al., 2024).

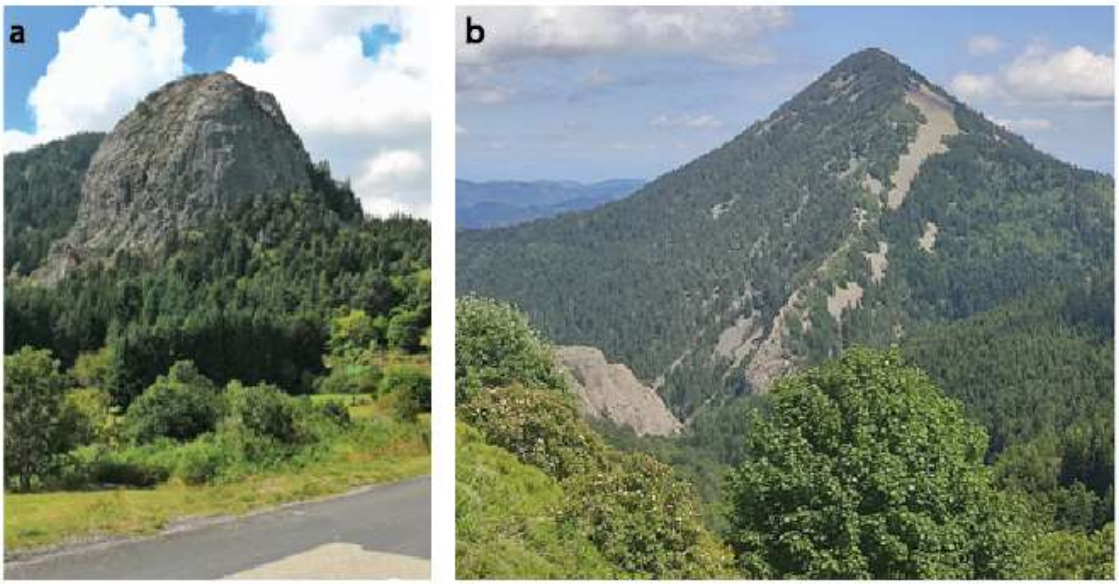

Figure VII.1. a) the Gouleiou neck (named also 'Petit Gerbier'). b) the Suc de Sara ring dyke.

These two volcanic bodies were chosen because,

- they represent the most common bodies that classically developed at shallow depth in volcanic settings, neck and dykes geometries. The Petit Gerbier is a near surface structure, probably a near surfafe volcanic neck, so it has undergone rapid cooling (Arbaret et al., 1993). On the other hand, the Suc de Sara is a deeper emplaced volcanic

dyke with an annular shape and it has undergone slower cooling as illustrated by its tingaïte texture in its core (Mergoil, 1968; Mergoil and Biovin, 1993; Pereira et al., 2024));

- Both are issued from the same volcanic province and they exhibit a close, phonolitic, chemistry and mineralogy.
- Both show evidence of late magmatic, melt segregation assisted by strain localization (Arbaret et al., 1993; Pereira et al., 2024), (see Appendix G for further details);
- these volcanic bodies well outcrop and are easily accessible. Sampling was carried out with a good control on the position of the samples with respect to the margins along which highest shear deformation is known to develop.

2. Geological setting

The Petit Gerbier and the Suc de Sara are part of the Velay volcanic province, located in the southeast of the French Massif Central (fig. VII.2). The area is formed by a thinned Variscan granitic and migmatitic basement and it is characterised by a series of Tertiary horsts and grabens oriented towards N140 (Couzinié et al., 2014; Mergoil, 1968). Monogenic volcanic eruptions over the last 15 Ma have covered the area with alkaline lavas. In the upper Miocene, the area is composed of calcareous sands and lake sediments with Miocene's flora and fauna (de Goer and Mergoil, 1971). The volcanic activity has begun 11.4 Ma with basalts emission, followed by the deposition of stratified pipernoid tuff-lava, covered by layers of basalts that constituted the plateaux of Mezenc. As a result of fissural volcanism, layers of oligoclase aphanitic trachyandesite have been erupted. Between 7.5 and 6.5 Ma there was the formation of the Gerbier de Jonc with alkaline to hyperalkaline phonolitic and trachytic dykes and the formation of the Suc de Sara and de Touron, consisting of volcanic domes and annular structures (Mergoil, 1968) . The Gerbier de Jonc, the Suc de Sara and de Touron form a chain oriented in the NE-SW direction, located in two grabens: the Emblaves graben to the north and the Boutieres graben to the south.

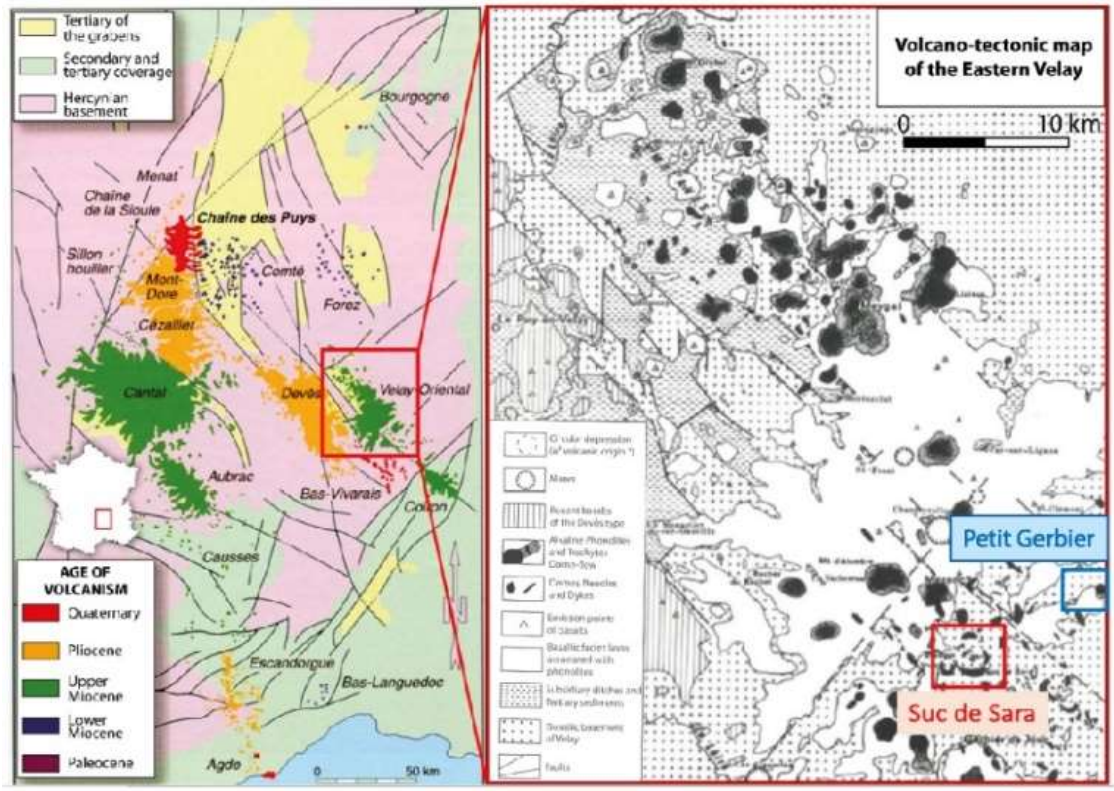

Figure VII 2. a) Geographic positioning of the Velay volcanic province in relation to the different volcanic fields of the French Massif Central (modified from (Boivin et al., 2004)). b) Volcano-tectonic map of Eastern Velay (modified from (Jung, 1971; Pereira et al., 2024)).

The latter is located at the foot of the eastern side of the Mezenc plateau and it represents a depression of 200-300 m. At the margins and inside the graben there are numerous phonolitic bodies. Near the annular structure of Suc de Touron rises a volcanic neck, the Petit Gerbier, where the contact with the underlying granite rock is hidden by abundant scree.

The Petit Gerbier (or Gouleiou) is a needle-shaped structure with an altitude of 1290 m. It is located 1400 m south-east of the village of Borée, near the ring structure of the Suc de Touron (fig. VII.3). It is a phonolite with a trachytic texture, characterised by the abundance of elongated K-feldspar phenocrysts. (Arbaret et al., 1993) showed that there are two mineral shape preferred orientations in the neck: the first corresponds to a pervasive mineral foliation (S plane, fig. VII.3) and the second to C'-type localised bands croscutting the latter (these C'type bands are called inproperly C-type bands by (Arbaret et al., 1993) fig. 3). The microstructure formation hypotheses involve two phases: the

first takes place during the movement of the magma in the magmatic conduit, which produces pervasive foliations and lineations. The second stage occurs in the late magmatic phase, when the crystal fraction increases drastically leading to strain localization that generate the C'-type shear bands.

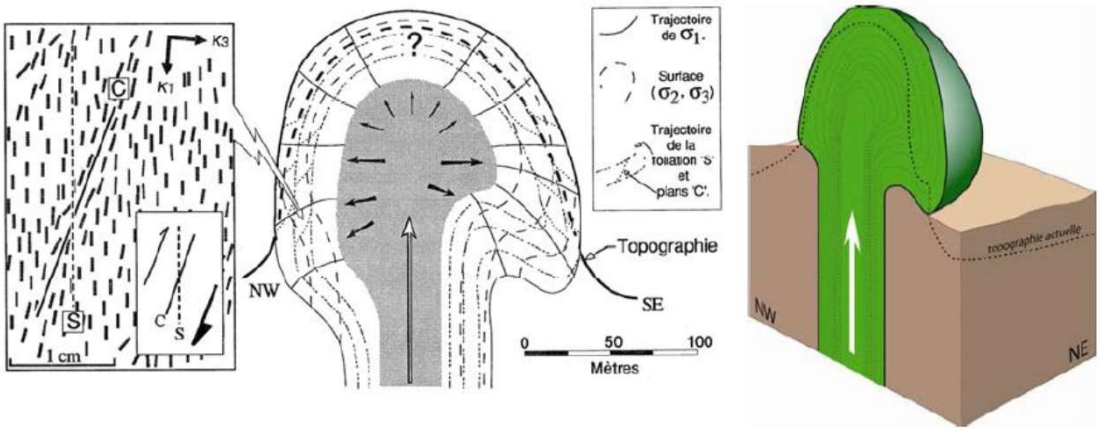

Figure VII.3. Left: local rearrangement of feldspar crystals on the C plane crosscutting the S folaition plane. Centre: schematic section NO – SE showing the radial disposition of the C microbands reorganising the mineral foliation S. Right: Formation of phonolitic extrusion Gouleiou (modifed from (Arbaret et al., 1993)).

The Suc de Sara is a 6.5 Ma old volcanic L-shaped dyke (fig. VII.4a). It is emplaced at shallow depth, equivalent to less than 1.5 kbar, in the Boutières graben in a NW-SE regional compressional stress field (Mergoil, 1968; Mergoil and Biovin, 1993). Its maximum height is 1.521 m. It is the most differentiated and peralkaline volcanic body of the Velay province, undersaturated in silica, with a phonolitic composition. The inner part of the dyke is composed of a homogeneously foliated, fine-grained tinguaïte that contains sodium pyroxenes (aegirine) and alkaline feldspar (orthoclase, sanidine, anorthoclase), the latter being often included in plagioclase. When approaching the outer margin of the dome, the tinguaïte texturally evolves to a nepheline phenocryst-rich phonolite crosscut by an anastomosing pattern of shear bands that are mostly parallel to the mineral foliation (fig. VII.4b). These shear bands, filled by late magmatic melts with analcime and aegirine, express the strain localization during a near solid state close to the chilled margin during its final emplacement (Pereira et al., 2024).

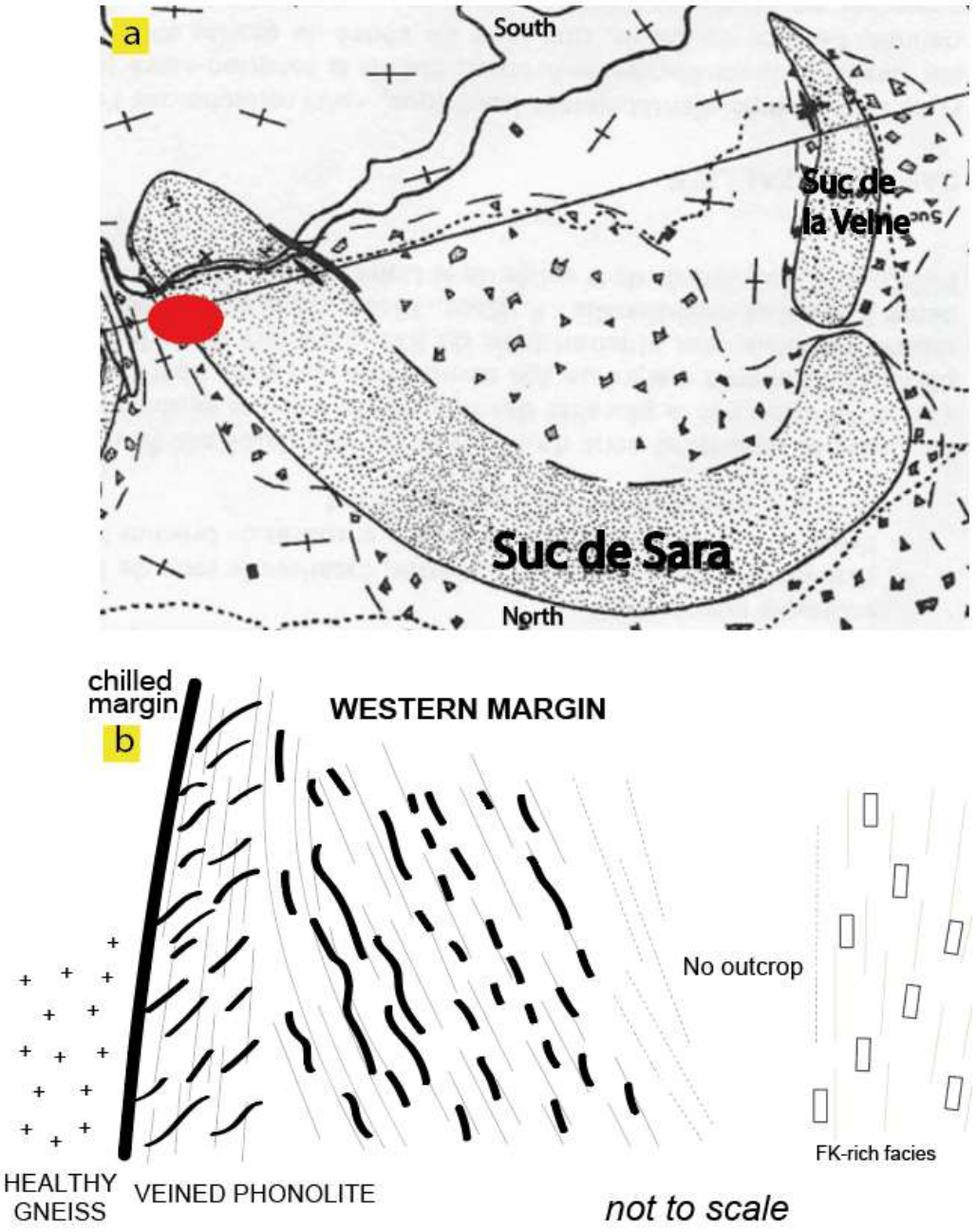

Fig. VII.4. a) Annular structure of Suc de Sara. The sampling area is highlighted in red (modified from (Mergoil, 1968)). b) Cross section of the the western margin of the Suc de Sara intrusion (Pereira et al., 2024).

3. Sampling strategy

The areas selected in the two volcanic bodies for sampling are representative of different deformation intensities encoutered in the deformation gradient developed near the margins. Therefore, samples were taken as close as possible from the margins and they were completed with samples representative of inner, and therefore potentially less deformed, facies (fig. VII.5).

For Petit Gerbier neck (fig. VII.5a), two samples were collected. One was taken in the outcrop close to the D378 road, this place being interpreted as the closest to the hidden margin of the neck (PG3, fig. 5a; (Arbaret et al., 1993)). At the sample scale, the phonolite appears strongly foliated. The second sample was taken on the Northwest wall where the most inner part of the volcanic body is outcropping (PG1, fig. VII.5a). This sample does not show any structural anisotropy but its foliation and lineation is known through the AMS measurement performed by (Arbaret et al., 1993).

For the Suc de Sara dyke, 2 samples were chosen (SA1 and SA4) among the sample collection acquired over the complete section of the dyke performed by Pereira et al., 2024. They correspond to the southwestern margin of the dyke outcropping near the "Coix de la Scie" crossroad (fig. VII.5b). This margin is caracterised by a chilled, 20 cm thick, zone that prevented outgassing and melt escape toward the country rock (Pereira et al., 2024).

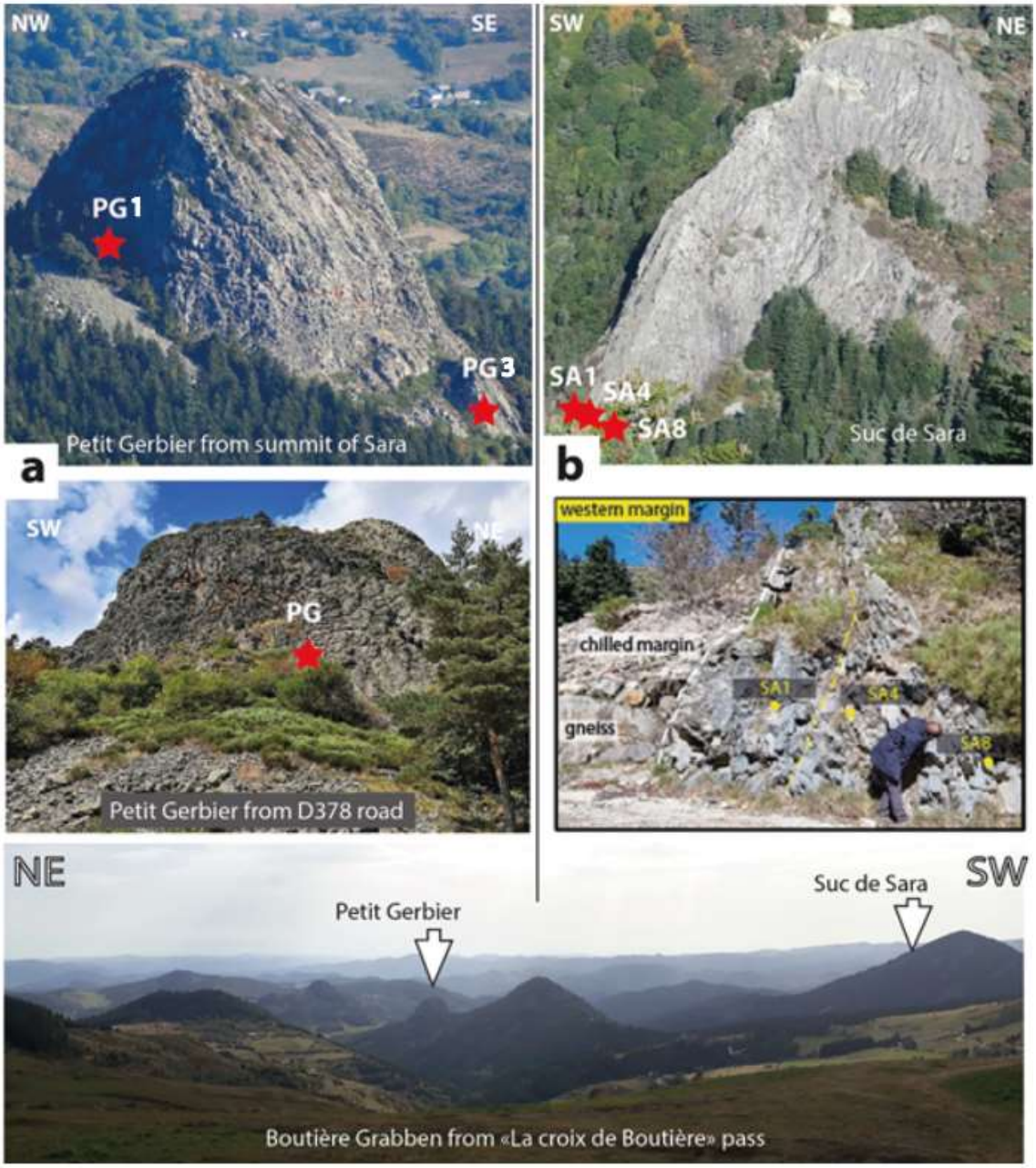

Figure VII.5. a) Sample location in Petit Gerbier neck. b) Sample location in the Suc de Sara dyke. Bottom, the two phonolitic bodies in the landscape. View taken from the "La croix de Boutière" pass and toward the Boutière grabben.

The excellent exposures along the path and in the riverbed of the Eysse river allow to observe microstructure variations from the margin toward the core (fig. VII.5). Sample SA1 is composed by a groundmass with a phonolitic texture crosscut by two populations of aegirine-rich veins: one population is closely parallel to the mineral foliation, while the second population, forming a dense anastomosing network, is secant to it (fig.

VII.6a). SA4 sample show a tinguaite texture characterized by a clear mineral foliation marked by millimetric aegirines, while rare rounded alkali felspar porphyroclasts show evidence of intense deformation (fig. VII.6b). This foliation is crosscut by rare, regularly spaced aegirine-rich veins.

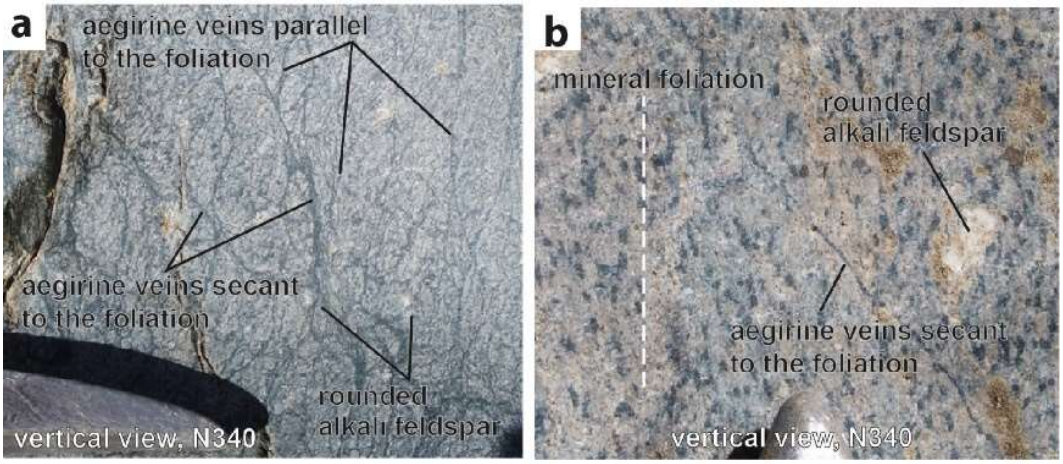

Figure VII.6. a) SA1 sample. B) SA4 sample. From Pereira et al., 2024.

4. Results

The following results present the microstructural and chemical analyses carried out on the natural samples. All samples were cut along a section parallel to the mineral lineation and perpendicular to the foliation. The structural plane is named XZ, where X is the lineation and Z is perpendicular to the foliation plane. Petit Gerbier and Suc de Sara samples were analysed by a scanning electron microscope (SEM, Merlin Compact Zeiss, ISTO) to study microstructures and textures. Chemical mapping and quantitative chemical analyses were performed using an electron microprobe (EMPA; Cameca SX Five equipped, ISTO) with an acceleration voltage of 15 kV and a beam current of 10 nA. Crystal structure and crystal orientation analyses were performed using Raman and EBSD.

4.1 Crystal morphology

Petit Gerbier neck and Suc de Sara dyke

In the following section, the equivalent diameter ϕ and aspect ratio R of PG3 sample (analyzed in the penetrative fabric and bands; fig. VII.7a), of PG1 sample (analyzed in the penetrative fabric and analcime-rich lenses; fig. VII.7b) and SA1 sample (analyzed in the penetrative fabric, fig. VII.7c) are calculated. Only K-feldspar crystals are considered because they represent more than 70% of the total crystals and therefore form the solid network.

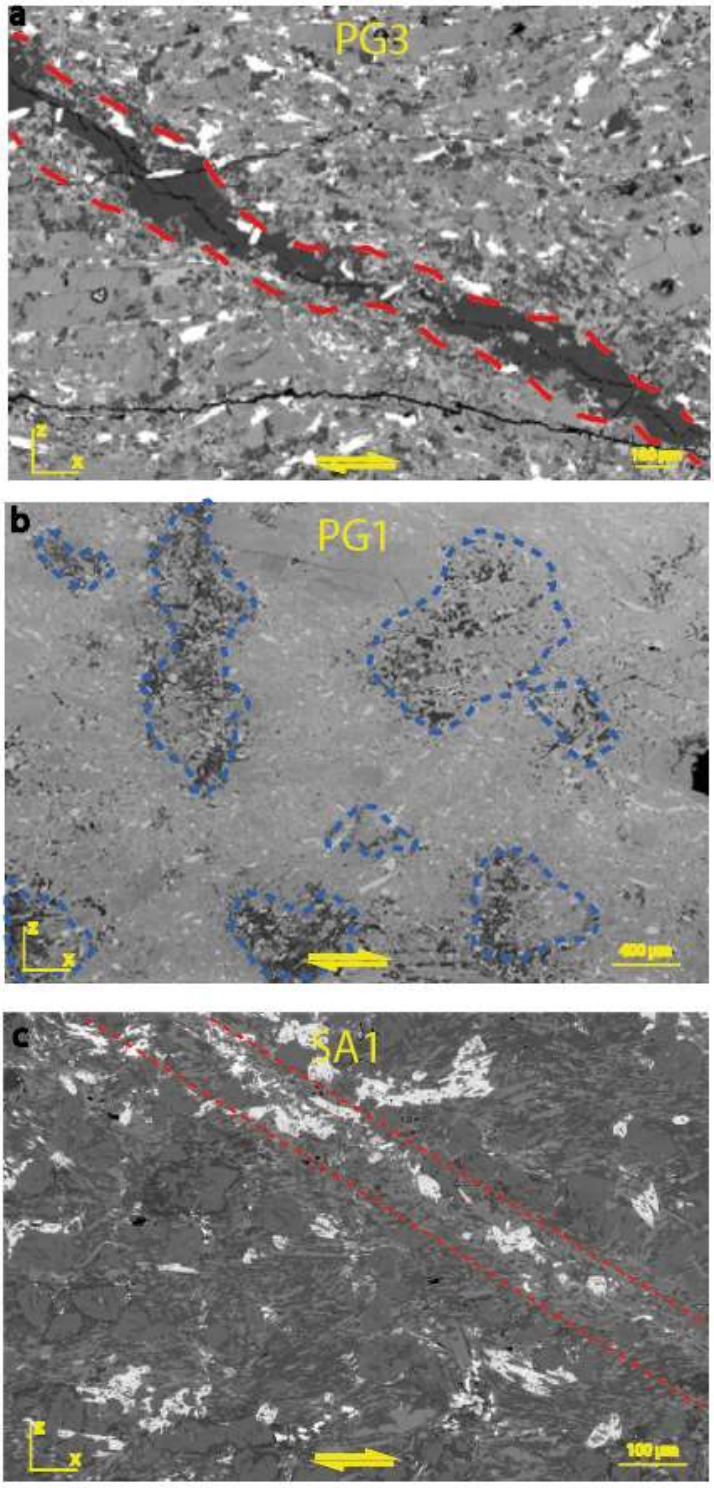

Figure VII.7. SEM picture of natural samples. a) PG3 sample. The red dotted lines highlight the analcime-rich band. b) PG1 sample. The blue dotted lines highlight the voids and analcime-rich lenses. c) SA1 sample. The red dotted lines highlight the aegirine-rich veins.

Equivalent diameter ϕ

The equivalent diameters ϕ of feldspar from PG3 sample show an arithmetic mean value of 18.10±18.62 μm, a harmonic mean value of 10.70 μm and a mode value of 7.5 μm (fig. VII.8a). Within the bands, ϕ is 20.58±21.93 μm and the harmonic mean is 12.47 μm, with a mode of 10 μm (fig. VII.8b).
The PG1 sample has an arithmetic mean of the equivalent diameter ϕ of 59.80±60.71 μm, a harmonic mean of 34.76 μm and a mode of 50 μm (fig. VII.8c).
The SA1 sample shows an arithmetic mean of the equivalent diameter ϕ of 11.74±12.75 μm, a harmonic mean of 9.30 μm and a mode at 9 μm (fig. VII.8d).

All crystal size populations exhibit a log-normal distribution. For the PG samples, the arithmetic mean values have a large deviation compare to the harmonic mean, while the harmonic mean and mode values are closely similar. The most representative values of the samples are the small crystals.
The shear band crystals of the PG3 sample (figure VII. 8b) have a larger equivalent diameter ϕ than the crystals in the penetrative fabric. This size difference could have promoted stress localization.
The crystals of the PG1 sample (fig. VII.8c) have a larger equivalent diameter ϕ than the PG3 sample (fig. VII.8a). This could be due to slower cooling in the inner part of the volcanic neck leading to the formation of larger crystals.
The crystals of the SA1 (fig. VII.8d) sample show minor differences between arithmetic mean, harmonic mean and mode. However, the log-normal trend is maintained and the most representative grain sizes are the smaller ones. Compared to PG, SA1 has smaller equivalent diameters, probably due to the strong deformation it has undergone.

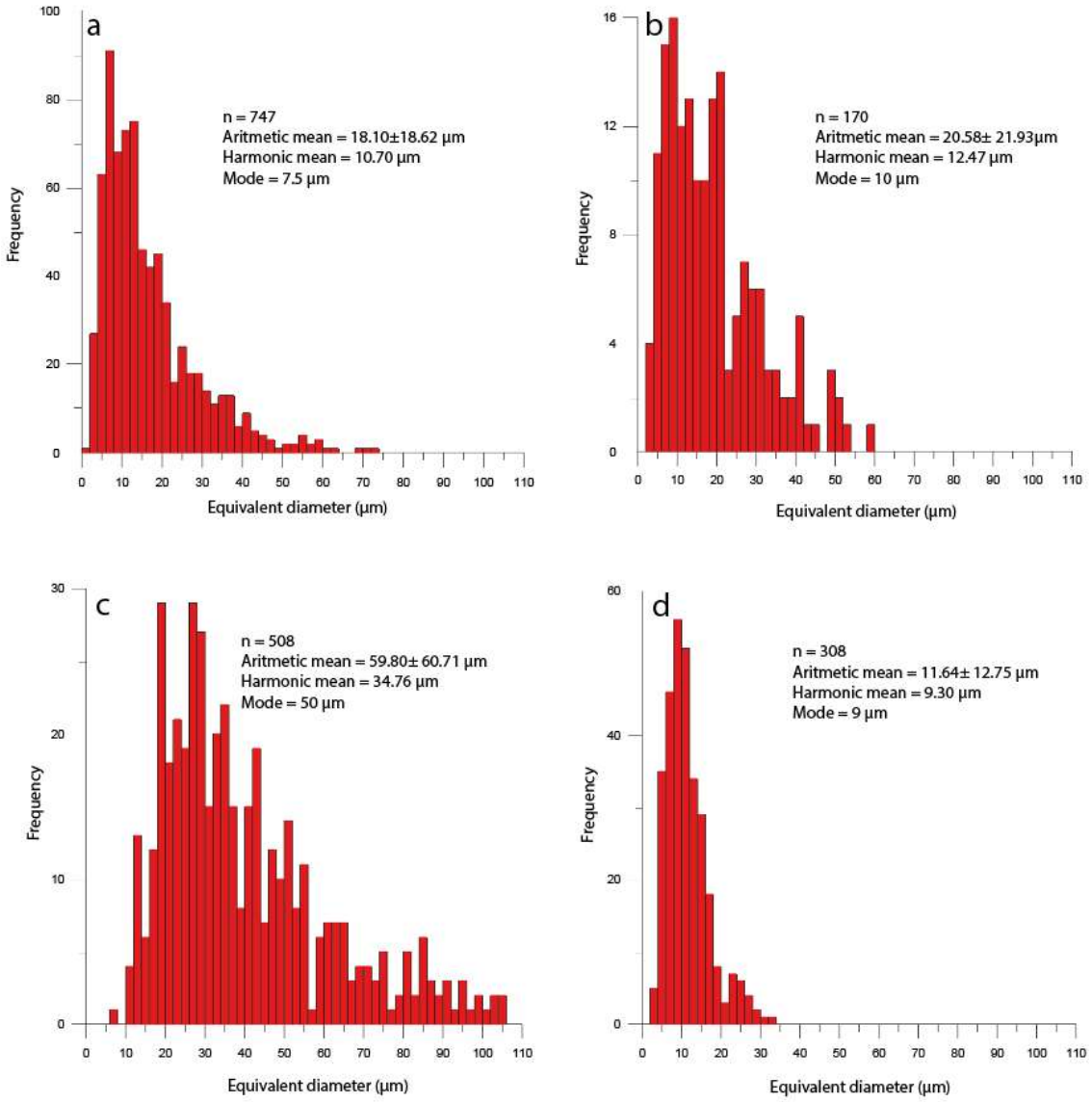

Figure VII.8. Histograms of equivalent diameters. a) Penetrative fabric of PG3 sample. b) Bands area of PG3 sample. c) Penetrative fabric of PG1 sample. d) Penetrative fabric of SA1 sample.

Aspect ratio R

The PG3 sample in its penetrative fabric shows an arithmetic mean value of aspect ratio R of 3.77±2.11, a harmonic mean value of 2.92 and a mode of 3.0 (fig. VII.9a). In the bands of PG3 sample, the arithmetic mean is 4.04±2.09, the harmonic mean is 3.17 and to modes are found at 2.80 and 4.20 (fig. VII.9b).

The PG1 sample shows an arithmetic mean of the aspect ratio R of 4.78±2.15, a harmonic mean of 3.99 and a mode of 3.20 (fig. VII.9c).

The SA1 sample has an arithmetic mean of 4.52±0.73, a harmonic mean of 3.89 and a mode at 3.50 (fig. VII.9d).

The PG3 sample shows a double population of crystals in its shear bands. The first population of feldspars show an aspect ratio R similar to those forming the penetrative fabric while the second population is composed of more elongated crystals.

The PG1 sample shows higher aspect ratio R values than the PG3 sample. This may be due to the same reason as in the previous paragraph for the equivalent diameter ϕ: slow cooling in the inner zone of the volcanic neck caused the formation of larger crystals with lower aspect ratio R.

The crystals of sample SA1 show very similar R aspect ratios to those of sample PG1.

For all samples the trend is log-normal and the most realistic mean is the harmonic.

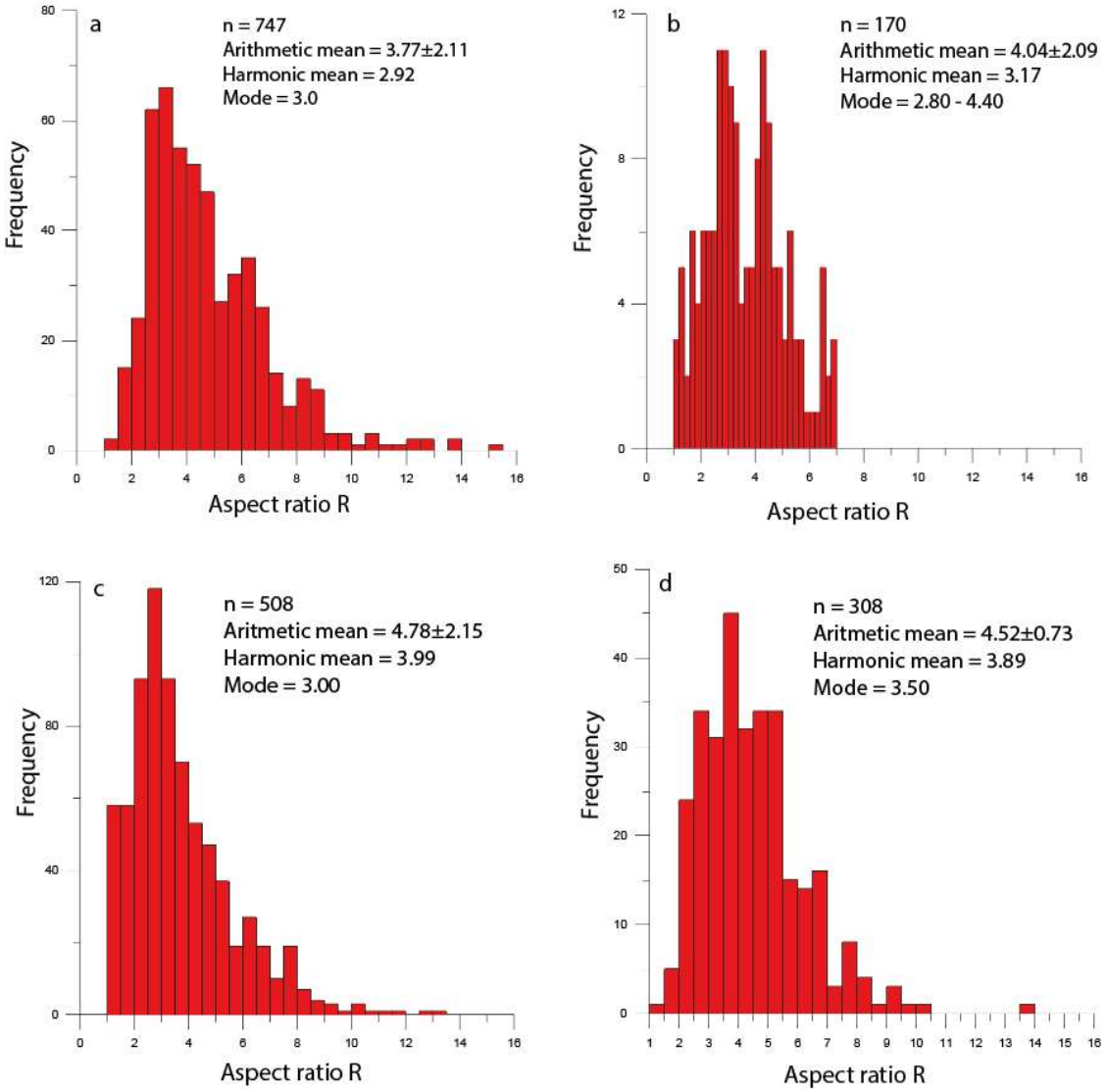

Figure VII.9. Histograms of aspect ratio R calculated in a) penetrative fabric of PG3 sample, b) bands area of PG3 sample, c) penetrative fabric in PG1 sample, d) penetrative fabric of SA1 sample.

5. Chemical composition

It is presented in this paragraph the chemical analyses of samples from Petit Gerbier neck (data in table VII.1), while the analyses of Suc de Sara dyke are summarized in detaill in (Pereira et al., 2024).

5.1. Petit Gerbier neck

Both PG3 and PG1 samples show the same paragenesis in the penetrative fabric. It includes K-feldspars, plagioclases, pyroxenes and rare amphiboles (fig. VII.10 and table VII.1). Analcime is well developed as late magmatic phase in the bands (fig. VII.10) and in lenses (fig. VII.7b).

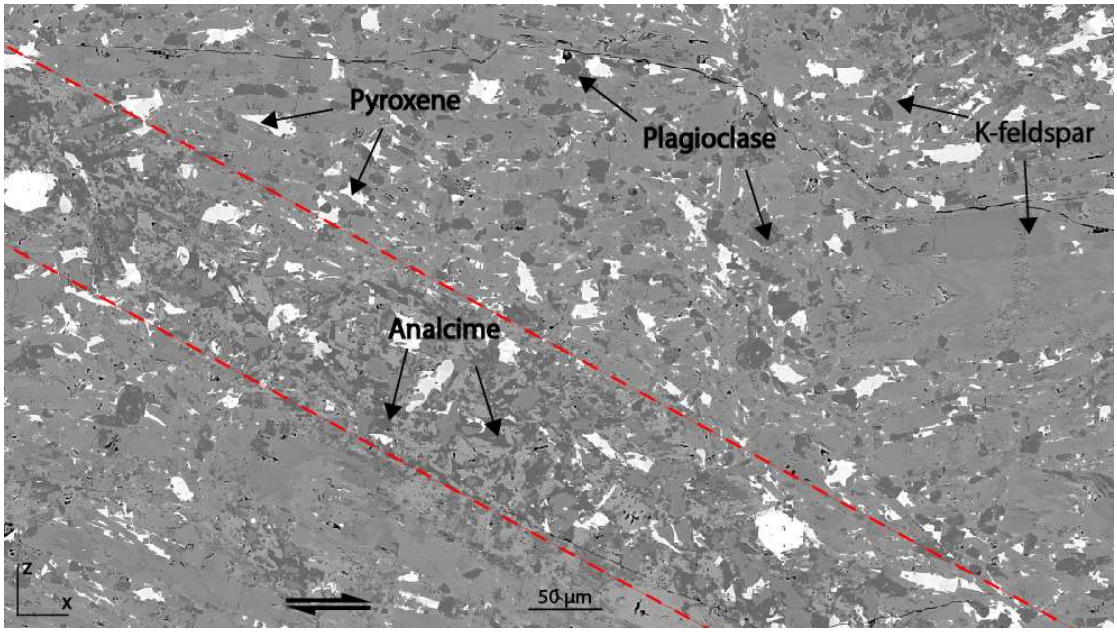

Figure VII.10. SEM picture of PG sample. Minerals analyzed by microprobe are shown. The dotted red line indicates the edges of a C'-type band.

Several EDS maps were performed on both the PG3 and PG1 samples in order to highlight the chemical difference between the penetrative fabric and the bands or altered areas. The results are shown in figures VII.11 and VII.12. Further EDS maps are shown in Appendix E. In the bands and lenses there is a depletion in potassium and silica and an enrichment in sodium compared to the minerals located in the penetrative fabric.

a

Mineral	Sanidine		Plagioclase		Aegirine		Aegirine-augite		Kaersutite		Analcime	
Sample	PG3		PG3		PG3		PG3		PG3		PG3	
n	18		20		14		PG3		10		17	
		±		±		±		±		±		±
Na_2O	6.92	0.79	13.20	4.22	11.60	0.99	1.46	0.42	2.35	0.08	10.37	1.13
Al_2O_3	18.67	0.58	23.64	1.57	0.90	0.15	2.44	0.85	13.81	0.36	23.30	0.56
SiO2	65.34	0.97	52.53	2.31	51.47	0.75	47.17	0.71	38.53	0.29	56.28	0.53
K_2O	6.12	1.40	0.18	0.09	0.02	0.02	0.03	0.03	1.30	0.09	0.31	0.25
CaO	0.56	0.31	0.56	0.39	3.36	1.78	20.00	0.68	11.97	0.08	0.06	0.06
TiO_2	0.04	0.05	0.01	0.01	2.70	0.76	1.28	0.42	5.57	0.17	0.01	0.02
FeO	0.19	0.16	0.11	0.09	26.63	1.35	20.36	1.15	12.60	0.45	0.23	0.10
MnO	0.06	0.11	0.03	0.04	0.68	0.25	1.47	0.33	0.13	0.06	0.05	0.04
MgO	0.00	0.01	0.03	0.01	0.84	0.67	3.84	1.26	11.10	0.62	0.01	0.01
Total	97.90		90.29		98.20		98.05		97.36		90.62	

b

Mineral	Sanidine		Albite		Aegirine-augite		Analcime	
Sample	PG1		PG1		PG1		PG1	
n	17		10		PG1		12	
		±		±		±		±
Na_2O	6.65	0.49	9.06	1.32	2.36	0.94	12.34	1.14
Al_2O_3	19.24	0.30	25.71	0.62	1.62	0.78	23.45	0.67
SiO_2	65.98	0.26	63.57	1.42	47.92	1.06	53.62	1.53
K_2O	7.59	0.82	0.86	0.75	0.04	0.05	0.14	0.05
CaO	0.19	0.13	0.09	0.07	19.04	1.62	0.16	0.21
TiO_2	0.02	0.03	0.06	0.03	0.98	0.30	0.01	0.02
FeO	0.02	0.14	0.50	0.21	21.11	1.79	0.37	0.36
MnO	0.02	0.03	0.06	0.05	1.74	0.19	0.05	0.06
MgO	0.00	0.01	0.01	0.01	4.14	1.06	0.01	0.01
Total	99.71		99.92		98.95		90.15	

Table VII.1. Chemical composition of natural samples analysed by electron microprobe. n = number of analyses. a) PG3 sample, b) PG1 sample. Because analcime is an anhydrous phase and the amount of water can not be quantified with the electron microprobe, the error is high.

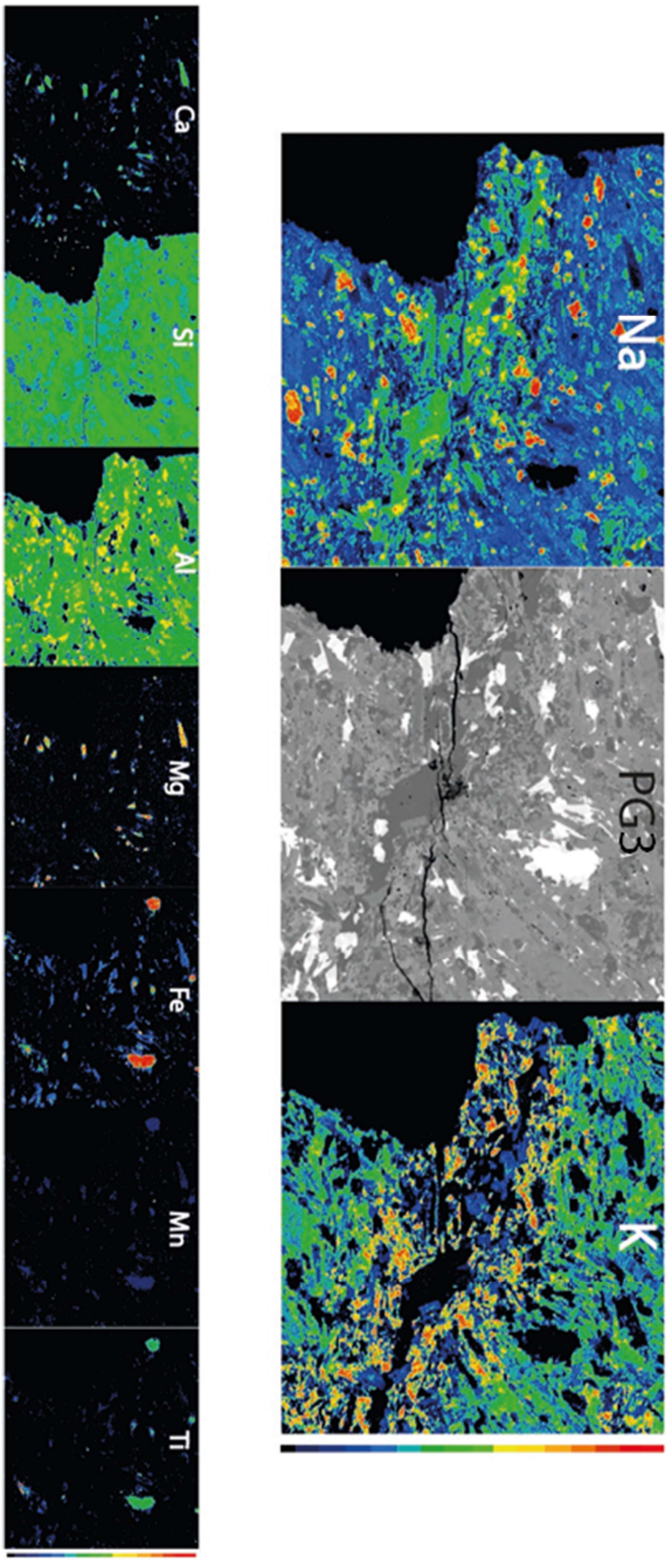

Figure VII.11. EDS mapping of Na, Ca, K Si, Al, Mg, Fe, Mn, Ti on a selected area of PG3 sample.

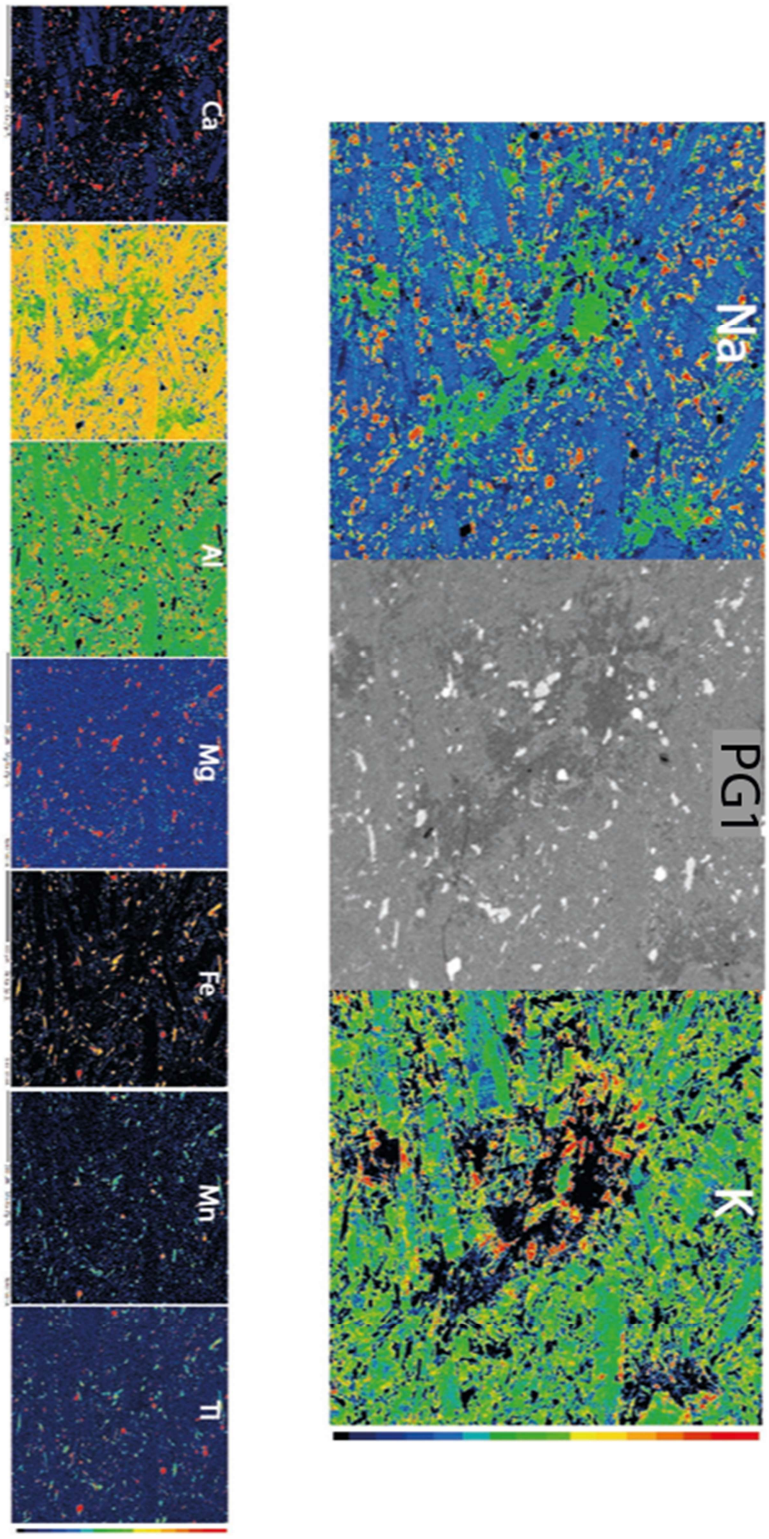

Figure VII12.. EDS mapping of Na, Ca, K Si, Al, Mg, Fe, Mn, Ti on a selected area of PG1 sample.

5.2. Suc de Sara dyke

The petrology and geochemistry of all the different facies encountered in the Suc de Sara dyke are detailed in the work of (Pereira et al., 2024). The phonolitic facies developed near the chilled western margin of the dyke is composed of idiomorphic phenocryst of alkali feldspar that exbibit potassium-rich overgrows, and nepheline (fig. VII.13; (Pereira et al., 2024)). Alkali feldspars phenocrysts are also affected by late albite recrystallization mainly developed on the periphery of phenocrysts, but also locally propagated into the phenocryst by following the crystallographic planes (Peireira et al., 2024). The phenocrysts are embedded in a groundmass composed of feldspathoids (nepheline and sodalite), sodic pyroxene (aegirine), aenigmatite, alkali feldspar and albite. Pyroxenes are idiomorphic and exhibit a poikilitic texture as they have included smallest idiomorphic feldspar microlites. Aenigmatites are also often idiomorphic and usually associated with pyroxenes. As also observed with feldspar phenocrysts, square sections of nepheline grains exhibit a reactional rim of albite composition (fig. VII.13). Finally, the matrix shows a porosity expressed as isolated pores entrapped between feldspar microlites (fig. VII.13). In the shear bands the paragenesis change as it is composed of aenigmatite, aegirine, lavenite, analcime and iron oxides. In the inner tinguaite facies the groundmass is similar but the texture change with larger idiomorphic phenocrysts of aegirine, alkali feldspar and abundant square shaped nepheline (fig. VII.14). Aegirine-rich bands alternate with domains characterized by a fine groundmass wrapping around abundant idiomorphic square-shaped nepheline crystals. The mineral foliation is well developed and clearly marked by the orientation of elongated aegirine crystals. The porosity is much less developed than in the phonolitic facies close to the margin and the analcime-rich lenses does not show any significant anisotropy. No C'-type shear bands are noticed (fig. VII.14).

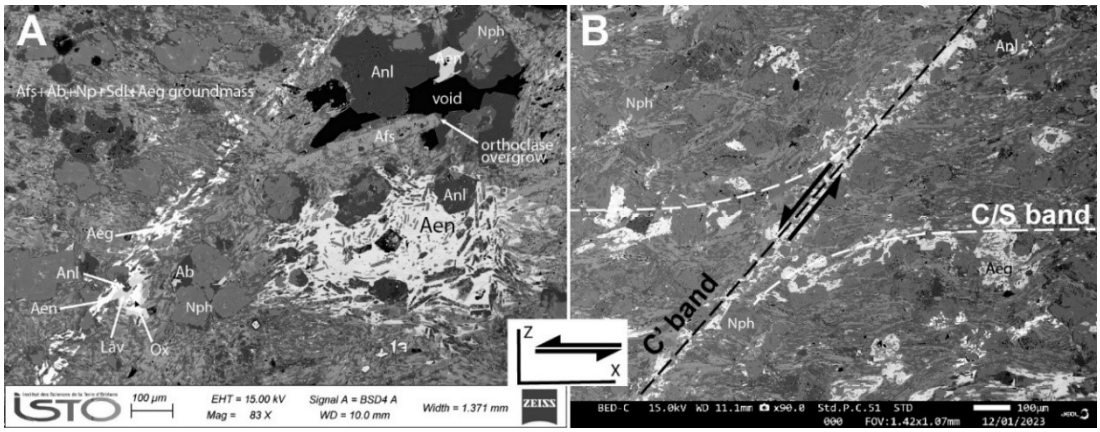

Figure VII.13. Backscattered electron (BSE) image of the veined phonolite near the Western chilled margin (SA3) showing the textural relationships between magmatic and late-magmatic assemblages. [X, Z] sections with the lineation x horizontal, sinistral bulk sense of shear. a) The magmatic assemblage is composed of alkali feldspar (Afs), albite (Ab), sodalite (Sdl) and idiomorphic grains of aegirine (Aeg). The late magmatic assemblage that fill the aegirine-bearing veins is mainly composed of analcime, aenigmatite (Aen), aegirine, låvenite (Lv) and iron oxides (Ox). Aenigmatite appears also as a poikilitic phase in the groundmass while idiomorphic analcime is present in voids. b) The late magmatic assemblage fills the anastomosed pattern of veins formed by the C bands parallel to the mineral foliation S and the C' bands along which normal synthetic shearing with respect to the bulk sense of shear is highlighted by the bending of the C/S planes. (Pereira et al., 2024).

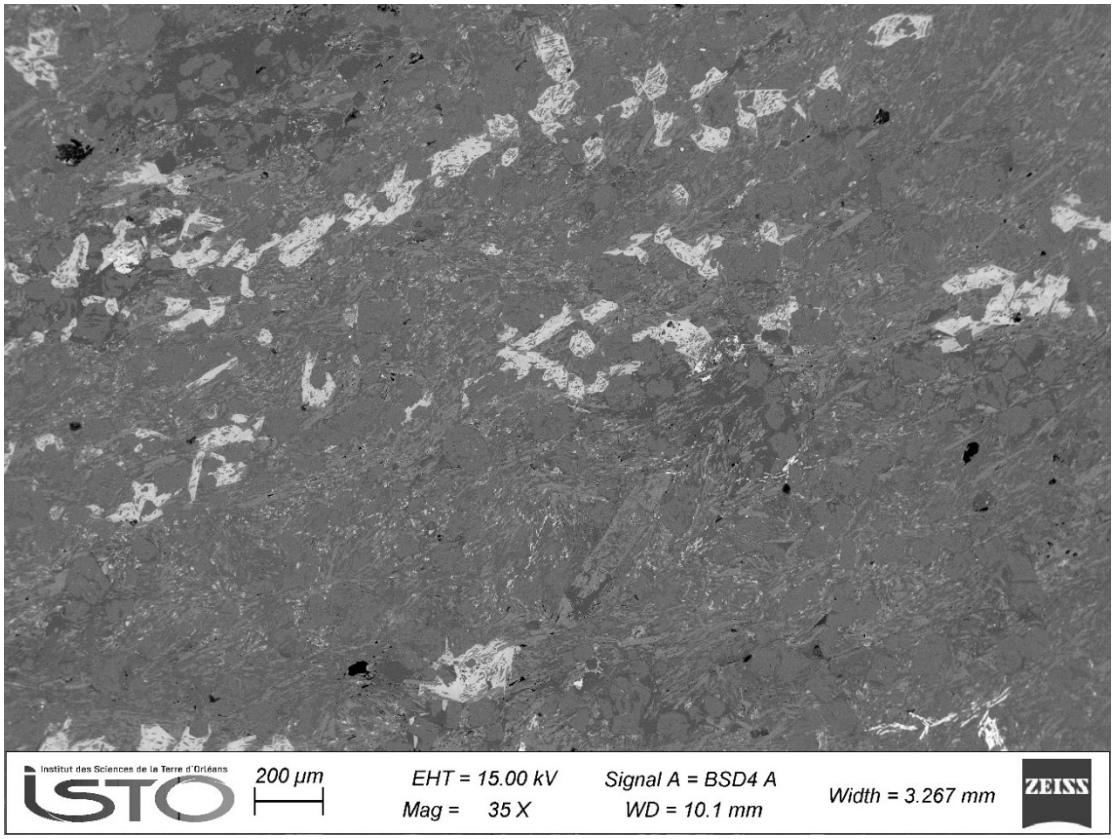

Figure VII.14. Backscattered electron image of the banded tinguaite facies few meters away from the western margin of the Suc de Sara (SA4 sample).

6. Raman spectra

Raman analyses were carried out on analcime crystals present either in C'-type bands or lenses developed found in both volcanic bodies (see example for the Petit Gerbier neck in fig. VII.15). Låvenite crystals were found in Suc the Sara. The results were compared with the spectra issued from the RRUFF database, ID R040128 and ID R120044 respectively. The Raman spectrometry confirms the presence of these two mineral phases in the late magmatic assemblage that fill the voids and the aegirine-rich veins of the phonolite facies (fig. VII.16).

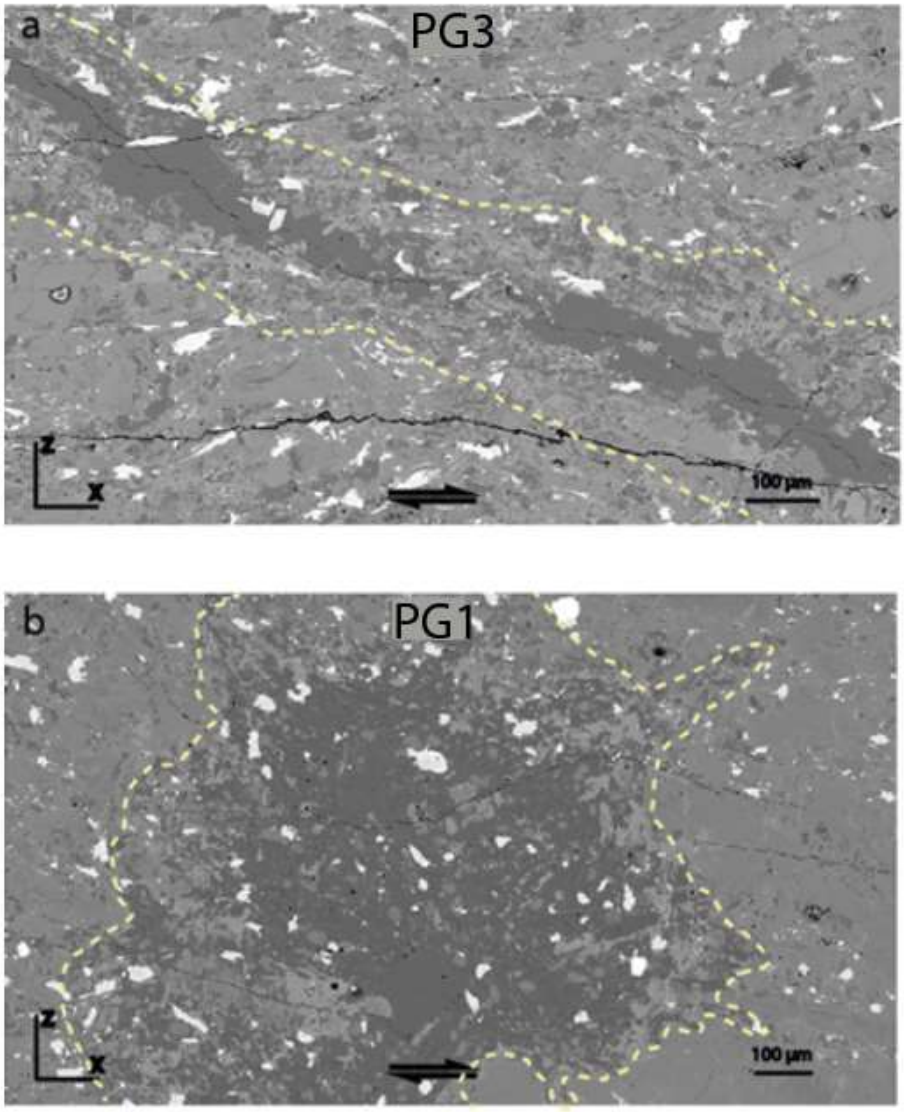

Figure 15. SEM images of the areas analyzed by Raman. Dashed yellow lines border the bands and lent of melt areas. a) PG3 sample, b) PG1 sample.

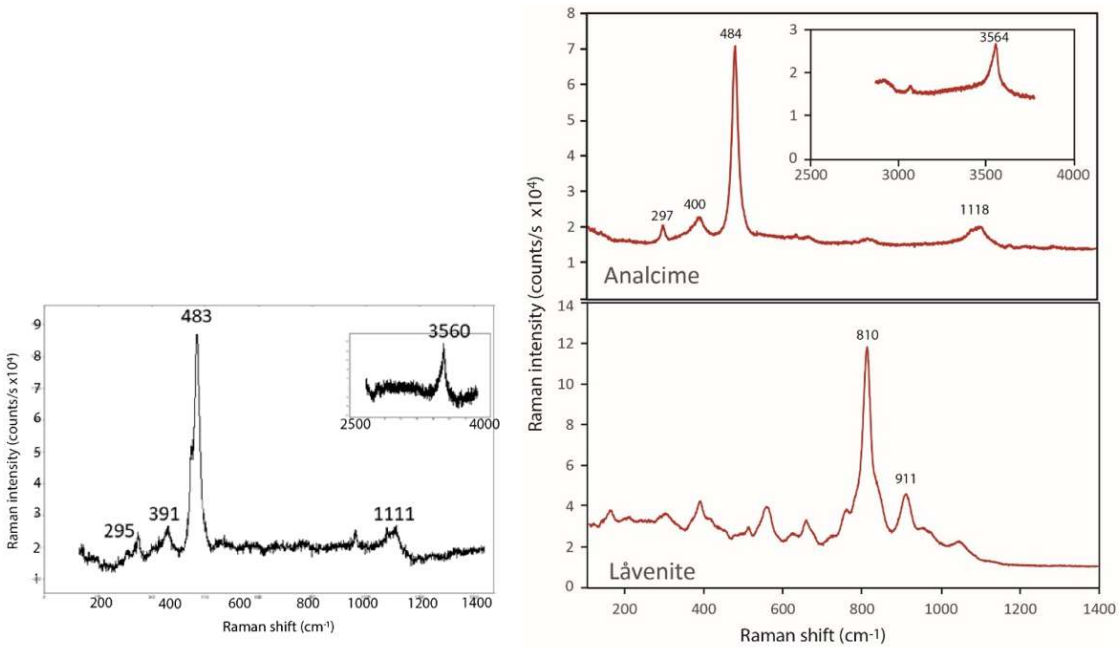

Figure 16. Left: Raman spectra of analcime measured in PG3 and PG1 samples. Right: Raman spectra of analcime and Lavenite measured in the Suc de Sara dyke (Pereira et al., 2024).

7. Microstructural analysis

In this section, the microstructures formed in samples PG3, PG1 (Petit Gerbier, outer and inner part) and SA1 (Suc de Sara, outer part) were analyzed and studied.

7.1. Petit Gerbier

Performing large-scale analyses, PG3 sample (XZ section, fig. VII.17a) shows bands with a preferential orientation at -15° with respect to the shear direction (fig. VII.17b). The bands are distributed over the entire surface of the sample and the distance between one band and another is not uniform, it can range from tens of microns to 2-3 mm. The average thickness of the bands is between 50 µm and 100 µm.

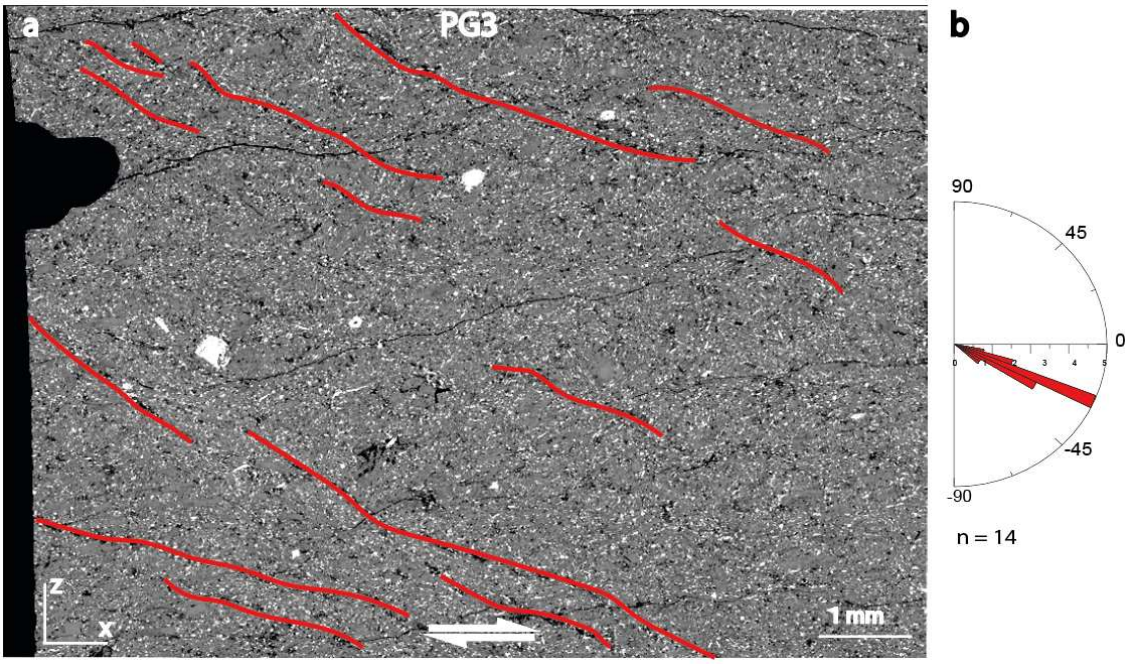

Figure VII.17. a) Panoramic view of PG3 sample. The red lines indicate the direction of the bands. b) Preferred orientation of the PG3 sample bands. n = number of measures.

Microstructural analyses were performed in the penetrative fabric and in the shear bands or lenses. Some area shows strong late magmatic recrystallizations (figure VII.18), so microstructural analyses were only performed on crystals that maintain their crystal habit. Figure VII.18 is an illustration of the crystals analyzed in a band of PG3 sample.

The analysis by intercept method of the penetrative fabric of sample PG3 (fig. VII.19a) shows the eccentricity value at R_i = 1.42 and the direction of orientation of the mean tensor ellipse at α = 1.20° from the shear plane (fig. VII.19b). The orientations of the long axes of the local tensor ellipse is at 15° (fig. VII.19c).

The crystals were then drawn by hand using Adobe Illustrator and colored using the SPO2003 software, in order to better characterize the orientations of the crystals. In the penetrative fabric (fig. VII.20a) the inertia tensor ellipse has an eccentricity R_x = 2.36 and an inclination α = 1.23° (fig. VII.20b). The orientations of the crystals were assembled in the rose diagram showing a preferential direction between 10° and -10° (fig. VII.20c).

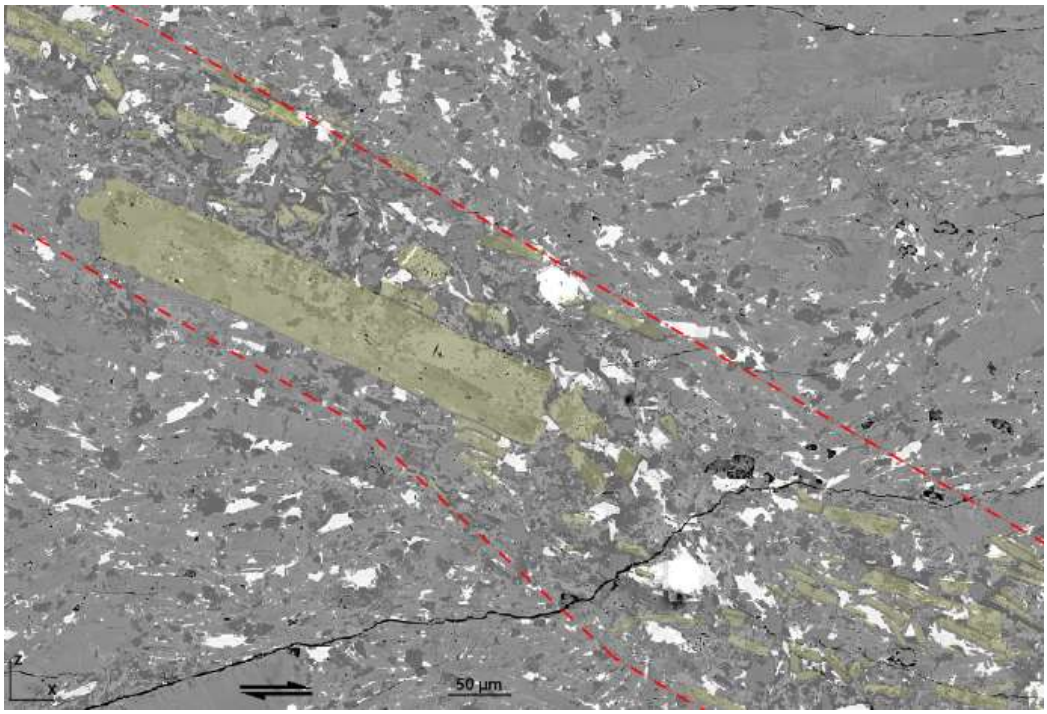

Figure VII.18. Zoom on a C'-type shear band of the PG3 sample. The band is outlined by the red dotted lines. Crystals that can be analysed by SPO and Intercept are coloured yellow.

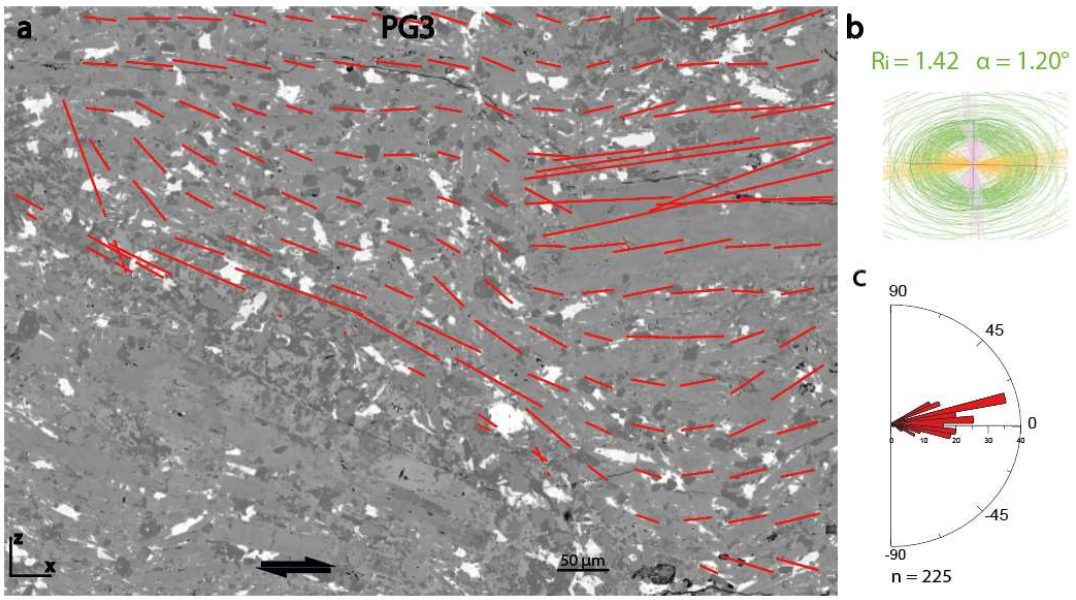

Figure VII.19. SEM image of sample PG3. The red lines represent the long axes of the local tensor ellipses of the shape fabrics of the penetrative fabric. b) Mean tensor ellipse of the shape fabric. α = orientation of the long axis of the ellipse, R_i = eccentricity of the mean ellipse. c) Rose diagram of long axes of local tensor ellipses. n = number of measures.

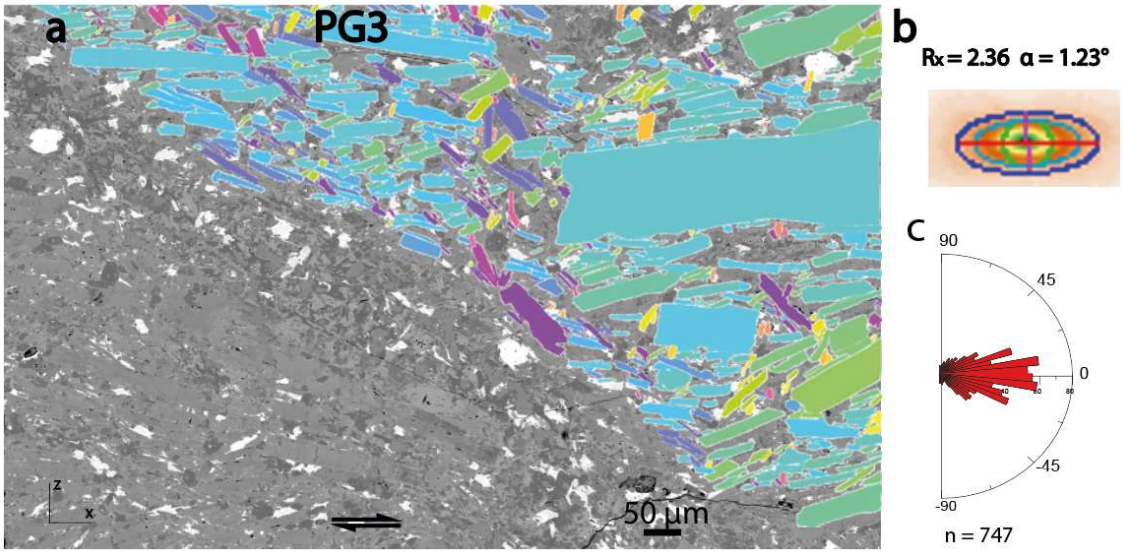

Figure VII.20. a) Preferential crystal orientation of sample PG3 in the penetrative fabric. b) Inertia tensor ellipse of the penetrative fabric. c) Rose diagram of the preferential direction of the crystals. n = number of measures.

In the bands of sample PG3 (fig. VII.21a) the eccentricity value is R_i = 2.03 and the direction of orientation of the mean tensor ellipse is α = -20.55° (fig. VII.21b). The orientations of the long axes of the local tensor ellipse is at -22° (fig. VII.21c).

The crystals analysed using the SPO software (fig. VII.22a) show a inertia tensor ellipse with R_i = 3.23 and α = 23.41° (fig. VII.22b). The rose diagram shows a preferential direction at -21° (fig. VII.22c).

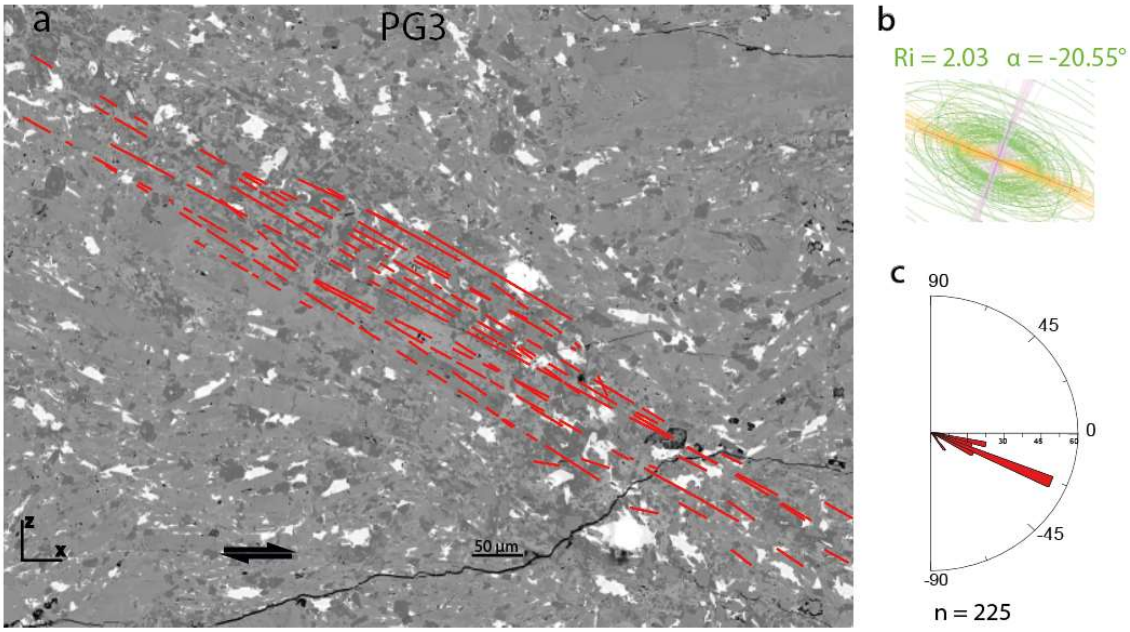

Figure VII.21. Preferential orientation of sample PG3 in a band. a) [XZ] SEM image of the sample. The red lines represent the long axes of the local tensor ellipses of the shape fabrics. b) Mean tensor ellipse of the shape fabric. R_i = eccentricity of the mean ellipse, α = orientation of the long axis of the ellipse. c) Rose diagram of long axes of local tensor ellipses. n = number of measures.

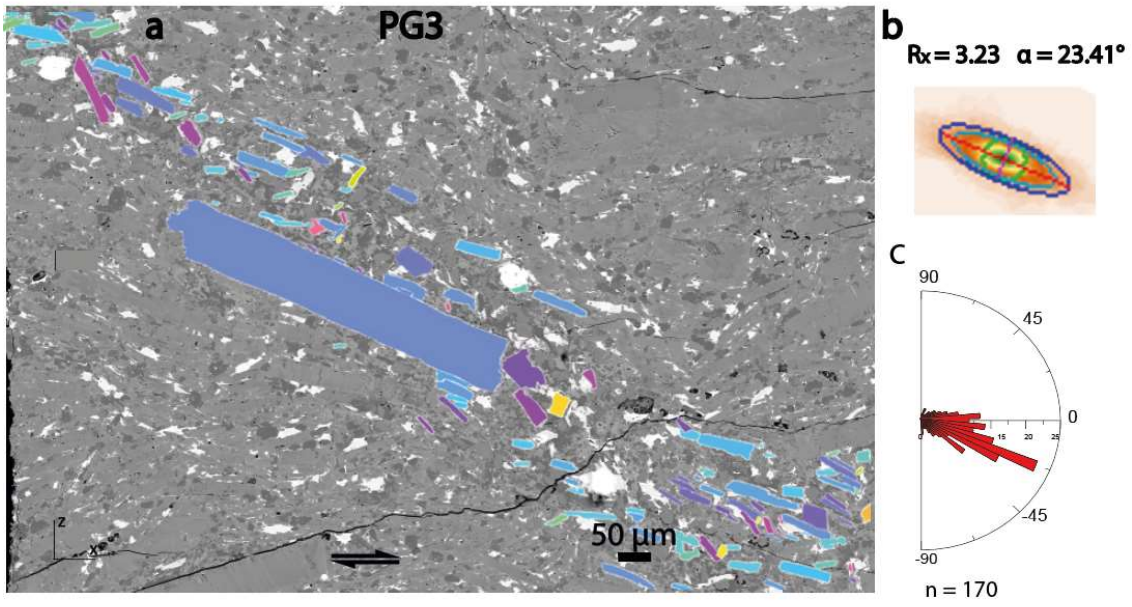

Figure VII.22. a) Orientation of the long axes of the K-feldspar in sample PG3. b) Inertia tensor ellipse in the shear band. c) Roses diagram of individual crystal orientations. n = number of measures.

The PG1 sample (fig. VII.23a) shows no bands of deformation, but rather a homogeneous deformation distributed over the entire sample area. No distinction is made between penetrative fabric and late magmatic lenses when analysing the sample. The resolution of the images and the similar colour of the crystals only allowed the microstructural study of a part of the minerals, about 50%. It is considered that this percentage is sufficient to obtain reliable results and a realistic average.

From the analyses performed with the Intercept software (fig. VII.23a), the sample has an eccentricity R_i value of 2.14 and it has the direction of orientation of the mean tensor ellipse α at 12.24° (fig. VII.23b). The preferred orientation of the long axis shows a preferred orientation at 25° (fig. VII.23c).

Crystals drawn by hand (fig. VII.24a) and analysed with the SPO software show a eccentricity of the inertia tensor ellipse R_x = 2.78 and α = 15.96° (fig. VII.24b). The rose diagram shows an orientation between -6° and 45° (fig. VII.24c).

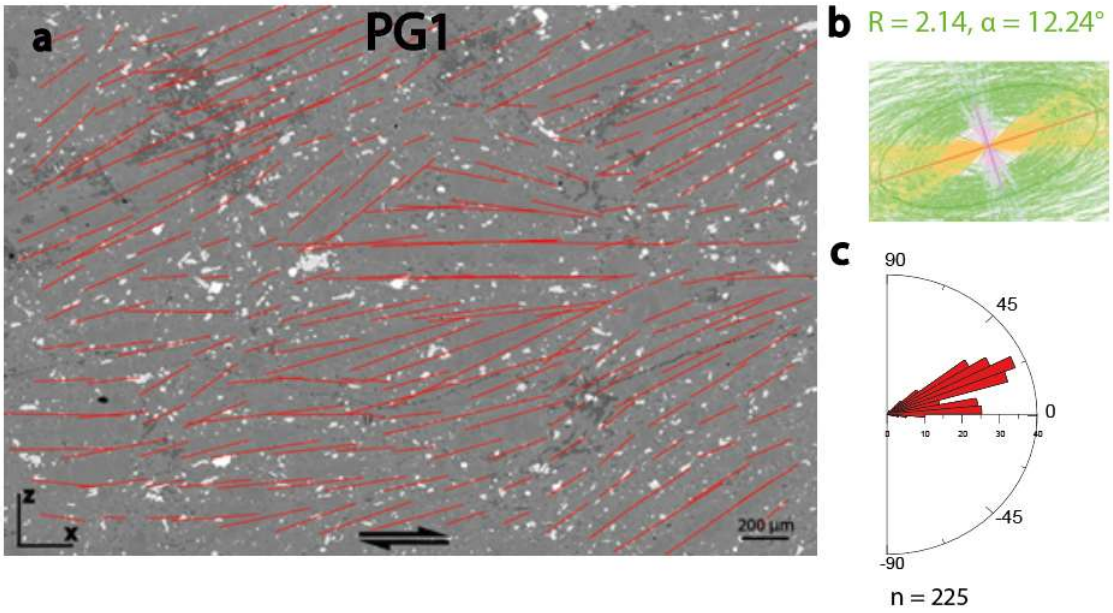

Figure VII.23. Preferential orientation of sample PG1. a) [XZ] section SEM image of the sample. The red lines represent the long axes of the local tensor ellipses of the shape fabrics. b) Mean tensor ellipse of the shape fabric. R_i = eccentricity of the mean ellipse, α = orientation of the long axis of the ellipse. c) Rose diagram of long axes of local tensor ellipses. n = number of measures.

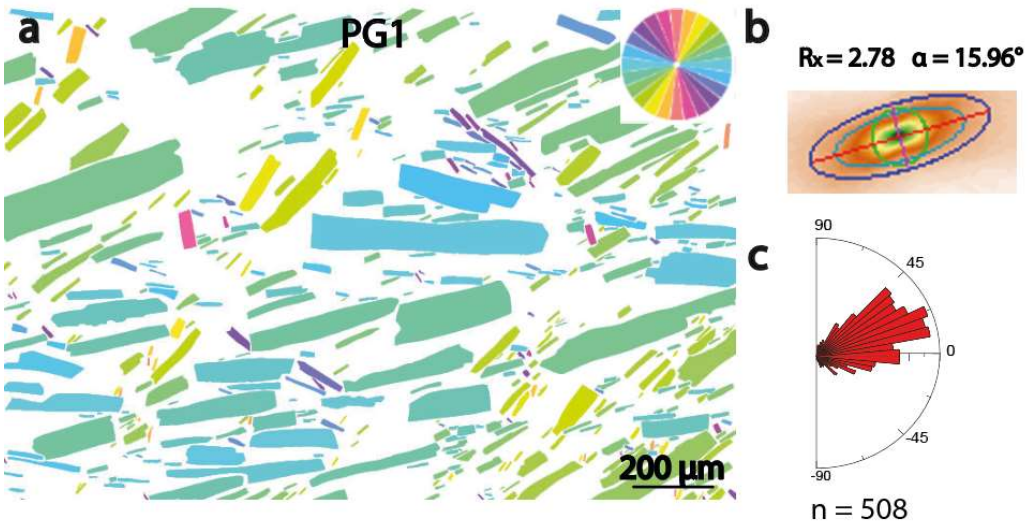

Figure VII.24. a) Orientation of the long axes of the K-feldspars of sample PG1. b) Inertia tensor ellipse in sample PG1. c) Roses diagram of individual crystal orientations of sample PG1. n = number of measures.

Panoramic pictures were taken for PG3 sample (fig. VII.25a) and PG1 sample (fig. VII.25b). The preferential direction of K-feldspars larger than 50 µm was studied. The orientation roses show a preferential direction between 23° and 2° for PG1 sample (fig. VII.25c) and a preferential direction between 21° and 0° for PG1 sample (fig. VII.25d). The orientations of the K-feldspars are in agreement with previous analyses carried out on smaller section of the samples. These preferential orientations show a wavy pattern of the sample at large scales.

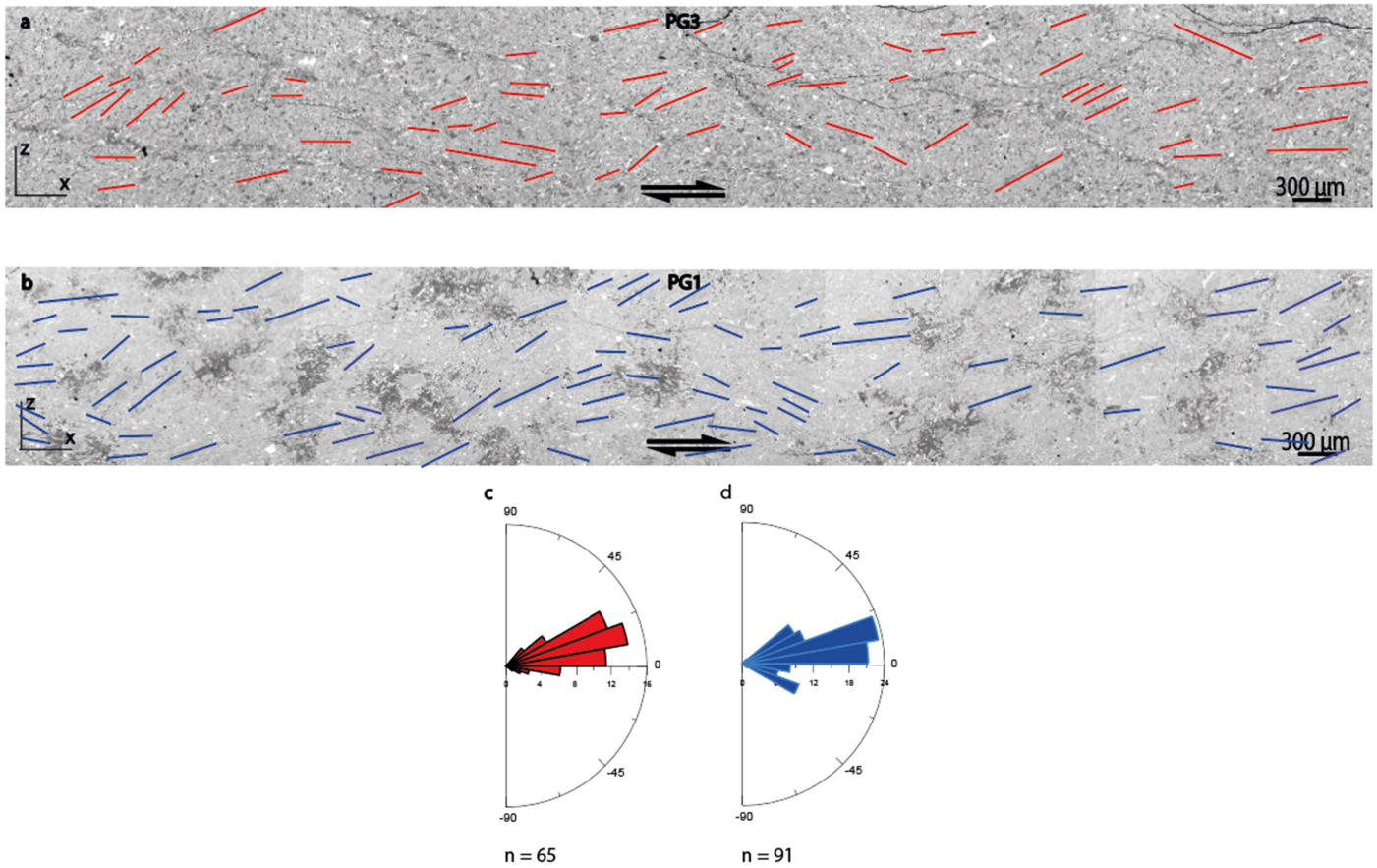

Figure VII.25. SEM panoramic image of natural samples. a) PG3 sample. The red lines represent the long axes of the K-feldspars. b) PG1 sample. The red lines represent the long axes of the K-feldspars. c) Orientation rose of the long axes of the K-feldspars of the PG3 sample. d) Orientation rose of the long axes of the K-feldspars of the PG1 sample.

7.2. Suc de Sara

In the sample SA1 (fig. VII.26a) the eccentricity of the ellipse of the mean tensor shows a value of R_i = 2.15, associated with a mean orientation direction α of 6.95° (fig. VII.26b). The orientations of the long axes of the local ellipses show a preferred orientation at 12° (fig. VII.26c).

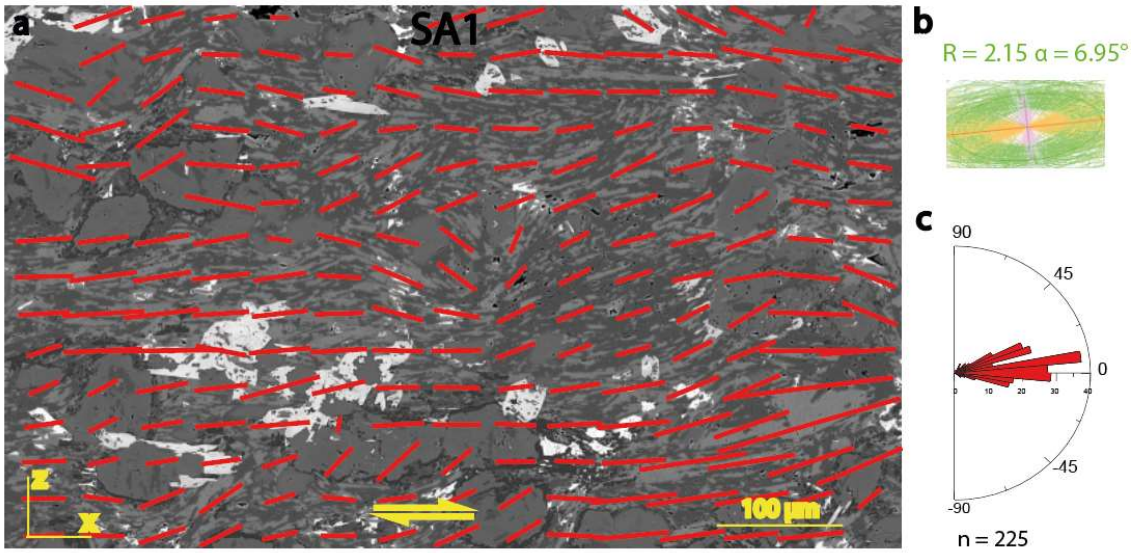

Figure VII.26. Preferential orientation of sample SA1. a) [XZ] section SEM image of the sample. b) Mean tensor ellipse of the shape fabric. R_i = eccentricity of the mean ellipse, α = orientation of the long axis of the ellipse. c) Rose diagram of long axes of local tensor ellipses.

The crystals were studied individually using the inertia method (fig. VII.27a). The inertia tensor ellipse shows an eccentricity R_x = 2.30 and α = 5.83° (fig. VII.27b). The analysis of the preferential orientation of the crystals shows a preferred orientation at -3° (fig. VII.27c).

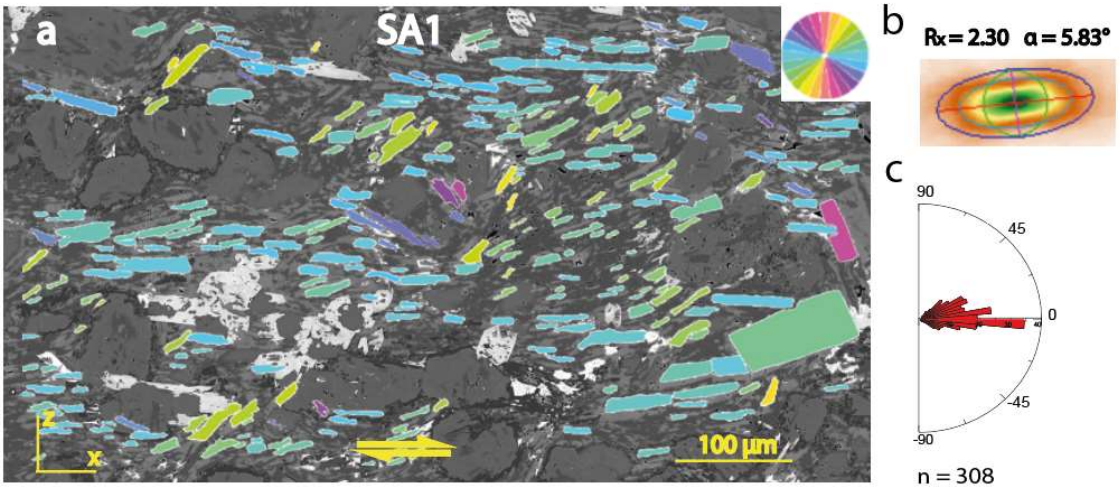

Figure VII.27. a) Individual crystal orientations of sample SA1. Crystals are colored according to their orientations b) Inertia tensor ellipse in sample SA1. c) Roses diagram of individual crystal orientations of sample SA1. n = number of measures.

In the same area as the previous figure, nepheline crystals were analyzed by the inertia method (fig. VII.28a) to compare them with the elongated K-feldspar crystals and to determine if they could provide further information. The inertia tensor ellipse shows an eccentricity R_x = 1.31 with α = 5.93° (fig. VII.28b). The rose diagram has a light preferred orientation between -5° and +5° (fig. VII.28c).

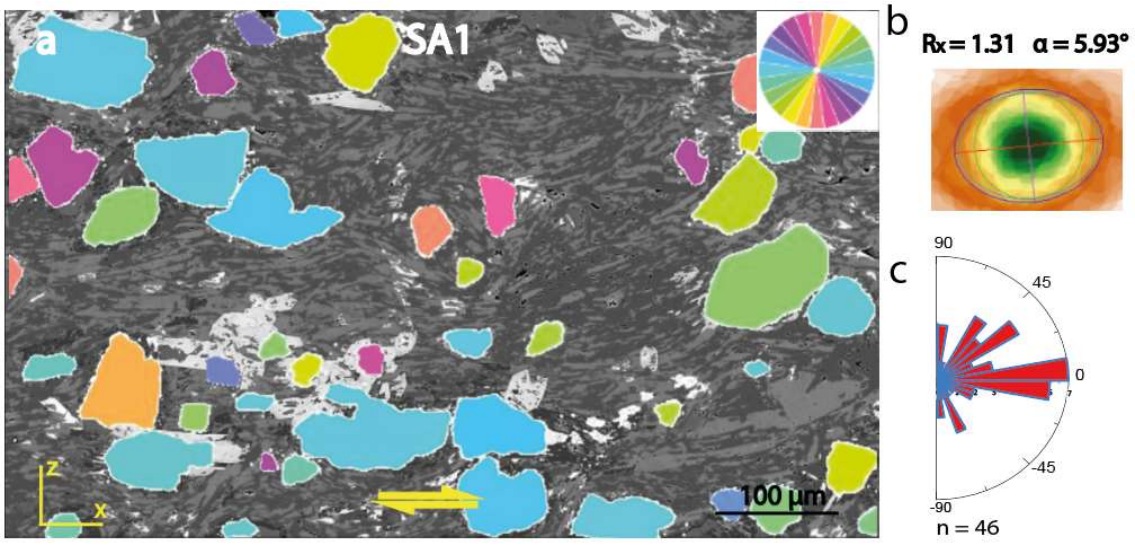

Figure VII.28. a) Individual crystal orientations of nepheline crystals of SA1 sample. Crystals are colored according to their orientations b) Inertia tensor ellipse of nepheline crystals. c) Roses diagram of individual crystal orientations of nepheline crystals. n = number of measures.

As mentioned above, the Suc de Sara has a rich mineralogy, including minerals with a non-elongated shape, such as nepheline. These crystals can strongly influence the propagation of deformation.

Although the 2D analysis using the inertia method and hand drawn crystals are not sufficient to understand the preferred direction of nephelines (figure VII.28 was made to give an idea of how the sample looks), interesting information can be gained by studying their equivalent diameter Φ and the percentage of area they cover in the sample.

Figure VII.29 shows the equivalent diameters Φ of the non-elongated crystals, the nephelines, of samples SA1 (fig. VII.29a) and SA4 (fig. VII.29b).

Sample SA1 (fig. VII.29a) has an arithmetic mean of 50.31±22.85 µm, a harmonic mean of 40.74 µm and a mode of 45 µm. These minerals cover 21% of the surface area.

Sample SA4 (fig. VII.29b) shows an arithmetic mean of 54.32±32.59 µm and a harmonic mean of 38.44 µm. Its mode at 25 µm and 45 µm. The percentage of the surface area covered by these minerals is 36%.

Sample SA1 has slightly lower equivalent diameter Φ than sample SA4. In addition, the area covered by these minerals is significantly smaller in sample SA1 than in sample SA4. These lower equivalent diameter Φ and area values favour localized deformation, resulting in different deformation structures between the two samples.

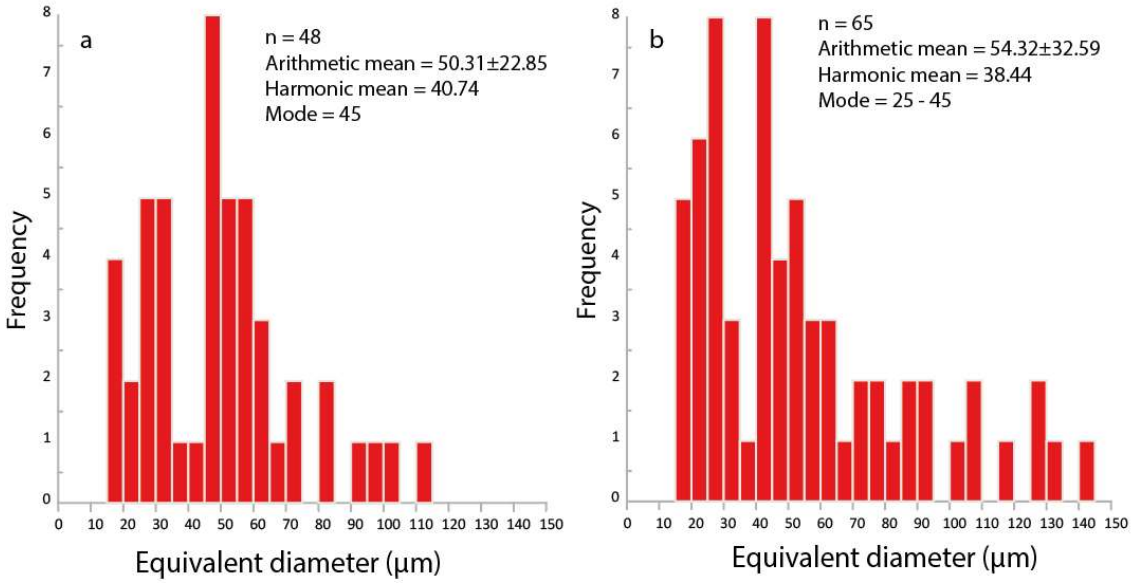

Figure VII.29. Histograms of the equivalent diameter Φ for the sample a) SA1 and b) SA4.

8. Contacts

The contacts of the PG3 sample were classified according to the definition (Azema and Radjaï, 2012) as it is shown in chaper II, paragraph 10. Only elongated crystals are considered and the contact changes depending on whether two crystals are in contact via the long side (S-S contact), via the short side (C-C contact), or via the long-short side (S-C contact). For this reason, only K-feldspars are considered.

The contacts of the PG1 sample were not taken into account as it was not possible to detect contacts between the small crystals. This is due to two reasons: the resolution of the images is not high enough and the chemical homogeneity of the K-feldspars makes them of the same colour at the boundaries. The sample from Suc de Sara also shows a similar problem: as can be seen in fig. VII.30, it is not possible to clearly delineate the contact types between the k-feldspars.

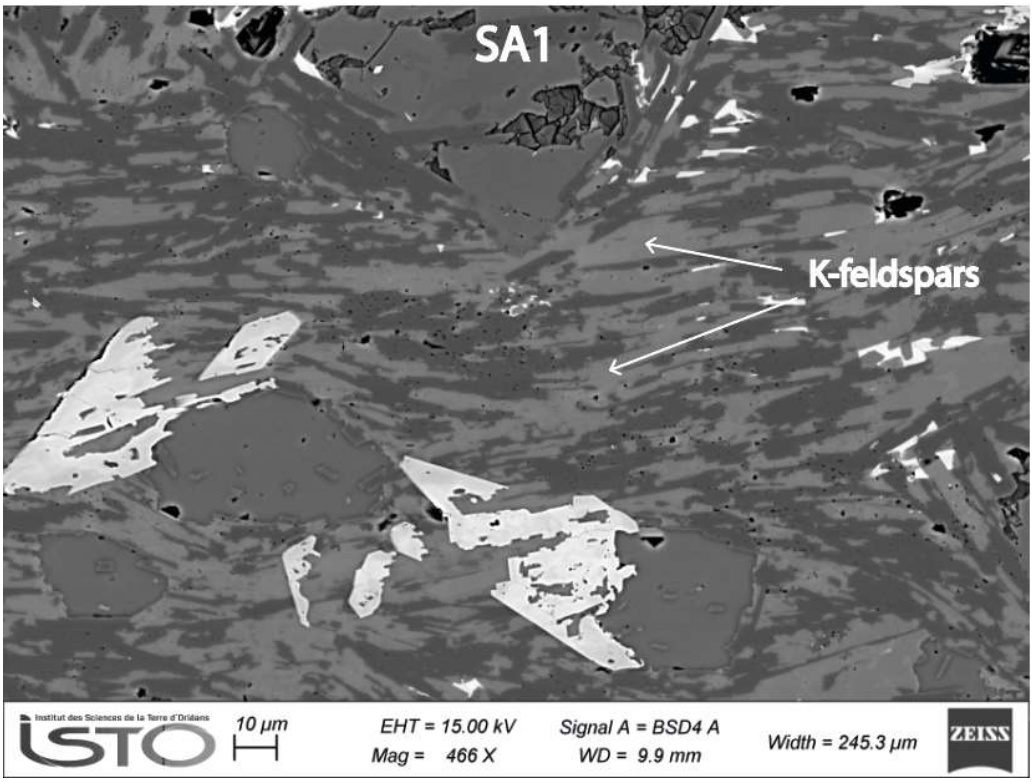

Figure VII.30. SEM picture of SA1 sample. The k-feldspars are in ligh grey.

The contacts of the PG3 sample were only considered in the area of the penetrative fabric, as the bands area is too alterated and no contact is visible.

The PG sample (fig. VII.31a) shows a majority of S-S contacts in its penetrative fabric (n = 236), representing 55% of the total contacts. The preferential orientation of the S-S contacts is between 10° and 15° (fig VII.31b). The C-C contacts, wh2ich are fewer in number (n = 63) and represent only 15% of the total contacts, have a double preferential orientation. The first at 90°/80° and the second at -90°/-75° (fig. VII.31c). The S-C contacts, which represent 30% of the total contacts (n = 132), have a preferential orientation at -10° and -25° (fig. VII.31d).

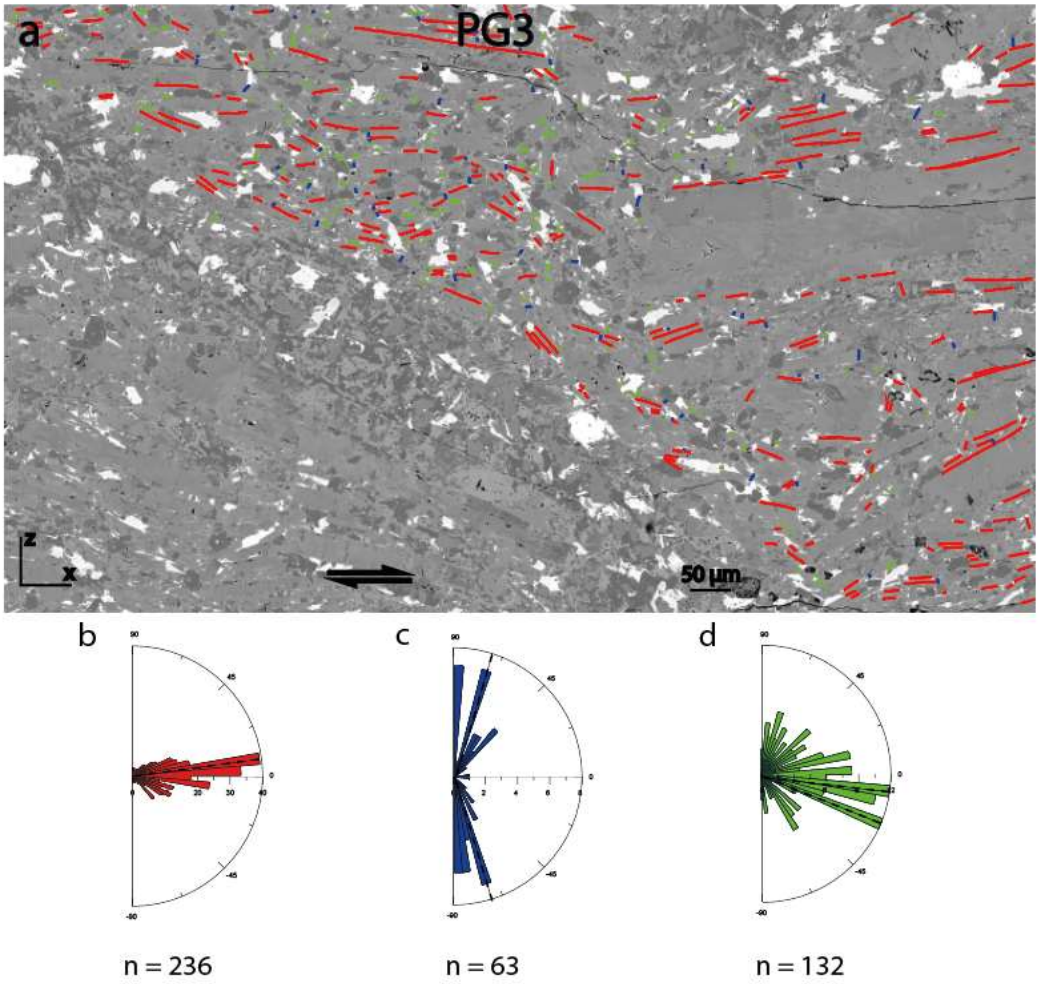

Figure VII.31. Penetrative fabric of PG3 sample. a) SEM picture of the sample with hand drawn contacts (red: S-S, blue: C-C, green: S-C). b) Rose diagram for the orientation of the S-S contacts. c) Rose diagram for the orientation of the C-C contacts. d) Rose diagram for the orientation of the S-C contacts. n = number of contacts.

9. Shape fabric of bubbles of PG samples

The PG3 and PG1 samples show low bubble content of 0.2%. The bubbles were drawn by hand for both PG3 (fig. VII.32a) and PG1 (fig. VII.33a) sample. The orientation rose show no preferred direction for the bubbles of PG3 sample (fig. VII.32b). The equivalent diameter Φ of the bubbles has an arithmetic mean of 4.19±0.86 µm, a harmonic mean of 4.05 µm and a mode of 3.4 µm (fig. VII.32c). The aspect ratio of the bubbles has an arithmetic mean of 2.64±1.52, a harmonic mean of 2.13 and a mode of 1.8 (fig. VII.32d).

The bubbles of PG1 sample has no preferred orientation (fig. VII.33b), they have an arithmetic mean value of the equivalent diameter Φ of 3.67±1.01 µm, a harmonic mean of 3.51 µm and a mode of 3.0 µm (fig. VII.33c). The aspect ratio of the bubbles is equal to 3.05±1.49 for the arithmetic mean, 2.42 for the harmonic mean and 2.8 for the mode (fig. VII.33d).

In both samples the bubbles are not deformed in the shear direction, but they have a high aspect ratio R, slightly higher in the PG1 sample. Both equivalent diameter Φ and aspect ratio R values are similar for arithmetic mean, harmonic and mode.

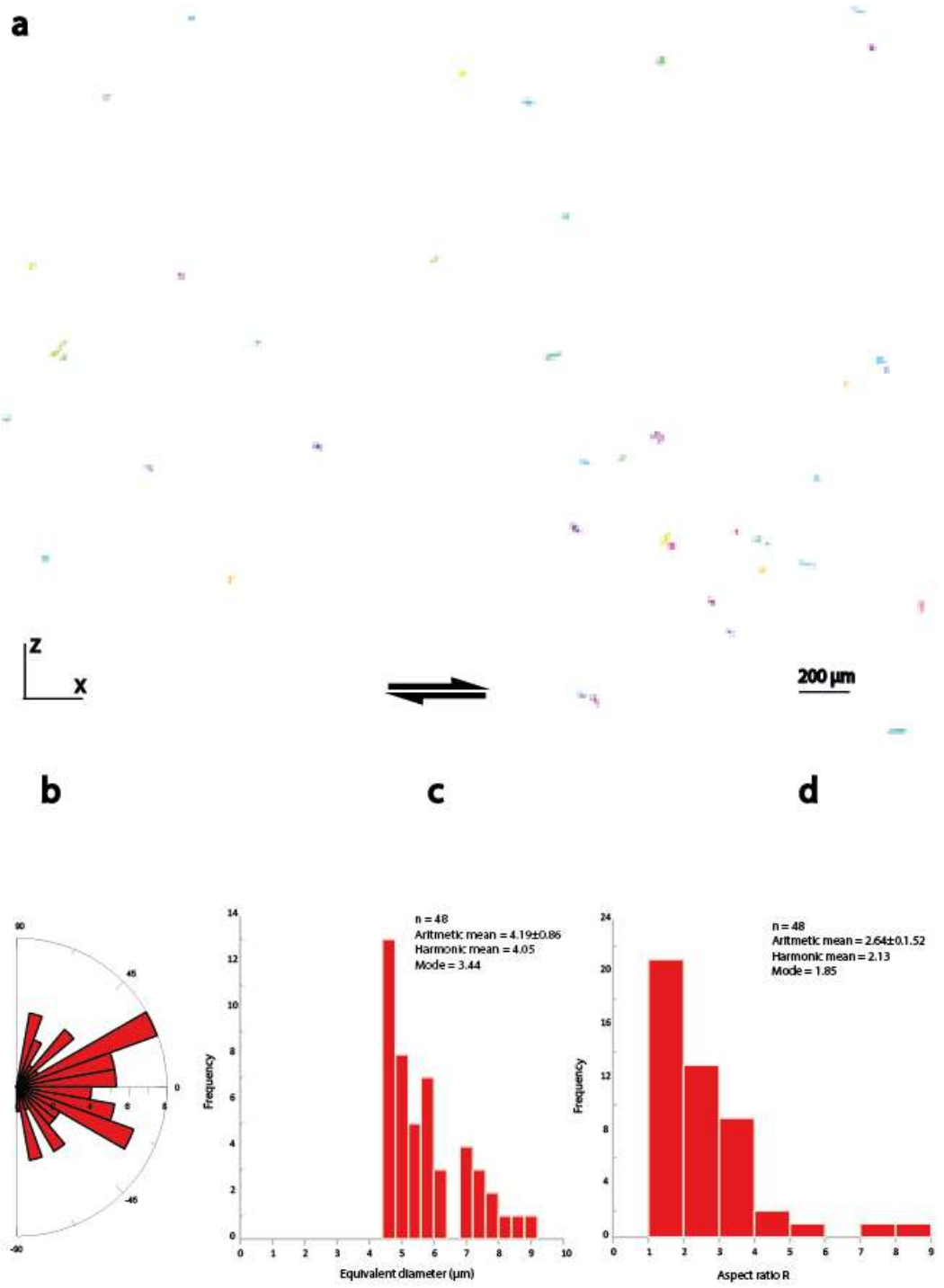

Figure VII.32. Bubbles orientation of sample PG3. a) Bubbles colored according to their orientations. b) Rose of directions of individual bubbles orientation. c) Equivalent diameter histogram for groups of bubbles. d) Equivalent diameter histogram for groups of bubbles.

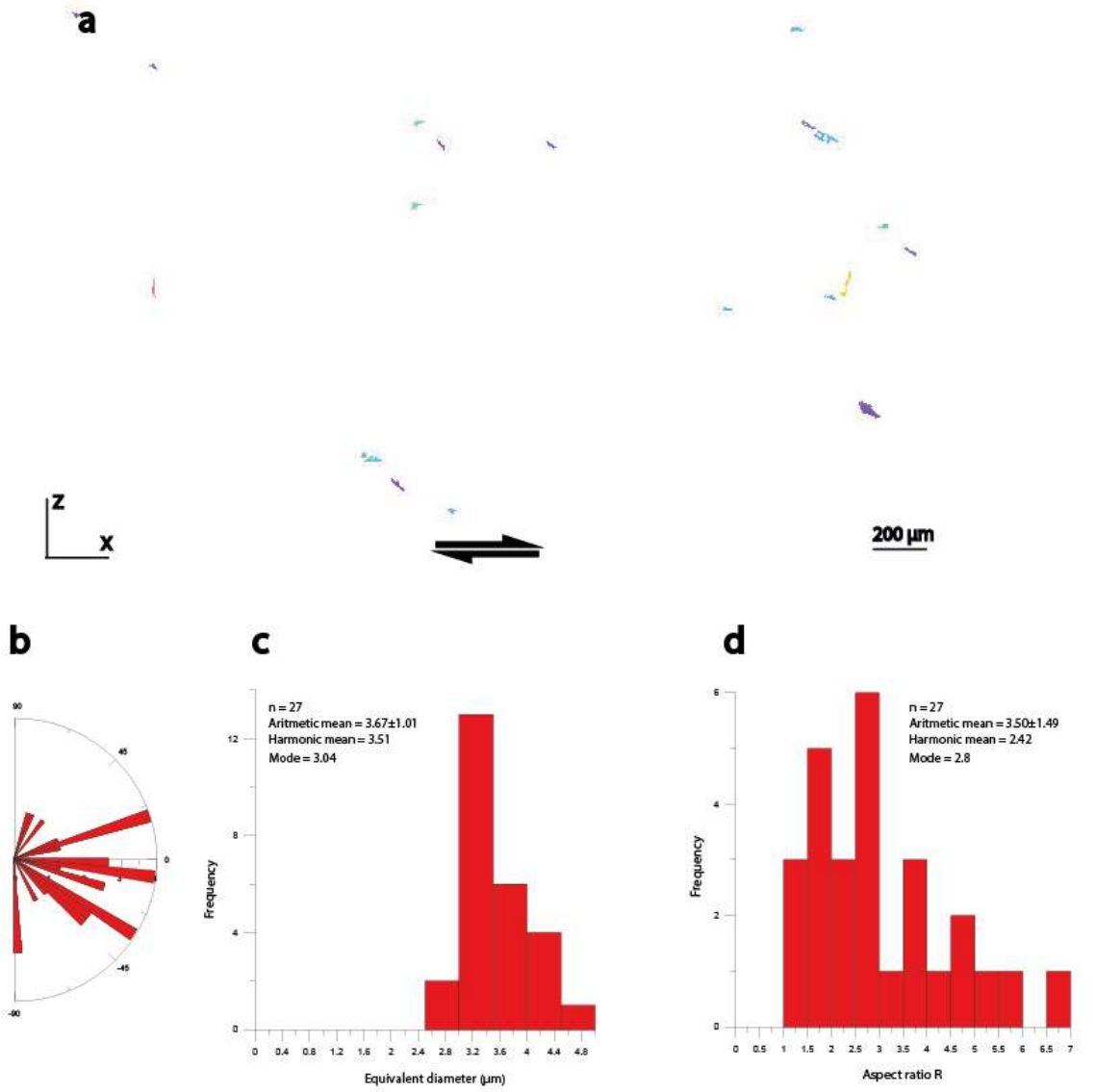

Figure VII.33. Bubbles orientation of sample PG1. a) Bubbles colored according to their orientations. b) Rose of directions of individual bubbles orientation. c) Equivalent diameter histogram for groups of bubbles. d) Equivalent diameter histogram for groups of bubbles.

10. Summary

In this chapter on natural samples, sections from the Petit Gerbier and Suc de Sara were analysed and compared. Sampling areas were selected from different zones to compare samples subjected to different stress.

The aspect ratio R and equivalent diameter ϕ values of the PG1 indicate slow cooling and less severe deformation, with crystals that are not very elongated and much larger than those of the PG3 sample.

The crystals show a preferred shape orientation according to the direction of deformation. In the penetrative fabric the crystals show a wavy pattern. The most deformed samples show shear bands, the moderately deformed samples show banding and the innermost samples show foliation.

The contacts between the crystals are well oriented but few in number due to the different mineralogical phases present in the penetrative fabric of PG sample.

There are two ways in which forces can be localized: by increasing the concentration of stable force chains, or by having areas of weakness formed prior to the onset of deformation. The PG1 sample, representing the initial phase of deformation, has areas of concentrated melt scattered throughout the sample. It is likely that these areas represent weaknesses where strain localization occur, such as the shear bands present in PG1 sample.

The percentage of bubbles in the Petit Gerbier is so low that the results of their analysis may be negligible.

Results - Electron Backscatter Diffraction – EBSD

Résumé du chapitre VIII - Résultats EBSD

Ce chapitre traite des analyses EBSD (Electron Backscatter Diffraction) réalisées sur des échantillons synthétiques et naturels. Toutes les analyses ont été effectuées dans la partie centrale des échantillons, là où la déformation est la plus forte. Les orientations préférentielles du réseau sont indiquées dans les figures du pôle de l'hémisphère inférieur pour les normales des plans (100), (010) et (001). Les iso-contours et les gradients de couleur indiquent les multiples de la distribution uniforme des points de données. Autour de chaque figure de pôle sont indiqués 1) le nombre de points de données, 2) les indices de texture (J) et de désorientation (M). Des cartes de figures de pôles inversées (IPF) et des cartes d'étalement de l'orientation des grains (GOS) sont également présentées pour chaque échantillon.

Toutes les orientations des échantillons sont par rapport à la direction de cisaillement. Le plan de cisaillement et la direction de foliation sont également pris en compte.

Les premiers échantillons décrits sont les matériaux de départ. Leur analyse montre que les échantillons ne présentent pas d'orientations cristallines préférentielles avant les expériences de déformation.

Les échantillons déformés ont été divisés en fonction de leur rapport d'aspect (R = 4 ou R = 2) et de leur teneur en cristaux (0,52 à 0,95).

Les échantillons avec un rapport d'aspect R = 4 présentent toujours une localization de cisaillement, mise en évidence par les figures polaires.

Les échantillons avec un rapport d'aspect R = 2 ne présentent pas de localization de cisaillement. L'interprétation des figures de pôles montre une orientation préférentielle des cristaux dans les directions moyennes entre 0° et 45°.

Les échantillons naturels PG1 et PG3 montrent une forte orientation des cristaux dans la direction de la déformation. Les bandes de cisaillement sont enrichies en liquide résiduel résiduelle.

VIII. Results - Electron Backscatter Diffraction – EBSD

In this study, it has been acquired EBSD maps on feldspar from experimentally and naturally deformed partially molten rocks. For experimental samples, exclusively composed of glass and plagioclase, inverse pole figure maps and lattice preferred orientations (grain mean orientations) are systematically given for different amount of aspect ratio and plagioclase content. It has been then provided crystallographic information of natural samples containing plagioclase, K-feldspar and analcime. In this case, the aim is to compare crystallographic preferred orientations, as deduced from EBSD, with shape preferred orientations, obtained with the SPO2003 and Intercept2003 softwares using the inertia and intercept methods.

1. Experimental deformation

As mentioned previously, deformation experiments have been performed on partially molten samples of plagioclase + glass. For samples affected by shear bands, EBSD analyzes were produced both, outside of shear bands in the main/penetrating foliation and within shear bands. For samples with fully distributed deformation, EBSD data were acquired in the central area where deformation is considered as the greatest, as for the undeformed starting material. Lattice preferred orientations are given in lower-hemisphere pole figures for the (100), (010) and (001) plane normals. Iso-contours and color gradients indicate multiple of uniform distribution of data points. Around each pole figure are indicated 1) the number of data points, 2) the texture (J) and misorientation (M) indices, which both provide the fabric strength respectively between J=1/M=0 (uniform distribution) and J=∞/M=1 (crystal-like distribution), as calculated from the Orientation Distribution Function (ODF; Bunge, 1982) and uncorrelated misorientation angle distribution (Skemer et al., 2005), and 3) percentages that quantify the geometry of the pole figure, i.e., punctual (P) vs. girdle (G) vs. random (R), based on the Eigen values (Boneh and Skemer, 2014). The pole figures were interpreted by considering the foliation direction, shear direction and shear plane (fig. VIII.1). To describe the intergranular deformations, inverse pole figure (IPF) and grain orientation spread (GOS) maps were analyzed for each deformed sample. The IPF gives the distribution of crystallographic axes with respect to the vorticity axis {Y} using the plagioclase lattice coordinates. GOS is a misorientation parameter that corresponds to

the average of misorientation angles between each pixel and the mean orientation of a given grain (Brewer et al., 2009). Rose diagrams have been used to highlight any shape preferred orientation (SPO) by considering the long axis distribution of grains, as calculated using the best-ellipse method.

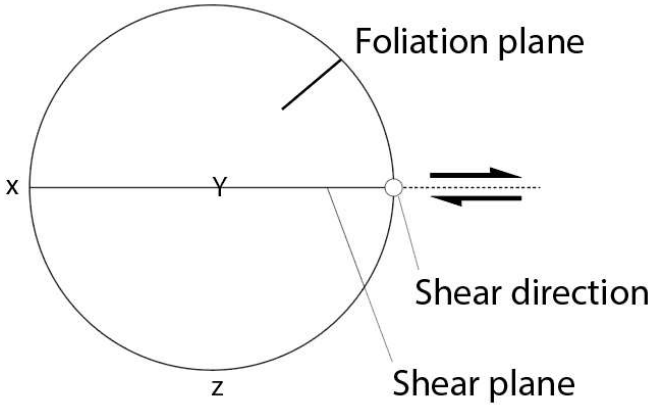

Figure VIII.1. Reference pole ellipse showing shear direction, foliation and shear plane.

2. Starting materials

The starting materials are the undeformed synthetic samples. They have been classified according to the aspect ratio, R, of feldspar grains (R = 4 or R = 2) and their proportion. Figure VIII.2 gives representative SEM images of the starting material for each category of aspect ratio R and phase content (fig. VIII.2 for samples with R = 4, ϕ_s = 0.52 - 0.58 - 0.59, for samples with R = 2 and low crystal content, ϕ_s = 0.58 - 0.59, for samples with R = 2 and high crystal content, ϕ_s = 0.73 - 0.76 and for the granular sample, ϕ_s = 0.95). For pole figures of the starting materials that include a significant amount of grains (>> 150 data points; (Skemer et al., 2005), a very weak fabric strength has been found (J between 1 and 2, and M < 0.1), validating the “almost-free-of-any-LPO” initial state of our samples before their deformation using the Paterson press. Only one starting sample has a strong fabric, but the number of grains is far below 150 (N = 61), so these values probably result from an artefact calculation (Précigout et al., 2022; Skemer et al., 2005).

In terms of geometry, most of the starting samples have their (010) plane poles that describe a girdle parallel to the “future” shear plane, sometimes tending towards punctual geometry parallel to the “future” shear direction. The other plane poles (100) and (001) are more randomly distributed and do not show any systematic LPO.

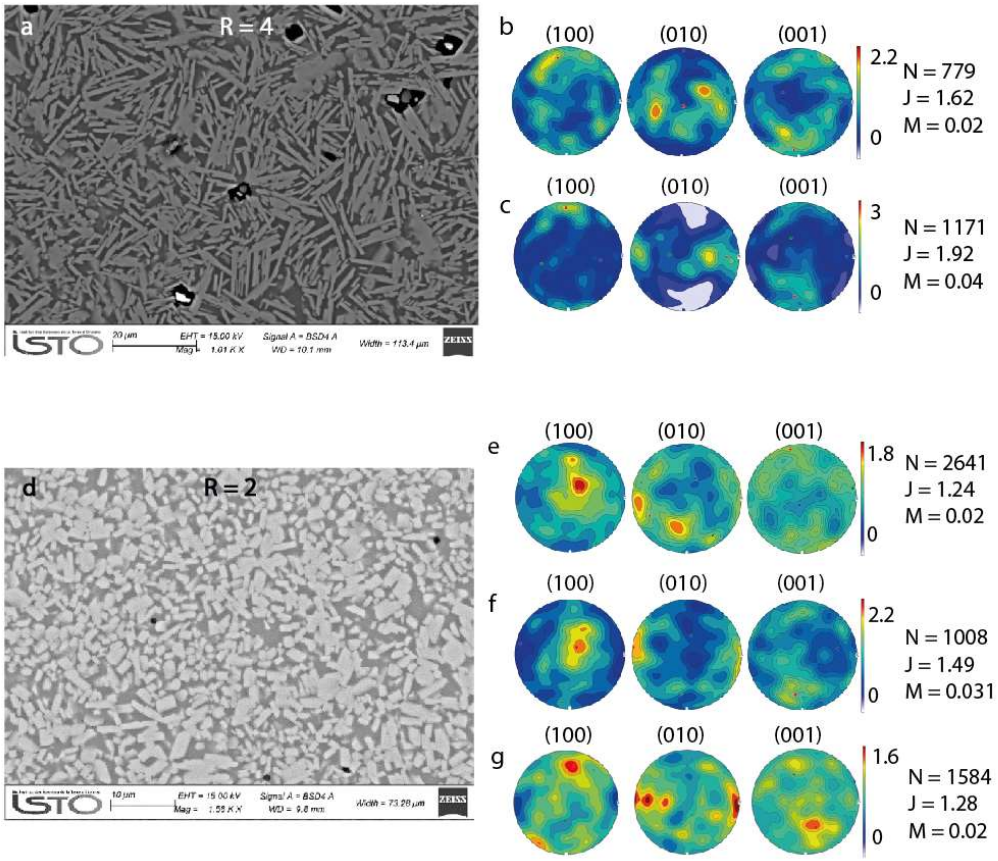

Figure VIII.2. a) SEM image representative of starting materials with R = 4 b) Pole figures of sample with ϕ_s = 0.52 and R = 4. c) Pole figures of sample with ϕ_s = 0.58 and R = 4. d) SEM image representative of starting materials with R = 2 e) Pole figures of sample with ϕ_s = 0.58, corresponding to the deformed sample PP669. f) Pole figures of sample with ϕ_s = 0.58, corresponding to the deformed sample PP676. g) Pole figures of sample with ϕ_s = 0.59.

3. Deformed samples

This section provides the EBSD analyses of the samples deformed in the Paterson press using the torsion deformation regime. A representative sample was selected for each sample type (R = 4, R = 2 low ϕ_s, R = 2 high ϕ_s) due to similarity of characteristics. They are classified according to their aspect ratio R and crystal content ϕ_s. For each type sample, a representative SEM image, pole figures, inverse pole map, GOS map and long-

axis rose diagram are given for plagioclase crystals. EBSD analyses of all samples are given in Appendix F.

3.1. Samples with aspect ratio R = 4

All samples with aspect ratio R = 4 show localized deformation with the development of shear bands, so the analyses were carried out in both the penetrative fabric and the shear bands.

$\phi_s = 0.58$

The sample with $\phi_s = 0.58$ (fig. VIII.3) was deformed with a bulk strain $\gamma = 1.4$ and a strain rate $\dot{\gamma} = 8.9*10^{-4}\ s^{-1}$. Shear bands developed obliquely to the shear plane with an angle of around 10°. Outside of the shear bands, the pole figures of the penetrative fabric are without any preferential orientation of plane poles (100) and (001), which gives rise to a random LPO pattern (fig. VIII.4a). In contrast, the shear bands show a concentration of (010) lying close to the shear plane, while (100) and (001) are concentrated in the shear direction (fig. VIII.4b). The rose diagrams of long axes distribution show no orientation for the penetrative fabric (fig. VIII.4c) and a preferred orientation parallel in the shear direction of the shearing for the shear band (fig. VIII.4d).
The IPF map (fig. VIII.4e) and GOS map (fig. VIII.f) of the penetrative fabric do not show any preferred orientation or intragranular deformation of the crystals. In the shear bands, the IPF map show a higher orientation of the crystals (fig. VIII.4g), but most of the grains have a GOS lower than 1, indicating very few intragranular deformation (fig. VIII.4h).

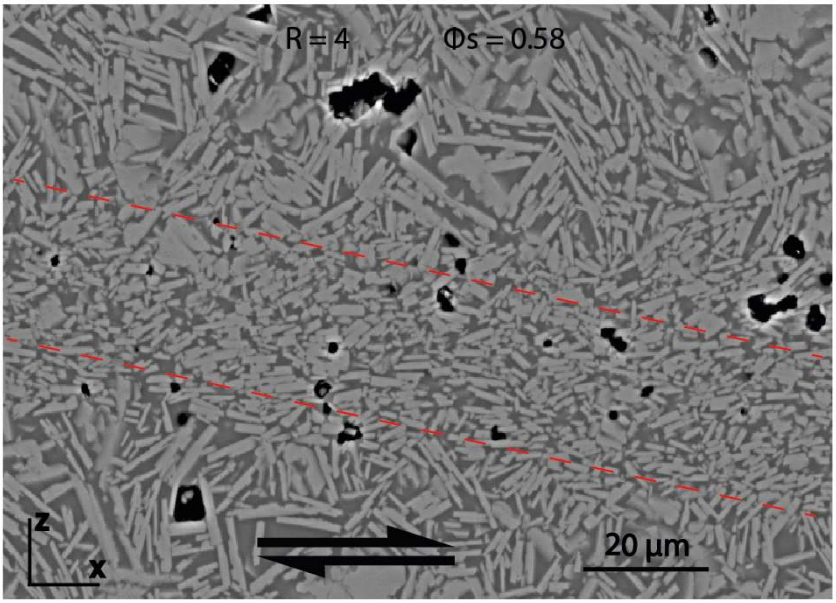

Figure VIII.3. SEM image of the sample with R = 4 and crystal content 0.58 (γ = 1.4, $\dot{\gamma}$ = 8.9*10^{-4} s^{-1}). The red dashed line highlights the shear band.

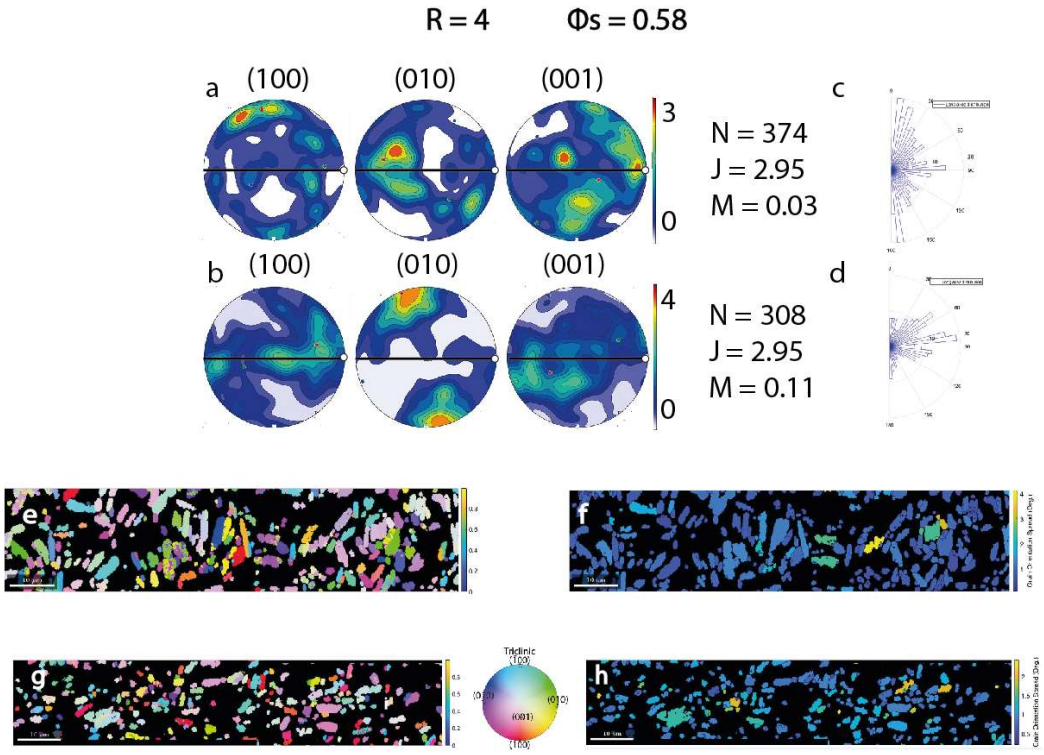

Figure VIII.4. a) Pole figures of the penetrative fabric. b) Pole figure of the shear band. c) Rose of long axis distribution of the plagioclase of the penetrative fabric. d) Rose of long axis distribution of the plagioclase of the shear band. e) Inverse pole figure map of the penetrative fabric. f) GOS map of the penetrative fabric. g) Inverse pole figure map of the shear band. h) GOS map of the shear band.

3.2. Samples with aspect ratio R = 2

This paragraph provides EBSD analyses of the samples with aspect ratio R = 2. Samples are described as a function of their crystal content, highlighting two distinct behaviors recorded during deformation, one related to low crystal content (ϕ_s), between 58% and 59%, and a second one related to a high content ranging between 73% and 95%.

Deformation at low crystal content (ϕ_s = 0.58 – 0.59)

The sample with R = 2 and low crystal content (fig. VIII.5) has been deformed applying a low strain of $\gamma = 0.5$ and a strain rate of $\dot{\gamma} = 1.0*10^{-4}\ s^{-1}$. There is no formation of shear bands, but a penetrative fabric develops with deformation, as confirmed by a – although weak – LPO characterized by (100) and (010) plane poles respectively parallel and normal to the foliation plane (fig. VIII.6a), while (001) poles are randomly distributed both (010) and (100) also concentrate at high angle to the shear plane. The rose diagram of the long axis distribution shows a very weak orientation parallel to the foliation plane (fig. VIII.6b). Accordingly, the IPF map does not show any preferred direction of the crystals (fig. VIII.6c) and the GOS map does indicate very few intragranular deformations (fig. VIII.6d).

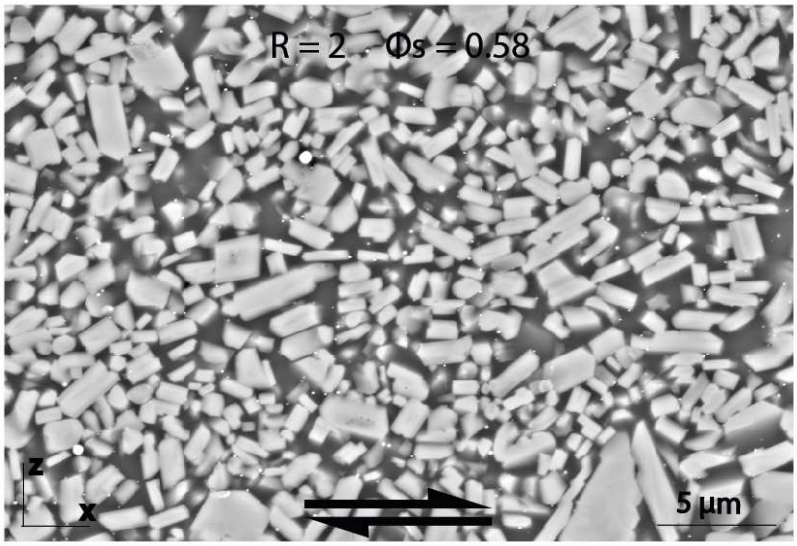

Figure VIII.5. SEM image of the sample with R = 2 and crystal content 0.58 (γ = 0.5, $\dot{\gamma}$ = $1.0*10^{-4}$ s^{-1}).

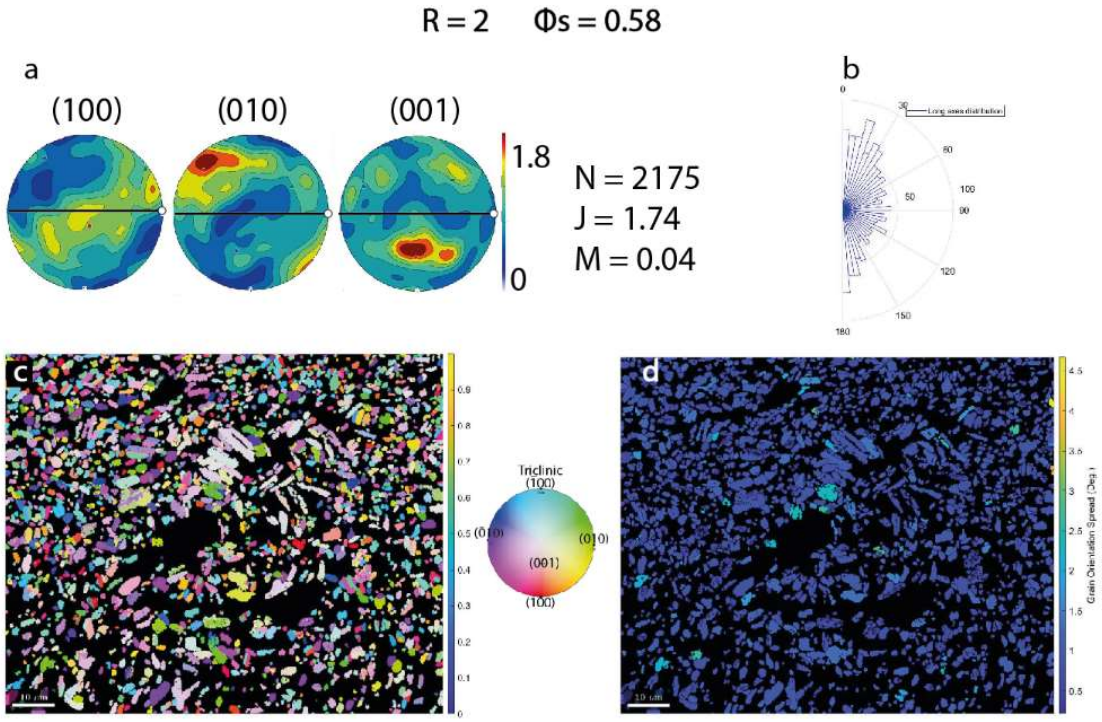

Figure VIII.6. a) Pole figures of sample with R = 2 and low crystal content. b) Rose of long axis distribution of the plagioclase of sample with R = 2 and low crystal content. c) Inverse pole figure map. d) Grain orientation spread map of sample with R = 2 and low crystal content.

Deformation at high crystal content (ϕ_s = 0.73, 0.76, 0.95)

This paragraph is about the pole figures of the penetrative fabrics of the samples with aspect ratio R = 2 and high crystal content (fig. VIII.7).

The experiment in the high crystallinity series was performed with a finite strain γ of 2.0 and strain rate $\dot{\gamma}$ of $2.5*10^{-4}$ s^{-1}.

The penetrative fabric (fig. VIII.8a) shows a concentration of the (010) planes close to the foliation direction, while the (100) and (001) planes are located in a girdle parallel to the foliation plane. The rose of the long axis distribution shows an orientation perpendicular to the shear direction (fig. VIII.8c). The crystals follow the foliation direction. The IPF map does not show any preferred direction of the crystals (fig. VIII.8c) and the GOS map does not indicate any intergranular deformation (fig. VIII.8d).

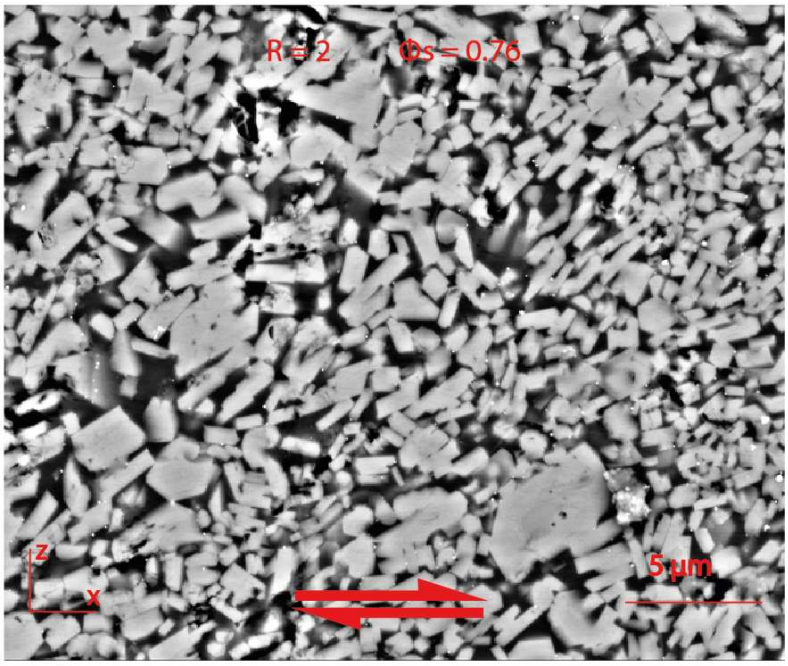

Figure VIII.7. SEM image of the sample with R = 2 and high crystal content.

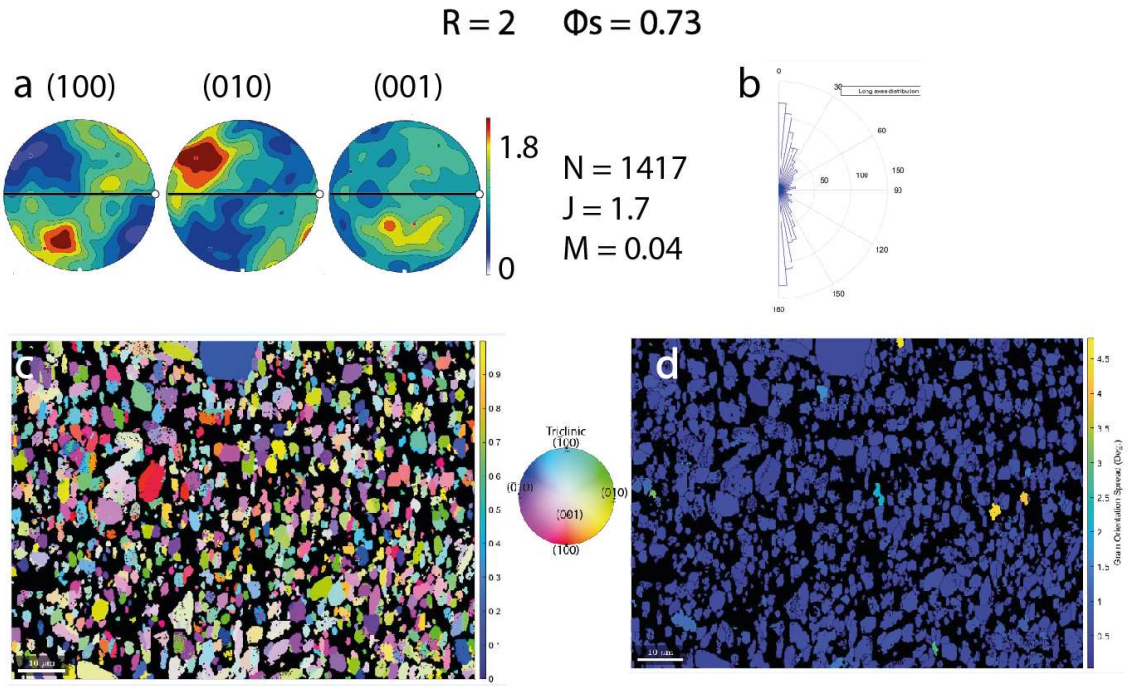

Figure VIII.8. a) Pole figures of sample with R = 2 and high crystal content. b) Rose of long axis distribution of the plagioclase of sample with R = 2 and high crystal content. c) Inverse pole figure map. d) Grain orientation spread map of sample with R = 2 and high crystal content.

4. Natural samples PG1 and PG3

The EBSD analysis of the natural samples were carried out on samples taken from the inner (PG1, fig. VIII.9a) and outer (PG3, fig. VIII.10a) areas of the Petit Gerbier. The PG1 sample shows a penetrative fabric area and a lenses area with an analcimic composition, here attributed to late melt crystallization. For the penetrative fabrics of PG1 and PG3, only K-feldspars were considered as they are the most abundant minerals and the most representative of the deformation.

The penetrative fabrics of the PG1 sample show a concentration of plane poles (010) parallel to the shear direction (fig. VIII.9b). Planes (100) shows a girdle within the shear plane and the (001) poles show a concentration around the vorticity axis (Y). Thus, the crystals orientations are consistent with the direction of the main strain axes. The IPF map shows an orientation of the crystal in the direction of deformation (fig. VIII.9c) and

the GOS map shows sporadic intragranular deformation (fig. VIII9d). The preferred direction of the long axes is close to the shearing direction (fig. VIII.9e).

The PG3 sample consists of a penetrative fabric and shear bands containing altered crystals and a residual melt with analcimic composition. Due to the strong alteration of the crystals in the shear bands, it was not possible to determine their CPO. The penetrative fabric (fig. VIII.10b) shows crystals strongly oriented in the main shearing direction, with the (010) planes aligned with the shear direction, the (100) and (001) planes concentrated in a girdle parallel to the shear plane. As for the previous sample, the IPF map shows an orientation of the crystal in the direction of deformation (fig. VIII.10c) and the GOS map shows sporadic intergranular deformation (fig. VIII.10d). The rose diagram of the shape preferred orientation highlight long axes that get close to parallel to the shear direction (fig. VIII.10e).

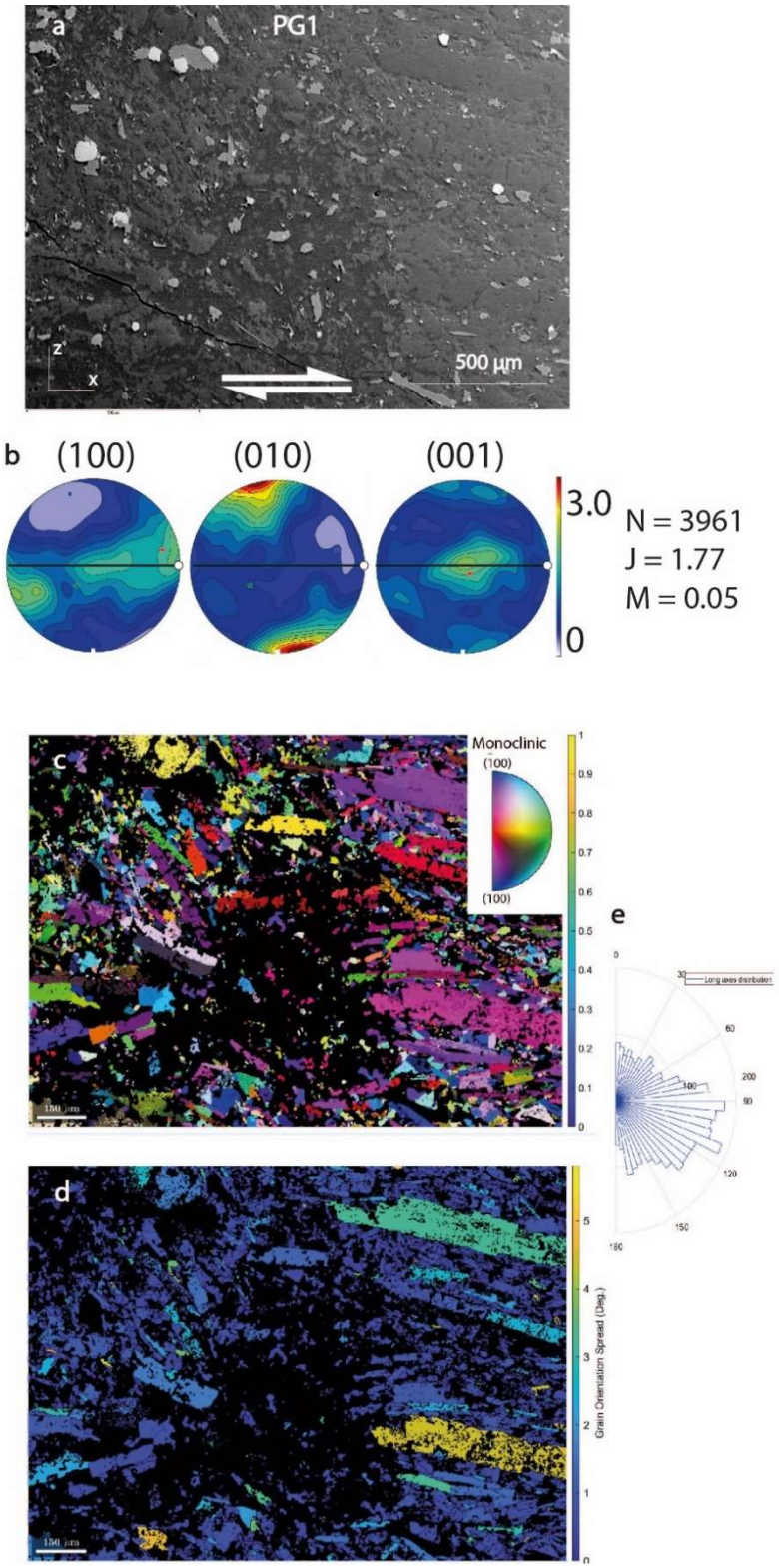

Figure VIII.9. a) SEM image of the natural sample PG1. b) Pole figures. c) Inverse pole figure map. d) Grain orientation spread map. e) Long axis orientation rose of the plagioclase.

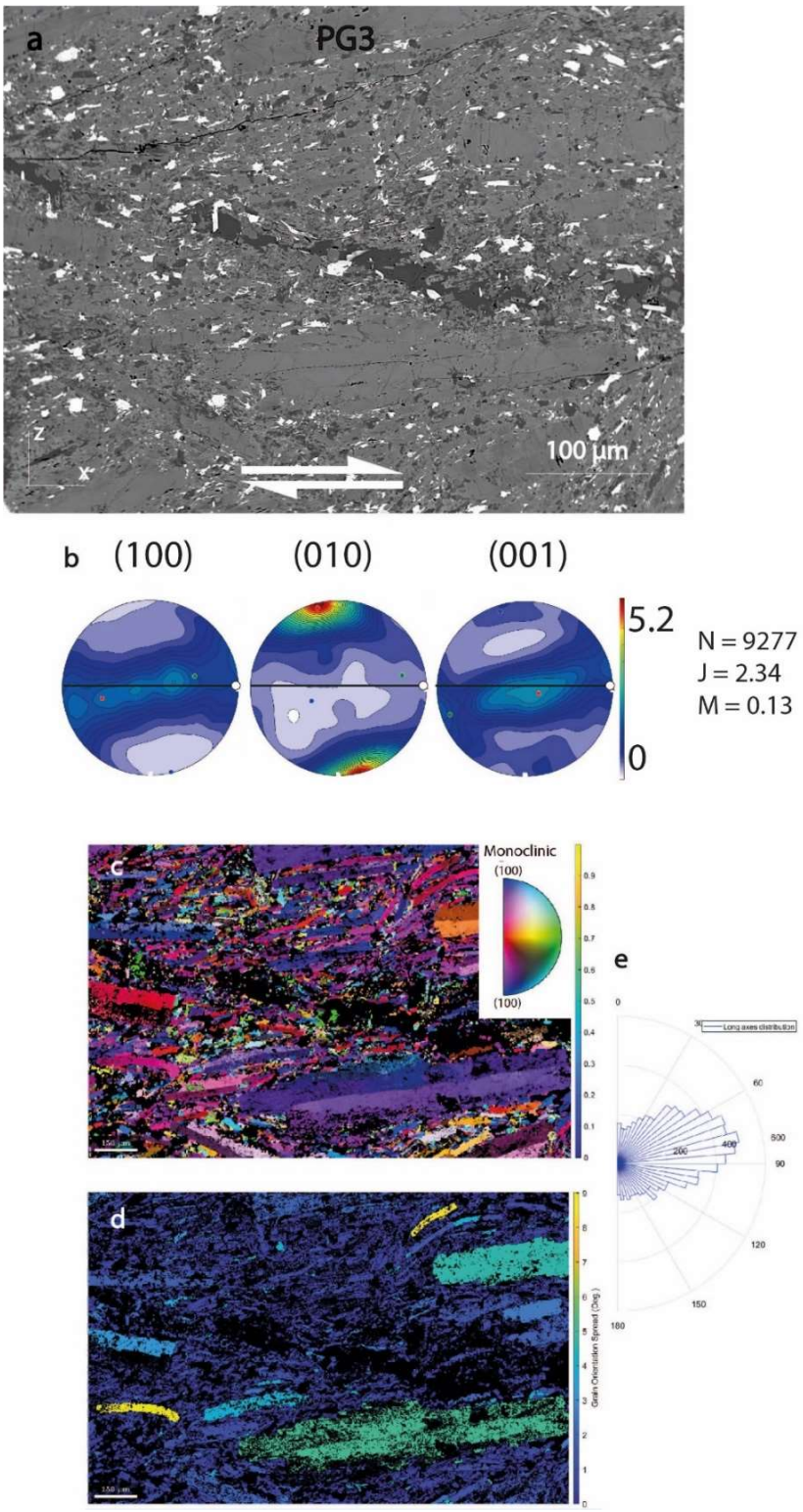

Figure VIII.10. a) SEM image of the natural sample PG3. b) Pole figures. c) Inverse pole figure map. d) Grain orientation spread map. e) Long axis orientation rose of the plagioclase.

For both samples, analyses were carried out in the analcime-rich areas (fig. VIII.11a). This mineral belongs to the cubic crystal system, so the pole figures do not give any information about the orientation of the crystals (fig. VIII.11b). However, IPF and GOS maps show that there are several randomly oriented crystals (figures VIII.11c-d). This suggests that the analcime could have been a residual melt that cooled rapidly and formed a few crystals.

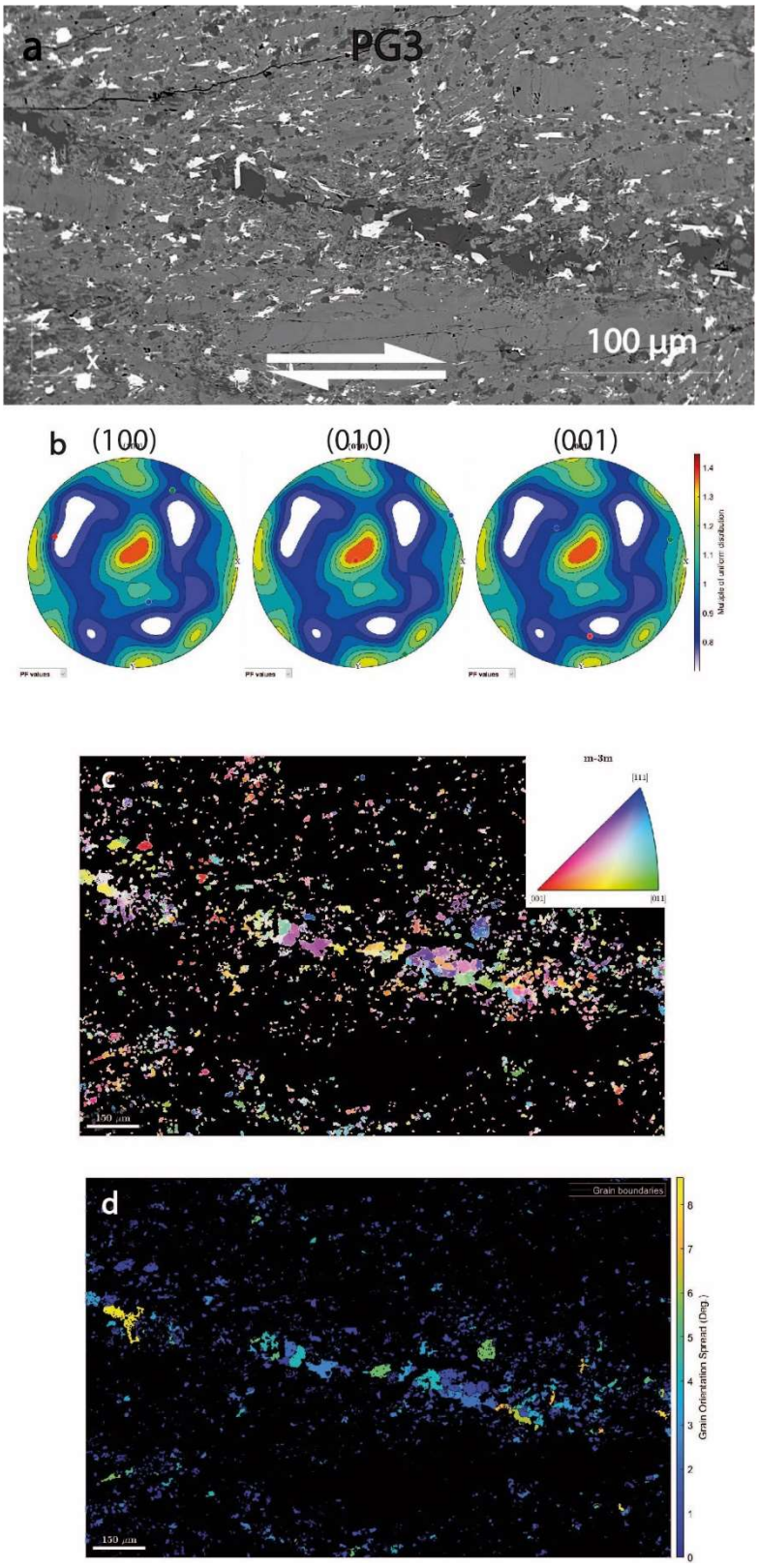

Figure VIII.11. a) SEM image of the natural sample PG3, zoom on analcime. b) Pole figure. c) Inverse pole figure map. d) Grain orientation spread map.

Discussion

Résumé du chapitre IX – Discussion

La première partie du chapitre explique les limites de cette thèse. Les expériences de déformation sont limitées à certaines valeurs de déformation finie et de vitesse de déformation, qui dépendent de la presse Paterson. En outre, la suspension synthétique utilisée dans cette thèse est "simplifiée", c'est-à-dire qu'elle n'est constituée que d'un seul type de minéral. Les résultats sont donc faciles à interpréter, mais les systèmes naturels sont formés de suspensions multicristallines. Néanmoins, cette suspension "simplifiée" est un bon point de départ pour de futures expériences de déformation dans des conditions plus compliquées.

La seconde montre toutes les relations entre les chaînes de force, les clusters et les échantillons déformés. Pour chaque échantillon, il est illustré comment les chaînes de force et les clusters se propagent.

Dans la troisième partie, les diagrammes rhéologiques sont illustrés. Ils n'ont été réalisés que pour les échantillons pour lesquels un changement de viscosité a pu être enregistré pendant les expériences de déformation. Ces diagrammes permettent d'étudier la dynamique et la chronologie de la déformation.

Il a été décrit comment différentes valeurs de déformation finie et de taux de déformation peuvent modifier les structures de déformation finales : à des taux de déformation élevés, on observe la formation de structures plus fragiles et de cataclasite, tandis qu'à des taux de déformation finie élevés, des bandes se développent.

Un autre paramètre pris en compte est le rapport d'aspect R des cristaux : pour des rapports d'aspect plus élevés, il y a une plus grande concentration des forces le long de la surface du cristal. Cela conduit à une plus grande localization de la déformation, avec le développement possible de bandes de cisaillement, et les cristaux deviennent plus orientés dans la direction de la déformation.

Il est possible de supposer que des modèles conduisent à la ségrégation et à la migration de liquide résiduel en raison de la concentration de la déformation, des chaînes de force et des clusters.

Une section est consacrée au comportement des bulles. Dans les échantillons avec R = 4, elles restent non formées, dans les échantillons avec R = 2, elles s'orientent dans la direction de la déformation, migrent et coalescent.

Enfin, les échantillons naturels sont discutés et comparés aux échantillons synthétiques. Les échantillons naturels et synthétiques présentent de bonnes corrélations. Les échantillons synthétiques sont donc représentatifs d'un environnement naturel.

IX. Discussion

1. Limitations of my experimental approach compare to magmatic system

Investigation of melt extraction mechanism from volcanic mush is the main objective of this thesis. However, representing the natural system using experimental methods is not easy. The concept of magmatic mush is relatively new, so experimental studies of melt extraction dynamics are still in their infancy. It is clear that natural samples, such as those considered in this work, show greater heterogeneity in terms of crystal textures, shapes, crystal sizes and mineralogy. It is important to study samples with homogeneous morphological characteristics. For this reason, synthetic samples were chosen to produce a simplified system. The experimental samples represent rocks with a haplotonalitic composition consisting exclusively of plagioclase crystals (except for the 95% crystal content experiment, which also shows quartz). They have an almost unimodal distribution of crystal size and shape, with an aspect ratio R ranging from about 2 to 4. It is important to study samples with homogeneous morphological characteristics, such as aspect ratio R, equivalent diameter, etc., in order to better understand the evolution of structural processes underlying volcanic systems. The simplicity of my system has allowed to study the evolution of force chains and strain localization in a crystal-rich system. In this work a parametric study has been carried out. The first two parameters studied are the aspect ratio R of the crystals and the crystal content of the samples (which varies as a function of the synthesis temperature). Two other parameters studied are the finite strain and the strain rate. The aim was to understand how these deformation parameters affect the formation of microstructures in torsionally deformed samples.

The synthetic mushes used here represent represent surface systems in a volcanic environment. The strain rate and finite strain values used in the deformation experiments are comparable to those of shallow dykes, necks or sills undergoing uplift and deformation. According to the works of (Chadwick Jr et al., 1988; Spera et al., 1988), strain rate values comparable to natural shallow systems are in the range of 10^{-3} to 10^{-7} s^{-1} and my deformation experiments have values in the range of 10^{-5} to 10^{-3} s^{-1}. Deep plutonic systems were not considered as the strain rate values comparable to deep environments would have required months of experiments. As shown by the work of (Petford, 2003), magmas located in depth have deformation rates around 10^{-10} s^{-1}.

In order to analyse melt segregation in synthetic samples, it was decided to perform strain experiments in simple shear rather than pure shear, since compressive deformation experiments of earlier work (Picard et al., 2013) did not show any particularly interesting deformation structures correlated to melt segregation. In addition, pure shear deformation is not usually evoked in (sub-)volcanic systems, as the simple shear geometry most represent the deformation encountered in ascending and flowing magmas.

The rheology of the synthetic samples with aspect ratio R = 2 could not be analysed. The samples with aspect ratio R = 2 show low viscosity and low resistance which did not allow the Paterson press load cell to measure the rheology of the samples. On the other hand, this rheological weakness has made it possible to carry out deformation experiments on synthetic samples with a very high crystal content of up to 95%. The experiments performed in the work of (Picard et al., 2011) show the opposite situation. Their plagioclases have an aspect ratio R = 4 and the viscosity of the samples is high. This made easy to measure the rheology and the viscosity of the samples using the Paterson press load cell. The samples with a high crystal content (60% or more) and aspect ratio R = 4 were not deformed, due to their high viscosity. In addition, no experiments were carried out at high finite strain values. The reason for this is probably due to their high viscosity, which made the sample susceptible to brittle deformation. The maximum finite strain value reached is 2.

Another limitation is that the Paterson is a closed system that cannot degas, so it is not possible to reproduce two-phase systems.

2. Aspect ratio R and force chains evolution as the main mechanisms for shear localization

Force chains are very important elements for stress localization. Force chains are formed when the sample undergoes deformation and they allow the deformation to propagate in a sample when different particles come into contact.

Geometrical disorder leads to an inhomogeneous distribution of force chains. Depending on the aspect ratio, shape and size of the crystals, the force chains show different intensities and directions. The type of contact formed between the different plagioclase crystals determines the intensity of the force chains. According to Azema's classification (Azema and Radjaï, 2012), the contacts are divided into S-S (side-by-side),

C-C (cap-cap) and S-C (S-C). S-S contacts are those that transmit the most intense force chains. It is not possible to measure the intensity of the force chains quantitatively (although numerical simulation could provide a quantitative measure). However, by analysing 2D images of synthetic samples, it is possible to determine the type of contact between the plagioclases and to determinate where the force chains are likely to be most intense. Once all contacts had been identified, the clusters were analysed. Clusters by definition are formed by at least three adjacent S-S contacts, allow the concentration of force chains in a particular area of the sample. By examination of the areas of highest concentration of force chains, corresponding to areas of high contact and clustering, it is possible to deduce which areas of the sample are likely to be subject to strain localization.

The following figures (figures IX.1a, IX.2a, IX.3a, IX.4a, IX.5a, IX.6a) summarise the deformation processes and deformation structures formed in the sample, while figures IX.1b, IX.2b, IX.3b, IX.4b, IX.5b, IX.6b show the processes and intensities of the force chains and clusters. The force chains are shown as red arrows, indicating their direction of orientation. Strong force chains correspond to thick, intensely coloured red arrows. Weak force chains correspond to thin and fine red arrows. Crystals that are subject to force chains and form clusters are coloured green. As with force chians, more intense greens represent more stable and strong clusters, faded greens represent unstable and weak clusters.

Figure IX.1 schematises the deformation structures of sample PP043 (R = 4, ϕ_s = 0.52, strain rate = $1.1*10^{-4}$ s^{-1} and finite strain = 1.4). In fig. IX.1b, the sample is undeformed. As deformation begins, the crystals start to rotate and translate until they reach an orientation in the direction of foliation (fig. IX.1b). At this point, the first stable contacts are formed (yellow crystals, fig. IX.1b), mainly of the S-S type, which spread over a large part of the sample surface. The movement of the crystals at 45° creates areas of compression in the penetrative fabric. When most of the crystals are oriented in the direction of foliation, C' shear bands form (fig. IX.1c - d). These structures are formed to accommodate the deformation produced by the crystals and thus to accommodate the volume. Shear bands C can also be formed, but they are less common. Thus the shear band is not formed due to the localization of the deformation, but to keep the volume stable.

The developed force chains system (fig. IX.1e) is distributed over almost the entire surface of the penetrative fabric. The force chains are therefore homogeneous in terms

of both their location and their intensity. A large number of clusters are formed which are also homogeneous and distributed over a large part of the sample surface. In this example, the arrows are a pale red because the deformation is not localized, but evenly distributed.

The crystals within the shear bands are oriented in the direction of deformation, almost all parallel to each other. In this area, the majority of the contacts is S-S type and there are a fair number of clusters. The sample shows C and C' shear bands distributed over the entire sample surface, with a strong abundance of C' shear bands. This abundance is an indication that the force chains are distributed over the entire surface of the sample and that their localization is not intense.

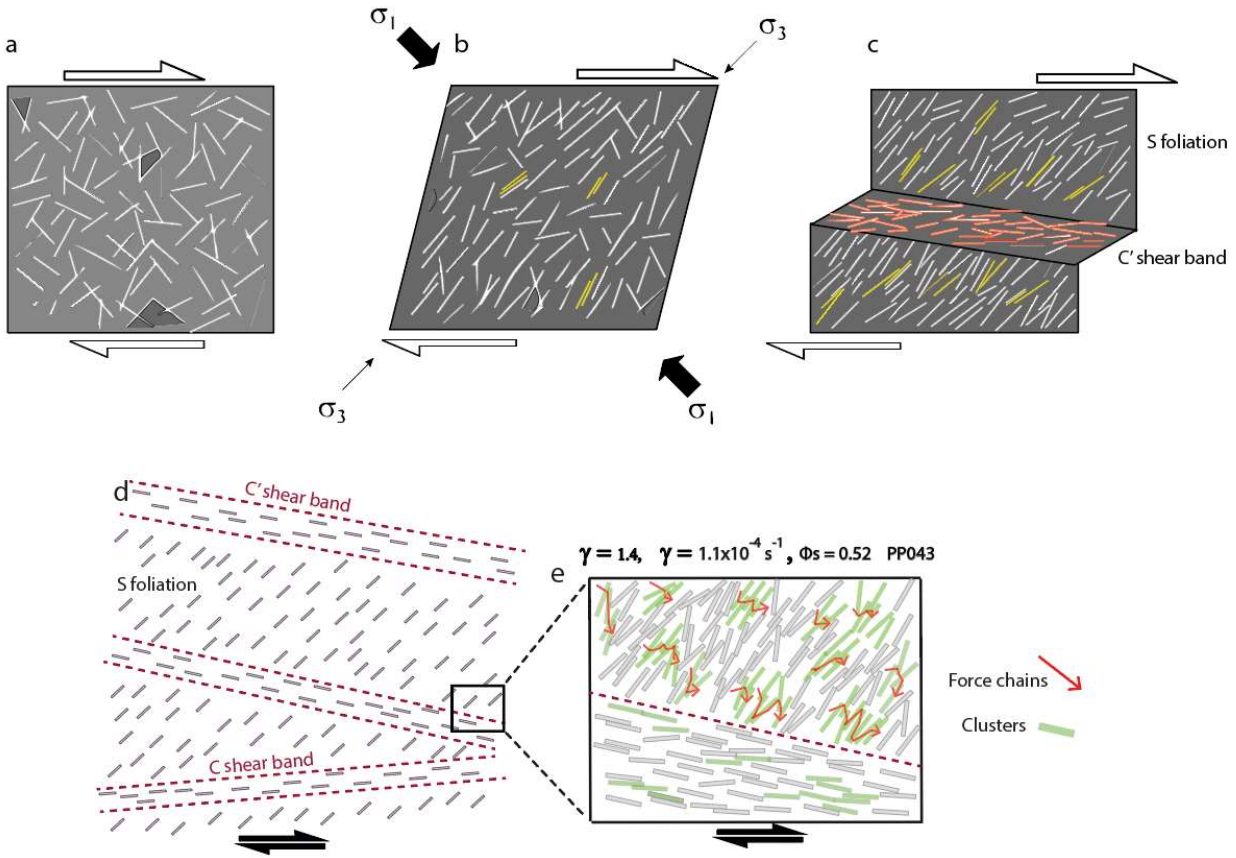

Figure IX.1. Deformation stages and forche chains propagation for PP043 sample (R = 4, ϕ_s = 0.52, strain rate = 1.1*10^{-4} s^{-1} and finite strain = 1.4). a) Undeformed sample. b) First stage of deformation, the contacts start to be formed (yellow crystals). c) Final stage of deformation, with formation of C' shear bands. d) Drawing of the microstructures formed at the end of the experiment. e) Force chains propagation and clusters. The red arrows indicate the direction of the force chains. The clusters are in green.

Figure IX.2 shows the PP029 sample (R = 4, ϕ = 0.59, strain rate = $8.9*10^{-4}$ s^{-1} and finite strain = 1.4) in its deformation structures (fig. IX.2a), in its force chains and clusters (fig. IX.2d).

When the sample begins to be deformed, the crystals cannot move much due to the high crystal content. The penetrative fabric shows no penetrative structure (fig. IX.2b) and the crystals are not oriented in any specific direction. The crystals touch each other (with S-S, C-C and C-S contacts, yellow crystals, fig. IX.2b) and these contacts remain stable over time, producing strong force chains and stable clusters. Due to the non-preferential orientation of the crystals, fewer contacts and clusters are formed. However, due to their stability and intensity, there is a strong localization of the forces. When the intensities of the force chains become too high, the deformation start to localize and the threshold values of the crystals are reached. As a result, the crystals break, creating areas of weakness that spread out to form C shear bands (fig. IX.2c). The crystals within the shear bands are parallel to each other and they have different grain sizes due to the breaking of some of the plagioclases. The result is an interconnected network of crystals oriented in the direction of deformation. Sample PP029 shows a lower number of shear bands than sample PP043, with an abundance of C type shear bands. These types of bands are typical of compressive deformations. The small number of shear bands and their C type indicate that the sample is subjected to strong force chains only in certain areas of the sample.

In the penetrative fabric, the force chains are strong and the clusters are stable (fig. IX.2e).

The force chains were able to localize and break the crystals due to their strong intensity. In the shear bands, due to the high intensity of the force chains, the sample is partially cataclased. The high amount of intact crystals and a small amount of cataclasite could allow a homogeneous distribution of force chains and clusters in the shear bands.

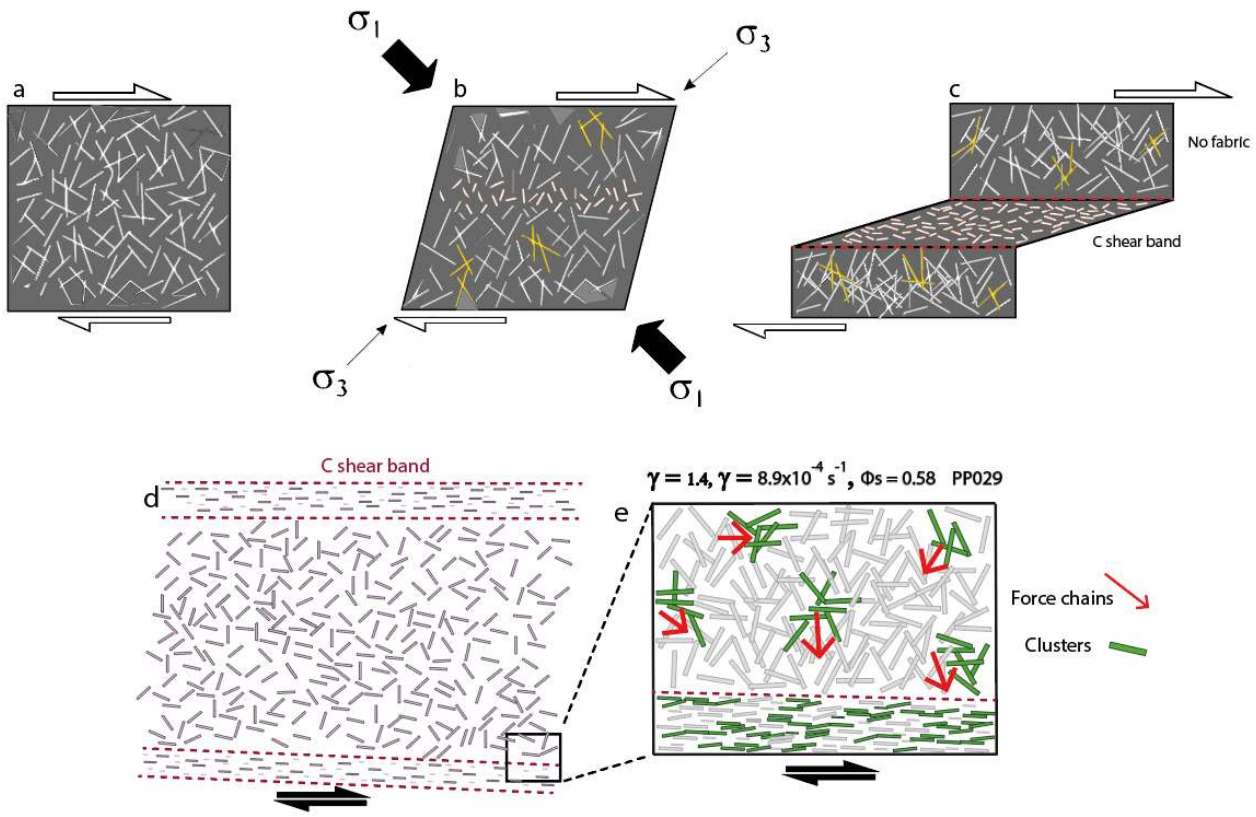

Figure IX.2. Deformation stages and forche chains propagation PP029 sample (R = 4, ϕ_s = 0.59, strain rate = $8.9*10^{-4}\ s^{-1}$ and finite strain = 1.4). a) Undeformed sample. b) First stage of deformation, the contacts start to be formed (yellow crystals). c) Final stage of deformation, with formation of C shear bands. d) Drawing of the microstructures formed at the end of the experiment. e) Force chains propagation and clusters. The red arrows indicate the direction of the force chains. The clusters are in green.

Figure IX.3 shows the deformation struct ures of sample PP249 (R = 4, ϕ_s = 0.59, strain rate = $2.1*10^{-3}$ s^{-1} and finite strain = 2.0). This sample has the same crystal content ϕ_s as the previous sample (fig. IX.2), so it is investigated how a higher finite strain and strain rate can affect deformation structures, force chains and clusters. At the microstructural level, sample PP249 (fig. IX.3) behaves like sample PP043 (fig. IX.2). Figure IX.3a is the undeformed sample. When the deformation starts, the crystals in the penetrative fabric do not orientate, the crystals are in contact and they maintain their positions, forming stable contacts (fig. 3b). When the deformation accumulated on the crystals is too strong, shear bands form (fig. IX.3c). Due to the higher strain rate and higher finite strain, a single central deformed area is formed, consisting of C-type, C' type and thrust shear bands with an anastomosing pattern (fig. IX.3d).

In the penetrative fabric, intense force chains and stable clusters are formed (fig. IX.3e). The shear bands show the plagioclase crystals oriented in the same direction as the shear band, indicating that the localization of forces and deformation is very strong within the shear bands, as highlighted also by the high amount of cataclasite (fig. XI.3e).

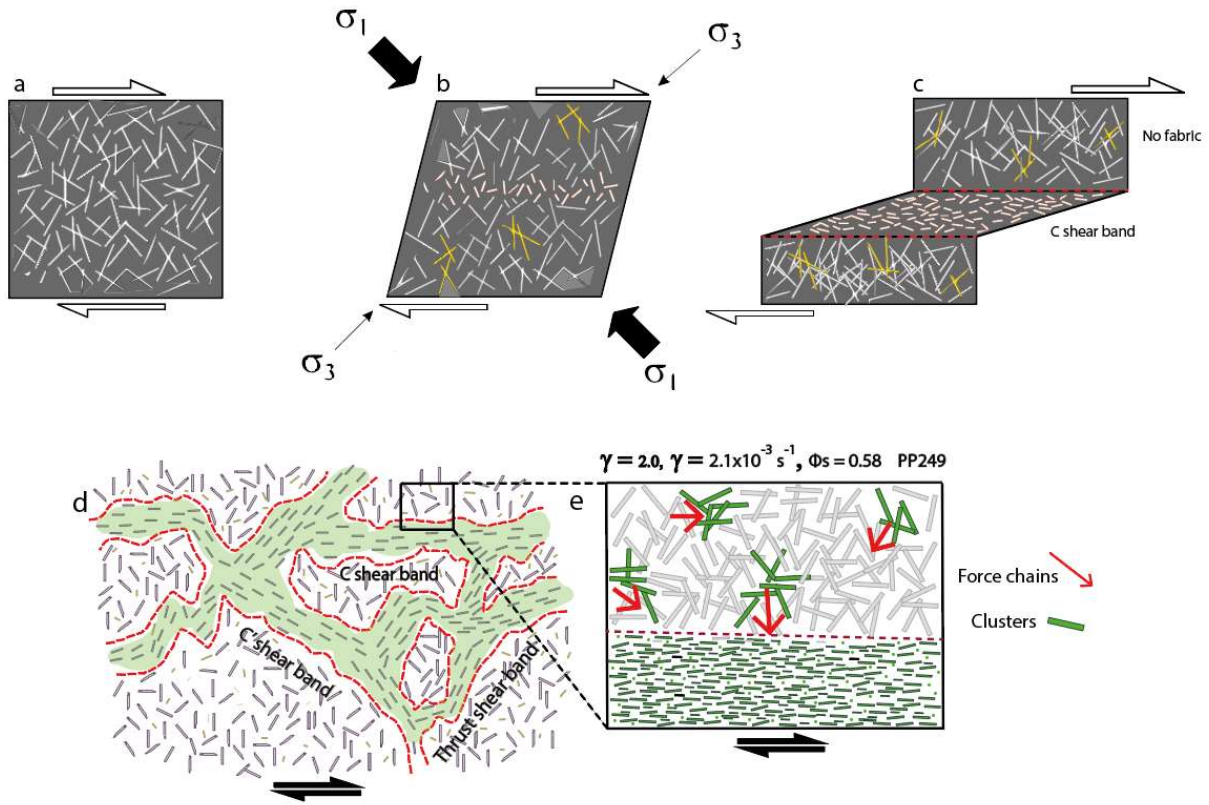

Figure IX.3. Deformation stages and forche chains propagation of PP249 sample (R = 4, ϕ_s = 0.59, strain rate = $2.1*10^{-3}$ s^{-1} and finite strain = 2.0). a) Undeformed sample. b) First stage of deformation, the contacts start to be formed (yellow crystals). c) Final stage of deformation, with formation of C shear bands. d) Drawing of the microstructures formed at the end of the experiment. e) Force chains propagation and clusters. The red arrows indicate the direction of the force chains. The clusters are in green.

Figure IX.4 shows the behaviour of samples with aspect ratio R = 2 and crystal content ϕ_s= 0.58 - 0.59. It has been done one representative plot of all these samples types as they all show similar structural behaviour, and therefore also similar force propagation and clusters formation.

Figure IX.4a is the undeformed sample. When the samples are deformed, the crystals orient between 0° and 45°, forming a dual orientation. There are areas of the sample where the crystals have an orientation closer to 0° and areas of the sample where the crystals have an orientation closer to 45° (fig IX.4b). Figure IX.4c shows weakly oriented crystals, with preferred directions parallel to the shearing or about 45°. In the latter case, the sample exhibits weak S foliation. Despite their high crystal content, plagioclases can move very easily, as their shape favours both translation and rotation. Force chains are formed along the entire surface of the sample, but they are not stable due to the continuous movement of the crystals (fig. IX.4d). The force chains are homogeneously distributed and they are not intense. The shape of the crystals also strongly influences the development of the clusters. The slightly elongated shape of the plagioclases favours a contact between S-S type crystals (in samples with aspect ratio R = 4, elongated crystals can 'wedge' the structure, even though they have a lower crystal content) and the formation of clusters composed of many elements. Like force chains, due to the mobility of the crystals the clusters are very unstable and weak.

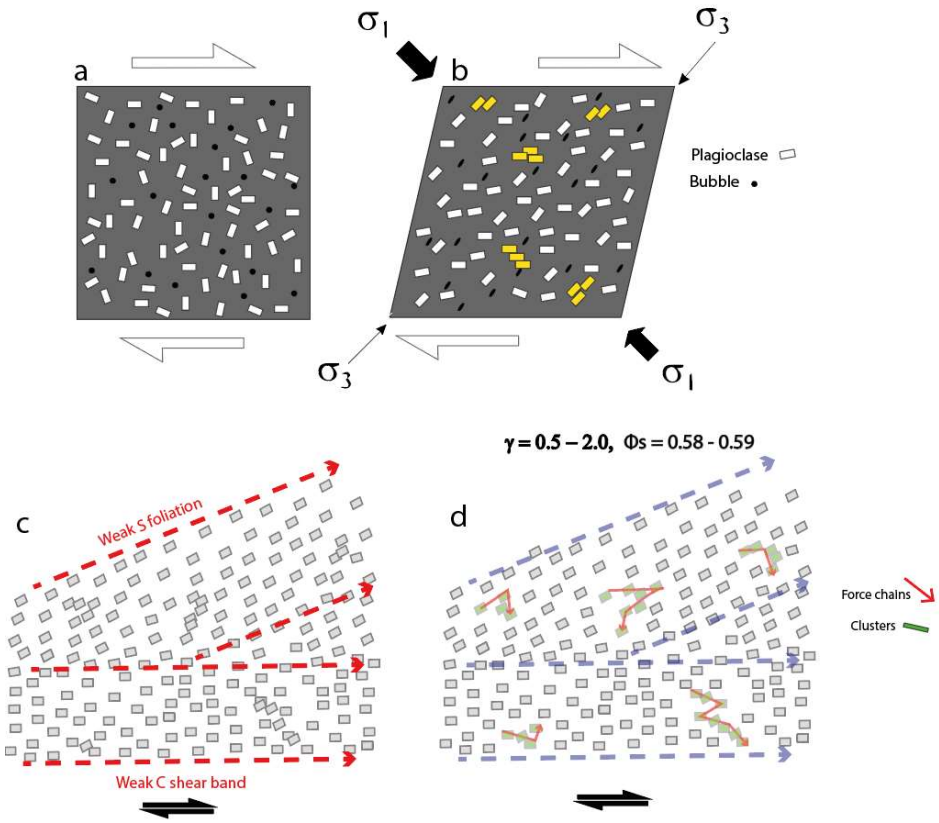

Figure IX.4. Deformation stages and forche chains propagation sample with aspect ratio R = 2 and crystal content ϕ_s = 0.58 – 0.59. a) Undeformed sample. b) Deformation begins and the contacts start to be formed (yellow crystals) c) Drawing of the microstructures formed at the end of the experiment. d) Force chains propagation and clusters. The red arrows indicate the direction of the force chains. The clusters are in green.

Figure IX.5 is a representation of all samples with an aspect ratio of R = 2 and a crystal content ϕ_S between 0.73 and 0.76. Figure IX.5a is the sample undeformed. When the sample is deformed, the crystals orient between -10° and 45° and the first stable contancts are formed (fig IX.5b - c). The crystals oscillate gradually to form a wave-like pattern. This curvilinear and homogeneous pattern can be produced for two reasons. The first is the high finite strain, which promotes more homogeneous strain propagation in the samples and give the crystals time to adapt better to the shearing. The second is the high crystal content, which can have an effect on the behaviour of the force chains. As deformation continues, an interconnected network of bands enriched with residual melt is formed (fig. IX.5d). These bands follow an anastomosing pattern and are all interconnected.

The crystals form a wavy pattern (fig. IX.5e). Due to the shape of the crystals, the force chains are uniformly distributed in the sample (fig. IX.5f), but the high crystalline content may favour the propagation of strain in 'crystal blocks' rather than in each individual crystal. In fact, groups of crystals, all of which are in close contact with each other, behave as a single body and propagate the force chains in a single direction. However, due to the shape of the crystals, the contacts and clusters are not stable and are weak.

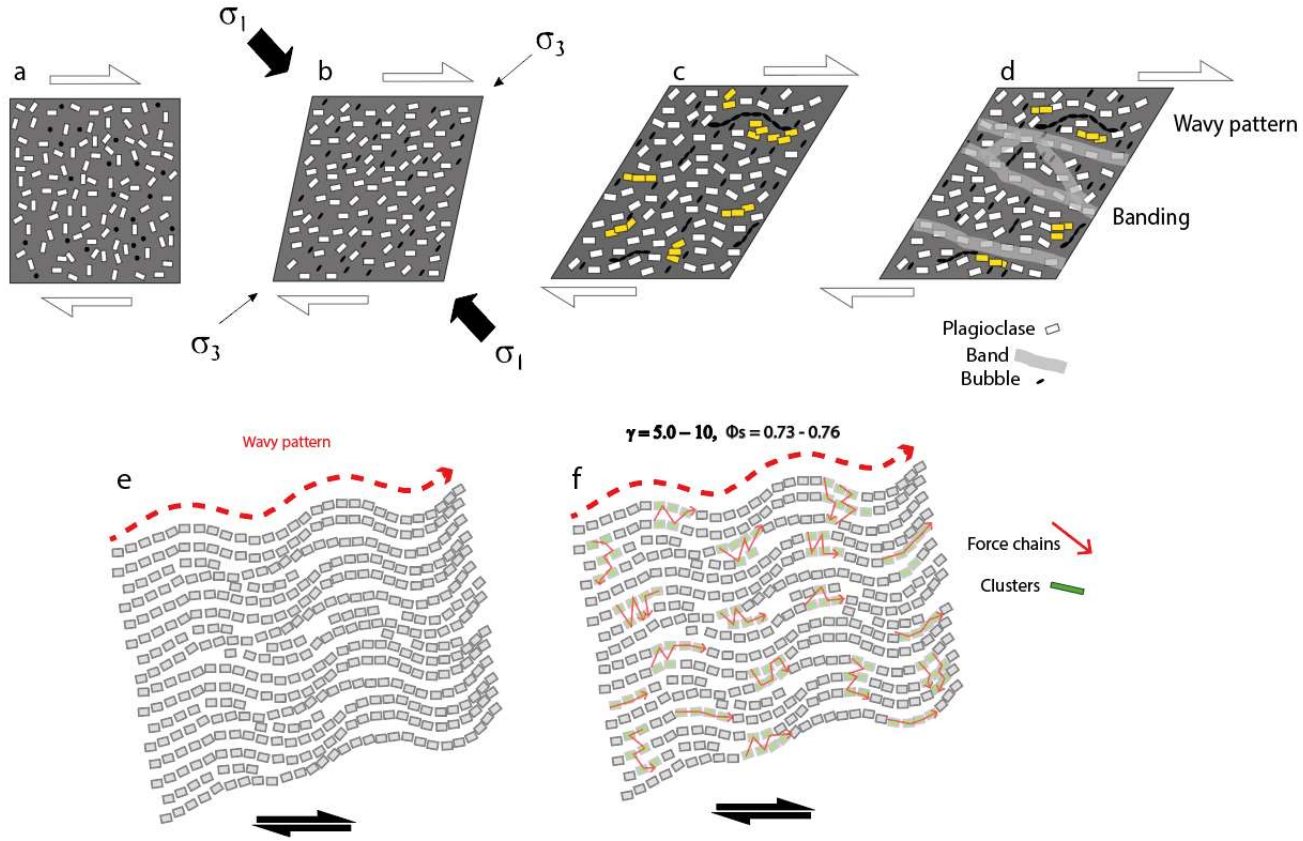

Figure IX.5. Deformation stages and forche chains propagation sample with aspect ratio R = 2 and crystal content ϕ_s = 0.73 – 0.76. a) Undeformed sample. b) Deformation begins and the crystals start to be oriented. c) the contacts start to be formed (yellow crystals) d) In the final stage of the experiment, the crystals are oriented and there is banding. e) Drawing of the microstructures formed at the end of the experiment. f) Force chains propagation and clusters. The red arrows indicate the direction of the force chains. The clusters are in green.

Figure IX.6 shows sample PP701 (R = 2, ϕ_s = 0.95, strain rate = $5.0*10^{-5}$ s^{-1} and finite strain = 1.8). The study of force chains and clusters is made difficult by the high crystallinity, as the resolution of the plagioclase crystals in the SEM images is not accurate enough to show all the boundaries between crystals. Although the sample has an aspect ratio R of 2, the high crystal content ϕ_s makes the behaviour of this sample granular. This behaviour results in a more brittle deformation of the sample.

In figure IX.6a the sample is undeformed. When the deformation starts (fig. IX.6b), the plagioclase crystals are oriented at about 45°, forming a slight foliation S. As deformation continues, a series of interconnected shear bands C' are formed with an anastomosing pattern (fig. IX.6c). The crystals within the C' shear bands follow the direction of the band and they have a smaller grain size than the crystals in the penetrative fabric (fig. IX.6d).

The contacts between the different crystals could not be delineated due to the resolution of the photo (fig. IX.6e). Based on the structural information, it has been hypothesised the behaviour of the force chains. The penetrative fabric is deformed over the entire surface of the sample and its orientation is restricted to a range of about 45°. This means that there is a good propagation of the force chains. Probably the stiffness of the system, given by the high crystallinity, makes the contacts between plagioclase crystals more stable. This stability leads to intense force chains deforming the entire surface. The shear bands are more complex. Due to their orientation, they can be referred to as C' shear bands, extensive deformation structures formed as a result of compression of adjacent areas (such as sample PP043). Within the shear bands, the crystals are fractured and they have a smaller grain size than the penetrative fabric. This may indicate a strong localization of the forces that caused the cataclasitic phenomena (such as in samples PP029 and PP249). It is likely that the force chains in the shear bands are also intense and formed by stable contacts.

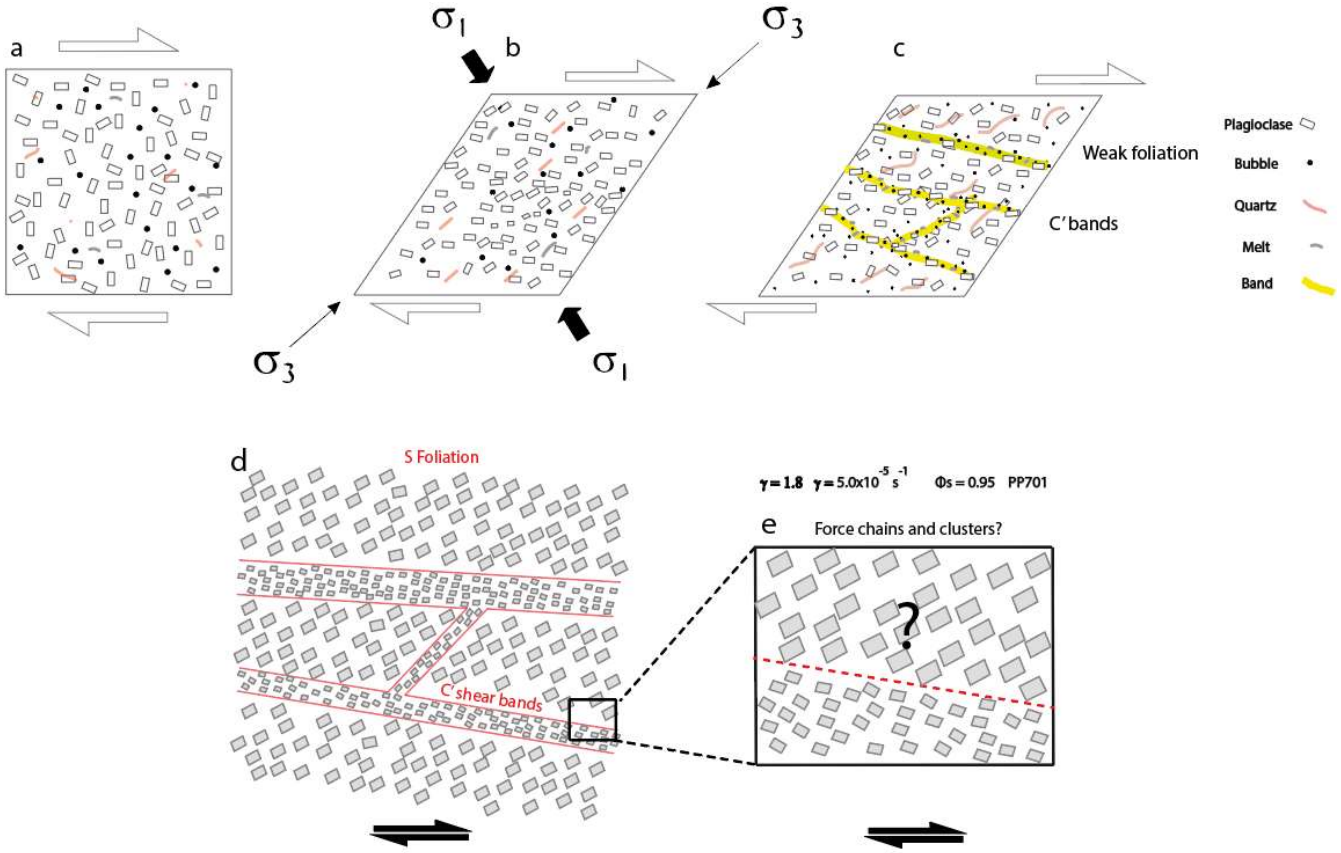

Figure IX. 6. Deformation stages and forche chains propagation sample with aspect ratio R = 2 and crystal content ϕ_s = 0.95 a) Undeformed sample. b) Deformation begins and the crystals start to be oriented. c) In the final stage of the experiment, the crystals are oriented and there is banding. e) Drawing of the microstructures formed at the end of the experiment. f) Force chains propagation and clusters.

3. Rheological diagrams

As previously mentioned, it was not possible to derive the viscosity values of all the synthetic samples. In this paragraph, the viscosity curves obtained for some of the samples have been compared and examined. The samples are PP043 and PP029 from the Picard's PhD thesis and the sample PP701.

The sample with crystal content ϕ_s 0.52 and aspect ratio R = 4 (PP043) initially shows an increase in differential stress as a function of strain rate (fig. IX.7a). At higher values of differential stress there is a plateau where the values remain constant. After the plateau there is a softening of the differential stress as the strain rate increases. The trend of the curve has been divided into 4 areas and the interpretation of these areas is as follows:

1) Elastic deformation with increasing stress, with values of shear strain ɣ starting from 0 up to 0.2. It is also hypothesised that there is an initial rotation of the crystals at this stage.

2) Crystal rotation, where the curve shows a plateau.

3) Formation of shear bands, which correlate with a softening of the curve and show shear thinning behaviour.

4) The system reaches a quasi-steady state.

The sample with crystal content 0.58 and aspect ratio R = 4 (PP029, fig. IX.7b) shows an initial increase in stress followed by a strong softening with increasing strain. As with the 0.52 crystallinity sample, there is an initial phase of elastic deformation corresponding to the initial increase in stress. The stress continues to increase until it reaches a crystal value at which the crystals can no longer resist deformation and they start to break. This phenomenon creates zones of weakness and the formation of shear bands. For this sample as well, the curve has been divided and interpreted as follows:

1) Initial elastic deformation, with shear strain ɣ untill 0.1.

2) Peak zone where the sample is subjected to severe deformation and it reaches a critical stress prior to breakage.

3) Crystal breakage and consequent softening of the rheological response.

4) Development of shear bands.

The sample with a crystal content of 0.95 and an aspect ratio of R = 2 (PP701, fig. IX.7c) shows a similar behaviour to the sample with a crystal content of 0.52 (PP043). There is an initial increase in differential stress as a function of strain rate. At high differential

stress there is a small plateau and then the differential stress decrease progressively. The interpretation of the curve is:

1) Initial elastic response, with shear strain ɣ untill 0.2. As for the sample with ϕ_s = 0.52 and aspect ratio R = 4, it has been hypothesised that there is an initial rotation of the crystals at this stage.

2) The weakly marked plateau corresponds to the maximum orientation of the crystals at about 45°.

3) Softened curve corresponding to shear softening and formation of C' shear bands.

Unlike the other samples, the curve of sample PP701 does not show a final phase parallel to the x-axis. This is probably due to the series of interconnected bands that are form and that increase in number as the deformation continues over time. The plateau is not as extensive as for sample PP043 because the high crystal content prevents some of the crystals from moving and it changes the rheology of the system more quickly.

All curves have non-Newtonian rheological behaviour. Their behaviour can be defined as pseudoplastic shear thinning.

No rheological data could be obtained for samples with aspect ratio R = 2 and crystal contents between 0.59 and 0.76. This is probably due to the low viscosity and low strength of the samples. The crystals, which have a non-elongated morphology, are able to move easily and do not make the sample hard. The analysis of the rheological curve of the sample with a crystal content of 0.95 was possible because the very high amount of crystals made the sample more resistant to deformation.

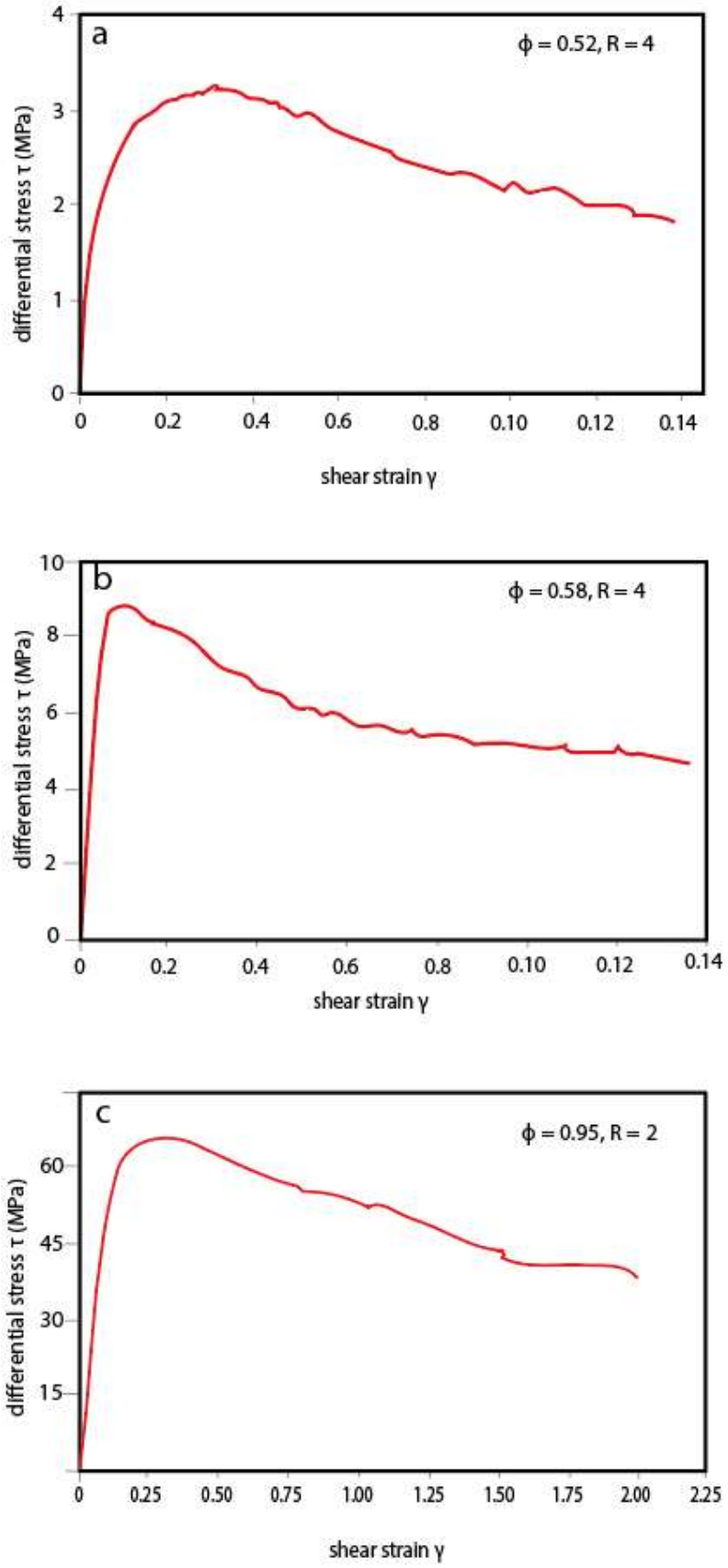

Figure IX.7. a) Rheological curve of sample PP043. b) Rheological curve of sample PP029. c) Rheological curve of sample PP701.

4. Influence of finite strain and strain rate

4.1. Strain rate

Strain rate is a very important parameter that can strongly change the microstructures of deformed samples. Depending on the morphological characteristics of the crystals (aspect ratio R and equivalent diameter Φ), plagioclases may or may not be able to absorb the strain rate. In the case of samples with aspect ratio R = 4, high strain rates lead to the formation of shear bands. The crystals do not have time to move and rotate, they accumulate stress on their surface and they tend to localize the forces. Higher is the strain rates, greater is the localization of deformation in the central part of the sample. This also leads to crystal breakage and cataclasite formation at high strain rates. These processes can be seen in samples PP043, PP029 and PP249. The first, which is the sample subjected to the lowest strain rate ($1.1*10^{-4}$ s^{-1}), shows shear bands scattered throughout the sample with a very regular spacing. This result is in agreement with the work of (Smith, 1997), where it is shown that the important parameters influencing the appearance of shear bands are both the crystalline content and the interaction between particles, which in turn depends on the strain rate. The bands are between 20 µm and 50 µm thick and the crystals within them show no breakage. The second sample (PP029) was subjected to higher strain rates ($8.9*10^{-4}$ s^{-1}). The crystals had less possibility to move and the force chains were localized in specific areas of the sample, in the central zone. The shear bands are fewer than in sample PP043, but they have a larger thickness, between 20 µm and 70 µm. Crystals within the shear bands are partially fractured and cataclasite is found. In sample PP249, which has the highest strain rate value ($2.1*10^{-3}$ s^{-1}), the deformation is localized only in the central part of the sample. There is a series of interconnected shear bands forming an anastomosing pattern. The breaking and cataclasite processes are extremely strong in the shear bands, which vary in thickness between 20 µm and 100 µm. As a result, higher strain rate values correspond to less crystal movement and bigger force localization. Increasing the strain rate values results in fewer shear bands, but they are localized in the central part of the sample, with greater thicknesses and cataclasite processes. At very high strain rates the deformation becomes so localized that it forms a network of interconnected shear bands.

In contrast, for samples with an aspect ratio R = 2, the strain rate does not appear to have affected the microstructures. The shape of the plagioclases allows them to move

and rotate even at high strain rates. As the strain rate increases, the crystals do not accumulate much deformation, but they rotate and move faster.

4.2. Finite strain

The finite strain parameter has not been studied in detail for samples with aspect ratio = 4. The highest value of finite strain obtained is 2, which is not high enough to show differences with the samples with lower finite strains.

For the samples with aspect ratio R = 2, the maximum finite strain value reached during the deformation experiments is 10, so it was possible to investigate how finite strain affects the microstructures. For finite strain of 2, the sample does not show any particular structure. From a finite strain of 5, the entire surface of the samples shows banding phenomena. For finite strain values between 5 and 10, the samples do not show much variation in banding, which appears with fairly regular band in thickness and in spacing. This is in agreement with the works of (Holtzman et al., 2005; Holtzman and Kohlstedt, 2007), which suggests simultaneous banding and a slight variation in band inclination at higher finite strains.

5. Aspect ratio as key parameter for strain localization - Influence of aspect ratio and equivalent diameter

The aspect ratio R of the synthetic samples is shown in the results chapters (see figures IV.3, V.3, VI.3). The graphs have a log-normal trend, so only the harmonic means are considered in the discussion, as they are more representative of the synthetic samples. The different sodium contents in the starting materials allowed the synthesis of monocrystalline samples with plagioclase crystals of different aspect ratio R and equivalent diameter Φ.

Synthetic samples with aspect ratio R = 2 show similar histograms of equivalent diameter Φ, with the harmonic mean decreasing in value as the crystal content increases. The average value of harmonic mean in samples with crystal content of 0.58 - 0.59 is 1.46 (see fig. V.2), while the average value of harmonic mean in samples with crystal content of 0.73 and 0.76 is 1.29 (see fig. VI.2). With increasing crystallinity, plagioclase crystals have limited space to nucleate, forming crystals with smaller equivalent diameters Φ,

but keeping a similar value of aspect ratio R. The same appears to synthetic samples with aspect ratio R = 4, but with some differences between the penetrative fabric and shear bands. The latter have lower values of aspect ratio R and equivalent diameter Φ. These areas are subjected to greater deformation with partial crystal fracture, a "crystal breakeage" (Forien et al., 2011). In addition, for the penetrative fabric and the shear bands, the aspect ratio R and equivalent diameter Φ values decrease with increasing deformation. This makes sense as greater deformation favours crystal breakage phenomena (Forien et al., 2011). Therefore, high aspect ratio values promote the localization of forces, as the morphology of the crystals not allow plagioclases to move, creating stable and intense force chains. Conversely, at low aspect ratio values, the plagioclases are able to move and rotate, propagating the deformation throughout the sample and creating weak and unstable force chains (Azema and Radjaï, 2012).

Figures V.12 and VI.30 in chapters V and VI show the aspect ratio R influences the orientation of the particles: the higher the aspect ratio R, the stronger the orientation of the crystals in the direction of extension. This is due to the tiling effect (Arbaret et al., 1996), where crystals with a larger surface area are subject to a stronger tilt (fig. IX.8). The force chains are able to propagate along the entire crystal surface and they act over a larger area, generating a higher force intensity on the individual crystal. This effect is only visible at aspect ratio R values greater than 4. There is no particular trend for lower aspect ratio values. This is probably due to the surface, which is not large enough for the accumulation of intense force chains. The tiling becomes slightly more intense when the finite strain is greater than 2, but a trend can also be seen at lower finite strains.

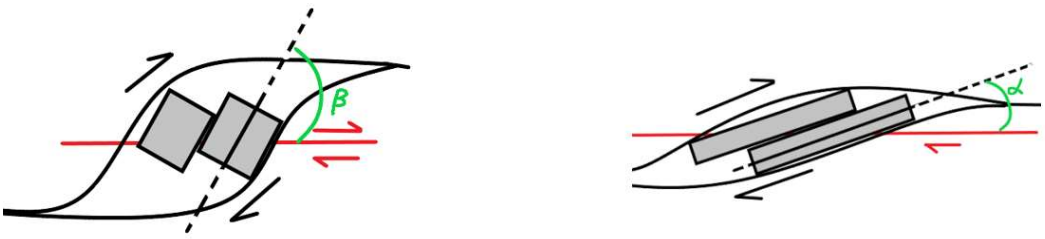

Figure IX.8. Tiling for not elongated (left) and elongated (right) particles.

6. Strain localization as driven component for melt segregation?

The mechanism of melt segregation that it has been considered in this chapter is shear localization. This mechanism can be observed in volcanic mush with a high crystal content, in a highly dynamic system when there are differential stresses acting for example near the walls of volcanic dykes and necks (Paterson et al., 1998; Smith, 1997). According to the work of (Katz et al., 2006), melt segregation can occur through melt channel formation by shear localization controlled by the dynamics of force chains (Bergantz et al., 2017). Different works show that shear bands and deformation structures resulting from shearing can be potential channels for melt segregation and extraction. (Geshi, 2001; Holness, 2018). In a volcanic system, the microlithic component increases as magma rises and cools. This forms a solid-dominated magma capable of transferring stress. When the crystalline content is sufficiently high, the crystal structure becomes stiff and the deformation applied to the volcanic mush can lead to localization of the deformation and subsequent formation of shear bands (Geshi, 2001; Picard et al., 2011; Smith, 1997). The formation of localized structures has been documented both in nature (Arbaret et al., 1993; Smith, 1996; Westerman et al., 2017) and in laboratory experiments (Holtzman and Kohlstedt, 2007; Laumonier et al., 2011; Picard et al., 2011). These structures can form potential channels for melt segregation. The best structures to promote this phenomenon are C' bands. They develop dilatancy (Koenders and Petford, 2007; Petford, 2009; Smith, 1997). So if there is deformation with area in compression, C'-bands are formed that have dilatancy and the melt moves into these areas under less pressure. In any case, all shear bands can be places of passage and extraction of residual melt.

The synthetic samples that show localization of deformation and consequent formation of shear bands are those with aspect ratio R = 4. The elongated shape of the crystals makes the system more rigid and favours brittle deformation. The shear bands found in samples with aspect ratio R = 4 are C' and C type. The former is formed when there is S foliation, producing compression zones. C' bands are extensional areas that accommodate the compression produced by the development of the S foliation. C' bands are associated with a strong localization of deformation in specific areas of the sample. The crystals accumulate the deformation until their threshold is reached. Once the threshold is exceeded, the crystals begin to break and zones of weakness are created. Over time, the zone becomes increasingly deformed until it forms a true shear band. Under conditions of strong deformation, as in the case of sample PP249 (R = 4, ϕ_s

= 0.59, strain rate = $2.1*10^{-3}$ s^{-1} and finite strain = 2.0), the deformation is localized in the central region of the sample. A series of interconnected shear bands are formed. Finally, the sample shows a complex anastomosing network. This could represent an extraction tunnel for residual melt if the magmatic system is open.

Another mechanism that has been subject of investigation in this work is the banding. This phenomenon can promote melt segregation processes and it is defined as the localization of residual melt in a network of interconnected bands with an anastomosing pattern. The bands typically have an inclination of between 15° and 25° with respect to the horizontal plane, with variable thicknesses. Previous work has shown how deformation experiments at high temperatures and pressures can produce this type of banding (Holtzman et al., 2003; Holtzman and Kohlstedt, 2007; Hustoft and Kohlstedt, 2006).

Banding was found on synthetic samples with aspect ratio R = 2 and crystal content ϕ_s at 0.76 and 0.95. The bands vary in orientation, up to a maximum of 25°. The bands are interconnected and they create an anastomosing network. A dynamics of band formation and melt migration is well hypothesised with "the pumping mechanism" ((Holtzman and Kohlstedt, 2007), fig. IX.8). In figure IX.9a, there is a sample subjected to right-handed shear deformation. This generates a series of connected bands (dark grey), which divide areas called 'lenses' (light grey). The bands can be at high angle (20°-25°) or low angle (5°-10°) with respect to the shear plane. All the lents are oriented at the same angle (Zimmerman et al., 1999), showing that this angle does not depend on the physical properties of the matrix, but on the stress.

The pumping mechanism has been schematised as follows: in the initial phase, when the sample begins to deform, bands are formed (fig. IX.9b). Some of the bands increase their slope due to the deformation, causing a decrease in normal stress and shear. As a result, the average pressure and melt pressure decrease, allowing the melt to flow within the band. Deformation partitioning is discussed by Holzman et al, 2005, who show how partitioning reduces the tendency of the band to rotate and stabilises the band at 20°-25°. (Katz et al., 2006) studied this deformation partitioning with numerical models. He shows how band rotation is reduced when melt transport in the bands is effective. The work of (Holtzman and Kohlstedt, 2007) shows that when the bands reach an inclination of about 30°, there is an increase in normal stress due to the strain partitioning. As a result, less strain is absorbed in the band. The adjacent lens is flattened and the converging walls increase the pressure in the low angle bands, which are compacted.

The melt is forced to go into the low angle bands. The cycle starts again, the low angle bands are rotated and decompressed until they are sufficiently compressed.
The banding process favours segregation of the melt in specific areas of the sample. Shear bands favours the extraction of melt by the formation of preferential tunnels through which the melt can migrate. Therefore, the ideal condition for extracting melt from a volcanic mush could be the formation of both banding and shear bands. This condition was not achieved in the experiments of this work and in the experiments used for comparison (from Picard and Laumonier's thesis, 2009). However, the samples show either shear localization or banding, demonstrating that it is possible to reproduce these processes in the laboratory. Only the samples with an aspect ratio of R = 2 and subjected to finite strain values greater than 5 show banding. This indicates how finite strain γ plays a very important role in melt segregation and how the banding is a late process. The bands have a constant inclination and thickness and are interconnected by an anastomotic network. These areas of residual melt concentration show a crystalline depletion of 10%.
Samples with aspect ratio R = 4 always show force localization. Shear bands can be formed by accommodation of compression (like for sample PP043) or by localization of forces with subsequent fracture of crystals and formation of areas of weakness (like for sample PP029).

To summarise, the presence of banding or shear localization C' bands indicates that:
1) The aspect ratio and the shape of the crystals strongly influence the propagation of the force chains and the localization of the deformation.
2) The force chains are uniformly distributed in samples with aspect ratio R = 2 at low finite strain. Their intensity remains low because there is no strain localization. The low intensity of the force chains and the homogeneity of their propagation cause the crystals of the sample to be orientated in the direction of deformation. Due to the tiling process, the crystals tend to follow a wavy pattern.
3) The melt can be segregated at high crystal contents, demonstrating that the mush is not a blocked structure with crystal contents above 0.65.
4) The force chains are inhomogeneous in the samples with aspect ratio R = 4 due to the formation of shear bands, so they maintain a high intensity.

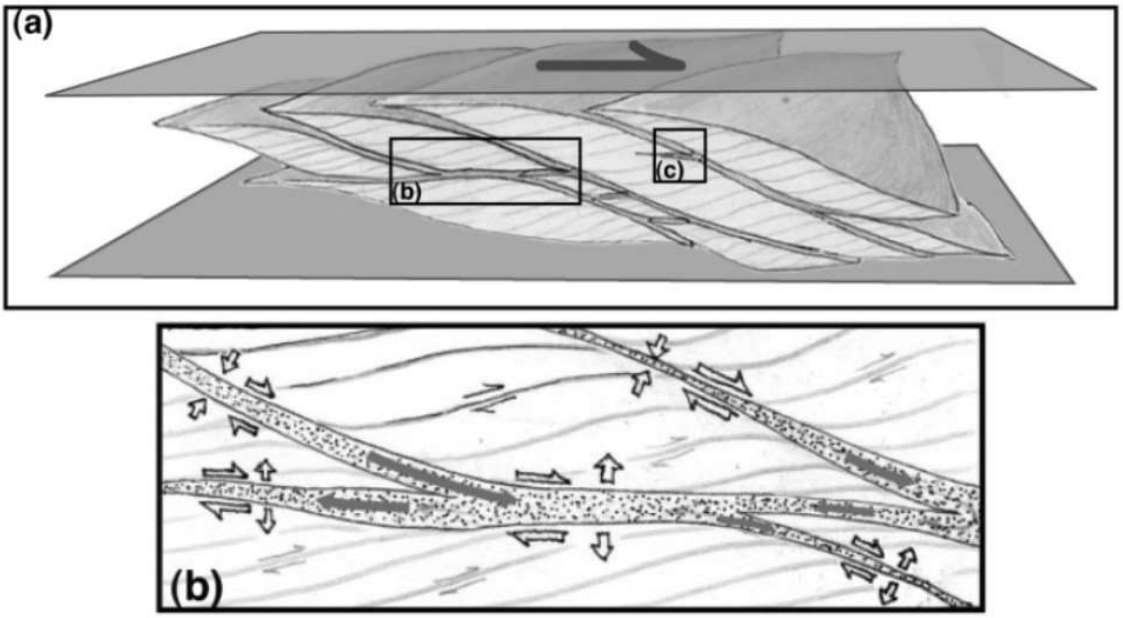

Figure IX.9. The pumping system. a) Samples undergoes torsion deformation. The bands are in dark grey. The lents are in light grey. b) Inset in a. The arrows indicate the directions of deformation. The normal stress switch to compressive stress when the band rich a critical angle (± 30°). As the bands increase their slope, the lents are compressed, the melt is "squeezed" from the lents and it goes in the bands. Modified from Holtzman et al., 2007.

7. Bubbles migration

Bubbles are an interesting element to consider as they can change the rheology of the samples and therefore the deformation structures. When subjected to deformation, bubbles can be oriented in different positions, migrate and coalesce. Conversely, if the sample is strongly viscous, the bubbles cannot be strongly deformed and they are poorly deformed, maintaining their shape and position. The shape of the crystals can also affect the deformation of the bubbles. At high aspect ratio, crystals hardly move and bubbles can get stuck between a row of crystals. At low aspect ratios, crystals can move easily and do not prevent bubbles from moving. In addition, for samples with an aspect ratio R = 2, the force chains are propagated homogeneously throughout the sample, resulting in homogeneous deformation of the bubbles. This is different for samples with aspect

ratio R = 4, where the force chains are more localized and therefore not all the bubbles undergo the same deformation.

In experiments with aspect ratio R = 4, only sample PP249 (R = 4, ϕ = 0.59, strain rate = $2.1*10^{-3}$ s^{-1} and finite strain = 2.0) shows bubble migration. The bubbles exhibit migration only in the shear bands, while they remain unchanged in the penetrative fabric. The shear bands are depleted of bubbles that have migrated into the surrounding penetrative fabric. Although the process is not fully understood, the migration of bubbles may indicate a strong force field in the shear bands that persists over time. As mentioned in the paragraph above, sample PP249 is deformed and it develops localized and intense force chains. When the force chains reach very high intensities, the crystals break, creating areas of weakness. These areas are ideal for the propagation of deformation and shear bands are formed. As the deformation continues over time, the shear bands grow and interconnect, creating an anastomosing pattern. A significant amount of cataclasite is formed in the shear bands and it is uncertain how cataclasite could affect the propagation of force chains (fig. IX.3c), but the bubbles migrate despite the cataclasite. It suggests that the force chains remain strong and intense in the shear bands, probably propagating along the entire surface of the anastomosing area. The bubbles are 'pushed' out of the shear bands and migrate into the penetrative fabric where the forces are less homogeneous and localized in specific areas. This migration of bubbles did not appear to affect the migration and segregation processes of the melt and it was not investigated further.

Samples with aspect ratio R = 2 show bubble orientation, coalescence and migration. At low finite strain values (finite strain = 2) the bubbles are oriented in the direction of deformation of maximum extension. At finite strain values of 5, the bubbles migrate and show coalescence. At finite strain values of 10, the sample shows strong bubble migration. The bubbles behave differently depending on the area of the sample analysed. In the unfractured area (see chapter VI, fig. VI.14) the bubbles have an orientation in the direction of extension with sporadic episodes of coalescence between bubbles. As the fractured area is approached, the number of bubbles increases significantly and the coalescence of the bubbles becomes very strong. The bubbles show a strong orientation (fig. IX.10) due to the high finite strain. As a result, the bubbles have a tendency to move in the direction of force propagation. The bubbles are concentrated in certain areas of the sample, changing its viscosity and making it weaker to deformation. The bubbles form 'coalescence bands' (fig. IX.11) oriented parallel to each other. When the deformation reaches high values, extensive structures are formed that

accommodate the deformation (fig. IX.12). As the deformation continues to increase, the sample reaches fracture. This interpretation could explain how areas of weakness are created in samples with an aspect ratio R = 2, which could ideally represent areas of melt migration.

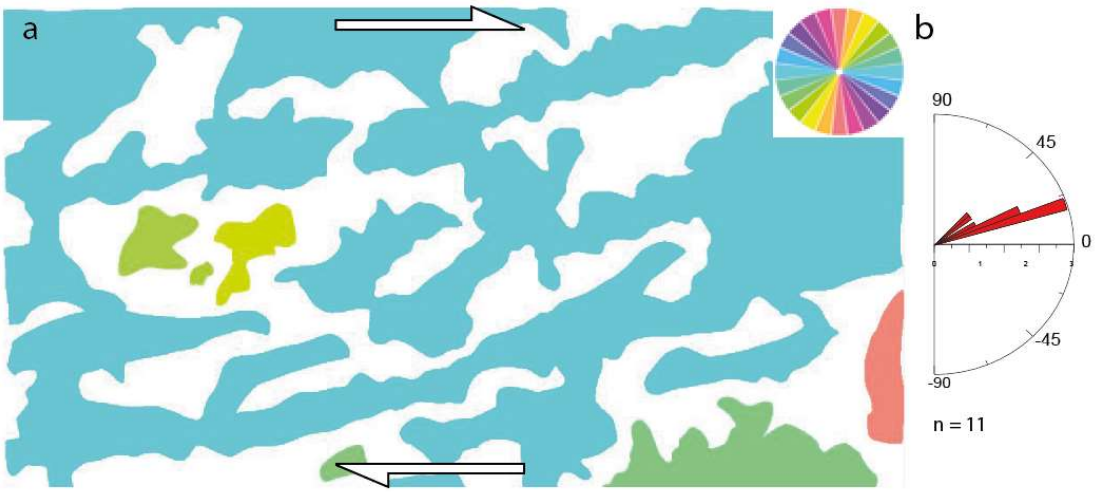

Figure IX.10. Bubbles orientation of the sample PP669 in the fractured area. Bubbles colored according to their orientations. b) Rose of directions of individual bubbles orientation.

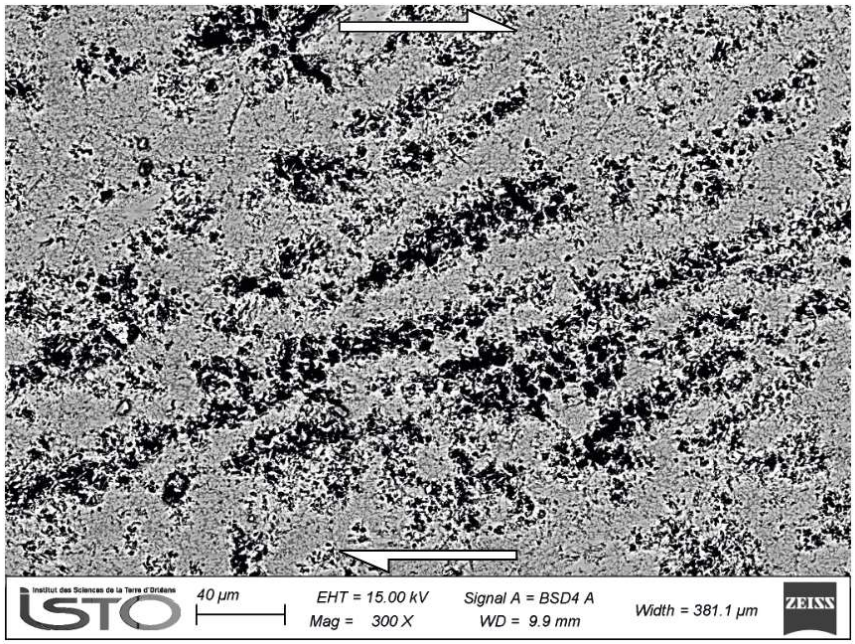

Figure IX.11. SEM picture of sample PP701 in the fractured area. The black line are bubbles forming “coalescence bands”.

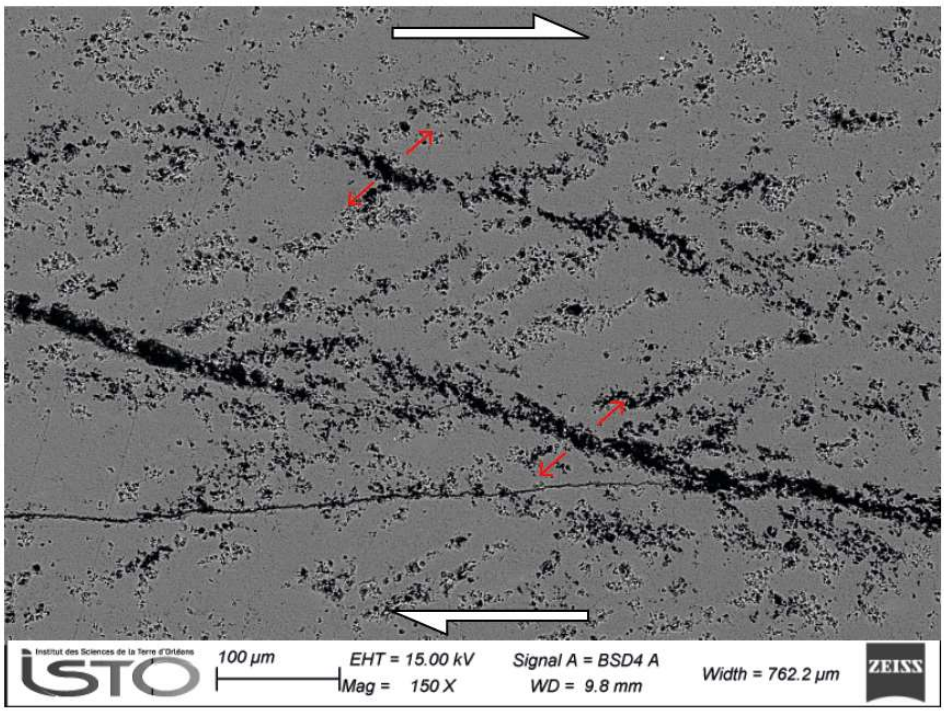

Figure IX.12. SEM picture of sample PP699 in the fractured area. The red arrows are the direction of the extensive fractures.

8. Bubbles and melt segregation

Sample PP701 (R = 2, ϕ = 0.95, strain rate = $5.0*10^{-5}$ s^{-1} and finite strain = 1.8) has a high crystal content. For this reason, it can be defined as a sample with granular behaviour and it undergoes more brittle deformation than other samples with aspect ratio R = 2. The sample is characterised by both melt and bubble migration and further studies are needed to fully understand the migration dynamics. As with the other samples with aspect ratio R = 2, sample PP701 shows a series of interconnected bands, which could follow the formation dynamics proposed by (Holtzman and Kohlstedt, 2007) and illustrated in the previous section. Compared to the other samples, PP701 does not show a wave pattern for the crystals, but there is foliation at about 45° in a penetrative fabric. Some area of the banding zones is so well defined that it could be described as C' shear bands. As C' shear bands, they are areas of extension formed as a result of compression due to foliation. These extensional zones may represent preferential migration areas for melt and bubbles.

9. Comparison between models

The investigation on how a volcanic mush can control melt segregation and extraction is one of the aims of this thesis. As mentioned in Chapter 1, the melt needs specific conditions to be extracted, such as certain temperatures, pressures, water and crystalline contents, and specific deformation processes, such as shearing. The type of deformation produces different structural characteristics of the samples and different propagation of the deformation. These conditions and processes define the “windows of extraction” (Burgisser and Bergantz, 2011; Dufek and Bachmann, 2010). Figure IX.13a shows the general correlations that can affect the definition of the mush and the area of the windows of extraction. Different crystal contents define whether a system is a suspension, a soft mush or a locked up mush. The present study shows that is that the aspect ratio R of the crystals has a huge influence on the propagation of the deformation in the deformed samples. The crystalline boundaries between different systems and the different types of microstructures formed during deformation change as a function of this parameter. The associated deformation structures also change. In this section, figure 13 has been used to highlight the different behaviour of the volcanic mush depending on whether it has an aspect ratio of R = 4 or R = 2.

Figures IX.13b and IX.13c show the behaviour of a volcanic mush with an aspect ratio of 4 and 2 respectively. Picard's thesis shows how a volcanic body has the characteristics of a suspension with a crystal content of less than 20%. The volcanic body has a Newtonian behaviour, a constant viscosity and consequently there is no localization of forces. Therefore, for both samples with aspect ratio R 4 and 2, the "suspension" range is defined at crystal contents lower than 20%, since the shape of the crystals does not strongly influence the deformation of the sample. From crystal contents greater than 20%, interconnectivity can be form between the crystals that are capable of transmitting stress (Petford, 2003), hence the transition from suspension to mush. Depending on the aspect ratio R of the crystals, there is a different propagation of the force chains and therefore a completely different localization of the deformation. Samples with aspect ratio R = 4 are able to generate intense and stable force chains. There is shear localization and the formation of shear bands starting from a crystal contents of 50% (from Picard's thesis, but simple shear experiments with lower crystal contents have not been carried out, so the formation of shear bands at lower crystallite contents cannot be excluded). For crystal contents higher than 59%, the deformation experiments carried out by Picard do not show shear localization due to the high viscosity of the

samples, which allowed low finite strain experiments. The system is defined as blocked, but shear localization might be possible if high finite strain experiments could be carried out.

For the mush of figure IX.13c and crystal contents higher than 20%, the propagation of the deformation is completely different compared to the mush of figure IX.13b. The force chains generated are not high enough to allow shear localization because they are very unstable and not very intense. The deformation is distributed throughout the sample and all the crystals orient to form a wavy pattern called the orientation domain. By increasing the crystal content, more stable and intense force chains are gradually formed, but never to the point where shear localization is achieved. At crystallinity higher than 73%, the deformation is such as to allow the melt to segregate into bands (segregation windows). At 95% crystallinity, the mush is still deformable and it shows melt segregation. This is a new boundary for the definition of volcanic mush.

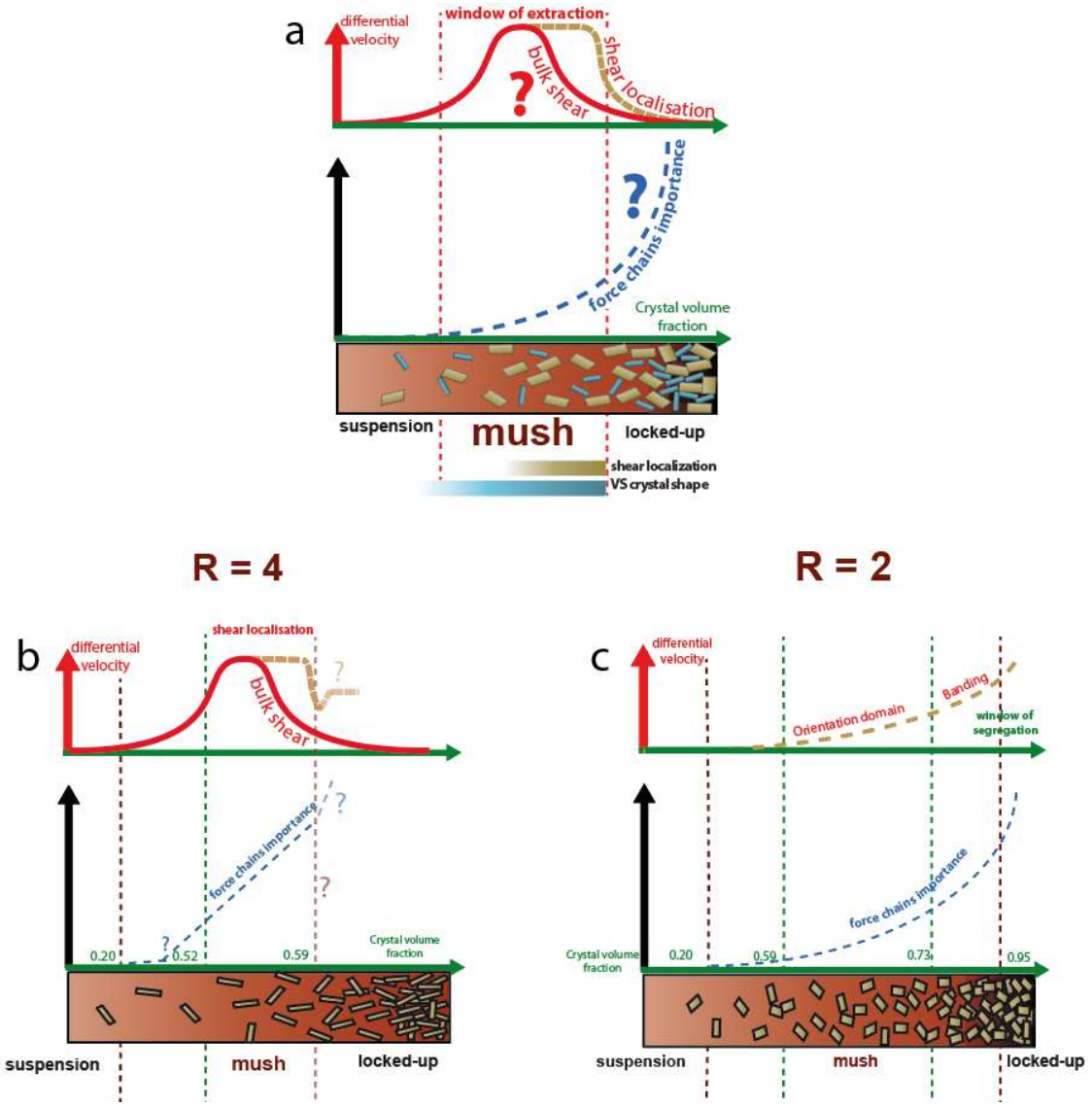

Figure IX.13. Summary diagrams of mush behaviour as a function of aspect ratio R. a) Mush with aspect ratio R = 4. b) Mush with aspect ratio R = 2. The red dashed lines highlight the boundaries of the mush (suspension or blocked solid system). The dashed green lines delineate areas of different deformation structures found during torsion experiments.

10. Natural samples

The natural samples studied in this work are the Suc de Sara, a volcanic dyke, and the Petit Gerbier, a volcanic neck. These two bodies were chosen because they are representative of volcanic structures undergoing surface deformation. They have similar chemistry, although the Suc de Sara has a more complex mineralogy than the Petit Gerbier. Both volcanic bodies were sampled in their inner and outer parts, which have higher and lower temperatures respectively. This shows how the thermal gradient affects crystal morphology and deformation structures. Another factor to consider is the cooling rate. The Suc de Sara is a volcanic dyke, it has emplaced at deeper depth than the Petit gerbied neck and it has therefore cooled more slowly than the Petit Gerbier, which has cooled more rapidly. Both the cooling rate and the sampling area strongly influence the morphology of the crystals. At slow cooling rates and in the inner areas of the volcanic body, crystals have time to nucleate and grow, forming very large crystals with a small aspect ratio R. Conversely, for volcanic bodies formed at a very fast cooling rate and in the outer areas of the neck, the crystals developed are smaller and they have a high aspect ratio R. These different morphologies change the deformation structures of the samples and the propagation of the force chains.

Figure IX.14a shows a drawing of the Suc de Sara. The stars indicate the sampling areas. In the inner part of the volcanic body, the sample is exposed to high temperatures due to its central position and the depth of the dyke. In addition, due to its location, the sample is subject to less deformation than in the outer areas. There are segregation phenomena that form banding. There is an alternation of areas formed by elongated crystals (feldspars) and areas formed by more rounded crystals (nepheline) with residual melt (fig. IX.14b). The low aspect ratio of the crystals favours their mobility. The crystals can easily move and rotate, so the force chains propagate over the entire surface of the sample, without localization and with low intensities (fig. IX.14c). The round shape of the crystals also favours homogeneous propagation. There are therefore no shear bands or structures from strain localization. In the outer dyke zone (fig. IX.14d), temperatures are lower and the deformation rate is higher. The crystals appear smaller, with a predominance of feldspars with a high aspect ratio. The elongated shape of the crystals makes hard their movement. The force chains are localized to specific areas of the sample and they are intense, forming shear bands (fig. IX.14e).

Figure IX.15a shows the Petit Gerbier. As with the Suc de Sara, sketches show the structures in the inner and in the outer parts of the sample and the relative directions and intensities of the force chains. Petit Gerbier is a shallower volcanic structure than Suc de Sara, which has experienced faster cooling rates. Probably for this reason, the inner sample (fig. IX.15b) does not show banding, but it shows orientated plagioclase crystals and melt lenses scattered over the sample surface. The rapid ascent of the neck did not allow the crystals and melt to segregate along the direction of deformation. The crystals have a low aspect ratio R and they are in motion, following a wave pattern. The force chains formed are temporally unstable, propagate over the entire surface of the sample and are of low intensity (fig. IX.15c). The localization of the forces is so low that there are no shear bands. The outer region of the neck (fig. IX.15d) has larger, elongated crystals that have limited movement. This produces very localized and stable force chains (as in sample SA4) which form shear bands (fig. IX.15e).

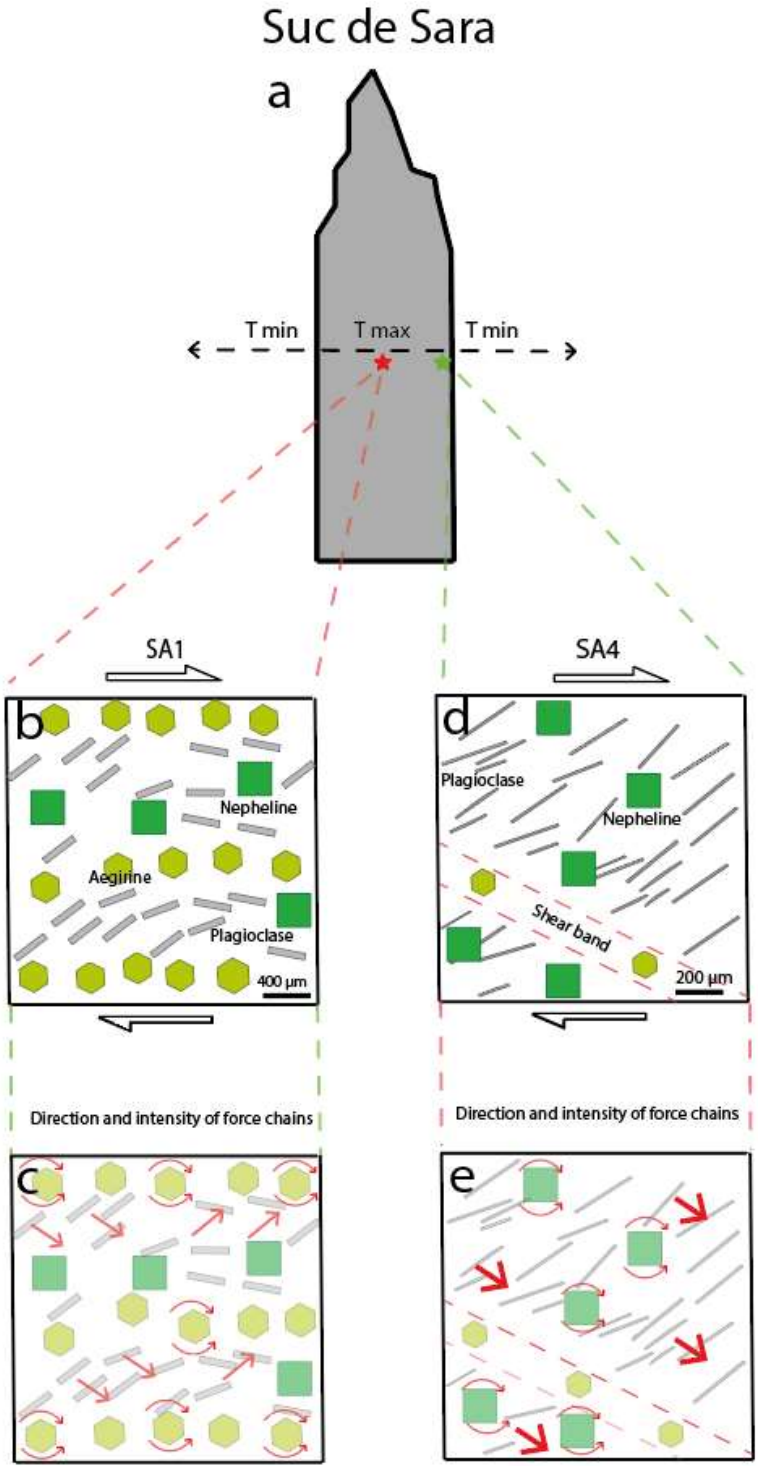

Figure IX.14. a) Schematic drawing of Suc de Sara. The stars indicate where the samples come from. b - d) Drawing of the deformation structures in the inner area (b) and outer area (d) of Suc de Sara. c - e) Drawing of the force chains direction and intensity in the inner area (c) and outer area (e) of Suc de Sara. The red arrows indicate the direction of the force chains.

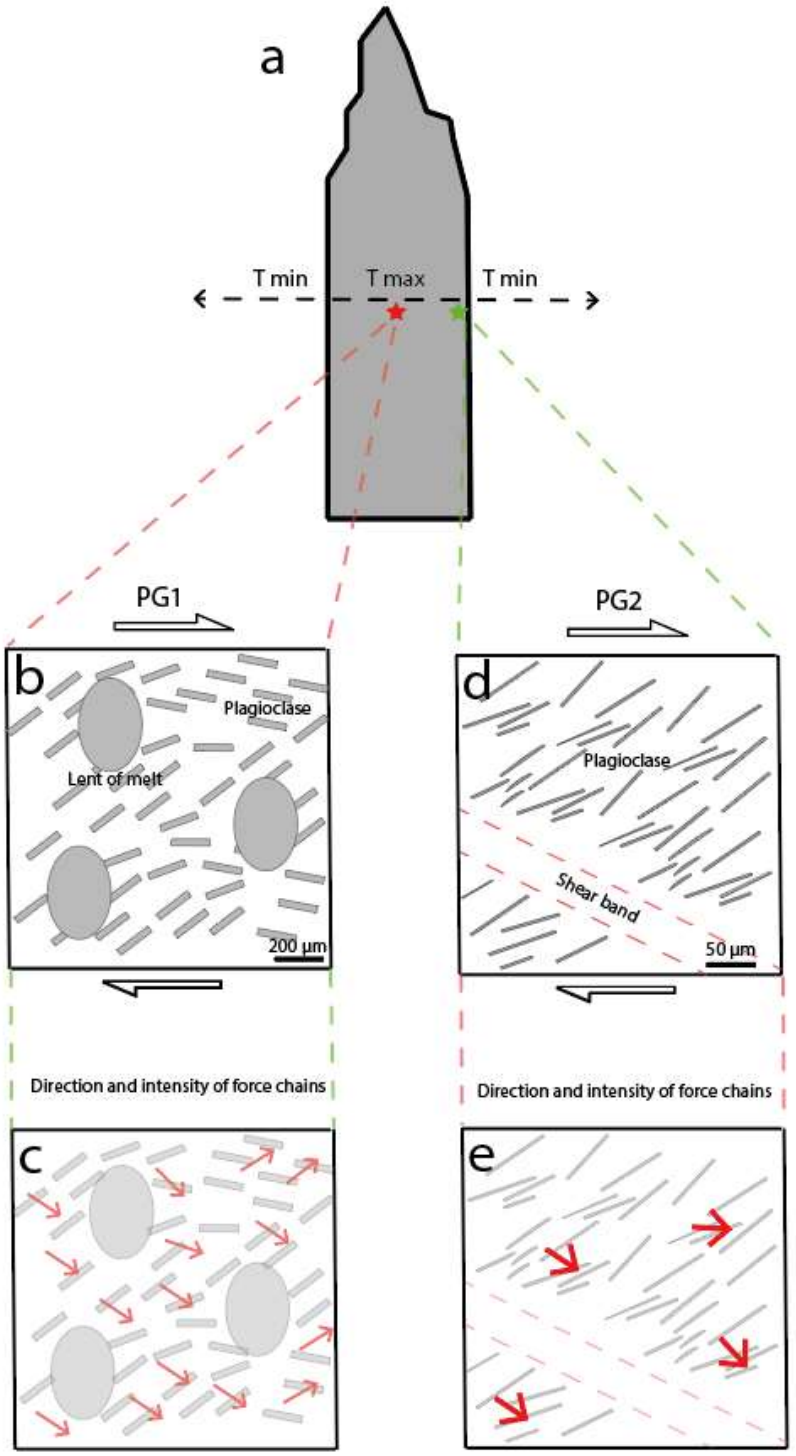

Figure IX.15. a) Schematic drawing of Petit Gerbier. The stars indicate where the samples come from. b - d) Drawing of the deformation structures in the inner area (b) and outer area (d) of Petit Gerbier. c - e) Drawing of the force chains direction and intensity in the inner area (c) and outer area (e) of Petit Gerbier. The red arrows indicate the direction of the force chains

11. Set up model

During the initial magmatic phase, the rising magma of Suc de Sara and Petit Gerbier has a low crystal content and the crystals are not in contact (figure IX.16 a and b, lower part). The crystals are able to translate and rotate, forming pervasive mineral fabrics, typical structures of magmatic flows in the initial phase of ascent (Smith, 2002; Vernon, 2000; Westerman et al., 2017). This situation can easily be imagined in both the inner and outer parts of magmatic bodies. As the magma continues to rise, these magmatic bodies undergo greater deformation and encounter lower temperatures. These two factors cause an increase in the crystal content, which reaches such proportions that an interconnected framework of crystals is formed. In this situation there is potential for force chain diffusion and thus strain localization. The magma continues to rise until it reaches the plug zone (figure IX.16 a and b, upper part). As deformation increases and the observation point moves from the inner to the outer part of the volcanic dike and neck, more pronounced deformation structures are observed. The shear deformation is high enough to cause segregation of the melt. In the inner areas of the Suc de Sara (fig. IX.16a, upper part), segregation is expressed as banding formed by C bands parallel to the S foliation. In the inner areas of the Petit Gerbier (fig IX.16b, upper part), segregation of the residual melt is not yet achieved. The melts remains concentrated in lenses and the crystals follow a wavy pattern. The initial deformation causes the accumulation of residual melt in these areas, which represent zones of weakness due to their structural composition. Approaching the margins of the two magmatic bodies, a more brittle deformation occurs. As a result of the strong deformation that has occurred, extensive C' shear bands are formed that accommodate the compressive deformation of adjacent areas. These extensional zones provide preferential regions for residual melt accumulation as they are subject to less pressure and the melt is 'pushed'. An anastomosing network of shear bands C' develops, where melt can concentrate.

In both the dyke and the neck, residual melt is not extracted. For the Suc de Sara, the western cooled margin (Pereira et al., 2024) prevented the extraction of melt. For the Petit Gerbier, the melt probably ascended very quickly and the structure was 'frozen' before the residual melt had a chance to be extracted.

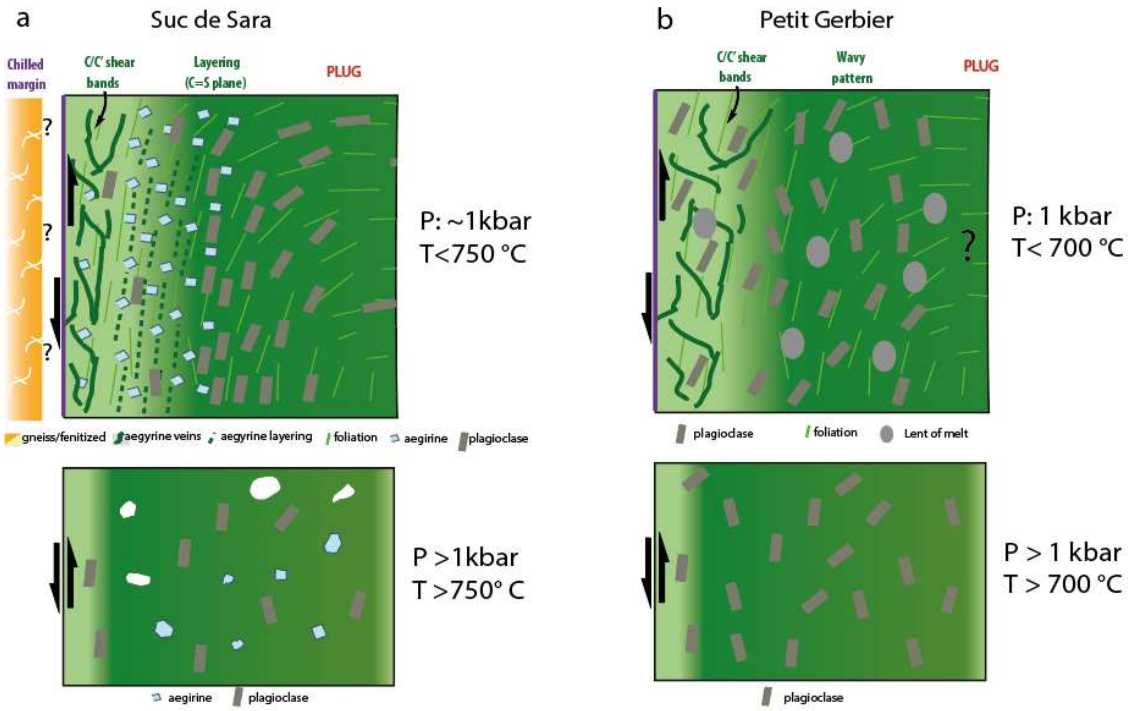

Figure IX.16. Evolution of deformation structures during magma ascent. a) Suc de Sara. b) Petit Gerbier. Modified from (Pereira et al., 2024).

12. Comparison between natural and synthetic samples

The natural samples from Suc de Sara and from Petit Gerbier were compared with the synthetic samples. Both natural samples show similarities with the synthetic samples. The outer samples of Suc de Sara (SA1, fig. IX.17a) and Petit Gerbier (PG3, fig. IX.18a) show similar deformation structures to the synthetic samples with aspect ratio R = 4 and crystal content between 0.58 and 0.59. All these samples show deformation localization expressed by the formation of shear bands (fig. IX.17b and fig, IX.18b). The minerals are oriented along the direction of deformation, forming either an S foliation or a wave pattern.

The internal samples from Suc de Sara (SA4, fig. IX.17c) and Petit Gerbier (PG1, fig. IX.18c) do not show shear localization, but the deformation is distributed over the entire surface of the sample. The crystals follow the deformation, orienting with inclinations between -10° and +10°. Sample SA4 shows a banding phenomenon. The bands are enriched in residual melt with an aegirine composition. The synthetic counterparts are the samples with aspect ratio R = 2 and crystal content between 0.73 and 0.76 (fig.

IX.17d). As with the samples with the same aspect ratio R and lower crystal content (0.58-0.59), mineral foliation occurs in the direction of deformation. High strain intensity and higher crystal content produce bands. A wavy trend is observed in the K-feldspar crystals of sample PG2. The same phenomenon is observed in the synthetic samples with aspect ratio R = 2 and crystal content between 0.58 and 0.59 (fig. IX.18d).

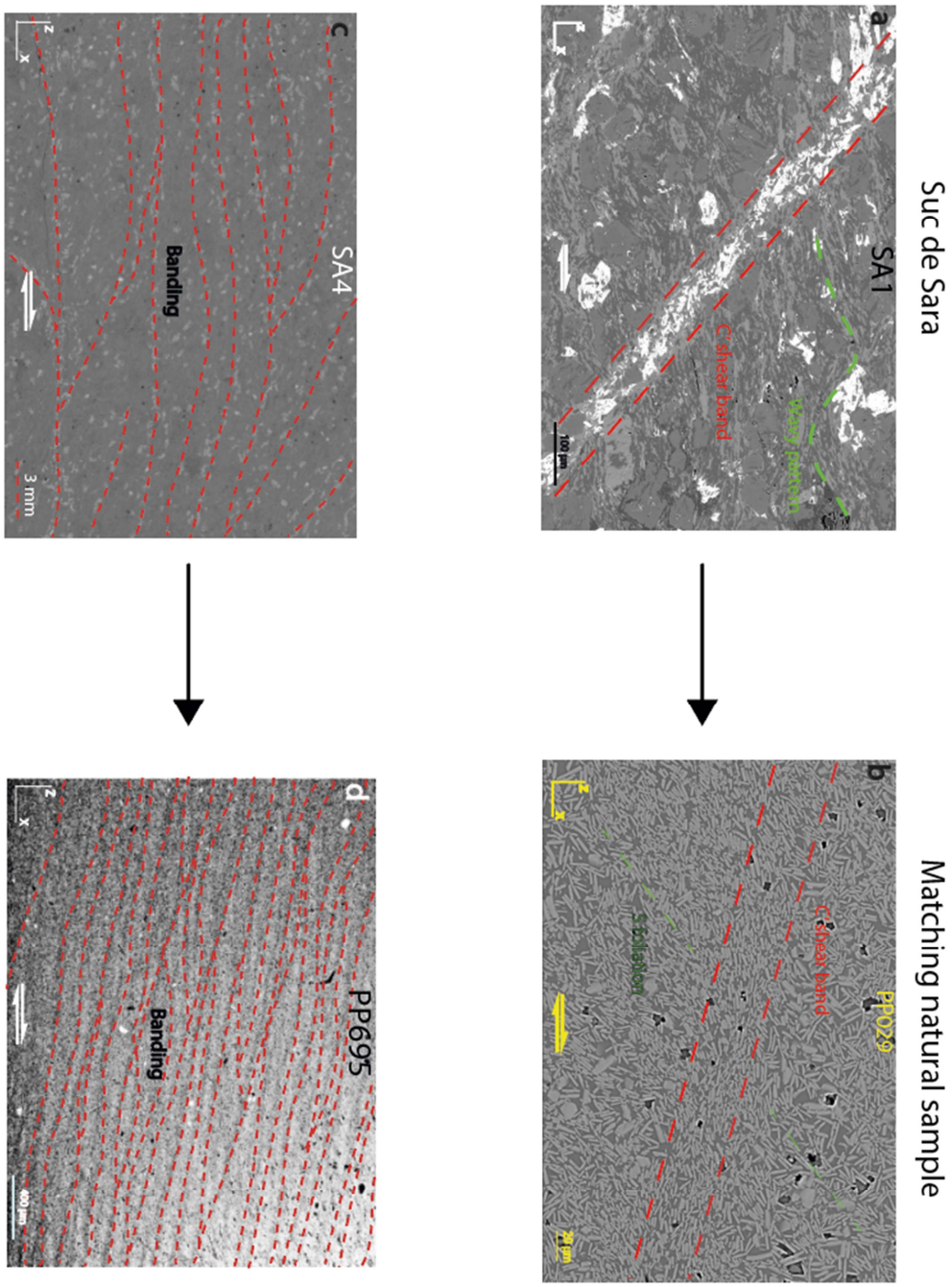

Figure IX.17. SEM pictures of natural and synthetic samples compared. Deformation structures are highlighted by the dashed red lines. a) Suc de Sara SA1, b) PP029, c) Suc de Sara SA4, d) PP695

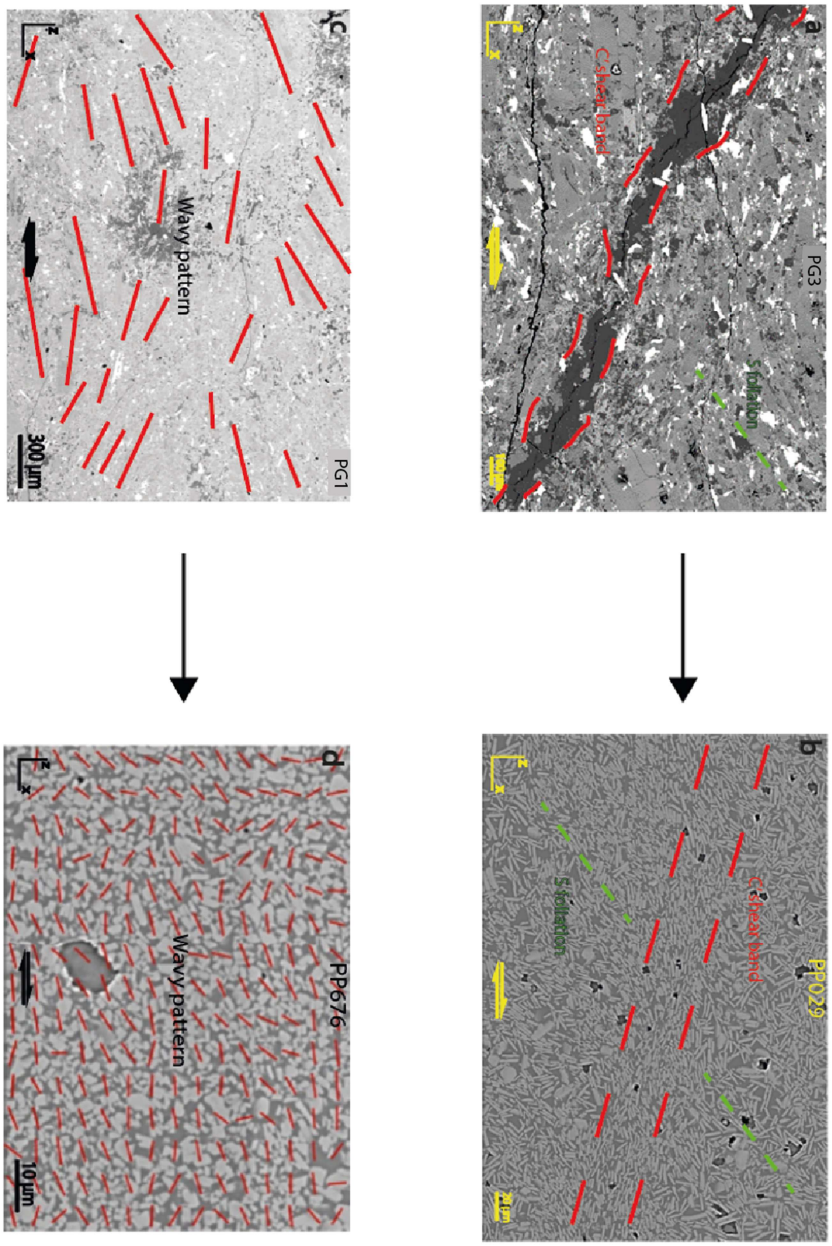

Figure IX.18. SEM pictures of natural and synthetic samples compared. Deformation structures are highlighted by the dashed red lines. a) Petit Gerbier PG3, b) PP029, c) Petit Gerbier PG1, d) PP676.

13. Crystal shape controls the window of deformable mush

As discussed in previous chapters, a mush is defined as a magmatic body dominated by crystals and containing a variable percentage of silicate fluid (Delph et al., 2017; Ward et al., 2014). Despite the high crystal content characteristic of mush, silicate fluid can be extracted and the mush can be deformed if external deformation, such as shearing, is applied. Crystalline domains describing the boundary between a mush and a solid-like system have not been well defined in the scientific literature (Arzi, 1978; Van Der Molen and Paterson, 1979; Lejeune and Richet, 1995; Vigneresse et al., 1996; Rosenberg and Handy, 2005). In this work, a boundary based on the deformability of the volcanic body is proposed: the transition between a mush and a solid-like system occurs when the mush subjected to deformation cannot be deformed, and thus neither deformation structures nor melt migration can happen. The deformation experiments performed in this work show how a mush can form the same deformation structures but at different crystal content depending on the aspect ratio R of the crystals.

Figure IX.19a shows a deformed sample with aspect ratio R = 4 and a crystal content ϕ_s of 0.52. The sample develops a penetrative fabric with foliation and a series of shear bands crossing the sample surface.

Figure IX.19b shows the deformed sample with aspect ratio R = 2 and a crystal content ϕ_s of 0.95. Similar to the previous sample, foliation and a series of shear bands are formed.

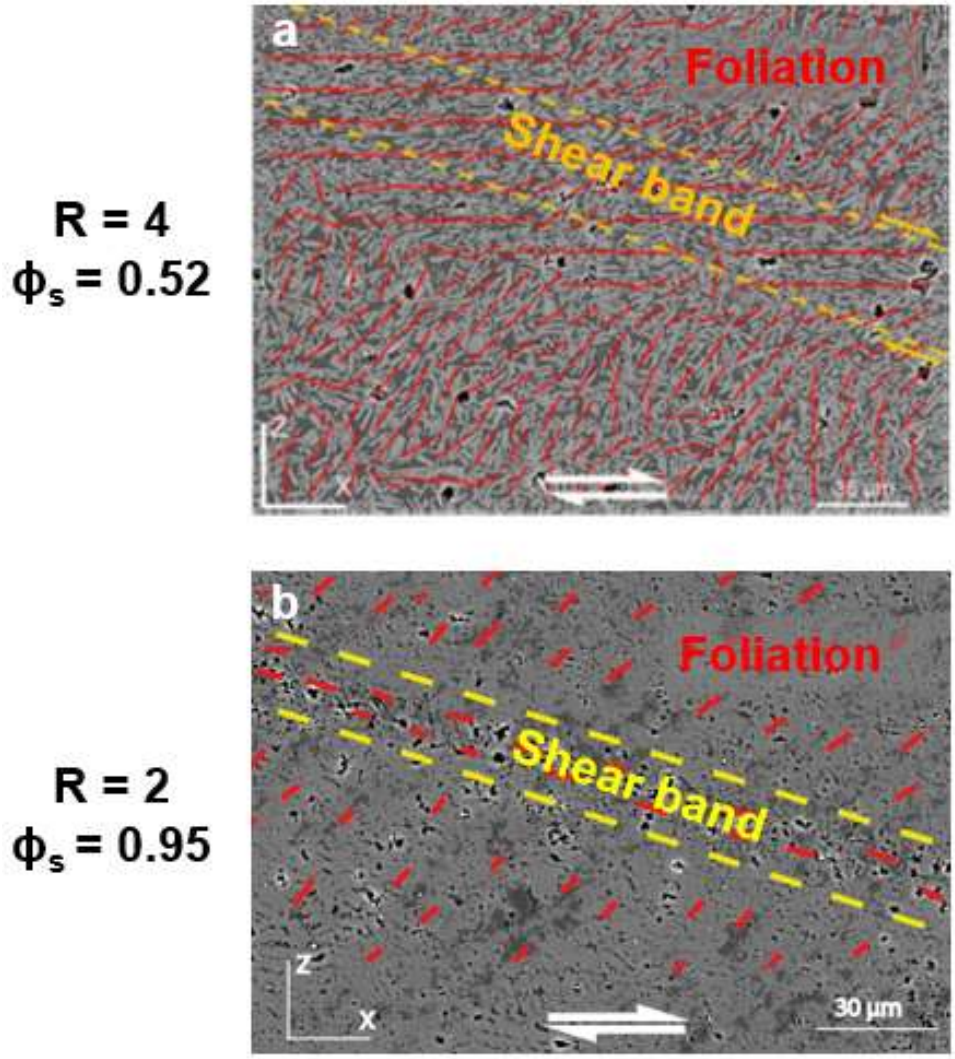

Figure IX.19. SEM images of the deformed samples with the deformation structures highlighted. a) Sample with aspect ratio R = 4 and cristal content ϕ_s of 0.52.
b) Sample with aspect ratio R = 2 and cristal content ϕ_s of 0.95.

This analogy of structures at different crystal contents illustrates how the mush field can change depending on the aspect ratio of the crystals (fig.IX.20.) At aspect ratio R = 4, the mush is deformed to crystal contents ϕ_s of 0.59, defining a narrow mush field. At aspect ratio R = 2, the mush is deformable up to crystal contents ϕ_s of 0.95, creating a very large mush field.

In conclusion, it can be seen that the boundary between the mush and the solid-like system changes as a function of the aspect ratio R for a given crystal contet ϕ_s.

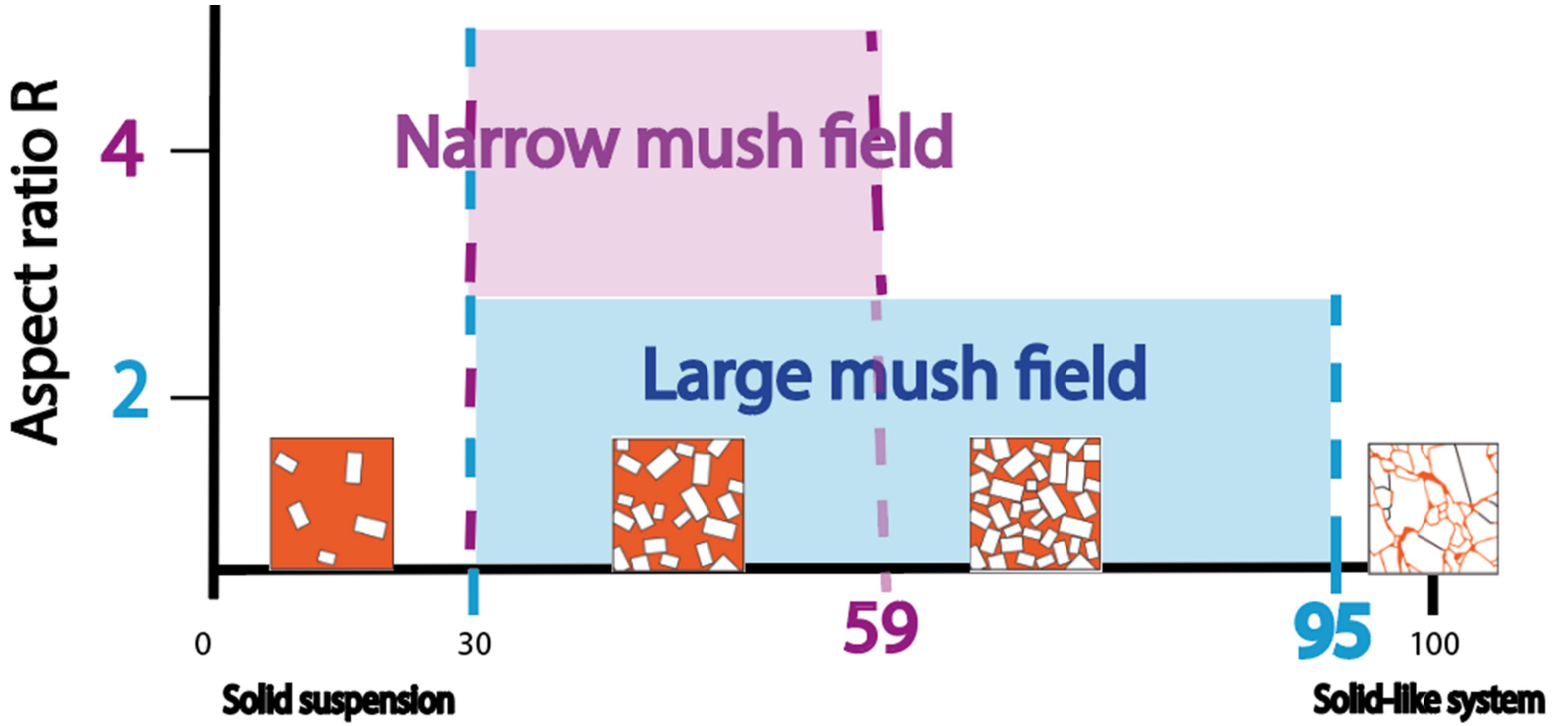

Figure IX.20. Crystal content ϕ_s vs aspect ratio R diagram. The purple area represents the domain of mushes with aspect ratio R = 4. The blue area represents the domain of mushes with aspect ratio R = 2.

Conclusions

Résumé du chapitre X. - Conclusions

Ce chapitre présente les principaux résultats obtenus. Il met en évidence l'influence de ces résultats sur les dynamiques de mobilisation de liquide résiduel e et sur le développement de microstructures déformantes.

En considérant le rapport d'aspect R des cristaux, les résultats montrent que :

- A un rapport d'aspect R = 4, les suspensions magmatiques soumises à la déformation et les teneurs en cristaux 0,52 < σs < 0,59 développent une série de structures de déformation e bandes de cisaillement.
- Au rapport d'aspect R = 2, les suspensions magmatiques soumises à la déformation ne présentent pas de bandes de cisaillement. Cependant, la déformation est répartie de manière homogène sur toute la surface des échantillons. Un système de bandes anastomosées interconnectées se forme. Ces bandes sont enrichies en liquide résiduel.

Les expériences menées avec un rapport d'aspect R = 2 ont permis de tirer deux conclusions essentielles. Premièrement, il a été démontré que les mush à forte teneur en cristaux peuvent présenter des processus de migration du liquide résiduel. Deuxièmement, la limite entre le mush et le système verrouillé a été élargie, ce qui indique qu'une bouillie peut être déformée au moins jusqu'à $\sigma_s = 0,95$.

Ce chapitre décrit également l'objectif futur : étudier la déformation de masses synthétiques avec différentes valeurs de déformation finie γ, de vitesse de déformation $\dot{\gamma}$, de teneur en cristaux σs et de forme des cristaux. Pour rendre le système plus réaliste, des expériences avec différentes phases minéralogiques pourraient être réalisées pour émuler l'hétérogénéité des échantillons naturels. Les expériences réalisées dans ce travail ne comportent qu'une seule phase minéralogique dominante, ce qui rend le système idéal pour la recherche initiale. Une fois que de bons résultats sont obtenus, il est nécessaire de procéder à un système plus complexe similaire à la réalité des échantillons naturels

X. Conclusion

The processes of melt migration, segregation, and extraction in volcanic mushes are influenced by many factors, including temperature, pressure, and water content. Some of the most important factors are deformation rate, crystal content, size, spatial distribution, and shape of crystals. All these factors affect the development of microstructures in magmatic suspensions and thus the processes of melt rise and melt transport. A low crystal content ($\sigma_s < 0.30$) results in Newtonian behavior of the magma, which behaves like a liquid. At medium and high crystal content ($0.31 < \sigma_s < 0.95$), there is a transition to Binghamian behavior, whereby the magmatic suspension is formed by a network of interconnected crystallites that can transmit deformation and form force chains. The samples develop shear thinning or shear thickening structures depending on crystal content, crystal shape, and deformation conditions.

This thesis presents the results of torsion deformation experiments on synthetic samples with haplotonalitic composition. The objectives of this thesis are twofold. Firstly, the impact of aspect ratio and crystal shape on deformation structures is investigated by performing experiments at medium and high crystal content ($0.52 < \sigma_s < 0.76$). The experiments consist of a magmatic suspensions comprising crystals with aspect ratio R = 2. The results of these experiments were compared with those of previous work (Picard et al., 2011) where magmatic suspensions were formed by crystals with aspect ratio R = 4. The second objective is to investigate the limit of the extraction window by conducting torsional deformation experiments on magmatic syntectic suspensions with high crystal content ($\sigma_s = 0.95$) and verify when the system becomes locked-up.

Therefore, all these experiments and analyzes were carried out to: study the microstructures formed that can facilitate melt migration, segregation and extraction processes; check whether there are melt extraction processes within the deformed samples; investigate the limits of extraction windows and the limits between the mush system and the locked-up system.

Considering the aspect ratio R of the crystals, the results show that:

- At an aspect ratio of R = 4, magmatic suspensions subjected to deformation and crystal contents $0.52 < \sigma_s < 0.59$ develop a series of deformation structures.

  At crystal content $\boldsymbol{\sigma_s = 0.52}$, there is foliation of crystals and C' shear bands are formed by dilatancy processes. Force chains are moderately strong in the penetrative fabric and in the shear bands, but they are not the main process leading

to mush deformation. Notably, clusters are distributed along the entire surface of the sample, resulting in fair deformation but not strong localization of force chains.
At a crystal content **σ_s = 0.59**, there is no foliation of minerals due to a lack of space for rotation and translation. This leads to an accumulation of force chains in specific areas of the sample. When the force chains become sufficiently intense, C-type (and less commonly, C' type) shear bands are formed. As the intensity of the force chains increases, very large clusters are formed.

- At aspect ratio R = 2, magmatic suspensions subjected to deformation do not show shear bands. However, the deformation is homogeneously distributed along the entire samples surface.
  At crystal contents **σ_s = 0.58 - 0.59**, due to their low aspect ratio, the crystals can rotate and translate, moving in the direction of deformation. The samples develop a uniform fabric with preferred directions of the plagioclases aligned with the direction of deformation, creating a wavy pattern. A higher aspect ratio indicates a crystal direction in closer proximity to the shear direction, whereas a low aspect ratio denotes a crystal direction in closer alignment with the foliation direction. The continuous movement of the crystals prevents the force chains from maintaining them stable over time. Consequently, the force chains cannot intensify and there is no concentration of forces. The shape of the crystals facilitates the formation of clusters, which, like the force chains, are not maintained over time. The bubbles are orientated in the direction of deformation, with an inclination of approximately 45°.
  At higher crystal contents **σ_s = 0.73 - 0.76**, the crystals display a stronger wavy pattern than samples with crystal contents σ_s = 0.58 - 0.59. The crystals are oriented on average between -10° and 45°. The bubbles also follow the same pattern. The bubbles are orienting in the direction of deformation, and show migration and coalescence phenomena. The coalescence of the bubbles generates wavy structures, which demonstrate that this geometry is the most stable at high crystal content and high finite strain. All samples with a high crystal content and a minimum finite strain γ of 5 exhibit banding. This phenomenon is characterized by the formation of a series of interconnected wavy bands in opposite direction of shearing. The bands are enriched of ± 7-10% residual melt compared to the surrounding areas. Therefore, the dynamics of melt migration was reached. These bands could form preferential channels for the extraction of residual melt. It remains to be clarified whether the determining factor for the formation of these bands is the high crystal content and/or the high finite strain.

At crystal content **σ_s = 0.95**, the sample has a granular behavior. The penetrative fabric is composed of plagioclase oriented in the direction of foliation. There is the formation of a series of interconnected bands, oriented in the opposite direction of deformation. The bands are enriched in residual melt. The plagioclases in the bands show smaller grain size than the plagioclases in the penetrative fabric. This means greater deformation and higher intensity of the force chains in these bands. It is unclear whether the formation of the bands is related to dilatancy or to strong strain localization or a mix of both. Interestingly, this sample also nucleated quartz, probably at the final stage when the melt was completely depleted in Na and Ca. The quartz is arranged in lines parallel to the foliation, despite the EBSD analysis showing no preferential orientation. From SEM observations, it is clear that the morphology of the quartz shows the typical characteristics of glass. It has been hypothesized that this quartz is residual melt crystallized at the final phase of the experiment, probably during quenching. The residual melt with quartz composition oriented parallel to the foliation during the torsion experiment, and during quenching it crystallized. This provides further confirmation of residual melt migration processes in high crystalline samples subjected to shearing.

The experiments at aspect ratio R = 2 yielded two key conclusions. First, it was demonstrated that mushes with high crystalline content can exhibit melt migration processes. Second, the boundary between the mush and locked-up system was expanded, indicating that a mush can be deformed at least up to $\sigma_s = 0.95$.

Two volcanic structures in the French Massif Central were studied: the Suc de Sara (volcanic dyke, deep geological body with slow cooling rate) and the Petit Gerbier (volcanic neck, shallower geological body with faster cooling rate). Natural and synthetic samples were compared, showing good correlations. The inner areas of the natural samples (SA4 and PG2, areas where cooling was slower than the dyke and neck external areas) show banding and wave patterns, similar to the synthetic samples at aspect ratio R = 2. The outer areas of the natural samples (SA1 and PG1, subject to rapid cooling) show strain localization with the formation of shear bands, as is also shown in the synthetic samples at aspect ratio R = 4. The natural samples demonstrate melt segregation and migration, which is represented by the movement of residual melt enriched in aegirin component (Suc de Sara) or analcim component (Petit Gerbier). With deformation, the melt is oriented parallel to the foliation and gathers the shear bands,

which potentially represent melt channels for melt extraction. Similarly, in the synthetic sample with granular behavior (PP695, $\sigma_s = 0.95$), the residual quartz component melt is oriented in the direction of foliation and migrates into the shear bands.

These similarities between natural and synthetic samples provide an excellent foundation for future deformation experiments. They make the concept of melt extraction in magmatic bodies with high crystal content through deformation processes realistic and applicable to deformed natural magmatic mushes.

Future goals include investigating the deformation of synthetic mushes with different values of finite strain γ, strain rate $\dot{\gamma}$, crystal content σ_s and crystal shape. To make the system more realistic, experiments with different mineralogical phases could be performed to emulate the heterogeneity of natural samples. The experiments carried out in this work have only one dominant mineralogical phase, which makes the system ideal for initial research. Once good results are reached, it is necessary to proceed with a more complex system similar to the reality of natural samples.

Bibliography

A

Aharonov, E., Whitehead, J.A., Kelemen, P.B., Spiegelman, M., 1995. Channeling instability of upwelling melt in the mantle. J. Geophys. Res. 100, 20433–20450. https://doi.org/10.1029/95JB01307

Allan, A.S.R., Morgan, D.J., Wilson, C.J.N., Millet, M.-A., 2013. From mush to eruption in centuries: assembly of the super-sized Oruanui magma body. Contrib Mineral Petrol 166, 143–164. https://doi.org/10.1007/s00410-013-0869-2

Amirrahmat, S., Druckrey, A.M., Alshibli, K.A., Al-Raoush, R.I., 2019. Micro Shear Bands: Precursor for Strain Localization in Sheared Granular Materials. J. Geotech. Geoenviron. Eng. 145, 04018104. https://doi.org/10.1061/(ASCE)GT.1943-5606.0001989

Annen, C., Blundy, J.D., Leuthold, J., Sparks, R.S.J., 2015. Construction and evolution of igneous bodies: Towards an integrated perspective of crustal magmatism. Lithos 230, 206–221. https://doi.org/10.1016/j.lithos.2015.05.008

Arbaret, L., Bystricky, M., Champallier, R., 2007. Microstructures and rheology of hydrous synthetic magmatic suspensions deformed in torsion at high pressure. Journal of Geophysical Research: Solid Earth 112.

Arbaret, L., Diot, H., Bouchez, J.-L., 1996. Shape fabrics of particles in low concentration suspensions: 2D analogue experiments and application to tiling in magma. Journal of Structural Geology 18, 941–950. https://doi.org/10.1016/0191-8141(96)00011-9

Arbaret, L., Diot, H., Launeau, P., 1993. THE PHONOLITIC BODY OF PETIT GERBIER (EASTERN VELAY, FRENCH MASSIF-CENTRAL, FRANCE)-MAGNETIC AND MAGMATIC STRUCTURES. COMPTES RENDUS DE L ACADEMIE DES SCIENCES SERIE II 316, 1603–1610.

Arbaret, L., Mancktelow, N.S., Burg, J.-P., 2001. Effect of shape and orientation on rigid particle rotation and matrix deformation in simple shear flow. Journal of Structural Geology 23, 113–125.

Arzi, A.A., 1978. Critical phenomena in the rheology of partially melted rocks. Tectonophysics 44, 173–184.

Azema, É., Radjaï, F., 2012. Force chains and contact network topology in packings of elongated particles. Phys. Rev. E 85, 031303. https://doi.org/10.1103/PhysRevE.85.031303

Azéma, É., Radjai, F., Dubois, F., 2011. Numerical simulation of granular media composed with irregular polyhedral particles: effect of particles' angularity, in: II International Conference on Particle-Based Methods-Fundamentals and Applications-PARTICLES 2011.

B

Bachmann, O., Bergantz, G.W., 2008. Rhyolites and their source mushes across tectonic settings. Journal of Petrology 49, 2277–2285.

Bachmann, O., Bergantz, G.W., 2004. On the origin of crystal-poor rhyolites: extracted from batholithic crystal mushes. Journal of Petrology 45, 1565–1582.

Bagdassarov, N., Pinkerton, H., 2004. Transient phenomena in vesicular lava flows based on laboratory experiments with analogue materials. Journal of Volcanology and Geothermal Research 132, 115–136.

Bagdassarov, N.S., Dingwell, D.B., 1992. A rheological investigation of vesicular rhyolite. Journal of volcanology and geothermal research 50, 307–322.

Bauer, P., Palm, S., Handy, M., 2000. Strain localization and fluid pathways in mylonite: inferences from in situ deformation of a water-bearing quartz analogue (norcamphor). https://doi.org/10.1016/S0040-1951(00)00065-2

Bergantz, G.W., Schleicher, J.M., Burgisser, A., 2017. On the kinematics and dynamics of crystal-rich systems. Journal of Geophysical Research: Solid Earth 122, 6131–6159. https://doi.org/10.1002/2017JB014218

Boivin, P., Besson, J.C., Briot, D., Camus, G., de Goër, A., Gourgaud, A., Labazuy, P., de Larouzière, D., Livet, M., Mergoil, J., 2004. Volcanologie de la Chaîne des Puys, carte et fascicule.

Boneh, Y., Skemer, P., 2014. The effect of deformation history on the evolution of olivine CPO. Earth and Planetary Science Letters 406, 213–222.

Bouchez, J.L., Delas, C., Gleizes, G., Nédélec, A., Cuney, M., 1992. Submagmatic microfractures in granites. Geology 20, 35–38.

Brewer, L.N., Field, D.P., Merriman, C.C., 2009. Mapping and Assessing Plastic Deformation Using EBSD, in: Schwartz, A.J., Kumar, M., Adams, B.L., Field, D.P. (Eds.), Electron Backscatter Diffraction in Materials Science. Springer US, Boston, MA, pp. 251–262. https://doi.org/10.1007/978-0-387-88136-2_18

Brophy, J.G., 1991. Composition gaps, critical crystallinity, and fractional crystallization in orogenic (calc-alkaline) magmatic systems. Contributions to Mineralogy and Petrology 109, 173–182.

Burgisser, A., Bergantz, G.W., 2011. A rapid mechanism to remobilize and homogenize highly crystalline magma bodies. Nature 471, 212–215.

Burgisser, A., Bergantz, G.W., Breidenthal, R.E., 2005. Addressing complexity in laboratory experiments: the scaling of dilute multiphase flows in magmatic systems. Journal of Volcanology and Geothermal Research 141, 245–265.

Burgisser, A., Poussineau, S., Arbaret, L., Druitt, T.H., Giachetti, T., Bourdier, J.-L., 2010. Pre-explosive conduit conditions of the 1997 Vulcanian explosions at Soufrière Hills Volcano, Montserrat: I. Pressure and vesicularity distributions. Journal of Volcanology and Geothermal Research 194, 27–41.

C

Caricchi, L., Burlini, L., Ulmer, P., Gerya, T., Vassalli, M., Papale, P., 2007. Non-Newtonian rheology of crystal-bearing magmas and implications for magma ascent dynamics. Earth and Planetary Science Letters 264, 402–419.

Caricchi, L., Giordano, D., Burlini, L., Ulmer, P., Romano, C., 2008. Rheological properties of magma from the 1538 eruption of Monte Nuovo (Phlegrean Fields, Italy): An experimental study. Chemical Geology 256, 158–171.

Cashman, K.V., Sparks, R.S.J., Blundy, J.D., 2017. Vertically extensive and unstable magmatic systems: A unified view of igneous processes. Science 355, eaag3055. https://doi.org/10.1126/science.aag3055

Cates, M.E., Wittmer, J.P., Bouchaud, J.-P., Claudin, P., 1998. Jamming, Force Chains, and Fragile Matter. Phys. Rev. Lett. 81, 1841–1844. https://doi.org/10.1103/PhysRevLett.81.1841

Chadwick Jr, W.W., Archuleta, R.J., Swanson, D.A., 1988. The mechanics of ground deformation precursory to dome-building extrusions at Mount St. Helens 1981–1982. Journal of Geophysical Research: Solid Earth 93, 4351–4366.

Champallier, R., 2005. Déformation expérimentale à Haute Température et Haute Pression de magmas partiellement cristallisés (phdthesis). Université d'Orléans.

Champallier, R., Bystricky, M., Arbaret, L., 2008. Experimental investigation of magma rheology at 300 MPa: From pure hydrous melt to 76 vol.% of crystals. Earth and

Planetary Science Letters 267, 571–583. https://doi.org/10.1016/j.epsl.2007.11.065

Cooper, R.F., 1990. Differential stress-induced melt migration: An experimental approach. Journal of Geophysical Research: Solid Earth 95, 6979–6992.

Cordonnier, B., Hess, K.-U., Lavallee, Y., Dingwell, D.B., 2009. Rheological properties of dome lavas: Case study of Unzen volcano. Earth and Planetary Science Letters 279, 263–272.

Couzinié, S., Moyen, J.-F., Villaros, A., Paquette, J.-L., Scarrow, J.H., Marignac, C., 2014. Temporal relationships between Mg-K mafic magmatism and catastrophic melting of the Variscan crust in the southern part of Velay Complex (Massif Central, France). Journal of Geosciences 59, 1–18.

Crozier, J., Tramontano, S., Forte, P., Oliva, S.J.C., Gonnermann, H.M., Lev, E., Manga, M., Myers, M., Rader, E., Ruprecht, P., 2022. Outgassing through magmatic fractures enables effusive eruption of silicic magma. Journal of Volcanology and Geothermal Research 430, 107617.

Cundall, P.A., Strack, O.D.L., 1983. Modeling of microscopic mechanisms in granular material, in: Studies in Applied Mechanics. Elsevier, pp. 137–149.

D

de Goer, A., Mergoil, J., 1971. Structure et dynamique des édifices volcaniques tertiaires et quaternaires, in: Symposium J. Jung: Gtologie Geomorphologie et Structure Profonde Du Massif Central Francais, Clermont-Ferrand. Plein Air Service. pp. 345–376.

deGraffenried, R.L., Larsen, J.F., Graham, N.A., Cashman, K.V., 2019. The Influence of Phenocrysts on Degassing in Crystal-Bearing Magmas With Rhyolitic Groundmass Melts. Geophysical Research Letters 46, 5127–5136. https://doi.org/10.1029/2018GL081822

Delph, J.R., Ward, K.M., Zandt, G., Ducea, M.N., Beck, S.L., 2017. Imaging a magma plumbing system from MASH zone to magma reservoir. Earth and Planetary Science Letters 457, 313–324.

Dingwell, D.B., Bagdassarov, N., Bussod, G., Webb, S.L., 1993. Magma rheology.

Dufek, J., Bachmann, O., 2010. Quantum magmatism: Magmatic compositional gaps generated by melt-crystal dynamics. Geology 38, 687–690.

F

Fernandez, A., Feybesse, J.-L., Mezure, J.-F., 1983. Theoretical and experimental study of fabrics developed by different shaped markers in two-dimensional simple shear. Bulletin de la Société géologique de France 7, 319–326.

Forien, M., Arbaret, L., Burgisser, A., Champallier, R., 2011. Experimental constrains on shear-induced crystal breakage in magmas. J. Geophys. Res. 116, B08217. https://doi.org/10.1029/2010JB008026

G

Geshi, N., 2001. Melt segregation by localized shear deformation and fracturing during crystallization of magma in shallow intrusions of the Otoge volcanic complex, central Japan. Journal of Volcanology and Geothermal Research 106, 285–300.

Gonnermann, H.M., Manga, M., 2007. The Fluid Mechanics Inside a Volcano. Annu. Rev. Fluid Mech. 39, 321–356. https://doi.org/10.1146/annurev.fluid.39.050905.110207

Graham, N.A., Larsen, J.F., Tasa, K.Y., deGraffenried, R.L., Cashman, K.V., McCartney, K.N., 2023. Controls of crystal shape on degassing mechanisms in crystal-rich magmas with rhyolitic groundmass melts. Earth and Planetary Science Letters 601, 117891.

Guo, P., 2012. Critical length of force chains and shear band thickness in dense granular materials. Acta Geotech. 7, 41–55. https://doi.org/10.1007/s11440-011-0154-3

H

Hildreth, W., 2004. Volcanological perspectives on Long Valley, Mammoth Mountain, and Mono Craters: several contiguous but discrete systems. Journal of Volcanology and Geothermal Research 136, 169–198.

Holness, M.B., 2018. Melt segregation from silicic crystal mushes: a critical appraisal of possible mechanisms and their microstructural record. Contrib Mineral Petrol 173, 48. https://doi.org/10.1007/s00410-018-1465-2

Holtzman, B.K., Kohlstedt, D.L., 2007. Stress-driven Melt Segregation and Strain Partitioning in Partially Molten Rocks: Effects of Stress and Strain. Journal of Petrology 48, 2379–2406. https://doi.org/10.1093/petrology/egm065

Holtzman, B.K., Kohlstedt, D.L., Morgan, J.P., 2005. Viscous energy dissipation and strain partitioning in partially molten rocks. Journal of Petrology 46, 2569–2592.

Holtzman, B.K., Kohlstedt, D.L., Zimmerman, M.E., Heidelbach, F., Hiraga, T., Hustoft, J., 2003. Melt Segregation and Strain Partitioning: Implications for Seismic Anisotropy and Mantle Flow. Science 301, 1227–1230. https://doi.org/10.1126/science.1087132

Hoyos, S., Florez, D., Pec, M., Huber, C., 2022. Crystal Shape Control on the Repacking and Jamming of Crystal-Rich Mushes. Geophysical Research Letters 49, e2022GL100040.

Huang, H.-H., Lin, F.-C., Schmandt, B., Farrell, J., Smith, R.B., Tsai, V.C., 2015. The Yellowstone magmatic system from the mantle plume to the upper crust. Science 348, 773–776.

Huber, C., Bachmann, O., Dufek, J., 2012. Crystal-poor versus crystal-rich ignimbrites: A competition between stirring and reactivation. Geology 40, 115–118.

Hustoft, J.W., Kohlstedt, D.L., 2006. The Role of Shear Deformation in Core Formation, in: AGU Spring Meeting Abstracts. pp. V31A-02.

I

Ildefonse, B., Launeau, P., Bouchez, J.-L., Fernandez, A., 1992. Effect of mechanical interactions on the development of shape preferred orientations: a two-dimensional experimental approach. Journal of Structural Geology 14, 73–83. https://doi.org/10.1016/0191-8141(92)90146-N

Ishibashi, H., Sato, H., 2007. Viscosity measurements of subliquidus magmas: Alkali olivine basalt from the Higashi-Matsuura district, Southwest Japan. Journal of Volcanology and Geothermal Research 160, 223–238. https://doi.org/10.1016/j.jvolgeores.2006.10.001

J

Jackson, M.D., Blundy, J., Sparks, R.S.J., 2018. Chemical differentiation, cold storage and remobilization of magma in the Earth's crust. Nature 564, 405–409.

Johannes, W., Holtz, F., 1996. Petrogenesis and Experimental Petrology of Granitic Rocks. Minerals and Rocks Series,. p. 335 pp.

Jung, J., 1971. Symposium: Géologie, géomorphologie et structure profonde du Massif Central français.

K

Katz, R.F., Spiegelman, M., Holtzman, B., 2006. The dynamics of melt and shear localization in partially molten aggregates. Nature 442, 676–679.

Keller, T., May, D.A., Kaus, B.J., 2013. Numerical modelling of magma dynamics coupled to tectonic deformation of lithosphere and crust. Geophysical Journal International 195, 1406–1442.

Kiser, E., Palomeras, I., Levander, A., Zelt, C., Harder, S., Schmandt, B., Hansen, S., Creager, K., Ulberg, C., 2016. Magma reservoirs from the upper crust to the Moho inferred from high-resolution Vp and Vs models beneath Mount St. Helens, Washington State, USA. Geology 44, 411–414.

Koenders, M.A., Petford, N., 2007. Shear-induced pressure changes and seepage phenomena in a deforming porous layer-III. Geophysical Journal International 171, 943–953.

Kohlstedt, D.L., Holtzman, B.K., 2009. Shearing Melt Out of the Earth: An Experimentalist's Perspective on the Influence of Deformation on Melt Extraction. Annual Review of Earth and Planetary Sciences 37, 561–593. https://doi.org/10.1146/annurev.earth.031208.100104

L

Laumonier, M., 2013. Mélange de magmas à HP-HT: contraintes expérimentales et application au magmatisme d'arc (PhD Thesis). Université d'Orléans.

Laumonier, M., Arbaret, L., Burgisser, A., Champallier, R., 2011. Porosity redistribution enhanced by strain localization in crystal-rich magmas. Geology 39, 715–718.

Laumonier, M., Scaillet, B., Arbaret, L., Andújar, J., Champallier, R., 2015. Experimental mixing of hydrous magmas. Chemical Geology 418, 158–170.

Launeau, P., 2004. Evidence of magmatic flow by 2-D image analysis of 3-D shape preferred orientation distributions. Bulletin de la Société Géologique de France 175, 331–350.

Lavallée, Y., Hess, K.-U., Cordonnier, B., Bruce Dingwell, D., 2007. Non-Newtonian rheological law for highly crystalline dome lavas. Geology 35, 843–846.

Lees, J.M., 2007. Seismic tomography of magmatic systems. Journal of Volcanology and Geothermal Research 167, 37–56.

Lejeune, A., Richet, P., 1995. Rheology of crystal-bearing silicate melts: An experimental study at high viscosities. J. Geophys. Res. 100, 4215–4229. https://doi.org/10.1029/94JB02985

Lejeune, A.M., Bottinga, Y., Trull, T.W., Richet, P., 1999. Rheology of bubble-bearing magmas. Earth and Planetary Science Letters 166, 71–84.

Lindoo, A., Larsen, J.F., Cashman, K.V., Dunn, A.L., Neill, O.K., 2016. An experimental study of permeability development as a function of crystal-free melt viscosity. Earth and Planetary Science Letters 435, 45–54.

Lofgren, G., 1974. An experimental study of plagioclase crystal morphology; isothermal crystallization. American Journal of Science 274, 243–273. https://doi.org/10.2475/ajs.274.3.243

Lyell, C., 1838. Elements of geology, lst American, from the lst London ed. ed. James Kay, Jun. and Brother, Philadelphia. https://doi.org/10.5962/bhl.title.51635

Lyon, M.K., Mead, D.W., Elliott, R.E., Leal, L.G., 2001. Structure formation in moderately concentrated viscoelastic suspensions in simple shear flow. Journal of Rheology 45, 881–890.

M

Majmudar, T.S., Behringer, R.P., 2005. Contact force measurements and stress-induced anisotropy in granular materials. nature 435, 1079–1082.

Manga, M., Castro, J., Cashman, K.V., Loewenberg, M., 1998. Rheology of bubble-bearing magmas. Journal of Volcanology and Geothermal Research 87, 15–28.

March, A., 1932. Mathematische Theorie der Regelung nach der Korngestah bei affiner Deformation. Zeitschrift für Kristallographie-Crystalline Materials 81, 285–297.

McKenzie, D., 1985. 230Th238U disequilibrium and the melting processes beneath ridge axes. Earth and Planetary Science Letters 72, 149–157.

McKenzie, D.A.N., 1984. The generation and compaction of partially molten rock. Journal of petrology 25, 713–765.

Mergoil, J., 1968. ANNULAR VEIN DEPOSIT OF PHONOLITES OF VELAY (FRENCH MASSIF CENTRAL). COMPTES RENDUS HEBDOMADAIRES DES SEANCES DE L ACADEMIE DES SCIENCES SERIE D 267, 12.

Mergoil, J., Biovin, P., 1993. Le Velay - son volcanisme et les formations associées: notice de la carte à 1/100 000 = The Velay - volcanism and related deposits. Ed. du BRGM, Paris.

Miallier D., Boivin P., Arbaret L., Burgisser A., Deniel C, Submitted. Microlitic crystal-venting episodes at two Quaternary, trachytic lava domes of the Chaîne des Puys (French Massif Central). Journal of Volcanology and Geothermal Research.

Miller, K.J., Zhu, W., Montési, L.G.J., Gaetani, G.A., 2014. Experimental quantification of permeability of partially molten mantle rock. Earth and Planetary Science Letters 388, 273–282. https://doi.org/10.1016/j.epsl.2013.12.003

Muthuswamy, M., Tordesillas, A., 2006. How do interparticle contact friction, packing density and degree of polydispersity affect force propagation in particulate assemblies? Journal of Statistical Mechanics: Theory and Experiment 2006, P09003.

N

Ness, C., Sun, J., 2016. Shear thickening regimes of dense non-Brownian suspensions. Soft Matter 12, 914–924. https://doi.org/10.1039/C5SM02326B

Ness, C., Xing, Z., Eiser, E., 2017. Oscillatory rheology of dense, athermal suspensions of nearly hard spheres below the jamming point. Soft Matter 13, 3664–3674.

Nicolas, A., 1992. Kinematics in magmatic rocks with special reference to gabbros. Journal of Petrology 33, 891–915.

P

Parmigiani, A., Huber, C., Bachmann, O., Chopard, B., 2011. Pore-scale mass and reactant transport in multiphase porous media flows. Journal of Fluid Mechanics 686, 40–76.

Paterson, S.R., Fowler Jr, T.K., Schmidt, K.L., Yoshinobu, A.S., Yuan, E.S., Miller, R.B., 1998. Interpreting magmatic fabric patterns in plutons. Lithos 44, 53–82.

Paulatto, M., Hooft, E.E.E., Chrapkiewicz, K., Heath, B., Toomey, D.R., Morgan, J.V., 2022. Advances in seismic imaging of magma and crystal mush. Front. Earth Sci. 10. https://doi.org/10.3389/feart.2022.970131

Pereira, T., Arbaret, L., Andújar, J., Laumonier, M., Spagnoli, M., Gumiaux, C., Laurent, G., Slodczyk, A., Di Carlo, I., 2024. Magmatic to solid-state evolution of a shallow emplaced agpaitic tinguaite (the Suc de Sara dyke, Velay volcanic province, France): implications for peralkaline melt segregation and extraction in ascending magmas. European Journal of Mineralogy 36, 491–524.

Peters, J.F., Muthuswamy, M., Wibowo, J., Tordesillas, A., 2005. Characterization of force chains in granular material. Phys. Rev. E 72, 041307. https://doi.org/10.1103/PhysRevE.72.041307

Petford, N., 2009. Which effective viscosity? Mineralogical Magazine 73, 167–191.

Petford, N., 2003. Rheology of granitic magmas during ascent and emplacement.

Philpotts, A.R., Asher, P.M., 1994. Magmatic flow-direction indicators in a giant diabase feeder dike, Connecticut. Geology 22, 363–366.

Phipps Morgan, J., Holtzman, B.K., 2005. Vug waves: A mechanism for coupled rock deformation and fluid migration. Geochem Geophys Geosyst 6, 2004GC000818. https://doi.org/10.1029/2004GC000818

Picard, D., 2009. Déformation HP-HT des magmas siliceux: contraintes expérimentales sur l'évolution structurale et les transitions rhéologiques aux moyennes et fortes cristallinités (PhD Thesis). Université d'Orléans.

Picard, D., Arbaret, L., Pichavant, M., Champallier, R., Launeau, P., 2013. The rheological transition in plagioclase-bearing magmas. Journal of Geophysical Research: Solid Earth 118, 1363–1377. https://doi.org/10.1002/jgrb.50091

Picard, D., Arbaret, L., Pichavant, M., Champallier, R., Launeau, P., 2011. Rheology and microstructure of experimentally deformed plagioclase suspensions. Geology 39, 747–750.

Pistone, M., Caricchi, L., Ulmer, P., Burlini, L., Ardia, P., Reusser, E., Marone, F., Arbaret, L., 2012. Deformation experiments of bubble- and crystal-bearing magmas: Rheological and microstructural analysis. J. Geophys. Res. 117, 2011JB008986. https://doi.org/10.1029/2011JB008986

Pistone, M., Caricchi, L., Ulmer, P., Reusser, E., Ardia, P., 2013. Rheology of volatile-bearing crystal mushes: mobilization vs. viscous death. Chemical Geology 345, 16–39.

Précigout, J., Ledoux, E., Arbaret, L., Spriet, C., 2022. Porosity induced by dislocation dynamics in quartz-rich shear bands of granitic rocks. Scientific Reports 12, 6141.

R

Radjai, F., Wolf, D.E., Jean, M., Moreau, J.-J., 1998. Bimodal Character of Stress Transmission in Granular Packings. Phys. Rev. Lett. 80, 61–64. https://doi.org/10.1103/PhysRevLett.80.61

Ramsay, J.G., 1967. Folding and fracturing of rocks. Mc Graw Hill Book Company 568.

Reid, M.R., Rudnick, R.L., 2003. Timescales of magma transfer and storage in the crust, in: The Crust. Elsevier Oxford, pp. 167–193.

Roscoe, R., 1952. The viscosity of suspensions of rigid spheres. Br. J. Appl. Phys. 3, 267–269. https://doi.org/10.1088/0508-3443/3/8/306

Rosenberg, C.L., Handy, M.R., 2005. Experimental deformation of partially melted granite revisited: implications for the continental crust. Journal of Metamorphic Geology 23, 19–28. https://doi.org/10.1111/j.1525-1314.2005.00555.x

S

Saar, M.O., Manga, M., Cashman, K.V., Fremouw, S., 2001. Numerical models of the onset of yield strength in crystal–melt suspensions. Earth and Planetary Science Letters 187, 367–379.

Schmitt, A.K., 2011. Uranium series accessory crystal dating of magmatic processes. Annual Review of Earth and Planetary Sciences 39, 321–349.

Scott, D.R., Stevenson, D.J., 1986. Magma ascent by porous flow. J. Geophys. Res. 91, 9283–9296. https://doi.org/10.1029/JB091iB09p09283

Scott, D.R., Stevenson, D.J., 1984. Magma solitons. Geophysical Research Letters 11, 1161–1164. https://doi.org/10.1029/GL011i011p01161

Seropian, G., Rust, A.C., Sparks, R.S.J., 2018. The Gravitational Stability of Lenses in Magma Mushes: Confined Rayleigh-Taylor Instabilities. JGR Solid Earth 123, 3593–3607. https://doi.org/10.1029/2018JB015523

Skemer, P., Katayama, I., Jiang, Z., Karato, S., 2005. The misorientation index: Development of a new method for calculating the strength of lattice-preferred orientation. Tectonophysics 411, 157–167.

Smith, J.V., 2002. Structural analysis of flow-related textures in lavas. Earth-Science Reviews 57, 279–297.

Smith, J.V., 1997. Shear thickening dilatancy in crystal-rich flows. Journal of Volcanology and Geothermal Research 79, 1–8.

Smith, J.V., 1996. Ductile-brittle transition structures in the basal shear zone of a rhyolite lava flow, eastern Australia. Journal of Volcanology and Geothermal Research 72, 217–223.

Spera, F.J., Borgia, A., Strimple, J., Feigenson, M., 1988. Rheology of melts and magmatic suspensions: 1. Design and calibration of concentric cylinder viscometer with application to rhyolitic magma. Journal of Geophysical Research: Solid Earth 93, 10273–10294.

Spiegelman, M., 2003. Linear analysis of melt band formation by simple shear. Geochemistry, Geophysics, Geosystems 4.

Stein, R.S., King, G.C., Lin, J., 1992. Change in failure stress on the southern San Andreas fault system caused by the 1992 magnitude= 7.4 Landers earthquake. Science 258, 1328–1332.

T

Thompson, R.N., 1972. Evidence for a chemical discontinuity near the basalt–andesite transition in many anorogenic volcanic suites. Nature 236, 106–110.

Tordesillas, A., 2007. Force chain buckling, unjamming transitions and shear banding in dense granular assemblies. Philosophical Magazine 87, 4987–5016.

Tordesillas, A., Steer, C.A.H., Walker, D.M., 2014. Force chain and contact cycle evolution in a dense granular material under shallow penetration. Nonlinear Processes in Geophysics 21, 505–519.

Tordesillas, A., Zhang, J., Behringer, R., 2009. Buckling force chains in dense granular assemblies: physical and numerical experiments. Geomechanics and Geoengineering 4, 3–16. https://doi.org/10.1080/17486020902767347

V

Van Der Molen, I., Paterson, M.S., 1979. Experimental deformation of partially-melted granite. Contr. Mineral. and Petrol. 70, 299–318. https://doi.org/10.1007/BF00375359

Vernon, R.H., 2018. A practical guide to rock microstructure. Cambridge university press.

Vernon, R.H., 2000. Review of Microstructural Evidence of Magmatic and Solid-State Flow. Vis Geosci 5, 1–23. https://doi.org/10.1007/s10069-000-0002-3

Vigneresse, J.L., Barbey, P., Cuney, M., 1996. Rheological transitions during partial melting and crystallization with application to felsic magma segregation and transfer. Journal of Petrology 37, 1579–1600.

Vigneresse, J.L., Tikoff, B., 1999. Strain partitioning during partial melting and crystallizing felsic magmas. Tectonophysics 312, 117–132.

W

Wambaugh, J.F., 2010. Simple models for granular force networks. Physica D: Nonlinear Phenomena 239, 1818–1826.

Ward, K.M., Zandt, G., Beck, S.L., Christensen, D.H., McFarlin, H., 2014. Seismic imaging of the magmatic underpinnings beneath the Altiplano-Puna volcanic complex from the joint inversion of surface wave dispersion and receiver functions. Earth and Planetary Science Letters 404, 43–53.

Weinberg, R.F., Vernon, R.H., Schmeling, H., 2021. Processes in mushes and their role in the differentiation of granitic rocks. Earth-Science Reviews 220, 103665.

Westerman, D., Rocchi, S., Breitkreuz, C., Stevenson, C., Wilson, P., 2017. Structures Related to the Emplacement of Shallow-Level Intrusions, in: Breitkreuz, C., Rocchi, S. (Eds.), Physical Geology of Shallow Magmatic Systems, Advances in Volcanology. Springer International Publishing, Cham, pp. 83–118. https://doi.org/10.1007/11157_2017_31

Willis, D.G., 1977. A kinematic model of preferred orientation. Geological Society of America Bulletin 88, 883–894.

Z

Zavada, P., Schulmann, K., Lexa, O., Hrouda, F., Haloda, J., Tỳcová, P., 2009. The mechanism of flow and fabric development in mechanically anisotropic trachyte lava. Journal of Structural Geology 31, 1295–1307.

Zimmerman, M.E., Zhang, S., Kohlstedt, D.L., Karato, S., 1999. Melt distribution in mantle rocks deformed in shear. Geophysical Research Letters 26, 1505–1508. https://doi.org/10.1029/1999GL900259

Appendices

Appendix A.

Table of deformation experiments

Sample	Crystal content	Aspect ratio R	Starting material	H_2O content (wt.%)	P (MPa)	T (°C)	Finite strain γ	Strain rate $\dot{\gamma}$ (s^{-1})
PP043	0.52	4	#7	3	300	800	1.4	$1.1*10^{-4}$
PP029	0.58	4	#6	3	300	800	1.4	$8.9*10^{-4}$
PP249	0.58	4	#6	3	300	700	2.0	$2.1*10^{-3}$
PP669	0.58	2	HTN4	3	300	800	0.5	$1.0*10^{-4}$
PP676	0.58	2	HTN8	3	300	800	1	$1.0*10^{-4}$
PP684	0.59	2	HTN9	3	300	800	2	$2.1*10^{-3}$
PP685	0.59	2	HTN9	3	300	800	2.3	$1.0*10^{-4}$
PP693	0.73	2	HTN11	3	300	810	2	$2.5*10^{-4}$
PP695	0.76	2	HTN13	3	300	810	5	$2.5*10^{-4}$
PP698	0.76	2	HTN14	3	300	810	5	$1.0*10^{-3}$
PP699	0.76	2	HTN14	3	300	810	10	$2.5*10^{-4}$
PP701	0.95	2	HTN12	3	300	790	1.8	$5.0*10^{-5}$

Table with all deformation experiments performed for both samples with aspect ratio R = 4 and aspect ratio R = 2. The aspect ratio R values are approximate and representative. This subdivision has been made to make it easier to read the samples with R = 4 and R = 2. In the results chapters (chapters IV, V, VI) the aspect ratio R values are presented in arithmetic mean, harmonic mean and mode.

Appendix B.

Preferential orientation and aspect ratio R of crystals

Starting materials, R = 4

	#6			#7	
diameter	angle°	a/b	diameter	angle°	a/b
9.54	90.72	14.78	0.96	89.33	24.48
1.51	177.55	1.66	4.01	46.08	4.93
1.11	166.28	2.32	3.96	39.43	6.63
2.99	157.87	4.45	2.49	56.44	3.74
1.93	81.47	5.62	2.95	68.73	3.41
2.43	34.64	7.77	2.89	170.36	4.30
4.12	75.59	4.50	4.04	22.19	6.57
1.66	54.29	3.25	2.17	165.30	1.20
2.14	133.35	1.29	1.52	85.57	3.18
4.31	57.39	2.15	2.92	117.16	5.78
2.73	79.69	2.35	2.77	110.34	4.20
3.58	176.32	3.69	2.92	17.56	5.35
2.40	162.78	4.72	3.11	156.65	4.70
2.27	160.84	4.02	4.61	60.13	2.99
3.31	171.54	5.10	2.20	143.30	7.71
2.91	9.09	3.85	3.72	115.73	3.64
1.78	80.38	2.03	2.19	39.33	7.98
1.72	170.69	4.44	3.93	62.24	5.07
2.90	61.71	1.96	2.63	73.60	2.70
4.21	97.63	6.60	1.97	47.41	1.62
1.89	97.84	2.74	4.73	119.43	5.63
1.63	71.52	1.52	3.36	159.83	4.22
2.60	103.47	4.57	5.33	16.64	5.63
3.24	172.32	1.20	3.79	13.20	4.26
2.53	94.71	4.38	4.41	8.11	7.49
2.43	89.15	6.05	3.34	71.29	6.61
1.78	50.12	2.26	0.90	158.26	2.87
2.13	118.74	2.09	2.27	142.68	3.40
2.22	101.14	7.20	5.59	118.65	5.23
2.81	169.99	3.28	4.29	72.65	3.20
1.51	102.32	5.41	2.27	136.54	3.50
2.04	120.83	8.03	3.22	2.40	6.33
4.21	10.37	4.90	2.11	115.50	3.56
1.90	85.14	4.82	6.37	160.43	5.32
2.53	117.03	4.56	2.78	63.43	3.03
2.35	89.99	2.53	2.79	26.29	4.13
2.02	103.17	5.85	4.53	34.58	4.51
6.18	69.63	2.73	0.13	87.20	2.26
1.86	145.50	1.52	6.03	143.25	2.09
2.61	96.87	6.89	5.86	117.17	4.64
1.86	79.48	2.04	6.43	171.03	2.09
2.15	106.65	3.08	2.33	104.24	3.04
2.61	101.06	2.13	2.01	106.17	4.74
2.46	102.78	5.92	0.15	180.00	2.81
1.69	116.73	3.32	2.26	36.61	6.35
1.72	21.15	2.11	1.92	66.41	5.86
1.76	43.18	3.50	3.83	176.51	6.68
2.12	91.71	4.77	1.46	148.58	2.89

Starting materials, R = 2

	HTN4			HTN8			HTN 9	
diameter	angle°	a/b	diameter	angle°	a/b	diameter	angle°	a/b
0.37	90.21	3.96	3.36	91.06	1.78	2.25	91.34	1.81
1.78	92.87	1.42	1.21	85.42	1.42	2.39	110.12	1.80
1.54	96.06	1.77	4.71	70.09	2.21	3.92	91.67	1.77
0.46	93.99	1.81	2.09	46.35	2.10	2.17	73.61	2.34
1.88	90.59	1.17	2.56	64.93	1.10	2.27	134.87	1.91
1.12	169.38	2.33	2.12	76.83	1.62	1.86	130.19	1.45
1.53	78.18	1.17	1.87	154.44	1.25	1.75	86.65	3.17
1.63	149.09	1.14	2.20	156.10	1.48	1.63	178.86	1.67
1.02	87.71	2.00	3.40	111.93	1.36	3.16	12.39	2.70
0.69	172.45	1.75	2.48	54.37	1.87	3.29	88.09	4.50
0.60	84.03	2.46	1.88	51.08	2.11	0.98	96.43	3.59
0.44	86.11	2.22	1.06	82.62	1.25	2.41	99.98	1.91
4.20	125.90	1.14	0.55	92.60	2.02	1.13	97.69	3.85
1.71	121.30	1.44	2.20	89.71	1.03	2.39	147.76	2.30
0.42	87.92	7.78	1.41	44.42	2.53	1.92	106.38	1.54
1.21	81.37	1.45	1.85	47.04	2.15	1.19	84.27	2.19
1.50	91.75	2.32	2.84	55.07	2.60	1.31	114.37	1.34
1.23	77.77	1.21	1.58	76.03	1.32	1.91	5.47	2.06
1.18	92.60	2.75	2.08	10.22	2.33	0.57	89.15	3.03
2.02	26.85	1.20	2.30	12.28	2.80	0.82	81.30	2.05
1.34	80.77	2.47	1.55	102.31	2.50	0.88	153.75	1.75
1.07	131.00	1.57	2.07	4.76	2.51	1.98	2.65	1.51
0.82	89.59	5.77	2.60	34.19	1.30	2.78	64.15	2.15
2.51	83.38	1.33	2.08	132.81	1.57	1.55	96.53	1.25
1.41	88.90	2.37	2.00	53.37	3.05	1.28	64.34	1.76
0.61	129.22	1.28	1.96	126.18	1.96	2.21	143.70	1.94
0.45	12.13	1.56	1.86	109.94	1.71	1.19	130.18	1.72
2.56	98.15	3.24	2.13	174.30	2.62	1.12	164.44	1.34
2.85	18.16	1.97	2.90	31.20	1.29	2.53	162.88	1.06
2.06	91.99	2.19	1.40	45.26	1.12	2.42	135.55	1.84
0.91	50.84	1.70	2.94	33.34	2.72	2.69	120.19	1.29
2.19	12.13	2.03	1.61	175.80	1.93	5.20	118.04	1.53
1.69	102.76	1.62	2.50	123.28	1.46	1.05	176.37	1.63
2.12	73.23	1.45	2.07	53.22	1.91	2.15	38.31	2.04
1.18	9.39	1.64	3.35	117.65	2.62	0.73	97.70	1.44
0.59	75.19	1.50	1.60	34.94	1.12	3.11	77.62	1.35
1.89	62.99	2.95	2.13	95.24	1.97	0.77	108.11	1.78
0.62	160.48	1.12	1.28	9.48	2.07	3.78	26.56	1.59
2.56	100.15	3.83	2.33	86.36	1.50	0.94	100.25	2.36
0.90	28.57	1.64	1.11	62.14	1.19	1.50	155.70	1.46
0.62	95.74	1.42	1.35	5.18	1.32	2.60	107.68	1.56
1.30	79.77	2.00	1.29	50.01	1.37	1.08	13.64	1.40
1.59	109.35	1.98	2.81	22.61	1.34	5.01	75.83	1.58
1.10	132.14	1.55	1.87	89.56	3.28	4.13	66.24	1.94
1.98	168.23	1.56	2.73	160.14	1.21	1.81	36.47	1.58
0.86	2.66	3.96	1.20	117.43	1.10	1.07	167.26	1.42
1.06	17.48	2.79	2.65	147.49	1.21	1.73	49.34	1.75
1.07	177.06	1.10	2.04	14.64	1.86	2.62	158.56	2.04
3.21	164.84	1.35	1.44	38.95	1.47	1.34	8.65	1.56
1.61	47.37	1.33	2.03	0.90	1.69	2.72	147.66	1.17
0.97	136.38	1.07	2.32	161.64	2.85	1.86	89.48	1.33

Starting materials, R = 2

	HTN11			HTN13			HTN14	
diameter	angle°	a/b	diameter	angle°	a/b	diameter	angle°	a/b
0.79	65.88	1.20	0.93	73.83	1.95	0.68	9.31	1.35
0.62	172.60	1.02	0.30	91.92	2.84	0.88	85.05	1.35
0.73	130.00	1.82	1.05	124.18	1.80	0.62	80.77	1.75
1.17	61.28	2.04	1.25	92.13	2.92	0.95	44.05	1.47
0.72	63.44	2.78	0.66	85.20	1.15	0.74	90.81	2.67
0.62	75.83	1.81	2.50	154.84	1.26	1.58	72.25	1.95
0.49	68.56	2.90	1.96	45.88	2.02	1.05	95.27	1.24
0.60	50.37	1.37	0.93	87.52	3.96	1.40	102.45	2.15
0.54	21.14	1.73	1.09	83.04	3.99	1.93	81.12	2.81
1.01	51.02	3.11	2.34	63.90	3.90	1.37	146.14	1.72
0.65	100.22	2.52	2.46	43.60	1.37	2.02	175.12	1.49
0.41	33.40	1.12	2.45	24.47	1.65	1.71	97.39	1.12
0.19	73.32	2.17	1.88	78.63	1.29	0.66	91.41	2.55
0.41	96.82	2.14	1.76	94.57	1.58	0.90	106.94	1.65
0.46	72.78	1.27	1.83	176.24	1.13	0.81	133.02	1.60
0.45	89.59	2.35	1.63	92.66	1.64	0.95	100.03	1.46
0.51	81.13	4.62	1.64	36.73	1.32	1.24	158.10	1.14
0.54	93.87	3.82	1.34	175.94	1.70	1.10	128.61	1.56
0.53	20.47	1.95	1.29	46.50	1.46	1.70	146.63	2.35
0.66	48.23	2.49	1.66	44.74	2.49	1.81	163.29	2.26
0.54	53.99	1.68	1.59	171.27	1.20	2.68	137.85	1.64
0.93	18.37	2.36	1.45	179.54	1.90	0.63	101.12	2.02
0.36	38.61	2.13	0.80	69.41	2.26	0.96	129.78	1.22
0.32	104.52	2.26	1.28	60.44	3.90	1.30	110.02	2.01
0.42	88.80	1.52	2.30	54.12	1.79	2.45	147.32	1.75
1.20	33.43	3.50	0.96	85.34	2.58	1.02	141.04	2.21
0.48	114.05	2.53	1.83	35.91	1.24	0.98	106.52	2.19
0.36	30.35	1.74	0.70	91.44	6.84	0.56	172.48	1.17
0.84	58.28	1.51	1.33	32.58	3.19	1.43	162.67	1.53
1.17	55.17	1.38	1.14	0.58	1.15	0.80	102.83	2.36
0.36	18.04	1.41	1.37	7.16	1.80	0.82	100.45	2.17
0.49	109.78	1.23	1.05	59.22	2.31	2.52	130.10	1.46
0.23	84.77	1.48	1.72	95.16	1.26	0.67	46.49	1.72
0.71	106.64	1.36	2.39	123.56	2.52	2.06	77.65	2.50
0.69	156.77	2.24	1.69	128.21	2.20	1.83	2.87	1.38
0.37	46.93	1.60	1.01	111.91	1.65	1.60	122.88	1.61
0.27	71.06	1.47	1.53	48.61	2.29	1.42	117.00	1.25
0.94	86.31	1.67	1.42	117.90	1.52	1.76	92.54	1.16
0.43	62.52	2.08	1.81	2.12	1.61	0.77	76.22	2.98
0.46	173.97	1.94	2.05	4.87	1.63	1.87	69.54	3.26
0.42	160.24	1.93	0.92	109.49	3.90	1.09	146.48	1.49
0.45	105.56	2.08	0.94	91.37	3.28	1.70	141.25	2.31
0.50	111.37	1.59	0.61	30.72	1.51	1.32	178.54	1.70
0.49	33.03	1.37	0.67	97.21	1.31	1.04	167.51	1.88
0.99	63.44	1.43	2.40	32.75	2.10	1.32	163.68	1.65
0.62	121.77	2.38	1.66	95.31	1.79	1.84	38.29	1.13
0.87	35.73	1.95	0.64	49.47	1.98	0.67	155.56	1.55
0.21	161.17	1.59	1.50	7.62	2.29	0.98	35.26	3.51
0.22	30.39	2.45	1.63	0.61	1.28	1.24	112.67	1.22
0.36	39.01	1.73	1.56	47.70	2.55	1.30	94.62	3.29
0.29	83.85	1.23	1.33	92.46	1.44	1.00	30.81	2.11

Deformed samples, R = 4

PP029 shear			PP249			PP249 shear		
diameter	angle°	a/b	diameter	angle°	a/b	diameter	angle°	a/b
4.31	78.50	1.33	0.75	97.73	1.45	3.03	61.17	1.94
1.67	79.12	2.51	0.88	108.59	2.16	2.22	102.54	7.88
4.76	106.41	1.38	1.47	171.08	7.73	5.04	115.59	1.35
1.56	57.85	1.35	3.52	148.10	1.45	3.32	76.13	2.53
2.81	38.56	3.40	4.05	163.92	3.43	4.83	117.79	2.59
1.60	107.88	1.93	3.56	146.57	2.00	4.95	68.94	2.76
3.06	87.16	1.66	0.86	173.38	2.43	2.88	91.25	1.99
1.97	91.42	5.50	1.71	115.15	3.31	3.07	83.13	2.06
1.42	117.92	2.35	2.07	178.03	3.72	3.61	82.24	2.21
1.50	77.80	3.43	4.44	178.25	2.20	4.19	95.49	1.85
1.33	34.10	1.94	4.63	44.23	3.40	7.25	87.07	3.11
3.65	111.57	2.36	2.24	134.71	2.11	3.13	85.57	1.80
1.30	85.10	2.93	1.93	71.44	2.01	3.89	69.53	2.63
2.45	98.26	1.74	0.57	1.01	1.59	4.19	74.66	2.51
4.43	47.94	4.01	4.02	102.51	4.16	3.25	103.80	2.54
1.22	153.22	1.69	3.12	100.45	3.20	2.98	33.31	1.09
2.95	111.52	5.14	4.07	34.67	3.11	0.09	90.00	3.00
2.11	78.54	2.05	2.01	111.96	1.92	0.09	90.00	3.00
4.47	51.80	1.46	3.17	55.63	2.18	0.04	90.00	3.00
0.96	43.27	1.53	0.51	98.56	1.54	0.07	90.00	3.00
1.90	109.84	2.39	2.91	113.78	1.32	3.88	90.00	2.66
0.82	31.46	1.56	1.75	133.06	1.16	4.01	62.10	3.28
1.54	54.99	1.59	2.71	66.40	1.87	3.35	76.94	3.59
1.76	121.85	2.91	0.60	35.76	1.44	5.20	75.22	1.94
3.36	76.95	1.66	3.81	53.24	3.91	4.12	83.54	2.15
3.18	78.04	1.99	5.59	22.96	1.51	5.21	73.06	3.34
1.70	84.22	1.37	1.52	135.00	1.23	4.60	73.16	2.23
2.79	111.43	2.82	1.10	75.53	2.54	4.07	70.37	2.81
0.99	80.46	3.55	5.60	39.50	2.50	3.89	78.29	3.36
1.38	117.54	1.75	2.76	95.33	2.46	3.72	96.29	2.46
1.98	90.65	3.64	4.25	27.95	3.05	4.19	79.18	2.06
1.60	97.44	3.87	0.69	0.63	4.89	2.89	76.77	2.05
1.55	77.95	1.99	2.86	120.36	3.33	4.55	93.81	1.72
1.35	83.06	1.75	1.06	124.26	3.05	5.11	84.33	3.58
1.46	72.57	2.36	7.12	106.46	2.48	4.63	175.28	1.12
3.44	121.31	4.69	3.13	115.70	4.18	3.40	91.31	3.51
3.13	27.79	2.78	0.73	14.08	1.53	4.24	92.66	2.47
2.86	94.52	5.35	0.83	153.80	2.76	3.85	123.23	1.73
1.47	108.80	1.34	8.91	103.90	2.18	3.45	66.02	2.67
3.43	20.25	2.95	5.08	141.78	2.98	3.02	81.56	1.95
2.23	93.35	2.99	0.92	144.13	2.47	2.14	82.83	2.40
3.53	113.55	4.69	3.07	101.77	2.09	3.00	83.84	1.83
2.11	94.10	2.81	1.73	160.03	2.22	3.69	89.36	3.18
2.92	80.41	3.95	0.76	144.43	3.43	3.37	109.21	2.45
1.86	85.70	1.96	2.25	159.21	2.78	4.44	97.69	2.71
2.17	89.30	2.97	1.84	14.59	3.65	3.57	31.99	1.51
1.72	93.91	2.14	4.12	110.43	2.39	3.15	79.52	1.52
3.05	110.27	2.71	4.13	109.25	1.99	3.84	92.87	1.80
1.49	95.36	2.81	2.38	80.70	2.03	4.05	33.37	1.80
3.78	43.36	1.32	1.62	70.98	1.93	3.18	105.89	1.39
2.69	106.33	2.89	3.98	8.08	3.12	4.15	86.73	2.09

Deformed samples, R = 4

PP043			PP043 shear			PP029		
diameter	angle°	a/b	diameter	angle°	a/b	diameter	angle°	a/b
1.87	29.89	4.52	4.31	78.45	3.05	1.61	17.92	1.27
1.35	21.02	1.26	1.66	79.19	1.99	2.51	19.61	1.80
2.08	50.65	2.65	4.75	106.36	4.21	3.23	50.56	2.69
2.68	42.19	6.13	1.57	58.05	6.74	4.41	42.23	6.26
3.66	32.02	2.16	2.81	38.57	2.94	4.89	168.74	5.53
4.05	71.44	3.65	1.60	107.52	2.66	2.83	20.95	1.85
2.35	22.25	2.98	3.05	87.17	3.00	3.21	31.85	2.17
2.66	89.71	3.21	1.97	91.39	2.38	2.54	89.51	3.24
2.11	62.34	4.57	1.43	117.63	3.99	2.24	29.92	4.71
2.46	19.64	1.80	1.51	77.79	3.25	2.97	71.36	3.69
0.67	168.73	5.43	1.33	34.09	3.84	2.73	62.25	4.72
2.27	20.78	1.82	3.73	111.88	2.62	3.75	22.17	3.02
3.12	91.62	3.44	1.29	85.23	2.43	4.09	166.75	5.53
3.39	81.18	2.49	2.45	98.27	7.28	0.80	91.11	3.44
2.70	43.59	1.04	4.43	47.93	1.90	3.25	10.33	3.80
2.65	147.96	1.83	1.23	152.51	2.72	3.20	81.33	2.51
3.05	95.67	2.39	2.94	111.51	5.83	3.67	44.87	1.04
2.10	15.93	2.91	2.11	78.44	2.88	2.53	147.92	1.86
2.38	10.27	3.76	4.45	51.73	3.96	2.86	51.10	1.71
3.90	51.64	1.69	0.96	43.82	5.91	4.70	95.65	2.41
4.06	45.55	1.16	1.90	109.73	2.04	4.89	82.24	3.89
1.14	166.70	5.41	1.54	55.15	3.64	1.37	44.87	1.15
3.86	91.70	1.78	1.76	121.61	3.44	4.65	15.83	2.94
3.61	81.39	4.78	3.35	77.00	1.35	4.35	14.44	5.87
2.34	14.43	5.76	3.60	82.47	4.58	2.82	65.78	3.19
3.25	65.81	3.13	2.78	111.36	1.53	3.91	10.74	5.23
4.28	10.70	5.14	1.00	80.46	4.84	5.16	111.29	3.38
4.48	111.34	3.35	1.39	117.10	2.04	5.40	144.71	8.02
3.28	144.70	7.87	1.98	90.62	1.85	3.95	18.75	4.69
3.97	18.73	4.61	1.60	97.61	13.41	4.78	149.49	3.64
1.77	149.48	3.60	1.55	78.00	1.68	2.13	83.04	2.08
2.69	75.55	2.92	1.35	83.23	5.34	3.23	75.58	2.97
5.21	83.54	2.06	1.46	72.69	4.54	6.28	151.49	7.70
4.79	151.48	7.60	3.44	121.34	3.78	5.77	27.44	7.15
2.87	27.41	7.03	3.12	27.79	4.42	3.46	17.51	5.20
2.62	17.52	5.06	2.85	94.52	1.75	3.16	78.48	6.04
2.66	78.48	5.87	1.47	108.11	5.96	3.21	123.70	1.68
1.59	123.59	1.67	3.42	20.23	2.51	1.92	46.61	5.67
2.40	46.36	5.52	2.22	93.37	3.03	2.90	133.15	4.52
4.24	133.26	4.44	3.52	113.56	1.85	5.11	49.30	2.16
2.14	49.21	2.14	2.11	93.98	4.77	2.58	92.57	2.01
6.57	92.88	2.00	2.91	80.35	4.88	7.92	160.49	3.61
2.98	160.50	3.60	1.85	85.72	2.95	3.59	83.62	3.80
1.36	83.65	3.74	2.17	89.33	2.56	1.63	48.65	6.77
2.43	48.83	6.32	1.72	93.85	3.21	2.93	17.22	3.30
2.30	144.35	3.45	3.05	110.32	1.42	2.77	23.45	3.83
3.81	17.08	3.24	1.49	95.38	1.92	4.59	144.28	3.51
3.16	23.45	3.76	3.78	43.36	4.67	3.80	68.73	4.84
1.78	68.70	4.73	2.69	106.30	2.99	2.15	55.83	3.51
1.25	55.70	3.40	2.41	114.76	3.28	1.50	114.51	2.34
3.63	114.01	2.28	2.50	92.10	1.99	4.37	134.89	5.23

Deformed samples, R = 2

PP669			PP676			PP684			PP685		
diameter	angle°	a/b	diameter	angle°	a/b	diameter	angle°	a/b	diameter	angle°	a/b
1.86	83.09	1.94	0.46	87.76	2.75	2.41	51.17	1.16	0.47	85.75	2.34
2.39	142.00	3.09	2.21	108.21	1.49	0.38	87.59	3.02	1.58	82.41	2.46
1.98	72.92	1.65	4.91	4.67	1.34	1.83	55.71	1.25	3.72	9.37	1.30
2.29	76.51	3.06	0.92	78.02	2.20	0.19	92.54	1.81	2.67	54.09	1.17
1.40	88.84	4.72	0.88	90.91	1.83	0.96	93.74	1.39	1.33	70.47	2.00
0.62	97.73	2.64	2.42	81.37	2.80	1.20	5.20	1.38	1.03	133.43	2.06
1.62	48.78	2.41	2.75	86.67	4.97	1.64	111.55	1.85	0.61	104.03	1.49
2.52	88.15	1.36	1.08	83.25	1.37	1.31	61.62	2.33	0.54	85.86	3.81
1.01	101.66	2.74	0.67	96.46	2.73	0.51	87.63	5.53	2.42	98.71	1.54
1.00	107.34	2.12	1.56	76.60	1.78	1.05	88.13	3.07	0.70	90.01	1.50
2.26	121.55	2.26	1.53	60.87	1.22	2.16	71.12	3.14	2.90	145.88	2.92
0.76	96.82	3.25	0.48	96.19	2.40	1.13	92.20	2.08	2.27	139.63	2.38
0.99	102.01	2.86	1.03	100.87	2.27	0.36	106.56	1.72	0.88	88.44	7.38
1.31	25.40	1.13	1.82	96.77	2.06	1.16	65.44	1.68	2.89	47.72	1.09
1.14	107.85	2.07	3.08	116.35	2.19	1.72	76.59	1.68	1.69	102.45	1.53
0.45	87.18	2.11	0.31	92.77	4.92	1.55	57.35	1.64	2.56	128.15	1.34
2.06	143.32	1.66	1.92	48.95	1.61	1.54	41.65	1.84	1.00	49.66	1.72
3.22	1.43	3.76	2.57	90.75	2.34	0.98	75.91	2.41	3.61	3.62	1.70
1.37	95.47	2.48	0.92	86.90	2.44	0.33	90.38	4.78	1.41	96.58	3.02
1.29	123.57	1.34	0.81	90.14	3.68	1.44	82.81	1.44	1.14	90.49	2.33
0.31	96.76	1.66	1.05	134.01	2.31	1.05	79.14	2.90	4.49	54.64	1.86
0.51	95.92	2.98	0.73	96.62	1.82	0.70	87.98	3.49	1.47	177.18	2.40
2.77	15.60	1.76	0.77	96.72	3.53	0.42	90.21	2.75	1.20	81.75	1.31
1.99	96.56	2.77	2.66	87.43	1.82	0.88	91.01	1.94	1.31	19.96	1.67
1.76	135.25	2.56	0.70	88.71	1.99	1.19	91.95	1.02	3.49	78.39	1.84
1.60	79.84	1.45	2.25	73.31	1.71	0.96	156.01	1.36	2.57	75.11	3.34
1.73	177.99	1.70	1.32	148.41	1.25	0.14	90.84	2.02	3.30	120.47	1.40
0.86	127.46	2.44	1.22	134.69	1.66	0.14	88.57	6.50	3.16	42.62	2.35
1.31	31.90	1.80	1.19	112.50	1.77	2.63	39.18	1.57	1.04	49.58	2.21
0.70	56.48	1.14	3.27	152.23	2.06	0.89	90.77	6.79	0.88	117.74	1.58
1.97	133.25	4.21	1.03	32.62	1.26	1.71	105.47	2.19	1.84	36.29	1.45
2.03	76.68	1.34	2.00	138.57	1.41	1.76	18.72	1.48	1.54	33.01	1.81
1.15	112.55	3.24	3.15	44.18	1.81	1.30	22.69	1.20	1.86	35.04	1.80
1.31	114.27	1.32	1.23	133.54	1.23	3.24	43.32	1.79	0.60	47.96	2.33
2.64	141.61	1.59	1.86	33.97	1.52	0.99	106.64	1.57	2.49	31.73	1.67
1.05	157.69	1.28	1.39	20.19	1.36	1.07	43.44	1.93	1.38	5.76	1.37
1.06	105.18	1.55	1.41	36.18	2.02	3.27	154.76	1.57	1.37	91.35	1.13
1.29	54.49	1.07	1.62	122.61	2.62	1.45	149.85	1.23	1.48	104.41	1.78
0.86	94.93	1.30	1.25	99.67	4.27	5.19	28.92	1.73	1.55	80.03	1.48
2.45	117.99	1.97	2.60	128.31	1.43	1.58	106.04	3.41	2.10	75.98	2.77
0.55	106.73	1.44	2.08	88.02	1.39	1.49	42.19	1.71	1.15	175.55	1.43
2.17	118.98	1.88	2.58	4.35	1.32	0.93	175.05	1.51	5.40	34.16	1.84
1.56	104.39	1.25	1.07	170.52	1.33	2.24	25.16	1.46	2.43	121.74	1.85
1.45	59.38	1.57	3.49	98.35	1.58	1.00	104.19	1.90	0.90	141.79	1.24
1.04	107.86	2.37	2.36	82.12	2.92	1.31	60.07	1.43	3.45	12.73	1.71
3.19	82.02	2.43	2.66	143.85	1.92	0.72	56.47	1.65	1.99	47.39	3.04
1.58	107.21	2.03	2.08	176.78	2.91	0.97	6.13	1.19	1.34	38.64	2.31
1.37	55.14	1.90	0.59	174.48	2.00	1.30	81.74	1.95	1.27	174.60	1.58
1.02	29.87	2.18	2.67	6.91	2.45	0.74	28.50	3.16	2.22	84.22	2.38
1.82	171.30	1.05	1.25	115.61	2.23	1.69	27.24	2.56	1.16	33.95	1.67
0.79	87.80	2.36	3.68	59.83	1.61	1.54	105.75	2.46	0.76	170.65	1.25

Deformed samples, R = 2

PP693			PP695			PP698			PP699		
diameter	angle°	a/b	diameter	angle°	a/b	diameter	angle°	a/b	diameter	angle°	a/b
4.04	70.58	1.47	1.82	59.92	1.71	1.28	174.24	2.79	2.27	87.96	4.09
3.58	65.21	1.75	1.78	42.81	2.40	1.30	93.16	1.62	1.49	3.73	1.18
2.71	95.51	2.17	1.59	41.81	4.74	1.70	100.86	2.19	1.15	151.92	1.99
2.41	92.21	8.38	1.72	103.85	3.26	2.54	88.97	5.40	2.43	135.44	1.70
2.92	108.15	1.59	1.37	72.35	2.17	2.49	102.82	1.11	1.18	99.05	1.71
1.32	60.69	2.52	0.88	71.19	1.55	2.76	98.38	2.70	1.18	32.83	2.10
1.85	90.76	2.00	1.18	67.96	5.37	0.63	99.81	3.14	0.91	59.74	1.75
1.57	70.71	3.58	1.48	22.25	2.56	1.09	98.90	3.68	1.22	45.43	2.11
1.88	38.57	2.10	3.40	45.09	4.15	1.04	90.77	4.68	2.93	48.75	4.37
1.63	90.56	7.25	1.35	39.92	3.12	1.37	10.43	1.75	1.46	47.86	1.39
1.61	96.66	1.19	0.72	33.42	4.50	0.53	93.40	4.41	1.33	58.88	1.94
1.67	68.47	1.63	2.84	40.55	1.93	1.25	58.29	2.32	1.83	79.41	2.43
2.02	77.31	2.94	1.66	49.75	1.50	1.07	47.91	1.76	1.29	24.88	1.51
1.66	72.46	1.38	1.33	69.14	2.06	1.03	5.25	1.17	1.14	59.75	2.24
1.22	31.31	2.33	2.36	74.35	2.14	1.04	18.02	2.53	1.98	36.89	2.01
2.15	81.73	2.55	0.60	84.38	3.60	1.44	61.41	1.27	2.18	43.68	1.71
2.09	98.65	1.67	2.46	81.79	4.08	1.73	108.97	1.99	1.85	48.07	1.97
1.36	89.72	4.58	0.93	62.69	2.00	1.80	45.46	1.53	2.07	47.71	3.93
1.81	32.75	1.64	2.18	65.26	4.69	1.12	37.50	1.35	2.64	20.43	1.29
2.36	82.19	1.84	1.93	179.18	1.62	0.52	98.43	1.41	2.35	17.08	2.06
2.10	22.39	1.20	1.10	48.58	3.12	2.36	83.83	1.20	1.18	69.75	2.23
0.96	83.49	4.29	1.49	89.36	4.01	0.98	128.79	1.21	2.72	33.86	2.10
2.10	73.49	1.59	1.90	1.57	1.68	1.14	84.39	1.89	2.23	38.47	3.97
2.76	88.19	3.68	1.91	178.47	4.07	1.04	55.37	1.26	2.09	133.75	2.86
2.20	85.74	2.12	2.21	21.51	1.13	1.13	88.16	1.86	1.16	114.13	3.07
1.76	83.66	1.67	0.78	128.72	1.78	0.88	72.47	1.17	2.53	174.26	1.75
0.78	48.86	1.48	1.55	118.04	2.55	2.39	96.80	3.43	1.55	30.59	2.75
1.30	35.84	2.19	3.07	31.86	2.89	1.07	149.25	1.33	3.47	42.68	3.31
3.04	81.41	1.90	2.38	102.27	1.18	1.55	85.63	2.06	2.31	84.30	1.42
1.77	101.89	2.50	1.39	112.13	1.72	0.43	103.66	3.36	0.95	153.51	1.28
1.84	1.09	3.63	1.44	105.79	1.25	1.43	127.56	1.76	2.53	43.94	1.67
1.91	41.00	2.93	1.69	146.86	1.82	1.18	59.95	1.86	1.22	29.33	1.15
2.20	40.65	2.56	2.98	85.56	1.68	1.18	60.46	1.24	1.74	16.67	2.58
1.71	46.32	1.25	1.63	58.86	2.12	2.06	104.18	1.48	1.61	146.57	1.21
3.00	71.77	2.13	1.19	103.23	1.93	1.62	92.71	2.97	2.17	70.86	1.67
2.12	89.70	1.46	1.27	16.26	2.98	0.94	81.56	1.79	2.03	60.06	2.02
2.59	34.98	2.04	1.29	76.59	1.51	1.15	122.65	2.14	1.69	45.36	3.18
2.11	26.08	2.51	2.07	73.21	2.51	2.26	78.54	2.41	1.83	64.32	1.29
1.65	46.77	2.25	1.42	89.21	1.71	1.44	123.74	1.50	2.02	125.00	2.86
0.97	17.31	3.94	1.11	39.55	1.07	1.44	108.74	1.33	1.17	44.29	1.77
1.03	73.90	2.84	2.24	124.35	1.89	1.30	86.67	1.73	3.10	61.59	1.65
1.04	64.30	3.00	2.53	91.39	1.25	0.91	68.45	1.99	0.99	32.64	1.86
2.02	163.06	1.28	0.66	65.78	2.82	2.42	76.32	2.36	1.29	15.66	1.53
2.43	98.93	2.05	2.15	177.84	1.90	1.04	76.89	1.17	0.84	116.37	1.27
1.34	109.00	2.05	1.50	82.42	3.11	1.80	85.50	2.32	2.01	19.22	2.31
1.12	5.47	1.47	1.29	39.81	1.63	1.72	51.72	1.82	1.41	170.77	1.39
1.55	110.21	1.82	1.34	134.54	1.55	1.38	122.63	1.46	0.69	60.74	1.54
1.14	14.76	1.51	0.83	79.34	1.64	1.71	52.35	1.30	1.33	45.72	2.70
1.65	14.68	2.85	1.78	77.70	3.28	2.62	4.62	1.08	1.09	115.99	1.46
1.91	34.64	1.41	2.79	172.83	1.94	0.78	66.46	2.02	2.22	103.46	1.04
1.81	93.78	3.08	0.88	95.28	2.69	0.76	76.49	1.98	2.07	56.44	2.49

Appendix C.

Preferential orientation and aspect ratio R of bubbles

Starting materials

#6		#7		HTN4		HTN8	
angle°	a/b	angle°	a/b	angle°	a/b	angle°	a/b
101.99	2.73	175.66	2.03	148.95	1.17	103.98	1.30
81.06	1.50	25.60	1.68	173.48	1.50	113.68	1.22
97.12	4.38	61.76	1.42	73.53	1.24	55.23	2.17
175.83	1.10	29.95	1.10	28.70	1.09	69.88	2.18
86.33	1.75	35.13	1.14	157.19	1.11	54.45	1.72
130.21	2.09	136.04	1.26	98.09	1.88	89.45	1.97
41.78	1.48	64.86	1.58	176.38	1.47	13.38	1.36
153.11	1.48	5.18	1.56	163.41	2.39	116.92	1.17
69.46	2.01	15.03	1.11	103.94	1.25	30.75	1.25
29.71	1.98	6.49	1.11	132.30	1.32	3.33	1.90
32.08	1.21	175.45	1.36	170.92	2.31	118.78	1.72
40.52	1.49	69.08	1.22	110.94	1.98	67.54	1.46
55.21	1.12	21.21	1.28	80.09	1.65	128.83	2.05
35.49	2.09	33.85	1.09	36.94	1.76	106.69	1.40
150.41	2.02	132.63	1.07	16.37	2.87	101.06	1.34
12.16	1.10	163.77	1.55	132.76	1.57	98.33	1.12
20.91	1.40	100.78	1.20	19.25	1.49	21.58	1.20
34.71	1.59	112.19	1.46	44.50	1.38	101.81	2.02
12.78	1.84	32.51	1.64	2.16	1.24	113.98	2.35
164.17	1.43	41.93	1.01	81.43	1.26	50.87	1.54
46.95	1.27	32.30	2.45	129.88	1.36	170.57	1.37
43.32	1.56	4.19	1.08	177.56	2.18	9.75	3.01
179.36	2.19	71.20	1.47	28.00	1.16	107.25	1.67
66.78	1.22	70.73	2.29	157.46	1.37	135.60	1.44
13.21	2.94	104.64	1.38	7.87	1.85	87.60	1.28
56.93	1.48	161.10	1.37	104.72	1.32	92.12	1.67
61.79	1.84	165.06	1.22	46.68	1.40	167.40	1.83
14.99	1.22	47.10	1.63	78.95	2.08	96.62	1.76
90.20	2.41	159.93	1.51	47.81	2.44	70.93	1.10
42.89	1.76	153.42	2.35	14.75	1.67	74.32	1.11
102.88	1.12	105.18	1.20	76.90	1.63	140.77	1.12
61.37	1.36	172.58	1.22	96.89	1.23	114.75	1.40
51.03	1.57	118.33	1.12	162.65	3.23	135.53	1.69
26.09	1.66	49.23	1.27	17.94	1.23	75.88	1.65
100.83	1.68	131.92	1.71	60.94	1.19	83.86	1.49
47.82	1.32	37.43	1.21	139.73	1.30	162.97	1.16
68.92	1.54	136.63	2.15	154.17	1.46	98.45	1.31
165.73	2.25	42.74	1.73	78.03	1.17	60.29	1.24
139.05	1.25	84.95	1.25	156.73	1.39	175.45	1.48
61.57	2.54	178.71	1.34	114.95	1.99	159.35	1.59
81.27	2.18	61.65	1.10	49.17	1.23	150.98	1.37
162.18	1.39	109.19	1.37	99.59	1.65	141.99	1.31
117.87	1.41	11.30	1.36	109.12	1.09	62.46	1.96
79.89	1.29	8.34	1.60	124.79	1.55	98.00	1.44
114.44	2.45	159.56	1.78	67.85	1.10	132.37	1.32
147.70	2.81	3.06	2.97	74.51	1.29	67.61	1.26
50.94	1.57	70.07	1.11	76.60	1.58	172.79	1.79
120.37	2.27	7.71	1.32	88.31	1.16	74.71	2.04
14.66	1.21	128.30	1.42	14.93	1.39	112.11	1.18
53.77	1.45	6.41	1.74	112.60	1.37	161.00	1.54
109.46	2.49	141.74	1.50	90.81	1.35	160.19	1.31

Starting materials

HTN 9		HTN11		HTN13		HTN14	
angle°	a/b	angle°	a/b	angle°	a/b	angle°	a/b
102.62	1.59	176.20	1.35	100.82	2.08	143.22	1.75
94.53	1.25	151.36	1.44	121.48	2.76	80.06	1.70
68.77	1.71	41.51	1.27	91.55	1.80	135.28	1.71
65.58	1.53	46.97	1.20	166.64	1.70	61.94	1.58
76.25	1.58	68.59	1.36	100.24	1.78	117.21	1.19
67.17	1.26	72.34	1.24	134.39	1.90	138.96	1.69
40.79	2.01	117.26	1.17	174.03	1.18	28.34	1.12
57.07	1.17	13.93	1.46	147.28	1.32	90.94	1.42
71.72	1.57	78.31	1.21	13.35	1.71	98.22	1.08
127.62	1.80	80.46	1.21	2.78	1.31	47.43	1.72
63.49	1.90	88.92	1.62	130.86	3.66	134.55	1.26
97.06	1.31	14.70	1.31	145.40	1.44	105.52	1.07
37.07	1.49	84.72	1.10	67.14	1.34	31.96	1.12
87.51	2.05	65.99	2.18	150.84	1.88	84.36	1.57
44.33	1.53	156.33	1.44	57.57	1.19	125.86	2.11
9.95	1.21	65.22	1.29	172.35	1.59	85.03	1.40
95.12	1.27	54.24	1.89	86.91	1.23	27.86	1.12
89.40	1.54	33.40	1.70	172.72	1.96	104.93	1.29
55.01	1.21	37.83	1.09	65.38	3.03	147.42	1.33
41.71	1.17	37.21	1.46	60.00	1.14	80.37	1.32
114.74	1.54	106.28	1.43	45.78	1.89	93.27	2.05
139.72	1.17	73.46	1.28	32.36	1.14	60.07	1.30
64.94	1.41	97.27	1.78	161.28	1.59	175.70	1.62
104.06	1.63	50.66	1.67	5.76	1.38	82.80	1.30
67.10	1.55	27.90	1.49	159.61	1.34	11.30	1.39
57.63	1.56	98.67	1.15	104.17	1.06	76.33	1.62
68.58	1.79	168.09	1.31	53.25	1.20	111.23	1.50
120.02	1.53	58.53	1.18	139.68	1.39	15.65	1.65
75.04	1.92	66.65	1.67	156.81	1.21	20.83	1.26
92.96	1.39	39.24	1.72	169.71	1.28	98.28	1.75
132.92	1.42	156.90	1.34	109.60	1.23	103.38	1.57
103.84	1.62	71.35	1.19	63.74	1.09	86.25	1.52
115.03	1.18	115.49	1.18	18.08	1.07	116.25	1.33
154.01	1.13	7.81	1.34	165.57	1.22	143.51	1.50
67.24	1.45	59.38	1.97	80.61	1.40	87.88	1.43
60.52	1.20	106.08	1.39	151.16	1.35	91.75	1.76
61.17	1.57	34.83	1.44	175.25	1.54	139.31	1.76
2.52	1.44	150.88	1.42	160.47	1.57	8.77	1.57
87.42	1.59	136.10	1.21	12.63	1.53	101.34	1.01
166.31	1.41	72.80	1.18	78.07	1.48	33.54	1.15
36.59	1.33	17.71	1.13	172.38	1.42	113.53	1.19
67.23	1.03	24.48	1.46	72.71	1.28	86.30	1.26
77.95	1.33	147.79	1.38	177.07	1.26	118.45	1.22
67.68	1.26	7.41	1.97	94.87	1.18	128.18	1.48
164.63	1.77	157.18	1.10	165.76	1.59	98.26	1.71
179.93	1.23	115.61	1.22	175.31	1.16	103.89	1.59
78.46	1.24	157.91	1.36	45.29	1.46	114.22	1.26
92.90	1.24	130.92	1.35	10.82	2.08	73.86	1.50
42.10	1.61	128.63	1.27	144.79	1.54	135.58	2.89
59.77	1.02	178.88	1.62	39.44	1.82	56.72	1.24
70.50	1.20	84.02	1.39	174.54	1.58	80.71	1.51

R = 4

PP043		PP029		PP249		PP249 shear bands	
angle°	a/b	angle°	a/b	angle°	a/b	angle°	a/b
22.38	1.35	97.98	1.20	154.58	1.26	88.24	1.94
28.73	1.71	89.68	2.80	169.74	2.42	82.32	1.49
89.38	1.31	68.45	2.52	94.73	2.52	100.82	1.14
59.95	1.20	74.57	2.35	158.52	1.33	128.87	1.30
164.05	2.69	87.71	2.15	80.76	1.58	75.83	1.25
80.64	1.54	46.56	1.63	58.07	2.52	108.76	3.47
179.96	2.05	67.97	1.91	52.31	1.35	116.00	2.04
51.90	1.65	61.66	2.14	101.21	1.64	86.60	2.71
88.22	1.32	79.32	1.94	57.99	1.41	133.41	1.11
57.33	1.47	113.93	1.08	71.96	1.89	100.41	2.68
97.83	1.19	66.07	1.94	95.38	1.42	113.63	1.40
84.91	2.21	41.55	4.92	144.66	1.18	107.24	1.72
36.91	1.60	87.40	2.17	100.88	2.56	128.98	1.41
5.00	2.33	42.94	1.86	89.18	1.31	67.07	1.39
18.86	1.17	28.89	2.82	140.82	2.07	98.92	2.07
11.53	3.51	68.76	1.64	122.88	1.18	89.37	1.71
83.57	1.33	73.64	2.99	147.09	1.42	98.40	1.50
27.31	1.71	25.61	1.51	109.08	1.61	102.03	1.87
8.88	1.11	83.05	1.12	114.34	1.22	44.14	1.59
2.56	1.79	74.90	1.48	33.55	1.12	81.81	1.72
23.38	2.34	117.29	1.45	79.98	1.71	125.98	1.28
167.61	1.96	40.92	1.54	143.08	1.02	116.49	1.27
106.54	1.27	33.35	1.56	55.74	1.47	130.19	1.03
126.14	1.16	128.79	1.33	140.40	2.21	105.42	1.25
48.26	3.52	120.50	1.18	90.62	1.88	89.10	2.37
65.72	1.81	83.55	1.54	77.16	1.39	129.96	1.73
166.12	3.34	67.53	1.63	163.64	1.38	61.15	1.86
22.41	2.10	9.94	1.81	82.16	1.84	127.06	1.47
16.59	1.86	132.97	1.92	85.76	1.33	93.78	1.24
12.49	2.37	82.96	1.82	98.25	1.59	137.20	1.91
84.76	1.68	40.17	1.52	60.93	1.69	149.59	2.40
31.19	1.90	92.67	1.54	23.22	1.96	80.34	1.36
17.45	1.07	76.43	1.03	126.69	1.24	138.72	2.14
75.52	1.49	4.67	1.52	150.13	2.04	46.06	1.26
110.19	1.34	120.44	2.36	51.43	1.22	143.59	1.49
21.64	1.26	103.73	1.40	175.70	1.35	99.48	1.25
10.47	1.82	151.33	1.45	64.26	1.91	77.31	1.27
154.33	2.57	71.55	1.67	25.84	1.39	138.46	1.23
14.41	3.18	49.97	1.63	125.34	2.42	88.84	1.35
43.81	1.49	39.77	2.83	65.56	2.58	151.71	2.47
33.73	1.87	164.95	2.38	21.43	1.63	91.28	1.57
162.89	1.40	87.04	1.09	87.44	1.48	97.91	1.44
92.29	1.79	145.36	1.14	43.64	1.17	138.51	1.37
98.22	1.45	16.42	2.53	18.90	1.47	53.22	1.74
60.92	1.25	127.20	3.84	11.08	1.86	65.88	1.41
126.96	2.44	122.62	1.42	45.64	1.31	104.55	1.66
50.90	2.00	31.02	1.47	9.18	1.35	113.51	2.10
15.53	2.01	123.55	1.38	5.72	3.09	118.95	1.09
77.51	1.20	104.20	1.79	133.34	1.17	62.56	1.80
15.31	1.35	14.61	1.38	32.33	1.60	67.44	1.46
158.21	1.84	89.48	1.68	62.71	1.11	0.55	1.40

R = 2

PP669		PP676		PP684		PP685	
angle°	a/b	angle°	a/b	angle°	a/b	angle°	a/b
65.93	1.93	173.21	1.14	87.44	1.81	72.24	1.81
34.82	1.13	98.86	1.23	68.52	2.47	74.67	1.70
3.91	1.07	57.89	1.63	70.67	1.34	85.59	1.77
38.10	1.88	75.66	1.62	38.85	1.35	77.17	1.75
35.86	1.84	33.46	1.29	60.84	1.71	58.31	1.76
33.30	1.86	52.87	1.71	82.11	1.37	89.14	1.58
150.19	1.22	74.89	1.56	104.42	1.55	67.65	1.71
21.52	1.57	16.96	1.49	79.24	2.55	64.94	1.90
65.53	1.62	45.38	1.35	70.06	2.16	97.89	1.52
47.94	1.64	59.62	1.81	47.45	1.58	69.30	1.88
76.89	1.24	52.93	2.08	75.99	4.00	119.16	1.61
68.13	1.62	97.80	1.89	89.78	1.55	79.46	1.53
61.56	1.19	59.89	1.44	16.52	1.59	97.47	1.79
45.81	1.59	38.58	1.72	54.30	2.46	84.33	1.42
58.22	1.62	53.76	1.52	54.18	1.60	60.82	1.97
49.19	1.38	43.92	1.66	79.16	1.64	85.87	1.55
43.36	1.88	125.07	3.18	63.85	2.43	86.98	1.71
40.91	2.40	13.04	1.49	114.76	2.32	45.78	1.81
62.34	1.44	65.08	1.77	174.40	1.19	140.79	1.45
55.89	1.61	62.36	1.58	123.04	1.48	86.03	2.46
83.64	1.57	100.53	1.12	160.03	1.20	104.92	1.20
20.53	1.62	80.66	1.82	86.55	1.72	67.13	1.48
42.42	1.66	51.59	1.83	78.64	1.53	110.27	1.55
47.43	1.86	92.70	1.34	72.82	1.66	70.31	1.64
80.00	1.76	72.90	1.57	71.55	1.90	83.74	1.79
55.64	1.31	68.13	1.47	74.26	1.64	17.53	1.19
53.65	2.08	159.34	1.71	117.13	2.01	95.22	1.40
29.86	1.76	42.75	1.99	49.74	1.90	70.21	1.31
160.72	1.10	76.03	1.98	80.40	1.29	75.60	1.70
57.70	1.33	18.06	1.10	72.14	2.64	81.50	1.90
34.89	1.69	94.69	1.42	75.65	2.00	75.69	1.71
41.24	1.27	31.79	1.10	0.70	1.12	89.08	1.86
46.93	2.16	52.81	1.50	79.77	1.92	98.73	1.88
164.63	1.40	76.13	1.61	146.95	1.21	77.61	2.92
57.70	1.23	20.84	1.12	167.21	1.33	56.53	1.41
52.34	2.19	78.18	3.28	29.88	1.03	80.84	1.92
67.22	1.49	51.73	1.22	112.93	2.53	72.96	2.07
27.87	1.50	42.16	1.50	24.60	1.69	75.11	1.92
63.84	1.78	152.34	1.22	35.43	3.51	73.33	1.54
49.48	1.77	23.59	1.34	75.86	2.08	88.03	1.93
56.00	1.11	27.78	1.63	0.40	1.61	76.73	2.69
60.08	2.29	147.61	1.47	63.68	1.87	91.74	1.59
40.06	1.52	72.58	2.15	68.41	4.14	83.35	1.51
43.14	1.72	81.41	1.95	69.48	2.38	107.32	1.34
9.96	1.04	38.22	1.66	58.51	1.95	104.99	1.59
19.78	1.54	30.05	1.20	50.75	2.60	72.77	1.81
50.86	1.84	119.58	1.51	68.39	2.68	85.57	1.72
45.80	1.64	169.98	1.40	77.24	2.12	70.96	2.54
43.49	1.51	74.44	2.07	62.74	2.30	73.79	1.42
52.58	1.31	23.67	1.12	83.37	1.66	95.14	1.99
59.12	1.15	59.81	2.05	76.06	1.82	93.40	1.45

R = 2

PP693		PP695		PP698		PP699.1	
angle°	a/b	angle°	a/b	angle°	a/b	angle°	a/b
138.72	1.63	42.87	3.21	101.14	1.31	59.87	1.73
73.49	1.97	158.70	2.01	96.31	1.77	83.90	1.43
127.57	1.51	106.60	1.30	94.19	1.67	52.41	1.33
49.98	1.35	68.38	1.71	21.04	1.49	37.08	1.40
62.22	1.72	91.95	1.77	68.49	1.24	62.26	1.87
49.07	2.06	59.47	1.70	47.74	1.47	55.67	1.41
134.43	1.19	69.53	2.50	79.71	1.24	74.09	1.50
149.84	1.14	63.14	1.41	11.89	1.17	27.89	1.32
119.49	1.10	102.85	1.52	47.60	2.00	59.29	2.01
87.47	2.57	50.11	2.42	176.52	1.18	39.49	1.08
42.54	1.57	105.11	1.72	27.62	1.39	56.80	1.24
87.42	2.05	48.52	1.51	45.51	1.19	60.91	1.18
147.38	1.54	77.50	1.54	30.46	1.73	82.84	1.21
0.67	1.28	53.06	2.05	16.65	1.43	89.95	1.20
71.29	1.15	53.38	3.11	59.90	1.90	97.85	1.46
97.55	1.73	68.80	3.33	74.43	1.82	97.21	1.25
32.16	1.56	28.46	2.19	88.09	1.40	74.75	1.94
47.36	1.69	88.91	5.08	75.66	1.66	129.11	1.32
88.30	1.52	104.21	1.91	45.47	1.25	67.25	2.82
79.61	3.30	60.50	2.56	20.75	2.78	71.07	1.32
81.01	1.80	48.83	1.78	47.68	1.53	70.31	1.19
87.46	1.13	86.70	2.86	82.21	2.19	36.45	1.28
56.69	1.64	107.93	2.55	115.55	1.14	147.26	1.05
100.45	1.55	71.55	2.44	39.52	1.99	67.75	1.51
135.78	1.01	161.68	1.27	44.74	1.87	30.35	1.23
99.84	1.53	55.06	1.46	4.52	1.94	98.43	2.01
47.30	2.53	91.17	1.10	44.08	1.75	1.77	1.22
64.25	1.52	48.43	1.84	48.42	2.35	79.82	1.28
113.51	1.56	70.93	2.03	8.19	1.68	53.84	1.70
60.34	1.93	64.90	1.50	62.68	2.63	80.26	1.96
78.30	1.48	83.63	3.67	172.00	1.10	69.03	1.24
33.94	1.96	27.29	1.26	129.33	1.17	102.54	1.68
73.10	2.30	68.97	4.00	76.82	2.13	166.87	1.23
79.50	1.69	99.56	2.82	57.27	1.68	100.14	1.33
39.00	1.85	57.37	1.38	83.17	1.96	56.20	1.16
95.84	1.23	154.62	1.48	18.47	1.54	162.80	1.20
55.88	1.39	87.31	1.47	66.84	2.81	118.79	1.63
54.60	3.84	115.22	1.17	103.29	1.52	44.55	1.20
85.74	1.17	104.26	1.79	71.85	3.77	65.37	2.27
160.26	1.18	148.51	1.40	64.72	1.47	124.52	1.75
136.57	1.51	15.03	1.54	6.83	1.94	94.10	1.12
96.97	1.14	47.76	2.35	56.93	1.21	178.33	1.12
85.86	1.47	58.12	2.84	149.53	1.23	58.00	2.05
163.49	1.30	70.95	1.28	19.06	2.33	57.67	1.71
60.58	1.72	55.65	1.89	175.17	1.09	111.81	2.29
31.85	1.41	92.72	1.22	56.56	1.67	34.87	1.40
109.12	1.16	123.51	2.52	39.44	1.33	101.37	1.47
36.84	1.52	113.53	1.84	77.73	1.50	176.48	1.22
29.21	1.81	45.83	1.25	147.32	1.45	75.05	1.50
125.15	1.28	137.03	2.71	67.03	1.56	59.65	1.57
47.54	2.16	27.67	2.39	4.72	1.37	70.27	1.48

R = 2

PP699.2		PP699.3		PP699.4	
angle°	a/b	angle°	a/b	angle°	a/b
76.51	4.32	117.91	1.23	36.32	1.47
76.61	1.20	104.75	1.38	8.21	1.72
127.84	2.12	95.29	1.78	117.86	1.26
130.02	2.35	87.68	5.47	124.04	1.53
28.01	1.97	91.72	1.73	73.15	1.27
159.22	2.14	53.42	3.44	103.83	2.27
90.65	4.51	105.42	2.19	140.13	5.41
114.58	3.28	138.98	1.76	100.56	1.72
71.27	2.01	153.78	1.63	1.10	1.67
14.09	1.68	136.26	1.47	152.78	1.49
5.11	2.59	105.78	1.22	41.18	1.49
88.05	2.89	37.90	1.31	69.44	2.85
165.73	2.04	175.31	3.12	145.97	1.83
177.67	1.23	88.74	1.33	74.59	2.10
136.39	1.82	16.65	2.74	100.22	1.62
77.89	2.51	90.40	2.13	100.89	2.93
89.22	2.81	106.48	2.03	63.28	1.69
73.65	3.01	159.69	2.36	97.63	2.10
137.39	4.74	54.86	1.70	170.72	2.05
73.01	2.41	96.10	1.44	27.28	3.50
87.32	1.97	86.71	1.80	152.74	1.13
14.61	1.35	90.16	2.82	72.58	2.35
117.16	1.56	53.77	1.94	88.16	1.45
158.13	2.64	146.90	1.57	115.38	1.77
77.18	3.03	159.92	2.82	54.29	2.30
84.24	1.71	65.90	1.53	167.17	2.81
107.11	2.09	6.07	2.63	30.32	1.46
52.33	2.91	4.45	1.65	93.20	1.47
76.78	1.32	141.12	2.35	149.12	2.37
110.72	4.00	177.49	1.07	19.31	1.63
91.37	2.22	39.07	1.25	71.86	1.70
106.57	1.72	107.19	1.72	122.78	1.59
71.51	1.95	96.16	1.80	31.03	2.33
94.95	2.80	98.93	1.66	127.69	1.42
131.80	2.83	37.03	2.37	48.50	1.61
29.06	2.27	3.24	1.26	78.69	1.14
162.00	1.23	26.74	1.87	119.27	1.52
106.28	2.08	10.03	1.58	96.87	1.33
96.20	1.55	80.42	1.97	54.14	2.18
97.46	3.98	123.57	3.62	161.01	1.18
56.93	1.66	48.23	1.76	36.34	1.40
29.89	2.05	146.47	1.11	91.93	1.28
86.87	2.94	103.55	1.72	90.90	2.22
117.26	1.48	165.65	2.15	136.05	1.84
80.93	2.30	94.19	2.12	91.87	2.13
81.01	2.05	23.72	2.83	85.02	6.99
35.10	1.29	143.12	1.05	155.90	1.84
63.34	1.63	7.77	1.63	145.18	1.31
43.28	1.02	13.15	1.56	115.82	2.00
125.43	1.46	107.61	1.73	107.25	2.17
61.03	2.05	114.23	1.63	168.84	1.88

Appendix D.

Chemical compositions of plagioclases and residual melt

Starting materials

R = 4

#6	Na_2O	Al_2O_3	SiO_2	CaO	Total
	7.39	22.19	65.46	4.50	99.66
	7.43	22.78	65.08	5.02	100.34
	7.09	21.95	66.45	4.22	99.74
	8.12	23.21	65.50	4.83	101.70
	8.25	22.05	64.42	4.36	99.09
	8.22	21.47	64.42	4.49	98.74
	8.17	22.34	63.99	4.54	99.05
	7.79	20.99	65.80	4.09	98.90
	8.16	22.77	63.01	4.94	99.01
	7.93	24.30	61.74	5.91	99.90
	8.00	22.27	63.74	4.87	99.02
	7.58	22.68	65.72	4.87	101.06
Average	7.84	22.42	64.61	4.72	99.68
Standard deviation	0.39	0.85	1.34	0.48	0.93

#7	Na_2O	Al_2O_3	SiO_2	CaO	Total
	7.85	24.72	61.78	6.54	100.89
	7.37	22.49	63.35	5.34	98.54
	7.69	24.36	61.27	6.36	99.68
	7.46	23.41	62.17	5.99	99.03
	6.69	22.33	66.96	5.00	100.98
	7.12	20.33	66.89	3.65	98.00
	7.42	21.01	65.02	4.82	98.27
	7.81	22.66	63.03	5.57	99.08
	7.50	22.57	64.54	5.22	99.83
	6.85	20.11	67.30	3.86	98.12
	7.01	20.26	67.29	3.85	98.41
	7.14	20.40	66.81	3.98	98.33
Average	7.33	22.05	64.70	5.02	99.10
Standard deviation	0.37	1.62	2.32	1.01	1.04

R = 2, Φs = 0.58 - 0.59

HTN4	Na_2O	Al_2O_3	SiO_2	CaO	Total
	6.37	26.77	56.85	9.41	99.72
	6.62	26.12	57.98	8.13	99.10
	5.80	27.05	56.43	9.87	99.22
	5.40	27.86	55.73	10.78	99.82
	5.46	28.82	54.00	11.13	99.49
	6.53	25.84	58.16	8.31	98.95
	6.26	26.88	58.06	8.99	100.42
	5.54	26.85	56.46	10.06	99.16
	5.71	28.17	55.60	10.41	99.96
	4.23	24.02	61.94	8.21	98.65
	5.11	29.48	53.71	11.50	100.03
	5.17	27.41	56.07	10.48	99.36
	5.16	26.22	57.33	9.61	98.44
	5.31	26.85	56.74	9.48	98.48
	5.03	24.66	61.44	8.22	99.41
	4.28	23.71	62.44	7.99	98.68
	5.30	26.51	59.37	9.53	100.78
	6.58	26.99	57.22	8.85	99.83
	5.62	28.22	55.78	10.22	99.95
	5.89	27.14	55.48	9.78	98.92
Average	5.57	26.78	57.34	9.55	99.42
Standard deviation	0.68	1.46	2.40	1.04	0.64

HTN8	Na_2O	Al_2O_3	SiO_2	CaO	Total
	7.32	25.45	59.15	7.34	99.82
	5.57	26.53	57.88	9.69	99.80
	4.63	21.79	65.80	6.01	98.83
	5.37	26.22	57.04	9.68	98.50
	6.41	25.91	57.52	8.65	99.04
	5.35	25.83	57.99	9.41	98.85
	5.69	27.59	55.34	10.22	98.90
	5.41	24.71	59.37	8.87	98.76
	5.32	26.36	57.36	9.87	99.09
	5.42	25.22	58.77	9.16	98.77
	5.05	25.38	60.13	8.74	99.55
	5.35	28.26	54.45	10.77	98.92
	5.62	27.19	55.50	10.43	98.96
	5.43	23.78	61.42	7.97	98.83
	5.36	26.40	56.84	9.72	98.48
	5.43	27.65	55.63	10.43	99.28
	5.28	24.76	60.81	8.31	99.43
Average	5.53	25.83	58.29	9.13	99.05
Standard deviation	0.58	1.56	2.76	1.23	0.40

HTN9	Na_2O	Al_2O_3	SiO_2	CaO	Total
	5.42	27.87	55.64	10.64	99.69
	4.77	24.90	61.68	8.43	99.97
	6.09	24.52	61.16	7.42	99.39
	5.31	24.74	60.69	8.62	99.53
	5.51	28.85	55.54	10.70	100.77
	5.54	27.33	57.75	9.78	100.62
	5.33	22.97	63.19	7.27	99.06
	5.66	26.79	57.72	9.74	100.12
	5.53	24.40	60.94	7.97	99.02
	5.82	25.76	59.23	9.26	100.47
Average	5.50	25.81	59.35	8.98	99.86
Standard deviation	0.35	1.84	2.61	1.24	0.63

Starting materials

R = 2, Φs = 0.73 - 0.76 - 0.95

HTN11	Na_2O	Al_2O_3	SiO_2	CaO	Total
	5.03	23.58	62.54	7.60	99.04
	5.15	23.93	62.70	7.61	99.68
	5.66	23.33	61.15	7.99	98.52
	5.96	26.11	59.32	9.04	100.49
	5.94	25.32	59.75	8.89	100.06
	5.44	24.56	61.25	8.13	99.75
	6.01	26.67	57.97	9.53	100.30
	7.19	24.10	60.36	7.11	99.21
	5.66	26.10	57.27	9.35	98.70
	5.66	23.84	61.76	7.98	99.53
	5.52	24.90	60.74	8.49	99.77
	6.01	26.93	56.38	9.77	99.34
	6.06	27.68	56.43	9.80	100.02
	5.54	24.53	60.01	8.58	98.91
	5.78	23.86	60.90	8.17	98.89
	5.43	24.43	61.40	8.03	99.41
	5.79	25.85	58.88	9.12	99.84
	5.83	25.66	62.19	8.47	102.35
	5.91	26.62	56.59	9.84	99.07
	6.20	26.30	58.46	8.86	100.09
	5.60	24.98	59.49	8.56	98.91
	5.61	23.46	62.14	7.89	99.41
	5.57	24.38	62.36	7.49	100.14
	5.47	24.67	60.51	8.61	99.62
	5.87	26.44	58.98	9.26	100.79
	5.92	27.39	56.67	9.74	99.95
	5.49	24.91	59.67	8.65	98.85
	5.77	25.66	59.77	8.81	100.15
	5.64	24.23	60.28	8.20	98.64
	6.01	24.96	61.50	8.47	101.15
	5.96	24.49	61.85	8.31	101.04
	5.81	26.26	58.70	9.19	100.30
	5.79	25.40	58.80	8.80	99.06
	6.11	26.42	58.84	9.05	100.67
	4.79	23.80	62.21	7.60	98.66
	6.20	26.21	58.03	9.05	99.64
	5.86	26.31	59.38	8.88	100.74
	5.09	25.22	59.42	8.52	98.54
	5.64	25.40	59.83	8.78	99.80
	5.92	24.63	60.39	8.62	99.74
	6.20	26.42	58.56	9.35	100.91
	6.68	26.27	58.62	8.35	100.26
	6.65	26.25	58.66	8.49	100.54
	5.71	25.26	59.46	8.70	99.25
	5.55	24.44	60.40	8.11	98.70
	5.24	24.84	59.84	8.55	98.68
	5.75	26.32	59.35	8.94	100.54
	6.18	27.15	57.55	9.50	100.50
	6.46	26.01	58.91	8.50	100.09
	5.87	26.56	58.01	9.48	100.16
	5.64	27.54	56.69	10.01	100.21
	5.39	24.55	61.06	8.07	99.33
	5.26	22.44	64.89	7.17	100.11
	5.57	25.25	59.88	8.46	99.54
	5.74	25.16	60.45	8.42	99.95
	5.92	26.89	57.14	9.59	99.71
	5.94	26.09	58.56	9.00	99.77
	5.90	24.06	61.76	7.87	99.84
	5.65	25.58	60.25	8.66	100.38
	5.96	25.70	58.96	8.92	99.64
	6.33	27.49	57.29	9.36	100.65
	5.74	26.24	59.66	8.93	100.72
	5.12	22.16	63.85	7.31	98.69
Average	5.78	25.37	59.76	8.64	99.79
Standard deviation	0.40	1.24	1.84	0.68	0.77

HTN12	Na_2O	Al_2O_3	SiO_2	CaO	Total
	4.89	20.71	67.63	6.41	100.01
	4.24	17.83	72.93	5.52	100.87
	6.08	26.69	59.80	8.87	101.82
	6.40	25.98	57.73	8.55	98.94
	6.49	25.36	58.04	8.49	98.66
	6.34	26.23	58.88	8.90	100.44
	6.41	25.26	57.77	8.72	98.63
	6.55	25.43	57.56	9.10	98.95
	6.65	25.08	57.91	8.22	98.65
	6.82	25.42	58.25	8.49	99.35
	6.51	25.74	57.67	8.72	99.01
	6.54	25.92	57.47	8.88	99.02
	6.50	25.92	57.73	8.73	99.10
	6.32	24.78	59.21	8.35	98.86
	4.94	16.88	71.72	5.37	99.33
	5.73	21.17	65.14	7.19	99.48
	6.09	24.02	60.96	8.03	99.45
	0.75	3.09	5.29	1.22	0.90

HTN13	Na_2O	Al_2O_3	SiO_2	CaO	Total
	5.87	22.69	62.07	7.70	98.46
	6.39	26.24	56.63	9.24	98.64
	6.02	23.70	60.23	8.08	98.40
	5.80	24.18	61.01	8.23	99.58
	5.64	23.56	60.81	8.07	98.45
	5.90	25.19	59.51	8.72	99.61
	5.65	23.25	62.01	7.52	98.62
	5.25	23.39	61.91	7.61	98.61
	5.96	24.21	59.91	8.54	98.77
	5.66	22.53	62.99	7.60	98.89
	5.89	22.88	61.85	7.54	98.46
	5.71	24.20	60.62	8.22	98.98
	6.55	26.62	57.71	9.01	100.08
	6.95	25.84	58.48	8.57	100.13
	5.63	21.80	65.40	7.08	100.23
	6.82	26.17	57.12	9.02	99.23
	6.35	24.60	61.32	8.03	100.61
	6.68	25.95	58.54	8.58	100.09
	6.34	26.37	57.53	9.01	99.57
	6.88	25.56	57.23	8.55	98.58
	6.57	26.01	57.75	8.70	99.23
	6.99	25.74	57.87	8.42	99.19
	6.01	23.54	62.97	7.72	100.60
	6.59	25.24	59.18	8.37	99.41
Average	6.17	24.56	60.03	8.26	99.27
Standard deviation	0.50	1.42	2.28	0.57	0.72

HTN14	Na_2O	Al_2O_3	SiO_2	CaO	Total
	5.81	58.71	25.29	8.72	98.56
	5.97	57.28	26.70	9.37	99.34
	6.22	56.58	26.68	9.41	98.90
	6.02	57.97	26.28	8.98	99.27
	6.05	57.18	26.43	9.21	98.88
	6.25	57.81	25.98	8.99	99.06
	5.49	63.75	22.68	7.04	98.97
	5.41	67.01	20.24	6.46	99.21
	6.06	63.03	23.39	7.46	99.95
	5.36	60.72	24.56	7.94	98.60
	6.06	57.83	26.63	9.07	99.61
	6.11	57.68	26.13	8.96	98.91
Average	5.90	59.63	25.08	8.47	99.10
Standard deviation	0.31	3.29	2.03	0.99	0.40

Deformed samples

R = 4 crystals

PP043	Na_2O	Al_2O_3	SiO_2	CaO	Total
	7.78	24.53	60.84	6.05	99.28
	7.43	24.22	60.17	6.60	98.53
	7.46	25.18	59.20	6.81	98.71
	7.69	22.08	64.43	4.71	98.99
	7.44	23.33	61.91	6.15	98.86
	7.79	24.47	60.73	6.18	99.37
	7.06	21.87	64.61	5.05	98.66
	7.92	23.78	61.98	5.58	99.36
	7.79	23.55	63.11	5.57	100.07
	7.86	24.29	62.13	6.13	100.55
	7.60	22.39	63.13	5.13	98.32
	8.19	25.14	60.53	6.33	100.20
Average	7.67	23.73	61.90	5.86	99.24
Standard deviation	0.29	1.13	1.69	0.65	0.71

PP029	Na_2O	Al_2O_3	SiO_2	CaO	Total
	6.57	20.45	67.56	4.08	98.70
	6.27	22.18	67.54	4.28	100.34
	7.71	21.51	64.38	4.47	98.11
	6.83	20.98	65.86	4.53	98.34
	7.69	21.54	66.12	4.36	99.91
	7.27	20.67	66.16	4.03	98.14
	7.68	21.57	65.94	4.44	99.64
	7.59	22.03	65.48	4.54	99.73
	7.69	21.54	66.12	4.36	99.91
	7.68	21.57	65.94	4.44	99.64
	7.59	22.03	65.48	4.54	99.73
Average	7.32	21.46	66.05	4.37	99.29
Standard deviation	0.52	0.56	0.89	0.18	0.80

PP249	Na_2O	Al_2O_3	SiO_2	CaO	Total
	7.32	24.28	60.98	6.92	99.54
	6.43	24.29	59.71	8.09	98.65
	6.94	24.62	60.33	7.55	99.54
	7.34	24.21	61.96	6.85	100.46
	6.90	25.72	58.68	8.14	99.52
	6.92	24.33	61.15	7.53	99.98
	6.90	23.42	61.92	6.69	99.01
	7.25	22.70	62.78	5.98	98.91
	8.32	19.93	67.51	3.10	98.95
	7.31	23.51	62.23	6.08	99.16
	7.00	22.08	65.17	5.66	100.01
Average	7.15	23.56	62.04	6.60	99.43
Standard deviation	0.47	1.55	2.49	1.42	0.56

R = 4 glass

PP043	Na_2O	Al_2O_3	SiO_2	CaO	Total
	6.22	16.97	67.67	2.61	93.73
	6.73	17.22	67.14	2.42	93.66
	5.96	16.04	70.59	1.88	94.62
	6.78	18.27	66.18	3.26	94.64
	5.34	11.53	69.34	1.51	88.16
	6.54	16.97	68.19	2.52	94.38
Average	6.26	16.17	68.18	2.37	93.20
Standard deviation	0.55	2.38	1.58	0.61	2.50

PP029	Na_2O	Al_2O_3	SiO_2	CaO	Total
	3.91	14.68	71.09	1.86	91.79
	4.84	15.99	69.79	2.40	93.16
	3.80	14.35	69.63	1.85	89.75
	5.03	15.18	69.92	2.07	92.41
	4.55	13.19	71.13	1.14	90.20
	6.09	15.94	67.46	2.47	92.08
	4.77	13.94	70.42	1.41	90.77
	2.54	7.82	80.52	1.56	92.62
	4.38	13.42	70.77	1.19	89.91
	5.36	14.87	69.74	1.73	91.87
	5.06	13.62	70.10	1.34	90.20
Average	4.6	13.9	71.0	1.7	91.3
Standard deviation	0.9	2.2	3.3	0.5	1.2

PP249	Na_2O	Al_2O_3	SiO_2	CaO	Total
	6.24	14.09	71.50	1.29	93.68
	4.03	15.93	71.05	2.31	93.77
	4.45	13.43	71.60	1.09	91.19
	5.62	14.12	70.73	1.36	91.92
	6.49	15.67	69.34	1.76	93.48
	6.69	19.83	65.68	4.35	96.68
	6.42	15.74	69.86	1.83	94.02
	6.57	15.69	69.99	1.55	93.90
	6.96	15.87	69.94	1.66	94.52
Average	5.94	15.60	69.97	1.91	93.68
Standard deviation	1.04	1.85	1.79	0.98	1.55

Deformed samples

R = 2 crystals, **Φs = 0.58 - 0.59**

PP669	Na_2O	Al_2O_3	SiO_2	CaO	Total
	6.63	26.02	58.84	8.39	100.18
	5.77	27.76	56.49	10.17	100.27
	5.45	28.12	55.79	10.65	100.09
	5.74	25.10	60.55	8.41	100.08
	4.73	25.41	62.54	9.01	101.94
	5.11	27.38	56.36	10.66	99.55
	4.96	28.61	55.96	11.25	100.86
	5.05	28.16	55.29	11.21	99.72
	4.81	25.62	59.53	9.35	99.48
	4.92	29.33	53.80	12.08	100.20
	5.16	25.23	61.00	8.98	100.53
	5.16	28.68	55.93	11.10	100.99
	4.90	28.84	55.06	11.42	100.27
	5.00	29.08	54.81	11.42	100.32
	6.60	26.22	58.18	8.54	99.92
	6.80	25.76	59.02	7.96	99.96
	5.32	26.94	58.95	9.75	100.97
	5.47	26.00	60.32	9.08	101.06
	4.87	29.49	54.43	11.67	100.48
	4.82	24.62	60.76	8.54	98.86
	5.10	23.53	62.49	7.79	99.11
	5.58	25.90	59.16	8.97	99.66
	5.29	29.09	55.45	11.30	101.18
	5.19	26.50	57.81	9.65	99.28
	4.84	29.48	54.92	11.63	100.98
	4.90	25.09	60.23	8.86	99.11
	5.26	28.70	55.29	11.17	100.42
	5.17	26.83	58.77	9.99	101.01
	5.53	23.95	61.53	7.80	98.94
	4.92	24.83	61.27	8.78	100.03
	5.17	26.63	56.96	10.12	99.01
	5.10	28.05	55.48	10.68	99.45
Average	5.29	26.91	57.90	9.89	100.12
Standard deviation	0.53	1.75	2.60	1.30	0.76

PP676	Na_2O	Al_2O_3	SiO_2	CaO	Total
	5.23	25.16	58.63	9.09	98.40
	5.35	26.08	58.03	9.85	99.46
	5.19	28.15	53.98	11.40	98.85
	5.07	26.69	56.93	9.87	98.67
	5.18	22.61	63.70	7.12	98.93
	4.91	29.46	54.00	11.50	99.96
	5.38	27.82	56.87	10.43	100.62
	5.64	25.75	57.97	9.15	98.75
	5.40	26.69	57.58	9.76	99.60
	5.07	27.38	55.48	10.56	98.66
Average	5.24	26.58	57.32	9.87	99.19
Standard deviation	0.21	1.88	2.77	1.27	0.70

PP684	Na_2O	Al_2O_3	SiO_2	CaO	Total
	5.26	28.30	55.69	11.24	100.59
	5.21	27.57	56.53	10.41	99.94
	5.78	24.70	59.66	8.32	98.73
	4.79	23.03	63.02	7.65	98.69
	4.79	24.30	61.23	8.17	98.61
	5.47	28.58	54.98	10.69	99.85
	5.22	28.04	55.91	10.45	99.81
	5.39	27.80	55.33	10.29	99.01
	5.57	27.52	56.50	9.96	99.87
	5.53	28.31	55.77	10.79	100.49
	5.32	28.87	53.66	11.27	99.20
	5.15	28.04	56.68	10.54	100.67
	5.40	28.22	55.53	10.59	99.87
Average	5.30	27.17	56.96	10.03	99.64
Standard deviation	0.28	1.88	2.68	1.19	0.73

PP685	Na_2O	Al_2O_3	SiO_2	CaO	Total
	4.71	22.73	64.09	7.08	98.85
	5.11	28.15	55.67	11.13	100.20
	5.07	28.40	54.37	11.04	99.12
	5.32	26.93	58.59	9.36	100.37
	4.90	28.84	53.45	11.18	98.50
	5.10	27.33	55.99	10.37	98.86
	4.97	28.65	54.82	11.32	99.86
	4.85	28.65	53.26	11.68	98.58
	5.11	28.38	54.81	10.89	99.35
	4.91	28.58	54.66	11.24	99.53
	4.83	28.47	53.12	11.63	98.12
	5.22	28.15	54.31	11.15	99.01
	4.82	28.10	55.58	11.17	99.84
	5.05	29.41	53.79	11.40	99.74
	5.04	28.68	53.64	11.46	99.04
	5.30	25.22	59.20	8.60	98.68
	4.89	26.01	59.22	9.56	99.98
	5.64	27.77	54.99	10.44	98.95
	4.67	27.28	57.12	10.51	99.74
	4.90	28.47	53.65	11.42	98.50
	4.85	29.21	53.23	11.56	98.86
	5.19	27.80	54.67	10.75	98.54
	5.21	27.77	55.08	10.84	98.98
Average	5.03	27.78	55.54	10.69	99.18
Standard deviation	0.22	1.46	2.60	1.10	0.61

R = 2 glass, **Φs = 0.58 - 0.59**

PP669	Na_2O	Al_2O_3	SiO_2	CaO	Total
	2.29	13.75	70.71	2.03	89.34
	2.42	13.35	69.66	2.24	87.97
	1.07	13.11	70.63	1.79	87.06
	1.00	12.51	71.02	1.67	86.70
	2.19	14.19	68.89	2.71	88.32
	2.58	13.80	69.16	2.21	88.33
	2.68	13.97	69.61	2.34	89.23
	1.96	14.51	69.98	2.65	89.53
	2.20	12.66	70.22	1.78	87.34
	2.24	12.64	69.66	1.84	86.76
	2.41	12.76	70.03	1.75	87.38
	2.27	12.80	71.29	1.77	88.62
	1.51	12.98	71.38	2.14	88.56
	2.41	13.55	69.09	2.17	87.66
	3.62	17.87	65.27	4.11	91.08
	2.54	13.10	70.25	2.09	88.38
	2.49	12.91	70.29	1.90	88.29
Average	2.23	13.56	69.83	2.19	88.27
Standard deviation	0.61	1.26	1.39	0.58	1.12

PP685	Na_2O	Al_2O_3	SiO_2	CaO	Total
	2.55	12.55	70.26	1.72	87.69
	2.85	13.56	70.33	2.19	89.41
	2.42	12.38	69.85	1.63	86.68
	2.45	13.15	70.41	2.08	88.60
	2.75	12.90	69.03	2.04	87.15
	2.14	12.87	69.18	1.96	86.62
	2.45	12.82	70.73	1.78	88.34
	2.64	12.64	70.05	1.82	87.82
	2.94	13.34	69.22	2.26	88.20
	3.27	13.71	69.22	2.47	89.22
	2.94	13.27	70.04	2.13	89.01
	2.72	13.10	70.51	1.85	89.04
	2.97	13.27	69.54	2.21	88.51
	2.23	12.99	69.05	1.95	86.77
	2.69	12.64	69.79	1.78	87.51
Average	2.67	13.01	69.81	1.99	88.04
Standard deviation	0.30	0.38	0.58	0.23	0.95

Deformed samples

R = 2 crystals, **Φs = 0.73 - 0.76 - 0.95**

PP693	Na_2O	Al_2O_3	SiO_2	CaO	Total
	6.06	27.17	57.81	9.65	100.92
	5.49	23.18	61.96	7.56	98.67
	5.47	22.87	62.30	7.66	98.83
	5.47	23.71	61.57	8.17	99.24
	5.49	24.69	60.65	8.48	99.78
	5.85	25.01	58.68	8.74	98.54
	5.79	25.59	59.67	8.82	100.13
	5.72	24.83	60.24	8.50	99.55
	5.71	25.62	59.09	8.98	99.58
	6.01	26.31	59.39	9.00	100.97
	5.61	25.41	59.42	8.59	99.29
	5.71	25.63	60.65	8.43	100.65
	5.19	24.04	61.81	7.96	99.27
	5.31	23.67	61.70	7.61	98.56
	5.73	26.89	57.97	9.32	100.13
	5.51	24.55	60.51	8.31	99.06
	5.45	24.73	61.41	8.09	99.90
	5.62	26.34	59.97	9.16	101.25
	5.18	24.54	60.86	8.10	98.88
	6.01	25.96	58.04	8.93	99.14
	5.57	24.06	61.53	7.83	99.09
	5.99	26.17	57.67	9.00	99.06
	6.12	26.48	57.53	9.47	99.73
	6.20	26.63	56.73	9.16	98.73
	5.81	25.24	59.43	8.45	99.04
	5.08	23.53	61.91	7.77	98.70
Average	5.66	25.11	59.94	8.53	99.49
Standard deviation	0.30	1.20	1.63	0.60	0.78

PP695	Na_2O	Al_2O_3	SiO_2	CaO	Total
	5.60	25.15	59.54	8.28	98.79
	5.86	25.98	57.96	8.86	98.89
	5.75	25.60	58.35	8.57	98.53
	5.76	24.44	59.91	8.12	98.43
	5.66	26.87	55.78	9.75	98.47
	5.36	24.56	60.72	7.94	98.60
	6.06	26.63	57.83	9.07	99.61
	6.11	26.13	57.68	8.96	98.91
	5.70	24.67	59.15	8.46	98.23
	5.64	25.37	58.23	8.69	98.17
	5.95	25.44	58.05	8.67	98.27
	5.86	26.31	57.04	8.98	98.28
Average	5.77	25.60	58.35	8.70	98.60
Standard deviation	0.21	0.81	1.33	0.48	0.41

PP698	Na_2O	Al_2O_3	SiO_2	CaO	Total
	7.35	24.54	61.03	6.70	100.26
	5.71	25.10	60.46	8.46	99.74
	5.65	25.22	58.64	8.75	98.44
	6.27	26.83	57.43	9.02	99.60
	5.88	27.55	56.40	9.86	100.08
	5.73	26.05	59.53	8.54	100.21
	6.25	27.19	56.83	9.45	99.99
	5.50	24.53	61.01	8.16	99.23
	6.02	25.60	58.07	8.74	98.69
	7.35	24.54	61.03	6.70	100.26
	5.71	25.10	60.46	8.46	99.74
	5.65	25.22	58.64	8.75	98.44
	6.27	26.83	57.43	9.02	99.60
	5.88	27.55	56.40	9.86	100.08
	5.73	26.05	59.53	8.54	100.21
	6.25	27.19	56.83	9.45	99.99
	5.50	24.53	61.01	8.16	99.23
	6.02	25.60	58.07	8.74	98.69
Average	6.04	25.85	58.82	8.63	99.58
Standard deviation	0.54	1.09	1.72	0.86	0.64

PP699	Na_2O	Al_2O_3	SiO_2	CaO	Total
	5.73	26.17	58.38	9.16	99.61
	5.73	24.78	59.73	8.36	98.85
	5.60	24.80	59.93	8.19	98.81
	5.30	24.65	60.22	8.19	98.74
	5.52	24.61	60.12	8.62	99.04
	5.21	24.15	60.91	7.89	98.46
	5.37	24.92	60.99	8.14	99.62
	5.55	25.18	60.26	8.45	99.63
	4.84	22.83	63.57	7.06	99.00
	6.20	27.15	57.52	9.13	100.13
	4.62	22.76	64.95	6.64	99.34
	5.70	24.77	61.24	8.11	100.17
	5.18	23.96	62.50	7.37	99.23
	5.96	25.97	59.09	8.48	99.58
	5.94	25.06	59.35	8.49	98.87
	5.88	25.75	59.17	8.83	99.90
	5.79	25.56	58.62	8.83	98.97
	4.97	23.42	62.62	7.24	98.59
	5.59	25.72	60.48	7.97	99.99
	5.16	24.09	63.09	7.19	99.80
	6.28	24.99	59.61	7.96	99.30
	5.24	24.93	60.19	8.19	98.73
Average	5.52	24.83	60.57	8.11	99.29
Standard deviation	0.42	1.05	1.82	0.67	0.52

PP701	Na_2O	Al_2O_3	SiO_2	CaO	Total
	5.25	20.27	67.03	6.41	99.40
	6.15	23.51	61.58	7.67	99.15
	5.85	23.01	62.74	7.17	99.16
	6.50	25.82	58.48	8.49	99.55
	6.59	25.02	58.96	8.19	99.03
	6.44	25.26	59.75	7.94	99.64
	4.75	18.96	69.25	5.99	99.37
	5.59	21.40	64.19	7.03	98.60
	6.05	23.00	62.50	7.47	99.40
	4.95	19.71	69.09	6.27	100.32
	5.34	20.25	66.89	6.13	99.03
	5.43	20.88	65.63	6.52	98.75
	6.32	24.01	60.41	7.76	98.82
	5.03	20.45	66.75	6.65	99.24
	6.22	24.29	61.04	7.72	99.81
	6.08	23.26	62.09	7.35	99.33
	4.71	18.36	69.89	5.59	99.23
	6.46	25.18	59.13	8.04	99.05
	6.30	24.73	59.83	7.84	99.09
	6.37	25.04	58.90	7.95	98.66
Average	5.82	22.62	63.21	7.21	99.23
Standard deviation	0.63	2.37	3.83	0.84	0.41

Natural sample - Petit Gerbier - PG1

K-feldspar	Na_2O	MgO	Al_2O_3	SiO_2	K_2O	CaO	TiO_2	MnO	FeO	Total
	6.90	0.02	19.25	66.49	6.74	0.32	0.00	0.00	0.30	100.03
	7.50	0.00	19.85	66.63	6.41	0.32	0.00	0.00	0.22	100.93
	6.88	0.00	19.56	66.11	6.77	0.40	0.01	0.04	0.21	99.99
	6.90	0.00	19.32	65.36	7.27	0.25	0.06	0.00	0.10	99.28
	6.67	0.00	19.42	65.95	7.75	0.09	0.00	0.00	0.33	100.21
	6.51	0.00	18.96	65.77	7.80	0.11	0.00	0.00	0.36	99.52
	7.14	0.00	19.40	65.82	6.65	0.34	0.00	0.00	0.28	99.63
	6.93	0.00	19.47	65.23	7.26	0.29	0.04	0.01	0.15	99.37
	5.92	0.00	18.58	65.16	8.71	0.05	0.01	0.02	0.42	98.88
	7.28	0.01	19.17	66.09	6.46	0.17	0.00	0.00	0.31	99.50
	6.04	0.01	18.76	66.09	8.34	0.00	0.10	0.06	0.56	99.98
	6.29	0.01	19.30	65.19	8.09	0.06	0.00	0.00	0.34	99.28
	6.49	0.01	18.78	65.18	7.81	0.09	0.03	0.00	0.32	98.73
	5.70	0.00	19.17	65.25	9.04	0.06	0.03	0.03	0.26	99.56
	6.57	0.00	18.98	65.37	7.77	0.15	0.00	0.00	0.37	99.22
	6.25	0.01	18.76	66.33	8.05	0.01	0.08	0.10	0.64	100.25
Average	6.62	0.00	19.17	65.75	7.56	0.17	0.02	0.02	0.32	99.65
Standard deviation	0.50	0.01	0.34	0.51	0.80	0.13	0.03	0.03	0.14	0.56

Plagioclase	Na_2O	MgO	Al_2O_3	SiO_2	K_2O	CaO	TiO_2	MnO	FeO	Total
	8.77	0.00	23.03	56.33	0.61	0.06	0.01	0.07	0.46	89.35
	8.21	0.00	22.42	56.49	1.12	0.01	0.06	0.08	0.77	89.15
	8.37	0.01	23.00	56.75	0.09	0.17	0.07	0.12	0.50	89.08
	7.85	0.00	23.45	57.16	0.08	0.05	0.03	0.00	0.45	89.09
	9.64	0.00	23.96	55.40	0.44	0.06	0.06	0.02	0.16	90.07
Average	8.57	0.00	23.17	56.42	0.47	0.07	0.05	0.06	0.47	89.35
Standard deviation	0.69	0.01	0.57	0.66	0.43	0.06	0.03	0.05	0.21	0.42

Pyroxene	Na_2O	MgO	Al_2O_3	SiO_2	K_2O	CaO	TiO_2	MnO	FeO	Total
	1.80	4.16	3.51	45.89	0.04	19.84	1.65	1.34	20.36	98.60
	2.60	4.11	1.30	47.82	0.02	18.70	0.91	2.00	21.81	99.28
	2.91	3.42	1.12	48.49	0.00	18.08	0.75	1.77	21.99	98.53
	2.82	4.32	1.52	47.83	0.01	18.54	1.39	1.84	20.71	98.99
	1.51	4.23	2.53	46.22	0.03	20.38	1.23	1.51	20.63	98.30
	1.59	6.09	0.91	49.68	0.14	20.46	0.68	1.84	17.85	99.26
	1.05	4.57	1.28	47.64	0.00	21.12	0.75	1.73	20.85	99.00
	2.84	4.11	1.88	48.32	0.09	18.49	1.02	1.61	21.04	99.40
	2.13	5.41	1.55	48.69	0.04	19.61	0.88	1.70	19.33	99.35
	3.37	2.37	0.87	48.27	0.05	17.15	0.73	1.99	23.74	98.55
	4.27	2.40	0.90	48.77	0.00	15.56	0.83	1.89	24.55	99.17
	1.42	4.46	2.05	47.45	0.11	20.57	0.99	1.68	20.47	99.21
Average	2.36	4.14	1.62	47.92	0.04	19.04	0.98	1.74	21.11	98.97
Standard deviation	0.94	1.06	0.78	1.06	0.05	1.62	0.30	0.19	1.79	0.38

Analcime	Na_2O	MgO	Al_2O_3	SiO_2	K_2O	CaO	TiO_2	MnO	FeO	Total
	11.15	0.01	22.46	53.45	0.24	0.42	0.00	0.20	1.18	89.11
	11.91	0.01	23.40	55.01	0.19	0.07	0.00	0.03	0.17	90.80
	13.94	0.01	23.88	53.22	0.17	0.01	0.00	0.00	0.14	91.36
	12.74	0.00	22.51	55.66	0.06	0.00	0.05	0.00	0.02	91.05
	12.08	0.00	23.74	55.41	0.16	0.30	0.00	0.08	0.39	92.17
	11.95	0.00	23.52	53.59	0.16	0.63	0.00	0.07	0.38	90.32
	11.65	0.00	23.76	54.73	0.10	0.00	0.02	0.04	0.13	90.43
	14.27	0.00	24.40	50.68	0.15	0.00	0.00	0.00	0.00	89.50
	13.16	0.00	23.11	52.20	0.12	0.04	0.06	0.00	0.39	89.10
	13.07	0.01	23.04	52.64	0.16	0.35	0.00	0.06	0.34	89.69
	11.80	0.00	23.02	54.68	0.14	0.02	0.00	0.05	0.33	90.06
	10.33	0.03	24.57	52.18	0.04	0.10	0.03	0.06	0.99	88.34
Average	12.34	0.01	23.45	53.62	0.14	0.16	0.01	0.05	0.37	90.16
Standard deviation	1.14	0.01	0.67	1.53	0.05	0.21	0.02	0.06	0.36	1.09

Natural sample - Petit Gerbier - PG3

K-feldspar	Na_2O	MgO	Al_2O_3	SiO_2	K_2O	CaO	TiO_2	MnO	FeO	Total
	8.13	0.02	19.10	65.20	3.97	0.95	0.01	0.00	0.18	97.56
	6.16	0.01	17.80	66.23	7.47	0.15	0.00	0.00	0.55	98.36
	7.06	0.00	18.41	66.37	5.93	0.59	0.00	0.00	0.26	98.63
	6.97	0.00	18.74	65.52	5.62	0.38	0.05	0.12	0.13	97.53
	5.71	0.00	18.08	65.80	7.95	0.25	0.07	0.00	0.18	98.04
	6.94	0.00	18.53	65.40	6.03	0.50	0.13	0.00	0.26	97.81
	7.38	0.00	18.77	64.84	5.21	0.87	0.00	0.02	0.10	97.17
	8.43	0.01	20.29	65.50	3.66	1.19	0.04	0.22	0.01	99.36
	6.16	0.01	18.89	65.95	8.03	0.18	0.01	0.40	0.07	99.71
	6.60	0.00	19.02	63.00	7.10	0.69	0.09	0.08	0.01	96.58
	8.13	0.02	19.10	65.20	3.97	0.95	0.01	0.00	0.18	97.56
	6.16	0.01	17.80	66.23	7.47	0.15	0.00	0.00	0.55	98.36
	7.06	0.00	18.41	66.37	5.93	0.59	0.00	0.00	0.26	98.63
	6.97	0.00	18.74	65.52	5.62	0.38	0.05	0.12	0.13	97.53
	5.71	0.00	18.08	65.80	7.95	0.25	0.07	0.00	0.18	98.04
	6.94	0.00	18.53	65.40	6.03	0.50	0.13	0.00	0.26	97.81
	7.38	0.00	18.77	64.84	5.21	0.87	0.00	0.02	0.10	97.17
	6.60	0.00	19.02	63.00	7.10	0.69	0.09	0.08	0.01	96.58
Average	6.92	0.00	18.67	65.34	6.12	0.56	0.04	0.06	0.19	97.51
Standard deviation	0.79	0.01	0.58	0.97	1.40	0.31	0.05	0.11	0.16	97.47

Plagioclase	Na_2O	MgO	Al_2O_3	SiO_2	K_2O	CaO	TiO_2	MnO	FeO	Total
	10.63	0.00	22.26	56.04	0.13	0.01	0.00	0.07	0.06	89.22
	14.71	0.01	24.05	51.39	0.16	0.93	0.02	0.00	0.12	91.39
	13.44	0.01	22.68	51.11	0.19	0.41	0.03	0.08	0.00	87.95
	14.75	0.01	22.65	52.86	0.10	0.87	0.00	0.02	0.06	91.31
	12.01	0.00	22.92	51.81	0.27	0.98	0.01	0.00	0.25	88.26
	10.63	0.00	22.26	56.04	0.13	0.01	0.00	0.07	0.06	89.22
	14.71	0.01	24.05	51.39	0.16	0.93	0.02	0.00	0.12	91.39
	13.44	0.01	22.68	51.11	0.19	0.41	0.03	0.08	0.00	87.95
	14.75	0.01	22.65	52.86	0.10	0.87	0.00	0.02	0.06	91.31
	12.01	0.00	22.92	51.81	0.27	0.98	0.01	0.00	0.25	88.26
	15.33	0.04	27.10	51.11	0.39	0.81	0.00	0.08	0.11	94.96
	11.37	0.03	26.44	52.98	0.27	0.47	0.00	0.00	0.13	91.68
Average	13.15	0.01	23.55	52.54	0.20	0.64	0.01	0.03	0.10	90.24
Standard deviation	1.74	0.01	1.62	1.78	0.09	0.37	0.01	0.04	0.08	2.13

Amphibole	Na_2O	MgO	Al_2O_3	SiO_2	K_2O	CaO	TiO_2	MnO	FeO	Total
	2.43	11.83	13.78	38.46	1.12	11.99	5.43	0.18	11.82	97.03
	2.38	11.98	13.88	39.00	1.26	11.83	5.34	0.11	12.16	97.95
	2.27	10.43	13.90	38.75	1.27	11.89	5.46	0.10	12.91	96.98
	2.25	10.87	14.49	38.39	1.38	11.94	5.80	0.14	12.88	98.13
	2.25	10.80	14.00	38.50	1.41	12.16	5.77	0.19	12.99	98.07
	2.39	11.94	13.68	38.65	1.31	11.98	5.57	0.19	12.00	97.70
	2.34	10.34	13.98	38.35	1.36	11.96	5.54	0.21	12.96	97.04
	2.31	10.45	13.86	38.42	1.44	11.99	5.87	0.13	12.91	97.37
	2.44	11.51	13.50	37.90	1.21	12.00	5.45	0.09	12.30	96.40
	2.47	10.87	13.03	38.85	1.27	11.99	5.45	0.00	13.03	96.97
Average	2.35	11.10	13.81	38.53	1.30	11.97	5.57	0.13	12.60	97.37
Standard deviation	0.08	0.62	0.36	0.29	0.09	0.08	0.17	0.06	0.45	0.55

Natural sample - Petit Gerbier - PG3

Aegirine	Na_2O	MgO	Al_2O_3	SiO_2	K_2O	CaO	TiO_2	MnO	FeO	Total
	11.10	0.15	0.70	51.46	0.00	4.26	2.95	0.70	26.55	97.86
	11.46	0.15	0.73	51.62	0.01	3.25	1.53	0.71	27.81	97.27
	11.68	1.53	1.04	52.04	0.00	3.42	3.27	0.59	25.17	98.75
	12.34	1.54	0.84	52.23	0.01	2.28	2.33	1.02	25.76	98.34
	10.91	2.04	1.13	51.32	0.04	4.61	3.67	0.57	24.76	99.05
	12.47	0.96	0.91	51.54	0.03	1.90	2.71	0.49	26.48	97.49
	12.51	1.17	0.98	52.06	0.00	1.82	2.61	0.81	26.53	98.50
	11.94	1.15	1.05	52.07	0.00	2.64	3.30	0.45	26.48	99.08
	12.09	1.26	1.02	51.63	0.03	2.64	3.55	0.51	25.19	97.92
	11.90	1.20	0.95	51.78	0.02	2.84	3.19	0.52	26.01	98.42
	10.54	0.14	0.69	50.76	0.06	4.99	0.98	0.77	29.38	98.31
	8.89	0.32	0.68	49.24	0.07	8.38	2.81	1.31	26.17	97.88
	12.50	0.06	0.94	51.47	0.00	1.54	2.14	0.40	28.44	97.48
	12.12	0.08	0.87	51.31	0.04	2.49	2.77	0.67	28.16	98.51
Average	11.60	0.84	0.90	51.47	0.02	3.36	2.70	0.68	26.63	98.20
Standard deviation	0.99	0.67	0.15	0.75	0.02	1.78	0.76	0.25	1.35	0.57

Aegirine- augite	Na_2O	MgO	Al_2O_3	SiO_2	K_2O	CaO	TiO_2	MnO	FeO	Total
	1.39	4.26	1.77	47.67	0.02	20.35	0.86	1.63	21.27	99.21
	1.82	5.46	3.28	47.36	0.04	19.82	1.84	1.05	19.12	99.79
	1.61	4.04	3.50	45.85	0.05	20.03	1.77	1.35	19.50	97.69
	1.49	4.75	3.27	47.12	0.06	20.13	1.63	1.42	19.90	99.77
	1.66	4.52	3.46	46.30	0.00	20.09	1.88	1.20	20.75	99.86
	1.55	4.89	2.48	47.21	0.00	20.41	1.25	1.14	20.73	99.65
	2.02	4.74	2.67	47.26	0.02	19.76	1.32	1.37	19.28	98.44
	1.69	4.53	2.41	47.22	0.00	20.19	1.18	1.64	20.50	99.36
	1.73	4.57	2.22	47.94	0.06	20.19	1.17	1.39	20.30	99.57
	1.54	4.67	2.40	47.36	0.07	20.62	1.06	1.20	20.55	99.46
	2.16	3.17	0.82	48.12	0.05	19.48	0.71	2.28	23.18	99.98
	1.05	4.24	1.25	48.47	0.09	20.96	0.74	1.90	21.41	100.11
Average	1.64	4.49	2.46	47.32	0.04	20.17	1.28	1.46	20.54	99.41
Standard deviation	0.29	0.55	0.86	0.72	0.03	0.40	0.42	0.35	1.11	0.69

Analcime	Na_2O	MgO	Al_2O_3	SiO_2	K_2O	CaO	TiO_2	MnO	FeO	Total
	11.14	0.00	23.84	56.51	0.06	0.04	0.00	0.01	0.11	91.70
	11.81	0.01	23.75	56.08	0.01	0.00	0.00	0.06	0.13	91.86
	11.63	0.00	24.31	54.99	0.09	0.02	0.03	0.00	0.08	91.16
	11.58	0.02	24.01	55.27	0.08	0.00	0.00	0.07	0.07	91.12
	11.33	0.01	26.76	52.04	0.18	0.08	0.02	0.09	0.16	90.68
	11.28	0.00	26.77	52.89	0.16	0.06	0.03	0.00	0.09	91.28
	9.49	0.00	24.11	56.79	0.16	0.08	0.00	0.00	0.24	90.85
	9.35	0.00	23.01	56.03	0.56	0.07	0.08	0.19	0.55	89.85
	11.00	0.02	26.86	52.28	0.17	0.11	0.00	0.00	0.03	90.46
	10.12	0.07	24.54	50.96	0.27	2.76	0.26	0.00	1.66	90.64
	9.24	0.01	23.48	56.83	0.18	0.01	0.00	0.00	0.27	90.03
	10.83	0.01	23.25	56.24	0.31	0.17	0.00	0.04	0.14	90.98
	9.90	0.00	24.04	56.84	0.85	0.02	0.01	0.08	0.24	92.01
	10.25	0.00	23.81	56.70	0.24	0.05	0.00	0.07	0.17	91.27
	9.53	0.02	22.78	56.65	0.67	0.06	0.00	0.09	0.38	90.20
	12.00	0.00	23.75	55.55	0.27	0.00	0.04	0.06	0.21	91.87
	9.69	0.01	22.84	56.22	0.07	0.14	0.00	0.00	0.18	89.16
Average	10.60	0.01	24.23	55.23	0.25	0.22	0.01	0.05	0.28	90.89
Standard deviation	0.95	0.02	1.32	1.93	0.23	0.66	0.02	0.04	0.38	0.78

Appendix E.

EPMA maps

Petit Gerbier - PG1

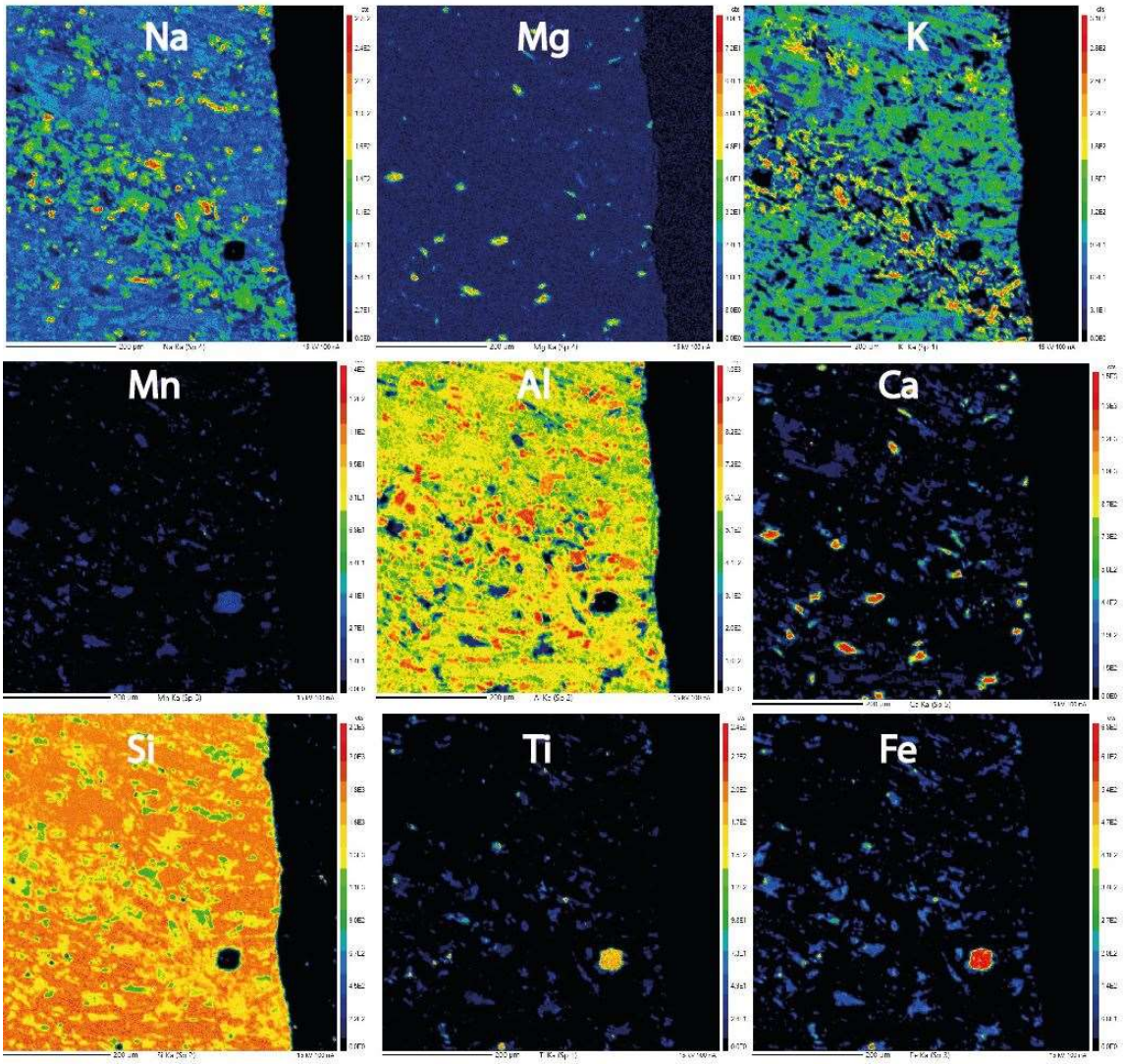

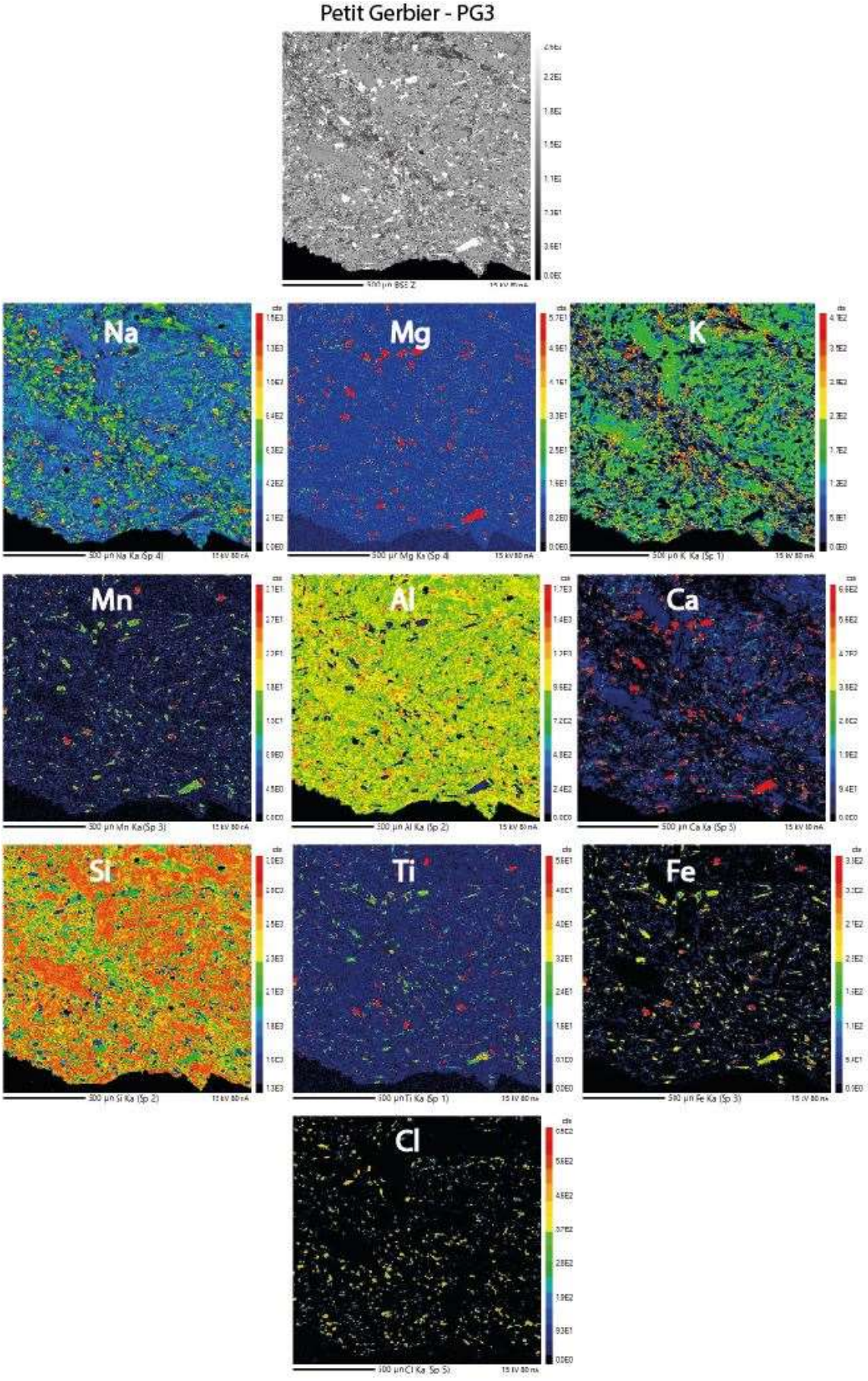
Petit Gerbier - PG3
Na
Mg
K
Mn
Al
Ca
Si
Ti
Fe
Cl

Suc de Sara

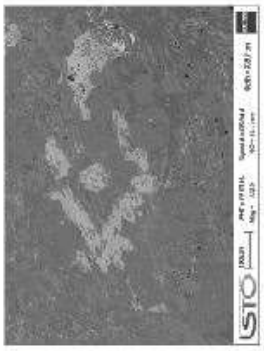

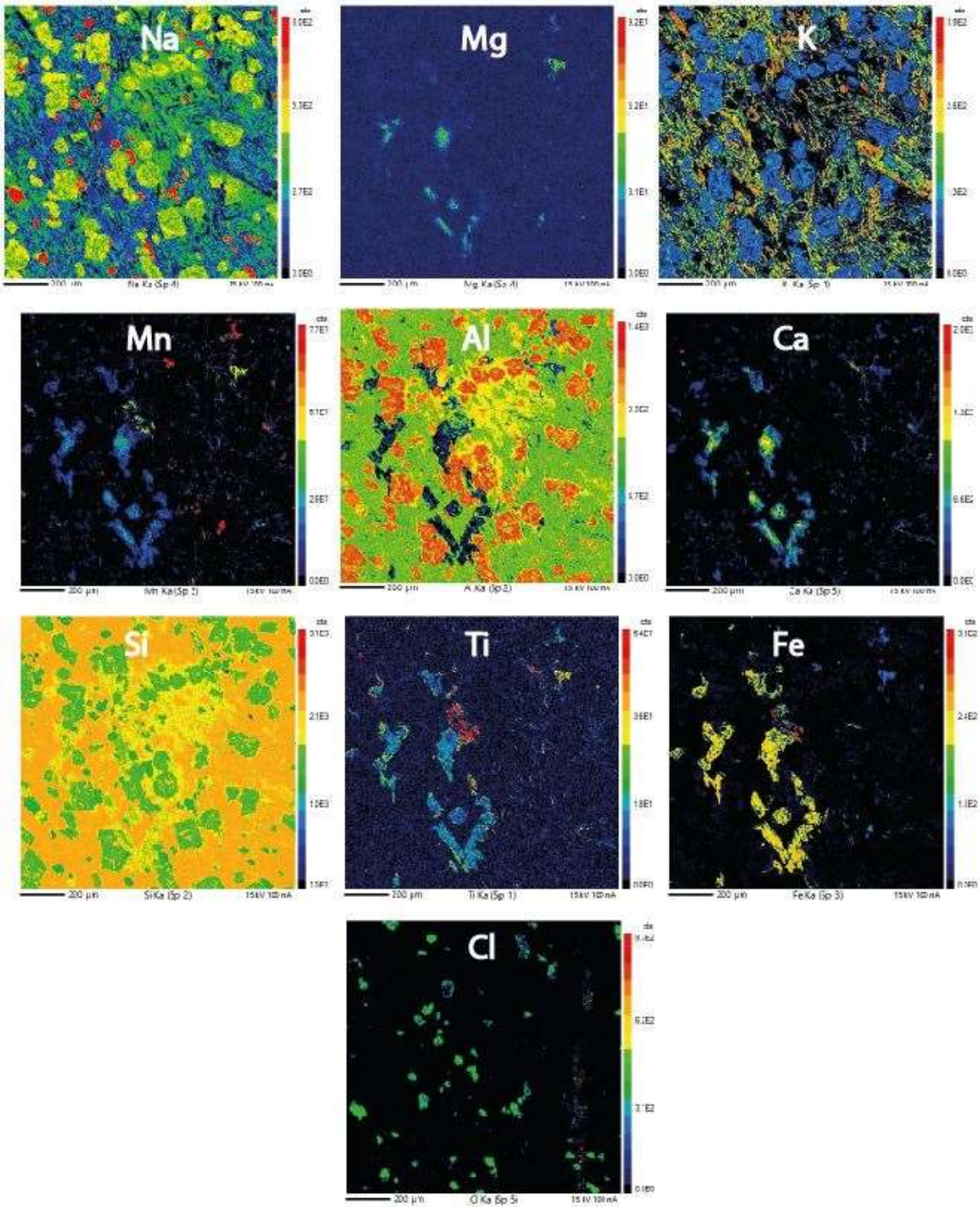

PP701.1

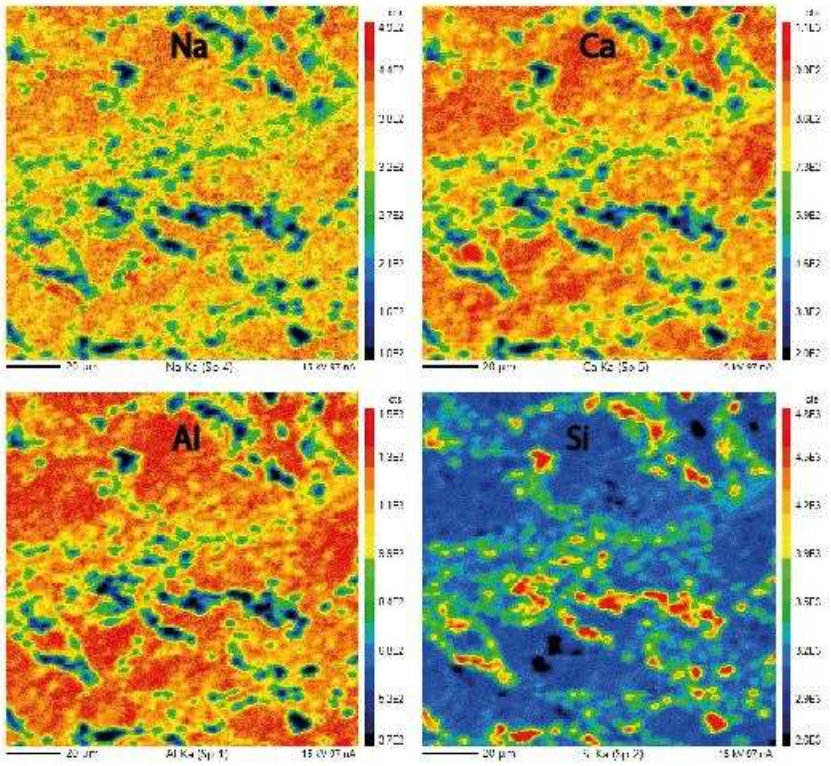

PP701.2

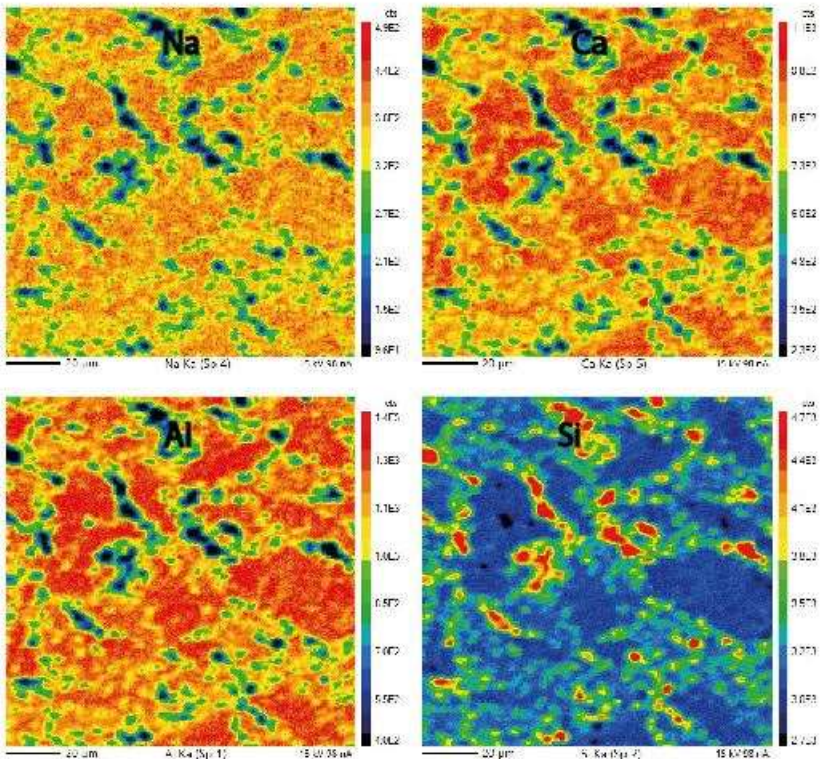

Appendix F.

EBSD data

Deformed samples, R = 2, ϕ_s = 0.58 – 0.59

PP669, γ = 0.5, $\dot{\gamma}$ = 1.0*10^{-4} s^{-1}

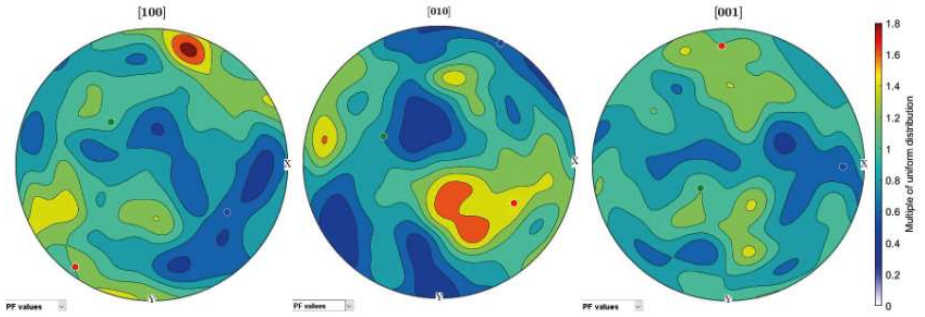

PP676, γ = 1.0, $\dot{\gamma}$ = 1.0*10^{-4} s^{-1}

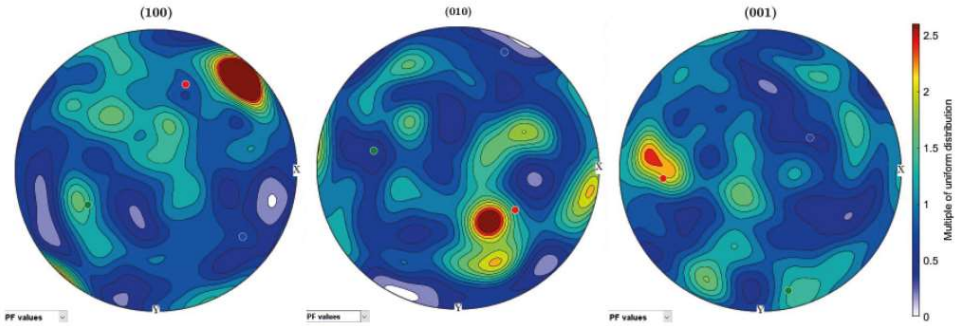

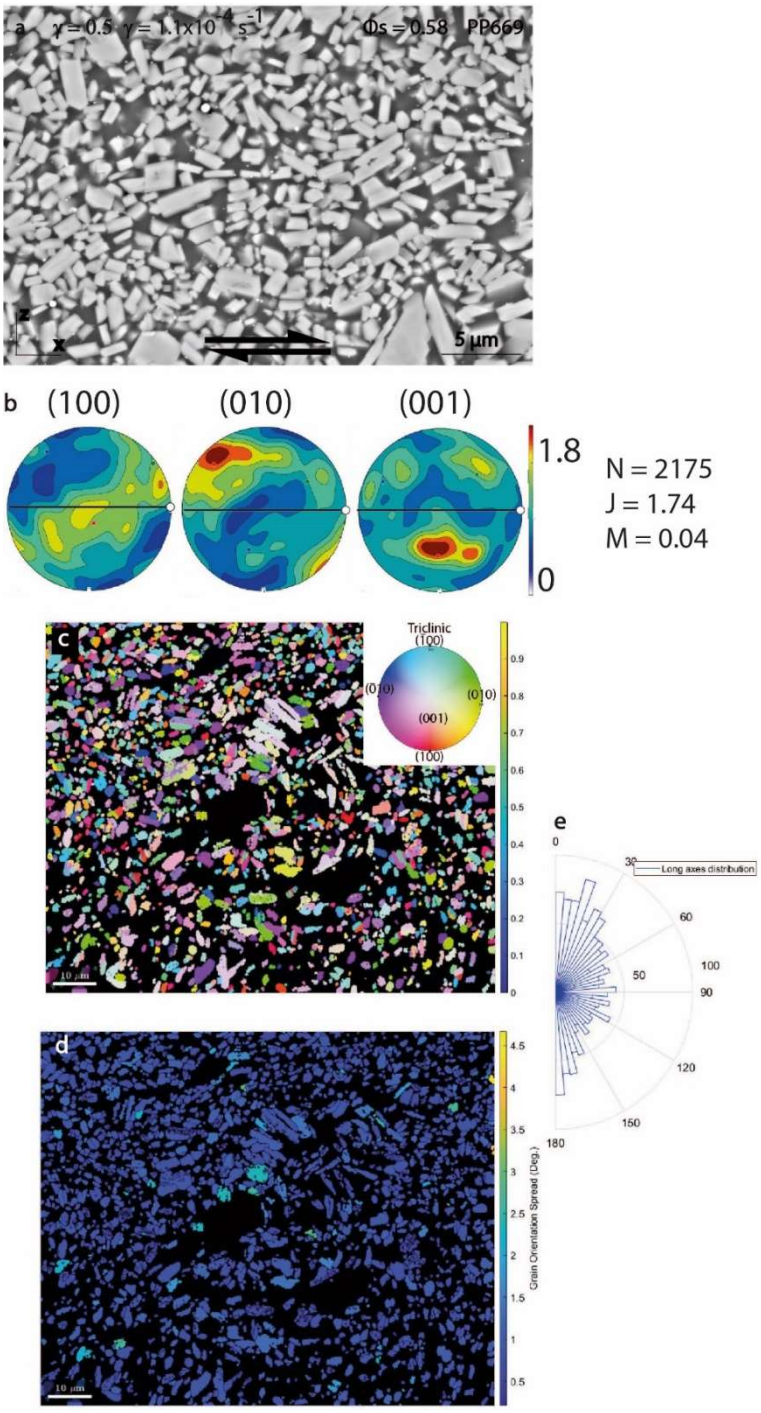

The LPO does not reveal any fabric. No preferred direction of crystals on the IPF map and very few intragranular deformation on the GOS map are observed. The rose diagram of the long axis distribution describes a weak, but clear, SPO at high angle to the shear plane.

PP684, γ = 2.0, $\dot{\gamma}$ = 2.1*10^{-3} s^{-1}

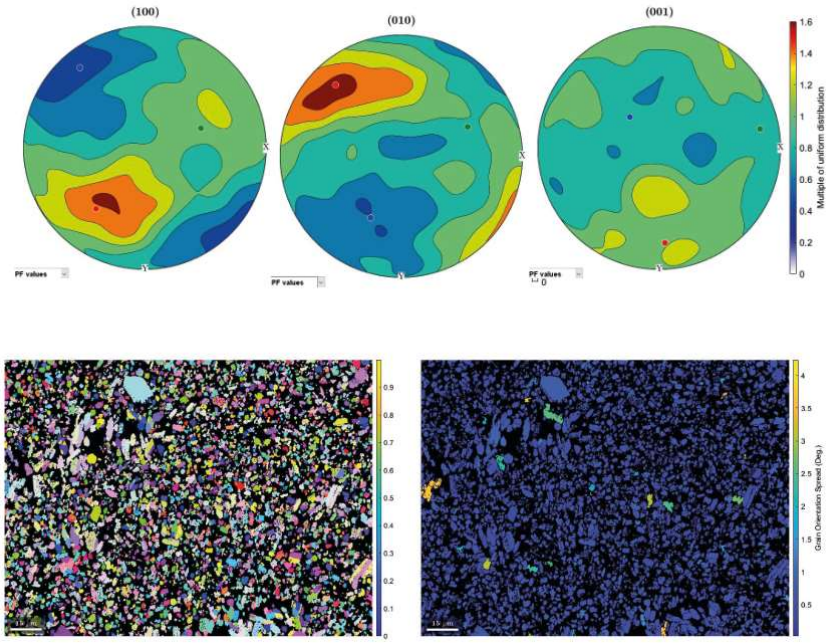

The (010) poles are concentrated close to the line direction, while (100) ones form a girdle parallel to the foliation plane and (001) ones have no preferred orientation. The IPF map does not show any preferential direction of the crystals and the GOS map does not show any intragranular deformation. The orientation rose of the long axes shows a preferred direction parallel to the shear direction.

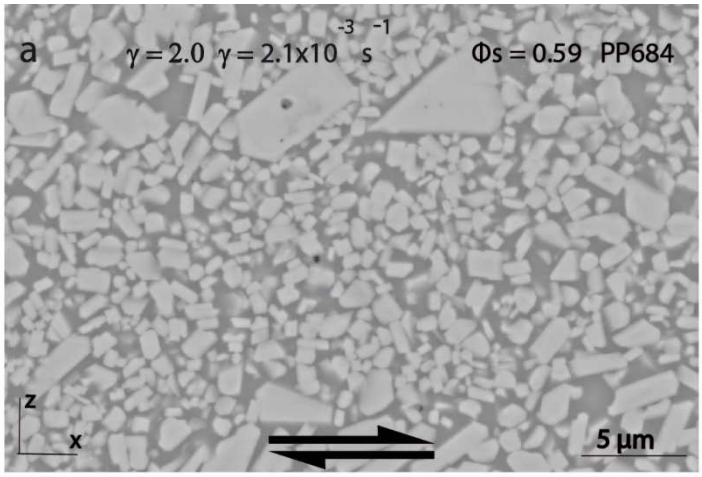
a
γ = 2.0 γ = 2.1x10 -3 -1 s
Φs = 0.59 PP684
z
x
5 µm

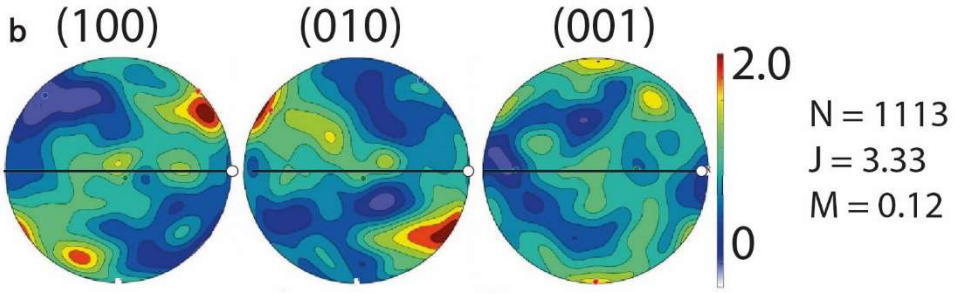
b (100) (010) (001)
2.0
0
N = 1113
J = 3.33
M = 0.12

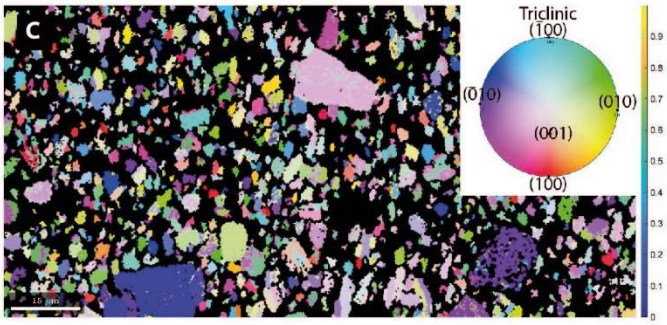
c
Triclinic
(100)
(010)
(010)
(001)
(100)

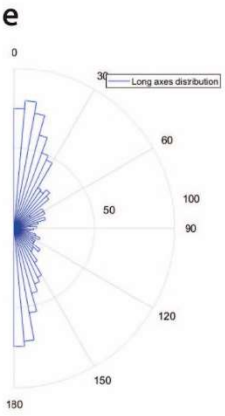
e
Long axes distribution
0
30
60
90
100
120
150
180
50

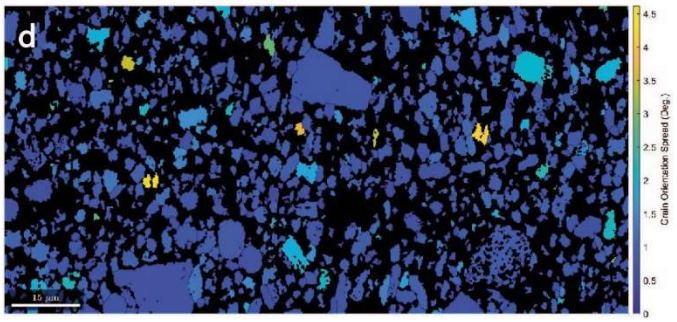
d
Grain Orientation Spread (Deg.)

PP685, γ = 2.3, $\dot{\gamma}$ = 1.0*10^{-4} s^{-1}

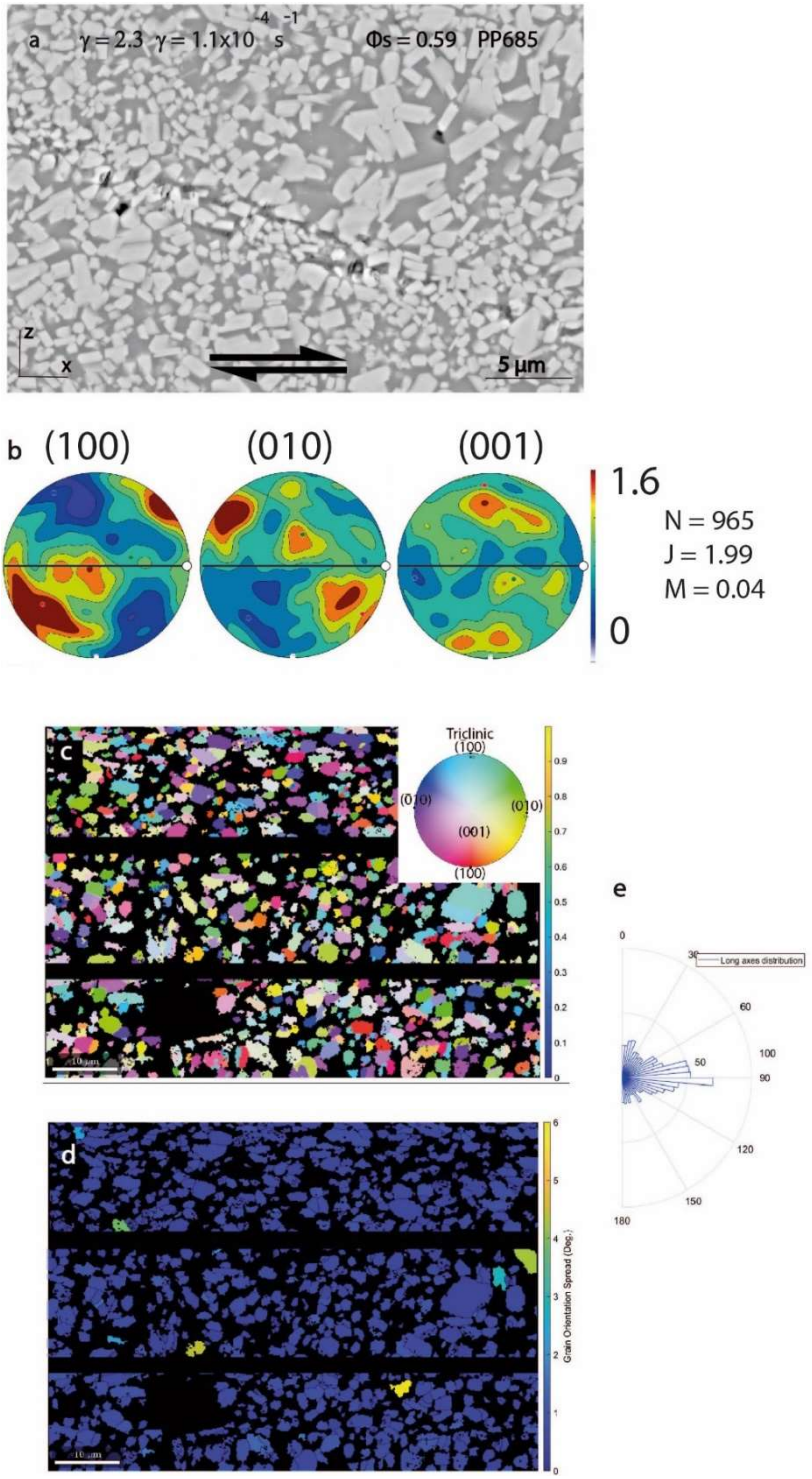

The penetrative fabric has the (100) poles located in a girdle parallel to the foliation plane, the (010) ones concentrated close to the line direction and the (001) poles randomly distributed. As with the previous samples, the IPF map and GOS map do not

show preferential orientation and intergranular deformation of crystals respectively. The rose of the long axis distribution shows a preferential orientation perpendicular to the shear direction.

Deformed samples, R = 2, ϕ_s = 0.73 – 0.76 – 0.95

PP693, γ = 2.0, $\dot{\gamma}$ = 1.0*10^{-4} s^{-1}

The penetrative fabric shows a concentration of the (010) planes close to the foliation direction, while the (100) and (001) planes are located in a girdle parallel to the foliation plane. The crystals follow the foliation direction. The IPF map does not show any preferred direction of the crystals and the GOS map does not indicate any intergranular deformation. The rose of the long axis distribution shows an orientation perpendicular to the shear direction.

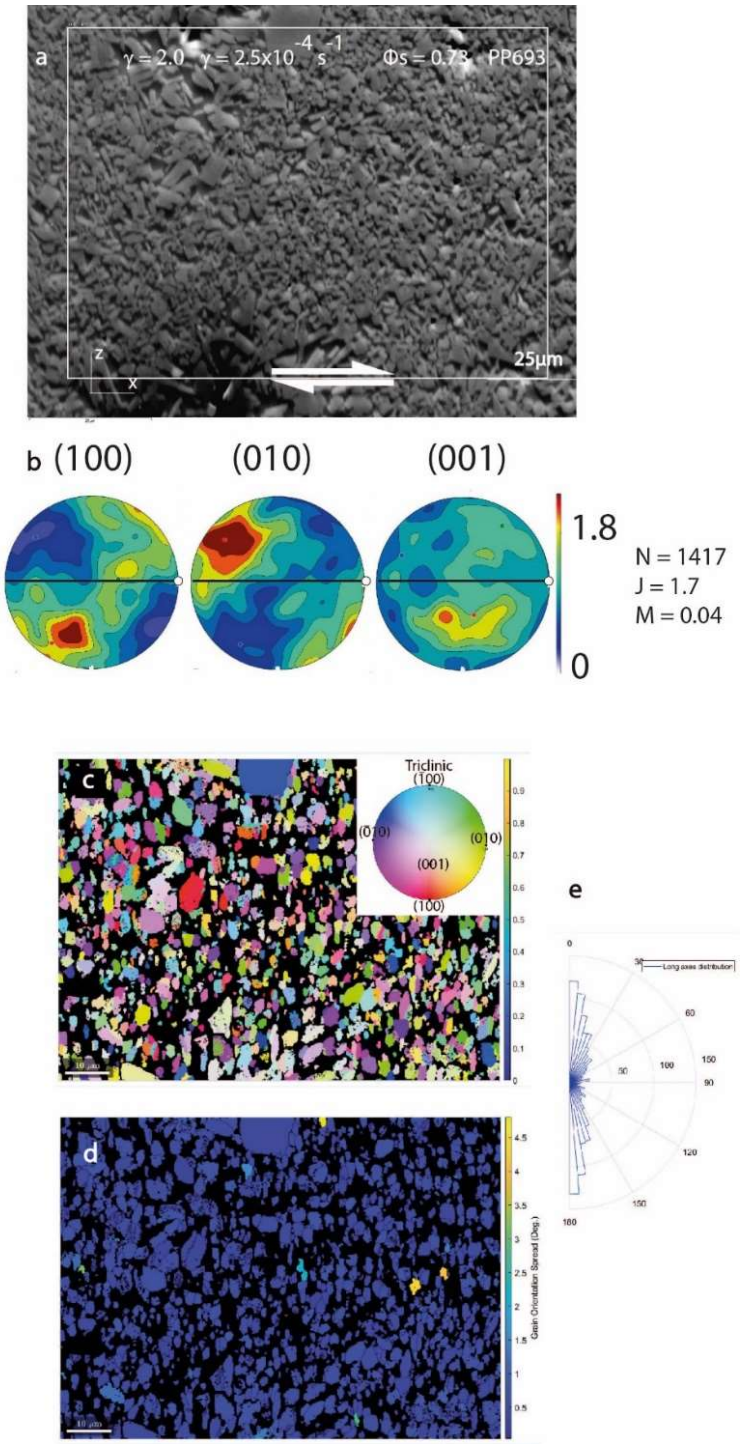
a
γ = 2.0 γ = 2.5x10 -4 s -1 Φs = 0.73 PP693
z
x
25µm
b (100) (010) (001)
1.8
0
N = 1417
J = 1.7
M = 0.04
c
Triclinic
(100)
(010)
(010)
(001)
(100)
d
e

PP698, γ = 5.0, $\dot{\gamma}$ = 1.0*10^{-3} s^{-1}

The (010) planes of the penetrative fabric form a girdle orientated perpendicular to the foliation direction, the (100) planes form a poorly defined girdle that crosses the central area of the pole figure and the (001) planes show no area of concentration. No preferred direction of crystals on the IPF map and no intergranular deformation on the GOS map. The rose of the long axis distribution follows the direction of the foliation.

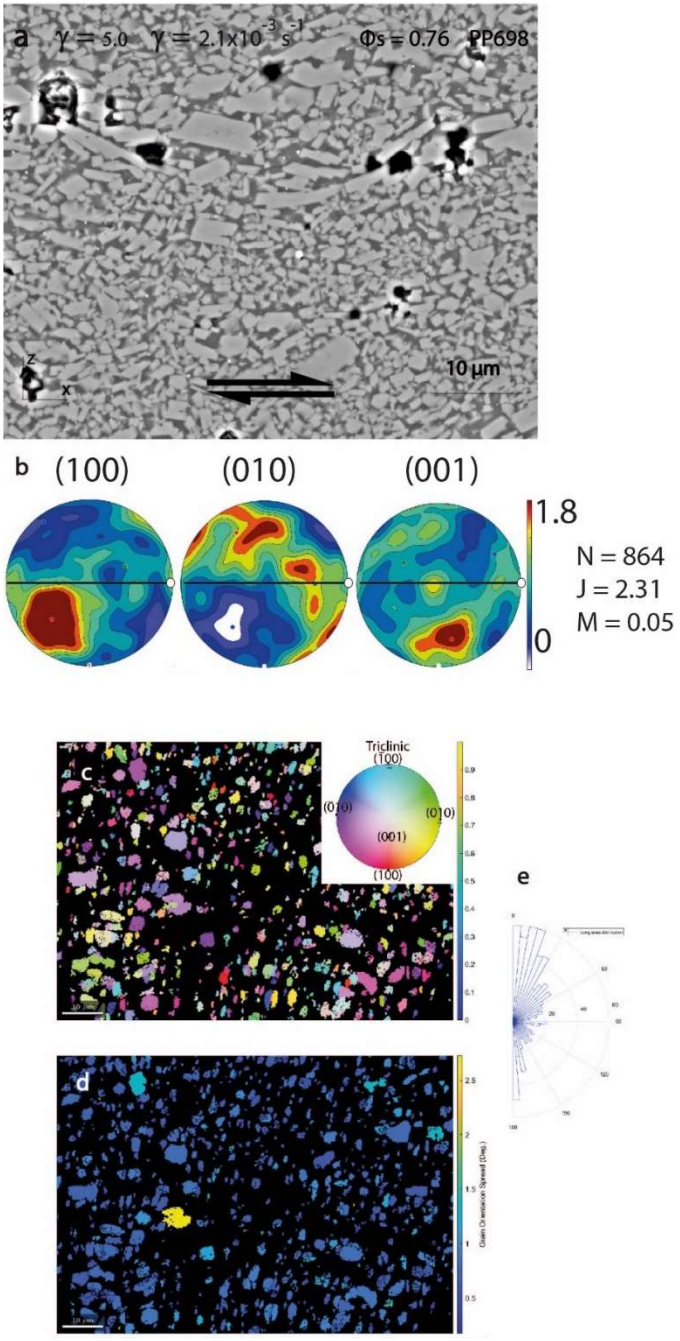

PP699, γ = 5.0, $\dot{\gamma}$ = 2.5*10^{-4} s^{-1}

The penetrative fabric does not show any preferential orientation of the planes. This may be due to the breakage of the sample during the final phase of the deformation experiment, which caused a lower orientation of the crystals in certain areas of the sample. The IPF map and GOS map do not show preferential orientation and intergranular deformation of crystals respectively. The rose of the long axis distribution shows a preferential orientation perpendicular to the shear direction.

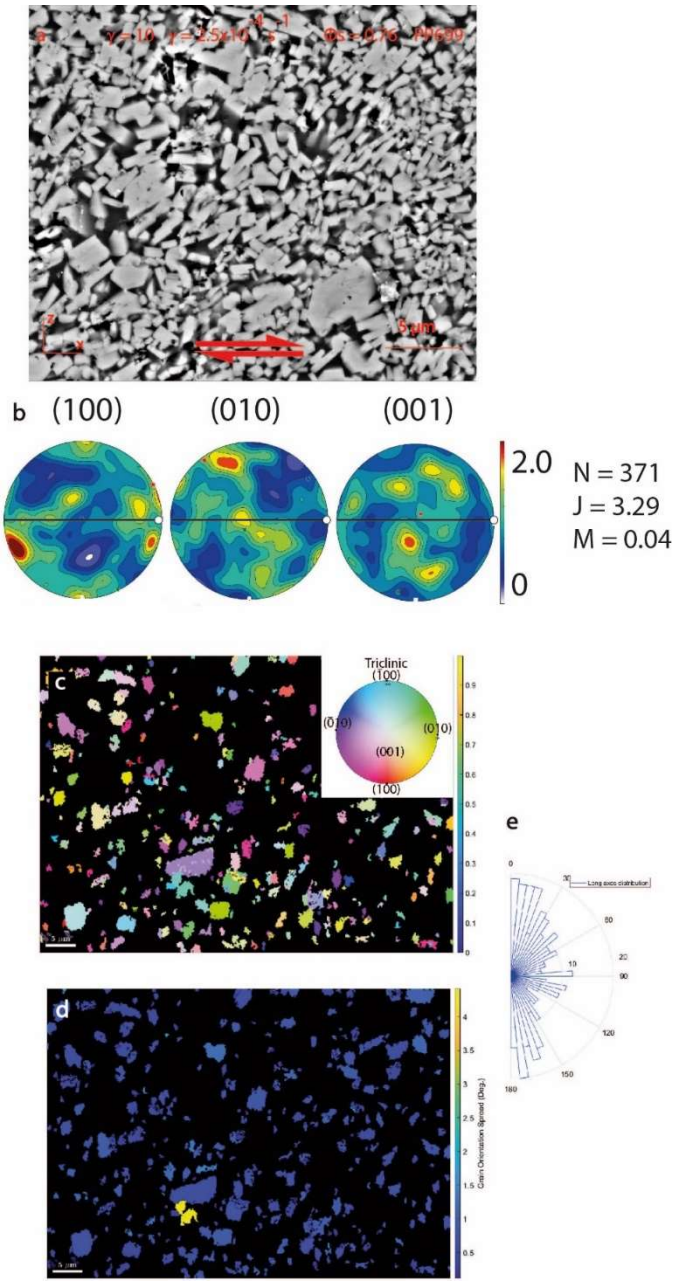

PP701, γ = 1.8, $\dot{\gamma}$ = 5.0*10^{-5} s^{-1}

The plagioclases of the penetrative fabric show a concentration of the (010) planes close to the foliation direction. The (100) planes form a girdle parallel to the foliation plane. The (001) planes have no orientation. The crystals are oriented in the direction of the foliation, as shown in the 2D analyzes. The IPF map does not indicate any preferred directions of the crystals. The GOS map does not indicate any intergranular deformation. The rose of the long axis distributions shows a slight orientation perpendicular to the shearing. The quartz in the penetrative fabric shows no preferential orientation of the (0001) and (11-21) planes. The IPF map does not show any preferred direction.

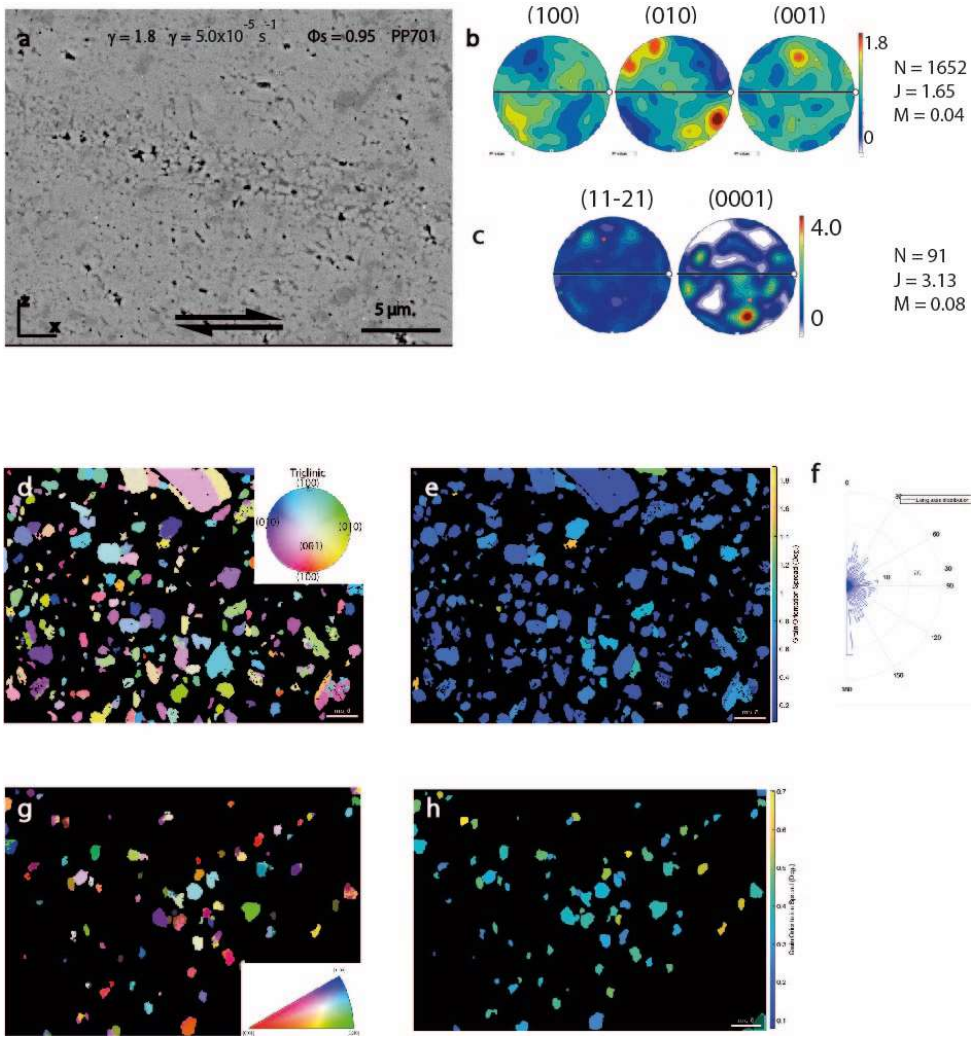

Deformed samples, R = 4

PP043, γ = 1.4, $\dot{\gamma}$ = 1.0*10^{-4} s^{-1}

The penetrative fabric shows a concentration of the (010) plane poles close to the foliation direction, while the (100) and (001) planes are located in a girdle parallel to the foliation plane. In the shear band, the (010) plane poles show an alignment close to the shear direction, while the (100) and (010) planes form a girdle in the foliation plane. The IPF map of the penetrative fabric does not highlight any orientation of the crystals and the GOS map indicates very few intragranular deformation. In contrast, the rose diagram of long axes distribution shows a preferential orientation parallel to the lineation. The IPF map of the shear band highlights a concentration in the shear direction. The GOS map shows no intergranular deformation. Accordingly, the rose diagram indicates a

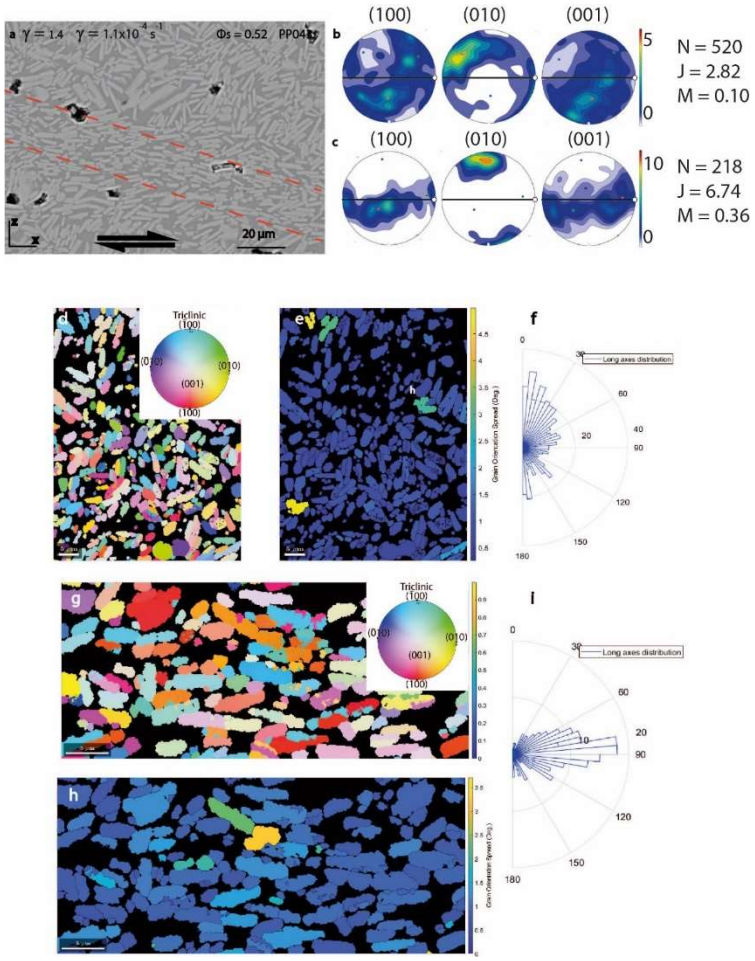

shape preferential orientation parallel to the shear direction.

PP249, γ = 1.4, $\dot{\gamma}$ = 2.1*10^{-3} s^{-1}

The penetrative fabric shows a very weak orientation of the crystals, with a concentration of (010) parallel to the lineation, and (100) and (001) forming a girdle at 90° from the line direction. The shear band shows a strong alignment of (010) close to the pole of the shear plane and an alignment of (100) and (001) as girdles parallel to the shear plane. The IPF map show no preferred crystal orientation in the penetrative fabric and a slight crystal orientation in the shear band, while the GOS map indicate very few

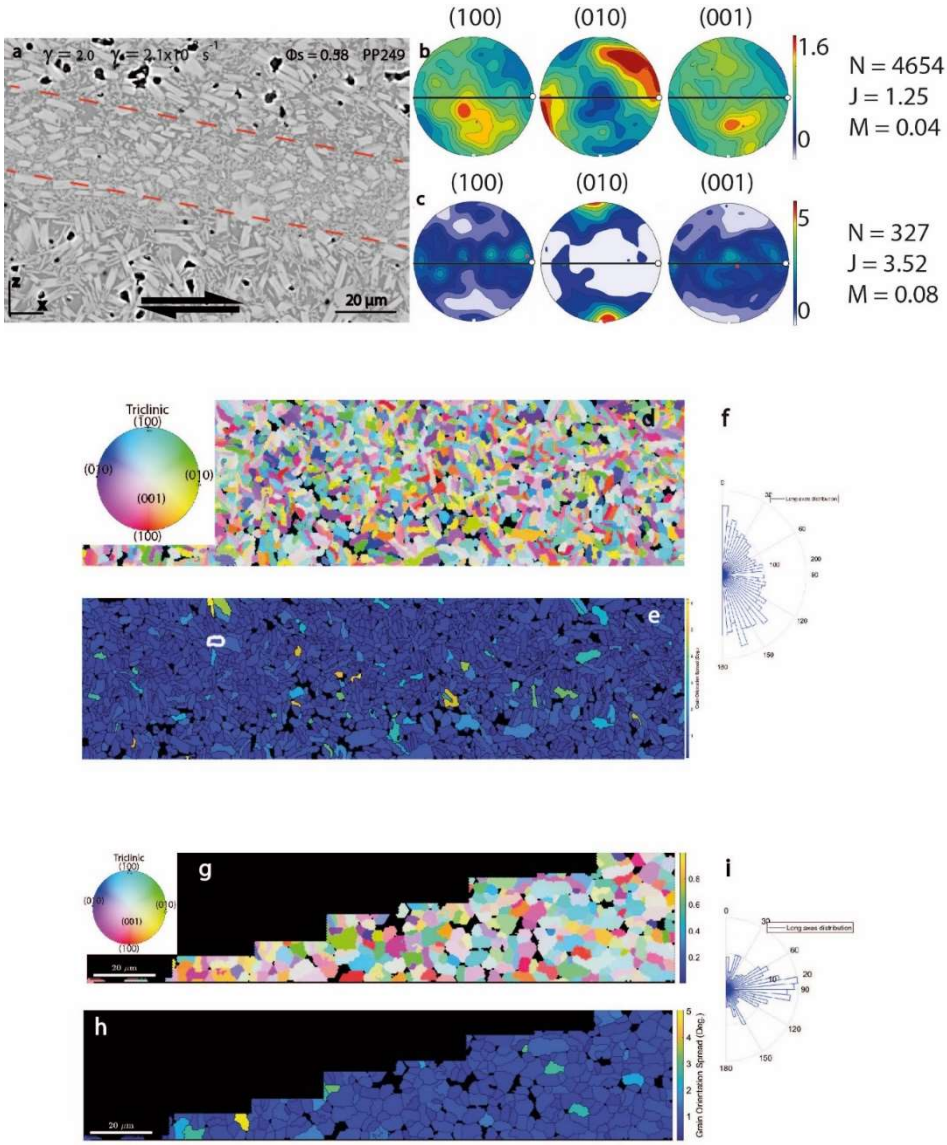

intragranular deformation. The rose diagram does not show any shape preferred orientation for the penetrative fabric, while a strong SPO arises close to parallel to the shear direction.

Natural sample – PG1

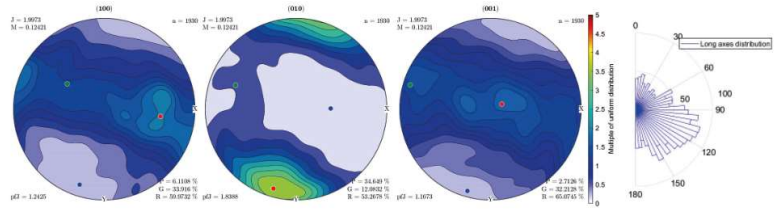

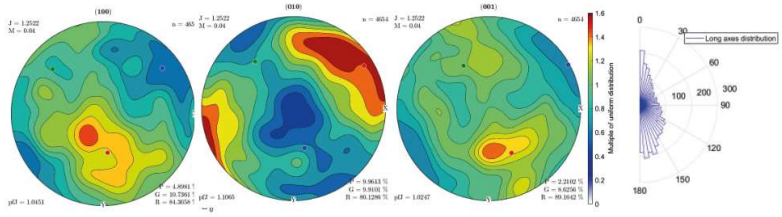

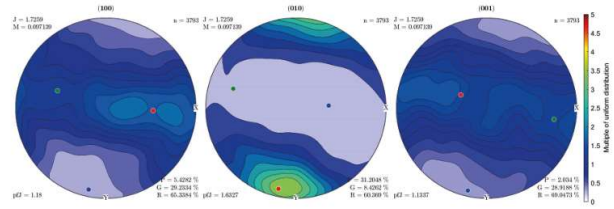

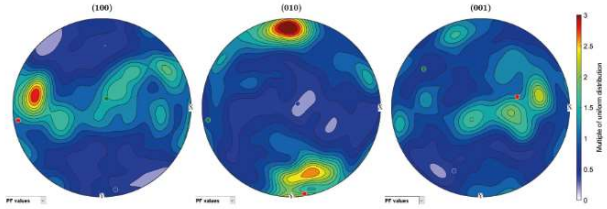

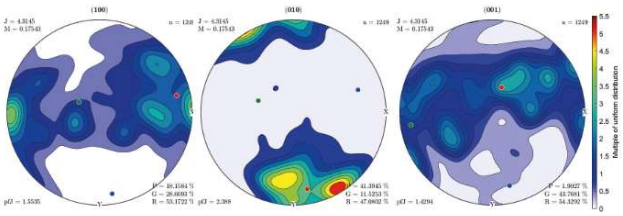

Appendix G.

Paper

Magmatic to solid-state evolution of a shallow emplaced agpaitic tinguaite (the Suc de Sara dyke, Velay volcanic province, France): implications for peralkaline melt segregation and extraction in ascending magmas.

Thomas Pereira [(1)], Laurent Arbaret [(1)], Juan Andújar [(1)], Mickaël Laumonier [(2)], Monica Spagnoli [(1)], Charles Gumiaux [(1)], Gautier Laurent [(1)], Aneta Slodczyk [(1)] and Ida Di Carlo [(1)]

[1] Institut des Sciences de la Terre d'Orléans, UMR 7327 (CNRS-Université Orléans-BRGM), Orléans, France.

[2] Université Clermont Auvergne, CNRS, IRD, OPGC, Laboratoire Magmas et Volcans, F-63000 Clermont-Ferrand, France.

Correspondence: Thomas Pereira (thomas.pereira@univ-lorraine.fr); Laurent Arbaret (laurent.arbaret@univ-orleans.fr)

Abstract

Since last decades the mush model have been generalized to the complete Trans-Crustal Magmatic System in which differentiation would be driven by segregation and extraction of trapped melts from crystal-rich mushes. Melt extraction Processes involved are porous flow and strain localization, the latter being regarded as the main process acting during transfer

through dykes and necks along which high differential stresses are acting on. We combine structural measurements together with petrological analyses and textural observations to constrain the model of emplacement and finally emphasize how shear deformation and strain localization structures promoted the residual melt segregation that occurred in a shallow silica-undersaturated peralkaline intrusion (Suc de Sara, Velay volcanic province, French Massif Central).

In this study, we demonstrate that segregation and subsequent extraction of the CO_2-rich residual melt occurred during magma ascent and final emplacement of the Suc de Sara tinguaite. Contrasting features of shear deformation between the margins that exhibited different permeabilities highlight that melt segregation started by compaction as a loose packing of emerging microlites and continued with melt filling of an anastomosed C/C' bands network developed in the crystal-rich mush subjected to high shear strain. Subsequent melt extraction throughout the country rock was controlled by the permeability of the hanging wall. Along the Western hanging wall of the intrusion, extraction of the residual melt was prevented by the 15 cm thick chilled margin. In contrast, segregated melt circulated through the highly porous and permeable Eastern margin, causing the fenitization of the country rock.

Keywords: strain localization, melt segregation and extraction, phonolite, tinguaite, Velay.

1. Introduction

Since few decades there is a paradigm shift in progress: instead of mostly liquid, magma bodies are now inferred to be bodies dominated by crystal-rich mush, a mix of crystals, and silicate liquid (Ward et al., 2014; Delph et al., 2017). This model of a mush zone with limited pockets of mobile magmas (Bachmann and Bergantz, 2008) has been generalized as a continuum over

the entire crust from the deep ductile hot crust to the shallower chambers opened to volcanic systems and it is called the Trans-Crustal Magmatic System (TCMS, Cashman et al., 2017; Allan et al., 2013; Holness, 2018). In this model, the fundamental process of differentiation is driven by segregation and extraction of trapped melts from highly viscous crystal-rich mushes (Dufek and Bachmann, 2010; Burgisser and Bergantz, 2011). Melt transfer architecture arises from compaction and shear: (1) Melt transfer by porous flow, where crystal network permeability is the controlling parameter (Dufek and Bachmann, 2010), and (2) melt channel formation by shear localization (Katz et al., 2006). Strain localization in crystal-rich zones is commonly observed in highly dynamic magmatic system such as convective cells in magma chambers and hanging walls of dykes and necks along which high differential stresses are acting on (Smith, 1997; Paterson, 1998). While it is nearly impossible to obtain examples of a "living mush" in deeply emplaced pluton, sub volcanic systems may preserve various stages of deformed mushes that were fossilized during rapid cooling (Geshi, 2001).

We combine structural measurements at the regional scale and along a complete cross-section of the silica-undersaturated Suc de Sara Intrusion (6.5 Ma; Mergoil and Boivin, 1993), together with petrological analyses and textural observations. Thus, we better constrain the model of emplacement and finally emphasize how shear deformation and strain localization structures promoted the residual melt segregation that occurred in this differentiated intrusion during its shallow emplacement (< 1.5 kbars) in the Boutières graben (Mergoil and Boivin, 1993). We emphasize that melt segregation began by forming planar distribution domains in a loose stack of emerging microlites. During cooling, increasing crystal fraction led to the development of localised melt-rich shear bands. Finally, we point out the control of the contrasted permeability of the hanging wall on melt extraction throughout the country rock.

2. Geological settings

The Velay volcanic province is located in the Southeast of the French Massif Central (Fig. 1a). This region is characterized by a series of N140E directed tertiary horsts and grabens affecting the thinned granitic and migmatitic Variscan basement (Mergoil, 1968; Couzinié et al., 2014; Fig. 1b) covered by alkaline lavas from monogenetic volcanoes over the last 15 Ma.

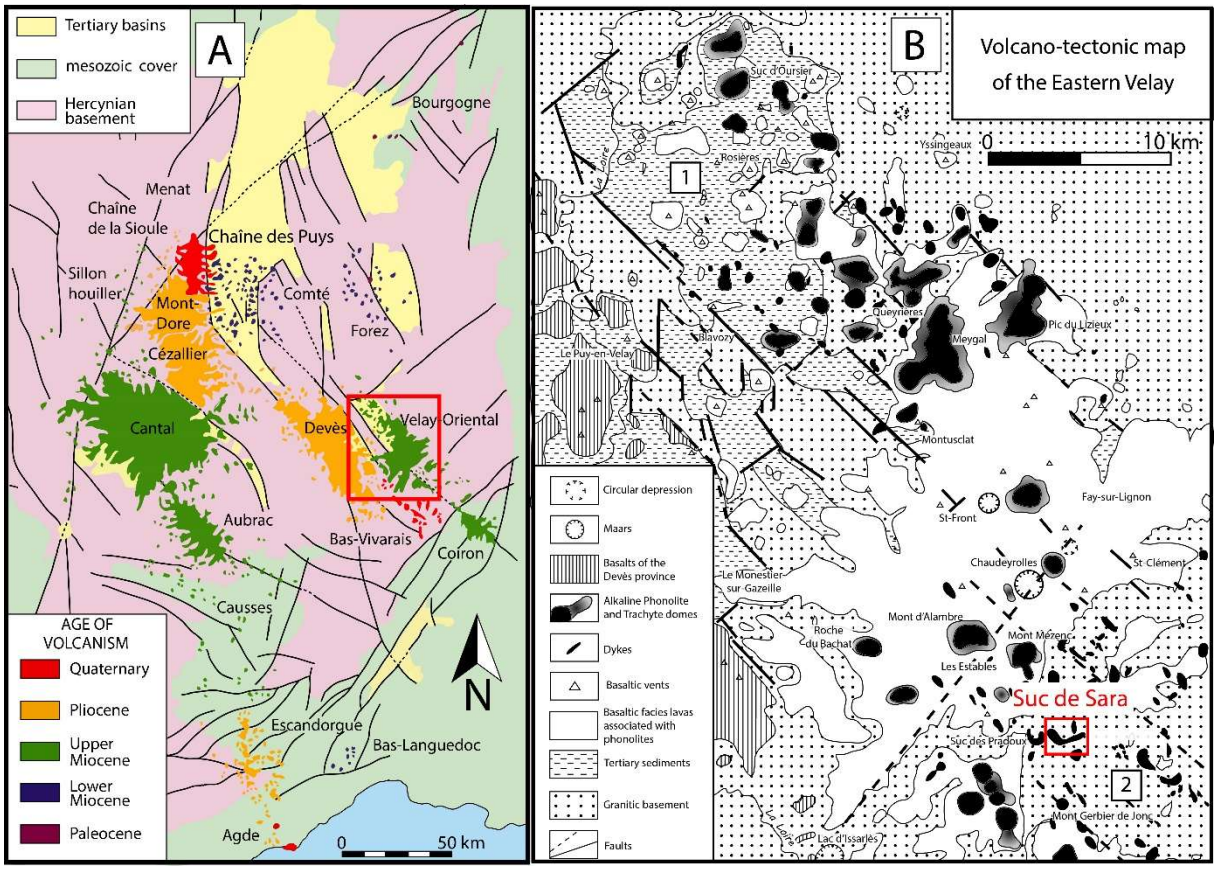

Figure 2. a – Geographic positioning of the Velay volcanic province in regard to the different volcanic fields of the French Massif Central (modified from Boivin et al., 2004). The red inset represents the zoom shown in b. **b –** Volcano-tectonic map of the Eastern Velay (modified from Jung, 1971). The red inset corresponds to Fig. 3a. (1) = Emblavès graben; (2) Boutières graben.

2.1 The Velay basement

The Velay basement is composed of a set of granites and migmatites emplaced during the Westphalian (Carboniferous sub-stage), after the anatexis of a metamorphic series including prior monzogranitic, paragneiss, orthogneiss, amphibolite and basic massifs (Dupraz and Didier, 1988; Couziné et al., 2014; Barbey et al., 2015). The formation of the Velay migmatitic complex was established in the Upper Carboniferous, at the end of the collision episode that generated the Variscan Chain, which was built during a period from the Devonian to the Carboniferous (between 400 and 300 Ma). Beneath the Velay, the crust is strongly thinned, with a thickness of about 25 km (Mergoil and Boivin, 1993 and references therein) lying above a very heterogeneous lherzolitic mantle (Berger and Vannier, 1984). Tectonically, the Velay basement is affected by large NW-SE faults associated with NE-SW faults. Particularly in the Eastern Velay, the compartmentalization of the basement into horsts and grabens is controlled by two networks of regional faults almost oriented N080E-N090E and N140E respectively (Fig. 1b; Blès et al., 1989). For the period corresponding to the volcanic activity of the Velay province, the E-W Oligocene extension continued during most of the Miocene with the activation of this pair of normal faults network (Bout, 1966; Mergoil and Boivin, 1993). At the end of the Miocene, the period for the Suc de Sara formation, a NW-SE compression caused the reactivation of the preexisting fault network with mainly horizontal displacement. Finally, in the Pliocene, basaltic lava flows of the Devès are synchronous of the Velay basement extension marked by normal faults.

2.2 The Velay volcanism

From the late Oligocene to the Holocene, the Massif Central experienced two major magmatic episodes (Maury and Varet, 1980; Merle and Michon, 2001). The first episode ranging from 24 to 12 Ma, was essentially expressed in the North of the French Massif Central induced and associated with a strong crustal thinning (25% maximum). The second episode ranging from

14 Ma to less than 10,000 years was characterized by the emplacement of large magmatic provinces (Eastern Velay, Devès, Cantal…) in the South. This major volcanic phase is contemporaneous with a general uplift with two paroxysm peaks from 9 to 6 Ma and from 3.5 to 0.5 Ma. After Malcles et al (2020), the uplift occurred mainly in the Pliocene-Quaternary (last 4 Ma).

The volcanic massif of Velay includes three volcanic areas: the Devès, the Meygal and the Mézenc where the Suc de Sara is located (Fig. 1a). In the Eastern Velay (Fig. 1b), the volcanic formations of the Mézenc volcanic field can be separated into three distinctive episodes that are visible on the wall of the graben (Cirque des Boutières valley, Jung, 1971; Mergoil and Boivin, 1993): (1) a basal level composed of basalt flows and strombolian scoria cones; (2) above, stratified pipernoid tuffo-laves covered by several layers of more or less differentiated basalts; (3) trachy-andesite lava flows ending the sequence. This volcanism began around 13.5 Ma during a period of tectonic extension (Fig. 2a) essentially by extrusions of phonolites (Emblavès sector to the NW) preceding the emission of subalkaline trachytes with a paroxysm around 12 to 10 Ma. In the SE sector (Boutières graben), eruptions of differentiated lavas (phonolites, trachytes) occurred between 8.5 and 5.7 Ma (Mergoil and Boivin, 1993). The youngest eruptions (< 5 Ma) were exclusively basaltic and confined to the Western Velay (Devès and Le Puy basin, Fig. 1, 2a).

The Velay volcanic province has the particularity of being composed of a continuous series from basalts to differentiated SiO_2-oversaturated and undersaturated products (Mergoil and Boivin, 1993). While experimental work demonstrates that phonolitic liquids can be obtained directly by low melting rate of peridotites (Laporte et al., 2014), differentiation to saturated, oversaturated or undersaturated terms is generally due to crustal contamination or mineral fractionation from a basaltic or basanitic parent liquid such as alkali feldspar (Jeffery and Gertisser, 2018) plagioclase and pyroxene (Ablay et al., 1998) or amphibole (Legendre et al.,

2005). In the case of the differentiated lavas of the Velay series, the differentiation is explained by a strong fractionation of alkali feldspars, the crustal contamination remaining insignificant (Dautria et al., 2004).

For several years, miaskitic and agpaitic parageneses have been put forward to define peralkaline rocks. The distinction between the two was then based on the $\frac{Na}{Al-K}$ ratio and the crystallization sequence of the various mineral phases (e.g. Batard, 1974; Hodges, 1991; Mergoil and Boivin, 1993). A recent review proposes new definitions for the terms miaskitic and agpaitic: in some cases, the extreme enrichment of alkalis, halogens (F, Cl, Br, and I), high field strength elements (HFSEs, such as Zr, Hf, Nb, Ta, and U), and rare earth elements (REEs) during the differentiation of peralkaline magmas may result in the precipitation of a wealth of otherwise rare minerals. The presence of these diverse and structurally complex HFSEs defines the so-called agpaitic rocks as opposed to miaskitic rocks, in which HFSEs are hosted by zircon and titanite, as is typical of most other igneous rocks (Marks and Markl, 2017). The differentiated products of the Velay are represented by trachytes and phonolites with alkalinity $\left(\frac{Na}{Al-K}\right)$ ranging from 0.8 to 1.3 (Batard, 1974; Fig. 2b, c; Macdonald et al., 2021 for another recent review). Batard (1974) showed that phonolites are derived from a normal crystallization sequence at depth (magnetite, ilmenite, apatite, zircon, sphene, pyroxene, plagioclase, amphibole, alkali feldspar, feldspathoid) that was surimposed by reverse paragenesis (feldspathoid, alkali feldspar, Zr/Ti silicates, alkali pyroxene) developed at lower depth. The role of CO_2 transfers during the development of these phonolites has been proposed by Batard and al. (1977). Mergoil (1968) has pointed out an intense transfer of CO_2-rich fluids that affected the phonolite of the Suc de Sara along its Eastern margin including the surrounding metamorphic basement during its final emplacement. The possible origin of theses volatile-rich melts is discussed by Martin et al. (2017).

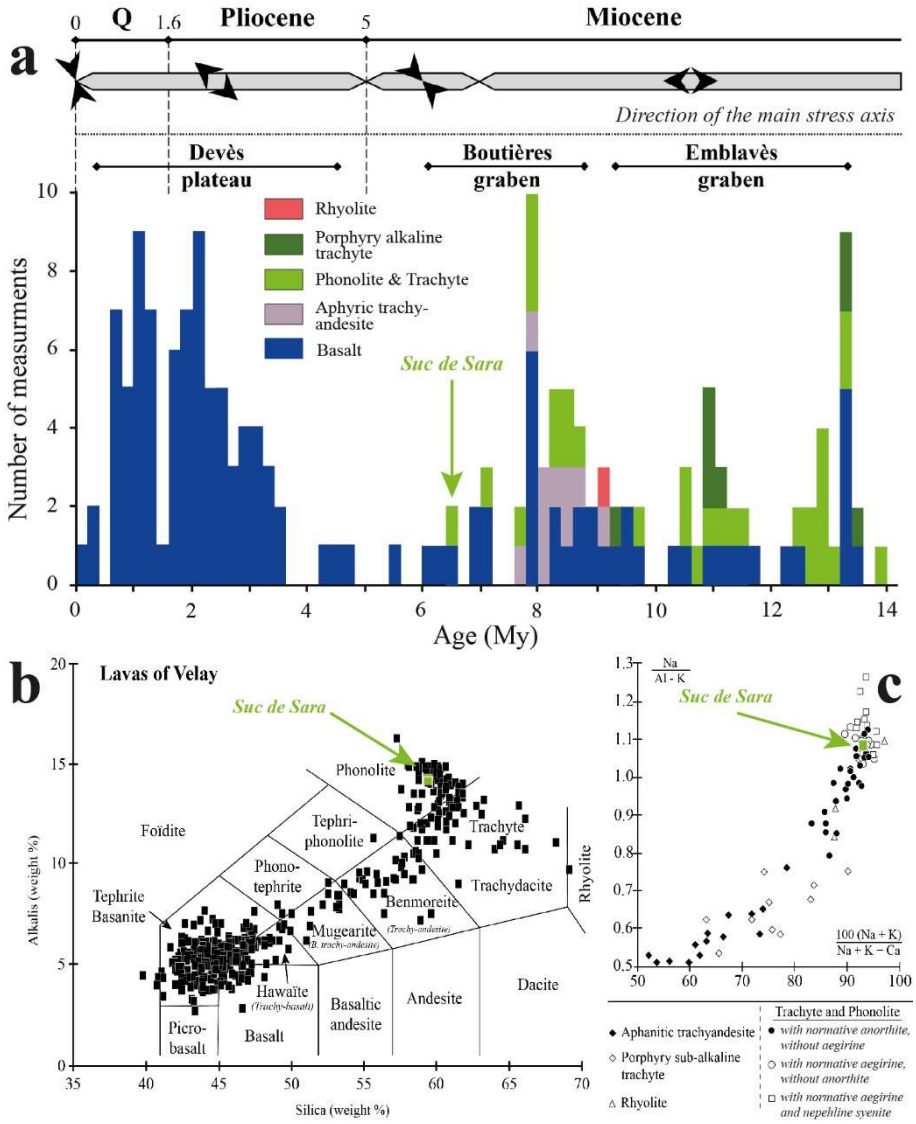

Figure 2. a – Histogram summarizing the number of geochronological ages of volcanic edifices in the Velay massif according to their composition (modified after Mergoil and Boivin, 1993) and direction of the main constraints represented by the black arrows (modified after Blès et al., 1989). The 6.5 Ma old Suc de Sara represents the youngest phonolitic edifice. **b –** TAS diagram (Le Bas et al., 1986) of the Velay alkaline series (modified after Mergoil and Boivin, 1993). **c –** Peralkalinity diagram for differentiated products from the Velay province (modified after Mergoil and Boivin, 1993).

2.3 The Suc de Sara intrusion

The Suc de Sara intrusion has been the subject of studies since the 1970s (Mergoil, 1968). This vertical arched structure is located in the "Cirque des Boutières" and culminates at 1,521 meters (Saint Martin, 2009; Fig. 1, 3a, b). It is interpreted so far as a ring dyke structure shallow emplaced in a late Miocene graben free of sedimentation affecting a variscan basement composed of gneiss and metatexite (Mergoil and Boivin, 1993; and references therein). This intrusion is a phonolite with a thickness varying between 50 and 390 m (Fig. 3a). It is defined by $\frac{Na+K}{Al} > 1$ (Mergoil, 1968). According to Mergoil (1968), its alkaline chemical composition grants a mineralogy enriched in sodium and potassium with the presence of sodic pyroxenes (aegirine-augite), aenigmatite and alkali feldspars (sanidine, orthoclase or microcline). Moreover, the rock contains a large proportion of feldspathoids (nepheline and sodalite), testifying to its undersaturation in SiO_2 (Mergoil, 1968).

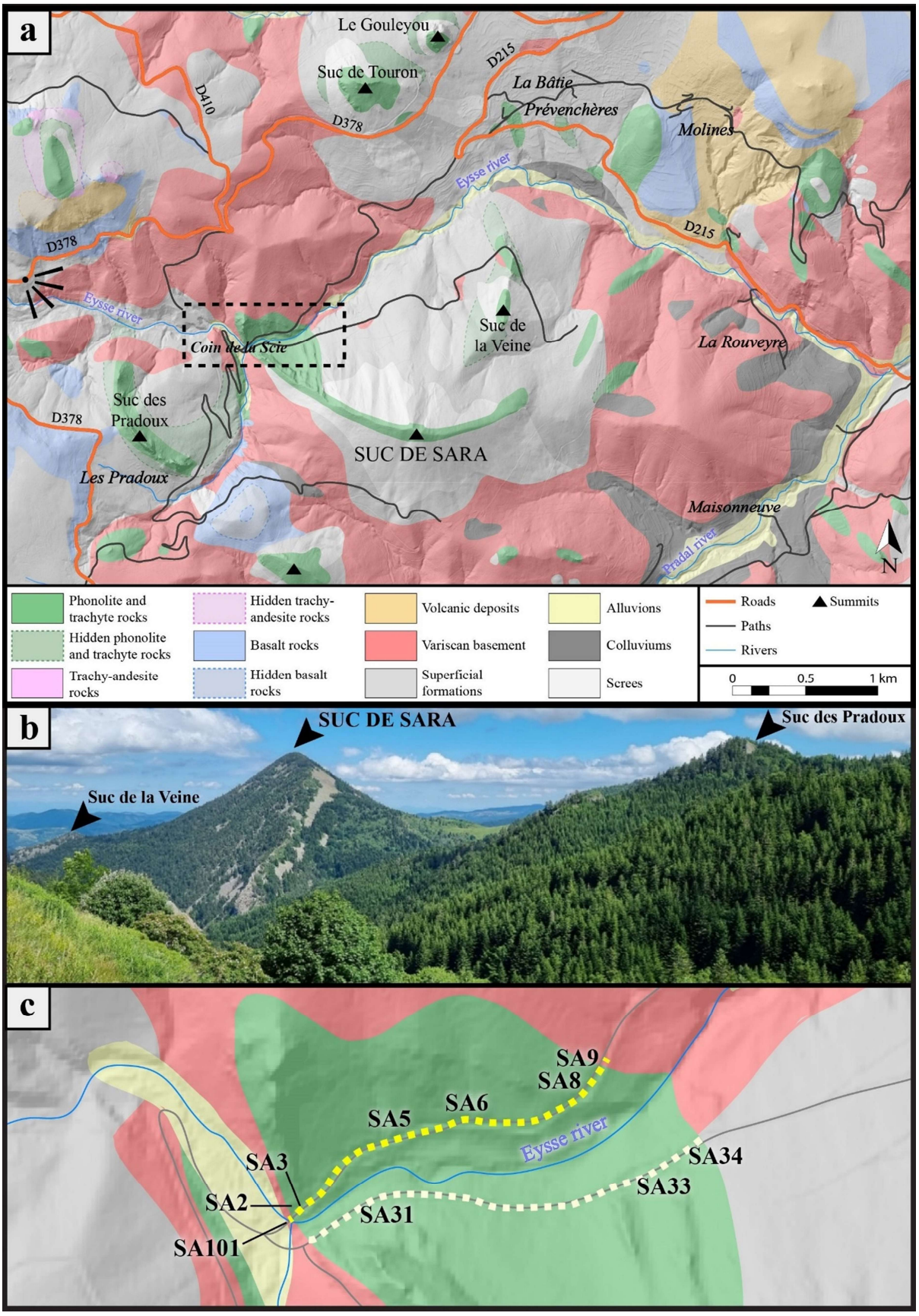
a
Le Gouleyou
Suc de Touron
D215
La Bâtie
Prévenchères
Molines
D410
D378
Eysse river
D215
D378
Eysse river
Coin de la Scie
Suc de
la Veine
La Rouveyre
Suc des
Pradoux
D378
SUC DE SARA
Les Pradoux
Maisonneuve
Pradal river
N
Phonolite and trachyte rocks
Hidden phonolite and trachyte rocks
Trachy-andesite rocks
Hidden trachy-andesite rocks
Basalt rocks
Hidden basalt rocks
Volcanic deposits
Variscan basement
Superficial formations
Alluviums
Colluviums
Screes
Roads
Summits
Paths
Rivers
0
0.5
1 km
b
SUC DE SARA
Suc des Pradoux
Suc de la Veine
c
SA9
SA8
SA6
SA5
Eysse river
SA3
SA34
SA2
SA33
SA31
SA101

Figure 3. a – Simplified geological map of the Suc de Sara area ("Cirque des Boutières" graben, see location in Fig. 1b. Modified from BRGM (2011) 1:50,000 geological map no. 816, Le Monastier-sur-Gazeille, Define et al., 2011). Digital terrain model generated from Data supplied by Institut Géographique National, https://geoservices.ign.fr/rgealti. The pictogram corresponds to the panoramic view of Fig. 3b. The red insert corresponds to Fig. 3c. **b** – Panoramic view of the ‘‘Cirque des Boutières’’ with three visible summits: the Suc de la Veine; the Suc de Sara and the Suc des Pradoux. **c** – Close view from Fig. 3a on the Western part of the intrusion which represents the two sections on either side of the river Eysse where we carried out our observations and sampling. Each sample code name is listed in Table 1. The yellow dotted line corresponds to the section presented in Fig. 7.

3. Analytical methods

3.1 Linear analysis with Hough transform

We analyzed the regional-scale spatial distribution and determined the best alignment directions of the 505 monogenetic vents identified in the area of 1,800 km² of the Eastern Velay (Mergoil and Boivin, 1993). We used three 1:50,000 geological maps: Le Puy (number, 791; Girod et al., 1979), Le Monastier-sur-Gazeille (number 816; Define et al., 2011) and Burzet (number 840, Bambier et al., 1985). We applied the Hough Transform method which is a pattern recognition technique used in digital image processing. The principle of this method is based on the detection of potential alignments on an image, despite imperfections such as noise (Hough, 1959). The technique consists in placing objects of interest in a Cartesian space (x, y) and transforming them into curves in the Hough space according to a distance and an angle (ρ, θ). The formula linking both is as follows:

$$(D) : \rho = x \cdot \cos(\theta) + y \cdot \sin(\theta) \quad (1)$$

In the Hough space, cartesian equation of a line (D) is expressed by polar coordinates with ρ the distance of the line from the origin of the reference frame and θ (between 0° and 360°) the angle that the perpendicular to the line makes with the x axis. Each point identified in the Cartesian space will allow a projection in the plane of the polar coordinates of all the lines that pass through this point (Hart and Duda, 1972). An example of calculation performed with the software coded in Python language is presented in Fig. A1.

3.2 Structural and textural cross-section

An East-West detailed cross-section along the Eysse valley, including textural observations, structural measurements and sampling, was made along the Northwestern thicker part of the Sara dyke till the surrounding metatexites (Fig. 3c). Structural measurements included fractures population analyses in the basement, and foliation, vein and mineral banding measurements in the dyke. Ten phonolite samples were selected as representative of the different facies observed in the field (Fig. 3c). The criteria were local enrichment in alkali feldspar and nepheline phenocrysts and the transition from medium-grained phaneritic to aphanitic, porphyritic textures, the latter locally being cut by aegirine veins and localized shear bands.

3.3 Textural and chemical analyses

The samples selected for petrography, scanning electron microscope (SEM) textural characterization, mineral chemistry and bulk rock composition are listed in Table 1. Samples selected for microstructural and petrographic analyses were cut following a section parallel to

the mineral lineation and perpendicular to the foliation ([x,z] structural plane with x the mineral lineation and z the normal of the foliation plane). The resulting thin sections were first observed under a polarizing optical microscope in order to characterize all the different textures and the associated mineral paragenesis recognized in the Sara intrusion. Subsequent analyses included backscattered high-resolution image acquisition using a scanning electron microscope (Merlin Compact Zeiss hosted in ISTO) with an acceleration voltage of 15 kV and a working distance of 10 mm. In addition, semi-quantitative chemical mapping was performed by using a Bruker QUANTAX – XFlash6 Wavelength Dispersive Spectroscopy (WDS) available on the SEM. Quantitative chemical mineral analyses and mapping were performed using two electron microprobes (EPMA; Cameca SX Five and JEOL IhP200F, both equipped by 5 WDS spectrometers and hosted in ISTO) with an acceleration voltage of 15 kV and a beam current of 10 nA. Counting time for each element was 10 sec/peak for punctual analysis; a dwell time of 100 ms was used for chemical maps. The detection limits are of the order of 900 ppm for Si and K, of 400 ppm for Al, Na and Ca and of less than 2,000 ppm for Fe and Ti.

Coordinates			Analysis			
Sample SA-	X	Y	Petrography	SEM textural analysis	EPMA phase analysis	Bulk rock chemistry
2	44.877860	4.207730	•			
3	44.877860	4.207730	•	•	•	•
5	44.878530	4.209210	•			
6	44.878710	4.210400	•	•	•	•
8	44.878770	4.211650	•			
9	44.878920	4.211970	•	•	•	
31	45.079335	4.093647				•
33	45.079335	4.093647				•
34	44.878432	4.213421				•

101	44.877860	4.207730	•

Table 1. List of samples used in this study with their geographical coordinates and the type of analysis performed on each sample.

3.4 Whole-rock analysis

Major elements were analyzed by ICP-OES at Laboratoire Magmas et Volcans (LMV, Clermont-Ferrand, France). Powdered samples were melted with $LiBO_2$ in a magnetic induction oven at 1,100°C for 5 min using graphite crucibles. The glass beads were then dissolved in a solution of deionized water and nitric acid (1 M) and diluted by a factor of 2,000 to produce the solution to be analyzed by an Agilent 5,800 VDV ICP OES in radial mode. Analytical uncertainties ($\pm 2\sigma$) vary between 1 and 3% except for K_2O, MnO (4%) and P_2O_5 (7%) for the DR-N standard (diorite). The conditions of analysis are as follows: plasma flow 12 L/min, nebulizer flow 0.7 L/min, RF power 1.2 kW.

3.5 Raman spectroscopy

The structural/chemical identification of late magmatic phases was performed using Raman spectroscopy. The spectra were recorded using micro-Raman apparatus hosted in ISTO and equipped with a monochromatic 532 nm Coherent Genesis MX SLM laser as exciting source, a Nikon ECLIPSE Ni-U microscope, an Andor Shamrock 500i spectrometer and Peltier cooled back illuminated CCD Andor Newton detector. The use of long working distance Nikon objective (100×, N.A. 0.8) allowed micro-scale analysis with lateral resolution down to 1–2 μm^2. The 1,200 lines/mm grating was employed to record two spectral windows of interest: the main silicate network spanning from 100 to 1,400 cm^{-1} and the OH stretching region from

to 2,800 to 3,800 cm^{-1}. Each spectrum was recorded during 60 seconds (2 acquisitions of 30s) under the laser power output of 200 mW. Daily calibration of the Raman micro-spectrometer was performed based on the main 520 cm^{-1} peak of silicon.

4. Results

4.1 Lineament analysis

A simplified map that includes the 505 vents identified on geological maps to be analyzed with the Hough transform analysis is shown in Fig. A2.

First, we applied the Hough Transform to all 505 vents (Fig. 4). For this first case, one node stands out clearly at N146E (symmetrically, the same node stands at N326) but more discreet directions not calculated can be recognized such as the N010E and N110E directions (Fig. 4a, b). In a second analysis, we discriminated the mafic and felsic vents (Fig. 4c, d, e, f). The Hough transform analysis on mafic vents show four main alignments: N011E, N103E, N112E and N140E; while the felsic vents show only two major directions: N110E and N142E.

Complementary field measurements on fracture networks affecting the Variscan gneisses in several locations near the Suc de Sara intrusion and in the phonolite itself were performed (Fig. 5). Analyses confirm the existence of two main associated populations of brittle structures mostly oriented N080E-N090E and N140E affect the basement. In addition, a third minor direction represented by N050E fractures is identified (Fig. 5a). Measurements within the Suc de Sara allow us to follow the foliation direction of this intrusion from the "Coin de la Scie" to the summit (Fig. 5b). It can be seen that the main foliation plane rotates between the NW end and the summit of the Suc de Sara.

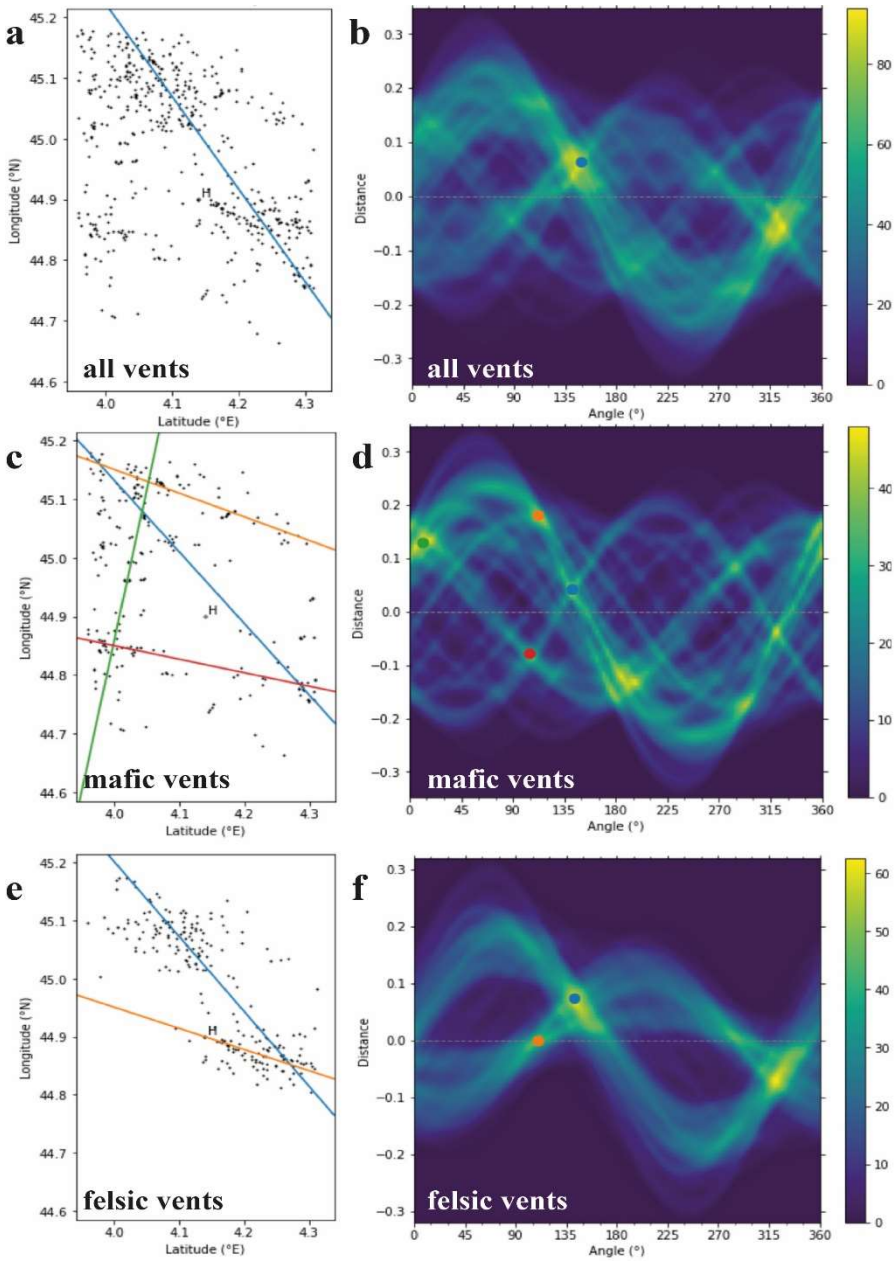

Figure 4. Hough transform applied to monogenic vents of the Eastern Velay (**a** and **b**), only to mafic vents (**c** and **d**) and only to felsic vents (**e** and **f**). The diagrams on the left (a, c and e) correspond to Cartesian spaces. The H points corresponds to the Hough center from which the distance ρ is calculated. The points on the right diagrams represent the main nodes and their associated line is drawn on the Cartesian space. The blue to yellow gauges represent the number of curves that overlap in Hough space.

4.2 Fracture network analyses

We conducted a regional, joints and shear fractures analysis based on 16 sites: 9 sites distributed in the country rock and 7 sites located in the intrusion (Fig. 5). Low dipping fractures, i.e. fractures dipping less than about 10 degrees, were not measured as they generally can to either exfoliation or unloading joints.

In the Velay basement two main fractures populations are recognized (Fig. 5a). N120E-N140E striking fractures are associated with N010E-N020E striking fractures, all being highly dipping. These two fracture sets are observed in the far field (stereographic diagrams 3, 8 and 9 in Fig. 5a) but also in the vicinity of the Suc de Sara intrusion (stereographic diagram 1 in Fig. 5a). A third fracture population composed by almost East-West striking fractures is also observed (stereographic diagrams 4, 5, 6 and 7 in Fig. 5a). This population consists of two associated sets of fractures moderately dipping (from 20° to 45°) either to the North or to the South.

In the Suc de Sara intrusion, three populations of fractures are observed (Fig. 5b). The orientation and dip of these fractures evolve with respect to their location in the intrusion. The main population is composed of fractures parallel to the closet hanging wall of the intrusion, while the two associated populations exhibit nearly perpendicular striking directions. The first population corresponds to fractures parallel to the local mineral foliation (see measurements hereafter) while the two other populations are identified as prismatic joints. The associated N120-N140 and N10-N20 striking fractures recognized in the country rock are not developed in the intrusion, meaning that they were not anymore active during and after the emplacement of the intrusion.

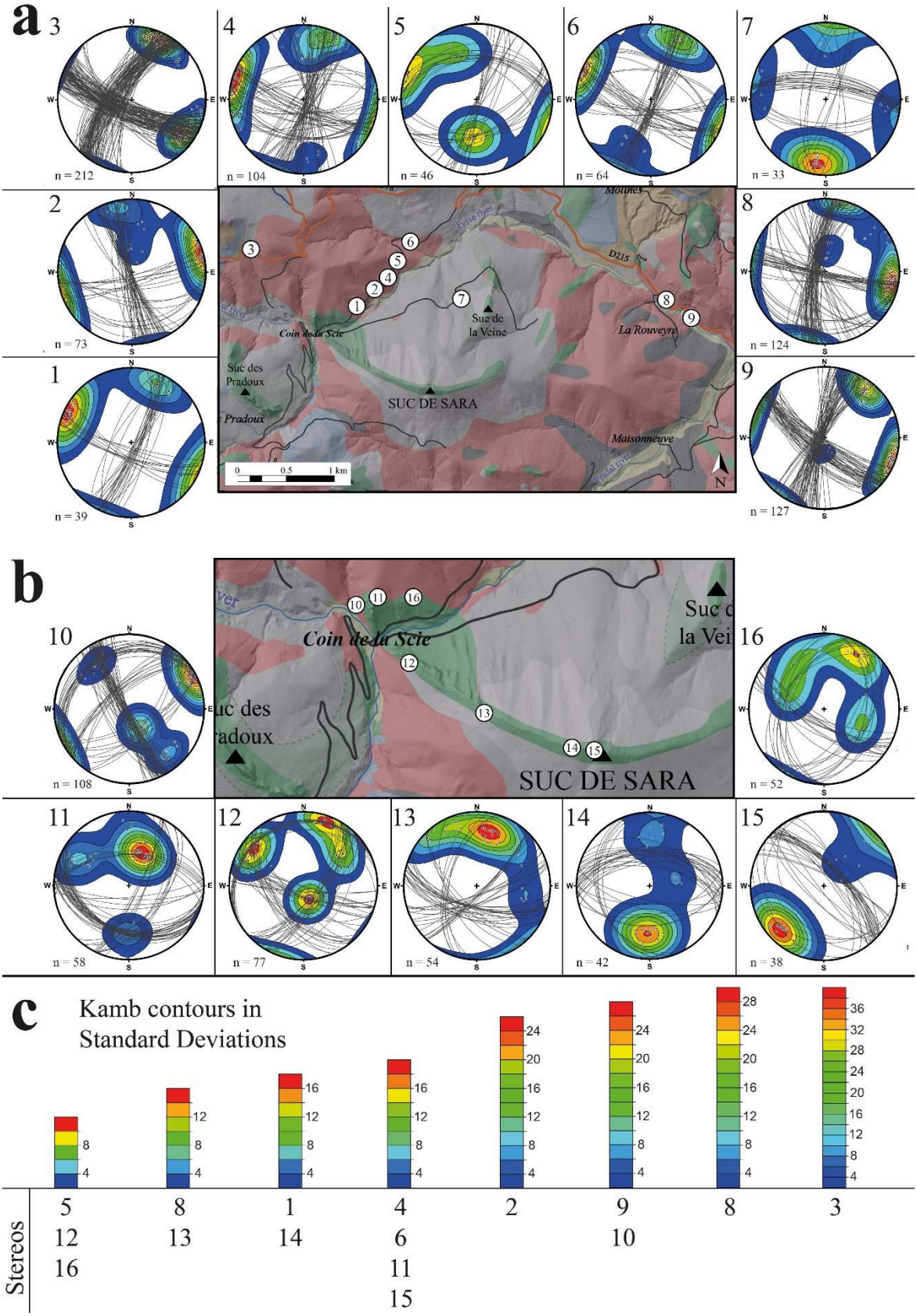

Figure 5. a – Fragile tectonic history of the late-Variscan basement around the Suc de Sara since 295 Ma (Cirque des Boutières). **b –** Fracturing recorded since 6.5 Ma by the Suc de Sara with anisotropy

linked to foliation. **c –** Statistical densities of the pole population contoured at interval of standard deviation following the Kamb contour method. Equal area stereographic projections, lower hemisphere. The map legend as in Fig. 3. Geological maps modified from BRGM (2011) 1:50,000 geological map no. 816, Le Monastier-sur-Gazeille, Defive et al. (2011).

4.3 Mineral fabrics

Mineral foliations and lineations were measured within the Suc de Sara intrusion by using the shape preferred orientation of elongated pyroxene, and alkali feldspar porphyroclasts, when present. Mineral lineation is usually hardly distinguishable in the field; only 5 lineations were measured in the Eastern area. Their orientations range from N0E to N030E and from N110E to N170E. The associated dips range from 30° to 45°, with an almost horizontal dip measured at the heart of the structure (Fig. 6).

In the vicinity of the intrusion margin, the mineral foliation always trends parallel to the margin. They dip between 35° and 75° along the Northwest margin, but they are more generally dipping at 80° in average. In the core of the structure, the foliation progressively evolves to a 20° dip to the North (Fig. 6). The inferred foliations trajectories based on our measurements express an axial structure.

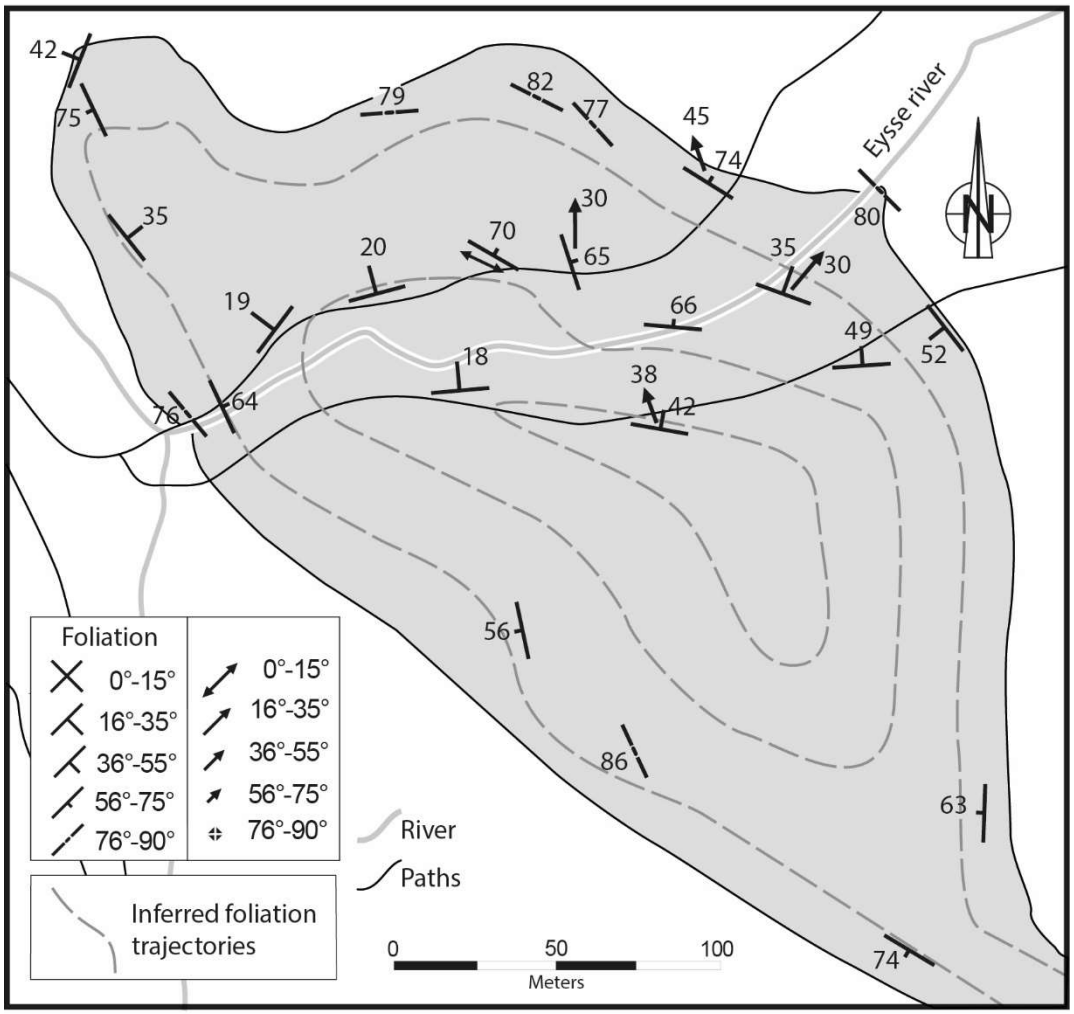

Figure 6. Mineral foliations and lineations measured in the Northwestern extension of the Suc de Sara intrusion. Inferred trajectories exemplify the axisymmetric nature of the thicker Northwestern part of the intrusion.

4.4 Cross-section

The detailed cross-section that lies perpendicularly to the margins of the intrusion was performed by combining observations along the two pathways on both sides of the Eysse river, and in the riverbed (Fig. 7a).

On the Western margin of the intrusion, the surrounding Variscan metamorphic basement formed of biotite-rich metatexites outcrop in the riverbed. The margin of the dyke trend

N140E and dip 76° to the West (Fig. 6). It is composed of a 10 to 15 cm thick glassy phonolite in which rare alkali feldspar phenocrysts are present. The inner zone is constituted by an aphanitic porphyritic phonolite whose mineral foliation is parallel to the margin of the dyke (Fig. 7a and 7b). Rare alkali feldspar phenocrysts show rounded shape (Fig. 8a, b). These two facies are crosscut by two set of veins filled by aegirine (Fig. 8a). The first set is composed of long and locally thick veins parallels to the main foliation. They are connected to a second set of veins, both forming an anastomosed pattern (Fig. 8a). From place to place, and in particular close to the glassy margin, this second set becomes predominant. The orientation of the shear planes C (parallel to the foliation planes S) and the associated planes C' marked by certain aegirine veins and further from the glassy margin by aegirine crystals is schematized in Fig. 9. From the margin and about 2 meters to the East, the texture changes as the rock exhibits progressively a phaneritic texture (tinguaite facies) with infra-centimetric feldspar, idiomorphic nepheline and elongated aegirine; the orientation of the later defining a clear foliation parallel to the margin of the dyke. Scattered fractures are still present but are progressively replaced when moving away from the margin by a dense network of veins parallel to the main mineral foliation and composed of aligned aegirine grains (Fig. 8b, c).

Approaching the center of the intrusion the tinguaite becomes rich in alkali feldspar phenocrysts while aegirine-rich veins are no longer present (Fig. 8d). Aegirine phenocrysts define a S-type fabric as the well-marked foliation does not include any lineation (Fig. 8d). At the same location the N75-oriented bending discrete foliation rapidly bent to become almost horizontal; before to get a 65° bending to the East, 100 meters eastward (Fig. 7a). The intrusion is crosscut by two N145E and N016E trending brittle faults (Fig. 7).

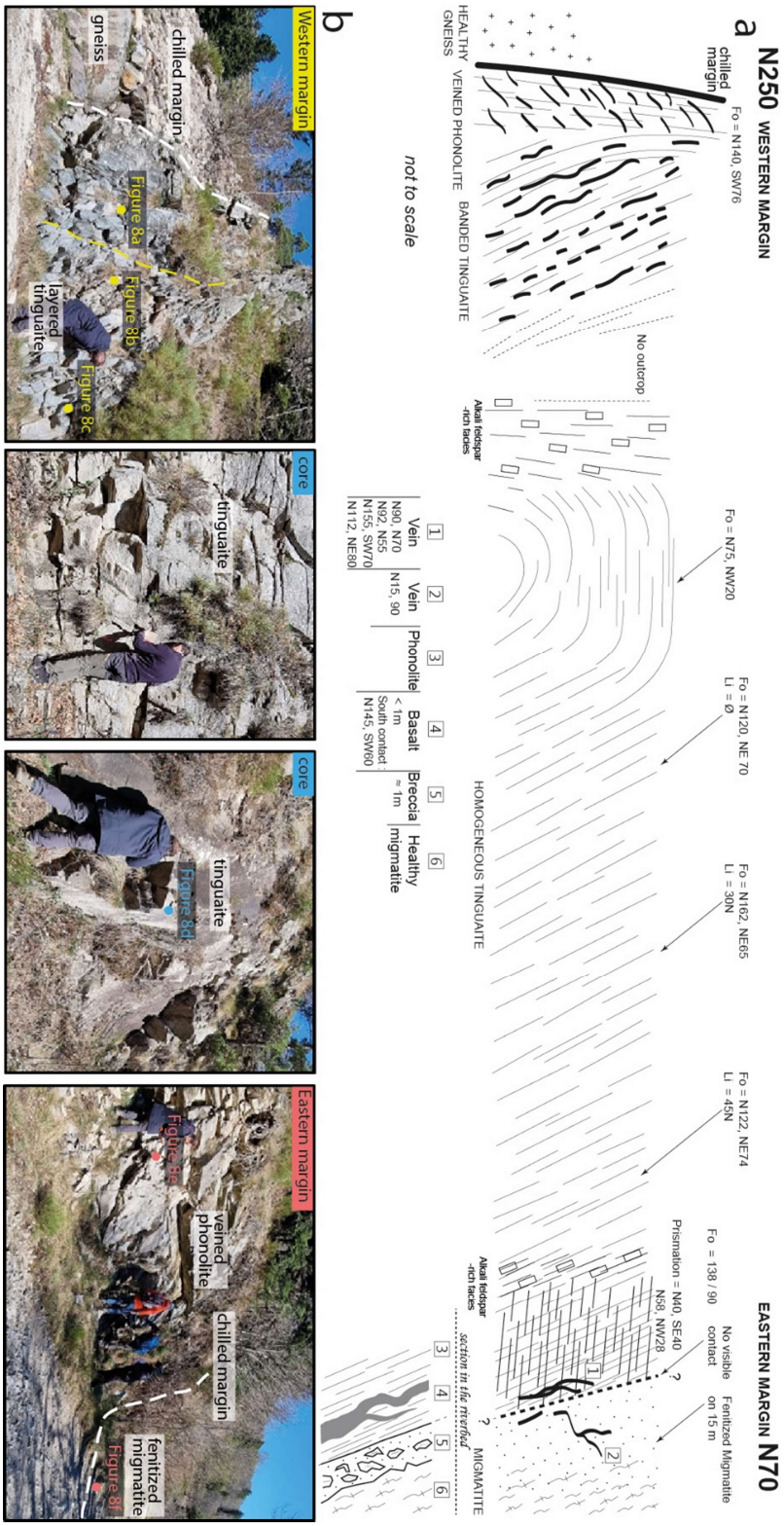

Figure 7. a – Detailed cross-section of the Suc de Sara phonolitic intrusion at the level of the path above the Eysse River, based on the outcrops on the left and right banks. The location of the section is

available in Fig. 3. **b –** Photos of outcrops on the North bank. Fo = mineral foliation, Li = mineral lineation, P = fault plane with L = striae.

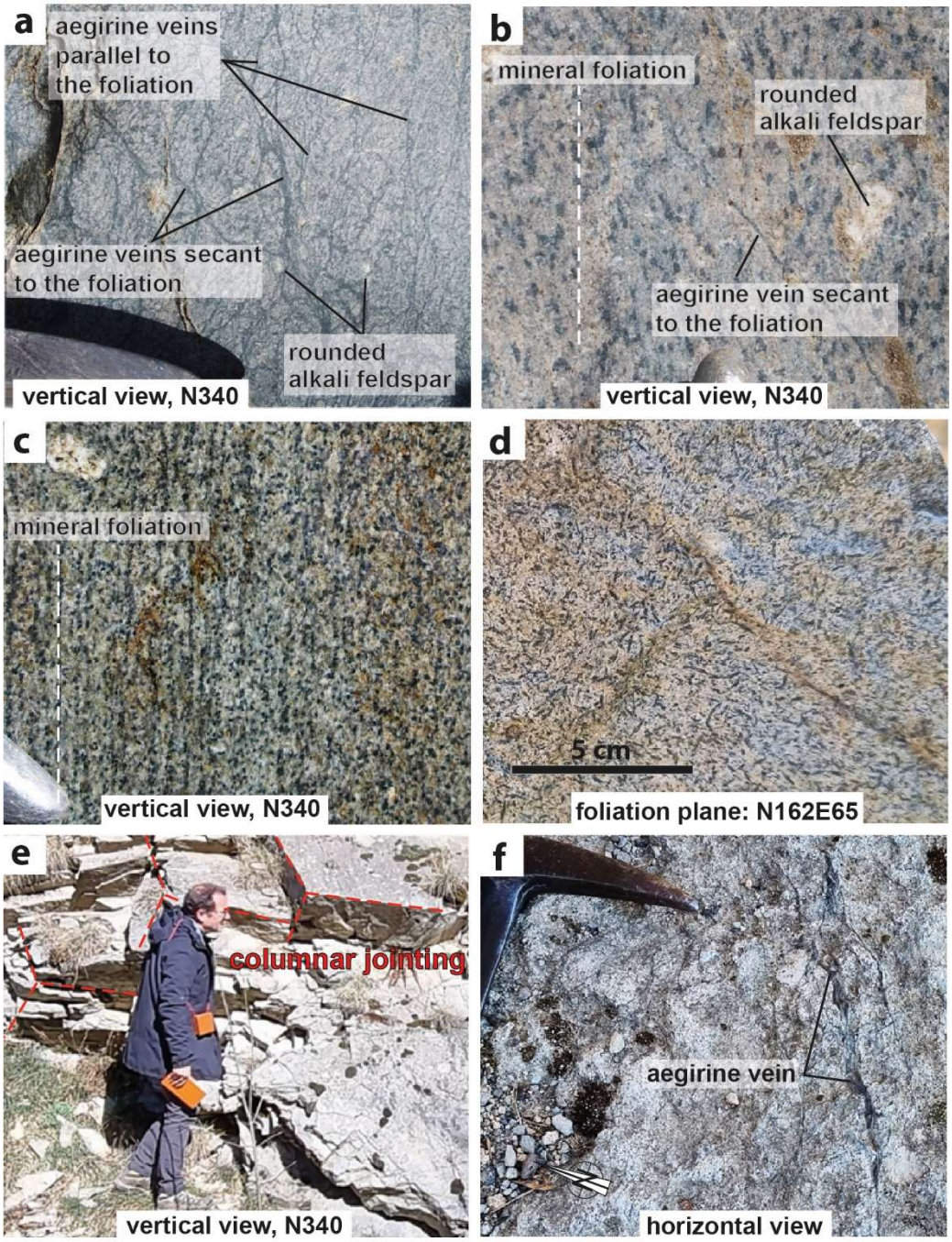

Figure 8. Field photographs detailing the main structures observed across the intrusion. The position of each figure is shown in Fig. 7. **a** – Aegirine-bearing vein network and alkali feldspar phenocrysts observed on the Western margin. **b** – Aegirine-bearing veins crosscut the mineral foliation that wraps around an alkali feldspar phenocryst. **c** – Aegirine banding and alkali feldspar phenocrysts observed in

the tinguaite away from the Western margin. **d** – Idiomorphic aegirine and alkali feldspar phenocrysts exhibiting a weak shape fabric orientation observed in the core of the structure. **e** – Sub-horizontal columnar jointing of the phonolite observed near its Eastern margin. **f** – Aegirine-bearing veins observed in the fenitized migmatitic host rock at about one meter from the Eastern margin.

Along the Eastern margin the tinguaite is crosscut by rare, aegirine-rich veins without preferred orientation observed. In addition, the tinguaite exhibits a horizontal columnar jointing (Fig. 7a, 8e) indicating that no shearing affected the tinguaite during the late cooling magmatic stage. The Eastern margin between the intrusion and the country rock well crops out in the Eysse riverbed and it is characterized by the presence of a one-meter-thick composite polygenic breccia consisting of phonolitic and gneissic blocks embedded in a porous, coarse-grained matrix (Fig. A3, A4). Close to this breccia, a basaltic dyke, barely parallel to the margin of the intrusion, intrudes the tinguaite as it was already fully crystallized (Fig. A3). The metatexite forming the country rock is strongly altered over about 15 meters from the contact margin. This metasomatic alteration that involves the removing of the silica corresponding to the so-called fenitization is caused by the circulation of magmatic fluids under pressure from the intrusion into the surrounding rock (Mergoil, 1968). This alkaline alteration is expressed by the disappearance of the biotite and a strong dequartzification, this latter process left spaces that are locally filled by aegirine as geodic crystallizations while veins of similar origin than those affecting the phonolite are also presents (Fig. 8f, A4).

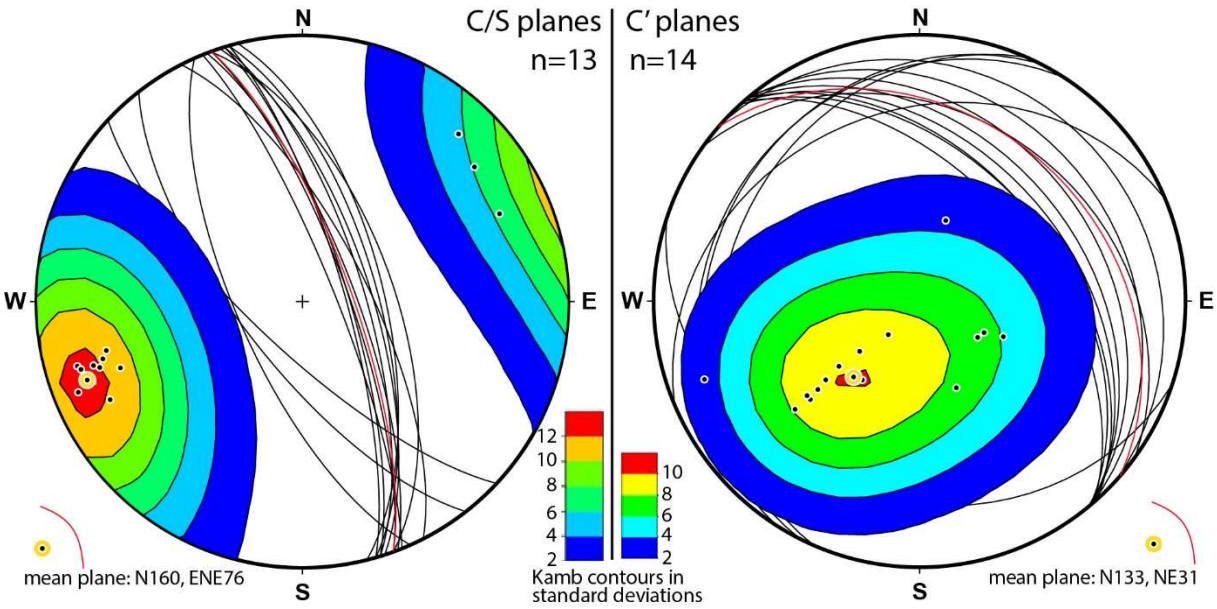

Figure 9. Stereographic diagrams (Schmidt equal are projection, lower hemisphere) of associated C (left, parallel to the mineral foliation S) and C' (right) aegirine-bearing shear bands measured near the chilled Western margin (SA3 location in Fig. 7 and picture in Fig. 8a). Statistical densities of the pole population contoured at interval of standard deviation following the Kamb contour method. Equal area stereographic projections, lower hemisphere.

4.5 Whole-rock geochemistry

The whole-rock analyses of 6 representative samples are presented in Table 2. The locations of the samples SA3, SA31, SA6, SA33, SA34 and SA101 are shown in Fig. 3c.

All whole rock analyses of the Suc de Sara intrusion point in the phonolite domain (Fig. 2b): SiO_2 (60.18 ± 0.12) and Na_2O + K_2O (16.62 ± 0.28) contents confirm the general SiO_2-undersaturation of the Suc de Sara intrusion. Among the analyzed oxides, only Na_2O show a significant variation from the margin to the core of the intrusion (Fig. 10a). In particular, the Western margin of the structure represented by sample SA3 is the most alkali-rich; in agreement with the large amount of idiomorphic nepheline phenocrysts. In the peralkalinity diagram, the $\frac{Na}{Al-K}$ ratio values range from 1.07 for SA33 to 1.20 for SA101 (Fig. 10b).

	This study						Mergoil and Boivin, 1993
Sample name	SA101	SA3	SA31	SA6	SA33	SA34	73-79
Location	Western margin	Western margin	Core	Core	Eastern margin	Eastern margin	Core
SiO_2	59.60	60.34	60.11	60.12	60.27	60.05	59.52
Al_2O_3	19.99	20.27	20.08	20.16	20.04	20.11	20.05
Fe_2O_3	2.84	3.09	2.95	3.06	2.89	2.98	3.34
MgO	0.03	0.09	0.04	0.02	0.03	0.02	nd
CaO	0.66	0.75	0.72	0.77	0.70	0.68	0.66
Na_2O	10.36	10.04	9.48	9.45	9.23	9.47	9.11
K_2O	5.22	5.05	5.14	5.09	5.10	5.05	4.97
TiO_2	0.15	0.16	0.16	0.16	0.16	0.16	0.23
MnO	0.25	0.29	0.28	0.29	0.28	0.29	0.28
Ba	0.0005	0.0015	0.0013	0.0009	0.0013	0.0008	nd
Sr	0.0001	0.0004	0.0007	0.0004	0.0007	0.0004	nd
H_2O+	0.04	0.25	0.34	0.26	0.36	0.29	nd
H_2O-	0.062	1.11	2.01	1.52	2.00	1.71	nd
Total	101.30	101.42	101.30	100.89	101.05	100.80	98.18

Table 2. Whole-rock analyses of the Suc de Sara. Analysis of Mergoil and Boivin (1993) performed on a sample taken in the core along the same section is given for comparison (n.d.: no data).

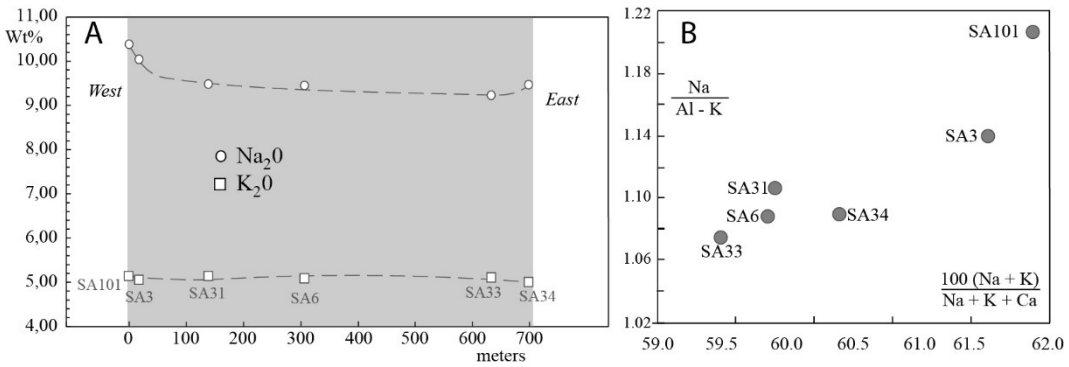

Figure 10. a – Variation in Na_2O and K_2O along the cross-section. **b –** Position of representative samples in the peralkalinity diagram.

4.6 Microscopic analysis

To unravel the mineral associations and textures present in the different facies of the Sara intrusion, we selected 6 [x,z] oriented thin sections representative of the main textures recognized in the field (Table 1). In order to simplify the description, they are grouped in three main zones, namely the Western margin (SA2 and SA3), the core of the intrusion (SA5 and SA6) and the Eastern margin (SA8 and SA9). The glassy zone that marks the Western contact with the basement is not taken in consideration.

4.6.1 Petrography

The different facies of the margins and the core facies of the Suc de Sara intrusion were observed under a polarizing optical microscope (Fig. 11). At the Western margin, the phonolite exhibits an aphanitic, feldspathoids-rich (nepheline and sodalite) porphyritic and trachytic texture formed by rare alkali feldspar phenocrysts embedded in a groundmass composed of aligned alkali feldspar and aegirine microlites. The rod-like habit of some aegirines suggests a rapid crystallization consistent with the frozen wall facies.

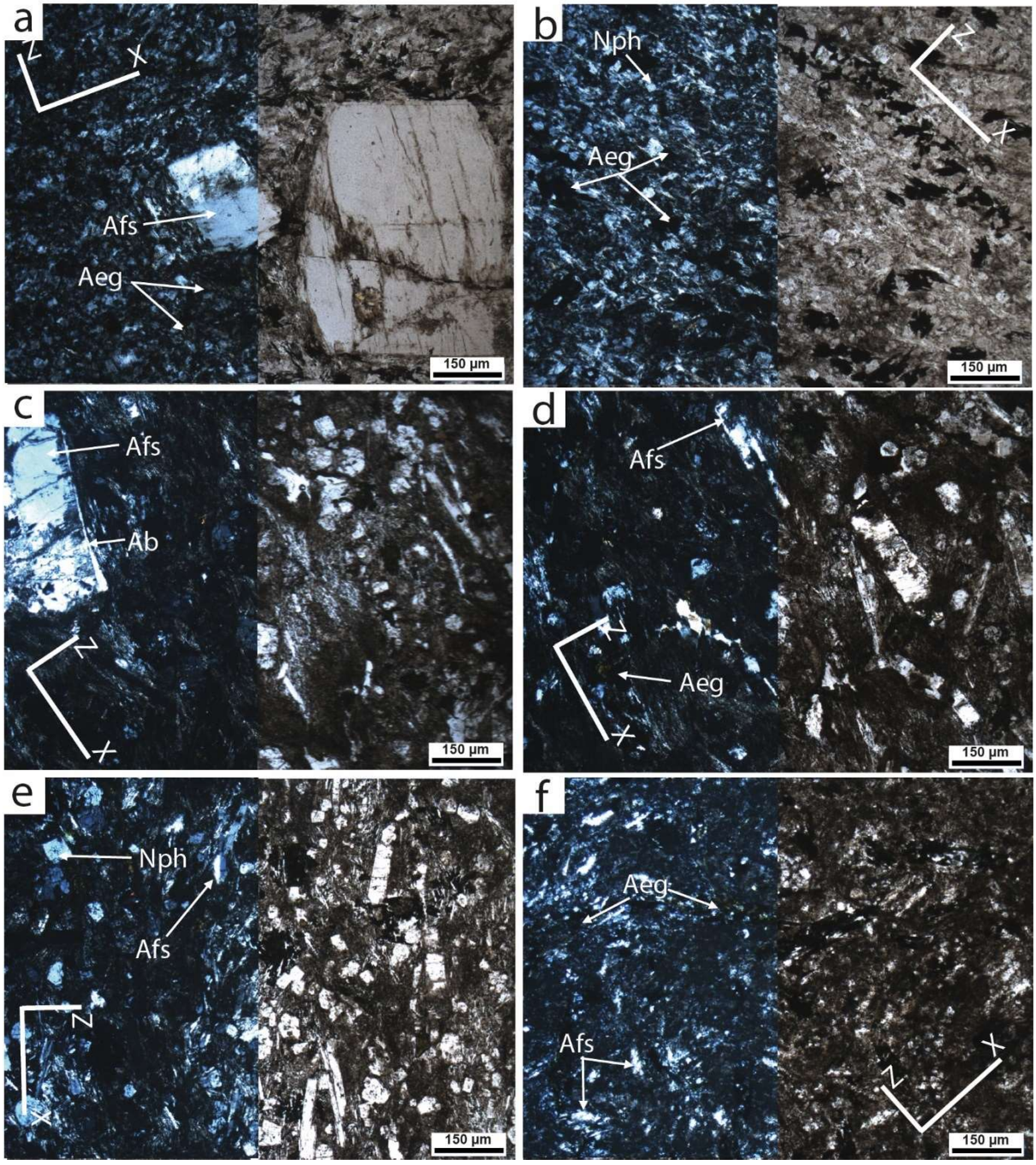

Figure 11. Characteristic textures observed in the Sara intrusion. All images are [x,z] sections (with x as the lineation) and divided in cross polarized light half image (left) and in plane polarized light half image (right). The position of the samples is shown in Fig. 3c. (**a**) and (**b**) represent trachytic textures of the Western margin. (a) is the veined phonolite (SA101, corresponds to the field view of Fig. 8a) characterized by idiomorphic pristine alkali feldspar with albite corona embedded in an aegirine (Aeg)-rich aphanitic groundmass. (b) is the banded phonolite (SA2, corresponds to the picture of Fig. 8c)

characterized by alignment of 100 µm-long poikilitic aegirine (upper left corner). (**c**) and (**d**) represent the texture of the tinguaite forming the core area (SA5 in Fig. 8d). Note the abundance of aligned prismatic alkali feldspar phenocrysts showing Carlsbad twinning, all being intensively altered. They are just a little less present at the apex of the intrusion. (**e**) and (**f**) represent the transition from tinguaite texture (e, SA7) and the phonolite texture (f, SA9) approaching the Eastern margin. The pristine alkali feldspars mark the lineation in the nepheline-rich tinguaite. In both facies the aegirine is present as poikilitic, 100-200 µm long, crystals in the groundmass. The mineral abbreviations are derived from Warr, 2021: Ab = Albite; Aeg = Aegirine; Afs = Alkali feldspar; Nph = Nepheline.

The core facies is represented by the tinguaite (Fig. 11c, d). Its paragenesis is broadly similar to those observed in the phonolite of the margin with sparse phenocrysts of alkali feldspars and albites. However, feldspars are in lower proportion at 130 m from the Western margin (Fig. 11c). But they are again more present further away (Fig. 11d) to the East where aegirines are in lower abundance and most often interstitial. Moving to the East, the phaneritic texture changes as it becomes progressively aphanitic and porphyritic approaching the Eastern margin (SA7, Fig. 11e, f). Nepheline is present as microlites together with alkali feldspar and albite in the groundmass (Fig. 11f).

4.6.2 SEM textural analysis

Scanning electron microscopy (SEM) analyses were done on the three main facies by combining Back Scattered Electron (BSE) images (Fig. 12) and compositional mapping using Wavelength dispersive X-ray spectroscopy (WDS; Fig. A5, A6).

In the thin section SA3 representative of the Western margin, idiomorphic alkali feldspar phenocrysts exbibit potassium-rich overgrows (Fig. 12a, A5, A6). In addition, they are affected by late albite recrystallization mainly developed on the periphery of phenocrysts, but also

locally propagated into the phenocryst by following the crystallographic planes (Fig. 12b). The phenocrysts are embedded in a groundmass composed of feldspathoids (nepheline and sodalite), sodic pyroxene (aegirine), aenigmatite, alkali feldspar and albite. Pyroxenes are idiomorphic and exhibit a poikilitic texture as they have included smallest idiomorphic feldspar microlites. At larger scale not shown in Fig. 12, these pyroxenes locally form ribbons as observed on a macroscopic scale in the field (Fig. 8c). Aenigmatites are also often idiomorphic and usually associated with pyroxenes. As also observed with feldspar phenocrysts, square sections of nepheline grains exhibit a reaction rim of albite composition (Fig. 12b). Finally, the matrix shows a limited porosity expressed as isolated pores entrapped between feldspar microlites (Fig. 12a).

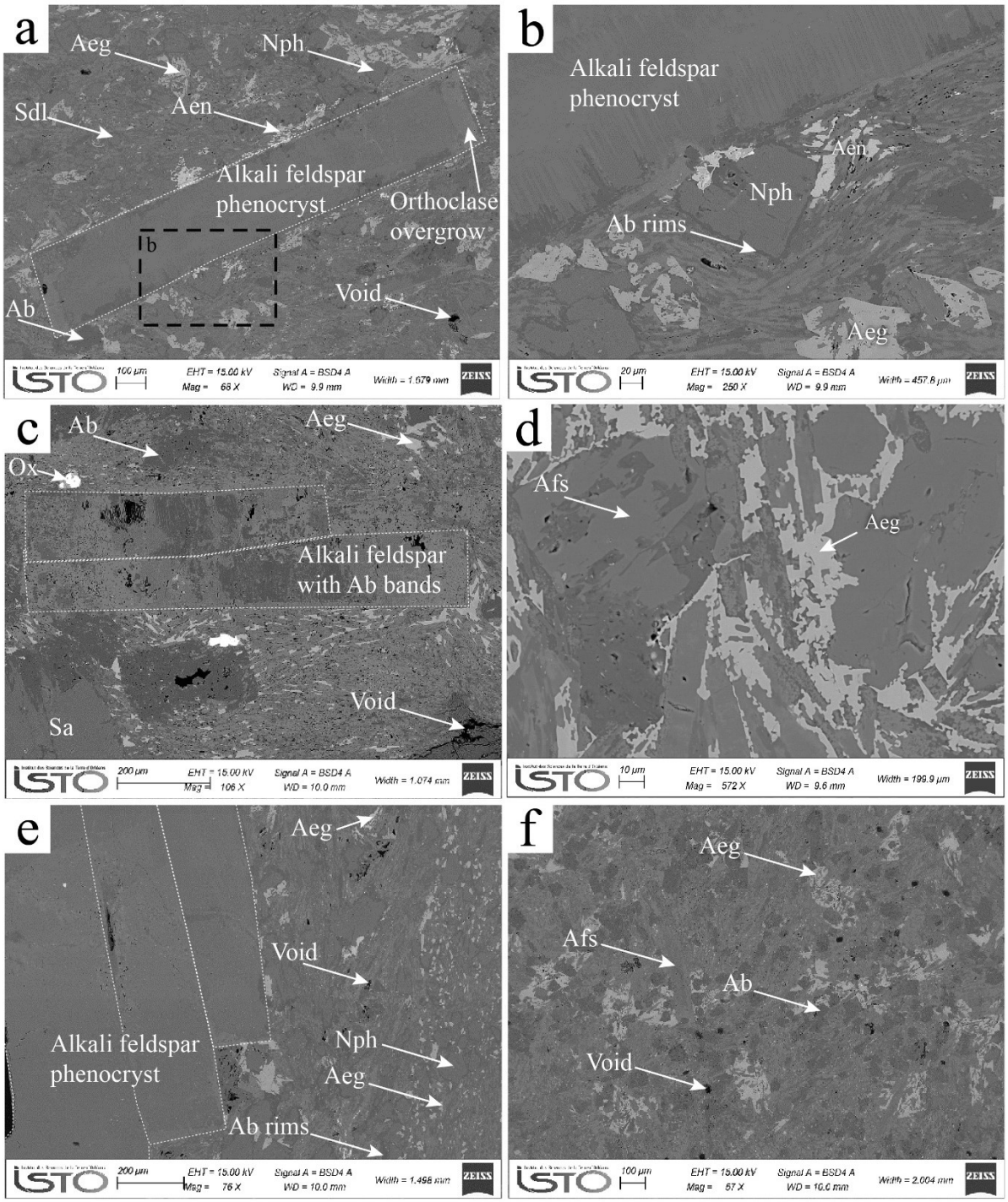

Figure 12. Back Scattered Electron (BSE) photography **a –** Section SA3 (Western margin). The dotted rectangle represents the enlargement in Fig. 12b. **b –** Zoom from Fig. 12a showing the albitic rims developed around alkali feldspars and nepheline phenocrysts. **c –** Section SA5 (core). **d –** Close view from section SA6 (core). Note the partially resorbed alkali feldspars microliths in contact with the interstitial aegirine. **e –** Section SA8 (Eastern margin). **f –** Section SA9 (Eastern margin).

The mineral abbreviations are derived from Warr, 2021: Ab = Albite; Aen = Aenigmatite; Aeg = Aegirine; Afs = Alkali feldspar; Nph = Nepheline; Ox = Oxide; Sa = Sanidine; Sdl = Sodalite.

In the central part of the intrusion, where the foliation is nearly horizontal, the tinguaite contains a larger population of phenocrysts with a centimetric size (SA5, Fig. 11c). The coarser grains are alkali feldspar, some of them with a sanidine composition. Many of these large phenocrysts are intensively recrystallized with the development of large domains of albitic composition associated with an extensive porosity (Fig. 12c). Nepheline is still present but as rounded grains with a maximum diameter of 50 µm (Fig. 12d). Aenigmatite is absent. The groundmass exhibits a strong shape fabric marked by the alignment of the feldspar microlites wrapping around the phenocrysts. Other microlites are rounded albite grains and, punctually, idiomorphic oxides (titanomagnetite) smaller than 50 µm. Locally in this groundmass, millimetric poikilitic crystals of aegirine are present (Fig. 12d). The alkali feldspar embedded in these poikilitic aegirine exhibits rounded shape, implying re-equilibration processes with the pyroxene (Fig. 12d). The porosity is also present in abundance in the groundmass.

Close to the Eastern margin (SA8 and SA9) the paragenesis is similar to the one observed on the Western side (Fig. 12a, b, e, f). Both idiomorphic alkali feldspar phenocrysts and nepheline microlites exhibit albitic rim overgrowth (Fig. 12e). In the feldspar-rich groundmass, aegirine remains abundant, still with a poikilitic texture as it encompasses both square shaped albite grains and alkali feldspar microlites.

4.6.3 Mineral chemistry

The chemical data are presented in the appendix. For iron-containing minerals, we used the Droop (1987) method to separate Fe^{2+} and Fe^{3+} from the total-FeO content.

Alkali feldspar

Alkali feldspar is the most abundant phase and spread over a wide compositional range in the ternary diagram between the potassium and sodium poles (Fig. 13a; Table A1, A2). The core of the feldspar phenocrysts found in the three facies are potassic anorthoclase to sanidine in composition in the range $Ab_{68-44}Or_{32-56}An_{0-4}$. All phenocrysts exhibit a margin of sodic anorthoclase to albite with composition in the range $Ab_{98-80}Or_{2-20}An_{0-9}$. The albitic composition constitutes the irregularly developed most external rim in contact with the groundmass (Fig. A5, A6). Finally, potassium-dominated sanidine to nearly pure orthoclase ($Ab_{2-18}Or_{81-98}An_{0-6}$; Fig. 13a) overgrowth occurs, particularly in phonolite from the Western margin of the intrusion.

The feldspar microlites are predominantly potassium-dominated sanidines in the range $Ab_{3-18}Or_{81-98}An_{0-4}$. Most of them are wrapped by a rim of albite to sodium-rich anorthoclase except for those that are embedded in the poikilitic pyroxenes for which rims are systematically absent.

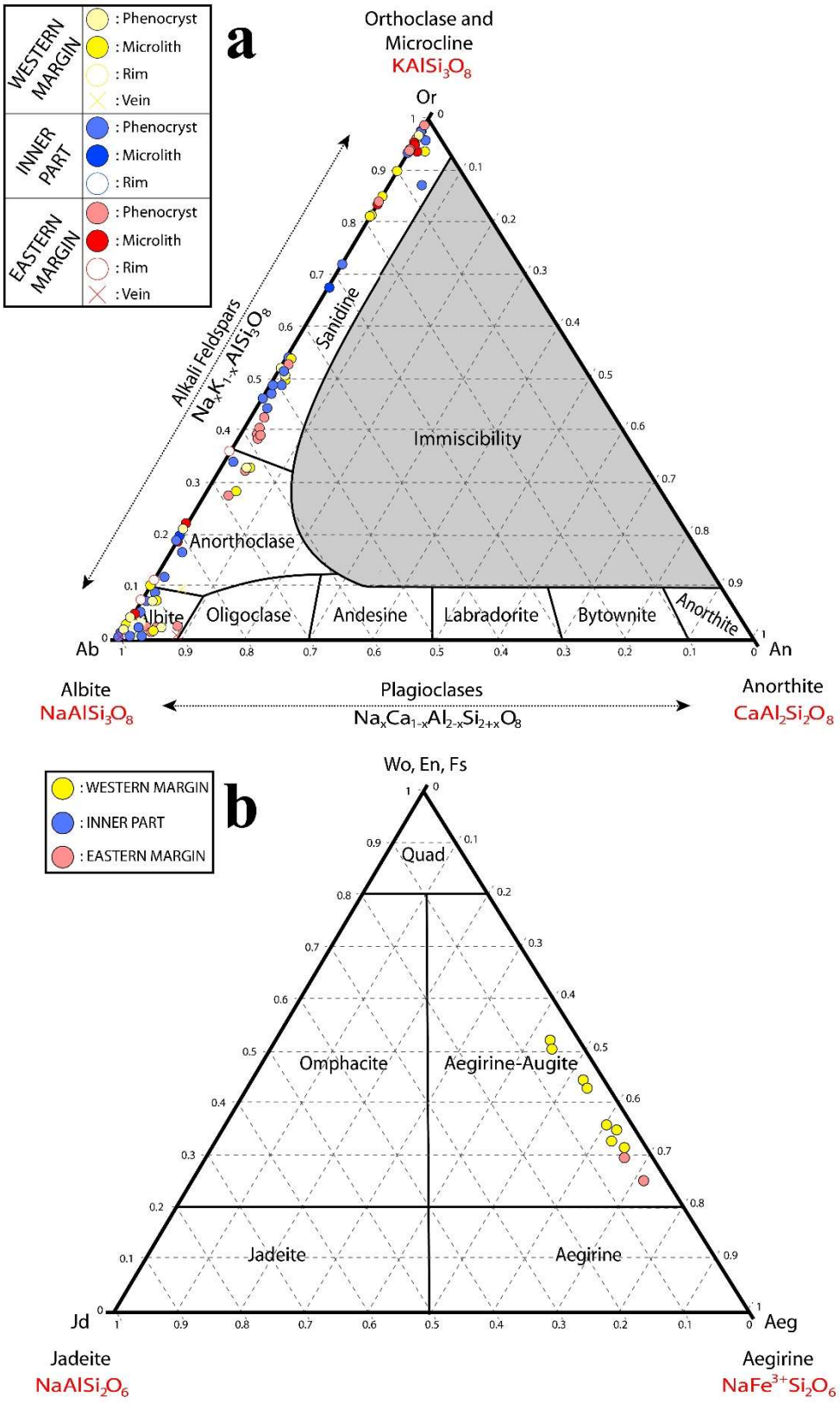

Figure 13. a – Ternary diagram of feldspars with our data going from the albite pole to the orthoclase pole for phenocrysts, their rim and the matrix; veins being exclusively albitic (after Greenwood and Earnshaw, 2012)**. b –** Ternary diagram of Ca-Na and Na pyroxenes with our data from the two margins

of the intrusion. Quad represents the Ca-Mg-Fe pyroxene pole with wollastonite (Wo), enstatite (En) and ferrosilite (Fs) after Morimoto (1989). Calculation of the aegirine (Aeg), jadeite (Jd) and Quad poles was determined using the MinPlot program presented by Walters (2022).

Pyroxene

Most of the idiomorphic to poikilitic pyroxenes form a continuous trend that lies in the aegirine-augite domain (Fig. 13b, A5, A6). One has to note that the core of pyroxene crystals is usually more calcic than the rim. Compositions range from $Aeg_{43-61}Jd_{3-5}Quad_{35-62}$ for the Western margin to $Aeg_{62-71}Jd_{3-5}Quad_{25-33}$ for the more evolved Eastern margin (with values within ± 0.1, Table A3).

Aenigmatite

This mineral is always interstitial and shows a poikilitic texture in the groundmass (Fig. A5, A6). Aenigmatite is common over the intrusion except in the plug area where it is absent. However, this phase is not very abundant in the intrusion, as confirmed by the proportion of titanium in the total rock (0.16 wt%). Average compositions is $Na_{1.99}(Fe^{2+}_{3.67}Fe^{3+}_{1.12})Ti_{0.84}Si_{5.83}O_{20}$ for the Western margin (with values within ± 0.1, Table A4). In general, this mineral phase carries the majority of the titanium present in the tinguaite, not to mention the titanomagnetites.

Magnetite-ulvöspinel solid solution

Iron oxides represent the second Ti-rich mineral phase present over the intrusion as isolated, sometimes poikilitic, grains of less than 50 µm in diameter in the groundmass (Fig. 12c, A5, A6). The largest, idiomorphic and unaltered grains are found in the central area and more particularly in the plug where they have a mean composition of $(Mn_{0.11}Fe^{2+}_{1.13}Fe^{3+}_{1.56})Ti_{0.27}O_4$

(with values within ± 0.1, Table A5). In contrast, the oxides become smaller, systematically xenomorphic and acicular with evidence of resorption, and exhibit a composition of $(Mn_{0.19}Fe^{2+}_{1.23}Fe^{3+}_{1.17})Ti_{0.47}O_4$ for the Western margin (with values within ± 0.1, Table A5).

Feldspathoids

Two feldspathoids have been recognized in the Suc de Sara intrusion (Fig. A5, A6).

- *Nepheline*

Nepheline is the dominant feldspathoid (Fig. 12d) in the intrusion as it is abundant in all facies except at the apex. Nepheline phenocrysts are idiomorphic and exhibit square-shaped sections surrounded by sodium anorthoclase to albite overgrowth ($Ab_{98-80}Or_{2-20}An_{0-9}$). Their average compositions are $Na_{2.87}K_{0.56}Al_{3.55}Si_{4.43}O_{16}$ and $Na_{2.78}K_{0.45}Al_{3.56}Si_{4.52}O_{16}$ for the Western and Eastern margins respectively (with values within ± 0.1, Table A6). At the core, the few grains present have a composition of $Na_{3.05}K_{0.60}Al_{3.49}Si_{4.41}O_{16}$; a little higher in sodium than the margins.

- *Sodalite*

Sodalite is the secondary feldspathoid in abundance. It is found as small xenomorphic isometrics grains in the groundmass (Fig. A5). They are also present as rare and isolated grains in the groundmass of the core. The average composition is $Na_{7.63}(Al_{5.59}Si_{5.83}O_{24})Cl_{1.89}$ for the Western margin (with values within ± 0.1, Table A7).

Late magmatic phases

Two minerals that constitute, associated with aegirine, aenigmatite and rare titanomagnetite, the late magmatic to hydrothermal assemblages have been recognized (Fig. 14). The first

mineral is analcime (Table A8) and belongs to the zeolite group, while the second mineral is låvenite that belongs to the wöhlerite group ($Na_2Ca_2Mn_2Zr_2(Si_2O_7)_2O_2F_2$, Dal Bo et al., 2022). Låvenite and analcime have been determined by WDS analysis and both minerals were confirmed with Raman spectra analysis (RRUFF database, ID R040128-analcime and ID R120044-låvenite; Fig. A7). These late magmatic assemblages fill the voids and the aegirine-rich veins of the phonolite facies near the chilled Western margin (SA3, Fig. 13).

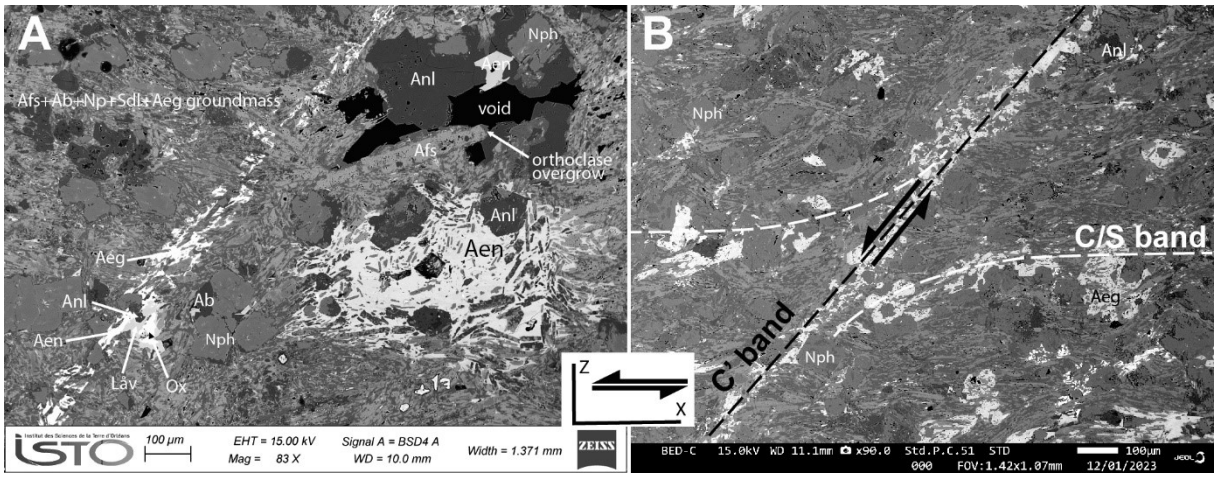

Figure 14. Backscattered electron (BSE) image of the veined phonolite near the Western chilled margin (SA3) showing the textural relationships between magmatic and late-magmatic assemblages. [x,z] sections with the lineation x horizontal, sinistral bulk sense of shear. **a –** The magmatic assemblage is composed of alkali feldspar (Afs), albite (Ab), sodalite (Sdl) and idiomorphic grains of aegirine (Aeg). The late magmatic assemblage that fill the aegirine-bearing veins is mainly composed of analcime, aenigmatite (Aen), aegirine, låvenite (Lv) and iron oxides (Ox). Aenigmatite appears also as a poikilitic phase in the groundmass while idiomorphic analcime is present in voids. **b –** The late magmatic assemblage fills the anastomosed pattern of veins formed by the C bands parallel to the mineral foliation S and the C' bands along which normal synthetic shearing with respect to the bulk sense of shear is highlighted by the bending of the C/S planes.

- *Analcime*

Analcime constitutes an abundant late-magmatic to hydrothermal hydrous mineral phase present over the intrusion. It is abundant as large idiomorphic crystals in voids and as smaller grains in aegirine-rich veins in particular in the banded phonolite close to the chilled Western margin (Fig. 14). Analcime can locally form the most external secondary rim that covers the preexisting albite rims previously formed around alkali feldspar and nepheline phenocrysts. The average compositions of analcime are $Na_{0.63}Al_{0.99}Si_{2.09}O_6 \cdot H_2O$ for the Western margin, and $Na_{0.57}Al_{1.03}Si_{2.08}O_6 \cdot H_2O$ for the Eastern margin (with values within ± 0.1, Table A8). For the analcimes present in the core, their average composition is $Na_{0.93}Al_{1.00}Si_{2.01}O_6 \cdot H_2O$.

- *Låvenite*

The Låvenite has been first recognized as a late magmatic phase in some phonolitic domes of the Velay province by Lacroix 1891 and Batard et al. (1977). This accessory mineral has only been found in the aegirine-bearing veins network developed near the Western margin together with aegirine, aenigmatite, analcime and rare oxide (Fig. 14a, A4).

5. Discussion

This work aimed at constraining the modality of segregation and further extraction of the fluid-rich residual melt differentiated during the late magmatic shallow emplacement stage of the of the 6.5 Ma old Suc de Sara intrusion. This intrusion was until now considered as a ring dyke resulting from the collapse of the roof of a hidden magma chamber causing the ascent at shallower level of a phonolitic magma (Mergoil, 1968; Mergoil and Boivin, 1993). By combining structural measurements at the regional scale and along a complete cross-section of this intrusion, together with petrological analyses and textural observations, we better

constrain the model of emplacement and finally emphasize how shear deformation and strain localization structures promote the late magmatic residual melt segregation that occurred in this differentiated intrusion during its emplacement at shallow depth.

The emplacement model elaborated by Mergoil (1968) considered the Suc de Sara and the Suc de la Veine, whose age remains undetermined, as forming together a unique arched structure. On the other hand, recent mapping suggests that the Suc de la Veine and the Suc de Sara are two different magmatic bodies as they appear not connected (Fig. 3; Define et al., 2011). Furthermore, Mergoil (1968) pointed out the hypovolcanic nature of the Suc de Sara on the basis of the textural evolution from phaneritic (tinguaite) texture present in the core of the intrusion to aphanitic (phonolite) and ultimately glassy textures approaching the chilled margins (Fig. 7, 8, 10, 11). In addition, sodalite found as an early magmatic phase forms only at a pressure of less than 1.5 kbar (Dorado et al., 2021).

5.1 Tectonic context of emplacement of the Suc de Sara intrusion

Paleotectonic studies (Blès et al., 1989, Mergoil and Boivin, 1993) and recent mapping (Define et al., 2011) evidence that associated dextral N080E – N090E and sinistral N140E regional faults were actives in a NW-SE regional compressional stress field during the late activity of the volcanism in the Boutières graben (Fig. 3a; Blès et al., 1989). In addition, N050E directed faults are also identified as active during the same period (basaltic dykes, Mergoil and Boivin, 1993). In our fracture analysis performed in the basement we also identified a ~N020E regional fracture network. Obviously, this direction, that corresponds likely to a late variscan brittle direction observed over the Eastern Massif Central (Faure, 1995), was not reactivated during the tectono-volcanic activity of the Cenozoic Velay province. At 6.5 Ma, opening under a NW-SE regional compressional stress of the northern, N140E striking thick intrusion extended as a

thinner, N080E-N090E directed, dyke to the East leading to the arced and asymmetric shape of the Suc de Sara body.

Orientation of the S/C structures of the northern part indicate an upward ascent of the magma (Fig. 14b). Moreover, foliation trajectories (Fig. 6) together with the general shape of the intrusion could be interpreted as the transition from a L-shaped dyke, as found in the Lake City caldera in Southwestern Colorado (Kennedy et al., 2018), to a neck in a similar geometry than those observed in the Shiprock volcanic complex in New Mexico (Philpotts and Ague, 2009). It should be noted that this model remains compatible with the ring dyke hypothesis of Mergoil (1968), a geometry well evidenced in the nearby Suc des Pradoux intrusion (Fig. 3a; Mergoil and Boivin, 1993). Furthermore, the development of the polygenic breccia along the Eastern margin may have resulted from the collapse of the country rock as a roof pendant, top of a hypothetic hidden magmatic chamber, following the model of Mergoil (1968). A simple model including the transition from a dyke to a neck is proposed in Fig. 15a. The two simplified geological sections present the position of the Suc des Pradoux and the Suc de Sara as well as the Suc de Sara and the Suc de la Veine, respectively (Fig. 15b). These three intrusions are independent.

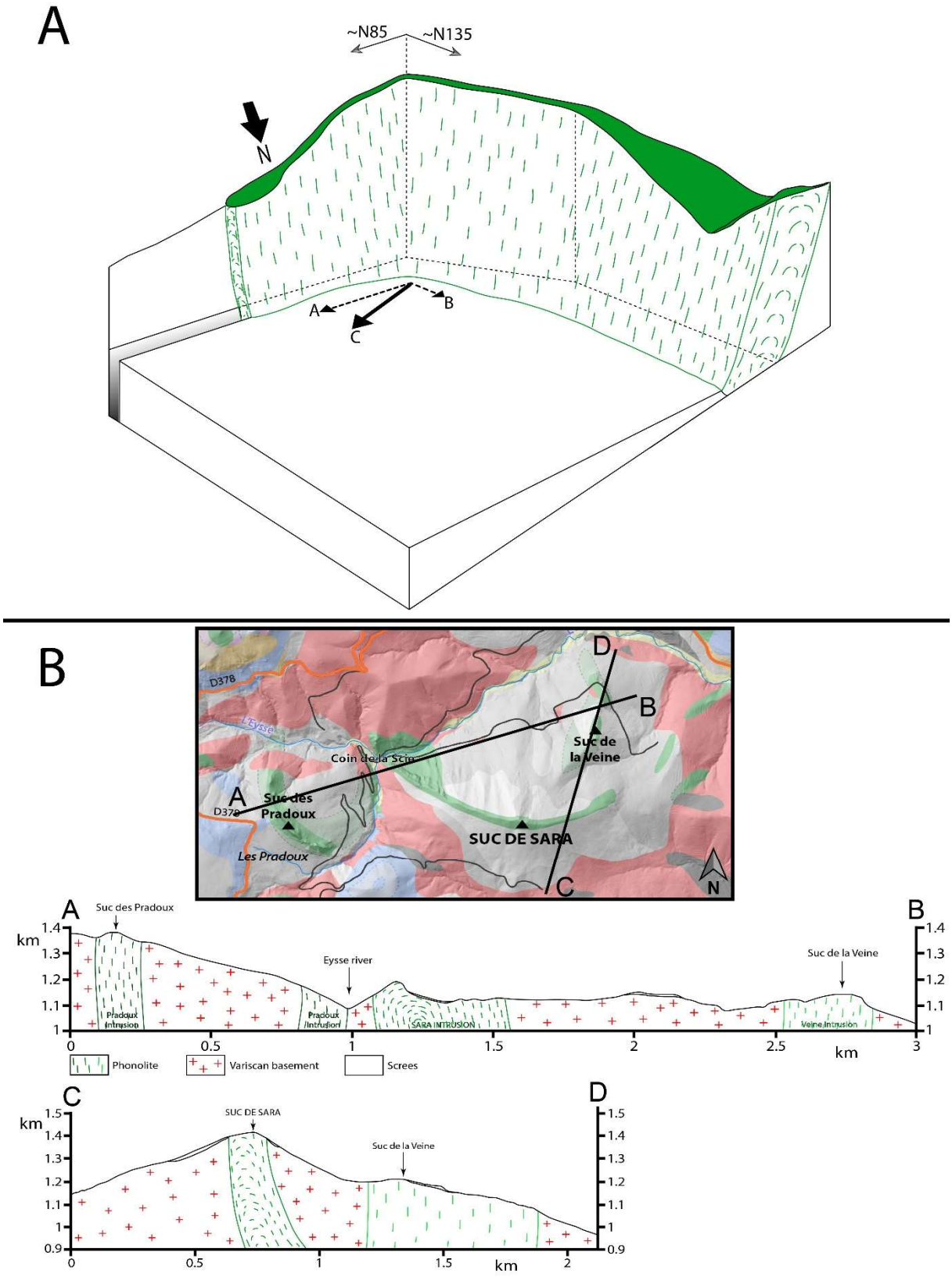

Figure 15. a – 3D model of the Suc de Sara illustrating the shallow emplacement of the phonolitic magma along two associated, ~N085E and ~N135E directed, fractures. Large opening in the ~N085E

direction (A vector) conjugate with a small opening in the ~N135E direction (B) vector giving the global opening vector C. **b** – synthetic geological sections through the three intrusions of Suc des Pradoux, Suc de Sara and Suc de la Veine (see also Mergoil and Boivin, 1993). The map is a close view from Fig. 3a.

Our detailed structural measurements including mineral foliation, aegirine- and låvenite-filled shear localization bands and columnar jointing, when present, have evidenced the asymmetric nature of the architecture of the Northwestern thicker part of the intrusion (Fig. 7). This asymmetric structure is synthetized in Fig. 16. First, the asymmetry is well expressed by the position of the axis of this Bingham-shaped plug marked by the nearly horizontal mineral foliation. The axis of this plug is offset towards the Western margin (Fig. 7, 16). Second, asymmetry further comes from the two margins that are structurally different. By combining these structural observations with the different mineral assemblages, an evolution from the early magmatic emplacement to the near solidus shear localized deformation can be drawn (Fig. 16).

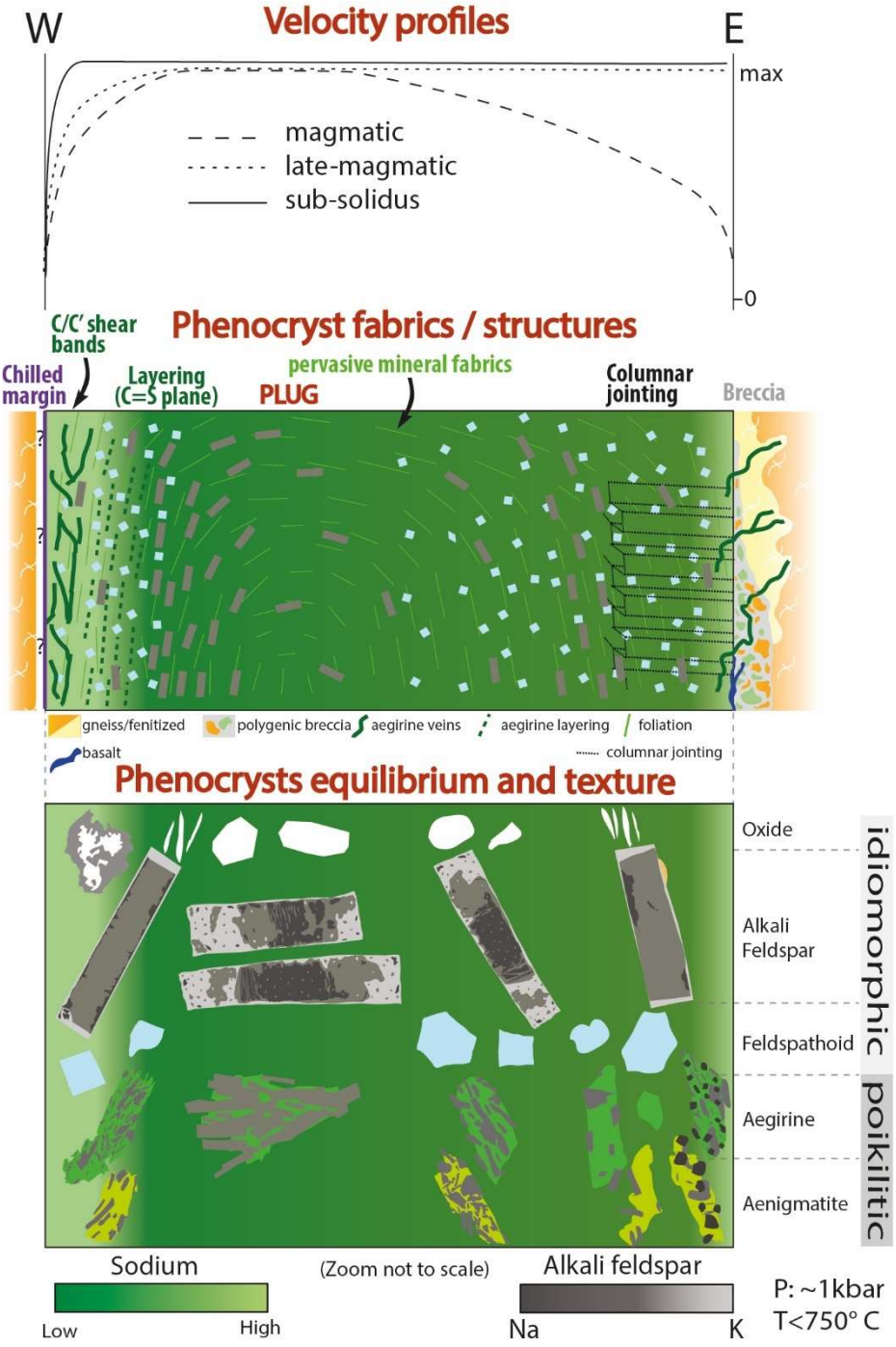

Figure 16. Synthetic scheme of the textural and structural evolution from the magmatic to solid state of the tinguaite. The top diagram shows the schematic evolution of the relative velocity profiles of the ascending magma from the magmatic stage, characterized by an asymmetric curved geometry approaching the margins, to a near-solidus deformation localizing only along the Western margin and which results in a plug geometry.

5.2 Early magmatic mineral assemblages and penetrative fabrics over the intrusion

The early magmatic assemblage is observed near the margins. It comprises anorthoclase + nepheline + sodalite + aegirine. Orthoclase with evidence of compositional zoning and nepheline are present as both euhedral phenocrysts and microlites. Aegirine + albite ± sodalite are also present in the microlithic groundmass.

This early magmatic assemblage progressively evolves to compositions with lower Na_2O concentrations toward the plug: nepheline phenocrysts and sodalite microlites are progressively resorbed until their complete disappearance, while anorthoclase phenocrysts are becoming scarce and are all intensively affected by late magmatic compositional re-equilibration into potassium-rich feldspar (Fig. 16). On the contrary, titanomagnetite becomes abundant approaching the plug as idiomorphic unaltered microlites, while it is rare and always strongly resorbed approaching the margins of the intrusion (Fig. 16). The Suc de Sara intrusion is one of the undersaturated magma established in the Velay alkaline series which was recognized by Batard et al. (1977) as an agpaitic phonolite with relict minerals of an initial miaskitic stage such as Ti-bearing oxides (Fig. 3a; Batard et al., 1977; Mergoil and Boivin, 1993). Such peralkaline phonolite was either derived from extensive plagioclase fractionation of an alkali basaltic magma (Marks et al., 2011; Marks and Markl, 2017; Dautria et al., 2004) or from the low degree of partial melting of enriched mantled lithologies, at temperatures close to the solidus (Laporte et al., 2014).

The early mineral assemblages exhibit a penetrative plano-linear shape fabric characterized by a foliation and a lineation marked by the anorthoclase and aegirine, when present, respectively. This mineral foliation is penetrative over the dyke and displays a curved geometry. However, an asymmetry is noticed as the plug axis, marked by a horizontal foliation, is closest to the western margin. (Fig. 16).

5.3 Late magmatic to near solidus mineral assemblages and shear deformation structures

5.3.1 The Western margin

West of the plug, and up to a few meters away from the Western margin, the tinguaite is characterized by a compositional layering formed by aegirine rich bands. Magmatic layering is another feature often encountered in agpaitic rocks (Marks and Markl, 2017 and references therein). The formation of this compositional layering could be attributed to the high strain partitioning in the magma that produced D-type shear bands (principal deformation shear bands of Tchalenko, 1968) in which the interstitial melt expressed by poikilitic aegirine was concentrated. Approaching the chilled margin, the thermal gradient was responsible for the transition from the phaneritic to the aphanitic texture (tinguaite to phonolite). The western margin is characterized by a strong mineral foliation parallel to the margin and surrounding rounded alkali feldspar phenocrysts. Progressive transition from D shear bands in the tinguaite to P- and Y-type (following the terminology of Westerman et al., 2017) Riedel shear bands in the phonolite indicate that the later was highly crystallized. Such Riedel-type shear bands are commonly developed at the late magmatic to solid-state transition in sheared magmas by dilatancy (Geshi, 2001; Smith, 2002; Westerman et al., 2017) that promoted late melt segregation in the anastomosed pattern of shear bands (Katz et al., 2006). All these structures point out that the Western margin suffered an intense magmatic, to late magmatic, upward shearing. On the contrary, the preservation of the glassy chilled margin without any associated breccia points out that no brittle, post magmatic, deformation affected the contact with the surrounding gneiss (Fig. 7b, 8). This suggests that the tinguaite accommodated most of, if not all the late magmatic related shearing.

The interstitial assemblage that developed during the intense strain localization is composed of aegirine + albite ± sodalite, the former developed as large poikilitic micro-phenocrysts in

the groundmass. This assemblage implies a significant Na-enrichment of the melt during late crystallization as noticed already for the earlier magmatic assemblage (Marks et al., 2011). Marks and Markl (2017, and reference therein) point out that agpaitic rocks can only form under certain conditions, including reduced crystallization conditions (low fO_2) and relatively dry magmas (low a_{H2O}). Such conditions allow for later Fe enrichment, increased peralkalinity, halogen retention and extreme HFSE enrichment in evolving magmas.

The near solidus assemblage is represented by the growth of analcime over albite on both anorthoclase microlite and nepheline in micro miarolitic cavities (Chakrabarty et al., 2016; voids in Fig. 14), together with the crystallization of låvenite in aegirine-rich veins. The abundance of miarolitic voids in the vicinity of a well-preserved chilled margin, the abundance of D-type, and subsequent C/C'-type shear bands filled by late magmatic assemblage, together with the pristine nature of the gneiss of the country rock without evidence of Na-metasomatism in the vicinity of the contact are evidences to conclude that the late magmatic fluids remained mostly confined and segregated in the sheared intrusion near the hanging wall.

5.3.2 The Eastern margin

In contrast to the Western margin, the Eastern margin is characterized by the absence of shear localized structures that could have overprinted the pervasive magmatic shape fabric. In addition, horizontal columnar joints are developed along the contact (Fig. 8e). This shows that the magmatic shearing responsible for the mineral foliation was no longer active at the late magmatic stage, leading to the development of the horizontal columnar jointing. This could be explained by the asymmetry of the plug that may have promoted the concentration of stress and therefore shear localization in a highly crystalized magma along the closer Western

margin. However, the presence of a polygenic breccia along the contact with the country rock may indicate that the tinguaite was still ascending as a solid plug along its Eastern margin.

The interstitial, late magmatic assemblage observed in the tinguaite along its Eastern margin is similar to that of the Western margin. However, this assemblage is restricted to rare, aegirine-rich veins with irregular distribution and orientation, indicating that they consist of fractures possibly opened by excess pore fluid pressure near the solidus conditions. The late magmatic melt and the Na^+, Cl^-, H_2O and CO_2-rich fluids (Mergoil, 1968; Batard et al., 1977) escaped toward the migmatitic gneiss of the country rock through the highly porous polygenetic breccia. As a consequence, the migmatitic gneiss suffered an intense fenitization characterized by nearly full dequartzification and Na-metasomatism (Mergoil, 1968; and Mergoil-Daniel et al., 1986). Theses authors pointed out the importance of CO_2 in this fenitization process, together with Na-rich fluids. The regional activity of CO_2 has been also evidenced by carbonate-rich trachytes and sanidinites found in the Velay province (Hodges, 1991; Batard et al., 1977), as well as in melt inclusion of basanitic lavas in Bas-Vivarais province (Buso et al., 2022).

Most of the very late magmatic melt and fluids escaped through excess pressure in the bedrock along the Eastern margin of the intrusion during its final emplacement. Evidence of this fluid circulation are the rare and irregularly distributed aegirine-rich veins in the tinguaite, the development of a highly porous polygenic breccia instead of a chilled margin, and intensely fenitized bedrock over 8 meters thick (Fig. 16).

5.4 Consequences for late melt segregation and extraction in shallow intrusions

The pervasive mineral fabrics are magmatic-flow-related structures (Vernon, 2000; Smith, 2002; Westerman et al., 2017) that developed during the early magmatic stage during which

the amount of melt was sufficiently high to allow for the rotation of phenocrysts and early crystallizing microlites. During this early stage, no melt segregation may arise after crystal settling because the latter is hindered by moderate crystal fraction (Bachmann and Bergantz, 2004; Holness, 2018).

During ascent and subsequent cooling, the microlithic fraction increased and a loose connected framework of crystals – the mush (Bergantz et al., 2017; and references therein) – capable of transmitting emplacement-related magmatic, or tectonic, stress developed. This transition from magmatic flow (liquid dominated) to stress-directed (solid dominated) deformation is named the rheologic lock-up threshold (equivalent to the Rigid Percolation threshold of Vigneresse et al., 1996). While the solid fraction continued to increase, the crystal framework stiffened and high localized stress may lead to strain localization (Smith, 1997; Geshi, 2001; Picard et al., 2011). Although the process of initiation of the strain localization in magma, in particular possibly by crystal jamming (Petford, 2009), remains poorly constrained, the onset of shear localized structures such as mineral banding and discrete shear zones is well documented from natural (Arbaret et al., 1993; Smith, 1996; Westerman et al., 2017) and experimental observations (Holtzman and Kohlstedt, 2007; Picard et al., 2011; Laumonier et al., 2011). At medium crystal fraction (almost 40 to 50% of solid fraction; Lejeune and Richet, 1995; Picard et al., 2011), shear deformation includes S/C/C’ bands that may propagate lengthwise from moderate strain and connect to form an anastomosing pattern at high strain (Smith, 1997; Arbaret et al. 2000; Holtzman and Kohlstedt, 2007). Such features are documented along the Western margin (Fig. 8, 9). With increasing crystal fraction and/or shear rate, Riedel -type fractures (D, Y and R -type) may develop (Misra et al., 2009). Finally, tensile fractures may arise at sub-solidus conditions, but the process need relatively high

external tectonic load (Bouchez et al., 1992). Tensile fractures have not been observed in the Sara intrusion suggesting that final ascent of the magma ended before its full crystallization.

It is well documented that shear localized structures triggered by an external stress field are potential channels for segregation and further extraction of late magmatic melts and fluids (Geshi, 2001; Holness, 2018 and references therein). In particular, synthetic normal shear bands such as C' shear bands are the most efficient shear structures for melt segregation because they develop dilatancy (Smith, 1997; Koenders and Petford, 2007; Petford, 2009). As a consequence, residual melt may be sucked from compressional regions of the mush into the local region of negative pressure gradient created by the reorganization of the crystal framework in these dilational shear bands (Petford, 2009). Such behavior is well expressed along the Western margin of the Suc de Sara intrusion. Because of its proximity to the plug, the crystal-rich magma experienced along this margin high shear deformation that resulted in residual Na-rich melt segregation. This segregation expressed as a mineral banding (C shear bands parallel to the S foliation) in the less crystalized tinguaite, progressively replaced laterally by an anastomosing network of dilational C' shear bands in the cooler, microlite-rich, phonolite, approaching the chilled margin (Fig. 14b). Such segregation by localized shear deformation is a common mechanism observed in shallow intrusions (Geshi, 2001) and in lava flows (Smith, 1997). The presence of the chilled margin on the Western margin seems to have prevented the extraction of both segregated melt, fluid and gas that filled the anastomosing network of shear bands toward the country rock, leading to the preservation of aegirine-rich veins network and miarolitic voids into the intrusion (Fig. 14a).

In opposite, along the Eastern margin the tinguaite did not suffered late magmatic shear localization as the deformation remained distributed through a significant thickness. The segregation of the residual melt is only evidenced by the presence of rare and randomly

oriented aegirine filled fractures that propagated throughout the polygenic breccia and the country rock. The presence of very low residual porosity in the tinguaite and the pervasive fenitization of the country rock (Mergoil-Daniel et al., 1986; Fig. A4) suggests that extraction of the segregated residual melt and associated Na-rich fluids was efficient along the Eastern margin. The process that promoted melt segregation and subsequent extraction toward the country rock remains unconstrained from field observation. Dufek and Bachmann (2010) highlighted a reduction of pore spaces by compaction in a random loose packing of crystals by self-reorganization of the crystal framework triggered by crystal realignment during magmatic flow (Smith 2002; Dufek and Bachmann, 2010; Holness, 2018; Hoyos et al., 2022). Such compaction is expected to be the main process acting in moderately crystal-rich mush during shearing by repacking and jamming. These two mechanisms are enhanced for elongated crystals (Hoyos et al., 2022) such as the feldspar microlites forming the groundmass of the tinguaite. Based on these evidences we may expect that, during ascent of the phonolitic magma with a moderately crystallized groundmass, the interstitial differentiated melt may have been forced to migrate toward dilatant areas. Such a process is invoked to explain the dense network of aegirine-rich layers parallel to the main mineral foliation preserved in the tinguaite (Fig. 8b, c, 14b) that experienced high and distributed deformation near the Western margin. A similar melt partitioning developed along the Eastern margin, if any, may have been drained thanks to the initiation of fractures generated by near-solidus local excess fluid pressure. These fractures further propagate throughout the permeable polygenic breccia forming the hanging wall of the Eastern margin, and likely ensure the extraction of the last residual fluids and melts toward the country rock.

6. Conclusion

The 6.5 Ma old Suc de Sara intrusion is the youngest and most differentiated peralkaline phonolite of the Velay volcanic province. It emplaced at shallow depth (< 1.5 kbars) in the Boutières graben subjected to a NW-SE directed regional compressional stress field.

This intrusion provides an exceptional example of segregation and subsequent extraction of the Na^+, Cl^-, H_2O and CO_2-rich residual melt during magma ascent and final emplacement. Contrasting features of shear deformation between the margins that exhibited different permeabilities highlight the compaction-induced melt segregation as a loose packing of microlites emerged. This segregation further developed as residual melt filling of an anastomosed C/C' bands network in the crystal-rich mush subjected to high shear strain. Subsequent melt extraction throughout the country rock was controlled by the permeability of the hanging wall. Along the Western hanging wall of the Suc de Sara intrusion, extraction of the residual melt was prevented by the 15 cm thick chilled margin. In contrast, segregated melt circulated through the highly porous and permeable, polygenic breccia developed along the Eastern margin, causing the dequartzification of the country rock and subsequent recrystallization of geodic aegirines in the pores left vacant (Mergoil-Daniel et al., 1986).

Data availability. All data derived from this research are presented in the enclosed tables, figures, and the supplements. The code developed by TP and GL for the Hough Transformation is available at the following link: https://github.com/GeoISTO/GeoDataKit/

Author contributions. TP: structural measurements and treatment, sampling, petrology, writing of the original draft; LA: structural measurements, funding acquisition, project administration, writing of the original draft. JA: petrology; ML: sampling, petrology, geochemistry; MS:

sampling, petrology; CG: structural measurements, linear analysis, SIG conceptualization; GL: alignment analysis, Hough transform software; AS: Raman analysis; IDC: petrology.

Special issue statement. This article is part of the special issue "Probing the Earth: magma and fluids, a tribute to the career of Michel Pichavant". It is a result of the Magma & Fluids workshop, Orléans, France, 4–6 July 2022

Acnowledgments. The authors thanks Emma Saulnier and Geoffroy Rodrik for their contribution to the lineament analysis. This project has benefited from the expertise and the facilities of the Platform MACLE - CVL which was co-funded by the European Union and Centre-Val de Loire Region (FEDER). We thank François Holtz for his editorial handling and Michael Marks and Armel Menant for their comments that improved the manuscript.

Financial support. TP, JA, MS, AS and LA are supported by the French Agency for Research (Agence Nationale de la Recherche, ANR) through the grant MECAMUSH ANR-19-CE0315-0007.

References

Ablay, G. J., Carroll, M. R., Palmer, M. R., Marti, J., and Sparks, R. S. J.: Basanite-phonolite lineage of the Teide-Pico Viejo Volcanic Complex, Tenerife, Canary Islands, J. Petrol., 39, 905-936, 1998.

Allan, A. S., Morgan, D. J., Wilson, C. J., and Millet, M. A.: From mush to eruption in centuries: assembly of the super-sized Oruanui magma body, Contributions to Mineralogy and Petrology, 166, 143-164, 2013.

Arbaret, L., Diot, H., and Launeau, P.: Le suc phonolitique du Petit Gerbier (Velay, Massif Central); fabriques magnétiques et magmatique. Comptes Rendus de l'Académie des Sciences, Paris, 316(2), 1603-1610, 1993.

Arbaret, L., Burg, J. P., Zeilinger, G., Chaudhry, N., Hussain, S., and Dawood, H.: Pre-collisional anastomosing shear zones in the Kohistan arc, NW Pakistan, Geological Society, London, Special Publications, 170(1), 295-311, 2000.

Bachmann, O., and Bergantz, G. W.: On the origin of crystal-poor rhyolites: extracted from batholithic crystal mushes, Journal of Petrology, 45(8), 1565-1582, 2004.

Bachmann, O., and Bergantz, G. W.: The magma reservoirs that feed supereruptions, Elements, 4(1), 17-21, 2008.

Bambier, A., Berger, E., Mergoil, J., Valadas, B., Veyret, Y., and Weisbrod, A.: Carte géologique de la France à 1/50000 (840), 1985.

Barbey, P., Villaros, A., Marignac, C., and Montel, J. M.: Multiphase melting, magma emplacement and PT-time path in late-collisional context: the Velay example (Massif Central, France), Bulletin de la Société géologique de France, 186(2-3), 93-116, 2015.

Batard, F.: Les feldspaths dans les roches volcaniques différenciées du Massif Central Français, Thèse 3^{e} cycle. Univ. Clermont-Ferrand, 176p, 1974.

Batard, F., Mergoil-Daniel, J., and Mergoil, J.: Calcite et rôle possible du CO_2 dans la genèse des roches hyperalcalines et agpaïtiques du Velay oriental (Haute-Loire, Massif central français), Bulletin de Minéralogie, 100(6), 343-347, 1977.

Bergantz, G. W., Schleicher, J. M., and Burgisser, A.: On the kinematics and dynamics of crystal-rich systems, Journal of Geophysical Research: Solid Earth., 122(8), 6131-6159, 2017.

Berger, E. T., and Vannier, M.: Petrology of Megacrysts, Mafic and Ultramafic Xenoliths from the Pipe of Eglazines, Causses, France, In Developments in Petrology, Elsevier 11A, 155-168, 1984.

Blès, J. L., Bonijoly, D., Castaing, C., and Gros, Y.: Successive post-Variscan stress fields in the French Massif Central and its borders (Western European plate): comparison with geodynamic data, Tectonophysics, 169,79-111, 1989.

Boivin, P., Besson, J. C., Briot, D., Camus, G., Goër, A. de, Gourgaud, A., Labazuy, P., de Larouzière, F. D., Livet, M., Mergoil, J., Miallier, D., Morel, J. M., Vernet, G., and Vincent, P.: Volcanologie de la Chaîne des Puys. Carte et fascicule, 4e édition, Parc Naturel des Volcans d'Auvergne (ed.), 179p, 2004.

Bouchez, J. L., Delas, C., Gleizes, G., Nédélec, A., and Cuney, M.: Submagmatic microfractures in granites, Geology, 20(1), 35-38, 1992.

Bout, P.: Histoire géologique et morphogenèse du système Velay SE-Boutières-Coiron, Rev. Geogr. Phys. Geol. Dyn., Vol. 2,8., Num. 0003, 225-251, 1966.

Burgisser, A., and Bergantz, G. W.: A rapid mechanism to remobilize and homogenize highly crystalline magma bodies, Nature, 471(7337), 212-215, 2011.

Buso, R., Laporte, D., Schiavi, F., Cluzel, N., and Fonquernie, C.: High-pressure homogenization of olivine-hosted CO_2-rich melt inclusions in a piston cylinder: insight into the volatile content of primary mantle melts, Eur. J. Mineral., 34, 325-349, 2022.

Cashman, K. V., Sparks, R. S. J., and Blundy, J. D.: Vertically extensive and unstable magmatic systems: a unified view of igneous processes, Science, 355(6331), 2017.

Chakrabarty, A., Mitchell, R. H., Ren, M., Saha, P. K., Pal, S., Pruseth, K. L., and Sen, A. K.: Magmatic, hydrothermal and subsolidus evolution of the agpaitic nepheline syenites of the

Sushina Hill Complex, India: implications for the metamorphism of peralkaline syenites, Mineralogical Magazine, 80(7), 1161-1193, 2016.

Couzinié, S., Moyen, J. F., Villaros, A., Paquette, J. L., Scarrow, J. H., and Marignac, C.: Temporal relationships between Mg-K mafic magmatism and catastrophic melting of the Variscan crust in the southern part of the Velay Complex (Massif Central, France), Journal of Geosciences, 59, 69-86, 2014.

Dal Bo, F., Friis, H., and Mills, S. J.: Nomenclature of wöhlerite-group minerals, Mineralogical Magazine, 86(4), 661-676, 2022.

Dautria, J. M., Liotard, J. M., and Briot, D.: Particularités de la contamination crustale des phonolites : exemple du Velay oriental (Massif Central), C. R. Géoscience, 336, 2004.

Define, E., Courrioux, G., Ledru, P., Poiraud, A., and Prognon, C.: Carte géologique de la France (1/50000), feuille Le Monastier-sur-Gazeille (816), 2011.

Delph, J. R., Ward, K. M., Zandt, G., Ducea, M. N., and Beck, S. L.: Imaging a magma plumbing system from MASH zone to magma reservoir, Earth and Planetary Science Letters, 457, 313-324, 2017.

Dorado, O., Andújar, J., Martí, J., and Geyer, A.: Pre-eruptive conditions at satellite vent eruptions at Teide-Pico Viejo complex (Tenerife, Canary Islands), Lithos, Vol. 396-397, 106193, 2021.

Droop, G. T. R.: A general equation for estimating Fe3+ concentrations in ferromagnesian silicates and oxides from microprobe analyses, using stoichiometric criteria, Mineralogical magazine, 51(361), 431-435, 1987.

Dufek, J., and Bachmann, O.: Quantum magmatism: Magmatic compositional gaps generated by melt-crystal dynamics, Geology, 38(8), 687-690, 2010.

Dupraz, J., and Didier, J.: Le complexe anatectique du Velay (Massif central) : structure d'ensemble et évolution géologique, p74-87, Géologie de la France, n°4, 1988.

Faure, M.: Late orogenic carboniferous extensions in the Variscan French Massif Central, Tectonics, 14-1, 132-153, 1995.

Geshi, N.: Melt segregation by localized shear deformation and fracturing during crystallization of magma in shallow intrusions of the Otoge volcanic complex, central Japan, J. Volcano. Geotherm. Res., 106, 285-300, 2011.

Girod, M., Bouiller, R., Roche, A., Weber, F., Larque, P., Giot, D., Guerin, C., Bladier, Y., Laurent, P., and Bambier, A.: Geological map, 1:50000; n°791; XXVII-35; 31 P.; H.T. 1; Bibl. 2 P.; 4 Ill.; 1 CART. Univ. Claude Bernard, Paris, France, 1979.

Greenwood, N. N., and Earnshaw, A.: Chemistry of the Elements, Elsevier., 1600 p., 2012.

Hart, P. E., and Duda, R. O.: Use of the Hough transformation to detect lines and curves in pictures, Communications of the ACMk, 15(1), pp.11-15, 1972.

Hodges, S.: Petrogenesis of the phonolitic rocks of the Velay Oriental, France, Thèse PhD, Oxford Univ, 1 vol, pp. 1-207, 1991.

Holness, M. B.: Melt segregation from silicic crystal mushes: a critical appraisal of possible mechanisms and their microstructural record, Contributions to Mineralogy and Petrology, 173(6), 48, 2018.

Holtzman, B. K., and Kohlstedt, D. L.: Stress-driven melt segregation and strain partitioning in partially molten rocks: Effects of stress and strain, Journal of Petrology, 48(12), 2379-2406, 2007.

Hough, P.V.C.: Machine analysis of bubble chamber pictures. In Proc. of the International Conference on High Energy Accelerators and Instrumentation, Sept. 1959. pp. 554-556, 1959.

Hoyos, S., Florez, D., Pec, M., and Huber, C.: Crystal Shape Control on the Repacking and Jamming of Crystal-Rich Mushes, Geophysical Research Letters, 49(19), e2022GL100040, 2022.

Jeffery, A. J., and Gertisser, R.: Peralkaline felsic magmatism of the Atlantic islands, Frontiers in Earth Science, 6-145, 2018.

Jung, J.: Géologie, Géomorphologie et Structure Profonde du Massif Central Français, Plein Air Service, Éditions Scientifiques, 358-363, 1971.

Katz, R. F., Spiegelman, M., and Holtzman, B.: The dynamics of melt and shear localization in partially molten aggregates, Nature, 442(7103), 676-679, 2006.

Kennedy, B. M., Holohan, E. P., Stix, J., Gravley, D. M., Davidson, J. R., Cole, J. W. and Burchardt S.: Volcanic and igneous plumbing systems of caldera volcanoes, In Volcanic and Igneous Plumbing Systems, Elsevier, 259-284, 2018.

Koenders, M. A., and Petford, N.: Shear-induced pressure changes and seepage phenomena in a deforming porous layer-III, Geophysical Journal International, 171(2), 943-953, 2007.

Lacroix, A.: Sur l'existence de la låvénite dans les phonolites néphéliniques de la Haute-Loire, Bulletin de Minéralogie, 14(1), 15-16, 1891.

Laporte, D., Lambart, S., Schiano, P., and Ottolini, L.: Experimental derivation of nepheline syenite and phonolite liquids by partial melting of upper mantle peridotites, Earth Plante. Sci. Lett., 404, 319-331, 2014.

Laumonier, M., Arbaret, L., Burgisser, A., and Champallier, R.: Porosity redistribution enhanced by strain localization in crystal-rich magmas, Geology, 39(8), 715-718, 2011.

Legendre, C., Maury, R. C., Caroff, M., Guillou, H., Cotton, J., Chauvel, C., Bollinger, C., Hémond, C., Guille, G., Blais, S. Rossi, P., and Savanier, D.: Origin of exceptionally abundant phonolites

on Ua Pou island (Marquesas, French Polynesia): partial melting of basanites followed by crustal contamination, J. Petrol., 46, 1925-1962, 2005.

Lejeune, A. M., and Richet, P.: Rheology of crystal-bearing silicate melts: An experimental study at high viscosities, Journal of Geophysical Research: Solid Earth, 100(B3), 4215-4229, 1995.

Le Bas, M. J., Le Maitre, R. W., Streickeisen, A., and Zanettin, B.: A classification of igneous rocks and glossary terms, IUGS and Blackwell Sientific Pub., 1986.

Macdonald, R., White, J. C., Belkin, H. E.: Peralkaline silicic extrusive rocks: magma genesis, evolution, plumbing systems and eruption, Comptes Rendus, Géoscience, Tome 353 no. S2, 7-59, 2021.

Malcles, O., Vernant, P., Chéry, J., Camps P., Cazes, G., Ritz, J. F., and Fink D.: Determining the Plio-Quaternary uplift of the southern French Massif Central; a new insight for intraplate orogen dynamics, Solid Earth, 11, 241-258, 2020.

Marks, M. A., Hettmann, K., Schilling, J., Frost, B. R. and Markl, G.: The mineralogical diversity of alkaline igneous rocks: critical factors for the transition from miaskitic to agpaitic phase assemblages. Journal of Petrology, 52(3), 439-455, 2011.

Marks, M. A., and Markl, G.: A global review on agpaitic rocks, Earth-Science Reviews., 173, 229-258, 2017.

Maury, R. C. and Varet, J.: Le volcanisme tertiaire et quaternaire de France. 26th Int. Geol. Congr. (Paris), BRGM, 3, 142, 1980.

Martin, A.M., Médard, E., Righter, K., and Lanzirotti, A.: Intraplate mantle oxidation by volatile-rich silicic magmas, Lithos, 292, 320-333, 2017.

Mergoil, J.: Gisement en filons annulaires de phonolites du Velay (Massif Central français), C.R. Acad. Sc. Paris, t. 267, 12-14, 1968.

Mergoil, J., and Boivin, P.: Le Velay : Son volcanisme et les formations associées. Notice de la carte à 1/100 000, Géologie de la France n°3, 3-96, 1993.

Mergoil-Daniel, J., Labernardière, H., and Maisonneuve, J.: Épisyénites-fenites et source de l'uranium, C. R. Acad. Sc. Paris, t.302, Série II, n°5, 227-232, 1986.

Merle, O., and Michon, L.: The formation of the West European rift: a new model as exemplified by the Massif Central area. Bull. Soc. Géol. France, t. 172, n°2, 213-221, 2001.

Misra, S., Mandal, N., and Chakraborty, C.: Formation of Riedel shear fractures in granular materials: Findings from analogue shear experiments and theoretical analyses, Tectonophysics, 471(3-4), 253-259, 2009.

Morimoto, N.: Nomenclature of pyroxenes, Mineralogical Journal, 14(5), 198-221, 1989.

Paterson, S. R., Fowler Jr, T. K., Schmidt, K. L., Yoshinobu, A. S., Yuan, E. S., and Miller, R. B.: Interpreting magmatic fabric patterns in plutons, Lithos, 44(1-2), 53-82, 1998.

Petford, N.: Which effective viscosity?, Mineralogical Magazine, 73(2), 167-191, 2009.

Picard, D., Arbaret, L., Pichavant, M., Champallier, R., and Launeau, P.: Rheology and microstructure of experimentally deformed plagioclase suspensions, Geology, 39(8), 747-750, 2011.

Philpotts, A. R., and Ague, J. J.: Principles of Igneous and Metamorphic Petrology, Cambridge University Press., 667p, 2009.

Saint Martin, M.: Carte géologique harmonisée du département de l'Ardèche. BRGM/RP-57097-FR, 423p, 2009.

Smith, J. V.: Ductile-brittle transition structures in the basal shear zone of a rhyolite lava flow, eastern Australia. Journal of Volcanology and Geothermal Research 72, 217-223, 1996.

Smith, J. V.: Shear thickening dilatancy in crystal-rich flows, Journal of Volcanology and Geothermal Research, 79(1-2), 1-8, 1997.

Smith, J. V.: Structural analysis of flow related textures in laves, Earth-Science Reviews 57, 279-297, 2002.

Tchalenko, J. S.: The evolution of kink-bands and the development of compression textures in sheared clays", Tectonophysics, 6, 159-174, 1968.

Vernon, R. H.: Review of microstructural evidence of magmatic and solid-state flow, Visual Geosciences, 5, 1-23, 2000.

Vigneresse, J. L., Barbey, P., and Cuney, M.: Rheological transitions during partial melting and crystallization with application to felsic magma segregation and transfer, Journal of Petrology, 37(6), 1579-1600, 1996.

Ward, K. M., Zandt, G., Beck, S. L., Christensen, D. H., and McFarlin, H.: Seismic imaging of the magmatic underpinnings beneath the Altiplano-Puna volcanic complex from the joint inversion of surface wave dispersion and receiver functions, Earth and Planetary Science Letters, 404, 43-53, 2014.

Walters, J. B.: MinPlot: A mineral formula recalculation and plotting program for electron probe microanalysis, Mineralogia, 53(1), 51-66, 2022.

Warr, L. N.: IMA–CNMNC approved mineral symbols, Mineralogical Magazine, 85(3), 291-320, 2021.

Westerman, D., Rocchi, S., Breitkreuz, C., Stevenson, C., and Wilson, P.: Structures related to the emplacement of shallow-level intrusions, In Physical Geology of Shallow Magmatic Systems, Springer, Cham., 83-118, 2017.

Appendices

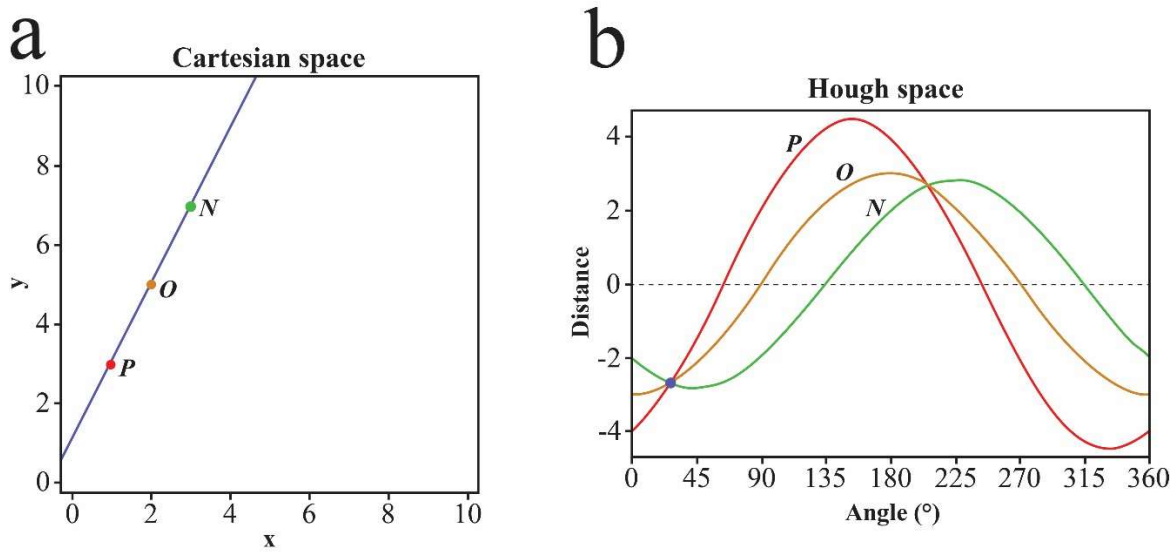

Figure A1. a – Representation of a Cartesian space with 3 points (N, O and P) aligned on a straight line. **b –** Representation of an associated Hough space with the 3 curves (N, O and P) corresponding to the points in Cartesian space and a blue point located at the intersection of the curves at θ ≈ 28° and corresponding to the straight line in Cartesian space.

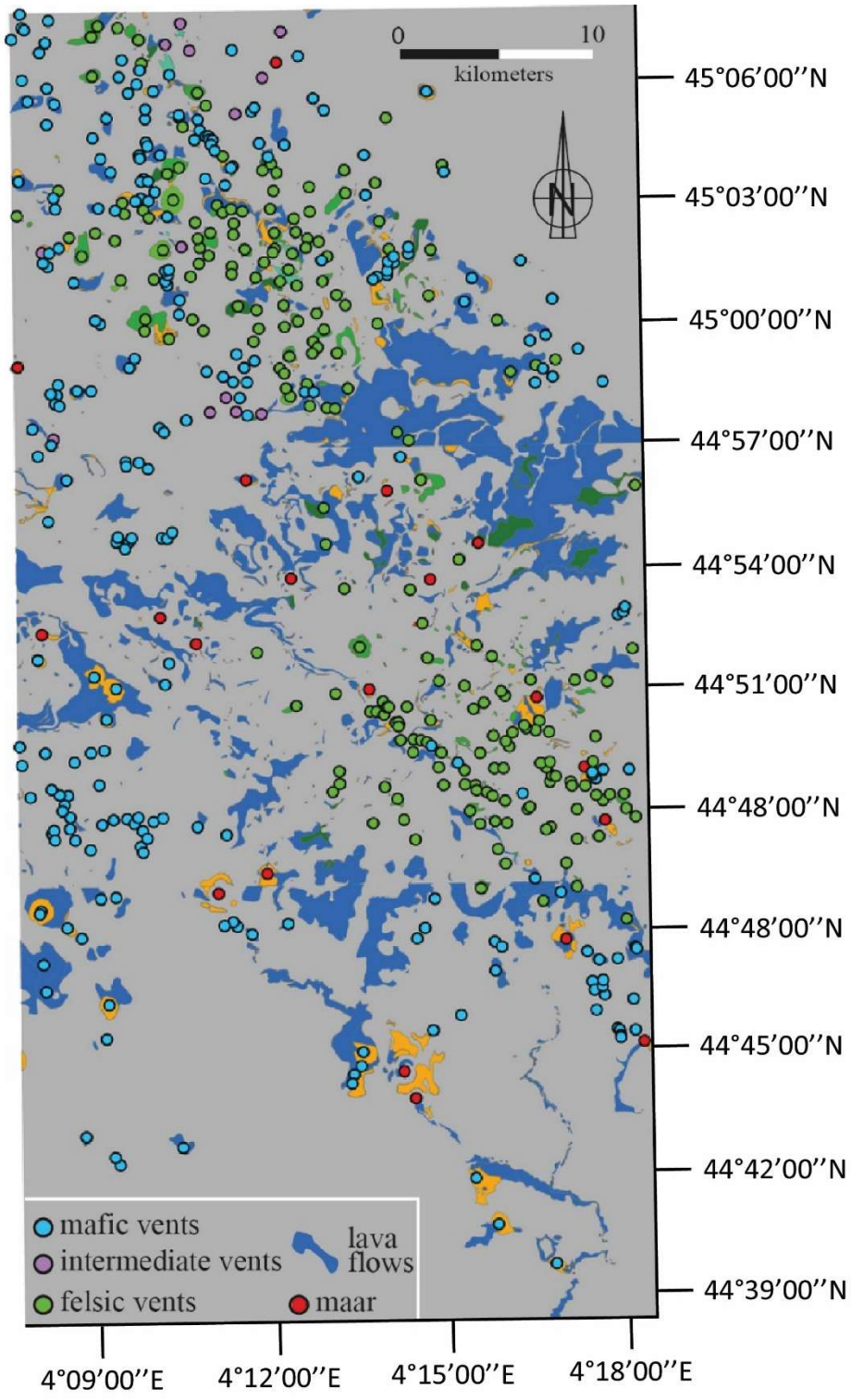

Figure A2. Simplified map of the volcanic formations of the Eastern Velay, including the Emblavès and Boutières grabens, with the positions of the 505 vents used for the Hough transform analysis.

Figure A3. a – Polygenic breccia observed on the right bank of the Eysse along the Eastern margin between the phonolite and the country rock. b – Lens of basalt emplaced in the solidified phonolite a few meters from the margin.

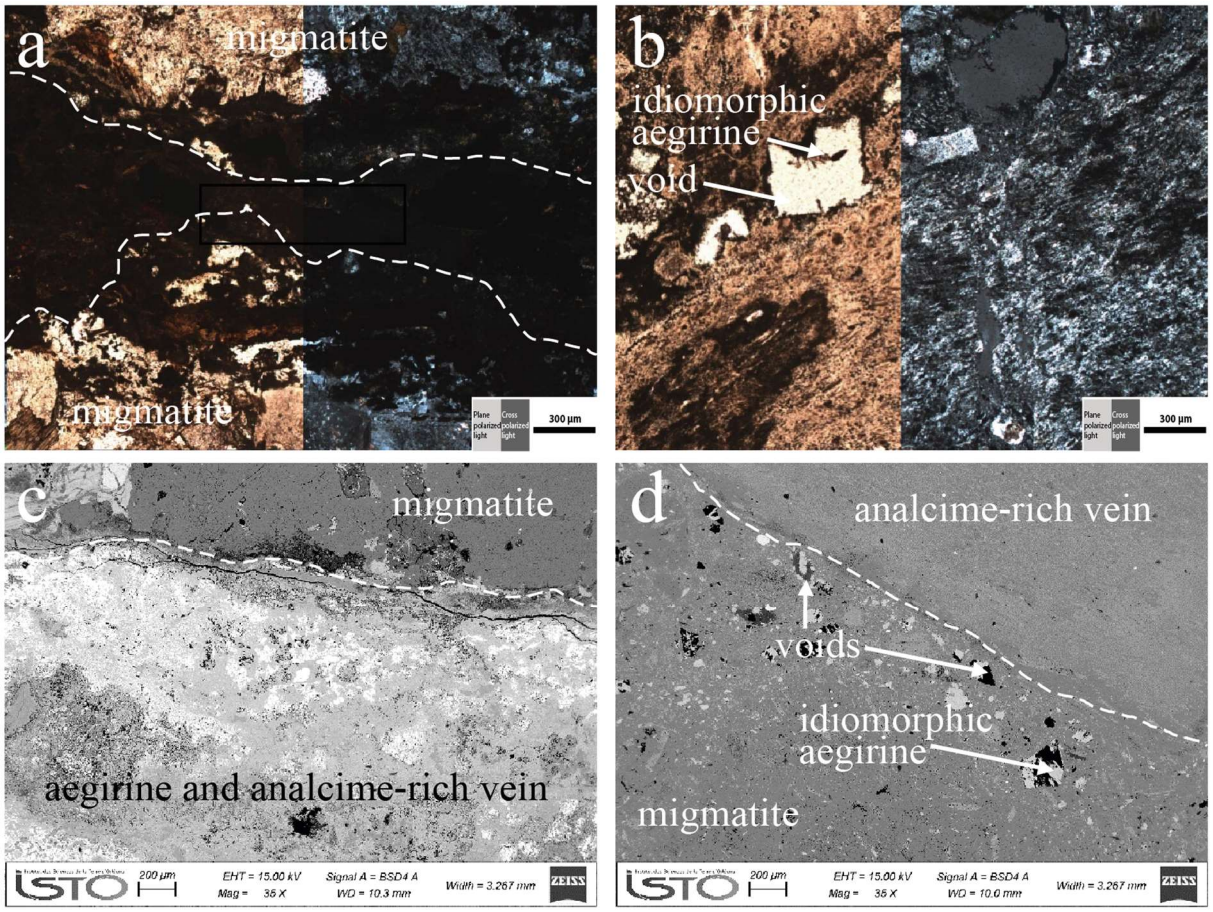

Figure A4. a – More marked vein of aegirine in the fenitized migmatite on the Eastern margin. **b –** Breccia on the Eastern margin comprising fragments of the host rock and phonolite as well as albite injections. **c –** SEM image of the more marked aegirine vein in the fenitized migmatite. d – SEM image of the breccia between the host rock and the phonolite in the Eysse riverbed.

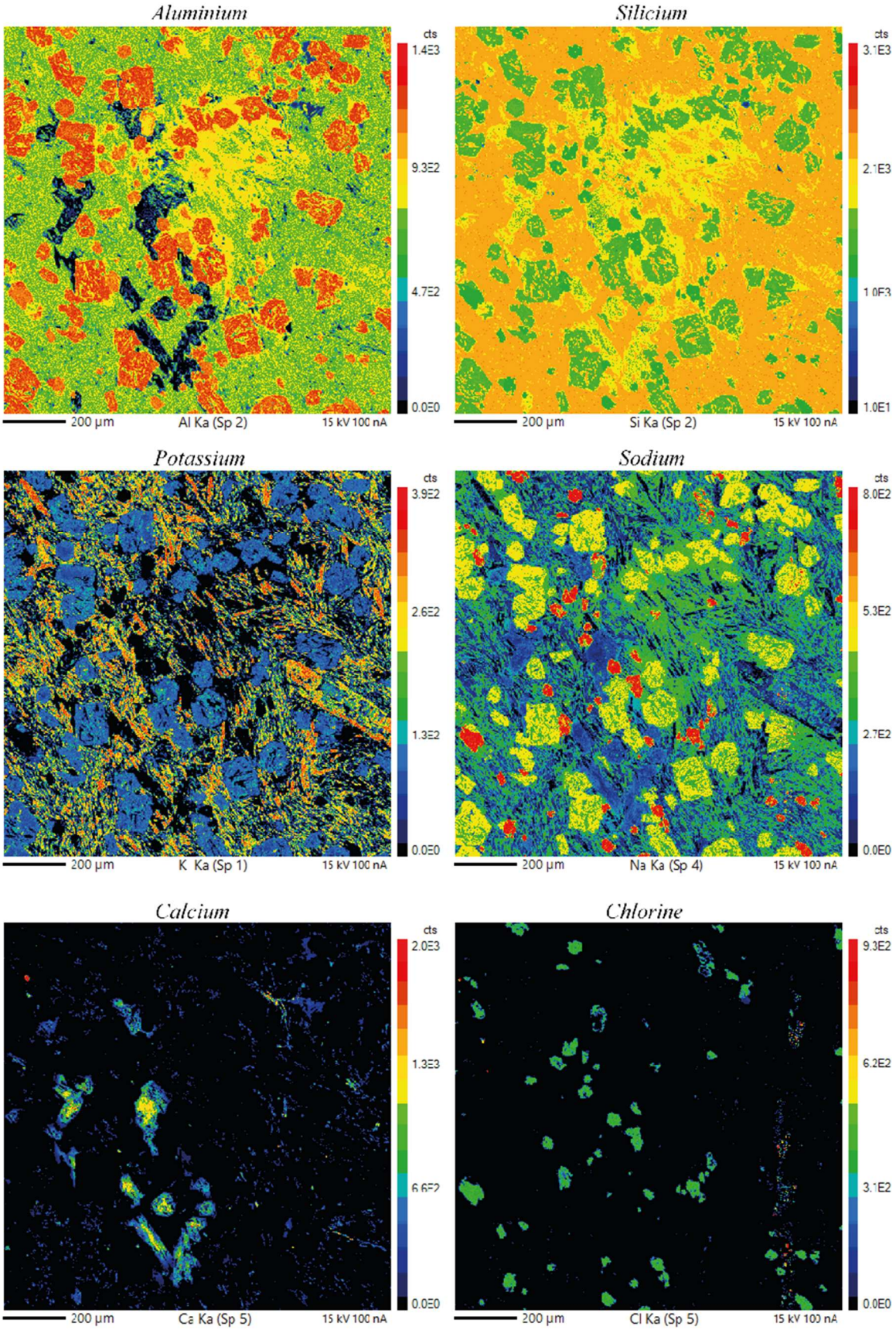
Aluminium
cts
1.4E3
9.3E2
4.7E2
0.0E0
200 µm
Al Ka (Sp 2)
15 kV 100 nA
Silicium
cts
3.1E3
2.1E3
1.0E3
1.0E1
200 µm
Si Ka (Sp 2)
15 kV 100 nA
Potassium
cts
3.9E2
2.6E2
1.3E2
0.0E0
200 µm
K Ka (Sp 1)
15 kV 100 nA
Sodium
cts
8.0E2
5.3E2
2.7E2
0.0E0
200 µm
Na Ka (Sp 4)
15 kV 100 nA
Calcium
cts
2.0E3
1.3E3
0.0E0
200 µm
Ca Ka (Sp 5)
15 kV 100 nA
Chlorine
cts
9.3E2
6.2E2
3.1E2
0.0E0
200 µm
Cl Ka (Sp 5)
15 kV 100 nA

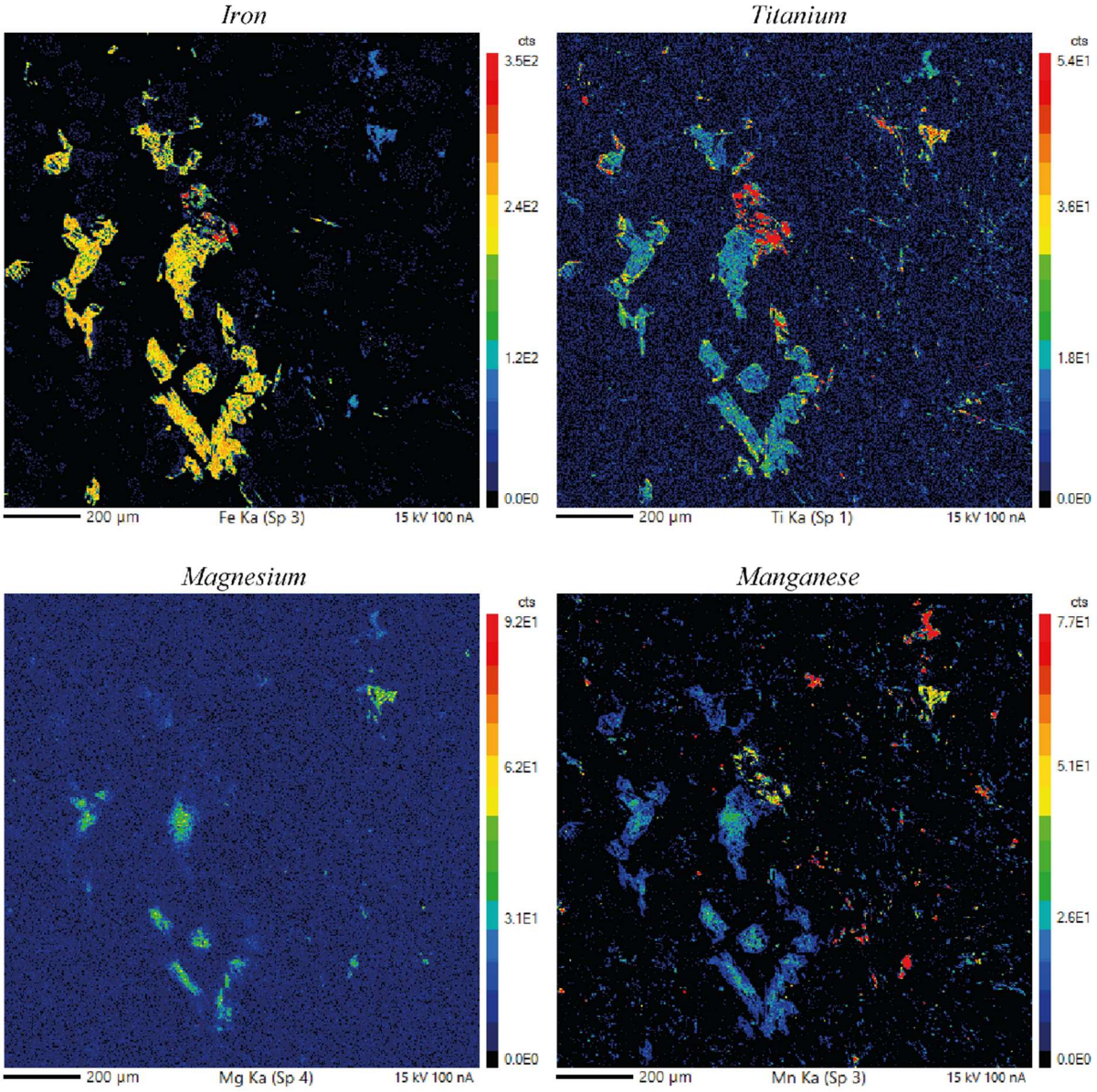

Figure A5. WDS mapping for 10 elements on thin section SA4 (near SA3; Western margin). Maps of aluminum, silicium, sodium and chlorine reveal the presence of feldspathoids. In particular, the sodium and chlorine maps allow distinguish between nepheline and sodalite, the latter being richer in sodium and containing chlorine. The potassium map reveals the presence of alkali feldspars. Calcium, iron and magnesium maps reveal the presence of aegirine. The titanium and iron maps, reveal aenigmatite.

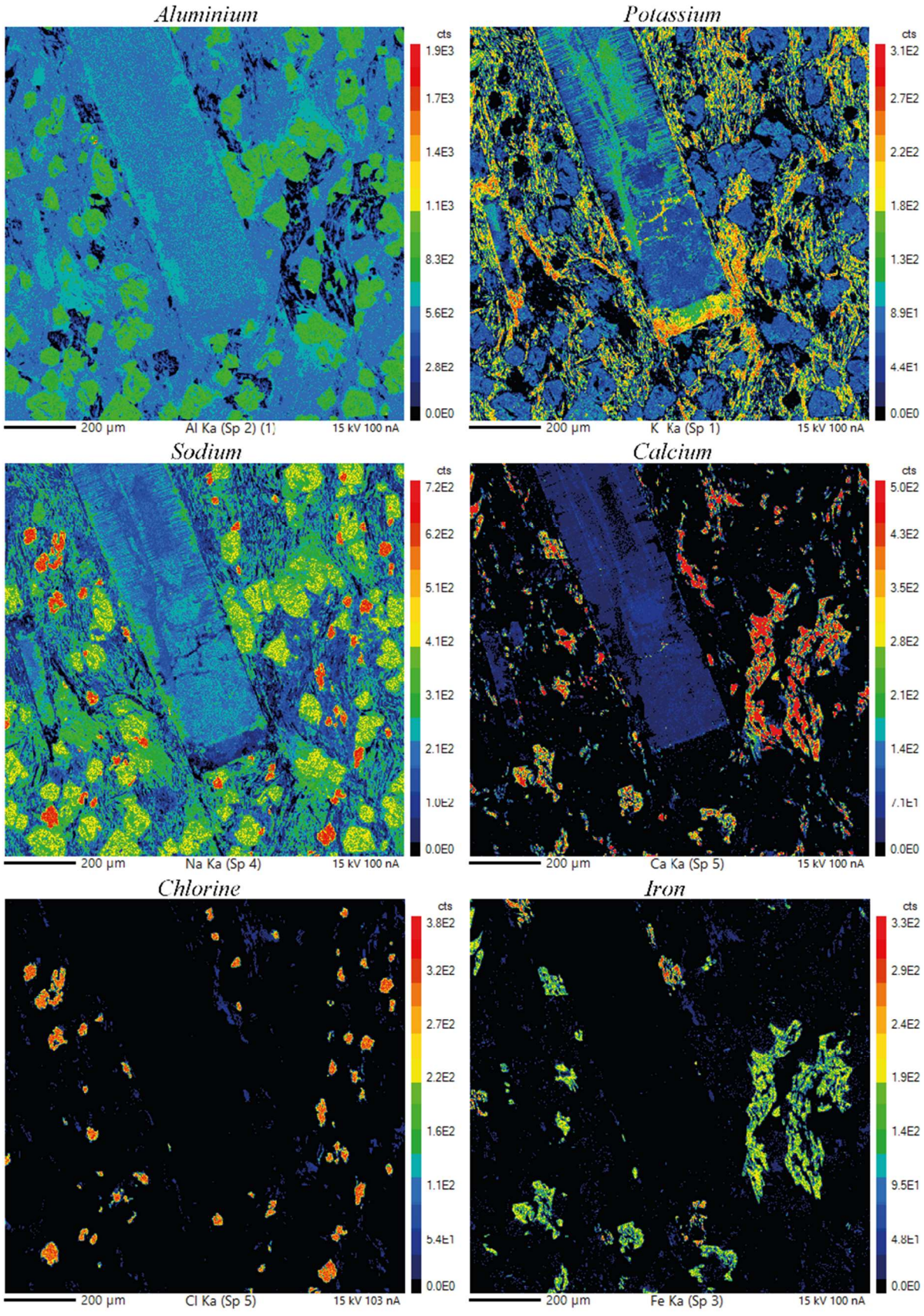
Aluminium
cts
1.9E3
1.7E3
1.4E3
1.1E3
8.3E2
5.6E2
2.8E2
0.0E0
200 µm
Al Ka (Sp 2) (1)
15 kV 100 nA
Potassium
cts
3.1E2
2.7E2
2.2E2
1.8E2
1.3E2
8.9E1
4.4E1
0.0E0
200 µm
K Ka (Sp 1)
15 kV 100 nA
Sodium
cts
7.2E2
6.2E2
5.1E2
4.1E2
3.1E2
2.1E2
1.0E2
0.0E0
200 µm
Na Ka (Sp 4)
15 kV 100 nA
Calcium
cts
5.0E2
4.3E2
3.5E2
2.8E2
2.1E2
1.4E2
7.1E1
0.0E0
200 µm
Ca Ka (Sp 5)
15 kV 100 nA
Chlorine
cts
3.8E2
3.2E2
2.7E2
2.2E2
1.6E2
1.1E2
5.4E1
0.0E0
200 µm
Cl Ka (Sp 5)
15 kV 103 nA
Iron
cts
3.3E2
2.9E2
2.4E2
1.9E2
1.4E2
9.5E1
4.8E1
0.0E0
200 µm
Fe Ka (Sp 3)
15 kV 100 nA

Figure A6. WDS mapping for 6 elements on thin section SA4 (Western margin). These maps reveal the presence of the same minerals as in Fig. A5, but also show variations in composition within an alkali feldspar phenocryst. The potassium-rich overgrowth of this idiomorphic feldspar is clearly visible.

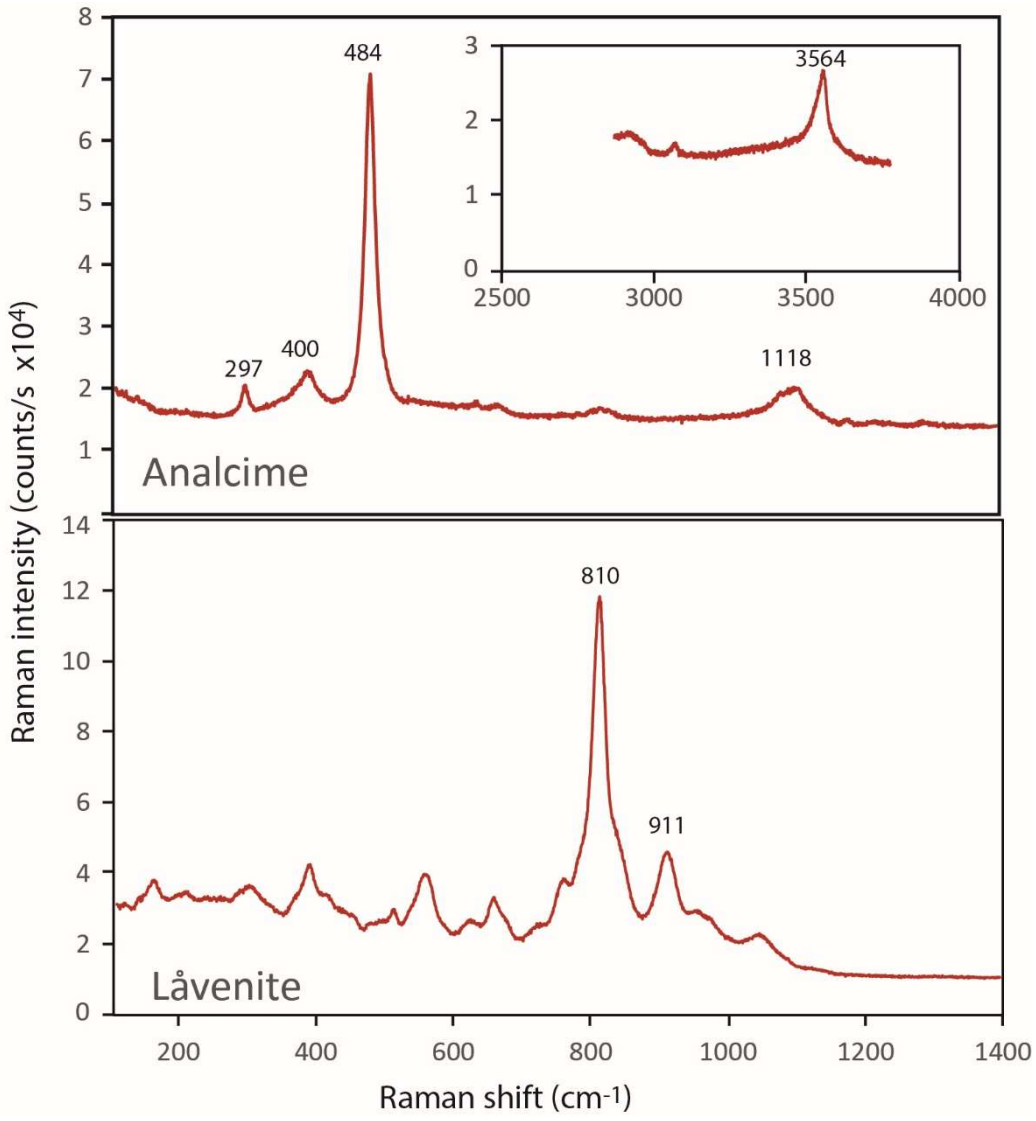

Figure A7. Raman spectra of analcime and låvenite measured in SA3 (see location in Fig. 14a).

	1	2	3	4	5	6	7	8	9	10	11	12	13	14	15
Sample	SA3	SA3	SA3	SA3	SA5	SA5	SA5	SA5	SA5	SA5	SA5	SA5	SA9	SA9	SA9
SiO_2	66.94	66.65	64.86	65.49	66.90	66.72	66.42	66.72	67.20	67.50	65.74	65.63	65.09	66.58	67.37
TiO_2	0.06	0.00	0.00	0.07	0.00	0.05	0.00	0.00	0.02	0.00	0.03	0.02	0.05	0.05	0.03
Al_2O_3	18.93	19.41	18.53	18.66	19.20	18.68	18.95	19.24	19.02	19.32	18.46	18.46	17.21	19.90	19.54
FeO_{TOT}	0.15	0.02	0.04	0.35	0.35	0.26	0.49	0.03	0.20	0.00	0.15	0.03	0.90	0.09	0.12
MnO	0.00	0.00	0.02	0.07	0.01	0.00	0.02	0.00	0.00	0.00	0.09	0.13	0.01	0.05	0.12
MgO	0.00	0.00	0.00	0.00	0.01	0.02	0.00	0.00	0.00	0.00	0.00	0.01	0.01	0.00	0.01
CaO	0.12	0.20	0.00	0.00	0.08	0.04	0.08	0.15	0.17	0.26	0.00	0.01	0.00	0.64	0.58
Na_2O	6.23	6.63	0.63	2.41	6.38	4.72	7.00	6.63	7.02	7.28	1.08	0.89	0.40	8.10	8.18
K_2O	7.27	7.02	16.28	13.37	6.83	9.75	6.66	7.08	6.35	5.93	14.37	14.80	15.97	4.23	4.25
Total	**99.70**	**99.93**	**100.36**	**100.42**	**99.76**	**100.24**	**99.62**	**99.85**	**99.98**	**100.29**	**99.92**	**99.98**	**99.64**	**99.64**	**100.20**
Number of ions on the basis of 8 oxygens															
Si	3.002	2.983	2.990	2.989	2.995	3.005	2.987	2.989	2.999	2.996	3.013	3.011	3.027	2.963	2.981
Ti	0.000	0.000	0.000	0.003	0.000	0.002	0.000	0.000	0.001	0.000	0.001	0.001	0.001	0.002	0.001
Al	1.001	1.024	1.007	1.004	1.013	0.992	1.005	1.016	1.000	1.010	0.997	0.998	0.943	1.044	1.019
Σa	**4.003**	**4.007**	**3.997**	**3.996**	**4.008**	**3.999**	**3.992**	**4.005**	**4.000**	**4.006**	**4.011**	**4.010**	**3.971**	**4.009**	**4.001**
Fe_{TOT}	0.005	0.001	0.000	0.004	0.013	0.010	0.000	0.001	0.008	0.000	0.006	0.001	0.035	0.003	0.004
Mn	0.000	0.000	0.001	0.003	0.000	0.000	0.000	0.000	0.000	0.000	0.003	0.001	0.000	0.002	0.005

Mg	0.000	0.000	0.000	0.000	0.000	0.001	0.000	0.000	0.000	0.000	0.000	0.001	0.001	0.000	0.001
Ca	0.006	0.010	0.000	0.000	0.004	0.002	0.040	0.007	0.008	0.012	0.000	0.000	0.000	0.030	0.028
Na	0.542	0.575	0.056	0.213	0.553	0.412	0.610	0.576	0.607	0.626	0.096	0.079	0.036	0.699	0.702
K	0.416	0.401	0.957	0.778	0.390	0.560	0.382	0.405	0.361	0.336	0.840	0.863	0.948	0.240	0.240
Σb	**0.969**	**0.987**	**1.014**	**0.998**	**0.960**	**0.985**	**1.032**	**0.989**	**0.984**	**0.974**	**0.945**	**0.945**	**1.020**	**0.974**	**0.980**
Total	**4.972**	**4.994**	**5.011**	**4.994**	**4.968**	**4.984**	**5.024**	**4.994**	**4.984**	**4.980**	**4.956**	**4.955**	**4.991**	**4.983**	**4.981**
(mol%)															
Or	43.2	40.6	94.5	78.5	41.2	57.5	38.4	41.0	37.0	34.3	89.8	91.6	96.4	24.8	24.7
Ab	56.2	58.4	5.5	21.5	58.4	42.3	61.2	58.3	62.2	64.3	10.2	8.4	3.6	72.1	72.4
An	0.6	1.0	0.0	0.0	0.4	0.2	0.4	0.7	0.8	1.2	0.0	0.0	0.0	3.1	2.9

Table A1. Representative microprobe analyses of alkali feldspars (in wt.%). Total iron is given in FeO. Cation values have been recalculated from the number of oxygens. Σa = Si + Al + Ti. Σb = FeTOT + Mn + Mg + Ca + Na + K.

	1	2	3	4	5
Sample	SA3	SA3	SA3	SA9	SA9
SiO_2	68.58	68.30	68.64	69.07	69.09
TiO_2	0.04	0.05	0.00	0.00	0.00
Al_2O_3	19.92	19.41	19.87	19.92	20.09
FeO_{TOT}	0.10	0.11	0.00	0.09	0.10
MnO	0.00	0.00	0.11	0.00	0.10
MgO	0.00	0.00	0.00	0.00	0.00
CaO	0.59	0.02	0.04	0.00	0.01
Na_2O	11.17	11.28	10.65	11.33	11.01
K_2O	0.15	0.31	0.30	0.47	0.18
Total	**100.55**	**99.48**	**99.61**	**100.88**	**100.58**
Number of ions on the basis of 8 oxygens					
Si	2.980	2.998	3.000	2.991	2.993
Ti	0.001	0.002	0.000	0.000	0.000
Al	1.021	1.004	1.024	1.017	1.026
Σa	**4.002**	**4.004**	**4.024**	**4.008**	**4.019**
Fe_{TOT}	0.004	0.004	0.000	0.003	0.003
Mn	0.000	0.000	0.004	0.000	0.004
Mg	0.000	0.000	0.000	0.000	0.000
Ca	0.028	0.001	0.002	0.000	0.001
Na	0.941	0.960	0.902	0.951	0.925
K	0.008	0.017	0.016	0.026	0.010
Σb	**0.981**	**0.982**	**0.924**	**0.980**	**0.943**
Total	**4.983**	**4.986**	**4.948**	**4.988**	**4.962**
(mol%)					
Or	0.9	1.8	1.8	2.7	1.0
Ab	96.3	98.1	98.0	97.3	98.9
An	2.8	0.1	0.2	0.0	0.1

Table A2. Representative microprobe analyses of albites (in wt.%).

	1	2	3	4	5	6	7
Sample	SA3	SA3	SA3	SA3	SA3	SA8	SA8
SiO_2	48.56	50.14	47.46	50.62	50.45	50.05	50.62
TiO_2	1.27	0.00	0.00	0.03	0.00	0.93	0.84
Al_2O_3	0.96	0.72	1.15	0.61	0.68	0.85	0.75
FeO_{TOT}	25.95	26.35	25.55	27.11	26.99	28.05	27.77
MnO	2.83	1.14	1.71	0.89	0.82	1.96	1.55
MgO	0.39	0.47	0.56	0.22	0.46	0.34	0.18
CaO	13.53	10.99	14.48	8.48	10.66	8.79	7.19
Na_2O	5.37	7.16	5.06	8.42	7.16	7.91	9.47
K_2O	0.05	0.02	0.00	0.00	0.00	0.05	0.05
Total	**98.91**	**96.99**	**95.97**	**96.38**	**97.22**	**98.93**	**98.42**
Number of ions on the basis of 6 oxygens							
Si	2.007	2.089	2.019	2.118	2.096	2.060	2.087
Al	0.000	0.000	0.000	0.000	0.000	0.000	0.000
Σa	**2.007**	**2.089**	**2.019**	**2.118**	**2.096**	**2.060**	**2.087**
Al	0.047	0.035	0.058	0.030	0.034	0.041	0.037
Ti	0.039	0.000	0.000	0.001	0.000	0.029	0.026
Fe^{3+}	0.424	0.524	0.464	0.591	0.506	0.592	0.703
Fe^{2+}	0.441	0.355	0.410	0.311	0.393	0.327	0.199
Mn	0.099	0.040	0.062	0.032	0.029	0.068	0.054
Mg	0.024	0.029	0.036	0.014	0.028	0.021	0.011
Σb	**1.074**	**0.983**	**1.030**	**0.979**	**0.990**	**1.078**	**1.030**
Ca	0.599	0.491	0.660	0.380	0.474	0.388	0.317
Na	0.431	0.578	0.417	0.683	0.577	0.632	0.757
K	0.003	0.001	0.000	0.000	0.000	0.003	0.002
Σc	**1.033**	**1.070**	**1.077**	**1.063**	**1.051**	**1.023**	**1.076**
Total	**4.114**	**4.142**	**4.126**	**4.160**	**4.137**	**4.161**	**4.193**

(mol%)

Or	42.9	53.2	43.8	61.4	51.8	70.9	62.0
Ab	4.5	3.5	5.2	3.0	3.3	3.5	4.7
An	52.6	43.3	51.0	35.6	44.9	25.6	33.3

Table A3. Representative microprobe analyses of pyroxenes (in wt.%). Σa = Si + Al. Σb = Al + Ti + Fe^{3+} + Fe^{2+} + Mn + Mg. Σc = Ca + Na + K. Al is distributed so that the sum of the cations at site "a" is as close as possible to 2. The Fe^{2+} / Fe^{3+} distinction was made using the method of Droop (1987). The aegirine (Aeg), jadeite (Jd) and Quad (Wo, En, Fs) poles were calculated with the program of Walters (2022).

	1	2	3	4	5
Sample	SA3	SA3	SA3	SA3	SA3
SiO_2	40.33	38.25	38.27	38.96	38.50
TiO_2	7.94	7.87	7.81	7.94	7.22
Al_2O_3	1.09	1.15	1.11	1.00	1.51
FeO_{TOT}	38.84	39.98	39.97	40.32	41.27
MnO	4.58	3.91	4.36	4.38	3.77
MgO	0.11	0.12	0.11	0.08	0.04
CaO	0.35	0.45	0.44	0.30	0.59
Na_2O	7.04	6.99	7.05	6.82	6.84
K_2O	0.07	0.07	0.02	0.00	0.00
Total	**100.35**	**98.79**	**99.14**	**99.80**	**99.74**
Number of ions on the basis of 20 oxygens					
Si	5.832	5.683	5.693	5.724	5.680
Al	0.168	0.202	0.193	0.173	0.262
Fe^{3+}	0.000	0.115	0.114	0.103	0.058
Σa	**6.000**	**6.000**	**6.000**	**6.000**	**6.000**
Al	0.019	0.000	0.000	0.000	0.000
Fe^{3+}	0.573	0.859	0.877	0.691	0.962
Ti	0.864	0.880	0.872	0.878	0.801
Fe^{2+}	4.058	3.873	3.810	4.063	3.943
Mn	0.561	0.493	0.548	0.545	0.472
Mg	0.023	0.026	0.023	0.017	0.009
Ca	0.000	0.000	0.000	0.000	0.000
Σb	**6.098**	**6.131**	**6.130**	**6.194**	**6.187**
Ca	0.053	0.071	0.071	0.047	0.093
Na	1.973	2.013	2.029	1.944	1.957
K	0.012	0.013	0.004	0.000	0.000
Σc	**2.038**	**2.097**	**2.104**	**1.991**	**2.050**
Total	**14.136**	**14.228**	**14.234**	**14.185**	**14.237**

Table A4. Representative microprobe analyses of aenigmatites (in wt.%). Σa = Si + Al + Fe^{3+}. Σb = Al + Fe^{3+} + Ti + Fe^{2+} + Mn + Mg + Ca. Σc = Ca + Na + K. Al and Fe^{3+} are distributed so that the sum of the cations at site “a” is equal to 6.

	1	2	3
Sample	SA3	SA5	SA5
SiO_2	0.02	0.10	0.11
TiO_2	14.06	7.43	7.66
Al_2O_3	0.76	0.15	0.18
FeO_{TOT}	76.18	83.84	85.54
MnO	5.02	2.71	2.90
MgO	0.04	0.00	0.00
CaO	0.02	0.03	0.02
Na_2O	0.03	0.00	0.00
K_2O	0.03	0.00	0.00
Total	**96.16**	**94.26**	**96.41**
Number of ions on the basis of 32 oxygens			
Si	0.007	0.040	0.041
Ti	3.734	2.126	2.141
Al	0.316	0.066	0.079
Σa	**4.057**	**2.232**	**2.261**
Fe^{3+}	9.372	12.459	12.419
Fe^{2+}	9.829	9.031	9.015
Mn	1.502	0.874	0.914
Mg	0.023	0.000	0.002
Ca	0.007	0.010	0.008
Na	0.022	0.000	0.000
K	0.000	0.000	0.000
Σb	**20.755**	**22.374**	**22.358**
Total	**24.812**	**24.606**	**24.619**

Table A5. Representative microprobe analyses of magnetite-ulvöspinels (in wt.%). Σa = Si + Ti + Al. Σb = Fe^{3+} + Fe^{2+} + Mn + Mg + Ca + Na + K.

	1	2	3	4	5	6	7	8	9	10	11	12	13
Sample	SA3	SA3	SA3	SA3	SA3	SA3	SA3	SA3	SA3	SA5	SA5	SA5	SA5
SiO_2	45.98	46.85	45.89	48.97	47.48	46.09	46.62	45.62	47.78	44.99	47.42	45.47	45.64
TiO_2	0.09	0.03	0.00	0.00	0.00	0.06	0.00	0.00	0.00	0.09	0.00	0.00	0.17
Al_2O_3	33.59	32.53	32.06	30.41	31.09	32.06	32.87	31.32	29.97	31.00	30.16	31.15	31.06
FeO_{TOT}	1.01	1.27	1.32	1.13	0.96	1.33	1.24	1.07	1.31	1.49	1.10	1.15	1.59
MnO	0.08	0.00	0.02	0.03	0.04	0.01	0.00	0.03	0.00	0.04	0.06	0.00	0.00
MgO	0.03	0.00	0.01	0.02	0.00	0.01	0.00	0.00	0.01	0.00	0.01	0.00	0.01
CaO	0.00	0.01	0.00	0.00	0.00	0.01	0.00	0.04	0.06	0.07	0.00	0.00	0.00
Na_2O	14.37	13.64	16.52	16.05	16.39	15.89	14.85	16.38	16.30	16.19	16.21	16.47	16.51
K_2O	5.42	4.80	5.16	3.36	4.40	4.97	4.56	4.99	4.00	5.28	4.13	5.00	5.10
Total	**100.57**	**99.13**	**100.98**	**99.97**	**100.36**	**100.43**	**100.14**	**99.45**	**99.43**	**99.15**	**99.09**	**99.24**	**100.08**
Number of ions on the basis of 32 oxygens													
Si	8.664	8.892	8.695	9.196	8.966	8.744	8.791	8.760	9.097	8.707	9.059	8.758	8.742
Ti	0.012	0.004	0.000	0.000	0.000	0.009	0.000	0.000	0.000	0.013	0.000	0.000	0.025
Al	7.461	7.277	7.159	6.731	6.920	7.168	7.306	7.089	6.726	7.072	6.971	7.072	7.013
Σa	**16.137**	**16.173**	**15.854**	**15.927**	**15.886**	**15.921**	**16.097**	**15.849**	**15.823**	**15.792**	**16.030**	**15.830**	**15.780**
Fe_{TOT}	0.159	0.202	0.210	0.177	0.152	0.211	0.195	0.171	0.209	0.241	0.176	0.185	0.255
Mn	0.013	0.000	0.003	0.004	0.006	0.002	0.000	0.005	0.000	0.007	0.010	0.000	0.000

Mg	0.007	0.000	0.002	0.006	0.000	0.002	0.000	0.001	0.002	0.000	0.002	0.000	0.002
Ca	0.000	0.001	0.000	0.000	0.000	0.002	0.000	0.009	0.012	0.015	0.000	0.000	0.000
Na	5.252	5.019	6.068	5.843	6.003	5.847	5.428	6.099	6.018	6.076	6.005	6.151	6.132
K	1.303	1.162	1.248	0.805	1.059	1.204	1.098	1.222	0.972	1.304	1.007	1.229	1.246
Σb	**6.734**	**6.384**	**7.531**	**6.835**	**7.220**	**7.268**	**6.721**	**7.507**	**7.213**	**7.643**	**7.200**	**7.565**	**7.635**
Total	**22.871**	**22.557**	**23.385**	**22.762**	**23.106**	**23.189**	**22.818**	**23.356**	**23.036**	**23.435**	**23.230**	**23.395**	**23.415**

Table A6. Representative microprobe analyses of nephelines (in wt.%). Σa = Si + Ti + Al. Σb = FeTOT + Mn + Mg + Ca + Na + K.

	1	2	3	4	5	6	7
Sample	SA3	SA3	SA3	SA3	SA3	SA3	SA3
SiO_2	36.76	36.61	36.47	36.94	37.76	36.97	37.70
TiO_2	0.00	0.03	0.02	0.03	0.02	0.06	0.08
Al_2O_3	30.08	29.68	29.47	29.95	30.77	30.63	30.21
FeO_{TOT}	0.80	1.07	1.03	1.17	0.51	0.66	0.64
MnO	0.01	0.05	0.06	0.05	0.01	0.02	0.07
MgO	0.00	0.00	0.00	0.00	0.00	0.00	0.00
CaO	0.00	0.00	0.02	0.08	0.00	0.07	0.00
Na_2O	25.28	25.47	24.80	25.02	25.71	23.61	24.87
K_2O	0.07	0.07	0.10	0.06	0.11	0.06	0.03
Cl	7.05	7.13	7.01	7.08	6.91	6.96	7.33
Total	**100.05**	**100.11**	**98.98**	**100.38**	**101.80**	**99.04**	**100.93**
Number of ions on the basis of 24 oxygens							
Si	5.807	5.803	5.831	5.822	5.833	5.847	5.888
Ti	0.000	0.003	0.002	0.004	0.002	0.007	0.009
Al	5.601	5.545	5.553	5.564	5.602	5.710	5.562
Σa	**11.408**	**11.351**	**11.386**	**11.390**	**11.437**	**11.564**	**11.459**
Fe_{TOT}	0.105	0.142	0.138	0.155	0.066	0.087	0.083
Mn	0.002	0.006	0.009	0.007	0.001	0.002	0.009
Mg	0.000	0.000	0.000	0.000	0.000	0.000	0.000
Ca	0.000	0.000	0.003	0.013	0.000	0.012	0.000
Na	7.743	7.828	7.688	7.646	7.700	7.240	7.532
K	0.015	0.015	0.020	0.012	0.021	0.012	0.007
Cl	1.889	1.916	1.900	1.891	1.809	1.866	1.940
Σb	**9.754**	**9.907**	**9.758**	**9.724**	**9.597**	**9.219**	**9.571**
Total	**21.162**	**21.258**	**21.144**	**21.114**	**21.034**	**20.783**	**21.030**

Table A7. Representative microprobe analyses of sodalites (in wt.%). Σa = Si + Ti + Al. Σb = FeTOT + Mn + Mg + Ca + Na + K + Cl.

	1	2	3	4	5	6	7	8	9	10	11
Sample	SA3	SA3	SA3	SA3	SA3	SA5	SA5	SA5	SA5	SA5	SA9
SiO_2	56.63	56.44	58.04	56.88	57.91	54.43	52.80	53.94	53.90	54.99	57.58
TiO_2	0.00	0.00	0.08	0.03	0.03	0.00	0.01	0.00	0.00	0.00	0.00
Al_2O_3	22.89	22.51	22.20	23.73	24.00	23.07	22.48	23.03	22.64	23.37	24.32
FeO_{TOT}	0.00	0.07	0.17	0.25	0.29	0.06	0.08	0.21	0.00	0.36	0.11
MnO	0.00	0.00	0.03	0.03	0.10	0.01	0.04	0.00	0.00	0.00	0.00
MgO	0.00	0.01	0.02	0.01	0.00	0.00	0.00	0.00	0.00	0.00	0.03
CaO	0.02	0.03	0.02	0.54	0.01	0.01	0.00	0.00	0.01	0.00	0.13
Na_2O	9.13	10.13	9.30	8.40	7.64	12.78	13.51	13.09	13.34	11.90	8.18
K_2O	0.15	0.15	0.06	0.19	2.03	0.08	0.14	0.16	0.08	0.08	0.17
H_2O	nd	nd	nd	nd	nd	nd	nd	nd	nd	nd	nd
Total	**88.82**	**89.34**	**89.92**	**90.06**	**92.01**	**90.44**	**89.06**	**90.43**	**89.97**	**90.70**	**90.52**
Number of ions on the basis of 96 framework oxygens											
Si	33.415	33.300	33.825	33.124	33.221	32.220	31.948	32.047	32.175	32.350	33.202
Ti	0.000	0.000	0.037	0.014	0.013	0.000	0.005	0.000	0.000	0.000	0.000
Al	15.919	15.658	15.248	16.287	16.231	16.099	16.033	16.132	15.930	16.205	16.532
Σa	**49.334**	**48.958**	**49.110**	**49.425**	**49.465**	**48.319**	**47.986**	**48.179**	**48.105**	**48.555**	**49.734**
Fe_{TOT}	0.000	0.035	0.082	0.119	0.140	0.030	0.043	0.104	0.000	0.177	0.052

Mn	0.000	0.000	0.014	0.016	0.048	0.008	0.020	0.000	0.000	0.000	0.000
Mg	0.000	0.005	0.018	0.012	0.000	0.000	0.000	0.000	0.001	0.000	0.026
Ca	0.011	0.022	0.010	0.336	0.005	0.008	0.000	0.003	0.006	0.000	0.080
Na	10.448	11.585	10.515	9.481	8.501	14.674	15.856	15.080	15.438	13.572	9.151
K	0.110	0.116	0.045	0.140	1.487	0.062	0.107	0.121	0.059	0.056	0.128
Σb	**10.569**	**11.763**	**10.684**	**10.104**	**10.181**	**14.782**	**16.026**	**15.308**	**15.504**	**13.805**	**9.437**
H_2O	nd	nd	nd	nd	nd	nd	nd	nd	nd	nd	nd
Total	**59.903**	**60.721**	**59.794**	**59.529**	**59.646**	**63.101**	**64.012**	**63.487**	**63.609**	**62.360**	**59.171**

Table A8. Representative microprobe analyses of analcimes (in wt.%). Σa = Si + Ti + Al. Σb = FeTOT + Mn + Mg + Ca + Na + K. Water is not analyzed (nd.: no data).

Monica SPAGNOLI

Ségrégation des liquides tardifs dans les mush magmatiques : approche expérimentale dynamique à haute pression

La différenciation planétaire ainsi que l'impact sociétal de l'activité volcanique sont tous liés aux transferts des magmas dans la croûte, ces derniers restant peu contraints. Depuis quelques années un changement de paradigme apparaît : au lieu d'être essentiellement liquides, les corps magmatiques pourraient être constitués pour en majorité par des mush : un mélange riche en cristaux (>>50%) constituants une charpente solide faible emprisonnant des poches de liquide plus ou moins connectées (Bachmann & Bergantz, 2004, 2008). Ce modèle a récemment été généralisé à l'ensemble de la croute continentale (Trans-Crustal Magmatic System; Cashman et al., 2017).
Les évidences géologiques mettent en avant que l'ubiquiste différenciation par extraction des liquides silicatés depuis les mush semble contrôlée par la physique des chaines de forces dans la charpente cristalline. Cette thèse a pour ambition de contraindre le comportement mécanique (rhéologie, structuration) des magmas riches en cristaux en s'appuyant sur une approche expérimentale en déformation à HP-HT. Les chaines de forces et leur influence sur la rhéologie des mush et sur l'initiation de la localisation de la déformation ont été caractérisées. On se concentre particulièrement sur l'effet de cette localisation de la déformation sur les capacités de ségrégation des liquides et fluides tardifs.
La stratégie novatrice de cette thèse est d'utiliser un approche expérimentale couplée à une étude sur des systèmes naturels. Les expériences sont menées en presse Paterson à l'ISTO (3 Kbars). Les produits de départ sont des mush de plagioclase issus de la cristallisation de liquides synthétiques haplotonalitique hydratés (Picard et al., 2013). Les analyses post-mortem sur les charpentes cristallines (topologie de la charpente cristalline, CPO, SPO, CSD, cataclase cristalline) sont réalisées en 2D au MEB, en 3D au EBSD. Les échantillons naturels sont constitués par des laves phonolitiques issues d'un neck et d'un dyke de la province volcanique du Velay oriental (Massif central français). Ces échantillons sont également préparés et analysés en 2D et 3D, en utilisant les mêmes techniques que les échantillons synthétiques.
Les résultats des expériences de torsion menées avec la presse Paterson montrent des structures de déformation localisantes qui évoluent en fonction de l'intensité des chaînes de forces ; cette intensité dépendant elle-même fortement de l'anisotropie des cristaux. La ségrégation des liquides résiduels apparait pour des déformations finies importantes et particulièrement dans des mush de cristaux peu anisotropes. Des structures de déformation localisante similaires, et dans lesquelles les liquides tardifs sont ségrégés, ont été également trouvées dans les échantillons naturels phonolitiques. Ces résultats montrent que la fenêtre d'extraction des liquides résiduels dans les mush soumis à une déformation cisaillante s'étend jusqu'à des teneurs en cristaux très élevées (>90%).

Mots clés : ségrégation, liquides tardifs, mush, expérimentation, haute pression, plagioclase

Segregation of late magmatic melt in mushes: experimental approach at high pressure

Planetary differentiation and the societal impact of volcanic activity are all linked to the transfer of magmas into the crust, which remains relatively unconstrained. In recent years, a paradigm shift has emerged: instead of being essentially liquid, magma bodies could be made up mainly of mush: a mixture rich in crystals (>>50%) forming a weak solid framework imprisoning pockets of liquid that are more or less connected (Bachmann & Bergantz, 2004, 2008). This model has recently been generalised to the entire continental crust (Trans-Crustal Magmatic System; Cashman et al., 2017).
Geological evidence suggests that ubiquitous differentiation by extraction of silicate liquids from mush appears to be controlled by the physics of chains of forces in the crystal framework. The aim of this thesis is to constrain the mechanical behaviour (rheology, structuring) of crystal-rich magmas using an experimental approach to deformation at HP-HT. The chains of forces and their influence on the rheology of mush and on the initiation of deformation localisation have been characterised. Particular emphasis is placed on the effect of this deformation localisation on the segregation capacities of liquids and late fluids.
The innovative strategy of this thesis is to use an experimental approach coupled with a study of natural systems. The experiments are carried out in a Paterson press at ISTO (3 Kbars). The starting products are plagioclase mush resulting from the crystallisation of hydrated haplotonitic synthetic liquids (Picard et al., 2013). Post-mortem analyses of the crystal frameworks (crystal framework topology, CPO, SPO, CSD, crystal breakage) are carried out in 2D using SEM, in 3D using EBSD. The natural samples consisted of phonolitic lavas from a neck and a dyke from the Eastern Velay volcanic province (French Massif Central). These samples were also prepared and analysed in 2D and 3D, using the same techniques as the synthetic samples.

The results of the torsion experiments carried out with the Paterson press show localised deformation structures that evolve as a function of the intensity of the chains of forces; this intensity itself being highly dependent on the anisotropy of the crystals. The segregation of residual liquids appears for large finite deformations and particularly in mush composed of crystals with low anisotropy. Similar localised deformation structures, in which late liquids are segregated, were also found in natural phonolite samples. These results show that the extraction window for residual liquids in mush subjected to shear deformation extends to very high crystal contents (>90%).

Keywords : segregation, magmatic melt, mushes, experimental, high pressure, plagioclase

Institut des Sciences de la Terre d'Orléans

1a, rue de la Férollerie, 45071 Orléans Cedex 2, FRANCE